

Department of Civil and Environmental Engineering

Imperial College London

# High-Fidelity Nonlinear Analysis of Composite Structural Systems

Alexandros N. Nordas, M.Eng., M.Sc., D.I.C.

A thesis submitted in fulfilment of the requirements for the degree of Doctor of Philosophy  
(Ph.D.) of Imperial College London and the Diploma of Imperial College London (D.I.C.)

March 2019



*To my parents,  
for their love and support.*



*'What a lot of things there are a man can do without.'*

Socrates (c. 470-399 B.C.)  
Classical Greek philosopher

*'Yes, we now have to divide up our time like that,  
between politics and our equations.  
But to me our equations are far more important,  
for politics are only a matter of present concern.  
A mathematical equation stands forever.'*

Albert Einstein (1879-1955)  
Physics Nobel Prize winner and developer of the theory of relativity

*'To improve is to change; to be perfect is to change often.'*

Sir Winston Churchill (1874-1965)  
UK prime minister and Literature Nobel Prize winner

*'Stay hungry. Stay foolish.'*

Steve Jobs (1955-2011)  
CEO and Co-founder of Apple Inc.



## **Declaration of Originality**

I hereby confirm that this thesis is my own work. Whenever published or unpublished work of others is used in any way, appropriate references are made.

## **Copyright Declaration**

The copyright of this thesis rests with the author. Unless otherwise indicated, its contents are licensed under a Creative Commons Attribution-Non Commercial 4.0 International Licence (CC BY-NC).

Under this licence, you may copy and redistribute the material in any medium or format. You may also create and distribute modified versions of the work. This is on the condition that: you credit the author and do not use it, or any derivative works, for a commercial purpose.

When reusing or sharing this work, ensure you make the licence terms clear to others by naming the licence and linking to the licence text. Where a work has been adapted, you should indicate that the work has been changed and describe those changes.

Please seek permission from the copyright holder for uses of this work that are not included in this licence or permitted under UK Copyright Law.



## **Abstract**

In large-scale metal composite systems, comprising independent plated components coupled along weld lines, the response and encountered failure modes are governed by complex interactions of local instabilities with the spread of plasticity. The system scale, as well as the requirement of achieving mesh conformity throughout the domain, pose severe limitations on the modelling front and increase the associated computational demand substantially, thereby rendering extensive nonlinear analyses prohibitive. This work is motivated by the necessity for a versatile modelling strategy, enabling the accurate nonlinear response evaluation and assessment of large-scale composite systems under extreme static and dynamic loading.

A high-fidelity modelling strategy is proposed, which enables the accurate response evaluation of composite systems in the range of large displacements, taking due account of geometric and material nonlinearity. The strategy utilises co-rotational Reissner-Mindlin shell elements, with an embedded hierarchic optimisation approach that addresses inaccuracies arising from locking phenomena. The proposed modelling approach is further enhanced with a dual super-element domain partitioning methodology, facilitating scalable parallel processing in High Performance Computing systems with distributed memory, which enables a substantial reduction in the computing wall-clock time to be achieved and potential memory bottlenecks to be overcome.

A systematic methodology for surface coupling along a line is developed, based on a novel 1-D coupling element formulation, which facilitates discrete constraint enforcement between surfaces of arbitrary relative spatial orientation discretised with non-conforming finite element meshes. The approach is applicable to any type of 2-D and 3-D elements and provides a systematic framework for geometric modelling of weld lines, coupling of independently discretised regions within a system, as well as for domain partitioning problems involving computationally heterogeneous partitions. Efficient translational and rotational coupling element formulations are further established for surfaces discretised with quadratic Reissner-Mindlin shell elements, and their performance is extensively assessed through patch tests, sensitivity analyses and verification studies.

Several application studies involving extensive nonlinear analyses of geometrically complex, large-scale, composite structural systems are presented, to illustrate the versatility and computational efficiency of the unified modelling framework, encompassing partitioned high-fidelity finite element modelling and the developed coupling capability.

## Acknowledgements

Firstly, I would like to extend my deepest and sincere gratitude to my supervisors, Professor Bassam A. Izzuddin and Dr Lorenzo Macorini, for their support and encouragement throughout the four dense years of my PhD degree. Beyond providing valuable guidance and constructive feedback in the drafting of this thesis, Professor Izzuddin has been an insightful mentor and a source of inspiration, who always helped me steer my potential in the right direction and unfailingly supported me in professional matters and beyond. I am also very grateful to Dr Macorini for his consistent encouragement, support and valuable suggestions.

Secondly, I wish to thank AMEC Foster Wheeler, POSCO and Worley Parsons for funding this research for 3.5 years. The contribution of the High Performance Computing system of Imperial College London in this work is also gratefully acknowledged.

The density and value of experiences one gathers during this process are virtually unquantifiable. The only viable way of expressing my appreciation for these in one paragraph is by thanking the people I shared this long journey with. First and foremost, I wish to express my gratitude to (Dr) Luis Santos, whom I shared every step of the way and the best moments of my PhD with. I would also like to sincerely thank Dr Alejandro Barrero, Dr Jean Paul Vella, Dr Ramandeep Singh, (Dr) Stanyslav Grosman, Dr Acile Sybella, Panagiotis and Nick, for sharing with me some of the most fulfilling experiences in my life so far. Moreover, I am grateful to Theodore Litsos, as well as my extended family, Tonia Psychari, Yiannis Moraloglou, Panagiotis Papanikolaou, Sotiris Aktipis, Romanos Mavridis, Nikos Lantzounis, George Papagiannidis and Vasilis Takas, for their unfailing support and unconditional friendship. Thanks is due also to Irene Pantazis, Kleio Manolopoulou, Yiannis Manalis, Lila Deli and Michael Vasileiadis, for their care and for increasing my life density. I would also like to extend my gratitude to Fionnuala Donovan for her immeasurable support, as well as to my colleagues in the Computational Structural Mechanics group for coping with me and shaping a friendly and productive working environment in the legendary 317A, which, although hard to admit, I will miss.

Lastly, I wish to sincerely thank my partner for her loving care and emotional support throughout this process, as well as my parents for never stopping believing in me and for teaching me to always strive to improve myself and make an impact by improving the lives of others. To you, I owe everything.

# Table of Contents

<b>Abstract</b>	<b>iii</b>
<b>Acknowledgements</b>	<b>iv</b>
<b>Table of Contents</b>	<b>v</b>
<b>List of Figures</b>	<b>xiii</b>
<b>List of Tables</b>	<b>xxviii</b>
<b>Nomenclature</b>	<b>xxix</b>
<b>Chapter 1: Introduction</b>	<b>1</b>
1.1 Preamble	1
1.2 Scope and objectives	6
1.3 Thesis outline	8
<b>Chapter 2: Literature Review</b>	<b>11</b>
2.1 Introduction	11
2.2 Metal honeycomb core sandwich composites	12
2.2.1 The sandwich concept	12
2.2.2 Materials	13
2.2.3 Metal sandwich composite core configurations	14
2.2.4 Modelling of all-steel honeycomb core sandwich composites	18
2.2.5 HF nonlinear analysis using partitioned modelling	25

2.3	Coupling methods in computational mechanics	26
2.3.1	Mathematical treatment of contact and coupling constraints	29
2.3.1.1	Lagrangian Multiplier formulation	30
2.3.1.2	Penalty formulation	31
2.3.1.3	Augmented LM formulation	33
2.3.1.4	Perturbed LM formulation	34
2.3.1.5	Nitsche formulation	34
2.3.1.6	Comparative evaluation of optimisation techniques for contact and coupling constraint enforcement	36
2.3.2	Contact/coupling interface discretisation	37
2.3.2.1	Node-to-node methods	38
2.3.2.2	Node-to-segment methods	39
2.3.2.3	Node-to-surface methods	43
2.3.2.4	Interface discretisation into contact/coupling segments: mortar methods	44
2.3.2.5	Comparative evaluation of interface discretisation methods	52
2.4	Concluding remarks	55
<b>Chapter 3: High Fidelity Nonlinear Analysis of Composite and Sandwich Structures</b>		<b>57</b>
3.1	Introduction	57
3.2	Local formulation of co-rotational Reissner-Mindlin shell elements	59
3.3	Assumed strain formulation via hierarchic optimisation	60

3.4	Local co-rotational framework	63
3.4.1	Bisector and zero-macrospin co-rotational frameworks	63
3.4.2	Co-rotational transformations	67
3.5	High-fidelity modelling of large-scale metal sandwich composites	68
3.6	Partitioned modelling for high performance computing	71
3.7	Partitioned modelling of large-scale metal sandwich composites	72
3.8	Concluding remarks	75
<b>Chapter 4: Surface Coupling along a 1-D Interface with Non-Conforming Meshes</b>		<b>77</b>
4.1	Introduction	77
4.2	Treatment of coupling constraints using Lagrangian Multipliers	79
4.3	Problem description and basic notation	85
4.4	Coupling element kinematic and additional DOFs	91
4.4.1	Shell element geometry and kinematics	92
4.4.2	Coupling interface segment geometry and LM field	94
4.5	Systematic methodology for progressive segmentation of coupling interface and active element identification	95
4.5.1	Discrete geometric description of coupled surfaces and coupling interface	96
4.5.2	Progressive segmentation of coupling interface and active shell FE identification	98
4.5.2.1	Algorithmic Process 1 (AP1) - Projection algorithm	103

4.5.2.2	Algorithmic Process 2 (AP2) - Conditional projection algorithm	109
4.5.2.3	Algorithmic Process 3 (AP3) – Adjacent active element identification	113
4.5.2.4	Algorithmic Process 4 (AP4) – Active element exit point identification	118
4.5.3	Coupling element identification	122
4.6	Coupling element formulation	124
4.6.1	Coupling interface contribution to total potential energy	125
4.6.2	Coupling element formulation notation	126
4.6.3	Coupling element contribution to total potential energy	127
4.6.4	Coupling element force vector	128
4.6.5	Coupling element tangent stiffness matrix	130
4.7	Numerical integration scheme	131
4.7.1	Gaussian quadrature integration scheme	131
4.7.2	Coordinate mapping	132
4.7.3	Gaussian integration at the coupling element level	136
4.7.3.1	Segment-specific integration scheme	137
4.7.3.2	Element-specific integration scheme	139
4.8	Concluding remarks	142
	<b>Chapter 5: 1-D Translational and Rotational Coupling Element</b>	<b>143</b>
5.1	Introduction	143

5.2	1-D translational coupling element formulation	144
5.2.1	Element contribution to total potential energy and internal force vector	145
5.2.2	Element tangent stiffness matrix	148
5.2.3	Basic comparative evaluation of coupling element	150
5.3	1-D rotational coupling element formulation	151
5.3.1	Element contribution to total potential energy and internal force vector	154
5.3.2	Element tangent stiffness matrix	161
5.4	Superposition of translational and rotational coupling formulations	163
5.5	Patch tests	164
5.5.1	Preliminaries	164
5.5.2	Coupling element patch tests	165
5.5.2.1	Coupling element patch configuration	166
5.5.2.2	Coupling element patch base-case and variants	167
5.5.3	Rigid body mode patch tests	170
5.5.4	Constant force/moment patch tests	172
5.5.5	Coupling element performance sensitivity analysis	177
5.5.5.1	Influence of master-slave surface classification	178
5.5.5.2	Influence of adopted integration scheme	181
5.5.5.3	Influence of adopted penalty parameter values	187
5.5.5.4	Influence of shell element geometric irregularities	189

5.6	Concluding remarks	193
<b>Chapter 6: 1-D Coupling Element Verification Studies</b>		<b>194</b>
6.1	Introduction	194
6.2	Rectangular plate subjected to uniform stress states	195
6.2.1	Uniform membrane force field	197
6.2.2	Uniform planar shear force field	200
6.2.3	Uniform transverse bending moment field	203
6.2.4	Uniform transverse shear force field	208
6.2.5	Uniform twisting moment field	214
6.3	L-frame subjected to end forces	219
6.3.1	Planar end loading in X-direction	221
6.3.2	Planar end loading in Y-direction	224
6.3.3	Out-of-plane end loading in Z-direction	228
6.4	Annular plate subjected to out-of-plane loading	231
6.5	Hinged cylindrical shell subjected to point load	235
6.6	Pinched hemispherical shell with cut-off	243
6.7	Imperfect I-beam subjected to transverse loading	246
6.8	Concluding remarks	252
<b>Chapter 7: Application studies on High-Fidelity Modelling of Composite Structural Systems</b>		<b>253</b>
7.1	Introduction	253



7.2	Application study 1: High-fidelity nonlinear analysis of large-scale all-metal sandwich composites	255
7.2.1	Problem Description	256
7.2.2	Response of large-scale all-metal sandwich composites subject to UDL	259
7.2.3	Response of large-scale all-metal sandwich composites subject to PL	264
7.2.4	Imperfection sensitivity analysis	268
7.2.5	Discussion	269
7.3	Application study 2: Computational benefits of dual super-element domain partitioning	271
7.3.1	Problem description	271
7.3.2	Comparative evaluation of domain partitioning configurations	271
7.3.3	Practical guidance for optimal partitioning	274
7.4	Application study 3: Computational and modelling benefits of 1-D translational and rotational coupling element	278
7.4.1	Problem description	278
7.4.2	Comparison of adaptive and monolithic HF modelling approaches	281
7.4.3	Computational benefits of adaptive HF modelling	283
7.5	Application study 4: Validation of high-fidelity nonlinear analysis - 4-point bending of all-steel sandwich composites	287
7.5.1	Sandwich composite specimen manufacturing and specifications	287
7.5.2	Coupon tests and nonlinear material constitutive model calibration	291
7.5.3	Results	293

7.6	Application study 5: Passive explosion-protective barrier on offshore platform topside module	298
7.6.1	Accidental explosion loading and passive explosion-protective barriers on offshore platform topside modules	298
7.6.2	Blast wall HF nonlinear FE modelling	300
7.6.3	Results	304
7.7	Concluding remarks	317
<b>Chapter 8: Conclusions</b>		<b>318</b>
8.1	Summary	318
8.1.1	HF partitioned modelling of composite and sandwich structures	319
8.1.2	Surface coupling along a 1-D interface with non-conforming meshes	320
8.1.3	1-D translational and rotational coupling element	322
8.1.4	1-D coupling element verification studies	324
8.1.5	Application studies on high-fidelity modelling of composite structural systems	325
8.2	Recommendations for future work	327
<b>Bibliography</b>		<b>331</b>

## List of Figures

Figure 1.1:	Typical jacket-based offshore platform topside (ESDEP [The European Steel Design Education Program], 2009)	2
Figure 1.2:	Typical design details for stacked (a) and flushed (b) composite deck panels (ESDEP [The European Steel Design Education Program], 2009) and conventional offshore topside deck system configuration (c)	3
Figure 1.3:	Envisioned offshore topside deck configuration comprising two-way spanning sandwich composites	5
Figure 2.1:	(a) One-way spanning sandwich composite core configurations, (b) conventional and I-core sandwich composites for ship decks (Taczała & Banasiak, 2004), (c) all-steel laser-welded unidirectional web (I-core) sandwich panel - courtesy of Meyer Werft (TWI - The Welding Institute, 2019b), (d) all-steel laser-welded corrugated (V-core) sandwich panel (Nilsson, 2017)	17
Figure 2.2:	All-metal sandwich core topologies (Wadley, 2003; 2005)	18
Figure 2.3:	Experimental investigation of small-scale, metallic, honeycomb core sandwich composite ultimate capacity to static (a, d, e) and impact loading (b, c): (a) hexagonal-aluminium faceplates and core (Crupi <i>et al.</i> , 2012), (b) hexagonal-steel faceplates and aluminium core (Nurick <i>et al.</i> , 2009), (c) rectangular-stainless steel alloy faceplates and core (Dharmasena <i>et al.</i> , 2008), (d)-(e) hexagonal-aluminium faceplates and core (Kee Paik <i>et al.</i> , 1999)	20
Figure 2.4:	Local buckling assessment of metal honeycomb core structures via FE modelling of individual cells and cell groups (a-c) and experimental testing (d): (a) (Liang & Chen, 2006), (b) (López Jiménez & Triantafyllidis, 2013), (c) (Zok <i>et al.</i> , 2005), (d) (Cote <i>et al.</i> , 2004)	22

Figure 2.5:	Simplified modelling of sandwich composites using three-layer shell finite elements with equivalent intermediate layer homogenisation (Liang & Izzuddin, 2016)	25
Figure 2.6:	Node-to-segment (NTS) interface discretisation approach (Zavarise & De Lorenzis, 2009b)	40
Figure 2.7:	(a) Nodal penetration due to local nodal constrain enforcement, (b) slave node projection inexistence and multiplicity (Zavarise & De Lorenzis, 2009b)	41
Figure 2.8:	(a) Standard contact patch test original configuration (Taylor & Papadopoulos, 1991), (b) alternative contact patch test configuration (Fischer & Wriggers, 2005)	42
Figure 2.9:	(a) Segment discretisation of 2-D contact/coupling interface (Simo et al., 1985), (b) non-overlapping of discrete geometric surface descriptions for non-conforming meshes, (c) smooth intermediate mortar surface (Puso, 2004)	46
Figure 2.10:	(a) Segment discretisation of 2-D mortar and non-mortar surface, (b) algorithmic treatment of Gaussian quadrature via projection (Fischer & Wriggers, 2005)	48
Figure 2.11:	LM shape function definition along 2-D interface segments: (a) Standard piece-wise linear, (b) dual piece-wise linear (Puso, 2004)	50
Figure 3.1:	Bisector local co-rotational system and global nodal displacement parameters for quadrilateral shell finite elements (Izzuddin & Liang, 2016)	64
Figure 3.2:	Zero-macrospin local co-rotational system and global nodal displacement parameters for triangular shell finite elements (Izzuddin & Liang, 2016)	66
Figure 3.3:	(a) High-fidelity finite element discretisation of sandwich panels with rectangular and hexagonal honeycomb core topologies, (b)	

	discretisation strategy for rectangular and hexagonal honeycomb cells, (c) sympathetic sinusoidal imperfection modelling idealisation for rectangular honeycomb core sandwich panels	70
Figure 3.4:	Domain decomposition of rectangular honeycomb core sandwich panels using dual super-element child partitions	74
Figure 3.5:	Drilling rotational constraint elements along smooth part of partition boundary	75
Figure 4.1:	Simplified mechanical model of elastic springs 1-D coupling	80
Figure 4.2:	1-D coupling of surfaces discretised with non-conforming shell finite element meshes and identification of active shell element subset on each surface	88
Figure 4.3:	(a) Coupling interface segmentation and active shell element couple identification procedure, (b) 1-D coupling interface with piecewise linear (dashed line) and piecewise quadratic (continuous line) distribution of the Lagrangian Multiplier field	89
Figure 4.4:	1-D coupling element comprising two shell finite elements and a coupling interface segment	90
Figure 4.5:	Algorithmic Process 1 (AP1) – projection algorithm	108
Figure 4.6:	Algorithmic Process 2 (AP2) – conditional projection algorithm ( $\xi=1$ )	113
Figure 4.7:	Algorithmic Process 3 (AP3) – adjacent active element identification	117
Figure 4.8:	Algorithmic Process 4 (AP4) – active element exit point identification	121

Figure 4.9:	Coordinate mapping between the natural and Cartesian coordinate systems of the shell element domains and the 1-D coupling interface segments	135
Figure 4.10:	Segment-specific integration scheme and mapping of GPs on the slave and master shell element natural coordinate systems (Gaussian quadrature order 5)	140
Figure 4.11:	Element-specific integration scheme and mapping of GPs on the slave and master shell element natural coordinate systems (Gaussian quadrature order 5)	141
Figure 5.1:	Rotational coupling based on the angle between the surface tangent vectors transverse to the coupling interface	154
Figure 5.2:	Vector mapping processes for the establishment of coupled shell element global tangent vector fields $\mathbf{b}_0^{(i)}$ and $\mathbf{b}^{(i)}$ in the initial undeformed and the current deformed configurations	158
Figure 5.3:	(a) Coupling element patch geometric configuration, material properties and coupling parameters, (b) coupling interface and integration segments	169
Figure 5.4:	Rigid body mode coupling element patch tests: (a) translation in X, (b) translation in Y, (c) translation in Z, (d) rotation about X, (e) rotation about Y, (f) rotation about Z	171
Figure 5.5:	Lagrangian Multiplier field error distribution with variable Gaussian quadrature order for base-case patch variant R1E2	174
Figure 5.6:	Lagrangian Multiplier field error distribution with variable Gaussian quadrature order for base-case patch variant R1E3	174
Figure 5.7:	Maximum Lagrangian Multiplier field error variation with specified projection algorithm tolerance for base-case patch variants R1E2 and R1E3	176

Figure 5.8:	Constant force/moment coupling element patch tests: (a) planar shear force field, (b) planar membrane force field, (c) out-of-plane bending moment field, (d) out-of-plane shear force and moment fields	177
Figure 5.9:	Lagrangian Multiplier field error distribution with variable Gaussian quadrature order for patch variant R2E2	179
Figure 5.10:	Lagrangian Multiplier field error distribution with variable Gaussian quadrature order for patch variant R2E3	180
Figure 5.11:	Lagrangian Multiplier field error distribution comparison for patch variants R1E2-R2E2	180
Figure 5.12:	Lagrangian Multiplier field error distribution comparison for patch variants R1E3-R2E3	181
Figure 5.13:	Lagrangian Multiplier field error distribution with variable Gaussian quadrature order for patch variant R1S2	182
Figure 5.14:	Lagrangian Multiplier field error distribution with variable Gaussian quadrature order for patch variant R1S3	183
Figure 5.15:	Lagrangian Multiplier field error distribution with variable Gaussian quadrature order for patch variant R2S2	184
Figure 5.16:	Lagrangian Multiplier field error distribution with variable Gaussian quadrature order for patch variant R2S3	185
Figure 5.17:	Lagrangian Multiplier field error distribution comparison for patch variants R1E2-R1S2	185
Figure 5.18:	Lagrangian Multiplier field error distribution comparison for patch variants R1E3-R1S3	186
Figure 5.19:	Convergence rate with increasing Gaussian quadrature order for patch variants R1E2/R2E2/R2S2 - R1S2	186

Figure 5.20:	Convergence rate with increasing Gaussian quadrature order for patch variants R1E3/R2E3/R2S3 - R1S3	187
Figure 5.21:	Maximum Lagrangian Multiplier field error variation with normalised translational and rotational coupling penalty parameters	188
Figure 5.22:	Convergence norm variation with normalised translational and rotational coupling penalty parameters	189
Figure 5.23:	Coupling element patch geometric configuration with irregular element geometry	190
Figure 5.24:	Convergence rate with increasing order of vertical mesh refinement for patch variants I1E2 and I1E3	191
Figure 5.25:	Coupling element patch geometric configuration for irregular element geometry and different vertical mesh refinement order: (a) 2, (b) 3, (c) 4	192
Figure 6.1:	Geometric configuration, material properties and FE meshes for plate models CM-1 and BM-1	196
Figure 6.2:	Geometric configuration, applied loading and boundary conditions for plate models CM-1 and BM-1	197
Figure 6.3:	Deformed configuration at maximum displacement for plate models CM-1 (a) and BM-1 (b)	198
Figure 6.4:	Contour plots of local shell FE membrane force $N_x$ at first yield for plate models CM-1 (a) and BM-1 (b)	199
Figure 6.5:	Nonlinear equilibrium path of translational DOF along the X-axis at right plate edge for plate models CM-1 and BM-1	199
Figure 6.6:	Geometric configuration, applied loading and boundary conditions for plate models CM-1 and BM-1	200



Figure 6.7:	Deformed configuration at maximum displacement for plate models CM-1 (a) and BM-1 (b)	201
Figure 6.8:	Contour plot of local shell FE planar shear force $N_{xy}$ at maximum displacement for plate models CM-1 (a) and BM-1 (b)	202
Figure 6.9:	Nonlinear equilibrium path of translational DOF along the Y-axis at right plate edge for plate models CM-1 and BM-1	202
Figure 6.10:	Geometric configuration, applied loading and boundary conditions for plate models CM-1 and BM-1	204
Figure 6.11:	Deformed configuration at first yield and maximum rotation for plate models CM-1 (a) and BM-1 (b)	205
Figure 6.12:	Contour plots of local shell FE bending moment $M_x$ at first yield and maximum rotation for plate models CM-1 (a) and BM-1 (b)	206
Figure 6.13:	Contour plots of local shell FE transverse shear force $Q_{xz}$ at first yield for plate models CM-1 (a) and BM-1 (b)	207
Figure 6.14:	Nonlinear equilibrium path of rotational DOF about the Y-axis at right plate edge for plate models CM-1 and BM-1	207
Figure 6.15:	Geometric configuration, applied loading and boundary conditions for plate models CM-1 and BM-1	209
Figure 6.16:	Deformed configuration at first yield and maximum displacement for plate models CM-1 (a) and BM-1 (b)	210
Figure 6.17:	Contour plots of local shell FE shear force $Q_{xz}$ at first yield and maximum displacement for plate models CM-1 (a) and BM-1 (b)	211
Figure 6.18:	Contour plots of local shell FE bending moment $M_x$ at first yield and maximum displacement for plate models CM-1 (a) and BM-1 (b)	212

Figure 6.19:	Contour plots of local shell FE membrane force $N_x$ at first yield and maximum displacement for plate models CM-1 (a) and BM-1 (b)	213
Figure 6.20:	Nonlinear equilibrium path of translational DOF along the Z-axis at right plate edge for plate models CM-1 and BM-1	214
Figure 6.21:	Geometric configuration, applied loading and boundary conditions for plate models CM-1 and BM-1	215
Figure 6.22:	Deformed configuration at a small twisting rotation state for plate models CM 1 and BM-1	216
Figure 6.23:	Contour plots of local shell FE twisting moment $M_{xy}$ at a small twisting rotation state for plate models CM-1 and BM-1	217
Figure 6.24:	Nonlinear equilibrium path of rotational DOF $\theta_x$ about the Y-axis at bottom right plate corner for plate models CM-1 and BM-1	218
Figure 6.25:	Nonlinear equilibrium path of rotational DOF $\theta_y$ about the X- axis at bottom right plate corner for plate models CM-1 and BM-1	218
Figure 6.26:	Geometric configuration, applied loading, boundary conditions and material properties for L-frame models CM-2 and BM-2	220
Figure 6.27:	Deformed configuration at maximum displacement for L-frame models CM-2 and BM-2	222
Figure 6.28:	Contour plots of local shell FE membrane force $N_x$ at plastic hinge formation and maximum displacement for L-frame models CM-2 (a, b, c) and BM-2 (d, e, f)	223
Figure 6.29:	Nonlinear equilibrium path of translational DOF along the X-axis at node P for L-frame models CM-2 and BM-2	224
Figure 6.30:	Nonlinear equilibrium path of translational DOF along the X-axis at node P for L-frame models CM-2 and BM-2	225

Figure 6.31:	Deformed configuration at maximum displacement for L-frame models CM-2 and BM-2	226
Figure 6.32:	Contour plots of local shell FE membrane $N_x$ for L-frame models: (a) CM 2 - plastic hinge formation, (b) BM-2 - plastic hinge formation, (c) CM-2 - maximum displacement, (d) BM-2 - maximum displacement	227
Figure 6.33:	Deformed configuration at maximum displacement for L-frame models CM-2 and BM-2	229
Figure 6.34:	Contour plots of local shell FE generalised stress entities at maximum displacement for L-frame models: (a) CM-2 - membrane force $N_x$ , (b) CM-2 - twisting moment $M_{xy}$ , (c) CM-2 - bending moment $M_x$ , (d) BM-2 - membrane force $N_x$ , (e) BM 2 twisting moment $M_{xy}$ , (f) BM-2 - bending moment $M_x$	230
Figure 6.35:	Nonlinear equilibrium path of translational DOF along the X-axis at node P for L-frame models CM-2 and BM-2	231
Figure 6.36:	Geometric configuration, applied loading, boundary conditions and material properties for annular plate models CM-3 and BM-3	233
Figure 6.37:	Deformed configuration at maximum displacement for annular plate models CM-3 and BM-3	234
Figure 6.38:	Nonlinear equilibrium path of translational DOF along the Z-axis at node P for annular plate models CM-3 and BM-3	235
Figure 6.39:	Geometric configuration, applied loading, boundary conditions and material properties for cylindrical shell models CM-4 and BM-4	237
Figure 6.40:	Deformed configuration at maximum displacement for cylindrical shell models CM-4 (a) and BM-4 (b)	238

Figure 6.41:	Contour plots of local shell FE generalised stress entities for cylindrical shell models with thickness $t = 12.7$ at a small displacement state: (a) CM-4 - bending moment $M_y$ , (b) BM-4 - bending moment $M_y$ , (c) CM-4 - membrane force $N_y$ , (d) BM-4 - membrane force $N_y$	239
Figure 6.42:	Contour plots of local shell FE generalised stress entities for cylindrical shell models with thickness $t = 12.7$ at limit point state: (a) CM-4 - bending moment $M_y$ , (b) BM-4 - bending moment $M_y$ , (c) CM-4 - membrane force $N_y$ , (d) BM-4 - membrane force $N_y$	240
Figure 6.43:	Contour plots of local shell FE generalised stress entities for cylindrical shell models with thickness $t = 12.7$ at a maximum displacement: (a) CM-4 - bending moment $M_y$ , (b) BM-4 - bending moment $M_y$ , (c) CM-4 - membrane force $N_y$ , (d) BM-4 - membrane force $N_y$	241
Figure 6.44:	Nonlinear equilibrium path of translational DOF along the Z-axis at node P for cylindrical shell models CM-4 and BM-4 ( $t = 12.7$ )	242
Figure 6.45:	Nonlinear equilibrium path of translational DOF along the Z-axis at node P for cylindrical shell models CM-4 and BM-4 ( $t = 6.35$ )	242
Figure 6.46:	Geometric configuration, applied loading, boundary conditions and material properties for hemispherical shell models CM-5 and BM-5	244
Figure 6.47:	Deformed configuration at maximum displacement for hemispherical shell models CM-5 (a, b, c) and BM-5 (d, e, f)	245
Figure 6.48:	Nonlinear equilibrium path of translational DOFs along the X- and Y-axes at nodes P1 and P2 for hemispherical shell models CM-5 and BM-5	246
Figure 6.49:	Geometric configuration, applied loading, boundary conditions and material properties for I-beam models CM-6 and BM-6	247

Figure 6.50:	Nonlinear equilibrium path of translational DOFs along the Y- and Z-axes at node P for I-beam models CM-6 and BM-6	249
Figure 6.51:	Deformed configuration at maximum displacement for I-beam models CM-6b (a) and BM-6b (b)	250
Figure 6.52:	Contour plots of local shell FE twisting moment $M_{xy}$ at maximum displacement for I-beam models CM-6b (a) and BM-6b (b)	251
Figure 7.1:	(a) Geometric configuration, applied loading, boundary conditions and material properties for sandwich composite models R-C, R-HF, H-C and H-HF, (b) core topology of R-C and R-HF, (c) core topology of H-C and H-HF	258
Figure 7.2:	Deformed configuration at maximum displacement for sandwich composite models subject to UDL: (a) R-HF, (b) H-HF	260
Figure 7.3:	Nonlinear equilibrium path of translational DOF along the Z-axis at bottom faceplate centre for sandwich composite models R-C and R-HF subject to UDL	261
Figure 7.4:	Nonlinear equilibrium path of translational DOF along the Z-axis at bottom faceplate centre for sandwich composite models H-C and H-HF subject to UDL	261
Figure 7.5:	Contour plots of local shell FE bending moment $M_y$ at maximum displacement for sandwich composite model R-HF subject to UDL: (a) intercellular buckling at panel centre, (b) penetration buckling of top faceplate and shear buckling of core strips at yield line vicinity, (c) intercellular buckling at cross-pattern lines	262
Figure 7.6:	Contour plots of local shell FE bending moment $M_y$ at maximum displacement for sandwich composite model H-HF subject to UDL: (a) intercellular buckling at panel centre, (b) penetration buckling of top faceplate and shear buckling of core strips at yield line vicinity	263

Figure 7.7:	Deformed configuration at maximum displacement for sandwich composite models subject to PL: (a) R-HF, (b) H-HF	265
Figure 7.8:	Nonlinear equilibrium path of translational DOF along the Z-axis at bottom faceplate centre for sandwich composite models R-C and R-HF subject to PL	266
Figure 7.9:	Nonlinear equilibrium path of translational DOF along the Z-axis at bottom faceplate centre for sandwich composite models H-C and H-HF subject to PL	266
Figure 7.10:	Contour plots of local shell FE bending moment $M_y$ at maximum displacement for sandwich composite model R-HF subject to PL: (a) penetration buckling of top faceplate and compressive/shear buckling of core strips at patch vicinity, (b) penetration buckling of top faceplate and shear buckling of core strips at yield line vicinity, (c) direct compressive buckling of core strips underneath the patch	267
Figure 7.11:	Contour plots of local shell FE bending moment $M_y$ at maximum displacement for sandwich composite model H-HF subject to PL: (a) penetration buckling of top faceplate and compressive/shear buckling of core strips at patch vicinity, (b) direct compressive buckling of core strips underneath the patch	268
Figure 7.12:	Imperfection sensitivity of sandwich composite model R-HF subject to UDL	270
Figure 7.13:	Imperfection sensitivity of sandwich composite model R-HF subject to PL	270
Figure 7.14:	Computing wall-clock time speedup for different domain partitioning configurations of sandwich composite models R-C and R-HF	274

Figure 7.15:	Parent and child partition process nodal quantities for different domain partitioning configurations of sandwich composite models R-C and R-HF	275
Figure 7.16:	Nonlinear equilibrium path of translational DOF along the Z-axis at bottom faceplate centre for monolithic and partitioned sandwich composite models R-HF	277
Figure 7.17:	Deformed configuration at maximum displacement for selectively-discretised sandwich composite model R-HF-A: (a) top faceplate, (b) core, (c) bottom faceplate	280
Figure 7.18:	Deformed configuration at maximum displacement for sandwich composite models R-HF and R-HF-A	281
Figure 7.19:	Nonlinear equilibrium path of translational DOF along the global Z-axis at bottom faceplate centre for sandwich composite models R-C, R-HF and R-HF-A	282
Figure 7.20:	Computing wall-clock time speedup for different domain partitioning configurations of sandwich composite models R-C, R-HF and R-HF-A	284
Figure 7.21:	(a) Geometric configuration, detailing and LVDT locations (in red) for all-steel sandwich composite specimens, (b) dimensions and detailing of longitudinal strips, (c) dimensions and detailing of transverse strips, (d) strain gauge arrangement	289
Figure 7.22:	Laser welding machine employed for specimen fabrication (a-c) and laser welding section with porosity defect (d), lack of penetration (e) and no defects (f)	290
Figure 7.23:	Experimental setup of the 4-point bending tests for all-steel sandwich panels	291

Figure 7.24:	(a) Experimental stress-strain curve obtained from coupon tests for the steel grade employed for specimen fabrication, (b) coupon test specimens	292
Figure 7.25:	Deformed configuration at ultimate state prior to laser weld delamination (transverse displacement 10 mm): (a) HF FE model, (b) specimen S1, (c) specimen S2	294
Figure 7.26:	Deformed configuration of specimens S1 (a) and S2 (b) at failure following laser weld delamination (transverse displacement 22 mm)	295
Figure 7.27:	Validation of high-fidelity FE model nonlinear response against experimental results for 4-point bending specimens S1 and S2	296
Figure 7.28:	Deformed configuration (a) and contour plots of local shell element planar shear force $N_{xy}$ (b) for high-fidelity FE model	297
Figure 7.29:	Typical deflagration pressure time-history in offshore platform topside modules (British Standards Institution, 2014)	299
Figure 7.30:	Blast wall corrugated profile geometric specifications and centreline distances	301
Figure 7.31:	HF FE model configuration, global component dimensions and 1-D coupling interface definition (slave surface continuous - master surface dotted) for integrated blast wall and surrounding structural elements	303
Figure 7.32:	Maximum transverse displacement time-history for blast wall models IM-1 and CM-1	307
Figure 7.33:	Maximum transverse displacement time-history for blast wall models IM-2 and CM-2	307
Figure 7.34:	Strain energy time-history for blast wall models IM-1/2 and CM-1/2	308



Figure 7.35:	Deformed configuration at maximum displacement for blast wall model IM-1	309
Figure 7.36:	Deformed configuration at maximum displacement for blast wall model IM-2 (scale factor 2.0)	310
Figure 7.37:	Deformed configuration at maximum displacement for blast wall model CM-1	311
Figure 7.38:	Deformed configuration at maximum displacement for blast wall model CM-2 (scale factor 2.0)	312
Figure 7.39:	Contour plots of local shell FE entities at maximum displacement for blast wall model IM-1: (a) strain $\varepsilon_y$ , (b) von Mises stress	313
Figure 7.40:	Contour plots of local shell FE entities at maximum displacement for blast wall model IM-2: (a) strain $\varepsilon_y$ , (b) von Mises stress	314
Figure 7.41:	Contour plots of local shell FE entities at maximum displacement for blast wall model CM-1: (a) strain $\varepsilon_y$ , (b) von Mises stress	315
Figure 7.42:	Contour plots of local shell FE entities at maximum displacement for blast wall model CM-2: (a) strain $\varepsilon_y$ , (b) von Mises stress	316

## List of Tables

Table 2.1:	Relative stiffness and strength of equivalent weight sandwich and solid components (Petras, 1999)	13
Table 7.1:	Computing wall-clock time and achieved speedup for different domain partitioning configurations of sandwich composite models R-C and R-HF	273
Table 7.2:	Parent and child partition process nodal quantities and nodal ratio for different domain partitioning configurations of sandwich composite models R-C and R-HF	276
Table 7.3:	Computing wall-clock time and achieved speedup for different domain partitioning configurations of sandwich composite model R-HF-A	285
Table 7.4:	Characteristic material properties for coupon test specimens A-1, A-2, B-1 and B-2 of the employed steel grade	292

# Nomenclature

All symbols and adopted notation in this work are defined when they first appear. For convenience, the definitions of the most relevant operators and symbols are collected hereafter. Symbols are arranged on the basis of the chapters where they are first introduced, while symbols for Chapters 2, 4 and 5 are presented together to avoid repetition. It is noted that some symbols may denote more than one quantity; in such cases, the context should provide disambiguation.

## General rules

- A horizontal bar on top of a 3-D vector denotes its respective planar components
- Subscript ‘0’ is used for reference to the initial undeformed configuration
- Superscript (*i*) is used for reference to an independent deformable surface

## Operators

- |   |                                      |
|---|--------------------------------------|
| • | Dot product or matrix multiplication |
| ⊗ | Outer product                        |

## Abbreviations

1-D, 2-D, 3-D	One-dimensional, two-dimensional and three-dimensional, respectively
CP	Collocation point
CS	Coupling segment
CPU	Central Processing Unit

DOF	Degree of Freedom
FE	Finite Element
GP	Gauss Point
HF	High-fidelity
HPC	High Performance Computing
ID	Identifier
IS	Integration segment
LM	Lagrangian Multiplier

### **Symbols in Chapter 3**

#### **Roman symbols**

$(\mathbf{c}_x, \mathbf{c}_y, \mathbf{c}_z)$	Triad of local shell element coordinate axes unit orientation vectors in the current deformed configuration
$(\mathbf{c}_{x0}, \mathbf{c}_{y0}, \mathbf{c}_{z0})$	Triad of local shell element coordinate axes unit orientation vectors in the initial undeformed configuration
$\mathbf{d}$	Local shell element displacement field
$\mathbf{d}_i$	Local shell element displacement vector at node $i$
$\mathbf{n}_i$	Local shell element normal vector at node $i$
$\mathbf{r}$	Local shell element rotational field
$\mathbf{r}$	Local shell element rotation vector at node $i$

$\mathbf{T}_0, \mathbf{T}, \bar{\mathbf{T}}$	Shell element local co-rotational coordinate system orientation matrices in the initial undeformed and the current deformed configurations
$\mathbf{u}$	Global shell element displacement vector
$\mathbf{u}_i$	Global shell element displacement vector at node $i$

### Greek Symbols

$\boldsymbol{\alpha}_o$	Objective strain parameter vector
$\boldsymbol{\alpha}_h$	Hierarchic strain parameter vector
$\boldsymbol{\varepsilon}^m$	Local shell element conforming membrane strain vector
$\boldsymbol{\varepsilon}^b$	Local shell element conforming bending strain vector
$\boldsymbol{\varepsilon}^s$	Local shell element conforming shear strain vector
$\boldsymbol{\varepsilon}_{GP}$	Local shell element conforming strain vector evaluated at Gauss points
$\boldsymbol{\Psi}_h$	Hierarchic corrective strain mode vector
$\boldsymbol{\Psi}_o$	Objective strain mode vector
$\boldsymbol{\Psi}_o^m$	Membrane objective strain components
$\boldsymbol{\Psi}_o^b$	Bending objective strain components
$\boldsymbol{\Psi}_o^s$	Shear objective strain components

## Symbols in Chapters 2, 4 and 5

### Roman symbols

$\mathbf{a}_0^{(i)}, \bar{\mathbf{a}}_0^{(i)}$	Local tangent vector fields transverse to coupling interface for shell elements on surface $i$ in the initial undeformed configuration
$\mathbf{a}_\xi, \mathbf{a}_\eta$	Tangent vectors on shell element surface along natural coordinate axes $(\xi, \eta)$
$\mathbf{a}_{\xi\xi}, \mathbf{a}_{\xi\eta}, \mathbf{a}_{\eta\xi}, \mathbf{a}_{\eta\eta}$	Derivatives of tangent vectors $\mathbf{a}_\xi, \mathbf{a}_\eta$ with respect to $(\xi, \eta)$
$\mathbf{b}_0^{(i)}, \mathbf{b}^{(i)}$	Global tangent vector field transverse to coupling interface for shell elements on surface $i$ in the initial undeformed and the current deformed configurations
$\mathbf{C}$	Connectivity matrix for coupling elements along the coupling interface
$\mathbf{C}_j$	Connectivity matrix for coupling elements associated with coupling segment $j$
$\mathbf{C}_{jk}$	Coupling element encompassing shell elements $j$ and $k$ as slave and master, respectively
$\mathbf{D}^{(i)}$	Structural nodal coordinate matrix for finite element mesh on surface $i$
$\mathbf{E}^{(i)}$	Element connectivity matrix for finite element mesh on surface $i$
$\mathbf{e}^{(i)}$	Array of active shell elements on surface $i$
$\mathbf{f}_e$	Coupling element internal force vector
$\mathbf{f}_g, \mathbf{f}_{g,\varepsilon}$	Coupling element internal force vector components associated with kinematic DOFs - distinct LM and penalty term contributions
$\mathbf{f}_a, \mathbf{f}_{\alpha,\varepsilon}$	Coupling element internal force vector components associated with additional LM DOFs - distinct LM and penalty term contributions

$\mathbf{f}_g^{(i)}, \mathbf{f}_{g,\varepsilon}^{(i)}$	Coupling element internal force vector components associated with the kinematic DOFs of surface $i$ - distinct LM and penalty term contributions
$\mathbf{G}$	Projection algorithm vector function
$\mathbf{g}$	Translational kinematic constraint vector function
$g_R$	Rotational kinematic constraint scalar function
$\mathbf{J}_G$	Jacobian matrix of vector function $\mathbf{G}$
$\mathbf{J}_0^{(i)}, \mathbf{J}^{(i)}$	Jacobian matrix of global coordinate mapping for shell elements on surface $i$ in the initial undeformed and the current deformed configurations
$\mathbf{j}^{(i)}, \bar{\mathbf{j}}_0^{(i)}$	Jacobian matrix of local coordinate mapping for shell elements on surface $i$ in the initial undeformed and the current deformed configurations
$\mathbf{k}_e$	Coupling element tangent stiffness matrix
$\mathbf{k}_{gg}, \mathbf{k}_{gg,\varepsilon}$	Coupling element tangent stiffness matrix components associated with kinematic DOFs - distinct LM and penalty term contributions
$\mathbf{k}_{ga}, \mathbf{k}_{ag}, \mathbf{k}_{ga,\varepsilon}, \mathbf{k}_{ag,\varepsilon}$	Coupling element tangent stiffness matrix components associated with both kinematic and additional LM DOFs - distinct LM and penalty term contributions
$\mathbf{k}_{aa}, \mathbf{k}_{aa,\varepsilon}$	Coupling element tangent stiffness matrix components associated with additional LM DOFs - distinct LM and penalty term contributions
$\mathbf{k}_{gg}^{(ij)}, \mathbf{k}_{gg,\varepsilon}^{(ij)}$	Coupling element tangent stiffness matrix components associated with the kinematic DOFs of surfaces $i$ and $j$ - distinct LM and penalty term contributions
$\mathbf{k}_{ga}^{(i)}, \mathbf{k}_{ga,\varepsilon}^{(i)}$	Coupling element tangent stiffness matrix components associated with the kinematic DOFs of surface $i$ and the additional LM DOFs - distinct LM and penalty term contributions

$m_i$	Number of nodes on shell elements of surface $i$
$m_\lambda$	Number of collocation points on coupling interface segments
$\mathbf{N}^{(i)}, \bar{\mathbf{N}}^{(i)}$	Matrix of 2-D Lagrangian polynomial shape functions for 3-D and 2-D vector interpolation for shell elements on surface $i$
$\mathbf{N}_{,\xi}^{(i)}, \mathbf{N}_{,\eta}^{(i)}, \bar{\mathbf{N}}_{,\xi}^{(i)}, \bar{\mathbf{N}}_{,\eta}^{(i)}$	1 <sup>st</sup> order derivative of shape function matrices $\mathbf{N}^{(i)}$ and $\bar{\mathbf{N}}^{(i)}$ with respect to $(\xi, \eta)$ for shell elements on surface $i$
$\mathbf{n}_0, \mathbf{n}$	Local shell element normal vector field in the initial undeformed and the current deformed configurations
$\mathbf{n}^+$	Local shell element normal vector field in the direction corresponding to counter-clockwise circulation of its boundary
$N_k^{(i)}$	Shell element shape function corresponding to node $k$ for elements on surface $i$
$n_{Di}$	Number of nodes on finite element mesh on surface $i$
$n_{Ei}$	Number of elements on finite element mesh on surface $i$
$n_{ei}$	Number of active coupled finite elements on surface $i$
$n_C$	Number of coupling elements along the coupling interface
$\mathbf{P}$	Global coordinate matrix of coupling interface linear sector control points
$\mathbf{R}^{(i)}$	Global coordinate matrix of the coupling interface intersection points with the active shell elements on surface $i$ – point images on coupling interface
$\mathbf{S}^{(i)}$	Global coordinate matrix of the coupling interface intersection points with the active shell elements on surface $i$ - point images on surface $i$
$\mathbf{t}^{(i)}$	Coupling interface linear sector orientation vector expressed in the local coordinate system of shell elements on surface $i$



$\mathbf{t}$	Matrix of global orientation vectors of coupling interface linear sectors
$\mathbf{t}_k$	Global orientation vector of linear sector $k$
$\mathbf{t}_{(e)}, \bar{\mathbf{t}}_{(e)}$	Coupling interface linear sector orientation vector expressed in the local coordinate system of active element $e$
$\mathbf{u}^{(i)}$	Global displacement field of points on surface $i$
$\mathbf{u}_k^{(i)}$	Global displacement vector of node $k$ for shell elements on surface $i$
$\mathbf{u}_e^{(i)}$	Global nodal displacement vector for shell elements on surface $i$
$(U^{(i)}, V^{(i)}, W^{(i)})$	Global displacement field components for points on surface $i$
$w_p$	Weighting factor of Gauss point $p$
$\mathbf{X}_0^{(i)}, \mathbf{X}^{(i)}$	Global coordinate vector for points on surface $i$ in the initial undeformed and the current deformed configurations
$\mathbf{X}_{k0}^{(i)}, \mathbf{X}_k^{(i)}$	Global coordinate vector of node $k$ for shell elements on surface $i$ in the initial undeformed and the current deformed configurations
$\mathbf{X}_{0e}^{(i)}, \mathbf{X}_e^{(i)}$	Global nodal coordinate vector for shell elements on surface $i$ in the initial undeformed and the current deformed configurations
$\mathbf{x}_0^{(i)}, \mathbf{x}^{(i)}, \bar{\mathbf{x}}_0^{(i)}, \bar{\mathbf{x}}^{(i)}$	Local coordinate vector for points on surface $i$ in the initial undeformed and the current deformed configurations
$\mathbf{x}_{k0}^{(i)}, \mathbf{x}_k^{(i)}, \bar{\mathbf{x}}_{k0}^{(i)}, \bar{\mathbf{x}}_k^{(i)}$	Local coordinate vector of node $k$ for shell elements on surface $i$ in the initial undeformed and the current deformed configurations
$\mathbf{x}_{0e}^{(i)}, \mathbf{x}_e^{(i)}, \bar{\mathbf{x}}_{0e}^{(i)}, \bar{\mathbf{x}}_e^{(i)}$	Local nodal coordinate vector for shell elements on surface $i$ in the initial undeformed and the current deformed configurations
$\tilde{\mathbf{X}}$	Global coordinate vector for points along the coupling interface in the current deformed configuration
$\tilde{\mathbf{X}}_k$	Global coordinate vector of coupling segment collocation point $k$ in the current deformed configuration

$\tilde{\mathbf{X}}_e$	Coupling segment collocation point global coordinate vector in the current deformed configuration
$\tilde{\mathbf{x}}_e$	Local coupling segment collocation point coordinate vector in the current deformed configuration
$\tilde{\mathbf{x}}$	Local coordinate vector for points along the coupling interface
$\tilde{\mathbf{x}}_k$	Local coordinate vector of coupling segment collocation point $k$
$(X^{(i)}, Y^{(i)}, Z^{(i)})$	Global Cartesian coordinates for points on surface $i$
$(x^{(i)}, y^{(i)}, z^{(i)})$	Local Cartesian coordinates for points on surface $i$

### Greek symbols

$\mathbf{a}_0^{(i)}$	Inverse Jacobian transformation of local tangent vector fields transverse to coupling interface for shell elements on surface $i$ in the initial undeformed configuration
$\Gamma_c$	1-D coupling interface
$\Gamma_c^{(i)}$	Projection of coupling interface on surface $i$
$\Gamma^{(i)}$	Domain of active coupled shell elements on surface $i$
$\Gamma_j^{(i)}$	Domain of active coupled shell element $j$ on surface $i$
$\Gamma_{cj}$	Coupling interface segment $j$
$\Gamma_{cj}^{(i)}$	Projection of coupling interface segment $j$ on surface $i$
$\gamma_1, \gamma_2$	Projection algorithm tolerances for Newton-Raphson iterative procedure and solution point coordinate admissibility, respectively
$\delta_{ij}$	Kronecker delta
$\varepsilon, \varepsilon_R$	Translational and rotational coupling penalty parameters

$\varepsilon^*, \varepsilon_R^*$	Normalised translational and rotational coupling penalty parameters
$\vartheta_0$	Relative orientation angle between surface slopes transverse to the coupling interface
$\lambda$	Lagrangian Multiplier vector field along coupling interface
$\lambda_k$	Lagrangian Multiplier vector at collocation point $k$
$\lambda_e, \lambda_{Re}$	Translational and rotational Lagrangian Multiplier field collocation point vectors
$(\lambda_X, \lambda_Y, \lambda_Z)$	Translational Lagrangian Multiplier field components
$\lambda_R$	Rotational Lagrangian Multiplier field component
$\xi^{(i)}, \eta^{(i)}$	Natural coordinate system abscissae for shell elements on surface $i$
$\tilde{\xi}$	Natural coordinate system abscissa for coupling interface
$\Pi_e$	Translational coupling element contribution to the system total potential energy
$\Pi, \Pi_\varepsilon$	Translational coupling element distinct LM field and penalty term contributions to the system total potential energy
$\Pi_{Re}$	Rotational coupling element contribution to the system total potential energy
$\Pi_R, \Pi_{Re}$	Rotational coupling element distinct LM field and penalty term contributions to the system total potential energy
$\Phi$	Matrix of 1-D Lagrangian polynomial shape functions for 3-D and 4-D vector interpolation along coupling segments
$\varphi$	Matrix of 1-D Lagrangian polynomial shape functions for 1-D vector interpolation along coupling segments
$\Phi_k$	Shape function of collocation point $k$
$\Omega^{(i)}$	Independent deformable coupled shell surfaces

## Symbols in Chapter 7

### **Roman Symbols**

$N_b^{(p)}$	Number of nodes along the partition boundary at the parent level for a partitioned model with $p$ child partitions
$NR_p$	Nodal ratio for a partitioned model with $p$ child partitions
$n^{(p)}$	Average number of child partition nodes for a partitioned model with $p$ child partitions
$n_b^{(p)}$	Average number of child partition boundary nodes for a partitioned model with $p$ child partitions
$n_i^{(p)}$	Average number of child partition interior domain nodes for a partitioned model with $p$ child partitions
$SF_p$	Speedup factor achieved by a partitioned model with $p$ child partitions

# Chapter 1

## Introduction

### 1.1 Preamble

Offshore platforms are large structural forms, designed to facilitate well drilling for the identification, extraction and processing of oil and natural gas deposits, alongside their temporary storage before transportation ashore and distribution to the global markets. A typical offshore platform configuration encompasses three principal compartments, namely the topside deck, the substructure and the foundation. The configuration of the last two is primarily dictated by the installation depth, and thereupon platforms can be fixed to the seabed with a jacket, compliance tower or tension leg sub-structure, semi-submerged, floating or installed on artificial floating islands. The most vital compartment is the topside deck, a large-scale integrated or modularised system where the essential equipment for extraction and processing of oil and gas deposits is installed. Typical topside modules include the well control, power generators, pumps/compressors for the product transportation ashore, helideck, flare boom and crane pedestals, while living quarters are further constructed to host the workforce in a great number of existing platforms (ESDEP [The European Steel Design Education Program], 2009). A typical piled steel jacket platform configuration is illustrated in Figure 1.1.

The conventional offshore topside deck configuration encompasses composite deck panels, consisting of a chequered or flat steel plate spanning over densely arranged stringers. Deck panels are classified as stacked or flushed, depending on their relative arrangement with respect to a grillage system of primary and secondary steel components, as illustrated in Figure 1.2 (a)-(b), respectively. The primary steel layout comprises either truss members or deep plate girders,

connected to the substructure compartment columns to form a portal frame configuration which facilitates vertical load transferring and provides lateral stability against wind, wave and earthquake loading. On the other hand, the secondary steel layout typically comprises regular hot-rolled steel beams, spanning between the primary components to form a supporting grillage system for the floor panels and overlying equipment (ESDEP [The European Steel Design Education Program], 2009). In critical deck locations where equipment is installed, the provision of a dense grid of secondary beams underneath the equipment supports is necessitated, to ensure adequate capacity and stiffness of the deck plate locally. Consequently, secondary deck beams are distributed over the deck in a non-uniform fashion, dictated by the equipment loading magnitude and variability, as illustrated in Figure 1.2 (c).

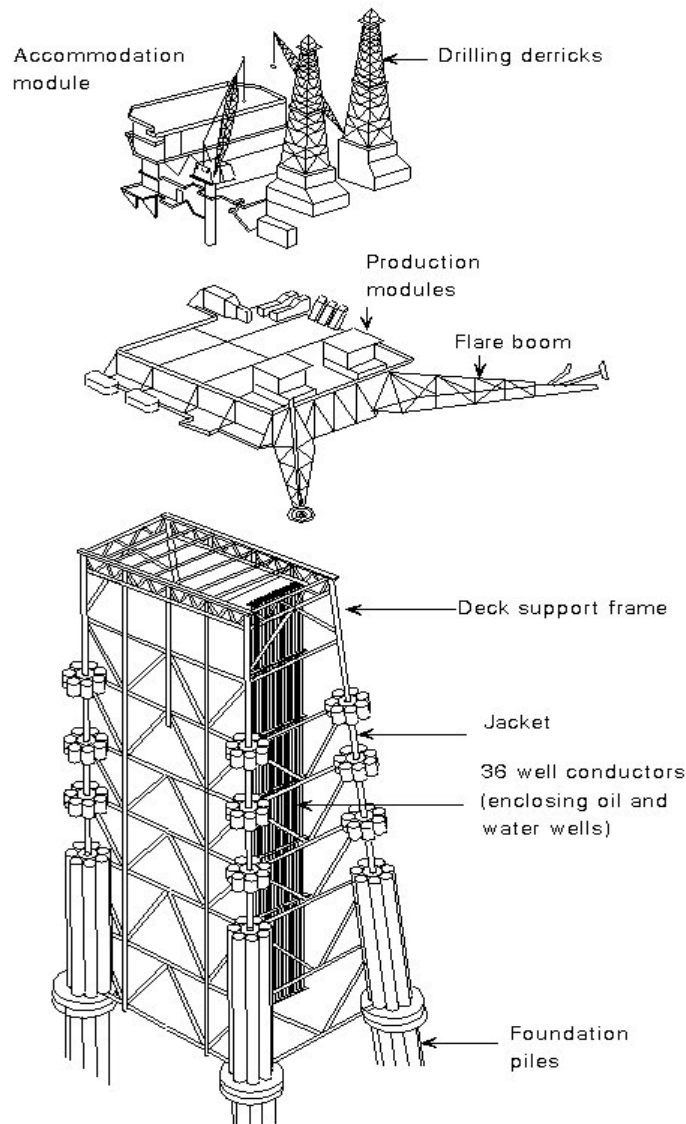


Figure 1.1: Typical jacket-based offshore platform topside (ESDEP [The European Steel Design Education Program], 2009)

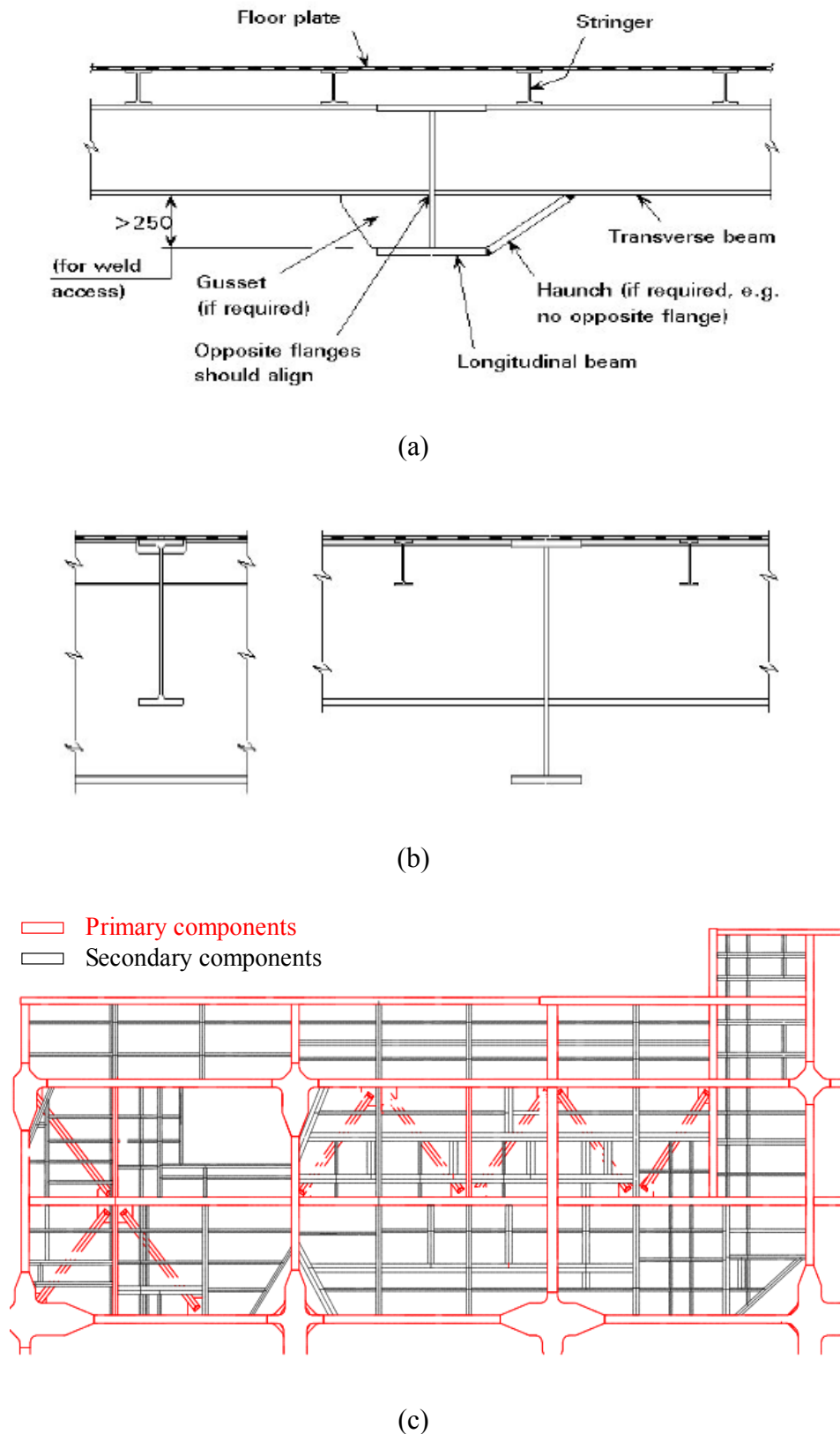


Figure 1.2: Typical design details for stacked (a) and flushed (b) composite deck panels (ESDEP [The European Steel Design Education Program], 2009) and conventional offshore topside deck system configuration (c)

The employment of the conventional deck configuration described above leads to several shortcomings: (i) the secondary steel contributes towards 50% of the global deck weight, thus rendering the conventional configuration cost-inefficient, inasmuch as the capital costs in the offshore oil and gas industry being dictated by structural weight; (ii) the localised stiffness and strength provision in critical equipment locations poses the requirement for multiple time-consuming and costly design modification processes, to accommodate equipment relocation during the platform design; (iii) the implementation of a large number of welded connections for the secondary steel layout is rendered cumbersome in offshore conditions, and hence the preassembly of the entire topside deck onshore and its subsequent transportation offshore is required, which is a resource-consuming and risky undertaking; and (iv) maintenance and life-cycle cost reduction requires the application of several tons of corrosion-protective paint-spray over the surface of environmentally exposed steel components, which, beyond being costly, contributes substantially towards the global structural weight.

Following the profit margin downturn in the offshore oil and gas industrial sector in 2014, significant research efforts have been initiated towards the establishment of a novel configuration for the topside deck. A joint industrial Research and Development (R&D) collaborative project between Imperial College London, POSCO and AMEC Foster Wheeler initiated in this direction in January 2015, entitled INFLOAT-INnovative FLoor systems for Offshore plAtform T<sub>opsides</sub>, with a specified duration of 4.5 years. The principal research objective of the project is the establishment of a systematic design methodology for offshore platform topside deck systems, underpinned by the employment of novel, all-steel, laser-welded, large-scale, two-way-spanning sandwich composites.

Sandwich composites comprise two thin and stiff faceplates connected to a structural core of discrete topological configuration via adhesion or welding. Owing to their discrete core topology, sandwich composites attain enhanced stiffness and strength characteristics in comparison to solid components of equivalent weight, as well as a fully efficient two-way spanning action with appropriate design. Furthermore, appropriate selection of the core topology allows for enhanced energy dissipation in cases of extreme accidental loading, such as blast, to be achieved, which is a governing design consideration in offshore topside decks. The identification and formal definition of geometric limitations, associated with the component manufacturing viability and the offshore application context, had been the focus of



several interactions between the INFLOAT project partners, where the provision of practical, technical and qualitative guidance from POSCO and AMEC Foster Wheeler was key.

Taking the above into consideration, the prospect of sandwich composite systematic incorporation in offshore topside decks is anticipated to be an innovation of significant merit: (i) the efficient two-way spanning action afforded by sandwich composites allows for a substantial reduction, or even elimination, of secondary components, thus leading to an estimated global deck weight reduction of the order of 30%; (ii) the stiffness and strength uniformity of sandwich composites enables equipment relocation to any desired extent to be accommodated with appropriate core design; (iii) the establishment of an efficient prescribed connection scheme amongst adjacent panels significantly limits the connection detailing workload and associated cost, thus further enabling their potential implementation offshore; and (iv) the restriction of environmentally exposed steel surfaces to the panel faceplates and the primary components leads to a considerable reduction in the corrosion protective paint weight and the associated maintenance cost. The envisioned configuration of an offshore topside deck encompassing large-scale sandwich composites is illustrated in Figure 1.3.

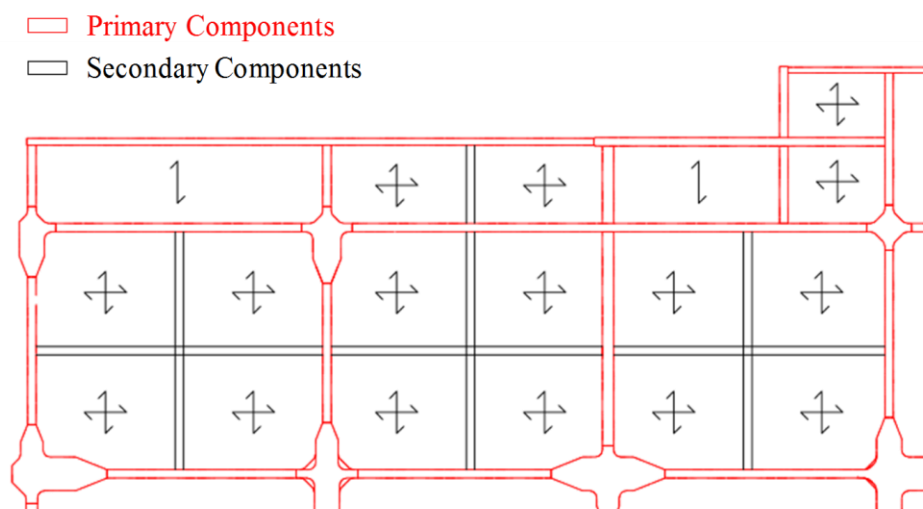


Figure 1.3: Envisioned offshore topside deck configuration comprising two-way spanning sandwich composites

Notwithstanding the superior performance attributes of sandwich composites in comparison with conventional deck panels, their incorporation in a systematic design methodology for topside decks, adopted by engineering practice, necessitates the establishment of a substantial level of confidence in their mechanical properties and response attributes. These have not been

documented in the existing literature hitherto, and hence a broad experimental investigation of their response and principal failure modes has been conducted in the context of the INFLOAT project. Beyond physical testing, however, the extensive response investigation of the novel composite response under a variety of complex loading conditions encountered in topside decks, as well as the robustness assessment of the envisioned novel deck systems at a global level, require the establishment of a high-fidelity (HF) Finite Element (FE) modelling strategy. Following its successful validation against the experimental results, a HF FE modelling strategy would provide a reliable, systematic and highly accurate computational tool for the individual component and deck system performance assessment, which, in turn, would enable the establishment of a systematic design methodology for engineering practice.

Nonetheless, in large-scale composite systems exhibiting substantial stress variations locally or comprising independent deformable plated components welded along a line, such as the sandwich composites core and faceplates or the faceplates and the primary steel components, the requirement of achieving mesh conformity poses severe limitations on the modelling front. Beyond compromising the modelling flexibility, the mesh conformity requirement unnecessarily increases the already substantial computational demand of large-scale systems, in respect of the wall-clock time and memory resources, potentially leading to memory bottlenecks in the case of extensive nonlinear analyses. The modelling of such systems would therefore greatly benefit from a selective discretisation approach, encompassing the employment of a dense mesh only in regions of substantial stress variation and the flexibility of coupling independently discretised substructures, as well as from the efficient use of modern parallel computing architectures. It is emphasised that the term non-conforming, which typically refers to types of FEs which do not fully observe the compatibility conditions, is employed here and throughout this thesis to refer to non-matching meshes, associated with lack of nodal alignment along the interface where they are adjoined.

## **1.2 Scope and objectives**

The response of large-scale metal composite structural systems, comprising independent deformable plated components coupled along weld lines, is characterised by the manifestation of various forms of local instabilities in several locations over the domain. The interaction of local buckling phenomena with the spread of plasticity in the range of large displacements

results in highly complex stress states, which govern the global structural response and dictate the encountered failure modes. The accurate capturing of these complex interactions over the full nonlinear response range is thus necessitated for an accurate response evaluation of these systems in the range of large displacements. In this context, the objectives of the present thesis are outlined hereafter:

- i. Development of a systematic and robust HF FE modelling strategy for realistic 3-D nonlinear analysis of large-scale metal composite structural systems. The modelling of such systems using plate or shell elements typically suffers from inaccuracies associated with various forms of locking phenomena, resulting in deteriorated element performance and the exhibiting of an overly-stiff response. The proposed strategy utilises recently developed geometrically nonlinear co-rotational shell elements, with an embedded hierarchic optimisation approach that effectively allows for the relief of locking inaccuracies (Izzuddin & Liang, 2016; 2017). The proposed approach aims at providing an original and systematic modelling framework for extensive nonlinear analysis of complex composite systems, including the novel sandwich composites and the envisioned topside decks, taking due account of geometric and material nonlinearity.
- ii. Validation of the HF FE modelling strategy against experimental results. Successful validation of the proposed modelling strategy against physical tests on the novel sandwich composites, conducted in the context of the INFLOAT project, aims at establishing its effectiveness for realistic 3-D modelling of individual sandwich composites and large-scale composite systems.
- iii. Incorporation of domain partitioning capabilities in the HF FE modelling strategy. The employment of the HF modelling strategy in large-scale composite systems imposes prohibitive computing wall-clock time and demands on memory resources, potentially leading to memory bottlenecks. These shortcomings can be effectively overcome via the systematic incorporation of a dual super-element domain partitioning approach (Jokhio & Izzuddin, 2015), allowing for scalable parallel processing in High Performance Computing (HPC) systems with distributed memory. The provision of qualitative guidance for the establishment of the optimal partitioning configuration, further aims at providing a systematic methodology towards this direction.

Within the HF modelling strategy framework, the constraints of mesh conformity between independent shell substructures intersecting along a line impose significant limitations on the modelling front, while substantially increasing the computational demands. The challenge of coupling intersecting non-conforming meshes along a line, traversing their domain in an arbitrary orientation, has motivated the development of a novel and systematic methodology for surface-to-surface coupling along a 1-D interface. Within this context, the principal research objectives, highlighting the originality of the present thesis, are outlined below:

- i. Development of a novel and systematic algorithmic treatment for enforcing discrete kinematic constraints along a 1-D interface of arbitrary orientation, extending to parallel or intersecting planar, curved and folded surfaces that are discretised with non-conforming meshes.
- ii. Development and implementation of original and computationally efficient 1-D translational and rotational coupling element formulations, applicable to surfaces discretised with 2-D and 3-D FEs.
- iii. Verification of the accuracy and effectiveness of the novel 1-D coupling element in enforcing translational and rotational constraints.
- iv. Demonstration of the combined modelling and computational benefits of the unified modelling framework, encompassing the partitioned HF FE modelling strategy and the novel 1-D coupling element, in realistic modelling of large-scale composite structural systems, via a series of practical application studies in the context of offshore topside structures.

### **1.3 Thesis outline**

Following a concise presentation of the background, scope and objectives of the research work in the present chapter, an extensive literature review on its underpinning aspects is provided in Chapter 2. An insight into sandwich structural composites is first given, in view of their envisioned incorporation in offshore platform topside deck systems. A brief description of the HF nonlinear FE modelling strategy principal aspects and the employed dual super-element domain partitioning methodology is provided thereafter. The chapter concludes with an

extensive review of contact and coupling methods applicable to mixed FE constrained equilibrium problems, and a comparative evaluation of alternative approaches for incorporation in the novel coupling formulation.

In Chapter 3 consideration is given to the HF nonlinear FE modelling strategy and the concept of domain partitioning, with specific focus on sandwich structural composites. An insight is first provided into the hierarchic optimisation approach embedded in the employed shell FE local formulation for the alleviation of locking phenomena (Izzuddin & Liang, 2017). Subsequently, alternative co-rotational framework definitions for establishing local element coordinate systems are presented and their benefits for large-displacement and rotation analyses are conferred (Izzuddin and Liang, 2016). The focus is thereafter shifted to the description of the dual super-element domain partitioning approach and the concept of scalable parallel processing in HPC systems with distributed memory (Jokhio & Izzuddin, 2015).

In Chapter 4, an original and systematic methodology for discrete kinematic constraint enforcement along a 1-D interface between shell surfaces of arbitrary relative spatial orientation with non-conforming meshes is presented. The general setting of surface-to-surface coupling along a line is first introduced, followed by an elaborate description of the algorithmic treatment for the 1-D interface discretisation into coupling elements, applicable to any surface type. The chapter proceeds with presenting the derivations of the general 1-D coupling element force vector and consistent tangent stiffness matrix expressions from energy variational principles and concludes with a discussion on the established integration schemes at the coupling element level.

In Chapter 5, the developed translational and rotational 1-D coupling element formulations are presented, with the expressions of the coupling element energy functional, force vector and tangent stiffness matrix being derived for each respective constraint type. Subsequently, the results of a set of patch tests are presented, verifying the element performance to effectively enforce translational and rotational constraints individually and in conjunction. The chapter concludes with a series of sensitivity analyses for the developed 1-D coupling element.

In Chapter 6, a series of verification studies for the novel 1-D coupling element is presented, which highlight its various performance aspects and potential shortcomings for a range of coupling problems, encompassing planar, curved and folded surfaces, intersecting or edgewise

adjoined along a straight or curved 1-D interface. The element performance in the range of large displacements is verified against equivalent monolithic FE models in each case.

In Chapter 7, a series of application studies focusing on offshore topside decks is presented, with consideration being given to large-scale metal sandwich composites employed as deck components and passive explosion-protective barriers. The presented numerical studies aim at showcasing the versatility of the unified modelling framework, encompassing partitioned HF FE modelling and the developed coupling capability, for extensive nonlinear analysis of geometrically complex, large-scale, composite structural systems.

In Chapter 8, a summary of the main conclusions and contributions of the current thesis is provided, alongside suggestions for future work towards further enhancements and extensions on partitioned modelling and the developed 1-D coupling formulation.

Throughout this research, the implementation of the coupling formulation and the numerical modelling simulations have been undertaken using ADAPTIC (Izzuddin, 1991), a sophisticated general FE code for the adaptive nonlinear analysis of structures under static and dynamic loading. Mesh generation capabilities have been developed using MATLAB R2017b (MathWorks Inc., 2017) and use has also been made of Maple 2016.2 (Maplesoft, 2016) symbolic and numeric computing environments, mainly as an alternative platform for verifying the implementation of the coupling formulation.

# Chapter 2

## Literature Review

### 2.1 Introduction

In the present chapter, a concise literature review on metal sandwich composites with rectangular and hexagonal honeycomb core topologies is provided, alongside a more extensive review on existing methods for discrete coupling constraint enforcement between non-conforming Finite Element (FE) meshes. The dual aim of the review presented herein is to provide: (i) insight into metal sandwich composites with honeycomb core topologies, highlighting the need for the systematic application of the high-fidelity (HF) partitioned modelling strategy discussed in Chapter 3; and (ii) insight into the principal mathematical optimisation formulations and discrete constraint algorithmic treatments employed in FE coupling problems, providing the context for the novel 1-D coupling element formulation developed and presented in Chapters 4 and 5. The main body of the chapter is therefore divided into two sections, individually addressing the objectives outlined above. It is emphasised that the term non-conforming is used herein to refer to non-matching coupled meshes, associated with lack of nodal alignment along the coupling interface, as discussed in Chapter 1.

It should be noted that the review provided herein focuses on the principal aspects underpinning the methods and developments presented throughout this thesis, however further references to the literature are also made at various points in the text, where in each case the relevant framework is explicitly specified and discussed.

## **2.2 Metal honeycomb core sandwich composites**

A literature review on sandwich composites is provided in this section, focusing on metal honeycomb core configurations. The sandwich concept and a short review on commonly employed materials in sandwich construction are presented first. The focus is subsequently shifted to metal composites, where an overview of relevant industrial engineering applications is provided, with particular emphasis to the respective core configurations. Within this context, a discussion on the principal aspects of viable core topologies for large-scale, two-way spanning, all-metal sandwich composite configurations is also provided, along the lines of the requirements and limitations outlined within the INFLOAT project framework. Subsequently, a review on existing modelling and analysis approaches and methods of investigation for metal honeycomb core composites is given, showcasing the necessity of establishing a systematic HF partitioned nonlinear analysis approach for large-scale applications. The section concludes with a brief overview of the principal aspects of the developed modelling strategy, which will be later elaborated in Chapter 3.

### **2.2.1 The sandwich concept**

Research undertaken in a broad spectrum of engineering fields over the past six decades, aiming towards the establishment of structural component configurations with optimal strength-to-weight (specific strength) and stiffness-to-weight (specific stiffness) ratios, progressively gave rise to sandwich construction. Owing to their cost-effectiveness, sandwich composites have been incorporated in the design of automotive, aeronautical, aerospace, naval and marine systems in a systematic fashion, while a substantial portion of the technical manufacturing industry is currently dedicated to their fabrication and mass-production.


Sandwich composites or sandwich panels comprise three principal compartments (Allen, 1969): (i) two thin and sufficiently stiff plates of dense material at the top and bottom of the panel, commonly referred to as faceplates, skins or covers; (ii) an intermediate thick layer of the same or lower density and material grade between the plates, commonly referred to as the core; and (iii) a certain connection scheme between the faceplates and the core, typically encompassing an adhesive material or welding. The mechanical properties and principal response attributes of sandwich composites, alongside their susceptibility to a variety of failure



modes, are primarily dictated by the core configuration and the material selection for the faceplates and core.

From a mechanical viewpoint, the most vital compartment is the structural core. Its significance can be highlighted in several ways: (i) it maintains a constant distance between the faceplates, thereby enhancing the composite flexural stiffness; (ii) it serves as the principal load transferring mechanism between the faceplates; (iii) it serves as the principal shear resistance mechanism of the sandwich composite; and (iv) it contributes to the faceplate out-of-plane stability. Owing to the core configuration and density, as well as potentially the choice of material, its beneficial action comes at a minimal weight trade-off, and hence sandwich composites attain substantially enhanced stiffness and strength characteristics in comparison to solid components of equivalent weight. This is highlighted in Table 2.1 for typical core configurations, densities and material properties employed in sandwich construction.

Table 2.1: Relative stiffness and strength of equivalent weight sandwich and solid components (Petras, 1999)



Relative Bending Stiffness	1	7.0	37
Relative Bending Strength	1	3.5	9.2
Relative Weight	1	1.03	1.06

### 2.2.2 Materials

Sandwich composites are currently employed in a wide range of weight-critical applications, extending from cardboard packaging and ski equipment to aerospace and ship vessels, or even composite satellite shells. The selection of material is primarily dictated by the type of application, environmental conditions, magnitude and type of loading, manufacturing process and life-cycle cost in relation to immediate cost for fabrication and construction.

In the vast majority of weight-critical applications, composite materials of intrinsically low density are employed, in order to further enhance the already substantial weight-saving potential of sandwich composites. In specialised automotive, aerospace and aeronautical

applications, Fibre-Reinforced Polymers (FRP), Fibre-Reinforced Glass (FRG) and Glass-Reinforced Plastic (GRP) are commonly employed for the faceplates, with the core potentially comprising a lower-density and/or strength material, such as aluminium, steel foil or resin-impregnated paper (Plantema, 1966). For less specialised applications, cheaper solutions for the faceplates include mild or structural steel, aluminium alloy and plywood (Allen, 1969).

In large-scale applications of sandwich composites, such as bridge decks and infrastructure systems, the magnitude and type of applied loading dictates the use of higher-density materials, attaining superior strength. Composite panels of reinforced or pre-stressed concrete and structural steel are employed in bridge construction, with more cost-effective alternatives for secondary components including plasterboard, glass-reinforced cement, lightweight concrete, foams and clay products (Allen, 1969). Recently, the use of hybrid polymer-steel-concrete (Pantelides *et al.*, 2008) or FRP composites (Morcous *et al.*, 2010) in bridge decks has been investigated, while FRP sandwich panels have also been employed for building floor rehabilitation of existing structures in Portugal (Correia & Garrido, 2018).

The complete list of materials used in sandwich construction is prohibitively long and outside of the present thesis scope. Shifting the focus to offshore applications, the environmental conditions and the predominant presence of water limit material selection to metallic materials, principally mild, high-strength and anti-corrosive structural steel. A widely accepted industrial practice is the use of mild steel, with an externally applied layer of specialised corrosion-protective paint-spray over the environmentally exposed surfaces. In this context, a brief overview of core configurations for all-steel sandwich composites employed in offshore and naval applications will be given in the following section, alongside a qualitative comparative evaluation of the most attractive candidate core topologies for employment within the INFLOAT project framework.

### **2.2.3 Metal sandwich composite core configurations**

The use of structural steel in offshore and naval applications dictates the employment of sandwich composites with discrete core topologies, potentially combined with a lightweight foam material filling. The range of viable configurations has been substantially expanded in the past two decades, following rapid advancements in welding technology leading to the

development of novel laser welding techniques (TWI - The Welding Institute, 2019a). Laser welding is currently employed for systematic all-steel sandwich composite fabrication at a mass-production level in various shipyards worldwide.

Several core configurations have been investigated within the framework of this application class, with the vast majority of research being oriented towards one-way spanning sandwich composites. These comprise core topologies characterised by substantial orthotropy in respect of their mechanical properties, thereby achieving superior stiffness and strength characteristics in a single principal planar direction. Such topologies include corrugated plates, I-, Z-, C- and V-shaped stiffeners, and elongated tubular cells, welded on the panel faceplates, as illustrated in Figure 2.1 (a)-(c).

For the INFLOAT project, a primary requirement has been the development of a sandwich panel system that achieves a two-way spanning capability. Within this framework, the most promising core topologies have been identified to be the cellular, corrugated prismatic and lattice truss. The mechanical properties and weight characteristics, alongside efficient fabrication approaches for these have been extensively investigated by Wadley (2003; 2005), and a brief overview of their main aspects is given hereafter.

Cellular topologies comprise a periodic arrangement of cells oriented transverse to the faceplates. Several alternative individual cell geometric configurations exist, such as the hexagonal, rectangular and triangular illustrated in Figure 2.2. The response of this topological class is generally orthotropic along the principal planar directions, with the potential of achieving planar isotropy via appropriate design and symmetry (Gibson & Ashby, 1999). The core density and orientation transverse to the faceplates allows for enhanced shear performance characteristics and buckling/indentation resistance under imposed localised loading to be achieved by this topological class. The manufacturing of cellular cores can be implemented in an automated manner, due to the relatively low geometrical complexity and their periodicity (Wadley, 2003), while welded connections can only be achieved with laser welding from the external faceplate surface.

Corrugated prismatic topologies comprise a sequence of prisms with longitudinal axes oriented along a single planar direction. The response of this topological class is typically characterised by substantial orthotropy, with triangular and rhombic prism topologies achieving enhanced load transferring transverse to the prism longitudinal axis, in comparison to corrugated, due to

their geometry allowing for a certain extent of truss action. Stacked configurations, encompassing two prism layers with mutually orthogonal longitudinal axes, as illustrated in Figure 2.2, exhibit a more isotropic response; however, the associated manufacturing process is more cumbersome and results in configurations of increased weight. The core orientation relative to the plates indicates an inferior shear, buckling and indentation resistance, in comparison to cellular topologies. The fabrication of the core requires bending of steel plates with a high degree of precision to attain the desired geometrical configuration, albeit the long and continuous contact surfaces between the core and the plates allow for a continuous and simple welding pattern to be established.

Lattice truss topologies comprise a densely arranged mesh of thin, slender bars in various spatial orientations. The density of the bar mesh allows for a virtually isotropic response to be afforded without increasing the global composite weight substantially, due to the voids generated between the bars. Nonetheless, the bar slenderness renders these susceptible to buckling under compressive localised loading, potentially resulting in extensive indentation failure, while the level of topological complexity renders the fabrication and welding of this class cumbersome. Variations of lattice truss core topologies are illustrated in Figure 2.2.

A comparative evaluation of various core topologies has been conducted in the INFLOAT project, in line with the set of requirements and limitations established in conjunction with AMEC Foster Wheeler and POSCO. In the selection process, consideration has been given to the stiffness and strength characteristics, two-way spanning efficiency, susceptibility to failure modes of interest for offshore topside decks and potential of mass-production. As a result, rectangular and hexagonal honeycomb core topologies were identified as the most viable alternatives, and hence consideration is henceforth given only to these.

A broad spectrum of publications and handbooks on analytical methods, experimental results and FE modelling for honeycomb sandwich composites can be identified in literature. The following section provides a concise review of the principal existing modelling and analysis methods for the mechanical property evaluation, response investigation and failure mode characterisation of honeycomb core composites, with particular emphasis on metal composites with rectangular and hexagonal core topologies.

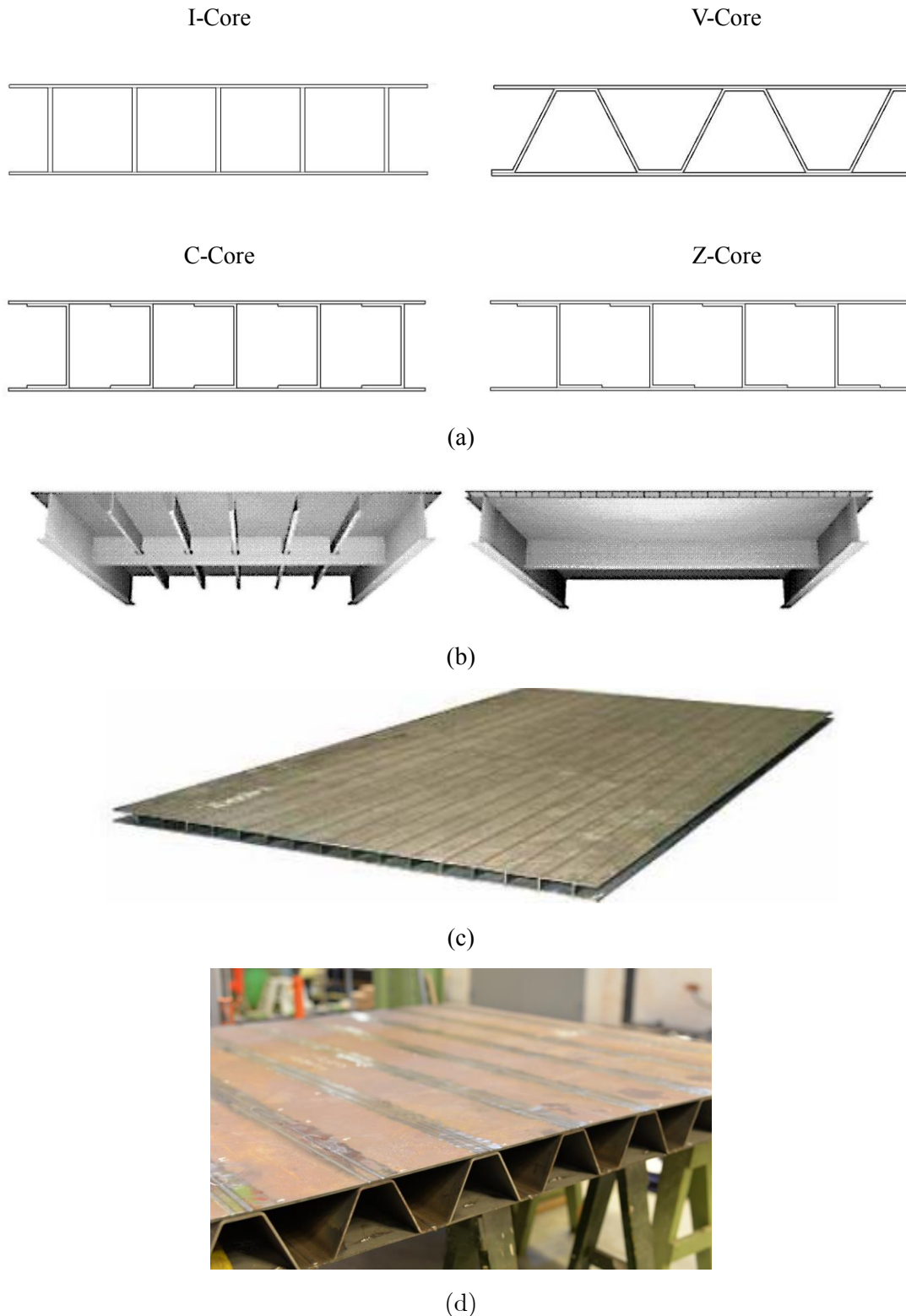


Figure 2.1: (a) One-way spanning sandwich composite core configurations, (b) conventional and I-core sandwich composites for ship decks (Taczała & Banasiak, 2004), (c) all-steel laser-welded unidirectional web (I-core) sandwich panel - courtesy of Meyer Werft (TWI - The Welding Institute, 2019b), (d) all-steel laser-welded corrugated (V-core) sandwich panel (Nilsson, 2017)

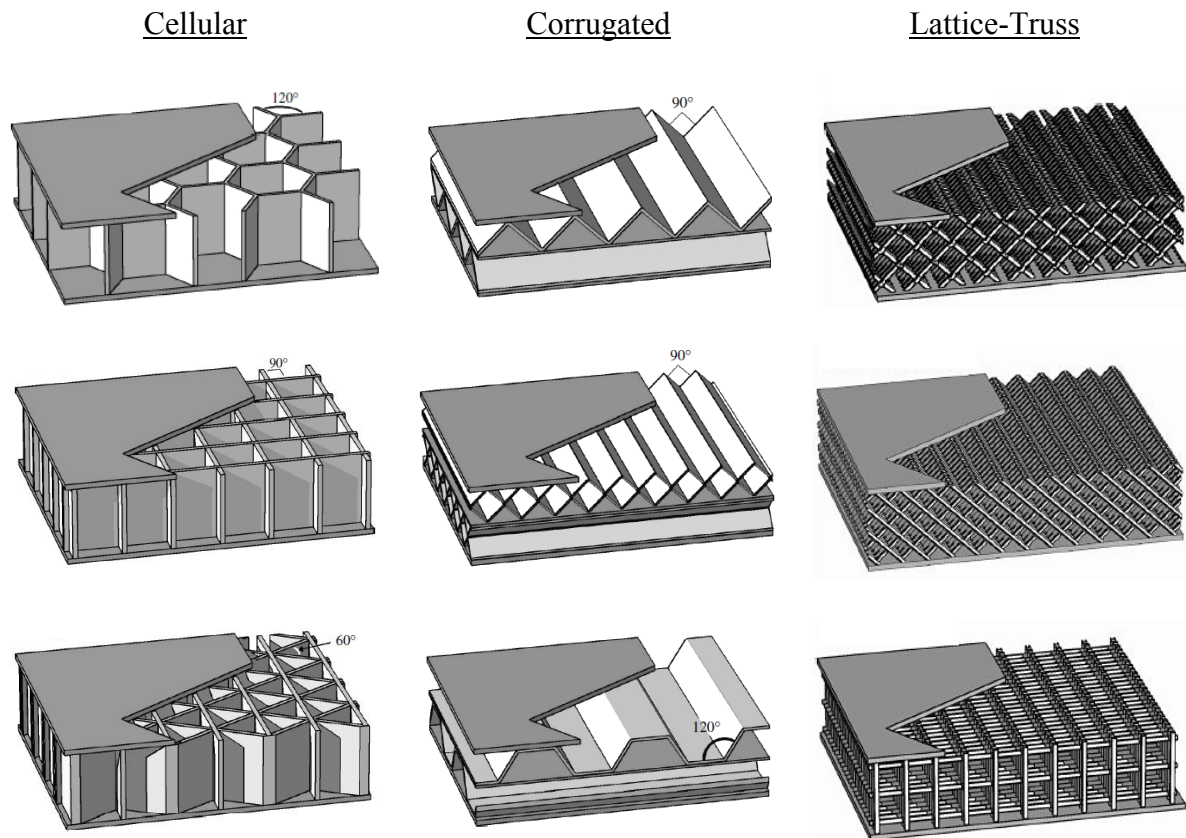


Figure 2.2: All-metal sandwich core topologies (Wadley, 2003; 2005)

#### 2.2.4 Modelling of all-steel honeycomb core sandwich composites

The theoretical principles underlying the analysis and design of structural sandwich panels, beams and struts can be found in the books of Allen (1969) and Plantema (1966), where analytical expressions and derivations of the governing differential equations for small deformation and second order sandwich theory are comprehensively presented. Contemporary guides include the books of Zenkert (1995; 1997), where the mathematical formulations derived by Allen and Plantema are further enhanced and guidance is provided on practical matters, including sandwich composites experimental testing, manufacturing methods and connection schemes.

The fundamental aspects of periodic and cellular solid mechanics are presented in the book of Gibson and Ashby (1999), where a rigorous experimentally-validated analytical framework for the analysis of honeycomb topologies is established, spanning between the microscale and the macroscale levels. Beyond the expressions derived by Gibson and Ashby, a variety of

analytical estimates have been established over the years for the elastic and elastoplastic moduli of rectangular and hexagonal honeycomb topological configurations (Grediac, 1993; Masters & Evans, 1996; Berggren *et al.*, 2001; Berggren *et al.*, 2003).

Owing to the undue complexity of the differential equations governing the response of sandwich composites, early design and analysis approaches were founded upon the simplified assumption of their treatment as beams. Such analytical expressions are widely applicable for the response evaluation of one-way composites in the linear elastic range, as well as their capacity estimation for design purposes, while providing crude conservative estimates for two-way spanning composites. Based upon this simplification, a variety of failure mode maps, as well as stiffness and capacity estimates, have been established for honeycomb core sandwich composites (Holt & Webber, 1982; Petras & Sutcliffe, 1999; Gibson & Ashby, 1999), while analytical approaches were later extended to provide more accurate capacity estimates for honeycomb core sandwich plates (Galletti *et al.*, 2008).

Shifting the focus to all-metal sandwich composites, experimentally-validated estimates for the ultimate capacity of metallic and aluminium hexagonal and rectangular honeycomb configurations were established for a variety of failure modes, including flexural and axial yielding, local core crushing and global buckling (Kee Paik *et al.*, 1999; Crupi *et al.*, 2012). The response of such composites to extreme loading has also received significant attention, due to their enhanced energy dissipation capability and their limited deflection, owing to the absorption of the impulse energy via core plastic deformation. The latter attribute makes them attractive for employment in displacement-critical blast mitigation applications, where the desired deformation of the protective barrier has to be limited (Dharmasena *et al.*, 2008). A wide spectrum of modelling strategies has thus been established in the literature, for the investigation of the impact energy dissipation via core crushing. The methods range from simplified modelling approaches (Andrews & Moussa, 2009) to experimentally validated detailed FE modelling (Karagiozova *et al.*, 2009; Nurick *et al.*, 2009), or even modelling of the fluid-structure interaction between the faceplate and the explosion wave-front (Zhu *et al.*, 2008; 2009). Some experimental investigations on the ultimate capacity of metallic honeycomb sandwich composites, subjected to static and blast/impact loading, are illustrated in Figure 2.3.

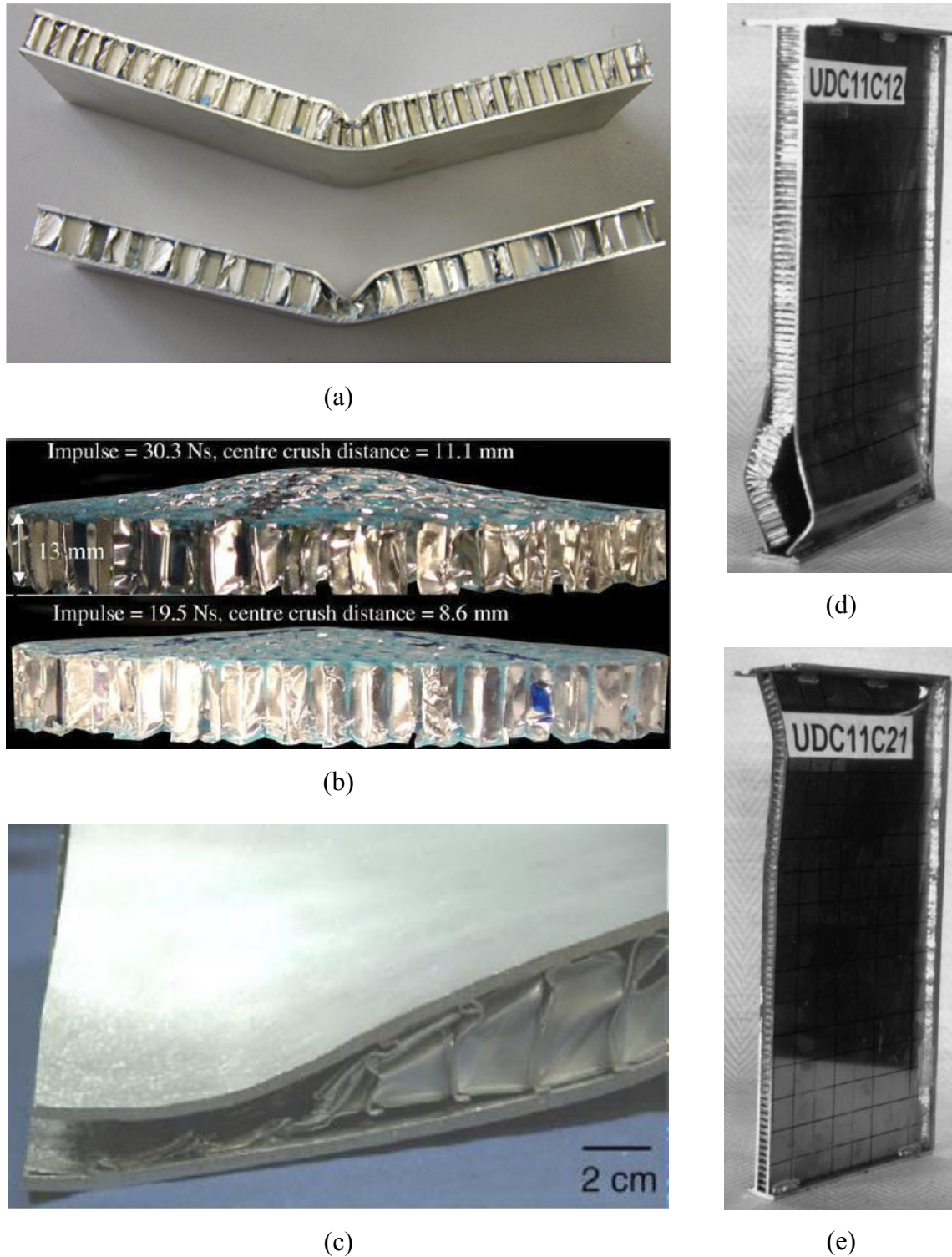


Figure 2.3: Experimental investigation of small-scale, metallic, honeycomb core sandwich composite ultimate capacity to static (a, d, e) and impact loading (b, c): (a) hexagonal-aluminium faceplates and core (Crupi *et al.*, 2012), (b) hexagonal-steel faceplates and aluminium core (Nurick *et al.*, 2009), (c) rectangular-stainless steel alloy faceplates and core (Dharmasena *et al.*, 2008), (d)-(e) hexagonal-aluminium faceplates and core (Kee Paik *et al.*, 1999)



The vast majority of available publications on failure mode characterisation and capacity assessment focus on small-scale composites, typically employed as vessels in lightweight systems in automotive, naval and aerospace applications. On the other hand, the investigation on the blast performance of metal honeycomb core structures is principally focused on composites employed as passive protective barriers, which are thus not designed to resist primary loading. Consideration is mainly given to core configurations associated with substantially inferior stiffness and strength characteristics in comparison to the faceplates, which enable an enhanced energy dissipation capability to be achieved. Despite providing an insight into the response of metal honeycomb core sandwich composites, the results of these investigations are not directly applicable to the context, scale and loading magnitude considered within the INFLOAT project investigation framework.

The response of metal honeycomb core sandwich composites in ultimate conditions is governed by local instabilities, due to their progressive manifestation in different regions and their interaction with global failure modes involving material yielding and the spread of plasticity. The resulting stress and deformation states are highly complex, particularly in cases of non-uniform loading, nonetheless their accurate capturing is essential for the composite design. A widely popular class of approaches for local buckling assessment of metallic honeycomb core structures is based upon the use of local-scale mechanical or detailed FE models, encompassing individual cells or cell groups with an appropriately introduced set of boundary conditions. These enable reliable estimates of the elastic and elastoplastic buckling capacity to be obtained locally and have been widely investigated.

Several analytical approaches for the buckling assessment of the core cell walls have been established and successfully validated against experimental results or verified against detailed FE models, for both rectangular and hexagonal topologies. Reliable estimates have been provided for the ultimate capacity in compressive buckling for rectangular (Zok *et al.*, 2005; Liang & Chen, 2006) and hexagonal (Zhang & Ashby, 1992; Kaman *et al.*, 2010; Jeyakrishnan *et al.*, 2012) honeycomb topologies, while a limited number of investigations on the shear buckling capacity of rectangular topologies in the elastoplastic regime also exist (Cote *et al.*, 2006). More sophisticated approaches encompass the development of mechanical models for elastoplastic buckling assessment under superimposed compressive and shear loading (López Jiménez & Triantafyllidis, 2013).

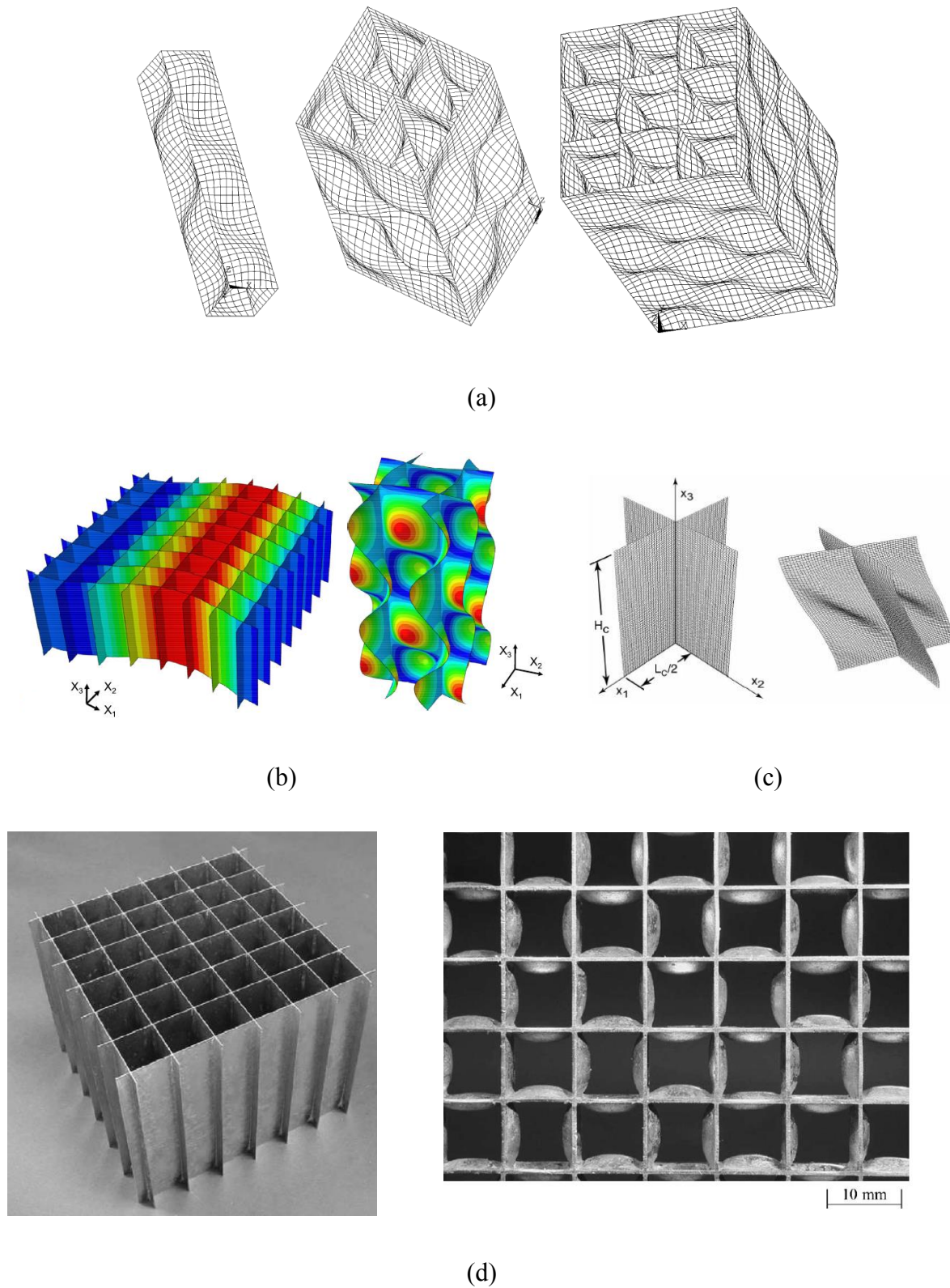


Figure 2.4: Local buckling assessment of metal honeycomb core structures via FE modelling of individual cells and cell groups (a-c) and experimental testing (d): (a) (Liang & Chen, 2006), (b) (López Jiménez & Triantafyllidis, 2013), (c) (Zok *et al.*, 2005), (d) (Cote *et al.*, 2004)

The accuracy of these estimates is highly sensitive to the established set of boundary conditions, which need to account for the extent of rotational and translational stiffness provided to the core cell walls by the faceplates and vice-versa. A thorough numerical and experimental investigation on the effect of the honeycomb core and faceplates relative density and degree of bonding, as well as of the cell aspect ratio, on the buckling capacity of all-steel rectangular honeycombs has been conducted by Cote *et al.* (2004). Examples of numerical and experimental investigations for local buckling assessment of metal honeycomb core structures are illustrated in Figure 2.4.

Recently, Santos *et al.* (2018) established an accurate analytical approach for the local buckling assessment of metal sandwich composites, which has been numerically verified and provides a systematic framework for the capacity assessment of individual plated components of the core cell walls or faceplates to intercellular, shear and compressive instability phenomena. The method is underpinned by the employment of a rotational spring analogy (Izzuddin, 2006; 2007), which enables the establishment of reliable estimates for the rotational restraints provided to each individual plated component of the cell walls or faceplates by the surrounding components, using realistic assumed buckling modes.

It is emphasised that this class of methods is particularly valuable within the scope of the INFLOAT project, in view of the necessity of establishing accurate analytical design expressions for the buckling capacity of faceplates and steel honeycomb cores, where several localised equipment loads are applied. Nonetheless, within the scope of the present thesis the focus remains on the establishment of an integrated modelling approach, enabling the capturing of the various instability forms and their effect on the global sandwich composite failure modes, rather than examining these phenomena locally. This is particularly important on two fronts: (i) to remove uncertainty associated with the boundary conditions employed for local models; and (ii) to assess the influence of local buckling on the overall system at various stages of the elasto-plastic response.

Existing publications on large-scale, all-steel, laser-welded sandwich composites, dimensionally equivalent to the envisioned components for application in offshore topside decks, are limited to one-way spanning configurations, employed mainly in naval applications, as discussed in Section 2.2.3. Consideration has been given to unidirectional web core (I-core) composites, several response aspects of which have been thoroughly investigated, in view of their systematic incorporation in industrial applications. A number of design-oriented

analytical approaches have been established for the analysis and design of such configurations in a variety of failure modes, while experimental and detailed numerical investigations have been conducted. Consideration has been given to the bending response of sandwich beams (Romanoff & Varsta, 2006; Romanoff *et al.*, 2007a), the bending response of sandwich plates and the extent of achieved composite action with underlying beam components (Romanoff & Varsta, 2007; Romanoff, 2011), the buckling and wrinkling of the faceplates in the elastoplastic regime (Kolsters & Zenkert, 2006a; 2006b; 2010) and the composite response subject to localised patch loading, considering the sensitivity of the response to the patch size, the plate aspect ratio and the rotational stiffness provided by the laser welds at the T-joint intersection (Romanoff *et al.*, 2007b). Moreover, a thorough investigation of the laser welding defects and corrosion effects on the composite response has been conducted and a 24% buckling capacity reduction has been estimated for the plated components (Jelovica *et al.*, 2012; Jelovica *et al.*, 2014). A complete experimental and numerical investigation of the I-core, alongside other one-way spanning, large-scale, all-steel sandwich composite configurations can be found in the S.A.N.D. Core practice guide for marine applications (2013).

The aforementioned investigations are evidently not directly applicable to two-way spanning composites with honeycomb core configurations; nonetheless due to the load types and magnitude, as well as the application context equivalence, they can provide guidance on the aspects requiring particular attention and consideration. This is important for steering the process of establishing a systematic methodology for offshore topside decks, within the context of the INFLOAT project.

Notwithstanding the significant research outlined above, the extensive nonlinear response investigation of large-scale metal sandwich composites with honeycomb core topologies at the component level has received much less attention. This is partially attributed to the lack of precedent of their application in the context considered herein, and largely to the associated modelling complexity and high computational demand posed by such intricate structures. A common approach to circumvent the aforementioned modelling challenges is based upon the employment of a simplified FE modelling approach, encompassing the use of conventional shell FEs with equivalent homogeneous cross-sectional properties (Berggren *et al.*, 2003). More efficient simplified FE modelling approaches based on the employment of sandwich shell FEs may also be used (Robbins Jr & Reddy, 1993; Carrera, 1998; Liang & Izzuddin, 2016), allowing for the definition of distinct properties for the faceplates and core, with the latter being

modelled as an equivalent homogeneous layer, as illustrated in Figure 2.5. Despite their efficiency for linear elastic analysis, as well as the sandwich shell FE capability of accurately approximating the capacity of failure modes involving plate yielding, simplified modelling approaches evidently fail to capture local instabilities.

Within the aforementioned backdrop, a HF nonlinear FE modelling strategy is proposed in this thesis, as elaborated in Chapter 3, utilising previous developments undertaken at Imperial College which are reviewed in the following sub-section.

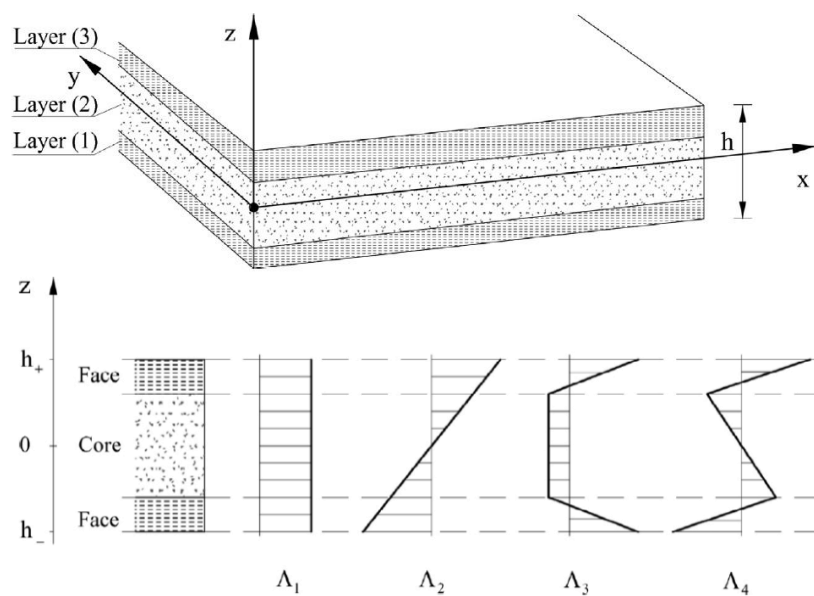


Figure 2.5: Simplified modelling of sandwich composites using three-layer shell finite elements with equivalent intermediate layer homogenisation (Liang & Izzuddin, 2016)

### 2.2.5 HF nonlinear analysis using partitioned modelling

The proposed HF modelling strategy encompasses the following key features: (i) accurate geometric modelling process for the core and plates, accounting for manufacturing and connection characteristics between individual cells, alongside initial imperfections; (ii) discretisation of the panel domain utilising advanced geometrically nonlinear shell elements, allowing for the effects of local buckling on the global panel response to be accurately captured; (iii) employment of sophisticated nonlinear constitutive models capable of accurately capturing yielding, strain-hardening and strain-rate effects; and (iv) utilisation of powerful domain

domain partitioning in High Performance Computing (HPC) systems that achieves considerable computational efficiency and overcomes memory bottlenecks.

The modelling strategy is underpinned by the employment of recently developed Reissner-Mindlin shell elements (Izzuddin & Liang, 2017), which enable the accurate capturing of geometric and material nonlinearity effects in the range of large displacements. The robustness and accuracy of the elements are attributed to the incorporation of two principal aspects in their local formulation: (i) an effective co-rotational framework for the shell element local coordinate system definition (Izzuddin & Liang, 2016); and (ii) a hierarchic optimisation approach for the relief of inaccuracies arising from locking phenomena (Izzuddin & Liang, 2017). The element local coordinate system definition within a co-rotational framework enables the exclusion of rigid body rotations from the element response, thus enabling simple local kinematic constitutive expressions to be obtained. On the other hand, the hierarchic optimisation approach enables the overcoming of inaccuracies associated with overly-stiff response of curved shell elements, commonly referred to as locking phenomena, when applied to relatively thin shells.

Extensive nonlinear analysis of large-scale sandwich composites imposes a prohibitive demand on computing wall-clock time and memory resources, potentially leading to memory bottlenecks. In view of these shortcomings, the proposed strategy is further enhanced by utilising recently developed domain partitioning capabilities based on a novel dual super-element concept (Jokhio & Izzuddin, 2015). Partitioned modelling allows for a substantial reduction in the computing wall-clock time and memory demands to be achieved in comparison to the monolithic approach, without compromising the convergence rate and accuracy of the latter, via scalable parallel processing in HPC systems with distributed memory.

As detailed in the next chapter, the overall strategy provides a powerful capability that enables the HF nonlinear analysis of large-scale, all-steel sandwich panels to be undertaken efficiently and within reasonable time.

### **2.3 Coupling methods in computational mechanics**

The novel coupling element formulation presented in Chapters 4 and 5 achieves translational and rotational constraint enforcement between surfaces or arbitrary relative spatial orientation

with non-conforming meshes along a 1-D interface. This requires the establishment of appropriate and systematic methodologies to facilitate the constraint enforcement in a discrete sense along the interface. The focus is thus shifted to the review of existing coupling methods in this section, in the scope of identifying the most efficient approach for incorporation in the coupling formulation.

Coupling methods facilitate the enforcement of kinematic constraints between independent computationally heterogeneous deformable bodies over a shared subdomain, henceforth referred to as coupling interface. Within the context of FE procedures, coupling methods have received significant attention over the past three decades, owing to their formulation providing a systematic framework for: (i) coupling of independently discretised domains, potentially comprising different FE types; (ii) domain decomposition approaches for process parallelisation, encompassing subdomains with generally non-conforming meshes; and (iii) the treatment of contact problems (Puso, 2004).

From a mathematical viewpoint, the introduction of kinematic constraints in the system global equilibrium can be treated as an optimisation problem, encompassing the extrema identification of the system total potential energy function subject to the given set of constraints. In the broader sense, these constraints are expressed in the form of inequalities, which physically correspond to the class of contact problems between deformable bodies, whereas in coupling problems the set of constraints is expressed in a strict equality form. Accordingly, coupling problems can be viewed as a particular case of contact problems, where permanent contact is enforced between the deformable bodies over a fixed interface, and the two classes of problems are hence treated equivalently.

In general contact problems, the shared interface between the two bodies is continuously changing to conform with the relative body deformations, inducing sliding and separation between these. The constraints are enforced by virtue of stress fields, acting normal and tangential to the interface in regions where contact occurs, and can be expressed in two distinct manners: (i) in a purely geometric sense, as a non-penetration condition, in which case the contact pressure over the interface is obtained solely from the constraint equations in accordance with *lege tertius* of Newtonian mechanics; and (ii) by virtue of a material constitutive model over the contact interface, in which case the contact pressure is implicitly or explicitly obtained from the interface deformations (Wriggers, 2006). Consideration will henceforth be given to the first of the above approaches, in which case the contact conditions

along the normal ( $N$ ) or one of the tangent to the interface directions ( $T$ ) can be mathematically formulated as follows:

$$\begin{aligned} g_{N/T} &\geq 0 \\ p_{N/T} &\leq 0 \\ p_{N/T} g_{N/T} &= 0 \end{aligned} \tag{2.1}$$

where  $p_{N/T}$  is the contact stress over the interface, and  $g_{N/T}$  is the gap function along the respective direction. Eq. (2.1) states that when the two bodies are not in contact, i.e.  $g_{N/T} > 0$ , no stresses develop over the contact interface, i.e.  $p_{N/T} = 0$ , while in the case of contact between the two bodies, i.e.  $g_{N/T} = 0$ , a set of equal and opposite compressive stress fields develop over the contact interface as reactions, i.e.  $p_{N/T} < 0$ . The above set of conditions is formally referred to as Hertz-Signorini-Moreau (HSM) in the field of computational contact mechanics, which is the equivalent of the Karush-Kuhn-Tucker (KKT) conditions in the field of mathematical optimisation (Wriggers, 2006).

Taking the above into consideration, coupling methods are a particular case of contact problems, where the HSM conditions are expressed in a strict equality form:

$$\begin{aligned} g_{N/T} &= 0 \\ p_{N/T} &\neq 0 \\ p_{N/T} g_{N/T} &= 0 \end{aligned} \tag{2.2}$$

Accordingly, sliding or separation are not allowed, and the contact interface remains thus unchanged throughout the range of exhibited relative body deformations. This is also commonly referred to as ‘stick’ condition in the field of contact mechanics (Wriggers, 2006).

In constrained equilibrium problems where FE procedures are employed, the treatment of kinematic constraints in a discrete sense is necessitated. The establishment of a systematic procedure for discrete constraint enforcement is founded upon of two principal classes of methods: (i) a consistent mathematical optimisation formulation for the kinematic constraint treatment over the interface, in the context of the global equilibrium problem; and (ii) a robust interface discretisation approach, ensuring accuracy and convergence of the solution procedure in a global sense. As is evident from the preceding discussion, coupling and contact problems



can be treated using identical procedures for the discrete constraint enforcement, owing to their mathematical equivalence.

Consideration is given hereafter to the two distinct classes of methods discussed above, where a comprehensive review of the existing variants for each respective class is provided. Following the presentation of each class of methods, a comparative evaluation of their respective variants is conducted, to identify the most efficient for employment within the novel 1-D coupling element formulation. It should be noted that the vast majority of existing publications investigate different approaches from the viewpoint of contact problems, with their specialisation to coupling problems, nonetheless, being a straightforward and well-established process.

### **2.3.1 Mathematical treatment of contact and coupling constraints**

The fulfilment of discrete system equilibrium conditions subject to an imposed set of kinematic constraints introduced over the interface, encompasses the establishment of an additional set of nodal forces and stiffness coefficients for the FEs located in the interface domain, and their subsequent assembly to the global system force vector and tangent stiffness matrix. These are derived from the potential energy function expressing the contribution of the imposed constraint over the interface to the system total potential energy, by employing 1<sup>st</sup> and 2<sup>nd</sup> order variational principles, respectively. The contact or coupling interface energy contribution for a given set of constraints can be expressed in a discrete-strong or continuous-weak form, where in the former case the constraint is introduced at specified distinct locations (most commonly nodes), while in the latter it is continuously interpolated over the interface domain (Wriggers, 2006).

The above procedure is the discrete equivalent of the total potential energy minimisation subject to the specified constraints, thus rendering the problem one of mathematical optimisation, as discussed. The vast majority of existing methods for formal treatment of contact and coupling constraints are thus based upon mathematical optimisation techniques for the extrema identification of functions subject to a set of inequality or equality constraints. A detailed description of constrained optimisation methods from a mathematical viewpoint can

be found in the books of Fletcher (2000) and Bertsekas (1982), while an overview of these in the context of their application to contact and coupling problems is given hereafter.

The most commonly employed optimisation techniques include the: (i) Lagrangian Multiplier (LM), (ii) penalty, (iii) augmented LM, (iv) perturbed LM and (v) Nitsche formulations (Wriggers, 2006), which are discussed in the subsequent sub-sections. For generality and simplicity, the constraints are introduced in all equations henceforth as a vector function  $\mathbf{g}(\mathbf{u}^{(1)}, \mathbf{u}^{(2)})$ , which is expressed in terms of the independent body displacement fields  $\mathbf{u}^{(1)}$  and  $\mathbf{u}^{(2)}$ . This encompasses all possible types of constraints along the tangential and normal to the interface directions. The LM or contact/coupling stress vectors are also expressed in a consistent vector format. The expressions therefore apply for the cases where the associated set of constraints described by  $\mathbf{g}$  are enforced individually, partially or in their entirety.

It should be noted that due to the employment of well-established mathematical optimisation formulations within the present context, the portion of the existing literature focusing exclusively on investigating their performance in contact problems is small, and mostly outdated, with the first publications dating back to 1985. Subsequent to the establishment of satisfactory accuracy and convergence characteristics from the employment of optimisation techniques in contact and coupling problems, the focus of research efforts has been shifted to the investigation of different interface discretisation techniques, which is still ongoing.

### 2.3.1.1 Lagrangian Multiplier formulation

The LM formulation is based upon the introduction of a set of additional LM Degrees of Freedom (DOFs) at distinct locations over the interface  $\Gamma_c$ , and their subsequent interpolation to obtain a continuous independent field  $\lambda$ , which facilitates the enforcement of the set of constraints  $\mathbf{g}$ . The LM field  $\lambda$  physically and dimensionally corresponds to a stress field along  $\Gamma_c$ , representing the pressure due to contact or coupling of the heterogeneous deformable bodies. Accordingly, the contribution of  $\Gamma_c$  to the total potential energy of the system can be expressed in the form of the following two-field Lagrangian functional:

$$\Pi(\lambda, \mathbf{u}^{(1)}, \mathbf{u}^{(2)}) = \int_{\Gamma_c} \lambda \cdot \mathbf{g}(\mathbf{u}^{(1)}, \mathbf{u}^{(2)}) \, d\Gamma_c \quad (2.3)$$

The term two-field is employed herein with reference to the two distinct  $\lambda$  and  $\mathbf{u} = (\mathbf{u}^{(1)}, \mathbf{u}^{(2)})$  fields incorporated in the formulation. Three-field approaches also exist, where the stress or strain field of the independent deformable bodies over  $\Gamma_c$  is also incorporated in the energy functional (Laursen & Heinstein, 2003), as will be also discussed in the context of the interface discretisation methods in Sub-section 2.3.2.

The LM formulation has been employed for the contact or coupling treatment in conjunction with various approaches for the interface discretisation, and it forms the basis for the mortar method (Puso, 2004; Fischer & Wriggers, 2005; Tur *et al.*, 2009), which is of principal interest in the context of the present research work. Its employment in coupling problems enables exact constraint enforcement at the locations where LM are introduced, and in a weak sense over the remaining part of  $\Gamma_c$  where these are interpolated, thus allowing for a substantial level of accuracy to be achieved in the case of non-conforming FE meshes, in a global sense.

The accuracy of the formulation comes at an increased computational demand, resulting from the introduction of additional LM parameters (pseudo DOFs) to the system. Therefore, the LM formulation employment in large-scale systems potentially leads to shortcomings in relation to the computing wall-clock time and memory resources demands. Several algorithmic treatments to circumvent these shortcomings have been established, with the most popular being the dual LM approach (Wohlmuth, 2000), which will be discussed in detail in Sub-section 2.3.2. Moreover, the LM method suffers from the well-known shortcoming of zero diagonal terms in the tangent stiffness matrix, which leads to intricacies depending on the adopted solution procedure, as will be discussed more extensively in Chapter 4.

### 2.3.1.2 Penalty formulation

As opposed to the LM formulation, the penalty method does not introduce additional unknowns to the system, but rather enforces the set of constraints  $\mathbf{g}$  in an approximate sense over  $\Gamma_c$ , by virtue of introducing a second order regularisation term of the following form to the system total potential energy:

$$\Pi(\mathbf{u}^{(1)}, \mathbf{u}^{(2)}) = \frac{1}{2} \varepsilon \int_{\Gamma_c} \mathbf{g}^2(\mathbf{u}^{(1)}, \mathbf{u}^{(2)}) \, d\Gamma_c \quad (2.4)$$

where the constant  $\varepsilon \geq 0$  is referred to as penalty parameter. The method owes its name to the penalisation of the constraint enforcement accuracy by the introduced parameter  $\varepsilon$ . The accuracy of the formulation increases with increasing values of  $\varepsilon$ , with convergence to the LM formulation being achieved when  $\varepsilon \rightarrow \infty$ , which nonetheless further leads to ill-conditioning (Luenberger & Ye, 2008).

A comparative evaluation of the LM and penalty formulation efficiency and accuracy for 2-D frictionless contact problems is presented in a series of numerical studies conducted by Fischer and Wriggers (2005), where the mortar method is employed for the contact interface discretisation. The obtained results highlight the capability of the penalty formulation to achieve comparable accuracy to the LM formulation in the stress distribution and global deformation, when a sufficiently, but not excessively, large value is adopted for the penalty parameter. A comparative evaluation of the penalty formulation with the augmented and perturbed LM formulations, conducted by Wriggers *et al.* (1985), indicates a comparable efficiency of the methods for an appropriately calibrated value of the penalty parameter, in the range of both small and large deformations.

Despite the non-introduction of additional unknowns to the system, the penalty method suffers from well-known shortcomings, the principal being the requirement for calibration of  $\varepsilon$  for an optimal balance between accuracy and stability to be established for a given system. While small values of  $\varepsilon$  lead to poor accuracy and very large values lead to ill-conditioning, an appropriate selection of the penalty parameter value to be at least three orders of magnitude greater than the characteristic stiffness of the bodies in contact in the respective constraint directions, allows for satisfactory accuracy and stability to be achieved (Wriggers, 2006). The main forms of inaccuracies of the penalty method are observed in the displacement field in the case of surface or body loading, with the application of displacement to the system, on the other hand, leading to substantial perturbations in the stress field (Wriggers, 2006).

It should be noted that different penalty parameters can be employed for the enforcement of the distinct constraints included in  $\mathbf{g}$ , for example along the normal and tangential directions of  $\Gamma_c$ , however an identical  $\varepsilon$  has been used in Eq. (2.4), and is also used in the expressions presented in the forthcoming sub-sections, on account of simplicity.

### 2.3.1.3 Augmented LM formulation

The augmented LM formulation encompasses the combined benefits of the classical LM and penalty approaches. The use of an independent LM field enables exact constraint enforcement at the LM locations and enhanced accuracy to be achieved, while the introduction of a penalty regularisation term enables the overcoming of potential ill-conditioning shortcomings, even with a moderate value. This expression for the total potential energy contribution of  $\Gamma_c$  to the global system is obtained by linear superposition of the expressions in Eqs. (2.3) and (2.4):

$$\Pi(\boldsymbol{\lambda}, \mathbf{u}^{(1)}, \mathbf{u}^{(2)}) = \int_{\Gamma_c} \boldsymbol{\lambda} \cdot \mathbf{g}(\mathbf{u}^{(1)}, \mathbf{u}^{(2)}) \, d\Gamma_c + \frac{1}{2} \varepsilon \int_{\Gamma_c} \mathbf{g}^2(\mathbf{u}^{(1)}, \mathbf{u}^{(2)}) \, d\Gamma_c \quad (2.5)$$

One of the first applications of the method has been presented by Simo *et al.* (1985) in the context of frictionless contact problems, with a primal mortar approach based on the interface discretisation into segments, where the attainment of a high level of accuracy in the range of large deformations is shown. Landers and Taylor (1986) also highlighted the superiority of the augmented LM in comparison to the classical LM, penalty and perturbed LM formulations, in relation to the control it offers over the accuracy and convergence rate for static and dynamic problems, through appropriate selection of the penalty parameter. Zavarise and Wriggers (1999) established a novel augmented approach, based on the update of the LM at every iterative step using a data set of converged states from all the previous iterative steps. This method has been shown to achieve superlinear convergence and virtually absolute invariance to the adopted penalty parameter value.

The method has been extended over the years to deal with contact problems encompassing a nonlinear constitutive (Wriggers & Zavarise, 1993) or Coulomb friction (Laursen & Simo, 1993a) law for the establishment of contact stresses over the interface domain. More recently, Cavalieri and Cardona (2013) illustrated the broad variety of benefits associated with the employment of the augmented LM formulation in conjunction with the mortar method in 3-D frictionless contact problems. The attainment of fast convergence with a monolithic Newton scheme and the accuracy insensitivity to the selection of the penalty parameter were demonstrated for the case of regions with non-conforming meshes, alongside the passing of the contact patch test. The application of the augmented LM to a class of problems extending beyond the pure geometric constraint treatment highlights its capability of preserving the accuracy and convergence characteristics in a broad range of cases and applications, which is

important in the context of the developed 1-D coupling formulation presented in Chapters 4 and 5.

#### 2.3.1.4 Perturbed LM formulation

The perturbed LM formulation is also a combination of the classical LM and penalty methods. A second order regularisation term is introduced in the energy functional, which, contrary to the augmented formulation, depends on both the penalty parameter  $\varepsilon$  and the LM field  $\lambda$ :

$$\Pi(\lambda, \mathbf{u}^{(1)}, \mathbf{u}^{(2)}) = \int_{\Gamma_c} \lambda \cdot \mathbf{g}(\mathbf{u}^{(1)}, \mathbf{u}^{(2)}) \, d\Gamma_c - \frac{1}{2\varepsilon} \int_{\Gamma_c} \lambda^2 \, d\Gamma_c \quad (2.6)$$

The regularisation term of the perturbed formulation can be viewed as the complementary energy contribution of the LM field  $\lambda$ , while, evidently, for  $\varepsilon \rightarrow \infty$  the perturbed LM degenerates into the classical LM formulation (Wriggers, 2006). The perturbed formulation has been shown to achieve convergence only in the cases of frictionless or ‘stick’ conditions in contact problems, due to the inability of explicitly stating incremental constitutive relationships, such as Coulomb’s frictional law, in a complementary form (Wriggers, 2006). Due to this shortcoming, the perturbed formulation has received limited attention in comparison with the rest of considered formulations, albeit its suitability for contact problems with stick conditions makes it eligible for employment in rigid translational coupling problems.

Some early applications of the method in contact problems can be traced back to the work of Simo *et al.* (1985), where satisfactory accuracy was demonstrated, while a comparative evaluation with the classical LM, penalty and augmented LM formulations was conducted by Landers and Taylor (1986), as discussed in the preceding sub-section.

#### 2.3.1.5 Nitsche formulation

A purely displacement-based alternative to the employment of LM formulations is based on a variational approach for the treatment of Dirichlet boundary conditions established by Nitsche (1971). Contrary to the LM-based formulations, which introduce additional DOFs to the global

system to facilitate constraint enforcement, the Nitsche method is based on the incorporation of the actual body stress fields in the energy functional:

$$\Pi(\mathbf{u}^{(1)}, \mathbf{u}^{(2)}) = -\frac{1}{2} \int_{\Gamma_c} (\mathbf{p}^{(1)}(\mathbf{u}^{(1)}) + \mathbf{p}^{(2)}(\mathbf{u}^{(2)})) \cdot \mathbf{g}(\mathbf{u}^{(1)}, \mathbf{u}^{(2)}) \, d\Gamma_c + \frac{1}{2} \varepsilon \int_{\Gamma_c} \mathbf{g}^2(\mathbf{u}^{(1)}, \mathbf{u}^{(2)}) \, d\Gamma_c \quad (2.7)$$

In the above expression,  $\mathbf{p}^{(1)}(\mathbf{u}^{(1)})$  and  $\mathbf{p}^{(2)}(\mathbf{u}^{(2)})$  are the stress fields of two independent deformable heterogeneous bodies  $\Gamma^{(1)}$  and  $\Gamma^{(2)}$  over the shared interface  $\Gamma_c$ . The independent body stress fields  $\mathbf{p}^{(1)}(\mathbf{u}^{(1)})$  and  $\mathbf{p}^{(2)}(\mathbf{u}^{(2)})$  are related to the independent displacement fields  $(\mathbf{u}^{(1)}, \mathbf{u}^{(2)})$  over  $\Gamma_c$ , by virtue of the respective material constitutive equations and the compatibility expressions founded upon Cauchy's theorem, and hence the functional in Eq. (2.7) is purely displacement-dependent. The Nitsche method enforces the constraints in an exact fashion, thus rendering the contribution of the penalty term inactive, with the latter being only employed to avoid ill-conditioning in the global equilibrium equation system, similar to the case of the augmented LM formulation discussed earlier.

An adaptation of the Nitsche method for domain decomposition with non-conforming FE meshes, using a mortar interface discretisation approach, has been presented by Becker *et al.* (2003). Wriggers and Zavarise (2008) employed different variants of the weak form Nitsche method for constraint enforcement in 2-D frictionless contact problems, based on the average or single stress fields of the bodies in contact, in conjunction with a segment discretisation approach for the interface. In the context of linear analysis, the Nitsche method has been shown to achieve superior accuracy and performance to the standard penalty formulation. On the other hand, the recovering of the independent body stress fields in the case of a geometrically or materially nonlinear response is rendered a cumbersome undertaking, thereby imposing limitations to the systematic employment of the Nitsche method in large-displacement problems.

### 2.3.1.6 Comparative evaluation of optimisation techniques for contact and coupling constraint enforcement

The classical LM formulation introduces an independent LM field over  $\Gamma_c$ , which enables exact constraint enforcement at the locations where the individual LM entities are introduced. Despite the method being substantially accurate, it suffers from potential ill-conditioning in cases where at least one of the coupled bodies is unrestrained against rigid body motion, when solvers that eliminate individual parameters using their corresponding equations, i.e. without performing row-switching, are employed, such as the frontal solver (Irons, 1970). This will be discussed in more detail in Chapter 4. Moreover, the introduction of additional DOFs increases the size of the global equilibrium problem at the system level, thereby potentially imposing an increased demand in respect of computing wall-clock time and memory resources for large-scale systems, in comparison with non-LM based formulations.

The penalty method enforces the constraints in an approximate sense over  $\Gamma_c$ , by means of a second-order penalty regularisation term, without introducing additional DOFs to the system. Therefore, contrary to LM-based formulations, it does not increase the computing resources demand, which comes at an inferior accuracy trade-off. The achieved level of accuracy is dictated by the selected value of the penalty parameter  $\varepsilon$ , with larger values generally leading to superior performance, but ill-conditioning of the global equilibrium equation system occurring for very large values. An appropriate calibration of  $\varepsilon$  is thereby required for a given system, if an approximation of enhanced accuracy is to be obtained.

The augmented LM formulation combines the benefits of both the classical LM and penalty formulations, enabling the exact constraint enforcement and the overcoming of ill-conditioning shortcomings with the employment of a moderate  $\varepsilon$  value, with the method being relatively insensitive to the selection of the latter. Despite the method allowing for the accuracy and convergence levels to be adjusted by the user, it introduces additional LM DOFs to the system.

The perturbed LM formulation is also a combination of the classical LM and penalty methods, with its principal difference from the augmented variant being the dependence of the regularisation term from the LMs to a second order. The regularisation term represents the complementary energy contribution of the LM field, and hence the application of the method



is limited to frictionless contact and coupling, where this can be explicitly stated. For  $\varepsilon \rightarrow \infty$  the perturbed LM degenerates to the classical LM formulation.

The Nitsche method enforces the constraints over  $\Gamma_c$  using the actual respective stress fields of the bodies, instead of additional LM DOFs, thereby constituting a purely displacement-based one-field formulation. Similar to the various LM-based variants, it enforces the constraints exactly, without however introducing additional unknowns, while the introduction of a penalty regularisation term allows for any potential ill-conditioning shortcoming to be effectively overcome. In the range of linear elasticity, the Nitsche formulation achieves superior performance characteristics in comparison to the penalty method; however in the presence of material or geometric nonlinearity the recovery of the independent stress fields becomes cumbersome, thus adversely affecting its performance and limiting its range of application.

Taking the above into consideration, the augmented LM formulation has been adopted in this work for the establishment and development of the coupling element formulation presented in Chapters 4 and 5, due to its capability of enforcing the constraints effectively and the control it offers over accuracy and convergence. The shortcoming related to the increased computing demand is minor, since coupling is typically performed over a relatively small portion of the problem domain.

### 2.3.2 Contact/coupling interface discretisation

A comprehensive review of the methods employed for the contact or coupling interface discretisation is given herein. Consideration is given to methods formulated within the framework of the Lagrangian and penalty approaches for the constraint enforcement, in accordance to what has been discussed in Sub-section 2.3.1

The general setting of the discrete contact/coupling problem, encompasses two independent deformable heterogeneous bodies  $\Gamma^{(1)}$  and  $\Gamma^{(2)}$  discretised with FEs, sharing an interface  $\Gamma_c$ . The constraint enforcement is achieved by virtue of an independent LM field introduced over  $\Gamma_c$ , which renders this a constrained equilibrium problem where both the displacement and LM fields need to be determined. Such discrete problems, where two independent fields are sought, are classified as mixed FE problems (Brezzi & Fortin, 1991).

This type of constrained equilibrium problem is referred to as a saddle point problem in a formal mathematical sense (Wriggers, 2006), and it requires the fulfilment of a set of stability conditions, alongside the passing of the contact patch test (Taylor & Papadopoulos, 1991), by the employed discretisation scheme, for solution uniqueness to be guaranteed (Bathe, 2001). The former encompasses the ellipticity condition, which is generally straightforward to satisfy, as well as the inf-sup condition, also commonly referred to as Ladyzhenskaya–Babuška–Brezzi (LBB) condition (Brezzi & Fortin, 1991). All contact/coupling interface discretisation methods described herein are formulated using interpolation functions for the displacement and LM fields which allow the LBB condition to be fulfilled, thus ensuring stability and uniqueness of the constrained equilibrium problem solution. The detailed review of the LBB conditions in mixed FE methods for contact problems from a mathematical viewpoint lies outside of the scope of the present thesis, however the interested reader is referred to Kikuchi and Oden (1988), Brezzi and Bathe (1990) and Bathe (2001).

The following classes of methods are discussed hereafter: (i) node-to-node, (ii) node-to-segment, (iii) node-to-surface, and (iv) segment-to-segment/mortar.

### 2.3.2.1 Node-to-node methods

Amongst the first and most simplistic approaches for the treatment of mixed FE problems where contact/coupling constraints are introduced is the node-to-node class of methods, encompassing the constraint enforcement on a purely nodal basis.

Early applications of the method were presented by Francavilla and Zienkiewicz (1975) for frictionless contact problems. Later on, the method was expanded to gap coupling elements by Stadter and Weiss (1979), where a stress invariance principle is enforced over the interface domain to achieve coupling, while a more extensive investigation of the formulation, the integration aspects and the various limitations of such elements can be found in Kikuchi and Oden (1988).

Evidently, the node-to-node class of methods is only applicable to contact/coupling problems where conforming FE meshes are employed for the discretisation of  $\Gamma^{(1)}$  and  $\Gamma^{(2)}$  over the interface  $\Gamma_c$ . In the case of contact problems, in particular, its applicability is limited to cases

of geometrically linear contact associated with small deformations, such that the contact domain is invariant to the body deformations and no relative nodal slip occurs (Wriggers, 2006). In the context of this research, consideration is given to methods applicable to non-conforming meshes, which are discussed hereafter. The node-to-node class of approaches is only mentioned here on account of completeness, and is thus not elaborated further.

### 2.3.2.2 Node-to-segment methods

The necessity of overcoming the shortcomings of the node-to-node approach, namely the requirement for nodal alignment, proportionality of element dimensions and FE discretisation pattern conformity in regions of contact, shifted subsequent research efforts towards the establishment of systematic discretisation approaches for non-conforming FE meshes. One of the most widely employed class of methods is the node-to-segment (NTS) approach, which has been extensively documented in the existing literature and incorporated in many commercial FE codes.

The NTS approach encompasses the constraint enforcement in a strong sense over the interface, between nodes on one region, commonly referred to as nodal collocation points, and a set of discretised segments on the other. The commonly adopted approach embodies: (i) the region classification as master and slave; (ii) the master and slave region discretisation into master and slave segments over the interface; (iii) the identification of a unique master segment associated with each slave node; and (iv) the constraint enforcement over the established set of coupling elements, where each comprises 1 slave node and 2 master nodes, corresponding to the master segment edge nodes (Zavarise & De Lorenzis, 2009b). The concept underlying the NTS interface discretisation approach is schematically illustrated in Figure 2.6.

The NTS approach field of application extends to large deformation contact problems, while its implementation in commercial FE codes effectively facilitates the constraint treatment when an automated meshing procedure for independent regions is adopted, potentially resulting into non-conforming meshes. The algorithmic process underpinning the NTS approach can be effectively applied for the constraint treatment in a pure geometric sense, i.e. non-penetration enforcement at nodal collocation points, or in conjunction with a nonlinear material constitutive or friction law (Zavarise & De Lorenzis, 2009b).

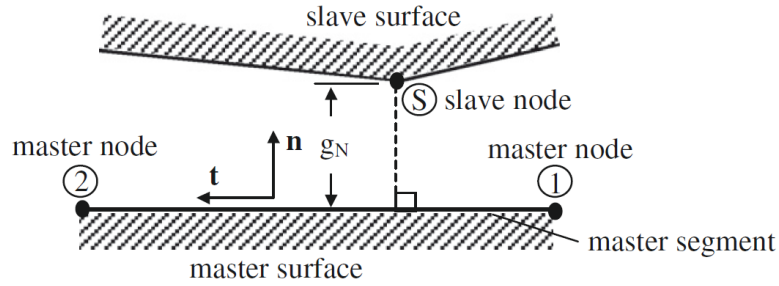


Figure 2.6: Node-to-segment (NTS) interface discretisation approach (Zavarise & De Lorenzis, 2009b)

A considerable amount of early applications of the NTS approach can be identified in the contact literature, focusing primarily on the establishment of a systematic approach for the coupling element identification and the constraint enforcement on a nodal basis. A primal implementation of the method in 2-D impact-contact problems was presented by Hughes *et al.* (1976). Simo *et al.* (1985) established a systematic methodology for the treatment of contact constraints, encompassing the use of the NTS approach for the interface segmentation and a perturbed LM formulation for the constraint enforcement, which achieves superior accuracy to other traditional penalty approaches. Hallquist *et al.* (1985) presented a similar methodology for the systematic identification of the unique sets of master segments-slave nodes over the interface, which has been implemented in the FE software DYNA2D. Bathe and Chaudhary (1985) extended the approach to 2-D frictional and large-deformation contact problems, using a LM formulation for the constraint enforcement over the interface, with Wriggers *et al.* (1990) applying it later on in the context of large-deformation dynamic impact-contact problems, encompassing a friction nonlinear interface constitutive law. Papadopoulos and Taylor (1992) established a geometrically consistent and directionally unbiased methodology for the systematic identification of contact segments using the NTS approach, in cases of arbitrary motion of the contacting bodies. The approach was employed in conjunction with a mixed penalty formulation, incorporating both the displacement and pressure fields of the contacting bodies, and was shown to be efficient for the treatment of general 2-D frictionless contact problems.

Despite the NTS approach providing a straightforward and systematic algorithmic process for the contact/coupling segment identification and the constraint enforcement in a discrete sense, it suffers from a variety of well-documented shortcomings. Primarily, the method is by definition sensitive to the domain classification as master and slave. This is attributed to the

constraint enforcement in a strong sense at the nodal locations of the slave domain, which are evidently different in the case of interchanged slave-master domains. The constraint enforcement on a slave-node basis results into the non-minimisation of gaps, as well as penetration occurrences, due to the master nodes penetration in the slave domain not being explicitly checked, as illustrated in Figure 2.7 (a). A widely-employed remedy for the alleviation of such inaccuracies is the two-pass NTS method, encompassing the gap evaluation based on a double identification of the set of contact elements, through an interchange of the slave and master domains (Taylor & Papadopoulos, 1991). Despite circumventing the penetration shortcomings, the double-pass NTS approach leads to potential over-constraining, thus impacting the accuracy and stability of the global constrained equilibrium problem solution (Puso, 2004).

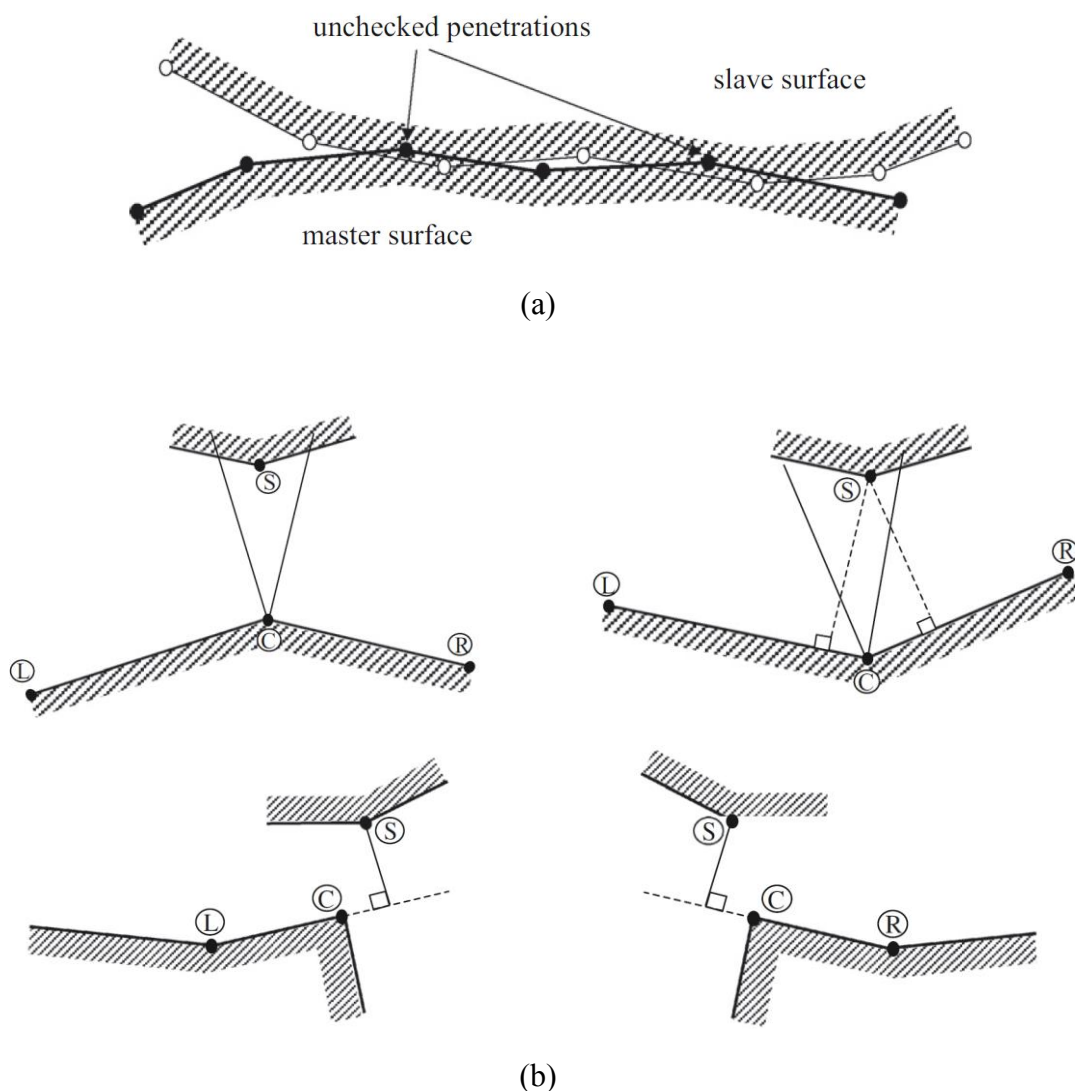


Figure 2.7: (a) Nodal penetration due to local nodal constraint enforcement, (b) slave node projection inexistence and multiplicity (Zavarise & De Lorenzis, 2009b)

Besides the result sensitivity to the surface classification, instabilities and convergence issues arise in cases where a slave node is projected either on multiple or to none of the master segments. These issues have been recently revisited and addressed by Zavarise and De Lorenzis (2009b), by means of a systematic approach for the treatment of slave node projection multiplicity or inexistence cases, as illustrated in Figure 2.7 (b).

The shortcomings of the NTS approach extend beyond discretisation inaccuracies that can be addressed with the workarounds discussed above, including the inability of the one-pass NTS approach of passing the standard contact patch test. The patch configuration of the latter was originally proposed by Taylor and Papadopoulos (1991) and is illustrated in Figure 2.8 (a), while several other authors have employed alternative configurations based on the original proposal in later years, as illustrated in Figure 2.8 (b). The issue arises when a LM formulation is employed for the constraint enforcement, with the accuracy further deteriorating with a penalty formulation. Several authors have re-visited the issue to address the aforementioned inaccuracies, due to the popularity of the approach and its consistent implementation in commercial FE codes. A number of workarounds have been proposed for the passing of the standard contact patch test by several authors, including Crisfield (2000), El-Abbasi and Bathe (2001), and more recently Zavarise and De Lorenzis (2009a).

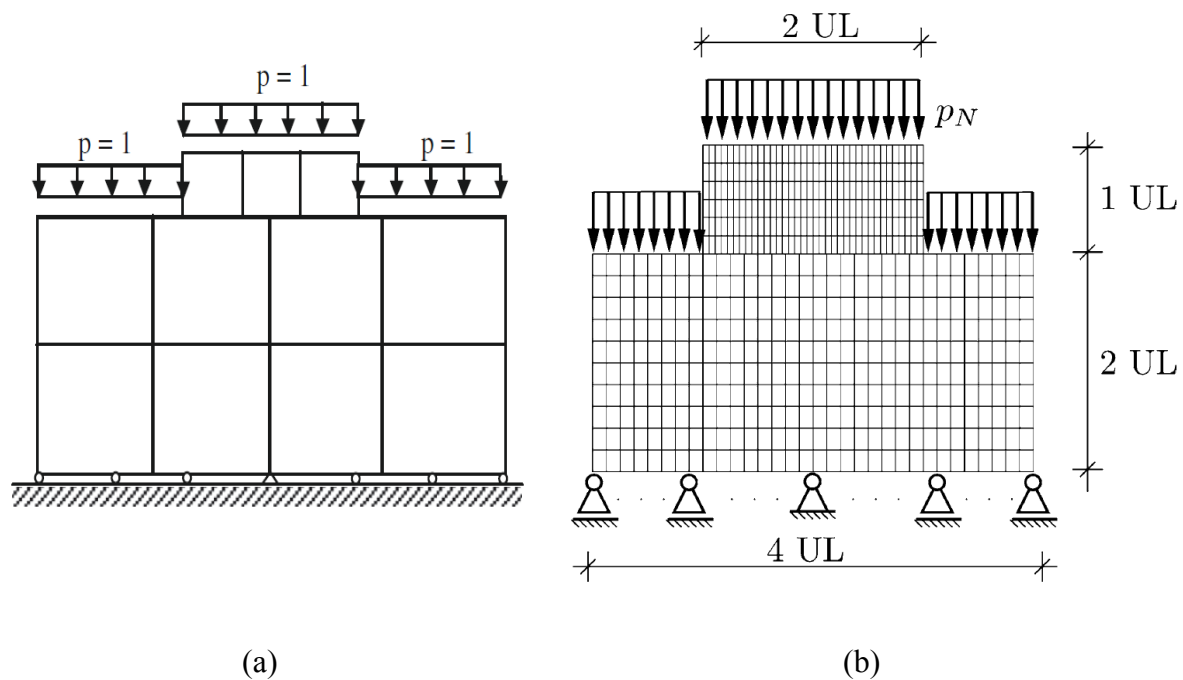


Figure 2.8: (a) Standard contact patch test original configuration (Taylor & Papadopoulos, 1991), (b) alternative contact patch test configuration (Fischer & Wriggers, 2005)

### 2.3.2.3 Node-to-surface methods

The extension of the NTS approach to 3-D contact problems is facilitated in the most general case via coupling of the slave nodes with the surface of the master domain FEs over the interface. This discretisation approach is referred to as node-to-surface and was first developed by Parisch (1989). A consistent tangent stiffness matrix for 3-D nonlinear frictionless contact problems with large deformations was established by the author, facilitating contact between solid and shell domains via a contact element with 3 or 4 nodes, consistent with the employment of LM and penalty formulations for the constraint enforcement. The method was later extended to incorporate a Coulomb frictional constitutive law over the surface by Perić and Owen (1992), using a penalty formulation for the constraint treatment and an approximation of the aforementioned consistent tangent stiffness matrix formulation. Both the frictionless and frictional cases discussed above achieve quadratic convergence when a Newton-Raphson scheme is employed for the incremental nonlinear solution procedure.

A robust and stable approach for the consistent treatment of 3-D nonlinear frictionless and frictional contact problems, with general applicability to a wide range of 2-D and 3-D deformable or rigid domains discretised with any FE type, has been presented by Laursen and Simo (1993b). The method owes its generality to the adoption first of a consistent continuum-based formulation for the derivation of the contact kinematics and underlying equations, and its subsequent expression in a discrete mixed FE form.

Parisch and Lübbing (1997) expanded their initial approach at a later point by developing a contact element for the treatment of 3-D frictionless and Coulomb frictional nonlinear contact problems in the most general context. The coupling element enables coupling of virtually any surface discretised with FEs, using a penalty formulation for the constraint treatment, and achieves quadratic convergence characteristics and enhanced numerical stability.

Notwithstanding the significant enhancements of the method discussed above, the 3-D node-to-surface approach inherits the shortcomings of the corresponding 2-D method and is thus rendered susceptible to the inaccuracies discussed in the preceding sub-section.

#### 2.3.2.4 Interface discretisation into contact/coupling segments: mortar methods

A widely employed class of 2-D contact/coupling interface discretisation methods is the segment discretisation approach, encompassing the identification of a unique set of segment couples on the coupled discretised domains, interacting over their shared interface. Different to the NTS methods, where the non-penetration constraint is enforced on a nodal basis, in the current approach this is achieved in a continuous weak sense within each distinct segment couple, over the part of the domain shared by both segments. The formulation of the method provides a systematic framework for the treatment of mixed FE coupling/contact problems, including cases of independently discretised bodies with non-conforming meshes.

The first formal presentation of the method for frictionless small-deformation 2-D contact problems can be found in Simo *et al.* (1985), where a perturbed LM formulation is employed for the constraint enforcement over the interface segments, using piece-wise constant and linear interpolations for the displacement and LM fields, respectively. Alternative approaches based on the augmented LM and penalty formulations were also explored by the same authors (Wriggers & Simo, 1985), as well as by Landers and Taylor (1986), while the extension of the concept to frictional problems was later facilitated by Simo and Laursen (1992). The fundamental concept of the interface discretisation into contact/coupling segments is schematically illustrated in Figure 2.9 (a).

The segment discretisation approach progressively gained significant attention, due to the systematic employment of automatic meshing tools in commercial FE codes and the development of domain decomposition approaches to exploit modern parallel computing architectures (Wriggers, 2006). This led to the development of a new class of approaches, referred to as mortar methods, the mathematical formulation of which presents a natural fit for mixed FE coupling/contact and domain decomposition problems with non-conforming meshes.

Mortar methods are applicable to both contact and coupling problems with non-conforming FE meshes and are underpinned by the employment of a LM-based formulation for the constraint enforcement, in accordance with Eqs. (2.3), (2.5) or (2.6). The latter encompasses the definition of LMs at discrete locations and the use of interpolation functions to obtain a continuous field over the interface. The mortar method has been shown to achieve optimal convergence (Laursen *et al.*, 2012) as well as pass the contact patch tests by design for planar surfaces (Puso & Laursen, 2004a). A number of different variants of the method have been established over



the years, corresponding to different combinations of two principal aspects: (i) the selection of the reference surface, (ii) the selection of interpolation spaces for the displacement and LM fields.

Two distinct cases can be identified in relation to the selection of the reference surface: (i) an independent intermediate surface between the two bodies is established, referred to as the mortar surface, and the interpolated LM field is defined on it; and (ii) the part of the surface of either of the two bodies over the contact/coupling interface is selected as the mortar surface, and the interpolated LM field is defined on the surface of the other body, referred to as the non-mortar surface.

The discretisation of the displacement fields  $\mathbf{u}^{(1)}$  and  $\mathbf{u}^{(2)}$  of the two bodies, alongside the specification of the respective interpolation space within the constraint function  $\mathbf{g}(\mathbf{u}^{(1)}, \mathbf{u}^{(2)})$ , are a priori limited to the nodal locations and the respective shape functions employed for the distinct field interpolations over the discretised domains. On the other hand, the discrete locations of LMs, also commonly referred to as collocation points, as well as the interpolation space of the LM field, can be defined independently, subject to the fulfilment of the LBB inf-sup conditions for global stability discussed earlier (Wriggers, 2006). It has been shown that appropriate selection of the LM interpolation functions leads to fulfilment of the LBB conditions, and hence to a stable discretisation approach from a mathematical viewpoint (Wohlmuth, 2000). A common approach for cases where the reference surface is defined on one of the two bodies is based upon the definition of collocation points at nodal locations on the non-mortar surface, alongside the use of linear, quadratic or higher order conventional or dual shape functions for the LM field interpolation. This has been generally shown to lead to stable interpolation schemes (Wohlmuth, 2000; Flemisch & Wohlmuth, 2007).

From a mathematical viewpoint, the formulation of mortar methods can be traced back to Bernardi *et al.* (1990). The formal establishment of the method a few years later in the context of domain decomposition can be found in the work of Bernardi *et al.* (1993), where a piecewise linear LM formulation based on the non-mortar surface displacement field shape functions is employed. The implementation of the mortar method in 3-D FE procedures was facilitated by Belgacem and Maday (1997), while its extension to contact problems using LM formulations for the constraint enforcement over the interface was elaborated by Belgacem *et al.* (1998) and Belgacem (1999).

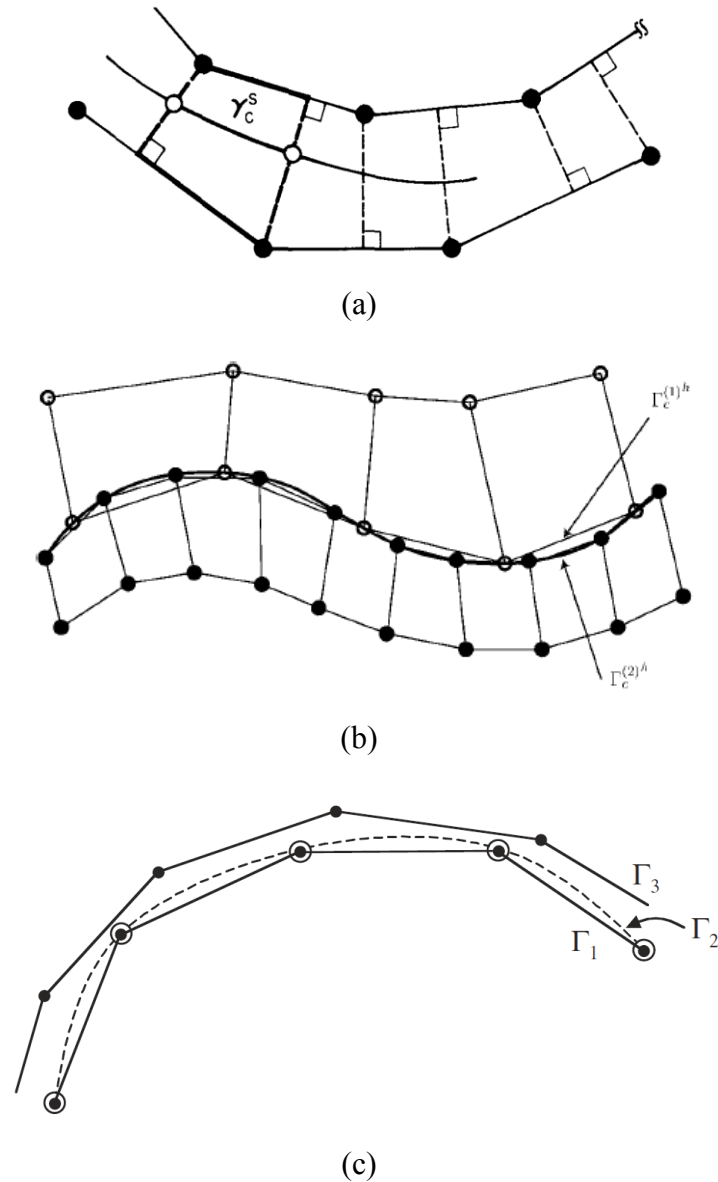


Figure 2.9: (a) Segment discretisation of 2-D contact/coupling interface (Simo *et al.*, 1985), (b) non-overlapping of discrete geometric surface descriptions for non-conforming meshes, (c) smooth intermediate mortar surface (Puso, 2004)

McDevitt and Laursen (2000) established a mortar approach for mesh tying in 2-D frictional contact problems based on the employment of an intermediate kinematically independent mortar reference surface. On the basis of this approach, Laursen and Heinstejn (2003) established an analogous method for coupling of non-conforming meshes, to alleviate inaccuracies arising from the non-overlapping of these in the undeformed configuration, as illustrated in Figure 2.9 (b). The method guarantees passing of the patch test, which had not been previously explicitly established. The employed approach is similar to the three-field formulation originally introduced by Dohrmann, *et al.* (2000), encompassing the introduction

of the independent body strain fields, i.e. displacement field gradients, in the constraint equations along the interface. Accordingly, the method is based on the introduction of an additional LM field along the coupling interface, to facilitate the consistent treatment of coupling constraints associated with the independent stress fields induced by the non-conforming surfaces.

A few years later, Rebel *et al.* (2002) formulated a novel approach along the same lines, encompassing an adaptive contact frame with independent kinematic DOFs. The frame acts as a third medium, facilitating contact force transferring between the non-conforming meshes in an indirect fashion, where constraint enforcement between the frame and each of the two surfaces is achieved using LMs, without violation of the global system equilibrium. Principal merits of the method include the passing of the contact patch test by design, due to the contact frame being associated with an independent set of kinematic DOFs, as well as the localisation of the integration to each side of the frame, which enables its establishment using only nodal data from the independent bodies. The method is thus invariant to the employed FE software and straightforward upgrade of existing FE codes can be easily facilitated. A similar formulation based on the frame concept has been recently proposed by Song *et al.* (2015), implemented in the form of a gap element and underpinned by the employment of a localised LM formulation for constraint enforcement.

Notwithstanding their numerical robustness, accuracy and the consistent treatment of coupling or contact between non-conforming meshes allowing the patch test passing, the methods discussed above impose an additional increase in the global system kinematic or additional DOFs, due to the introduction of respective independent fields over the intermediate surface. Despite this being seemingly unimportant for small 2-D contact problems, the efficiency of such methods is compromised in 3-D large-scale contact/coupling applications. The focus will henceforth be shifted to two-field methods, typically encompassing the original surface classification as mortar and non-mortar, as discussed earlier.

The basic formulation of the mortar method for 2-D frictionless contact and coupling problems, encompassing the use of the standard LM and penalty formulations for constraint enforcement, discussed in Sub-sections 2.3.1.1 and 2.3.1.2, respectively, has been presented by Fischer and Wriggers (2005) and Wriggers (2006). The method is summarised in a stepwise fashion hereafter: (i) classification of the original surfaces as mortar and non-mortar; (ii) establishment of distinct couples of interactive segments on the two coupled surfaces, over the

coupling/contact interface; (iii) establishment of an independent LM field on each segment of the non-mortar surface, using the nodal locations as collocation points and employing the non-mortar surface displacement field interpolation functions, or a dual approach (Wohlmuth, 2000) for LBB inf-sup condition fulfilment; (iv) numerical integration of the coupling/contact terms using Gaussian quadrature, based on the definition of Gauss Point (GPs) on the non-mortar surface and the employment of an algorithmic treatment for their projection identification on the mortar surface. The concept is schematically illustrated in Figure 2.10. The extension of the approach to 2-D Coulomb-frictional large-deformation contact problems was presented by Tur *et al.* (2009).

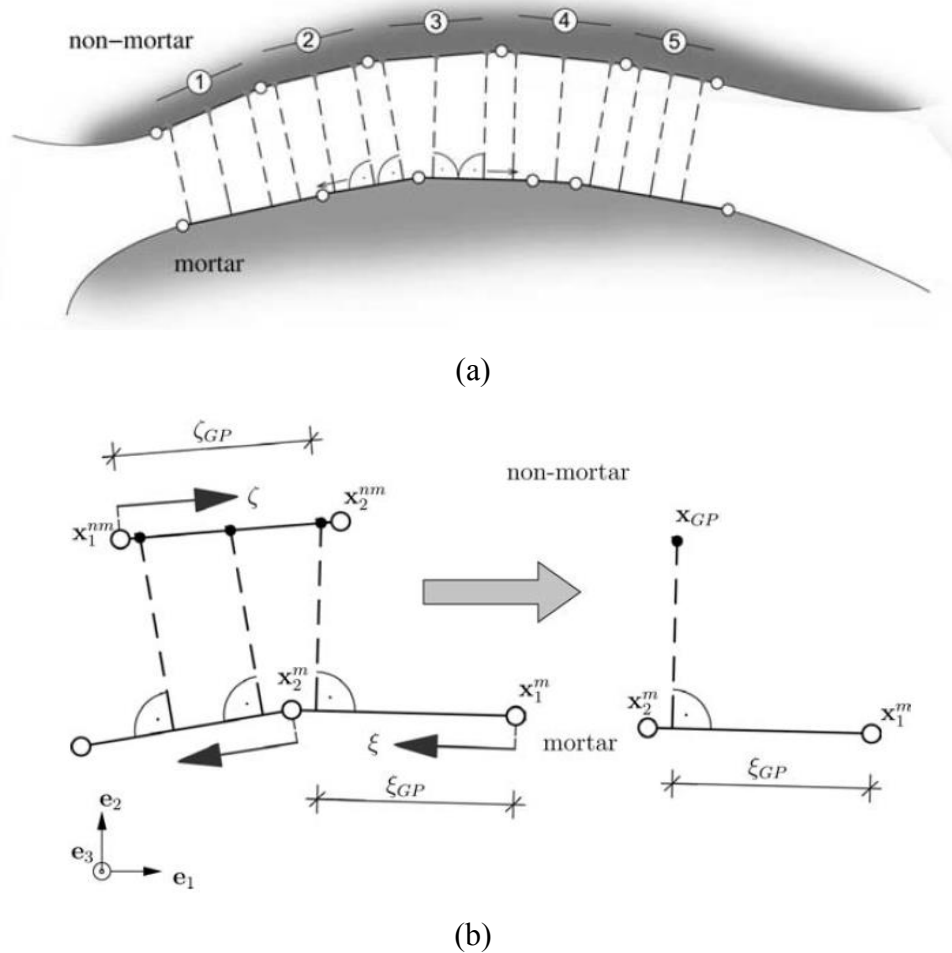


Figure 2.10: (a) Segment discretisation of 2-D mortar and non-mortar surface, (b) algorithmic treatment of Gaussian quadrature via projection (Fischer & Wriggers, 2005)

The formulation of the above method naturally leads to its implementation via a coupling/contact element, where each element corresponds to an interacting segment couple, identified by virtue of the GP projections from the non-mortar to the mortar segments. Dias *et*

*al.* (2015) presented an enhancement of the basic mortar formulation discussed above, using a hierarchic approach for the definition of the displacement and LM field interpolation spaces. A higher-order contact mortar element is thus obtained, encompassing an identical approach for the definition of the LMs at the non-mortar segments nodes and hierarchic shape function for the LM field interpolation.

Wohlmuth (2000) mathematically formulated the concept of a dual basis for the LM field on a segment-to-segment basis, using one of the two original surfaces as the mortar surface. The condition of duality for the displacement and LM field interpolation spaces over an interface segment  $\Gamma_c$  can be stated as follows:

$$\int_{\Gamma_c} N_j \bar{N}_k \, d\Gamma_c = \delta_{jk} \int_{\Gamma_c} N_j \, d\Gamma_c \quad (2.8)$$

where  $N_j$  are the displacement field interpolation functions for node  $j$  on the non-mortar side,  $\bar{N}_k$  are the dual basis functions for the LM field interpolation along  $\Gamma_c$  and  $\delta_{jk}$  is the Kronecker delta. The dual approach allows for the diagonalisation of the tangent stiffness matrix terms associated with the additional LM DOFs, thus enabling the direct evaluation of these from the displacement field, by virtue of inversion of a diagonal matrix within an iterative step of the incremental solution procedure. Owing to the computational benefits discussed above and its non-impingement on the optimality of the mortar method, the dual LM approach received attention by several authors and shaped a substantial part of the available literature on mortar methods. The dual basis for the LM shape functions, obtained for a piece-wise linear original interpolation, is illustrated in Figure 2.11.

Contrary to the standard LM approach, the use of dual LM spaces in problems involving substantially curved interfaces results in deteriorated accuracy and robustness, particularly when the individual surface mesh density varies considerably. These inaccuracies have been addressed for linear elements by Flemisch *et al.* (2005), as well as for quadratic elements by Popp *et al.* (2012), with extensions to contact problems in the latter case. Moreover, Popp *et al.* (2013) implemented a series of enhancements based on biorthogonalisation of the LM spaces and the employment of a Petrov-Galerkin LM approach, to remedy algorithmic shortcomings of the original dual LM method related to its robustness and consistency in 3-D contact problems. Extensions of the dual LM method to iso-geometric analysis have been recently presented by Seitz *et al.* (2016), however this lies outside of the scope of this work.

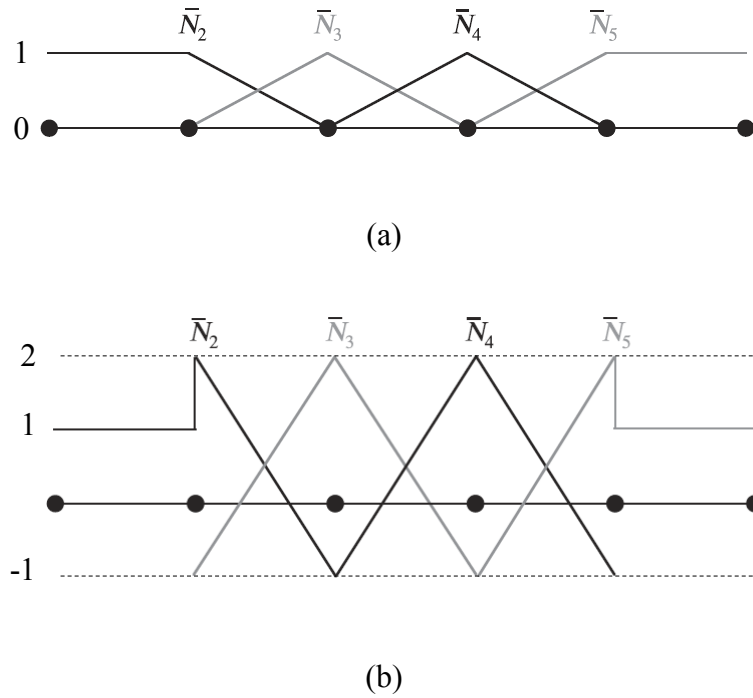


Figure 2.11: LM shape function definition along 2-D interface segments: (a) Standard piece-wise linear, (b) dual piece-wise linear (Puso, 2004)

The expansion of the mortar approach to 3-D mesh tying, i.e. coupling, problems of non-conforming curved surfaces discretised with linear hexahedral elements, was undertaken by Puso and Laursen (2003), encompassing a systematic algorithmic treatment of the coupling term integration using a projection scheme between non-overlapping surfaces. A comparison was conducted between the original mortar approach introduced by Bernardi *et al.* (1993), comprising a piece-wise linear LM interpolation, the dual LM formulation introduced by Wohlmuth (2000), as well as a piece-wise constant discontinuous LM field approach, and the attainment of a respective optimal convergence rate was demonstrated in all cases. The approach was later enhanced to achieve invariance to rigid body rotations for large-deformation 3-D mixed FE problems (Puso, 2004), which was proven to be achieved only when the constraints are enforced on both the displacement and discrete geometry fields. This is particularly important for the development of the coupling element proposed in this work, as discussed in Chapters 4 and 5. Enhancements were also presented to alleviate stiffening effects arising from the mesh non-conformity, based on the establishment of an intermediate mortar surface with distinct DOFs, corresponding to the Hermite smoothing of either of the original surfaces, and the treatment of both original surfaces as non-mortar, as shown in Figure 2.9 (c) (Puso, 2004).

The method was also extended to large-displacement 3-D contact problems involving linear elements by Puso and Laursen (2004a; 2004b), later incorporating quadratic elements (Puso *et al.*, 2008), and the superiority of the approach in comparison with 3-D NTS methods was established in both cases. An adaptation of the method using a mixed-penalty duality approach for 3-D contact problems, established on the basis of the augmented LM formulation, was presented by Cavalieri and Cardona (2013), where the method efficiency in respect of passing the contact patch test and its robustness for large displacement contact was demonstrated.

A coupling element formulation for non-conforming surfaces was developed by Minga *et al.* (2018), based on the 3-D mortar approach for mesh tying originally presented by Puso (2004). The developed formulation utilises a hierarchic augmented LM approach for constraint enforcement between linear and quadratic solid FEs, alongside a systematic algorithmic treatment for the GP projections over the coupling interface, and its effectiveness was demonstrated in the context of mesoscale partitioned modelling of masonry structures.

Very recently, Farah *et al.* (2018) established a systematic approach for fictional contact problems with non-smooth interfaces, sharing a number of fundamental principles with the developed coupling element formulation presented in Chapters 4 and 5 of this thesis. The established approach facilitates contact constraint enforcement at the point, edge and surface levels, as well as the transition between these cases, and employs mortar method principles for the interface discretisation, with consideration being given to the surface discretisation with linear FEs. The method further employs a dual LM formulation with a penalty regularisation term, for cases of non-parallel edge-to-edge contact.

One of the governing factors for the accuracy and robustness of all mortar variants discussed so far is the adopted scheme for the coupling term integration. In the vast majority of the existing literature, integration is undertaken using Gaussian quadrature, with the GPs being commonly defined over the non-mortar and projected to the mortar surface. Two principal algorithmic treatments for the GP projections in 2-D and 3-D coupling and contact problems exist, commonly referred to as segment-based and element-based integration schemes. Examples of segment- and element-based integration schemes can be found in Puso and Laursen (2004a) and Fischer and Wriggers (2005), respectively. A comprehensive study of the principal aspects of these integration schemes, alongside a comparative evaluation of their performance, was conducted by Farah *et al.* (2015), where qualitative guidance on the selection of the appropriate integration order is also provided for 2-D and 3-D problems. As expected,

the segment-based integration scheme was identified as substantially more efficient in comparison to the element-based approach, from a computing demand viewpoint. Nonetheless, contrary to the element-based approach, it fails to achieve exact or accurate integration in cases of quadratic interpolations and frictional problems. This issue is of primary importance in the context of the coupling formulation developed in this work, as discussed in Section 4.7, where consideration is given to both integration schemes, and their performance is compared.

Despite the development of the mortar method being underpinned by a LM formulation for the constraint treatment, alternative approaches based on the Nitsche method, discussed earlier in Sub-section 2.3.1.5, have also been proposed. A domain decomposition approach based on the Nitsche method, with extensions to coupling of non-conforming meshes, has been mathematically formulated by Becker *et al.* (2003), while Wriggers and Zavarise (2008) implemented a 2-D frictionless contact formulation within the framework of linear elasticity. As discussed, the employment of the Nitsche method enables the establishment of a purely displacement-based formulation, which does not require the introduction of an independent LM field to facilitate coupling or contact between non-conforming meshes, thus substantially reducing the global number of unknowns for large-scale applications. Nonetheless, its extension to nonlinear problems is rendered cumbersome, due to the requirement of establishing the traction field of the independent bodies over the interface using complex constitutive expressions.

Recent developments in the field of computational mechanics led to the establishment of methods extending beyond traditional FE approaches, such as iso-geometric analysis. The wide application spectrum of mortar methods in the framework of contact and coupling problems, motivated its incorporation in iso-geometric analysis by several authors; however, this is outside of the scope of the present thesis. The interested reader is referred to Kim and Youn (2012), Florez and Wheeler (2016) and Seitz *et al.* (2016).

### 2.3.2.5 Comparative evaluation of interface discretisation methods

As previously stated, one of the main objectives of this work is the development of a novel approach for surface-to-surface coupling along a line, which has not been previously addressed by researchers. A summary of the main features for the interface discretisation methods



presented in the preceding sub-sections is given herein from the perspective of their suitability as a basis for the developed coupling approach.

Node-to-Node approaches are only applicable to coupling of conforming meshes, with nodal alignment being a prerequisite, and are thus not considered.

NTS approaches enforce the constraints between distinct nodal locations (collocation points) on the master surface and a set of 2-D segments or 3-D surfaces on the slave surface in a strong sense. This class of methods is sensitive to the surface master/slave classification and is associated with non-minimal gaps and potentially substantial penetration of the two surfaces. Two variants of the methods exist, namely the single and double pass, where the former does not pass the contact patch test and the latter potentially leads to over-constraining.

Segment-to-segment and mortar methods enforce the constraints between a set of interacting couples of 2-D segments or 3-D surfaces in a continuous sense. This class of methods achieves optimal convergence with LM or penalty formulations and passes the contact patch test by design for planar surfaces. The establishment of the collocation points to coincide with nodal locations guarantees fulfilment of the LBB inf-sup conditions and leads to a stable discretisation scheme, for both conventional and dual LM shape functions. The performance of mortar methods is governed by the adopted algorithmic treatment for the GP projections from the non-mortar to the mortar surface, when Gaussian quadrature is employed, with a segment-based approach failing to achieve exact integration for quadratic elements, even with the employment of a large number of GPs, in contrast to the element-based approach. The two distinct variants of mortar methods, identified on the basis of the reference surface selection, are discussed separately hereafter.

The first variant, encompassing the establishment of an intermediate fictitious mortar surface, passes the patch test by design and provides a stable discretisation scheme with optimal convergence characteristics. However, the additional unknowns introduced to the global system, associated with the additional independent LM or displacement fields of the intermediate mortar surface, adversely affect the computational efficiency of the method for large-scale applications.

The second variant, encompassing the selection of one of the two surfaces as mortar and the establishment of an independent LM field on the non-mortar surface, has been proven to achieve enhanced accuracy, stability and optimal convergence in a wide range of 2-D and 3-D

applications, including large-deformation contact and coupling problems. The employment of dual spaces for the LM field interpolation leads to increased computational efficiency, however it suffers from deteriorated performance for curved surfaces, thus requiring the incorporation of complex algorithmic treatments to remedy these. The employment of a Nitsche approach allows for the elimination of the additional DOFs associated with the LMs, however it inherits the entanglements of the Nitsche formulation discussed in Sub-section 2.3.1.5 in large-deformation nonlinear problems, in relation to the establishment of the independent body stress fields over the interface.

Taking the above into consideration, the coupling element formulation is developed as an enhancement of the 3-D mortar approach, which facilitates continuous constraint enforcement over the 1-D interface. NTS approaches are not applicable in this context, due to the 1-D interface traversing the discretised domains in an arbitrary orientation in the general problem setting, and thus not passing through the nodes of all actively coupled FEs.

The introduction of an intermediate fictitious mortar surface and its discretisation into segments is an attractive option, enabling the substantial geometric complexity associated with the interface projection on the surfaces and the respective intersection identification to be overcome. Nonetheless, it does not guarantee stability of the discretisation scheme, while further complicating the algorithmic treatment of the numerical integration scheme, comprising the identification of GP projections on both surfaces. Therefore, an adaptation of the second mortar variant has been adopted, encompassing the definition of the interface independent of the surfaces and the establishment of the slave segments based on the intersections of its projection on the slave surface with the respective FE mesh.

As discussed in Sub-section 2.3.1.6, an augmented LM formulation is deemed more efficient in comparison with other alternatives, and is thus adopted in view of its enhanced accuracy and the overcoming of potential floating-domain ill-conditioning with the use of a moderate penalty parameter. The employment of a LM/penalty-based formulation enables the optimal convergence of the mortar method to be preserved, while the interpolation of both the displacement and LM fields using the same distinct collocation points enables for a stable discretisation to be achieved and coupling patch tests to be passed, as will be discussed in detail in Chapters 4 and 5. The displacement and LM field interpolation is performed within an iso-parametric framework, using conventional polynomial shape functions, while a hierarchic approach is also allowed for. Taking due account of the coupling element formulation

development for curved shell surfaces, the adoption of a dual LM basis has not been considered, in view of the requirement for special algorithmic treatment implementation to remedy inaccuracies of the dual approach related to curved surfaces.

The interface discretisation procedure, underpinned by the fundamental principles of the mortar approach, is outlined hereafter: (i) surface classification as slave (non-mortar)/master (mortar); (ii) establishment of interface projection on the slave and master surfaces; (iii) progressive interface segmentation on each surface, based on its intersection with the edges or passing through the nodes of the respective FE mesh; (iv) interface discretisation into coupling elements, encompassing a set of interacting slave and master segments, based on the active projection of the GPs defined on the slave segments to the mortar segments; (v) constraint enforcement at the element level using an augmented LM formulation, with the LMs defined at collocation points, corresponding to the edge points of the slave segments. For the coupling term integration, an element-based integration approach has been adopted. Finally, the element enables the employment of both piece-wise linear and quadratic shape functions for the LM field interpolation.

## 2.4 Concluding remarks

A comprehensive literature review has been presented in this chapter, which serves the dual purpose of providing: (i) an insight into the existing applications, as well as the modelling and analysis methods, of metal honeycomb core sandwich composites; and (ii) a broad review on existing coupling methods in computational mechanics.

In the first part of the literature review, an overview of the existing analytical, experimental and numerical investigations on metal honeycomb sandwich composites has been provided. The limited consideration given to the modelling of large-scale composites with honeycomb configurations has been highlighted, and the necessity of establishing an efficient HF nonlinear analysis approach for this class of composites has been argued for. Finally, a brief overview of the principal aspects underpinning the HF nonlinear FE modelling approach has been given, with further elaboration provided in Chapter 3.

In the second part of the literature review, an extensive review of coupling methods facilitating discrete kinematic constraint enforcement between non-conforming FE meshes has been

provided, aimed at establishing a suitable foundation for a novel treatment of surface-to-surface coupling along a line in the present work. Consideration has been given to two classes of methods: (i) mathematical optimisation formulations for the constraint treatment in the context of the mixed FE global equilibrium problem; and (ii) interface discretisation schemes for the constraint enforcement facilitation in a discrete sense. As discussed in Sub-sections 2.3.1.6 and 2.3.2.5, an augmented LM approach and a suitably enhanced variant of the 3-D mortar method will be developed for this purpose, as elaborated in Chapters 4 and 5.

# Chapter 3

## High-Fidelity Nonlinear Analysis of Composite and Sandwich Structures

### 3.1 Introduction

All-metal composite structural systems are widely employed in modern infrastructure, due to their intrinsically high specific strength and stiffness providing enhanced performance and robustness characteristics with minimal structural weight. A broad application spectrum can be identified for this structural class, with some of the most prominent structural applications encompassing: (i) composite floor systems, comprising corrugated or planar steel plates overlying a grillage system of beams, plate girders and floor braces; (ii) bridge decks comprising plate girders; (iii) sandwich composites employed in large-scale, weight-critical, structural and naval applications; (iv) composite shell structures employed as roof systems or in silo and storage facilities; and (v) composite and sandwich blast walls.

All-metal composite structures comprise independent deformable plated components coupled along weld lines, and hence their response is characterised by the manifestation and interaction of various local buckling phenomena in several locations over the structural domain. The interaction of these forms of local instability, along with the spread of plasticity in the large displacement range, result in a variety of complex phenomena which govern the global structural response and dictate the encountered failure modes. An accurate response prediction is typically required for the development of novel systems and for advanced applications, such as in the case of extreme accidental blast loading where the system energy dissipation must be quantified.

In this chapter, an accurate and robust high-fidelity (HF) nonlinear Finite Element (FE) modelling strategy for all-metal composite systems is presented. The proposed modelling approach utilises recently developed Reissner-Mindlin quadratic curved shell elements (Izzuddin & Liang, 2016; 2017), with two principal aspects underpinning their local formulation: (i) a co-rotational framework for the local element coordinate system definition, enabling the exclusion of rigid body rotations from the local element response and the establishment of simple kinematic constitutive relationships (Izzuddin & Liang, 2016); and (ii) a hierarchic optimisation approach for the relief of inaccuracies arising from shear, membrane and distortion locking phenomena, typically encountered in shell elements due to small shell thickness, curved shapes and the employment of isoparametric mapping for distorted element shapes, respectively (Izzuddin & Liang, 2017).

With the aim of its application to large-scale systems, the modelling strategy also utilises domain partitioning capabilities based on a novel dual super-element concept (Jokhio & Izzuddin, 2015), allowing for scalable parallel processing in High Performance Computing (HPC) systems with distributed memory. Partitioned modelling renders extensive nonlinear analyses of large-scale systems a realistic prospect, by allowing a substantial reduction in the computing wall-clock time and avoiding memory bottlenecks encountered with conventional modelling procedures.

As discussed earlier in Chapter 1, the proposed HF modelling strategy is applied within the framework of the INFLOAT project for the detailed response investigation of novel, large-scale, all-metal, honeycomb core sandwich composites and offshore platform topside deck systems. The modelling strategy and the partitioned modelling approach are therefore presented in this chapter with reference to individual sandwich composites, notwithstanding their more general applicability to the modelling of any all-metal, large-scale, composite structural system.

The chapter proceeds with reviewing the previously developed quadratic shell element local formulation and the associated Reissner-Mindlin kinematic constitutive expressions. The hierarchic optimisation approach (Izzuddin & Liang, 2017) embedded in the local element formulation is subsequently outlined, followed by a brief exposition of the utilised bi-sector and zero-macrospin local co-rotational frameworks (Izzuddin & Liang, 2016). The application of the HF modelling strategy to sandwich composites is demonstrated, and the focus is thereafter shifted to the description of the utilised dual super-element domain partitioning

approach (Jokhio & Izzuddin, 2015) and the concept of scalable parallel processing in HPC systems with distributed memory. The chapter concludes with a discussion on intricacies arising in the application of partitioned modelling with the adopted shell FEs, in respect of the treatment of the drilling rotational Degrees of Freedom (DOFs).

### 3.2 Local formulation of co-rotational Reissner-Mindlin shell elements

Consideration is henceforth given to the adopted quadratic shell elements developed by Izzuddin & Liang (2017), specifically the 9-noded quadrilateral and 6-noded triangular elements which employ 5 nodal DOFs in the local Cartesian coordinate system  $(x, y, z)$ , of which 3 are translational and 2 rotational.

For the local element shape and displacement fields interpolation, quadratic Lagrangian shape functions are employed in an isoparametric formulation framework, expressed in terms of the natural coordinates  $(\xi, \eta)$ :

$$\mathbf{x} = (x \ y \ z)^T = \sum_{i=1}^m N_i(\xi, \eta) \mathbf{x}_i \quad (3.1)$$

$$\mathbf{d} = (u \ v \ w)^T = \sum_{i=1}^m N_i(\xi, \eta) \mathbf{d}_i \quad , \quad \mathbf{r} = (\theta_x \ \theta_y)^T = \sum_{i=1}^m N_i(\xi, \eta) \mathbf{r}_i \quad (3.2)$$

where  $m$  is the number of element nodes,  $\mathbf{x}_i = (x_i \ y_i \ z_i)^T$  are the local nodal coordinates, and  $\mathbf{d}_i = (u_i \ v_i \ w_i)^T$  and  $\mathbf{r}_i = (\theta_{ix} \ \theta_{iy})^T$  are the translations and rotations of node  $(i)$ , respectively, in the local Cartesian coordinate system.

The Reissner-Mindlin theory underlies the element local kinematics, where the employment of a co-rotational approach enables the use of a simplified strain-displacement relationship through the exclusion of rigid-body modes from the local element deformation modes, as will be discussed in more detail in Section 3.4. The conforming element membrane strains  $\boldsymbol{\varepsilon}^m$ , bending strains  $\boldsymbol{\varepsilon}^b$ , and transverse shear element strains  $\boldsymbol{\varepsilon}^s$  can therefore be expressed in terms of the local element displacement fields  $(u, v, w)$  using the following equations:

$$\boldsymbol{\varepsilon}^m = \begin{Bmatrix} \varepsilon_x \\ \varepsilon_y \\ \gamma_{xy} \end{Bmatrix} = \begin{Bmatrix} \frac{\partial u}{\partial x} \\ \frac{\partial v}{\partial y} \\ \frac{\partial u}{\partial y} + \frac{\partial v}{\partial x} \end{Bmatrix} + \begin{Bmatrix} \frac{1}{2} \left( \frac{\partial z_0}{\partial x} + \frac{\partial w}{\partial x} \right)^2 - \frac{1}{2} \left( \frac{\partial z_0}{\partial x} \right)^2 \\ \frac{1}{2} \left( \frac{\partial z_0}{\partial y} + \frac{\partial w}{\partial y} \right)^2 - \frac{1}{2} \left( \frac{\partial z_0}{\partial y} \right)^2 \\ \left( \frac{\partial z_0}{\partial x} + \frac{\partial w}{\partial x} \right) \left( \frac{\partial z_0}{\partial y} + \frac{\partial w}{\partial y} \right) - \left( \frac{\partial z_0}{\partial x} \right) \left( \frac{\partial z_0}{\partial y} \right) \end{Bmatrix} \quad (3.3)$$

$$\boldsymbol{\varepsilon}^b = \begin{Bmatrix} \kappa_x \\ \kappa_y \\ \kappa_{xy} \end{Bmatrix} = \begin{Bmatrix} \frac{\partial \theta_x}{\partial x} \\ \frac{\partial \theta_y}{\partial y} \\ \frac{\partial \theta_x}{\partial y} + \frac{\partial \theta_y}{\partial x} \end{Bmatrix} \quad (3.4)$$

$$\boldsymbol{\varepsilon}^s = \begin{Bmatrix} \gamma_{xz} \\ \gamma_{yz} \end{Bmatrix} = \begin{Bmatrix} \theta_x + \frac{\partial w}{\partial x} \\ \theta_y + \frac{\partial w}{\partial y} \end{Bmatrix} \quad (3.5)$$

where the terms  $\frac{\partial z_0}{\partial x}$  and  $\frac{\partial z_0}{\partial y}$  denote the shell element curvature along its local planar axes.

### 3.3 Assumed strain formulation via hierarchic optimisation

The conforming kinematic assumptions presented in the preceding section introduce polluting higher-order nonlinear terms in the strain distributions (Izzuddin & Liang, 2017). These inaccuracies deteriorate the element performance, leading potentially to shear, membrane and distortion locking, which are the principal locking phenomena encountered in curved shell elements, arising from small shell thickness, curved shapes and the employment of isoparametric mapping for distorted element shapes, respectively.

In the adopted formulation, locking phenomena are relieved by correcting each of the conforming membrane, shear and bending strains with corrective hierarchic components  $\boldsymbol{\Psi}_h$ ,



towards an objective set of strains  $\Psi_o$  afforded by the original DOFs, using appropriate parameters (Izzuddin & Liang, 2017):

$$\boldsymbol{\varepsilon} + \boldsymbol{\varepsilon}_h \rightarrow \boldsymbol{\varepsilon}_o, \quad \boldsymbol{\varepsilon}_h = \boldsymbol{\Psi}_h \cdot \boldsymbol{\alpha}_h, \quad \boldsymbol{\varepsilon}_o = \boldsymbol{\Psi}_o \cdot \boldsymbol{\alpha}_o \quad (3.6)$$

The hierarchic and objective parameters,  $\boldsymbol{\alpha}_h$  and  $\boldsymbol{\alpha}_o$ , are determined by minimising the square of the error between the corrected and objective strains over the element domain, which leads to the following linear system of equations:

$$\left( \int_{\Omega^e} \begin{bmatrix} \boldsymbol{\Psi}_h^T \cdot \boldsymbol{\Psi}_h & -\boldsymbol{\Psi}_h^T \cdot \boldsymbol{\Psi}_o \\ -\boldsymbol{\Psi}_o^T \cdot \boldsymbol{\Psi}_h & \boldsymbol{\Psi}_o^T \cdot \boldsymbol{\Psi}_o \end{bmatrix} d\Omega^e \right) \begin{Bmatrix} \boldsymbol{\alpha}_h \\ \boldsymbol{\alpha}_o \end{Bmatrix} = \int_{\Omega^e} \begin{bmatrix} -\boldsymbol{\Psi}_h^T \\ \boldsymbol{\Psi}_o^T \end{bmatrix} \cdot \boldsymbol{\varepsilon} d\Omega^e \quad (3.7)$$

Considering the establishment of local kinematic and constitutive relationships for the shell elements in an isoparametric formulation framework, the integration of the above system of equations is most efficiently performed using Gaussian quadrature. The obtained strain parameters  $\boldsymbol{\alpha}_h$  and  $\boldsymbol{\alpha}_o$  can therefore be expressed in terms of the conforming strains at the Gauss Points (GPs), in the following form:

$$\boldsymbol{\alpha}_o = \boldsymbol{\Gamma}_o \cdot \begin{Bmatrix} \boldsymbol{\varepsilon}_1 \\ \boldsymbol{\varepsilon}_2 \\ \vdots \\ \boldsymbol{\varepsilon}_m \end{Bmatrix} = \boldsymbol{\Gamma}_o \cdot \boldsymbol{\varepsilon}_{GP}, \quad \boldsymbol{\alpha}_h = \boldsymbol{\Gamma}_h \cdot \begin{Bmatrix} \boldsymbol{\varepsilon}_1 \\ \boldsymbol{\varepsilon}_2 \\ \vdots \\ \boldsymbol{\varepsilon}_m \end{Bmatrix} = \boldsymbol{\Gamma}_h \cdot \boldsymbol{\varepsilon}_{GP} \quad (3.8)$$

where  $\boldsymbol{\varepsilon}_i$  is the conforming strain obtained at GP ( $i$ ) and  $m$  is the order of the employed Gaussian quadrature integration scheme. It is emphasised that the establishment of the strain parameters  $\boldsymbol{\alpha}_h$  and  $\boldsymbol{\alpha}_o$  independently from the element displacement field leads to an approach of enhanced computational efficiency, particularly in cases of complex nonlinear constitutive expressions at the element level (Izzuddin & Liang, 2017).

The enhanced strains can be expressed in terms of either the corrective or objective forms, as shown in Eqs. (3.9) and (3.10), respectively, with the error between the two reducing with the employment of higher order hierarchic corrective strains, or mesh refinement (Izzuddin & Liang, 2017):

$$\tilde{\boldsymbol{\varepsilon}}_{GP} = \boldsymbol{\varepsilon}_{GP} + \boldsymbol{\varepsilon}_{h,GP} = \boldsymbol{\varepsilon}_{GP} + \boldsymbol{\Psi}_{h,GP} \cdot \boldsymbol{\alpha}_h \cong \left( \mathbf{I} + \boldsymbol{\Psi}_{h,GP} \cdot \boldsymbol{\Gamma}_h \right) \boldsymbol{\varepsilon}_{GP} \quad (3.9)$$

$$\hat{\boldsymbol{\varepsilon}}_{GP} = \boldsymbol{\varepsilon}_{o,GP} = \boldsymbol{\Psi}_{o,GP} \cdot \boldsymbol{\alpha}_o \cong \boldsymbol{\Psi}_{o,GP} \cdot \boldsymbol{\Gamma}_o \cdot \boldsymbol{\varepsilon}_{GP} \quad (3.10)$$

This optimisation approach was originally developed for 9-noded shell elements (Izzuddin & Liang, 2017), leading to two alternative variants HnO9 and HnC9, where  $n$  indicates the order of employed hierarchic modes and O|C referring to the employment of Objective or Corrected strains to substitute the conforming field. It should be noted that the same approach is also directly applicable to 6-noded elements, leading to a respective family of elements with alternative branches HnO6 and HnC6 (Izzuddin & Liang, 2017).

For the individual membrane, bending and transverse shear strain components in Eqs. (3.3), (3.4) and (3.5), the hierarchic optimisation approach is employed separately to eliminate the associated locking phenomena. The distinct sets of objective strains are *a priori* defined in a polynomial form expressed in real Cartesian coordinates, thus allowing for the element sensitivity to geometric irregularities and distortion to be effectively overcome.

A total of 39 objective strain components are defined: (i) 15 membrane  $\boldsymbol{\Psi}_o^m$ , (ii) 15 bending  $\boldsymbol{\Psi}_o^b$ , and (iii) 9 transverse shear  $\boldsymbol{\Psi}_o^s$ . These correspond to the respective lower order modes afforded by the element local planar and transverse translational DOFs  $\mathbf{d} = (u \ v \ w)^T$ , as well as by the rotational DOFs  $\mathbf{r} = (\theta_x \ \theta_y)^T$ , encompassing the associated rigid body modes (Izzuddin & Liang, 2017). The respective objective strain components are given by the following expressions:

$$\boldsymbol{\Psi}_o^m = \begin{bmatrix} \frac{\partial}{\partial x} & 0 \\ 0 & \frac{\partial}{\partial y} \\ \frac{\partial}{\partial y} & \frac{\partial}{\partial x} \end{bmatrix} \boldsymbol{\Phi}_o^m \quad (3.11)$$

$$\boldsymbol{\Psi}_o^b = \boldsymbol{\Psi}_o^m \quad (3.12)$$

$$\boldsymbol{\Psi}_o^s = \left[ \boldsymbol{\Psi}_o^{s,z} \mid \boldsymbol{\Psi}_o^{s,\theta} \right], \quad \boldsymbol{\Psi}_o^{s,z} = \begin{bmatrix} \frac{\partial}{\partial x} \\ \frac{\partial}{\partial y} \end{bmatrix} \boldsymbol{\Phi}_o^{s,z}, \quad \boldsymbol{\Psi}_o^{s,\theta} = \begin{Bmatrix} -y \\ x \end{Bmatrix} \quad (3.13)$$

where:

$$\Phi_o^m = \begin{bmatrix} x & y & 0 & x^2 & xy & y^2 & x^2y & xy^2 & x^2y^2 & 0 & 0 & 0 & 0 & 0 & 0 \\ 0 & x & y & 0 & 0 & 0 & 0 & 0 & 0 & x^2 & xy & y^2 & x^2y & xy^2 & x^2y^2 \end{bmatrix} \quad (3.14)$$

$$\Phi_o^{s,z} = [x \quad y \quad x^2 \quad xy \quad y^2 \quad x^2y \quad xy^2 \quad x^2y^2] \quad (3.15)$$

Among the hierarchically optimised family of 9- and 6-noded shell elements, the H3O9 and H3O6 variants, employing 3<sup>rd</sup> order hierarchic corrective strain components, have been shown to achieve optimal performance in addressing all three forms of locking (Izzuddin & Liang, 2017), and are therefore employed herein.

### 3.4 Local co-rotational framework

The co-rotational approach encompasses the definition of a local coordinate system which follows the element in its deformed configuration. This enables the exclusion of rigid body rotations from the element response, thus enabling the use of simplified kinematic constitutive relationships at the local element level, such as those given in Eqs. (3.3) - (3.5).

The definition of an effective co-rotational framework is subject to the fulfilment of the following set of requirements: (i) simplified definition, (ii) nodal invariance, (iii) element spin reduction, and (iv) uniqueness in the local system definition, resulting in a symmetric tangent stiffness matrix (Izzuddin & Liang, 2016). For the optimised H3O9 and H3O6 shell elements employed herein, these requirements are achieved with the utilisation of bi-sector and zero-macrospin definitions of the local co-rotational system (Izzuddin & Liang, 2016), respectively, which are outlined hereafter.

#### 3.4.1 Bisector and zero-macrospin co-rotational frameworks

The bisector approach for quadrilateral shell elements encompasses a simple definition of the local x- and y-axes as the bisectors of the element diagonals linking the corner nodes, as illustrated in Figure 3.1. The relative orientation of the local co-rotational system in the element

deformed configuration with reference to the global system is uniquely defined by the unit orthogonal vector basis  $(\mathbf{c}_x, \mathbf{c}_y, \mathbf{c}_z)$ , where the unique triad is obtained as (Izzuddin, 2005; Izzuddin & Liang, 2016):

$$\mathbf{c}_x = \frac{\mathbf{c}_{13} - \mathbf{c}_{24}}{|\mathbf{c}_{13} - \mathbf{c}_{24}|}, \quad \mathbf{c}_y = \frac{\mathbf{c}_{13} + \mathbf{c}_{24}}{|\mathbf{c}_{13} + \mathbf{c}_{24}|}, \quad \mathbf{c}_z = \mathbf{c}_x \times \mathbf{c}_y \quad (3.16)$$

In Eq. (3.16) the unit vectors  $\mathbf{c}_{ij}$  are obtained by the following expression:

$$\mathbf{c}_{ij} = \frac{\mathbf{v}_{ij}}{|\mathbf{v}_{ij}|}, \quad \mathbf{v}_{ij} = \mathbf{v}_{ij}^o + \mathbf{u}_j - \mathbf{u}_i \quad (3.17)$$

where  $\mathbf{v}_{ij}^o$  and  $\mathbf{v}_{ij}$  are the vectors linking nodes  $(i)$  and  $(j)$  in the initial undeformed and the current deformed configurations, respectively, and  $\mathbf{u}_i = (U_i \ V_i \ W_i)^T$  is the global translation vector of node  $(i)$ .

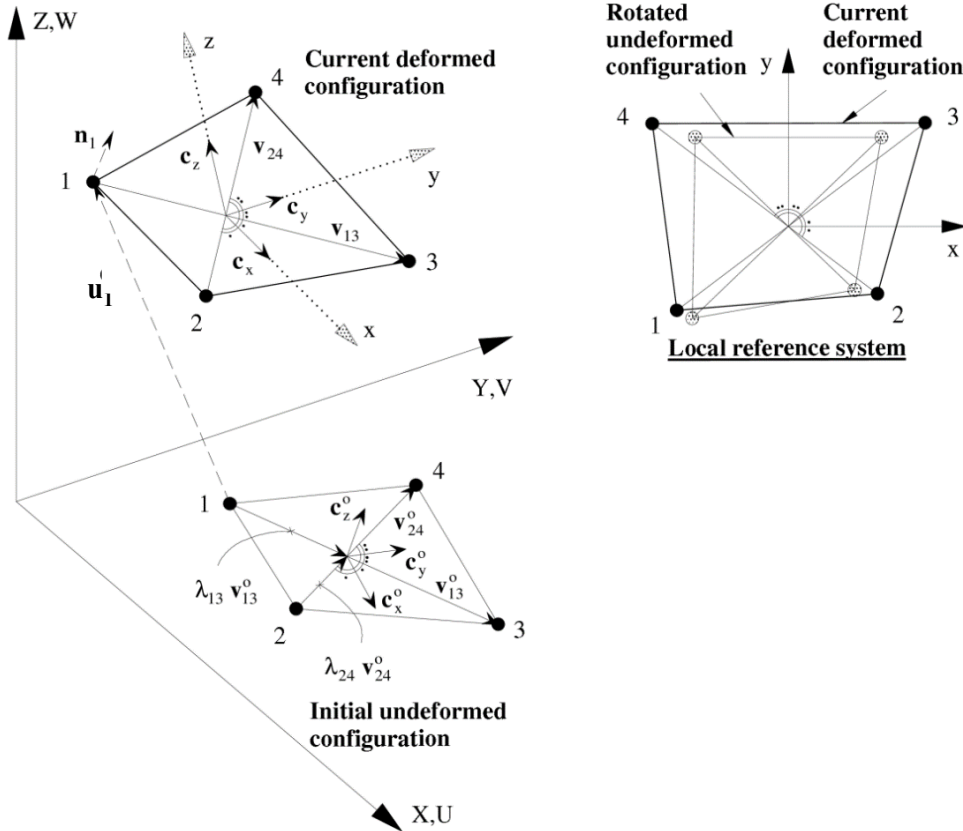


Figure 3.1: Bisector local co-rotational system and global nodal displacement parameters for quadrilateral shell finite elements (Izzuddin & Liang, 2016)

The zero-macrospin approach employed for triangular shell elements encompasses the optimal definition of the local x- and y-axes, such that the relative spin at the material point level in the current deformed configuration is zero in an aggregate sense, at the macro-element level, with reference to the corresponding rotated undeformed configuration. The orthogonal unit vectors defining the local co-rotational system relative orientation with reference to the global system in the element initial undeformed configuration,  $\mathbf{c}_x^o$  and  $\mathbf{c}_y^o$ , are defined such that  $\mathbf{c}_x^o$  is aligned with edge 1-2, as illustrated in Figure 3.2:

$$\mathbf{c}_x^o = a_{x1} \mathbf{v}_{12}^o + a_{x2} \mathbf{v}_{23}^o, \quad \mathbf{c}_y^o = a_{y1} \mathbf{v}_{12}^o + a_{y2} \mathbf{v}_{23}^o \quad (3.18)$$

where:

$$a_{x1} = \frac{1}{|\mathbf{v}_{12}^o|}, \quad a_{x2} = 0, \quad a_{y1} = -\frac{\mathbf{c}_{12}^{oT} \cdot \mathbf{c}_{23}^o}{|\mathbf{v}_{12}^o| \sqrt{1 - (\mathbf{c}_{12}^{oT} \cdot \mathbf{c}_{23}^o)^2}}, \quad a_{y2} = \frac{1}{|\mathbf{v}_{23}^o| \sqrt{1 - (\mathbf{c}_{12}^{oT} \cdot \mathbf{c}_{23}^o)^2}} \quad (3.19)$$

In the above expression, unit vectors  $\mathbf{c}_{ij}^o$  are obtained as follows:

$$\mathbf{c}_{ij}^o = \frac{\mathbf{v}_{ij}^o}{|\mathbf{v}_{ij}^o|} \quad (3.20)$$

where  $\mathbf{v}_{ij}^o$  are the vectors linking nodes ( $i$ ) and ( $j$ ) in the initial undeformed configuration.

In the current deformed configuration, the unit orthogonal vector basis  $(\mathbf{c}_x, \mathbf{c}_y, \mathbf{c}_z)$ , is uniquely obtained as:

$$\mathbf{c}_x = \frac{\mathbf{c}'_x + \mathbf{c}''_y}{|\mathbf{c}'_x + \mathbf{c}''_y|}, \quad \mathbf{c}_y = \mathbf{c}_z \times \mathbf{c}_x, \quad \mathbf{c}_z = \frac{\mathbf{v}_{12} \times \mathbf{v}_{23}}{|\mathbf{v}_{12} \times \mathbf{v}_{23}|} \quad (3.21)$$

where:

$$\mathbf{c}'_x = a_{x1} \mathbf{v}_{12} + a_{x2} \mathbf{v}_{23}, \quad \mathbf{c}''_y = \mathbf{c}'_y \times \mathbf{c}_z, \quad \mathbf{c}'_y = a_{y1} \mathbf{v}_{12} + a_{y2} \mathbf{v}_{23} \quad (3.22)$$

and  $a_{x1}$ ,  $a_{x2}$ ,  $a_{y1}$  and  $a_{y2}$  are given by Eq. (3.19). This is illustrated in Figure 3.2.

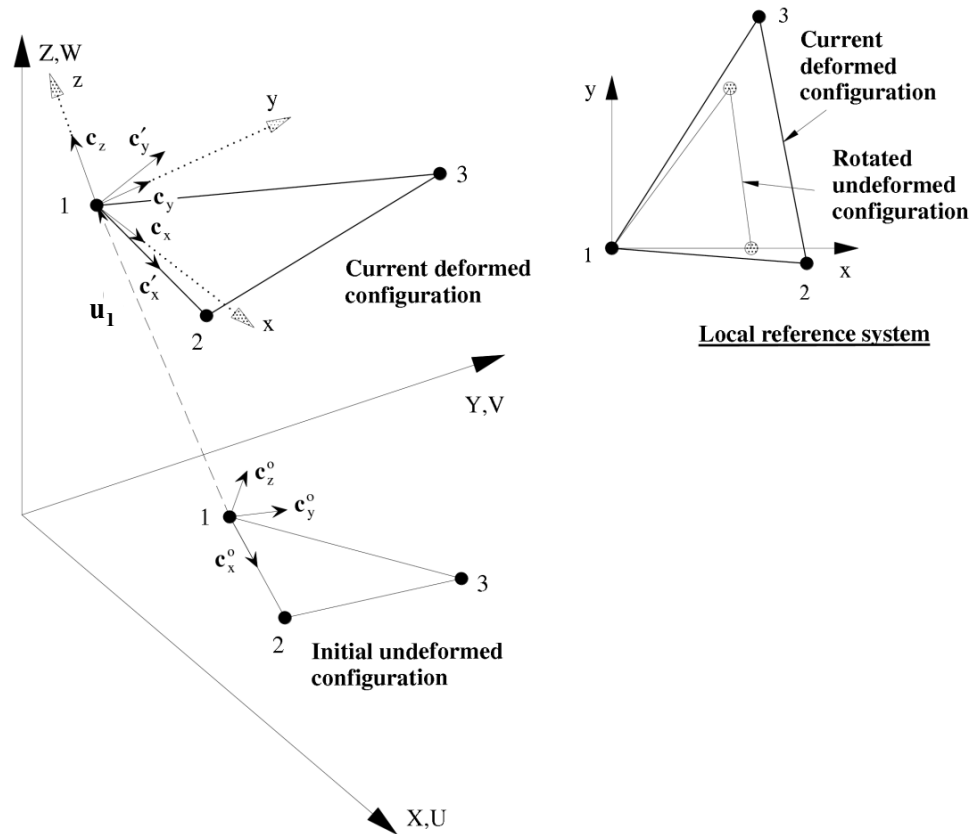


Figure 3.2: Zero-macrospin local co-rotational system and global nodal displacement parameters for triangular shell finite elements (Izzuddin & Liang, 2016)

Besides fulfilling the uniqueness and simplified definition requirements, both bisector and zero-macrospin frameworks outlined above are associated with reduced element spin, which is zero at the macro-element level in the latter case. Moreover, the definitions ensure nodal invariance, thus allowing for identical local and global element force vectors and tangent stiffness matrices to be obtained regardless of the adopted nodal ordering (Izzuddin & Liang, 2016). It must be emphasized that the above co-rotational framework definitions are independent of the element type and can thus be extended from 4-noded to 9-noded quadrilateral, as well as from 3-noded to 6-noded triangular, elements. Hence, they have been effectively applied to the formulation of the optimised H3O9 and H3O6 variants employed herein for the local coordinate system definition.

### 3.4.2 Co-rotational transformations

The co-rotational approach enables the element local internal force vector and tangent stiffness matrix to be obtained from local deformations, excluding the effect of rigid body rotations. Geometric nonlinearity is therefore incorporated in the global element response by means of relevant discrete transformations between the global and local coordinate systems. For the translational and rotational DOFs, these transformations are expressed in the following form (Izzuddin & Liang, 2016):

$$\mathbf{d}_i = \mathbf{T}\mathbf{u}_i + (\mathbf{T} - \mathbf{T}_0)\mathbf{v}_{io}^o \quad (3.23)$$

$$\mathbf{r}_i = -\bar{\mathbf{T}}\mathbf{n}_i \quad (3.24)$$

where  $\mathbf{n}_i$  is the normal vector,  $\mathbf{v}_{io}^o$  is the position vector of node ( $i$ ) about the local coordinate system origin ( $o$ ) in the initial undeformed configuration, while  $\mathbf{T}_0$  and  $\mathbf{T}$ ,  $\bar{\mathbf{T}}$  are the orientation matrices of the co-rotational system in the initial undeformed and current deformed element configurations. The expressions for the orientation matrices are given hereafter:

$$\mathbf{T}_0 = \begin{bmatrix} \mathbf{c}_x^o & \mathbf{c}_y^o & \mathbf{c}_z^o \end{bmatrix}^T \quad (3.25)$$

$$\mathbf{T} = \begin{bmatrix} \mathbf{c}_x & \mathbf{c}_y & \mathbf{c}_z \end{bmatrix}^T \quad (3.26)$$

$$\bar{\mathbf{T}} = \begin{bmatrix} \mathbf{c}_x & \mathbf{c}_y \end{bmatrix}^T \quad (3.27)$$

Two additional transformations from the local co-rotational to the global coordinate system are required for the element resistance forces and tangent stiffness matrix, which are obtained considering the first- and second-order derivatives of the above geometric relationships linking the local to global DOF parameters (Izzuddin & Liang, 2016).

It is worth noting that the orientation of the nodal normal  $\mathbf{n}_i$  at node ( $i$ ) is determined by three global rotational DOFs, but obviously the ‘drilling’ rotation will have no influence on the orientation of  $\mathbf{n}_i$ . This means that the element exhibits a singular behaviour in relation to the drilling DOF, which must either be excluded or restrained when discretising a smooth shell surface. In the modelling of complex shell structures, including parts with smooth surfaces and

other parts intersecting at an angle, the most effective approach encompasses the utilisation of three global rotational DOFs per node, alongside the restraining of the drilling DOF while accounting for the changing orientation of the drilling normal vector in large displacement analysis. This has implications on the application of the high-fidelity modelling strategy for all-metal sandwich composites, where careful consideration should be given to the treatment of drilling rotational DOFs, particularly along a partition boundary with domain decomposition. This will be thoroughly discussed at a later point in Section 3.7.

### **3.5 High-fidelity modelling of large-scale metal sandwich composites**

As discussed earlier in Chapter 2, the detailed nonlinear analysis of large-scale metal sandwich panels with honeycomb core topologies has received very little attention in the existing literature, largely due to the associated modelling complexity and high computational demand posed by such intricate structures.

In sandwich panels with honeycomb core configurations, as illustrated in Figure 3.3, the cell geometry and transverse orientation with respect to the panel faceplates result in the formation of discrete laterally unrestrained plated components of substantial slenderness, both at the cell walls and the faceplates. These are prone to elastoplastic compressive and shear buckling, which, alongside potential stress concentrations arising from the discrete nature of the core, lead to highly complex stress and deformation states throughout the panel domain. The establishment of reliable estimates for the critical buckling load of individual plated components, as well as the resulting reduction in the panel global capacity, is therefore rendered highly cumbersome for large-scale systems subject to complex loading conditions. The sensitivity of the aforementioned estimates to geometric constraints imposed by the cell wall interactions and the welded connections, as well as to the magnitude and sense of imperfections, further complicate the local buckling and response attributes assessment of the sandwich panel.

Taking the above into consideration, it is evident that an accurate global nonlinear response evaluation calls for an increased level of modelling sophistication. The application of the HF nonlinear FE modelling strategy discussed hitherto to sandwich composites encompasses the following principal features: (i) an accurate geometric modelling process for the core and

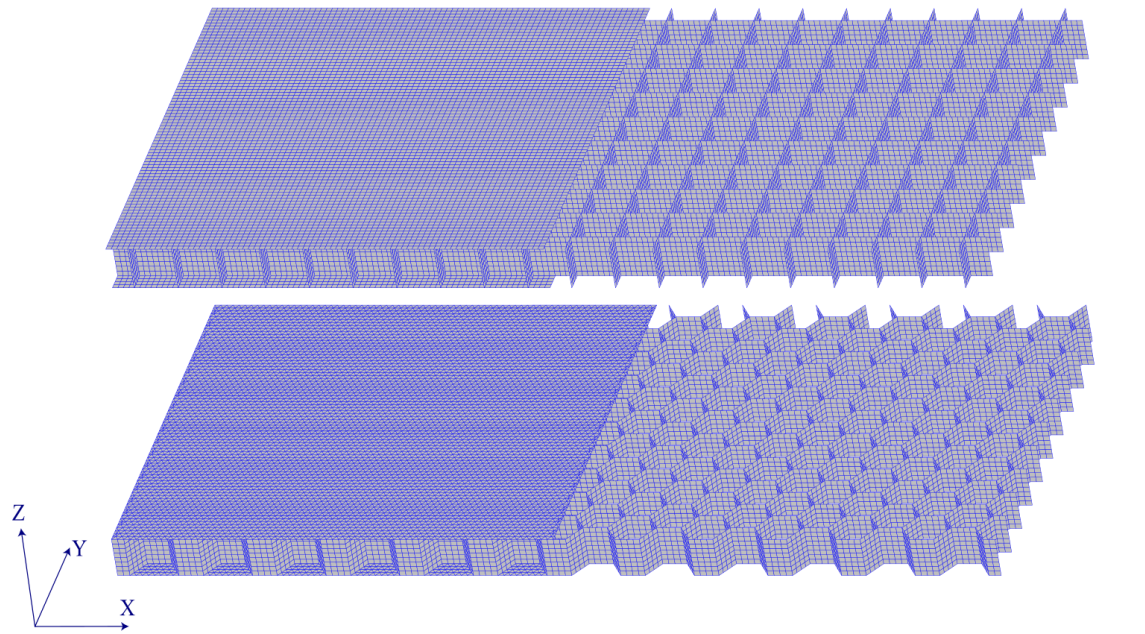


plates, accounting for manufacturing and connection characteristics between individual cells, alongside initial imperfections; (ii) an extensive discretisation of the panel domain with geometrically nonlinear shell elements, allowing for the effects of local buckling on the global panel response to be accurately captured; (iii) the employment of detailed nonlinear material constitutive models capable of accurately capturing local yielding and the spread of plasticity over the domain, including hardening and strain-rate effects; and (iv) the utilisation of powerful domain partitioning in HPC systems that achieves considerable computational efficiency and overcomes memory bottlenecks.

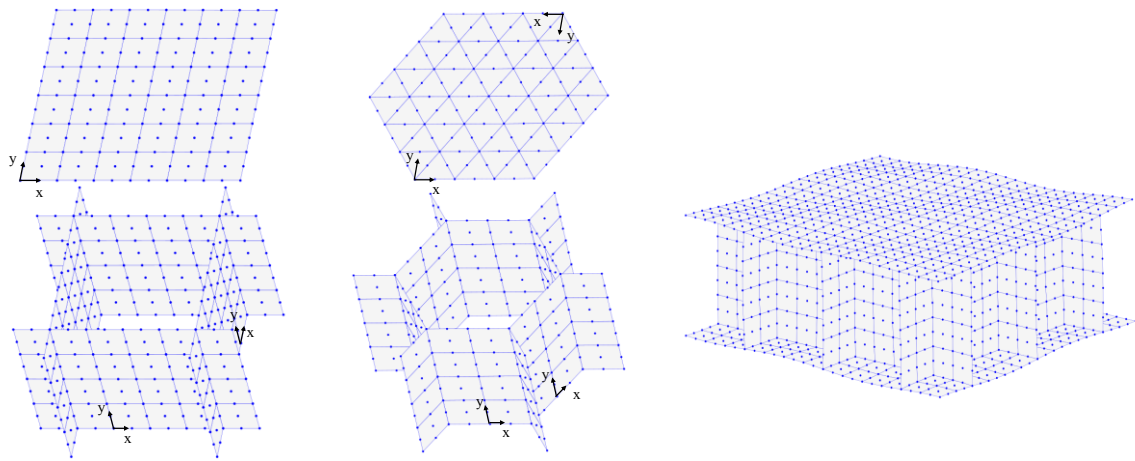
With respect to the first two features, for the domain discretisation of sandwich panels with rectangular and hexagonal honeycomb core topologies the previously reviewed 9-noded quadrilateral and 6-noded triangular shell finite elements have been employed (Izzuddin & Liang, 2017). 9-noded elements are utilised for the core cell wall discretisation in both configurations, while for the faceplates 9-noded and 6-noded elements are employed for the rectangular and hexagonal configurations, respectively. The detailed FE models are generated using a versatile mesh generation computing tool, developed to allow for the plates and core cells modelling to any desired level of discretisation detail, as illustrated in Figure 3.3 (a), (b). The mesh generator further enables the introduction of sympathetic imperfections in the system, by means of nodal dislocations, as illustrated in Figure 3.3 (c), which is imperative in the modelling of sandwich and composite systems due to their response imperfection sensitivity. The adopted strategy has been implemented in ADAPTIC (Izzuddin, 1991), a sophisticated general finite element code for the adaptive nonlinear analysis of structures under extreme static and dynamic loading.

The HF modelling strategy discussed above and illustrated in Figure 3.3 allows for an accurate nonlinear response evaluation of sandwich composites in the large displacement range, taking due account of geometric and material nonlinearity. The efficiency and accuracy of the HF modelling strategy will be illustrated in the context of application studies in Chapter 7, where consideration is given to large-scale, all-metal, honeycomb core sandwich composites employed as deck components in the envisioned novel topside deck systems discussed in Chapter 1. The HF modelling strategy is further validated against physical tests on the novel sandwich composites in Chapter 7, which enables its reliability for realistic 3-D modelling of composite structural systems to be established. As discussed earlier, notwithstanding the modelling strategy application to sandwich composites, this can be effectively employed for

the modelling and extensive nonlinear assessment of any large-scale all-metal composite system. Partitioned modelling and its application to sandwich composites are discussed in the forthcoming Sections 3.6 and 3.7.



(a)



(b)

(c)

Figure 3.3: (a) High-fidelity finite element discretisation of sandwich panels with rectangular and hexagonal honeycomb core topologies, (b) discretisation strategy for rectangular and hexagonal honeycomb cells, (c) sympathetic sinusoidal imperfection modelling idealisation for rectangular honeycomb core sandwich panels

### **3.6 Partitioned modelling for high performance computing**

In nonlinear static or dynamic analysis problems where finite element procedures are employed, the computational demand is inextricably related to the numerical solution of the algebraic system of equations of discrete equilibrium for a given set of essential and natural boundary conditions. The size of this system of equations is determined by the number of discrete nodal kinematic parameters employed for the domain discretisation, thus increasing substantially in the case of large-scale, geometrically complex and/or particularly dense FE meshes.

A detailed nonlinear response evaluation of large-scale metal sandwich panels subject to extreme static or dynamic loading, using the high-fidelity modelling strategy presented in Section 3.5, necessitates the employment of a dense mesh of shell FEs, typically associated with several hundreds of thousands of DOFs. The employment of a substantially dense mesh is essential for accurate modelling of the effects of the various progressively manifested forms of local geometric instability, alongside the spread of plasticity, on the global panel response. Consequently, extensive nonlinear numerical simulations are rendered prohibitively expensive, or even impossible, in relation to computing wall-clock time and memory resources.

These shortcomings are effectively overcome in this work by utilising a recently developed partitioned modelling approach based on the dual super-element concept (Jokhio & Izzuddin, 2015), facilitating scalable parallel processing in High-Performance Computing (HPC) systems with distributed memory.

The partitioned modelling methodology involves the domain decomposition of an initial parent structure into place-holder super-elements along the partition boundary, each representing a child partition. Place-holder super elements are treated as conventional finite elements in the parent process, and these communicate with dual super-elements that wrap the child partition which is analysed in a separate process (Jokhio & Izzuddin, 2015). At every iterative step of the solution procedure, the displacements at the partition boundary nodes are communicated from the place-holder to the dual super-elements. Subsequently, the condensed resistance forces vector and tangent stiffness matrix for each dual super-element are obtained via backward substitution and forward elimination processes at the level of the child partition, after which they are communicated back to the placeholder super-element in the parent process (Jokhio & Izzuddin, 2015). This two-way communication between pairs of place-holder and

dual super-elements allows for the discrete conditions of compatibility and equilibrium to be enforced within the individual partitions, including the parent partition, as well as along the partition boundary, while eliminating the requirement for communication between child partitions.

In applying the partitioned modelling approach to HPC parallel processing systems, individual child and parent processes are allocated to independent Central Processing Units (CPUs) or cores, distributed over single or multiple computing nodes. The reduced number of solver operations within separate child processes, alongside the effective parallelisation of the solution procedure, leads to a remarkable speed-up and reduction in the computing memory demand in comparison with the respective monolithic models (Jokhio & Izzuddin, 2015). Moreover, this capability overcomes the memory bottlenecks typically encountered in conventional monolithic models of large-scale structural systems, while achieving identical results and convergence rate (Jokhio & Izzuddin, 2015).

### **3.7 Partitioned modelling of large-scale metal sandwich composites**

An advanced high-fidelity mesh generation tool has been developed to facilitate the application of domain partitioning to the modelling of large-scale, metal sandwich composites using ADAPTIC (Izzuddin, 1991), in which the previously outlined partitioning approach has been implemented. This tool enables the effective domain decomposition of sandwich panel FE models into child partitions, each of which is in turn discretised with the adopted 9-noded and 6-noded shell finite elements, as previously described. A schematic representation of the concept is illustrated in Figure 3.4 for a sandwich panel partitioned model with 4 child partitions, where the partition boundary comprises only the nodes along the individual child partition domain perimeters.

As discussed in Section 3.5, the adopted shell elements utilise 6 DOFs, with 3 rotational DOFs, per node, though the local element response is formulated with 5 local DOFs, with 2 rotational DOFs for each node. This is typical of shell elements utilising the basic nodal parameters and makes these elements insensitive to ‘drilling’ nodal rotations, thus exhibiting a singular response under such rotations. Such singularity occurs for smooth surfaces but does not arise

for nodes along edges where elements intersect at an angle, such as for a folded plate or at the intersection of the honeycomb core with the faceplates for an all-metal sandwich panel.

Accordingly, the most general approach would be to utilise 3 rotational DOFs per node, and to constrain the drilling DOF at nodes where there are no intersections at an angle between adjacent shell elements (i.e. locations where the discretised domain is a smooth surface with no intersections). This is indeed the approach considered in ADAPTIC (Izzuddin, 1991) for the utilised 6- and 9-noded shell elements, where drilling DOF constraints are automatically introduced at non-intersecting nodal locations. The latter are achieved by means of a special constraint element that allows for the variation of the drilling orientation vector with large displacements.

In the context of dual super-element partitioned modelling, the automatic introduction of the drilling constraint element is restricted to the internal nodes of the partition domain. As discussed in Section 3.6, the two-way communication between dual and placeholder super-elements eliminates the need for inter-partition communication, while allowing for the former to be processed in parallel as independent substructures on separate CPUs or cores. Without more advanced communication between child processes, the establishment of whether the nodes on a partition boundary belong to a smooth part of the domain or to an intersection between two or more surfaces is impossible, and thus the automated drilling DOF constraint element introduction process is substantially encumbered.

Addressing the singularities associated with the drilling DOF on a partitioned boundary requires the introduction of additional constraint elements at the parent partition level, at nodal locations with no element intersections. This is shown in Figure 3.5 for the sandwich panel partitioned model illustrated in Figure 3.4, where additional constraint elements are introduced at all nodes on the partition boundary, except for those at faceplate-core intersection locations. This approach has been incorporated in the developed high-fidelity mesh generation computing tool for all-metal sandwich panel composites, enabling the automatic introduction of additional drilling DOF constraint elements at the partition boundary nodes, where this is required, and thus the effective partitioned modelling of such panels.

The effectiveness and computational benefits of the dual-super element domain partitioning methodology will be demonstrated in Chapter 7, in the context of application studies on large-scale, all-metal sandwich composites employed as deck components.

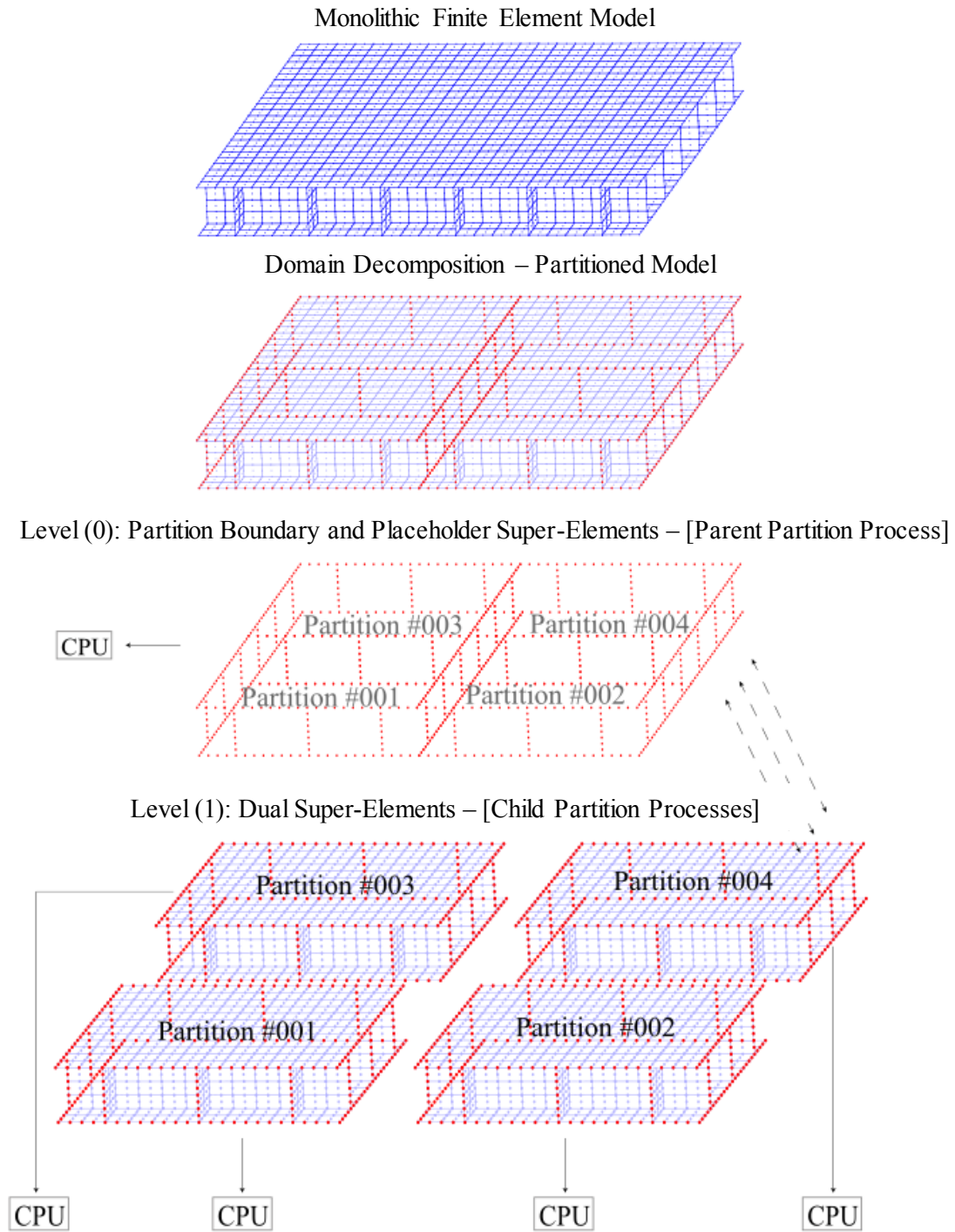


Figure 3.4: Domain decomposition of rectangular honeycomb core sandwich panels using dual super-element child partitions

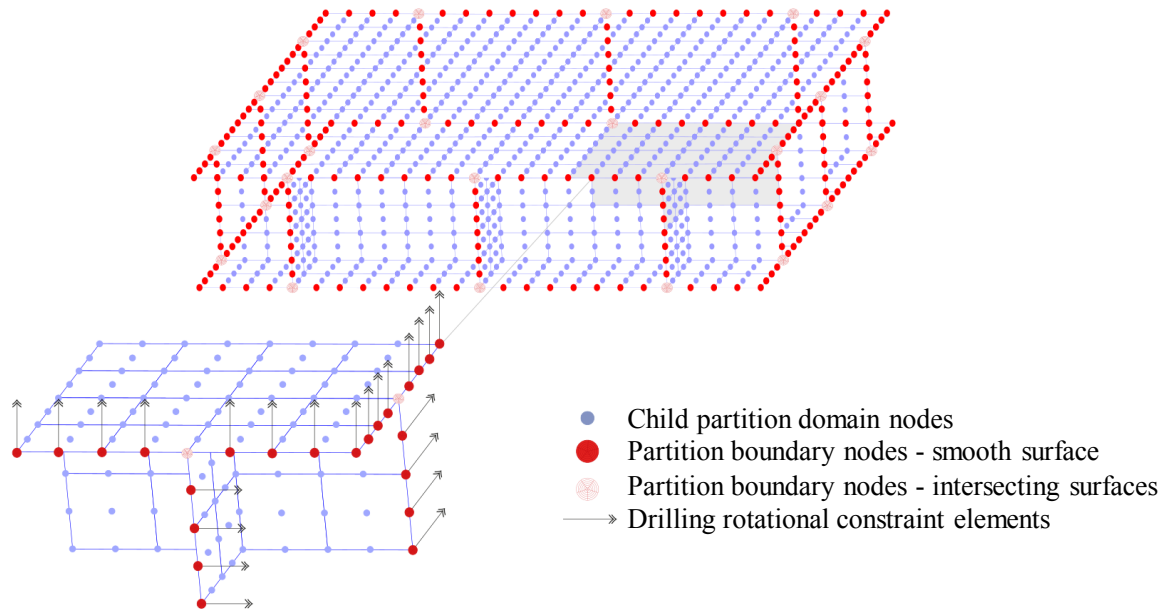


Figure 3.5: Drilling rotational constraint elements along smooth part of partition boundary

### 3.8 Concluding remarks

A HF nonlinear FE modelling strategy is presented in this chapter, which provides an accurate and systematic approach for realistic modelling of large-scale composite structural systems and sandwich composites. The proposed strategy is underpinned by the employment of co-rotational Reissner-Mindlin quadratic curved shell elements, attaining optimal performance through a hierarchic optimisation approach that enables membrane, bending and shear locking phenomena to be addressed (Izzuddin & Liang, 2016; 2017). The advanced features of the utilised shell elements enable the accurate nonlinear response evaluation in the range of large displacements, taking due account of geometric and material nonlinearity effects. This is imperative in the modelling of large-scale metal composite structures, particularly of sandwich composites with discrete core topologies, due to the global system response and failure modes being sensitive to the progressive manifestation and interaction of various local instability forms over their domain. The HF modelling approach is further enhanced with the utilisation of recently developed domain partitioning capabilities, based upon a novel dual super-element concept introduced by Jokhio and Izzuddin (2015). This allows for scalable parallel processing of individual partitions in HPC systems with distributed memory, without compromising the accuracy and convergence characteristics of the monolithic approach, thus enabling a

substantial reduction of computing wall-clock time to be achieved and potential memory bottlenecks to be effectively overcome. The significance of the proposed HF partitioned modelling methodology is highlighted in cases where computing resource limitations render nonlinear analyses prohibitively demanding or impossible. This applies in particular to the accurate nonlinear assessment of large-scale, metal composite structures subject to extreme static or dynamic loading, where the computational demands of the conventional HF modelling approach can be prohibitive.



# Chapter 4

## Surface Coupling along a 1-D Interface with Non-Conforming Meshes

### 4.1 Introduction

In the modelling of intricate composite structural systems comprising independent deformable components in contact, the efficiency and flexibility of the employed finite element (FE) discretisation procedure is significantly impacted by the requirement of achieving mesh conformity. The parameters of the employed FE mesh for the discretisation of different domains or plated components are mainly dictated by the requirement of accurately capturing geometric instabilities and material nonlinearity at a local level. However, the geometric complexity of the system, alongside the variability of natural and essential boundary conditions over the domain, often impose severe constraints on the meshing of the respective surfaces to achieve coupling. These include the requirement for nodal alignment, compliance of element shapes, edge orientations and mesh density, proportionality of element sizes and the use of complex transitional meshes.

When a high-fidelity (HF) nonlinear analysis of such systems is called for, the adopted computational modelling approach would significantly benefit from the employment of coupling methods for non-conforming meshes. These would enable the fulfilment of translational and rotational compatibility conditions and the accurate transferring of internal forces along the coupling interface for independently discretised domains, thereby leading to significant merits on the modelling front. The requirement of coupling independently

discretised deformable substructures in connection regions is rendered a cumbersome undertaking in such systems, due to the coupling constraint being enforced along a line of arbitrary orientation, rather than a surface. This corresponds typically to welded connections and intersections between nonparallel components, where the thickness of the coupling interface is sufficiently small compared to its length, thereby rendering the constraint enforcement between the two meshes a 1-D coupling problem. It is emphasised that the term non-conforming is employed herein to refer to non-matching coupled meshes with lack of nodal alignment along the coupling interface, as discussed in Chapter 1.

In this context, a novel coupling element has been developed and successfully implemented in ADAPTIC (Izzuddin, 1991) v2.16.5, facilitating discrete translational and rotational coupling of independently discretised surfaces of shell FEs along a 1-D coupling interface, for any spatial orientation of the line and the surfaces. The developed formulation is particularly applicable in the modelling of shell substructures coupled along a weld line, as well as in the case of partitioned models with a different level of discretisation detail in each child partition. The employment of the developed coupling element leads to a variety of merits on the modelling front: (i) discretisation flexibility in relation to the employed FE types and mesh parameters; (ii) overcoming of modelling shortcomings associated with the requirement of achieving mesh conformity; (iii) accuracy enhancement arising from the employment of component- or domain-specific optimal discretisation strategies at a local level; and (iv) substantial reduction of the associated demand in computing wall-clock time and resources.

The developed HF nonlinear FE modelling strategy for geometrically complex composite structural systems, presented in Chapter 3, utilises hierarchically optimised co-rotational Reissner-Mindlin curved shell FEs (Izzuddin & Liang, 2016; 2017). The coupling element formulation presented herein, as well as in Chapter 5, has been developed in compliance with the HF modelling strategy, aiming towards the establishment of a unified discretisation framework of enhanced computational efficiency, applicable to large-scale, geometrically complex, composite structural systems and beyond. Notwithstanding, its establishment within a general setting enables the straightforward upgrade of existing FE programs to incorporate coupling of different FE types.

Within the INFLOAT project scope, the incorporation of the developed coupling element in the HF modelling of large-scale sandwich composites and deck systems leads to substantial benefits on the modelling front, owing to the complete discretisation flexibility it provides.

These are highlighted in a variety of cases, encompassing: (i) modelling of laser-welded connections between sandwich composite core strips and faceplates, in cases where a selective discretisation is required for the capturing of local buckling effects; (ii) modelling of fillet-welded connections between sandwich composites and supporting plate girders of arbitrary relative spatial orientation; (iii) modelling of fillet-welded connections between sandwich composite faceplates and localised equipment patch plates in different locations and orientations over the panel domain; (iv) edgewise coupling of adjacent panels with different discretisation levels within a deck system or different regions within a panel, without the use of transitional meshes; and (vii) coupling of child partitions with non-conforming meshes along the partitioned boundary, when the domain partitioning approach discussed in Chapter 3 is employed.

This chapter proceeds with introducing the mathematical treatment of coupling constraints using Lagrangian Multipliers (LMs) on the basis of a simplified mechanical model, as well as the general setting of the surface-to-surface coupling problem. Subsequently, a systematic strategy for the mathematical treatment of surface coupling along a 1-D interface in a discrete form, using coupling elements, is presented, including: (i) the interface segmentation based on the surface mesh parameters, (ii) the identification of the set of coupling elements associated with each interface segment, and (iii) the discrete constraint enforcement along the interface. Lastly, the general coupling element formulation is presented, along with two alternative integration schemes for the coupling element internal force vector and consistent tangent stiffness matrix based on Gaussian quadrature, followed by a discussion on their relative accuracy and computational efficiency.

## **4.2 Treatment of coupling constraints using Lagrangian Multipliers**

The LM method is widely employed in mathematical optimisation for the extrema identification of a function subject to a set of constraints. As discussed in Section 2.3, the employment of LMs has become a prominent approach for the treatment of static and dynamic coupling problems in computational mechanics, where a system of physically or computationally heterogeneous components coupled over a shared interface is being looked at. This is due to the establishment of the respective static and dynamic equilibrium states

involving the minimisation of the system total potential energy function subject to a set of kinematic constraints defined over the coupling interface.

Shifting the focus to the 1-D coupling problem at hand, a qualitatively equivalent benchmark problem is considered herein. This involves a simplified mechanical model of 2 single degree of freedom (SDOF) elastic springs  $\Gamma^{(1)}$  and  $\Gamma^{(2)}$ , with stiffness parameters  $k_1$  and  $k_2$ , coupled along a shared interface  $\Gamma_c$ , as illustrated in Figure 4.1. By virtue of comparison of the obtained mathematical expressions for the simplified mechanical model and the actual system of coupled surfaces along a 1-D interface, the mathematical equivalence of the two systems can be established and an enhanced clarity of the concepts discussed in the following sections and in Chapter 5 can be achieved.

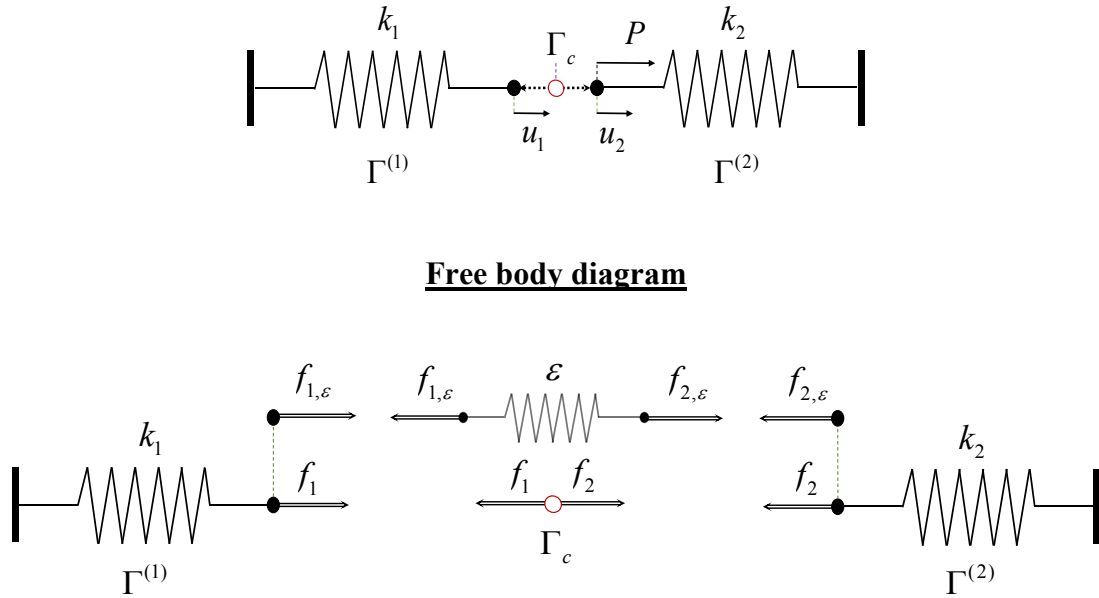


Figure 4.1: Simplified mechanical model of elastic springs 1-D coupling

The total potential energy of the simplified model consists of two parts: (i) the elastic strain energy stored in the springs  $\Gamma^{(1)}$  and  $\Gamma^{(2)}$ ; and (ii) the work done by the externally applied load  $P$ , which in this case is assumed to act on spring  $\Gamma^{(2)}$ , without loss of generality. This is given by the following expression, where energy storage in and energy dissipation from the system are taken as positive and negative, respectively:

$$\Pi(u_1, u_2) = \frac{1}{2}k_1u_1^2 + \frac{1}{2}k_2u_2^2 - Pu_2 \quad (4.1)$$

First order differentiation of the total potential energy function in Eq. (4.1) with respect to the kinematic DOFs  $u_1$  and  $u_2$  yields the system forces associated with each DOF, while its minimisation leads to an equilibrium state for the system under the externally applied loading.

Considering a system of two completely uncoupled, independent elastic springs, the minimisation of the energy function of Eq. (4.1) leads to an equilibrium state ( $u_1 = 0, u_2 = P/k_2$ ), where  $\Gamma^{(1)}$  stays intact and only  $\Gamma^{(2)}$  is displaced in the direction of the externally applied load  $P$ .

Considering a coupled springs system, where translational compatibility is desired to be achieved, the 1-D constraint can be expressed in the form of the following multivariate function:

$$g(u_1, u_2) = u_1 - u_2 = 0 \quad (4.2)$$

The establishment of the system equilibrium is therefore transformed into a mathematical optimisation problem, where the total potential energy objective function is minimised subject to the constraint function of Eq. (4.2):

$$\begin{aligned} &\text{minimise } \left\{ \Pi(u_1, u_2) = \frac{1}{2}k_1u_1^2 + \frac{1}{2}k_2u_2^2 - Pu_2 \right\} \\ &\text{subject to } \left\{ g(u_1, u_2) = u_1 - u_2 = 0 \right\} \end{aligned}$$

The employment of a LM formulation for the constraint enforcement on the coupled system encompasses the introduction of an additional term in Eq. (4.1), representing the LM contribution to the system energy, and the subsequent minimisation of the obtained Lagrangian function (Wriggers, 2006):

$$\Pi(u_1, u_2) = \frac{1}{2}k_1u_1^2 + \frac{1}{2}k_2u_2^2 - Pu_2 + \lambda(u_1 - u_2) \quad (4.3)$$

The new term comprises an additional DOF  $\lambda$ , with physical and dimensional correspondence to a fictitious force, multiplied by the kinematic constraint function  $g(u_1, u_2)$ . Despite the approach introducing an extra unknown to the system, it provides an elegant and systematic methodology for solving the constrained equilibrium problem, without necessitating the implementation of complex transformations or parametrisation of the constraint functions.

As discussed in Section 2.3, the augmented LM formulation introduces an additional term to the Lagrangian function, referred to as penalty term, which is related to the constraint function to a 2<sup>nd</sup> order. The penalty term introduced herein physically corresponds to a fictitious elastic spring of stiffness  $\varepsilon$  introduced between  $\Gamma^{(1)}$  and  $\Gamma^{(2)}$ , with deformation equal to their relative deformation, which is given by the constraint function. This leads to the following final form:

$$\Pi(u_1, u_2) = \frac{1}{2}k_1u_1^2 + \frac{1}{2}k_2u_2^2 - Pu_2 + \lambda(u_1 - u_2) + \frac{1}{2}\varepsilon(u_1 - u_2)^2 \quad (4.4)$$

First order differentiation of Eq. (4.4) with respect to the kinematic DOFs ( $u_1, u_2$ ) and the Lagrangian Multiplier  $\lambda$ , treated as an additional DOF, yields the system forces associated with each DOF. Equating the obtained expressions to zero for extrema identification leads to the following system of equilibrium equations, describing the minimum energy state of the coupled system subject to the kinematic constraint in Eq. (4.2):

$$\begin{Bmatrix} \frac{\partial \Pi}{\partial u_1} \\ \frac{\partial \Pi}{\partial u_2} \\ \frac{\partial \Pi}{\partial \lambda} \end{Bmatrix} = \begin{Bmatrix} k_1u_1 \\ k_2u_2 - P \\ 0 \end{Bmatrix} + \begin{Bmatrix} \lambda \\ -\lambda \\ u_1 - u_2 \end{Bmatrix} + \begin{Bmatrix} \varepsilon(u_1 - u_2) \\ -\varepsilon(u_1 - u_2) \\ 0 \end{Bmatrix} = \begin{Bmatrix} 0 \\ 0 \\ 0 \end{Bmatrix} \quad (4.5)$$

As shown in Eq. (4.5), the force vector of the system consists of three component vectors, corresponding to the spring, the LM and the penalty terms, respectively. Subsequent differentiation of the obtained force vector with respect to the kinematic and additional DOFs, allows for the determination of a consistent tangent stiffness matrix, with respective contributions from each of these components. Evidently, the LM term contribution extends to both the kinematic and additional DOFs, while the penalty term vanishes upon differentiation with respect to the additional DOFs.

Due to the system equilibrium being formulated in a discrete form, the contribution of the introduced LM and penalty coupling terms can be effectively accounted for by means of the corresponding force vector and tangent stiffness matrix component assembly to the global system of equations. Despite the coupling terms not being associated with material and mechanical properties, the incorporation of their contribution in a discrete manner via assembly naturally leads to the concept of a coupling element. In the simplified mechanical model at

hand, the coupling element comprises a set of DOFs associated with the coupling interface  $\Gamma_c$ , including both the kinematic DOFs  $(u_1, u_2)$  and the additional DOF  $\lambda$ , corresponding to the unknown value of the introduced LM.

The systematic mathematical treatment of kinematic constraints in discrete systems by employment of coupling elements is achieved on the basis of the following procedure: (i) establishment of the coupling term contributions to the total potential energy function of the system, accounting for both the LM and penalty term contributions; (ii) differentiation of these energy terms with respect to the set of kinematic and additional DOFs once, or equivalently application of 1<sup>st</sup> order variational principles, to obtain the coupling element internal force vector; (iii) differentiation of the energy terms twice with respect to the same parameters, or equivalently application of 2<sup>nd</sup> order variational principles, to obtain the consistent tangent stiffness matrix of the coupling element; (iv) assembly of the coupling element force vector and tangent stiffness matrix to the global force vector and tangent stiffness matrix of the system; and (v) solution of the system of equations to obtain the values of the unknown LMs and kinematic DOFs, which lead to an equilibrium state compatible with the imposed constraints.

For the simplified mechanical model of the two springs, the coupling element contribution to the system total potential energy is given by the following expression:

$$\Pi(u_1, u_2) = \lambda(u_1 - u_2) + \frac{1}{2} \varepsilon (u_1 - u_2)^2 \quad (4.6)$$

which in turn allows for the following expressions for the coupling force vector  $\mathbf{f}_e$  and tangent stiffness matrix  $\mathbf{k}_e$  to be obtained, by virtue of 1<sup>st</sup> and 2<sup>nd</sup> order differentiation, respectively:

$$\mathbf{f}_e = \begin{Bmatrix} \frac{\partial \Pi}{\partial u_1} \\ \frac{\partial \Pi}{\partial u_2} \\ \frac{\partial \Pi}{\partial \lambda} \end{Bmatrix} = \begin{Bmatrix} \lambda \\ -\lambda \\ u_1 - u_2 \end{Bmatrix} + \begin{Bmatrix} \varepsilon (u_1 - u_2) \\ -\varepsilon (u_1 - u_2) \\ 0 \end{Bmatrix} = \begin{Bmatrix} f_1 \\ f_2 \\ f_a \end{Bmatrix} \quad (4.7)$$

$$\mathbf{k}_e = \begin{bmatrix} \frac{\partial^2 \Pi}{\partial u_1^2} & \frac{\partial^2 \Pi}{\partial u_1 \partial u_2} & \frac{\partial^2 \Pi}{\partial u_1 \partial \lambda} \\ \frac{\partial^2 \Pi}{\partial u_2 \partial u_1} & \frac{\partial^2 \Pi}{\partial u_2^2} & \frac{\partial^2 \Pi}{\partial u_2 \partial \lambda} \\ \frac{\partial^2 \Pi}{\partial \lambda \partial u_1} & \frac{\partial^2 \Pi}{\partial \lambda \partial u_2} & \frac{\partial^2 \Pi}{\partial \lambda^2} \end{bmatrix} = \begin{bmatrix} 0 & 0 & 1 \\ 0 & 0 & -1 \\ 1 & -1 & 0 \end{bmatrix} + \begin{bmatrix} \varepsilon & -\varepsilon & 0 \\ -\varepsilon & \varepsilon & 0 \\ 0 & 0 & 0 \end{bmatrix} = \begin{bmatrix} k_{11} & k_{12} & k_{1\alpha} \\ k_{21} & k_{22} & k_{2\alpha} \\ k_{\alpha 1} & k_{\alpha 2} & k_{\alpha\alpha} \end{bmatrix} \quad (4.8)$$

The discrete equilibrium at the coupling element level can thus be stated as:

$$\mathbf{f}_e = \mathbf{k}_e \mathbf{u} \Rightarrow \begin{Bmatrix} f_1 \\ f_2 \\ f_a \end{Bmatrix} = \begin{bmatrix} k_{11} & k_{12} & k_{1\alpha} \\ k_{21} & k_{22} & k_{2\alpha} \\ k_{\alpha 1} & k_{\alpha 2} & k_{\alpha\alpha} \end{bmatrix} \cdot \begin{Bmatrix} u_1 \\ u_2 \\ \lambda \end{Bmatrix} \quad (4.9)$$

It can easily be inferred from Eq. (4.7) that the LM term introduces a couple of opposing forces  $f_1$  and  $f_2$  with values equal to the unknown LM  $\lambda$  in the direction of the kinematic DOFs, to enforce the kinematic constraint on the springs system. This confirms the physical and dimensional correspondence of LMs to forces in the case of translational coupling, as discussed earlier. The penalty term contribution to the system is also a couple of opposing forces on the two springs, albeit these vanish with the kinematic constraint fulfilment, and thus have no effect whatsoever on the obtained solution.

In the case of translational coupling, the stiffness contribution of the LM term is limited to the additional DOF, thereby leading to a sparse matrix form, as indicated by Eq. (4.8). The penalty term prominent contribution is the introduction of non-zero terms along the main diagonal of the tangent stiffness matrix. This is particularly crucial in large-scale multi-DOF systems where solvers that eliminate individual parameter using their corresponding equations, i.e. without performing row-switching, are employed, such as the frontal solver (Irons, 1970). Such solvers require non-zero pivots along the diagonals, and hence if one of the springs in this case, or one of the coupled substructures in large-scale systems, is unrestrained or associated with zero stiffness, then a penalty parameter would be the only way to eliminate the kinematic DOFs, after which the LM parameters can be eliminated. The penalty parameter therefore ensures that ill-conditioning of large-scale coupled nonlinear equilibrium equation systems, as well as potential convergence bottlenecks in the numerical solution of such systems, are avoided. This will also be discussed at a later point, in Section 4.6.



From Eqs. (4.7) and (4.8) it is evident that the extended system of equilibrium equations for the springs system, associated with both the kinematic and additional DOFs, is mixed-dimensional, i.e. comprising both force and displacement terms. In particular, its solution leads to a LM in the displacement vector representing the set of coupling forces, while the force vector term  $f_a$ , associated with the additional DOF in Eq. (4.7), is dimensionally correspondent to a displacement. This term is responsible for introducing the kinematic constraint function of Eq. (4.2) to the system of equations, which is equal to zero when the constraint is enforced, thus guiding the solution towards a kinematically compatible equilibrium state.

### **4.3 Problem description and basic notation**

The general setting of the coupling problem at hand considers two independent deformable surfaces, discretised with non-conforming shell FE meshes along a 1-D interface. For the coupling constraint enforcement in a discrete sense along the interface, an adaptation of the standard two-field mortar method (Fischer & Wriggers, 2005a; Puso, 2004) is employed herein, as discussed in Sub-section 2.3.2.5, leading to the development of a novel 1-D coupling element formulation.

The mortar method involves the surface domain classification as mortar and non-mortar, also commonly referred to as master and slave, respectively, which will be the adopted terminology henceforth. The surface classification into master and slave controls the interface discretisation into coupling elements and the efficiency of the adopted integration scheme at the coupling element level, as will be thoroughly explained in the current section, as well as in Sub-sections 4.5.2 and 4.7.3 at a later point of the present chapter.

An embedded assumption in the developed coupling element formulation, which primarily deals with thin plates and shells, is the constraint enforcement at the shell surface mid-plane, thus ignoring cross-sectional deformation and eccentricity over the shell thickness. For moderately thick shells, the inaccuracies associated with the mid-plane approximation can be partially alleviated by defining the coupling interface at a distance from the shell surfaces, to account for their respective half-thicknesses, however this is not considered in the present work.

In the general problem setting, the coupled surfaces can be planar or curved and parallel or intersecting, the coupling interface can be straight or curved, while the shell element domain geometry can be regular or irregular. A systematic algorithmic treatment for surface coupling along a line, applicable to curved surfaces discretised with irregular elements and curved interface geometries, for any relative spatial orientation of these, is presented and discussed in detail in Section 4.5.

To introduce the 1-D surface coupling problem and the adopted notation for the development of the coupling element formulation in a simple manner, the example system illustrated in Figure 4.2 is considered herein, comprising two parallel planar surfaces  $\Omega^{(i)} \in \mathbb{R}^3$ , ( $i=1,2$ ), discretised with regular 9-noded quadrilateral shell elements and coupled along a straight 1-D interface  $\Gamma_c$ . Surfaces  $\Omega^{(1)}$  and  $\Omega^{(2)}$  are classified as slave and master, respectively, without loss of generality, and the discussion following this point will be based on this assumption. To avoid overuse of the term element, referring to both the coupling elements and the shell elements on the two surfaces, the latter will be referred to as FEs henceforth.

The projection of  $\Gamma_c$  on  $\Omega^{(i)}$ , henceforth denoted  $\Gamma_c^{(i)}$ , traverses the respective discretised domains in an arbitrary orientation, intersecting the edges of a distinct set of FEs on each surface, as illustrated in Figure 4.2. This is the set of shell elements where the coupling constraint is enforced, henceforth referred to as active FEs of  $\Omega^{(i)}$  and denoted as  $\Gamma_j^{(i)}$ . The sub-domain of  $\Omega^{(i)}$  including these will henceforth be referred to as its active domain and denoted as  $\Gamma^{(i)}$ , with  $\Gamma^{(i)} = \bigcup_{j=1}^{n_{ei}} \Gamma_j^{(i)}$ , where  $n_{ei}$  is the number of active FEs on  $\Omega^{(i)}$ .

The discretisation of  $\Gamma_c$  into coupling elements is achieved by means of a progressive segmentation scheme. The progressive segmentation of  $\Gamma_c$  can be performed on the basis of either the slave surface or both the master and slave surfaces, henceforth referred to as slave-only and slave-master segmentation, respectively. The slave-only segmentation approach is adopted in the developed formulation, which is based on the intersection identification of the projection of  $\Gamma_c$  on  $\Omega^{(1)}$ ,  $\Gamma_c^{(1)}$ , with the edges of the active slave FEs  $\Gamma_j^{(1)}$ ,  $j=1,2,\dots,n_{e1}$ , where in the example system  $n_{e1} = 4$ . The set of identified slave interface segments, henceforth denoted as  $\Gamma_{c_j}^{(1)}$ , correspond to a set of segments on  $\Gamma_c$ , henceforth denoted as  $\Gamma_{c_j}$ . Each segment is subsequently projected on  $\Omega^{(2)}$  as  $\Gamma_{c_j}^{(2)}$ , and its intersections with a number of

active master FEs  $\Gamma_k^{(2)}$ ,  $k=1,2,\dots,n_{e_2}$ , in the active subdomain  $\Gamma^{(2)}$  are identified, where in the example system  $n_{e_2} = 4$ .

The adoption of this segmentation strategy provides a systematic approach for the identification of all interacting couples of active master and slave FEs along  $\Gamma_c$ . Furthermore, it enables each segment  $\Gamma_{cj}$ , and accordingly  $\Gamma_{cj}^{(1)}$ , to be associated with a unique active slave FE  $\Gamma_j^{(1)}$  on  $\Omega^{(1)}$  and a number of active master FEs  $\Gamma_k^{(2)}$  on  $\Omega^{(2)}$ , which varies in general amongst different segments. The coupling formulation can therefore be implemented in the form of a coupling element, comprising an active slave FE  $\Gamma_j^{(1)}$ , an associated active master FE  $\Gamma_k^{(2)}$ , and the corresponding slave segment  $\Gamma_{cj}^{(1)}$  of  $\Gamma_c$ . The procedure is schematically illustrated in Figure 4.3 (a).

The specified set of kinematic constraints are enforced at the coupling element level by virtue of a LM field  $\lambda$ . This is defined on the slave segment  $\Gamma_{cj}^{(1)}$  in a continuous sense, via interpolation of the LM parameters defined at predetermined discrete locations on the segment, henceforth referred to as Collocation Points (CPs). The concept is schematically illustrated in Figure 4.4. It should be noted that the definition of the LM field on  $\Gamma_{cj}$  in Figure 4.4 is due to this being identical to  $\Gamma_{cj}^{(1)}$  in the case of the example system, where parallel surfaces are considered and  $\Gamma_c$  is defined in a continuous sense on the surface domains. In the general case, the LM field should always be defined on  $\Gamma_{cj}^{(1)}$ . Moreover, the notation adopted in the figure has been simplified on account of generality, in compliance with what is later discussed in Sub-section 4.6.2.

In the formulation developed and presented herein, consideration is given to two or three CPs per coupling interface segment, defined at the segment end-points and, optionally, at their mid-point, leading to a linear or quadratic LM field interpolation, respectively. The limitation of the CP number is intended to avoid potential singularities in the nonlinear solution procedure of the coupled problem, arising from overly constrained coupling elements. The sharing of the CPs between adjacent segments leads to a piece-wise linear or quadratic continuous LM field along  $\Gamma_c$ , as graphically illustrated in Figure 4.3 (b), where  $\tilde{x}$ ,  $\tilde{y}$ ,  $\tilde{z}$  are the interface local Cartesian coordinate axes.

The CPs and the associated LM vectors along a given segment are shared between the set of coupling elements associated with it. Hence, the constraint enforcement in a continuous sense along this segment achieves coupling of the unique slave and all master FEs associated with the respective set of coupling elements. The subsequent assembly of all coupling element contributions achieves surface coupling along the entirety of  $\Gamma_c$ .

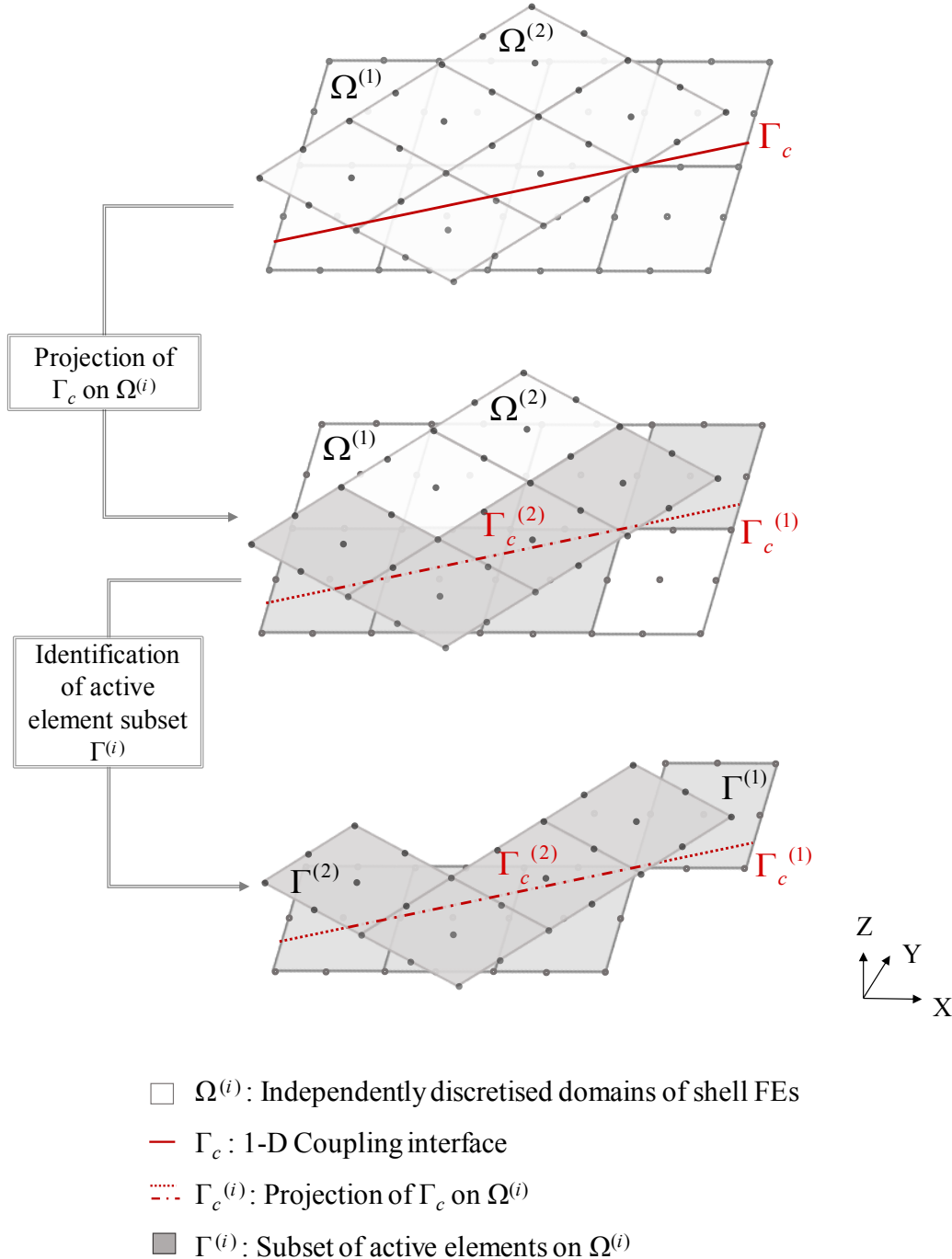
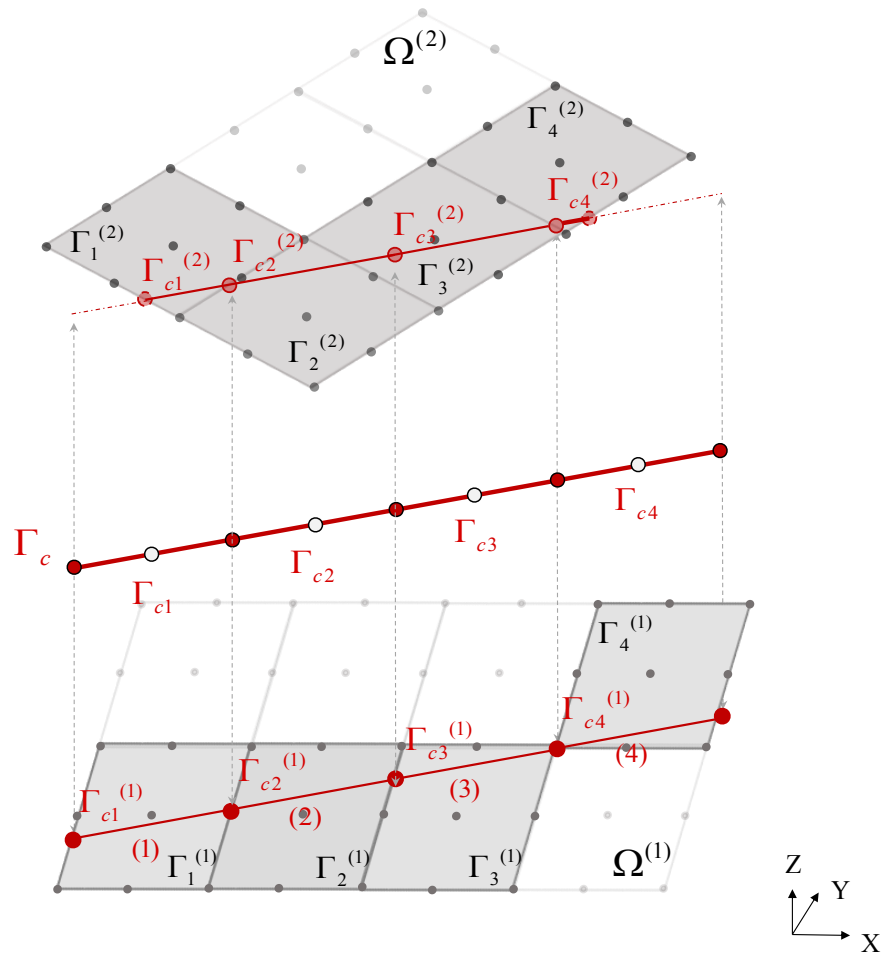
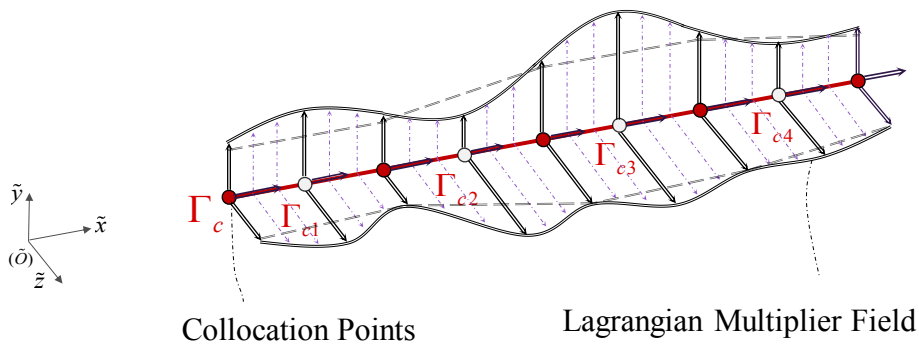


Figure 4.2: 1-D coupling of surfaces discretised with non-conforming shell finite element meshes and identification of active shell element subset on each surface



(a)



(b)

Figure 4.3: (a) Coupling interface segmentation and active shell element couple identification procedure, (b) 1-D coupling interface with piecewise linear (dashed line) and piecewise quadratic (continuous line) distribution of the Lagrangian Multiplier field

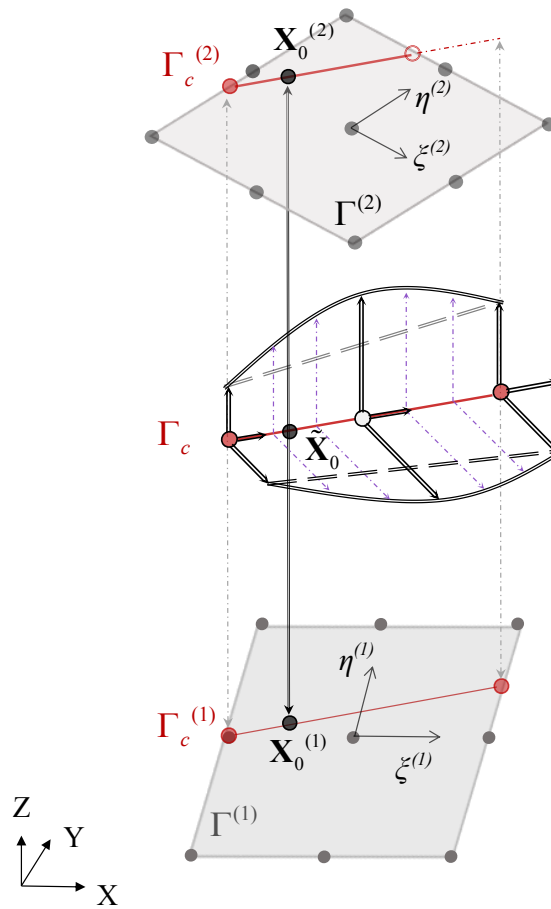


Figure 4.4: 1-D coupling element comprising two shell finite elements and a coupling interface segment

The coupling element formulation developed in the context of the present research work deals with the cases of translational and rotational surface coupling. As will be thoroughly discussed in Chapter 5, both these kinematic constraints are expressed in terms of the translational displacement field of the coupled surfaces in the global Cartesian coordinate system. This is due to the rotational constraint being associated with the coupling of the surface slopes along the interface, which can be related to the surface global translations, rather than the rotations of the surface normals. Accordingly, all expressions presented hereafter, related to the displacement fields of the two surfaces and the shell FEs employed for their discretisation, will be limited to the translational components.

In the case of continuous 1-D coupling between two deformable shell surfaces, the imposed constraint can be expressed as a function of the surface global displacement vector fields  $(\mathbf{u}^{(1)}, \mathbf{u}^{(2)})$  along  $\Gamma_c$ , similar to Eq. (4.2) for the simplified mechanical springs model. Each

component of the constraint vector function  $\mathbf{g}(\mathbf{u}^{(1)}, \mathbf{u}^{(2)})$  corresponds to an imposed kinematic constraint and requires the introduction of an additional set of LM DOFs at the CPs for its effective enforcement. In the context of the developed translational and rotational coupling formulations, consideration is given to a maximum of four LM field components, achieving coupling of the three global translational displacement components, as well as the relative surface slope orientation transverse to the coupling interface.

Before proceeding to the description of the systematic methodology for interface segmentation, coupling element identification and constraint enforcement in the general setting of the 1-D surface coupling problem, it is useful to define the coupling element kinematic and additional DOFs, as well as some useful expressions for the local geometry and LM field interpolation.

#### 4.4 Coupling element kinematic and additional DOFs

The constraint enforcement at the coupling element level requires the establishment of the constraint vector function  $\mathbf{g}(\mathbf{u}^{(1)}, \mathbf{u}^{(2)})$  along the associated segment projections on the slave and master shell FE domains. The displacement fields of  $\Omega^{(1)}$  and  $\Omega^{(2)}$  along the respective interface projections,  $(\mathbf{u}^{(1)}, \mathbf{u}^{(2)})$ , are obtained by means of interpolation of the respective shell FE nodal kinematic DOFs. Therefore, the inclusion of both slave and master shell FE nodal DOFs in the coupling element formulation is necessitated. These will be henceforth referred to as the set of primary or kinematic DOFs of a coupling element, and denoted as  $\mathbf{u}_e^{(1)}$  and  $\mathbf{u}_e^{(2)}$ .

As discussed in the preceding section, the introduction of CPs along the interface segments shifts the focus from the continuous to the discrete, with a continuous LM field  $\lambda$  being obtained via interpolation of the LM vectors evaluated at their discrete predetermined locations. Therefore, for the continuous constraint enforcement along the interface segment of a given coupling element, the LM vectors at two or three discrete CP locations are only required. These will henceforth be referred to as the additional DOFs of a coupling element and denoted as  $\lambda_e$ . As discussed earlier, the number of additional DOFs is dictated by the number of imposed constraints along the interface.

In the following two sections, the distinct isoparametric frameworks employed for the interpolation of the geometry and displacement field at the active shell FE domains, as well as of the geometry and LM field along the coupling segments, are presented. Special consideration is given to the translational and rotational coupling element formulations presented in Chapter 5, which achieve coupling of the global translational displacement field and the shell element slopes. A LM field  $\boldsymbol{\lambda} = (\lambda_X \quad \lambda_Y \quad \lambda_Z \quad \lambda_R)^T$  with four components is required to achieve coupling in this case, encompassing three LM force fields  $(\lambda_X \quad \lambda_Y \quad \lambda_Z)^T$  along the (X,Y,Z) global Cartesian coordinate axes and single moment field  $\lambda_R$ . The expressions presented in the following sections are derived along the lines of these considerations.

#### 4.4.1 Shell element geometry and kinematics

For any point along  $\Gamma_c^{(i)}$ , located in the domain of an active shell FE on  $\Gamma^{(i)}$ , the local and global coordinates,  $\mathbf{x}^{(i)} = (x^{(i)} \quad y^{(i)} \quad z^{(i)})^T$  and  $\mathbf{X}^{(i)} = (X^{(i)} \quad Y^{(i)} \quad Z^{(i)})^T$ , in the undeformed and the current deformed configurations, as well as the global translational displacement field  $\mathbf{u}^{(i)} = (U^{(i)} \quad V^{(i)} \quad W^{(i)})^T$ , can be obtained by interpolation of the respective nodal quantities using polynomial shape functions. This leads to an isoparametric representation of the local and global geometry, as well as of the global displacement field, over the shell element domain:

$$\mathbf{x}^{(i)} = \mathbf{x}^{(i)}(\xi^{(i)}, \eta^{(i)}) = \sum_{k=1}^{m_i} N_k^{(i)}(\xi^{(i)}, \eta^{(i)}) \mathbf{x}_k^{(i)} = \mathbf{N}^{(i)} \cdot \mathbf{x}_e^{(i)} \quad (4.10)$$

$$\mathbf{X}^{(i)} = \mathbf{X}^{(i)}(\xi^{(i)}, \eta^{(i)}) = \sum_{k=1}^{m_i} N_k^{(i)}(\xi^{(i)}, \eta^{(i)}) \mathbf{X}_k^{(i)} = \mathbf{N}^{(i)} \cdot \mathbf{X}_e^{(i)} \quad (4.11)$$

$$\mathbf{u}^{(i)} = \mathbf{X}^{(i)} - \mathbf{X}_0^{(i)} = \mathbf{u}^{(i)}(\xi^{(i)}, \eta^{(i)}) = \sum_{k=1}^{m_i} N_k^{(i)}(\xi^{(i)}, \eta^{(i)}) \mathbf{u}_k^{(i)} = \mathbf{N}^{(i)} \cdot \mathbf{u}_e^{(i)} \quad (4.12)$$

In the above expressions,  $m_i = 6$  or  $9$  is the number of element nodes in the case of triangular and quadrilateral quadratic shell elements considered herein;  $(\xi^{(i)}, \eta^{(i)})$  are the natural



coordinates of the shell FE in the active domain  $\Gamma^{(i)}$ ;  $\mathbf{x}_k^{(i)} = (x_k^{(i)} \ y_k^{(i)} \ z_k^{(i)})^T$  and  $\mathbf{X}_k^{(i)} = (X_k^{(i)} \ Y_k^{(i)} \ Z_k^{(i)})^T$  are the local and global coordinate vectors of node  $k$ , respectively;  $\mathbf{u}_k^{(i)} = (U_k^{(i)} \ V_k^{(i)} \ W_k^{(i)})^T$  is the global translation vector of node  $k$ ;  $\mathbf{x}_e^{(i)} = (\mathbf{x}_1^{(i)} \ \mathbf{x}_2^{(i)} \ \dots \ \mathbf{x}_{m_i}^{(i)})^T$  and  $\mathbf{X}_e^{(i)} = (\mathbf{X}_1^{(i)} \ \mathbf{X}_2^{(i)} \ \dots \ \mathbf{X}_{m_i}^{(i)})^T$  are the shell element local and global nodal coordinates, respectively;  $\mathbf{u}_e^{(i)} = (\mathbf{u}_1^{(i)} \ \mathbf{u}_2^{(i)} \ \dots \ \mathbf{u}_{m_i}^{(i)})^T$  are the shell element global nodal translations; and  $\mathbf{N}^{(i)}$  is a matrix containing the shell element shape functions, defined as follows for the interpolation of 3-D position vectors:

$$\mathbf{N}^{(i)} = \begin{bmatrix} N_1^{(i)} & 0 & 0 & N_2^{(i)} & 0 & 0 & \dots & N_{m_i}^{(i)} & 0 & 0 \\ 0 & N_1^{(i)} & 0 & 0 & N_2^{(i)} & 0 & \dots & 0 & N_{m_i}^{(i)} & 0 \\ 0 & 0 & N_1^{(i)} & 0 & 0 & N_2^{(i)} & \dots & 0 & 0 & N_{m_i}^{(i)} \end{bmatrix} \quad (4.13)$$

The assumption of the shell elements becoming virtually flat with mesh refinement is adopted herein, which allows for the local shell element geometry to be approximated as planar. This is attributed to the definition of the local element coordinate system, where, as the mesh is refined, the local z-abscissae become negligible compared to the x- and y- abscissae. The isoparametric representation of the local geometry using only the set of planar coordinates, henceforth denoted as  $\bar{\mathbf{x}}^{(i)} = (x^{(i)}, y^{(i)})$ , can be stated as follows:

$$\bar{\mathbf{x}}^{(i)} = \bar{\mathbf{x}}^{(i)}(\xi^{(i)}, \eta^{(i)}) = \sum_{k=1}^{m_i} N_k^{(i)}(\xi^{(i)}, \eta^{(i)}) \bar{\mathbf{x}}_k^{(i)} = \bar{\mathbf{N}}^{(i)} \cdot \bar{\mathbf{x}}_e^{(i)} \quad (4.14)$$

where the matrix of shape functions  $\bar{\mathbf{N}}^{(i)}$  employed for the interpolation of local planar quantities is given by the following expression:

$$\bar{\mathbf{N}}^{(i)} = \begin{bmatrix} N_1^{(i)} & 0 & N_2^{(i)} & 0 & \dots & N_{m_i}^{(i)} & 0 \\ 0 & N_1^{(i)} & 0 & N_2^{(i)} & \dots & 0 & N_{m_i}^{(i)} \end{bmatrix} \quad (4.15)$$

The flat shell limit assumption with mesh refinement is particularly useful for the establishment of the rotational coupling element formulation discussed in detail in Chapter 5.

#### 4.4.2 Coupling interface segment geometry and LM field

Based on the flat shell limit, or negligible shell out-of-flatness, assumption with mesh refinement, the interface segment out-of-straightness can also be considered negligible in the limit, thus enabling the approximation of the local geometry using a single local coordinate  $\tilde{x}$  along the segment longitudinal axis. An isoparametric representation is employed, allowing for the local and global coordinates,  $\tilde{x}$  and  $\tilde{\mathbf{X}} = (\tilde{X} \ \tilde{Y} \ \tilde{Z})^T$ , as well as the LM field  $\boldsymbol{\lambda}$ , to be obtained by interpolation of the respective quantities at the discrete CPs:

$$\tilde{x} = \tilde{x}(\tilde{\xi}) = \sum_{k=1}^{m_\lambda} \Phi_k(\tilde{\xi}) \tilde{x}_k = \boldsymbol{\Phi} \cdot \tilde{\mathbf{x}}_e \quad (4.16)$$

$$\tilde{\mathbf{X}} = \tilde{\mathbf{X}}(\tilde{\xi}) = \sum_{k=1}^{m_\lambda} \Phi_k(\tilde{\xi}) \cdot \tilde{\mathbf{X}}_k = \boldsymbol{\Phi} \cdot \tilde{\mathbf{X}}_e \quad (4.17)$$

$$\boldsymbol{\lambda} = \boldsymbol{\lambda}(\tilde{\xi}) = \sum_{k=1}^{m_\lambda} \Phi_k(\tilde{\xi}) \cdot \boldsymbol{\lambda}_k = \boldsymbol{\Phi} \cdot \boldsymbol{\lambda}_e \quad (4.18)$$

In the above expressions,  $m_\lambda = 2$  or  $3$  is the number of CPs defined along the segment, for a linear or quadratic LM field, respectively;  $\tilde{\xi}$  is the natural coordinate along the segment;  $\tilde{x}_k$ ,  $\tilde{\mathbf{X}}_k = (\tilde{X}_k \ \tilde{Y}_k \ \tilde{Z}_k)^T$  are the local and global coordinate vectors of CP  $k$ , respectively;  $\boldsymbol{\lambda}_k = (\lambda_{Xk} \ \lambda_{Yk} \ \lambda_{Zk} \ \lambda_{Rk})^T$  is the LM field vector of CP  $k$ ;  $\tilde{\mathbf{x}}_e = (\tilde{x}_1 \ \tilde{x}_2 \ \dots \ \tilde{x}_{m_\lambda})^T$ ,  $\tilde{\mathbf{X}}_e = (\tilde{\mathbf{X}}_1 \ \tilde{\mathbf{X}}_2 \ \dots \ \tilde{\mathbf{X}}_{m_\lambda})^T$  and  $\boldsymbol{\lambda}_e = (\boldsymbol{\lambda}_1 \ \boldsymbol{\lambda}_2 \ \dots \ \boldsymbol{\lambda}_{m_\lambda})^T$  are the coupling segment local and global coordinates and LMs at the discrete CPs, respectively; and the matrices of LM shape functions  $\boldsymbol{\Phi}$  and  $\boldsymbol{\Phi}$  are given by the following expressions:

$$\boldsymbol{\Phi} = [\Phi_1 \ \dots \ \Phi_{m_\lambda}] \quad (4.19)$$

$$\boldsymbol{\Phi} = \begin{bmatrix} \Phi_1 & 0 & 0 & 0 & \dots & \Phi_{m_\lambda} & 0 & 0 & 0 \\ 0 & \Phi_1 & 0 & 0 & \dots & 0 & \Phi_{m_\lambda} & 0 & 0 \\ 0 & 0 & \Phi_1 & 0 & \dots & 0 & 0 & \Phi_{m_\lambda} & 0 \\ 0 & 0 & 0 & \Phi_1 & \dots & 0 & 0 & 0 & \Phi_{m_\lambda} \end{bmatrix} \quad (4.20)$$

$$\mathbf{\Phi} = \begin{bmatrix} \Phi_1 & 0 & 0 & \dots & \Phi_{m\lambda} & 0 & 0 \\ 0 & \Phi_1 & 0 & \dots & 0 & \Phi_{m\lambda} & 0 \\ 0 & 0 & \Phi_1 & \dots & 0 & 0 & \Phi_{m\lambda} \end{bmatrix} \quad (4.21)$$

where Eqs. (4.20) and (4.21) are employed for the LM field and global geometry interpolations, respectively. As will be discussed in Chapter 5, the translational and rotational coupling formulations have been developed independently, allowing for coupling of surface translations and rotations or translations only, where in the latter case  $\boldsymbol{\lambda} = (\lambda_x \quad \lambda_y \quad \lambda_z)^T$  and the matrix of shape functions in Eq. (4.21) is employed for the LM field interpolation in Eq. (4.18).

The isoparametric mapping process for the shell element surfaces and the coupling interface segment is imperative for achieving an effective numerical integration of the coupling element force vector and tangent stiffness matrix, as discussed in detail in Sub-section 4.7.2.

#### 4.5 Systematic methodology for progressive segmentation of coupling interface and active element identification

In the general setting of 1-D surface coupling with non-conforming FE meshes, involving planar, curved or folded surfaces discretised with irregular shell FEs and coupled along a straight or curved interface, the establishment of a systematic methodology for the coupling interface progressive segmentation requires a rigorous algorithmic process. This is attributed to the requirement of establishing distinct coordinate mapping parametric frameworks for the surface and interface domain geometric descriptions, as well as to the intrinsic complexity of the embedded geometric and intersection point search processes.

A systematic methodology for the coupling interface discretisation into coupling elements encompasses: (i) the mathematical description of the coupled surfaces and the coupling interface geometry in a discrete sense; (ii) the active shell FE identification on each coupled surface based on the geometric progression of the interface projection in the respective domain, including the entry and exit points and the adjacent element identification for each active element; and (iii) the identification of distinct couples of master and slave shell FEs on the two surfaces interacting along each interface segment, and the establishment of a set of discrete coupling elements along the 1-D interface.

An advanced computational tool has been developed and implemented for this purpose, which provides an efficient strategy for the systematic treatment of the aforementioned processes. The progressive segmentation algorithm presented herein is applicable to planar, curved and folded surfaces, discretised with geometrically regular or irregular, isoparametric, 9-noded quadrilateral or 6-noded triangular, shell FEs and coupled along a straight or curved 1-D interface. The employment of the developed geometric algorithm in conjunction with the translational and rotational coupling element formulations presented in Chapter 5, allows for a systematic and consistent methodology to be established for discrete 1-D constraint enforcement between any two independently discretised deformable shell surfaces. The consideration of a broad and generic application framework in the development of the present methodology, as well as the coupling formulations presented in the next chapter, enables the straightforward upgrade of existing FE programs to incorporate coupling elements for any type of 2-D and 3-D FEs.

The current section is divided into three sub-sections, which shed light on the mathematical and computational treatment of the three main geometric processes previously outlined. The notation introduced in Section 4.3 is adopted throughout.

#### **4.5.1 Discrete geometric description of coupled surfaces and coupling interface**

The parametric framework for the discrete geometric description of the coupled deformable 2-D surfaces  $\Omega^{(i)}$  and the 1-D coupling interface  $\Gamma_c$  is described herein. The framework is applicable to parallel and intersecting planar, curved and folded surfaces, as well as to straight and curved line interfaces. The interface is defined in an arbitrary orientation in the case of parallel surfaces, while being limited to the line of intersection in the case of intersecting non-parallel surfaces.

The discrete geometric description of the coupled surface is achieved in an approximate sense, by virtue of the shell FE mesh employed for their discretisation. The required data includes: (i) a grid of nodes with known coordinates in the global Cartesian coordinate system; and (ii) a set of FEs with well-defined connectivity, where each FE domain geometry is approximated via interpolation of the respective nodal coordinates.

The arrays of structural nodal coordinates and FE connectivity for the mesh of surface  $\Omega^{(i)}$ , henceforth denoted as  $\mathbf{D}^{(i)}$  and  $\mathbf{E}^{(i)}$ , respectively, are expressed in the following formats:

$$\mathbf{D}^{(i)} = \begin{bmatrix} D_1^{(i)} & X_{D_1^{(i)}} & Y_{D_1^{(i)}} & Z_{D_1^{(i)}} \\ D_2^{(i)} & X_{D_2^{(i)}} & Y_{D_2^{(i)}} & Z_{D_2^{(i)}} \\ \vdots & \vdots & \vdots & \vdots \\ D_{n_{Di}}^{(i)} & X_{D_{n_{Di}}^{(i)}} & Y_{D_{n_{Di}}^{(i)}} & Z_{D_{n_{Di}}^{(i)}} \end{bmatrix} \quad (4.22)$$

$$\mathbf{E}^{(i)} = \begin{bmatrix} E_1^{(i)} & D_{11}^{(i)} & D_{12}^{(i)} & \dots & D_{1m_i}^{(i)} \\ E_2^{(i)} & D_{21}^{(i)} & D_{22}^{(i)} & \dots & D_{2m_i}^{(i)} \\ \vdots & \vdots & \vdots & \ddots & \vdots \\ E_{n_{Ei}}^{(i)} & D_{n_{Ei}1}^{(i)} & D_{n_{Ei}2}^{(i)} & \dots & D_{n_{Ei}m_i}^{(i)} \end{bmatrix} \quad (4.23)$$

In the above expressions,  $D_j^{(i)}$ , ( $j=1,2,\dots,n_{Di}$ ), are the nodal IDs and  $E_k^{(i)}$ , ( $k=1,2,\dots,n_{Ei}$ ), are the FE IDs on the mesh of  $\Omega^{(i)}$ , with  $n_{Di}$  and  $n_{Ei}$  being the total number of nodes and FEs on the respective surface. Array  $\mathbf{D}^{(i)}$  includes the global Cartesian coordinates  $(X_{D_j^{(i)}}, Y_{D_j^{(i)}}, Z_{D_j^{(i)}})$  of each node  $j$  on  $\Omega^{(i)}$ , while array  $\mathbf{E}^{(i)}$  includes the FE connectivity, where  $D_{k1}^{(i)}, D_{k2}^{(i)}, \dots, D_{km_i}^{(i)}$  are the nodes of element  $k$ , with  $m_i = 6$  or  $9$  for 6-noded triangular and 9-noded quadrilateral shell elements, respectively. A counter-clockwise sense is adopted for the nodal ordering in each FE, with the vertex nodes first, followed by the intermediate edge nodes, as well as the central node in the case of 9-noded shell FEs.

For the coupling interface line geometric description in 3-D space, a piece-wise linear approximation can be employed, considering a sufficiently large number of linear sectors for an accurate approximation in the case of curved geometry. A sequence of interpolation points  $\mathbf{P}$  is defined along the interface, henceforth referred to as control points. These need not be defined on  $\Omega^{(i)}$ , and are expressed in the global Cartesian coordinate system as follows:

$$\mathbf{P} = \begin{bmatrix} P_0 & X_{P_0} & Y_{P_0} & Z_{P_0} \\ P_1 & X_{P_1} & Y_{P_1} & Z_{P_1} \\ \vdots & \vdots & \vdots & \vdots \\ P_{n_p} & X_{P_{n_p}} & Y_{P_{n_p}} & Z_{P_{n_p}} \end{bmatrix} \quad (4.24)$$

where  $(X_{P_l}, Y_{P_l}, Z_{P_l})$  are the global coordinates of control point  $P_l$ , ( $l=0,1,\dots,n_p$ ),  $n_p + 1$  being the total number of control points along  $\Gamma_c$ . It should be clarified that the control points are generally different from the CPs.

A set of linear sectors is defined in between each couple of adjacent control points, and a linear interpolation of their coordinates is employed for the interface geometry approximation along a given sector. It should be noted that the term linear sector is employed herein for the purpose of distinction with the linear segments of the coupling interface, where the constraint is enforced.

It is also essential to define the constant orientation vector of each linear sector, which will subsequently be employed to guide the active shell FE identification process discussed in the following sub-section. These are given by the following expression:

$$\mathbf{t} = \begin{bmatrix} \mathbf{t}_1 \\ \mathbf{t}_2 \\ \vdots \\ \mathbf{t}_{n_p} \end{bmatrix} = \begin{bmatrix} \mathbf{X}_{P_1} - \mathbf{X}_{P_0} \\ \mathbf{X}_{P_2} - \mathbf{X}_{P_1} \\ \vdots \\ \mathbf{X}_{P_{n_p}} - \mathbf{X}_{P_{n_p}-1} \end{bmatrix} \quad (4.25)$$

The use of linear sectors provides a systematic and simplistic methodology of enhanced flexibility for the geometric description of  $\Gamma_c$ . The curved line geometry can be crudely approximated using a small number of appropriately defined control points outside of  $\Omega^{(i)}$ , while the interface projections  $\Gamma_c^{(i)}$  on  $\Omega^{(i)}$  can still be accurately determined by employing a systematic projection algorithm developed for this purpose. This is particularly useful in the case of curved or folded surfaces, where the definition of  $\Gamma_c$  on either of  $\Omega^{(i)}$  is rendered cumbersome, necessitating the employment of a considerably large number of control points, with the additional constraint of defining these on  $\Omega^{(i)}$ .

#### 4.5.2 Progressive segmentation of coupling interface and active shell FE identification

The present section describes the strategy employed for the active shell FE identification on  $\Omega^{(i)}$ , based on the previously outlined discrete geometric description approach. This is based

on primarily establishing  $\Gamma_c^{(i)}$ , and subsequently identifying the subset of  $E_k^{(i)}$  whose domain  $\Gamma_k^{(i)}$  or boundary is traversed by  $\Gamma_c^{(i)}$ , henceforth denoted as  $\mathbf{e}^{(i)}$ , with  $e_k^{(i)}$  being the individual active shell FEs, ( $k=1,2,\dots,n_{ei}$ ).

As discussed earlier, a piece-wise linear approximation is employed for the geometric description of  $\Gamma_c$ , using a set of control points which define a sequence of linear sectors with distinct orientation vectors, as given in Eqs. (4.24) and (4.25). The approximation of  $\Gamma_c$  with control points defined outside  $\Omega^{(i)}$  requires the employment of a projection algorithm for the establishment of its respective projection  $\Gamma_c^{(i)}$  in a continuous sense. The process outlined herein is based on the simultaneous progression along  $\Gamma_c$  and  $\Gamma_c^{(i)}$ , and the identification of the points of  $\Gamma_c$  projecting on  $\Gamma_c^{(i)}$  along the edges of active elements. In practice, it is only required to identify: (i) the start and end points  $P_0$  and  $P_{n_p}$  of  $\Gamma_c$  and their corresponding projections on  $\Gamma_c^{(i)}$ , henceforth denoted  $Q_0^{(i)}$  and  $Q_{n_p}^{(i)}$ , respectively; and (ii) the sequence of points  $R^{(i)}$  along  $\Gamma_c$ , corresponding to entry or exit points  $S^{(i)}$  of individual active elements  $e_k^{(i)}$  on  $\Gamma_c^{(i)}$ .

In the context of the developed active element identification strategy, four algorithmic processes are systematically employed, including: (i) a projection algorithm, which allows for the projection of a point with given global Cartesian coordinates on a curved shell FE surface described in a parametric form to be determined; (ii) a conditional projection algorithm, which allows for the point along a line in 3-D space and its corresponding projection on a curved shell FE surface described in a parametric form to be determined, subject to the condition that the latter lies on a given boundary of the surface domain; (iii) an adjacent element identification algorithm, which allows for the next active element in the direction of progression of  $\Gamma_c^{(i)}$  to be identified amongst a shortlist of candidate elements sharing a given node or edge; and (iv) an exit point identification algorithm, which allows for the intersection point of  $\Gamma_c^{(i)}$  in the direction of its progression with the boundary of a given active shell FE domain to be identified.

The active element identification strategy is outlined in a step-wise fashion hereafter, while the individual algorithmic processes discussed above, referred to as AP1-AP4, respectively, are subsequently presented in Sub-sections 4.5.2.1 - 4.5.2.4.

**Step 1:** Identification of coupling interface projection  $\Gamma_c^{(i)}$  entry element on the mesh of  $\Omega^{(i)}$

The establishment of the coupling interface projection  $\Gamma_c^{(i)}$  progression over the domain of the respective coupled surface  $\Omega^{(i)}$  primarily requires the identification of the entry shell element on the respective mesh,  $e_1^{(i)}$ . The entry element can either be known *a priori*, in which case this step is skipped, or the employment of the search process described hereafter is necessitated for its identification.

The search process aims at establishing a unique element  $e_1^{(i)}$  which fulfils two distinct criteria: (i) the starting point  $P_0$  of  $\Gamma_c$  has an active projection  $Q_0^{(i)}$  on its domain or boundary; and (ii) the orientation vector of  $\Gamma_c$  in the first linear sector traverses its domain. Criterion (i) can be fulfilled by multiple elements on  $\Gamma^{(i)}$ , which is the case when  $Q_0^{(i)}$  lies on an edge or a node shared by multiple elements. Criterion (ii) is therefore employed to ensure that the search process is narrowed down to a unique element.

Step 1.1: the distance of point  $P_0$  from the centroid of all elements of surface  $\Omega^{(i)}$  within a specified radius is evaluated and sorted in ascending order. The radius can be typically related to the maximum characteristic element size in the mesh.

Step 1.2: Starting from the element with the smallest distance, AP1 is employed to establish whether  $P_0$  has an active projection on its domain. Three cases can be distinguished:

- i.  $Q_0^{(i)}$  lies well within the domain of a unique element  $e_1^{(i)}$ .
- ii.  $Q_0^{(i)}$  coincides with a vertex node shared by multiple shell elements.
- iii.  $Q_0^{(i)}$  coincides with a perimetric non-vertex node or lies along one of the edge boundaries of  $e_1^{(i)}$  in between vertex nodes, and is thus shared by a maximum of two adjacent elements.



Conversely to case (i), where the entry element  $e_1^{(i)}$  is well established and the search process is terminated, in cases (ii) and (iii) the orientation vector  $\mathbf{t}_1$  of the first linear sector is employed to guide the unique entry element identification process, using AP3.

Step 2: Identification of exit point from active element

At the system level, the process starts with the starting point  $P_0$  of  $\Gamma_c$  and its projection  $Q_0^{(i)}$  on the domain  $\Gamma_1^{(i)}$  of the first active element  $e_1^{(i)}$  on  $\Omega^{(i)}$ , which defines the starting point of  $\Gamma_c^{(i)}$ . Orientation vector  $\mathbf{t}_1$  is employed as the trial vector for the respective exit point search process, leading to two trial points  $R_1^{(i)}$  and  $S_1^{(i)}$  on  $\Gamma_c$  and  $\Gamma_c^{(i)}$ , respectively. If the determined trial point  $R_1^{(i)}$  is located in a different linear sector, then the projection  $Q_1^{(i)}$  of control point  $P_1$  on the domain of  $e_1^{(i)}$  is established and a new search process is subsequently initiated from  $Q_1^{(i)}$  using orientation vector  $\mathbf{t}_2$ . The procedure is repeated at the active element level, until a set of points  $R_1^{(i)}$  and  $S_1^{(i)}$  conforming with the selection of the linear sector and its respective orientation vector is successfully identified.

For an active element  $e_k^{(i)}$ , ( $k=1,2,\dots, n_{ei}$ ), with entry point  $S_{k-1}^{(i)}$  on  $\Gamma_c^{(i)}$ , corresponding to the projection of a point  $R_{k-1}^{(i)}$  along  $\Gamma_c$ , AP4 is employed for the exit point  $S_k^{(i)}$  and its corresponding point  $R_k^{(i)}$  identification on  $\Gamma_c^{(i)}$  and  $\Gamma_c$ , respectively, as well as for the exit edge/vertex identification. AP4 further enables the monitoring of transitions between different linear sectors of  $\Gamma_c$ , which is particularly important in cases where the entry and exit points are associated with different linear sectors.

The process is repeated for all active elements along  $\Gamma_c^{(i)}$ , until the end points  $P_{n_p}$  and  $Q_{n_p}^{(i)}$  on  $\Gamma_c$  and  $\Gamma_c^{(i)}$  are reached, which allows for a distinct set of entry and exit points to be identified for each active element on the respective surface, as shown in Eq. (4.27).

Step 3: Identification of adjacent active element

Following the identification of the exit point edge/vertex on  $e_k^{(i)}$ , the adjacent active element  $e_{k+1}^{(i)}$  identification requires the distinguishing of two cases:

- i. The exit point coincides with a vertex node, which is shared by multiple elements in the most general context. These can be up to four for 9-noded quadrilateral and any number for 6-noded triangular shell elements. In this case, the element connectivity array  $\mathbf{E}^{(i)}$  given by Eq. (4.23) is scanned, in order for the elements sharing this vertex node to be identified. Subsequently, AP3 is employed for the identification of the unique element whose domain is traversed by  $\Gamma_c^{(i)}$ , using the orientation vector of the corresponding linear sector, as established in Step 2. It should be noted that the search process can be narrowed down to the elements within a specified radius from  $e_k^{(i)}$ , in order for the process to be accelerated in large-scale meshes.
- ii. The exit point lies on an edge of  $e_k^{(i)}$ , in between vertex nodes, potentially coinciding with a perimetric non-vertex node. In this case, the element connectivity array  $\mathbf{E}^{(i)}$  given by Eq. (4.23) is scanned, in order for the unique element sharing all three nodes or the non-vertex intermediate node of the respective edge to be identified.

Step 4: Repetition of steps 2, 3 for  $k=2,3,\dots,n_{ei}$

Having identified  $e_{k+1}^{(i)}$ , the exit point  $S_k^{(i)}$  of  $e_k^{(i)}$  becomes the new entry point, and steps 2 and 3 are repeated until one of the following process termination criteria is met:

- i. If the end point  $Q_{n_p}^{(i)}$  of  $\Gamma_c^{(i)}$  lies on surface  $\Gamma^{(i)}$ , the process is terminated when this is reached. This can be either on the surface boundary, in which case it coincides with the exit point of the last active element  $e_{n_{ei}}^{(i)}$ , or inside the surface domain, in which case it can be either on the boundary or within the domain of  $e_{n_{ei}}^{(i)}$ .
- ii. If the end point  $Q_{n_p}^{(i)}$  of  $\Gamma_c^{(i)}$  is outside the domain of surface  $\Gamma^{(i)}$ , the process is terminated when its boundary is reached by  $\Gamma_c^{(i)}$ .

Step 5: Repetition of steps 1-4 for both coupled surfaces.

The employment of the strategy outlined above for each individual coupled surface, yields as an output the subset of  $n_{ei}$  active shell elements  $\mathbf{e}^{(i)}$  on each surface, alongside the sets of entry/exit points  $\mathbf{R}^{(i)}$  and  $\mathbf{S}^{(i)}$  on  $\Gamma_c$  and  $\Gamma_c^{(i)}$ , respectively:

$$\mathbf{e}^{(i)} = \begin{bmatrix} e_1^{(i)} \\ e_2^{(i)} \\ \vdots \\ e_{n_{ei}}^{(i)} \end{bmatrix} \quad (4.26)$$

$$\mathbf{R}^{(i)} = \begin{bmatrix} R_0^{(i)} \equiv P_0 & X_{R_0^{(i)}} & Y_{R_0^{(i)}} & Z_{R_0^{(i)}} \\ R_1^{(i)} & X_{R_1^{(i)}} & Y_{R_1^{(i)}} & Z_{R_1^{(i)}} \\ \vdots & \vdots & \vdots & \vdots \\ R_{n_{ei}}^{(i)} & X_{R_{n_{ei}}^{(i)}} & Y_{R_{n_{ei}}^{(i)}} & Z_{R_{n_{ei}}^{(i)}} \end{bmatrix}, \quad \mathbf{S}^{(i)} = \begin{bmatrix} S_0^{(i)} \equiv Q_0^{(i)} & X_{S_0^{(i)}} & Y_{S_0^{(i)}} & Z_{S_0^{(i)}} \\ S_1^{(i)} & X_{S_1^{(i)}} & Y_{S_1^{(i)}} & Z_{S_1^{(i)}} \\ \vdots & \vdots & \vdots & \vdots \\ S_{n_{ei}}^{(i)} & X_{S_{n_{ei}}^{(i)}} & Y_{S_{n_{ei}}^{(i)}} & Z_{S_{n_{ei}}^{(i)}} \end{bmatrix} \quad (4.27)$$

Arrays  $\mathbf{e}^{(i)}$ ,  $\mathbf{R}^{(i)}$  and  $\mathbf{S}^{(i)}$  effectively allow for the segmentation of  $\Gamma_c$  and  $\Gamma_c^{(i)}$ , which is essential for their discretisation with coupling elements.

Step 6: Repetition of steps 1-5 for all coupling interfaces, if multiple interface specifications are defined within the context of the coupling problem

---

#### 4.5.2.1 Algorithmic Process 1 (API) - Projection algorithm

The projection algorithm described herein enables the determination of the natural coordinates of a given point projection on a curved shell surface, when the point coordinates in the global Cartesian coordinate system are initially known. This is achieved by means of satisfying two orthogonality conditions, between the vector  $\mathbf{r}$ , connecting the point and its projection, and two tangent to the surface vectors  $\mathbf{a}_\zeta$  and  $\mathbf{a}_\eta$ , along the planar axes  $\zeta$  and  $\eta$ , evaluated at the

projection location. This can be mathematically formulated in the system of equations given below:

$$\begin{cases} \mathbf{r} \cdot \mathbf{a}_\xi \\ \mathbf{r} \cdot \mathbf{a}_\eta \end{cases} = \begin{cases} 0 \\ 0 \end{cases} \quad (4.28)$$

In the context of the 1-D surface coupling problem under consideration,  $\mathbf{r}$  is defined as the unit vector connecting a given point  $P$ , with a fixed natural coordinate  $\tilde{\xi}$  along a coupling interface segment or sector, to its trial projection  $Q$  on a given shell element surface, with natural coordinates  $\xi = (\xi, \eta)$  in the respective natural coordinate system. Vector  $\mathbf{r}$  can therefore be expressed as:

$$\mathbf{r} = \frac{\hat{\mathbf{r}}}{\|\hat{\mathbf{r}}\|}, \quad \hat{\mathbf{r}} = \tilde{\mathbf{X}}(\tilde{\xi}) - \mathbf{X}(\xi, \eta) = \Phi \cdot \tilde{\mathbf{X}}_e - \mathbf{N} \cdot \mathbf{X}_e \quad (4.29)$$

The unit tangent vectors  $\mathbf{a}_\xi$  and  $\mathbf{a}_\eta$  in the direction of the orthogonal natural coordinate system axes of the curved shell surface at  $Q$  are given by the following expressions:

$$\mathbf{a}_\xi = \frac{\hat{\mathbf{a}}_\xi}{\|\hat{\mathbf{a}}_\xi\|}, \quad \hat{\mathbf{a}}_\xi = \frac{\partial \mathbf{X}}{\partial \xi} = \mathbf{N}_{,\xi} \cdot \mathbf{X}_e \quad (4.30)$$

$$\mathbf{a}_\eta = \frac{\hat{\mathbf{a}}_\eta}{\|\hat{\mathbf{a}}_\eta\|}, \quad \hat{\mathbf{a}}_\eta = \frac{\partial \mathbf{X}}{\partial \eta} = \mathbf{N}_{,\eta} \cdot \mathbf{X}_e \quad (4.31)$$

It should be noted that the superscript  $(i)$ ,  $i=1,2$ , referring to the coupled surfaces  $\Omega^{(i)}$ , is omitted in the derivations presented in the current section, on account of simplicity and generality.

The projection point  $Q$  is determined in an iterative fashion using a Newton-Raphson procedure, within an acceptable tolerance  $\gamma_1 > 0$ . The system of orthogonality conditions is formulated as a vector function  $\mathbf{G}$  as follows:

$$\mathbf{G} = \begin{cases} G_1 \\ G_2 \end{cases} = \begin{cases} \mathbf{r} \cdot \mathbf{a}_\xi \\ \mathbf{r} \cdot \mathbf{a}_\eta \end{cases} \cong \begin{cases} 0 \\ 0 \end{cases}, \quad |G_1| \leq \gamma_1 \text{ and } |G_2| \leq \gamma_1 \quad (4.32)$$

The Newton-Raphson procedure leads to the following system of equations, upon Taylor expansion of  $\mathbf{G}$  to a 1<sup>st</sup> order and rearrangement:

$$\mathbf{G}^{\{k+1\}} = \mathbf{G}^{\{k\}} + \mathbf{J}_G^{\{k\}} \cdot (\boldsymbol{\xi}^{\{k+1\}} - \boldsymbol{\xi}^{\{k\}}) = \mathbf{G}^{\{k\}} + \mathbf{J}_G^{\{k\}} \cdot \Delta \boldsymbol{\xi}^{\{k+1\}} = 0, \quad k = 0, 1, \dots, k_{\max} \quad (4.33)$$

$$\therefore \Delta \boldsymbol{\xi}^{\{k+1\}} = -(\mathbf{J}_G^{\{k\}})^{-1} \cdot \mathbf{G}^{\{k\}}$$

$$\therefore \boldsymbol{\xi}^{\{k+1\}} = \boldsymbol{\xi}^{\{k\}} + \Delta \boldsymbol{\xi}^{\{k+1\}}$$

where  $\boldsymbol{\xi}^{\{k\}} = (\zeta^{\{k\}}, \eta^{\{k\}})$  and  $\mathbf{J}_G^{\{k\}}$  correspond to the natural coordinate vector and the Jacobian matrix of vector function  $\mathbf{G}$  at iterative step  $k$ , with the latter being given by the following expression:

$$\mathbf{J}_G^{\{k\}} = \left. \frac{\partial \mathbf{G}}{\partial \boldsymbol{\xi}} \right|_{\boldsymbol{\xi}=\boldsymbol{\xi}^{\{k\}}} = \begin{bmatrix} \frac{\partial G_1}{\partial \zeta} & \frac{\partial G_1}{\partial \eta} \\ \frac{\partial G_2}{\partial \zeta} & \frac{\partial G_2}{\partial \eta} \end{bmatrix} \bigg|_{\boldsymbol{\xi}=\boldsymbol{\xi}^{\{k\}}} = \begin{bmatrix} -\mathbf{a}_\zeta \cdot \mathbf{a}_\zeta + \mathbf{r} \cdot \mathbf{a}_{\zeta\zeta} & -\mathbf{a}_\eta \cdot \mathbf{a}_\zeta + \mathbf{r} \cdot \mathbf{a}_{\zeta\eta} \\ -\mathbf{a}_\zeta \cdot \mathbf{a}_\eta + \mathbf{r} \cdot \mathbf{a}_{\eta\zeta} & -\mathbf{a}_\eta \cdot \mathbf{a}_\eta + \mathbf{r} \cdot \mathbf{a}_{\eta\eta} \end{bmatrix} \bigg|_{\boldsymbol{\xi}=\boldsymbol{\xi}^{\{k\}}} \quad (4.34)$$

where  $\mathbf{a}_\zeta^{\{k\}}$  and  $\mathbf{a}_\eta^{\{k\}}$  are the unit tangent vectors along  $\zeta$  and  $\eta$ , as defined in Eqs. (4.30) and (4.31), and  $\mathbf{a}_{\zeta\zeta}^{\{k\}}$ ,  $\mathbf{a}_{\zeta\eta}^{\{k\}}$ ,  $\mathbf{a}_{\eta\zeta}^{\{k\}}$  and  $\mathbf{a}_{\eta\eta}^{\{k\}}$  are their derivatives, at iterative step  $k$ , which are given by the following expressions:

$$\mathbf{a}_\zeta^{\{k\}} = \frac{\hat{\mathbf{a}}_\zeta^{\{k\}}}{\|\hat{\mathbf{a}}_\zeta^{\{k\}}\|}, \quad \hat{\mathbf{a}}_\zeta^{\{k\}} = \frac{\partial \mathbf{X}^{\{k\}}}{\partial \zeta} = \mathbf{N}_{,\zeta} \cdot \mathbf{X}_e^{\{k\}} \quad (4.35)$$

$$\mathbf{a}_\eta^{\{k\}} = \frac{\hat{\mathbf{a}}_\eta^{\{k\}}}{\|\hat{\mathbf{a}}_\eta^{\{k\}}\|}, \quad \hat{\mathbf{a}}_\eta^{\{k\}} = \frac{\partial \mathbf{X}^{\{k\}}}{\partial \eta} = \mathbf{N}_{,\eta} \cdot \mathbf{X}_e^{\{k\}} \quad (4.36)$$

$$\mathbf{a}_{\zeta\zeta}^{\{k\}} = \frac{\mathbf{I}_3 - \mathbf{a}_\zeta^{\{k\}} \otimes \mathbf{a}_\zeta^{\{k\}}}{\|\hat{\mathbf{a}}_\zeta^{\{k\}}\|} \cdot \hat{\mathbf{a}}_{\zeta\zeta}^{\{k\}}, \quad \hat{\mathbf{a}}_{\zeta\zeta}^{\{k\}} = \frac{\partial^2 \mathbf{X}^{\{k\}}}{\partial \zeta^2} = \mathbf{N}_{,\zeta\zeta} \cdot \mathbf{X}_e^{\{k\}} \quad (4.37)$$

$$\mathbf{a}_{\zeta\eta}^{\{k\}} = \frac{\mathbf{I}_3 - \mathbf{a}_\zeta^{\{k\}} \otimes \mathbf{a}_\zeta^{\{k\}}}{\|\hat{\mathbf{a}}_\zeta^{\{k\}}\|} \cdot \hat{\mathbf{a}}_{\zeta\eta}^{\{k\}}, \quad \hat{\mathbf{a}}_{\zeta\eta}^{\{k\}} = \frac{\partial^2 \mathbf{X}^{\{k\}}}{\partial \zeta \partial \eta} = \mathbf{N}_{,\zeta\eta} \cdot \mathbf{X}_e^{\{k\}} \quad (4.38)$$

$$\mathbf{a}_{\eta\xi}^{\{k\}} = \frac{\mathbf{I}_3 - \mathbf{a}_\eta^{\{k\}} \otimes \mathbf{a}_\eta^{\{k\}}}{\|\hat{\mathbf{a}}_\eta^{\{k\}}\|} \cdot \hat{\mathbf{a}}_{\eta\xi}^{\{k\}}, \quad \hat{\mathbf{a}}_{\eta\xi}^{\{k\}} = \frac{\partial^2 \mathbf{X}^{\{k\}}}{\partial \eta \partial \xi} = \mathbf{N}_{,\eta\xi} \cdot \mathbf{X}_e^{\{k\}} \quad (4.39)$$

$$\mathbf{a}_{\eta\eta}^{\{k\}} = \frac{\mathbf{I}_3 - \mathbf{a}_\eta^{\{k\}} \otimes \mathbf{a}_\eta^{\{k\}}}{\|\hat{\mathbf{a}}_\eta^{\{k\}}\|} \cdot \hat{\mathbf{a}}_{\eta\eta}^{\{k\}}, \quad \hat{\mathbf{a}}_{\eta\eta}^{\{k\}} = \frac{\partial^2 \mathbf{X}^{\{k\}}}{\partial \eta^2} = \mathbf{N}_{,\eta\eta} \cdot \mathbf{X}_e^{\{k\}} \quad (4.40)$$

where the evaluation of the unit vector  $\mathbf{a}_\xi^{\{k\}}$  and  $\mathbf{a}_\eta^{\{k\}}$  derivatives is based on the following expressions, which are presented here in their most general form for a unit vector  $\mathbf{a}$ <sup>1</sup>:

$$\frac{\partial \mathbf{a}^{(i)}}{\partial \xi} = \frac{\partial \mathbf{a}}{\partial \hat{\mathbf{a}}^T} \cdot \frac{\partial \hat{\mathbf{a}}}{\partial \xi} = \frac{\mathbf{I}_3 - \mathbf{a} \otimes \mathbf{a}}{\|\hat{\mathbf{a}}\|} \cdot \frac{\partial \hat{\mathbf{a}}}{\partial \xi} \quad (4.41)$$

$$\frac{\partial \mathbf{a}^{(i)}}{\partial \eta} = \frac{\partial \mathbf{a}}{\partial \hat{\mathbf{a}}^T} \cdot \frac{\partial \hat{\mathbf{a}}}{\partial \eta} = \frac{\mathbf{I}_3 - \mathbf{a} \otimes \mathbf{a}}{\|\hat{\mathbf{a}}\|} \cdot \frac{\partial \hat{\mathbf{a}}}{\partial \eta} \quad (4.42)$$

The Newton-Raphson iterative procedure proceeds until the vector function  $\mathbf{G}$  converges within the desired tolerance  $\gamma_1$ , which is set to  $1e^{-8}$ , while the maximum number of iterations  $k_{\max}$  is introduced to enhance the computational efficiency of the method in cases of diverging solutions.

A stepwise description of the iterative procedure is given below, while the concept is schematically illustrated in Figure 4.5.

---

Step 1: Initialisation of natural coordinates vector of trial projection point  $\xi^{\{0\}}$  :

---

<sup>1</sup> The derivative of a normalised unit vector  $\mathbf{a}$  with respect to the non-normalised vector  $\hat{\mathbf{a}}$  is evaluated as follows

$$\begin{aligned} \frac{\partial \mathbf{a}}{\partial \hat{\mathbf{a}}^T} &= \frac{\partial}{\partial \hat{\mathbf{a}}^T} \left( \frac{\hat{\mathbf{a}}}{\|\hat{\mathbf{a}}\|} \right) = \frac{\frac{\partial \hat{\mathbf{a}}}{\partial \hat{\mathbf{a}}^T} \cdot \|\hat{\mathbf{a}}\| - \hat{\mathbf{a}} \cdot \frac{\partial \|\hat{\mathbf{a}}\|}{\partial \hat{\mathbf{a}}^T}}{\|\hat{\mathbf{a}}\|^2} = \frac{\mathbf{I}_3 \cdot \|\hat{\mathbf{a}}\| - \hat{\mathbf{a}} \cdot \frac{\partial \sqrt{\hat{\mathbf{a}} \cdot \hat{\mathbf{a}}}}{\partial \hat{\mathbf{a}}^T}}{\|\hat{\mathbf{a}}\|^2} = \\ &= \frac{\mathbf{I}_3 \cdot \|\hat{\mathbf{a}}\| - \hat{\mathbf{a}} \cdot \frac{1}{2\sqrt{\hat{\mathbf{a}} \cdot \hat{\mathbf{a}}}} \left( 2\hat{\mathbf{a}}^T \cdot \frac{\partial \hat{\mathbf{a}}}{\partial \hat{\mathbf{a}}^T} \right)}{\|\hat{\mathbf{a}}\|^2} = \frac{\mathbf{I}_3 \cdot \|\hat{\mathbf{a}}\| - \hat{\mathbf{a}} \cdot \frac{1}{\|\hat{\mathbf{a}}\|} (\hat{\mathbf{a}}^T \cdot \mathbf{I}_3)}{\|\hat{\mathbf{a}}\|^2} = \frac{\mathbf{I}_3 - \mathbf{a} \otimes \mathbf{a}}{\|\hat{\mathbf{a}}\|} \end{aligned}$$

$$\xi^{\{0\}} = \mathbf{0}$$

Step 2: Evaluation of global coordinates vector, tangent vectors and tangent vector derivatives at initial trial projection point  $\xi^{\{0\}}$  :

$$\mathbf{X}^{\{0\}}, \mathbf{a}_{\xi}^{\{0\}}, \mathbf{a}_{\eta}^{\{0\}}, \mathbf{a}_{\xi\xi}^{\{0\}}, \mathbf{a}_{\eta\eta}^{\{0\}}, \mathbf{a}_{\xi\eta}^{\{0\}}, \mathbf{a}_{\eta\xi}^{\{0\}}$$

Step 3: Evaluation of  $\mathbf{r}^{\{0\}}$ ,  $\mathbf{G}^{\{0\}}$  and  $\mathbf{J}_G^{\{0\}}$  for Newton-Raphson procedure at initial trial projection point  $\xi^{\{0\}}$  .

Step 4: While  $(G_1^{\{k\}} > \gamma_1)$  and  $(G_2^{\{k\}} > \gamma_1)$  and  $(k \leq k_{\max})$  iterate through steps 4.1, 4.2 and 4.3,  $k=0, 1, \dots, k_{\max}$ :

-----  
Step 4.1: Evaluation of updated vector of natural coordinates at trial projection point  $\xi^{\{k+1\}}$  .

$$\therefore \Delta \xi^{\{k+1\}} = -(\mathbf{J}_G^{\{k\}})^{-1} \cdot \mathbf{G}^{\{k\}}$$

$$\therefore \xi^{\{k+1\}} = \xi^{\{k\}} + \Delta \xi^{\{k+1\}}$$

Step 4.2: Evaluation of updated global coordinates vector  $\mathbf{X}^{\{k+1\}}$ , tangent vectors  $\mathbf{a}_{\xi}^{\{k+1\}}$ ,  $\mathbf{a}_{\eta}^{\{k+1\}}$  and tangent vector derivatives  $\mathbf{a}_{\xi\xi}^{\{k+1\}}$ ,  $\mathbf{a}_{\eta\eta}^{\{k+1\}}$ ,  $\mathbf{a}_{\xi\eta}^{\{k+1\}}$ ,  $\mathbf{a}_{\eta\xi}^{\{k+1\}}$  at trial projection point  $\xi^{\{k+1\}}$

Step 4.3: Evaluation of updated position vector  $\mathbf{r}^{\{k+1\}}$ , vector function  $\mathbf{G}^{\{k+1\}}$  and Jacobian  $\mathbf{J}_G^{\{k+1\}}$  at trial projection point  $\xi^{\{k+1\}}$

-----

Step 5: Check projection point  $\xi$  admissibility, in respect of it lying within the shell element boundaries within an acceptable tolerance  $\gamma_2$ , which has been specified as  $10^{-8}$ :

- For 9-noded curved shell elements:

$$\therefore |\xi| \leq 1.0 + \gamma_2$$

$$\therefore |\eta| \leq 1.0 + \gamma_2$$

- For 6-noded curved shell elements:

$$\therefore 0 - \gamma_2 \leq \xi \leq 1.0 + \gamma_2$$

$$\therefore 0 - \gamma_2 \leq \eta \leq 1.0 + \gamma_2$$

$$\therefore 0 - \gamma_2 \leq \xi + \eta \leq 1.0 + \gamma_2$$

In the case of planar surfaces, the employment of the projection algorithm allows for a unique projection point to be identified on the surface, for any point in 3-D space. Conversely, in the case of curved surfaces with sufficiently large curvature or a closed domain, such as in the case of cylindrical vessels, a point is potentially associated with projections on multiple element domains where the orthogonality conditions stated in Eq. (4.32) are fulfilled. It is therefore essential to define the starting point  $P_0$  of the coupling interface  $\Gamma_c$  on, or at a sufficiently small distance from, the surface in this case, in order to ensure the uniqueness of the first active element  $e_1^{(i)}$  and the initiation of the segmentation process at the appropriate location on each surface mesh.

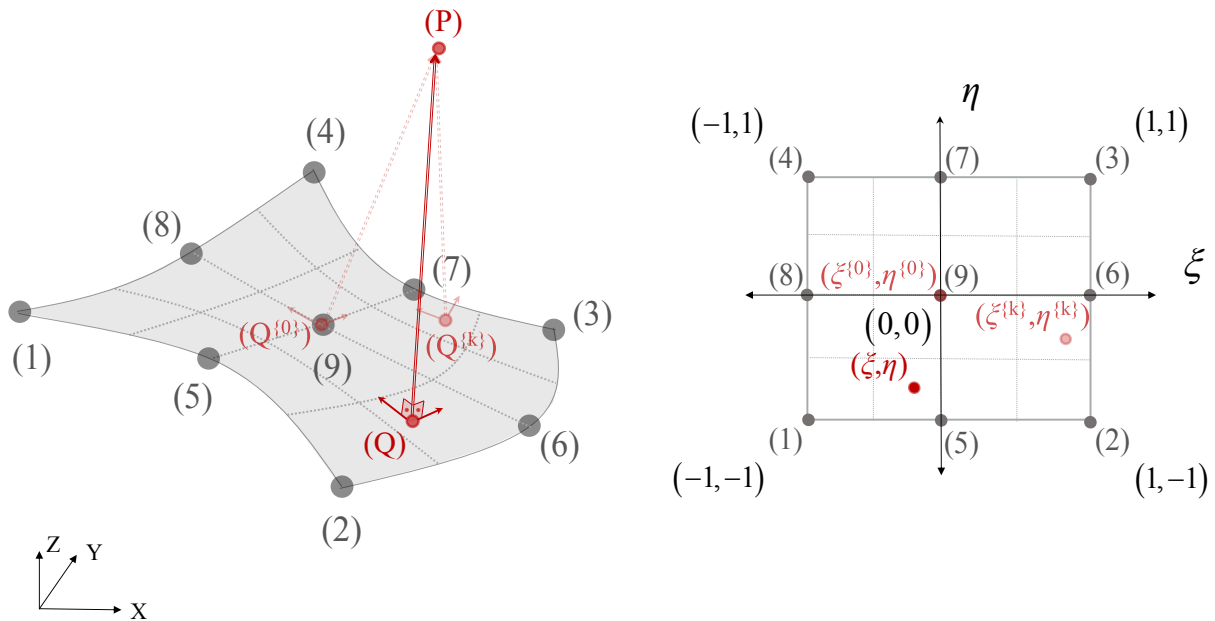


Figure 4.5: Algorithmic Process 1 (AP1) – projection algorithm



#### 4.5.2.2 Algorithmic Process 2 (AP2) - Conditional projection algorithm

The projection algorithm outlined herein is an expansion of AP1, where the point  $P$  has a variable natural coordinate  $\tilde{\xi}$  along a coupling interface segment or sector, however it is known that its projection  $Q$  lies along a given boundary of a shell element domain.

Similar to AP1, the identification of  $P$  and  $Q$  is achieved by means of satisfying two orthogonality conditions between the unit vector  $\mathbf{r}$  connecting these, as given by Eq. (4.29), and two tangent to the curved surface vectors  $\mathbf{a}_\xi$  and  $\mathbf{a}_\eta$  evaluated at  $Q$ , as given by Eqs. (4.30) and (4.31). However, the system of equations is now subject to a given linear constraint  $g(\xi, \eta)$ , and is thus mathematically formulated as follows:

$$\begin{cases} \mathbf{r} \cdot \mathbf{a}_\xi \\ \mathbf{r} \cdot \mathbf{a}_\eta \\ g(\xi, \eta) \end{cases} = \begin{cases} 0 \\ 0 \\ 0 \end{cases} \quad (4.43)$$

The conditional projection algorithmic process enables the determination of the natural coordinate  $\tilde{\xi}$  of point  $P$  along a given linear segment or sector of the coupling interface with orientation vector  $\mathbf{t}$ , as well as the set of natural coordinates  $(\xi, \eta)$  of its projection  $Q$  on the shell element surface. The introduction of the constraint function  $g(\xi, \eta)$  enforces the triplet of coordinate parameters  $\xi = (\xi, \eta, \tilde{\xi})$  yielded as the solution of the above system to map into a set of points  $P$  and  $Q$ , where the latter lies on a specified shell element edge determined by the constraint function. The linear constraint function  $g(\xi, \eta)$  introduces the equation of an element edge in Eq. (4.43), and it can therefore be expressed in the following general form, for both 9-noded quadrilateral and 6-noded triangular shell elements:

$$g(\xi, \eta) = g(\xi^*) = \xi^* - c \quad (4.44)$$

where the following cases can be distinguished:

- Vertical edges:  $\xi^* = \xi$ ,  $c = \pm 1$  for 9-noded and  $c = 0$  for 6-noded elements
- Horizontal edges:  $\xi^* = \eta$ ,  $c = \pm 1$  for 9-noded and  $c = 0$  for 6-noded elements
- Diagonal edges:  $\xi^* = \xi + \eta$  and  $c = 1$  (for 6-noded elements only)

It should be noted that, similar to the preceding sub-section, the superscript ( $i=1,2$ ) referring to  $\Omega^{(i)}$  is omitted in the derivations presented herein, on account of simplicity and generality.

The projection is determined in an iterative fashion within an acceptable tolerance  $\gamma_1 > 0$  using a Newton-Raphson procedure, where the system of orthogonality conditions is formulated as a vector function  $\mathbf{G}$  as follows:

$$\mathbf{G} = \begin{Bmatrix} G_1 \\ G_2 \\ G_3 \end{Bmatrix} = \begin{Bmatrix} \mathbf{r} \cdot \mathbf{a}_\xi \\ \mathbf{r} \cdot \mathbf{a}_\eta \\ g(\xi, \eta) \end{Bmatrix} \cong \begin{Bmatrix} 0 \\ 0 \\ 0 \end{Bmatrix}, \quad |G_1| \leq \gamma_1, \quad |G_2| \leq \gamma_1, \quad |G_3| \leq \gamma_1 \quad (4.45)$$

The Newton-Raphson procedure leads to the system of equations described by Eq. (4.33), where in this case  $\xi^{\{k\}} = (\xi^{\{k\}}, \eta^{\{k\}}, \tilde{\xi}^{\{k\}})$  is the natural coordinate parameter vector, and the Jacobian matrix  $\mathbf{J}_G^{\{k\}}$  of vector function  $\mathbf{G}$  at iterative step  $k$  is given by the following expression:

$$\mathbf{J}_G^{\{k\}} = \left. \frac{\partial \mathbf{G}}{\partial \xi} \right|_{\xi=\xi^{\{k\}}} = \begin{bmatrix} \frac{\partial G_1}{\partial \xi} & \frac{\partial G_1}{\partial \eta} & \frac{\partial G_1}{\partial \tilde{\xi}} \\ \frac{\partial G_2}{\partial \xi} & \frac{\partial G_2}{\partial \eta} & \frac{\partial G_2}{\partial \tilde{\xi}} \\ \frac{\partial G_3}{\partial \xi} & \frac{\partial G_3}{\partial \eta} & \frac{\partial G_3}{\partial \tilde{\xi}} \end{bmatrix} \bigg|_{\xi=\xi^{\{k\}}} = \begin{bmatrix} -\mathbf{a}_\xi \cdot \mathbf{a}_\xi + \mathbf{r} \cdot \mathbf{a}_{\xi\xi} & -\mathbf{a}_\eta \cdot \mathbf{a}_\xi + \mathbf{r} \cdot \mathbf{a}_{\xi\eta} & \mathbf{t} \cdot \mathbf{a}_\xi \\ -\mathbf{a}_\xi \cdot \mathbf{a}_\eta + \mathbf{r} \cdot \mathbf{a}_{\eta\xi} & -\mathbf{a}_\eta \cdot \mathbf{a}_\eta + \mathbf{r} \cdot \mathbf{a}_{\eta\eta} & \mathbf{t} \cdot \mathbf{a}_\eta \\ g_{,\xi} & g_{,\eta} & 0 \end{bmatrix} \bigg|_{\xi=\xi^{\{k\}}} \quad (4.46)$$

where  $\mathbf{a}_{\xi^{\{k\}}}$ ,  $\mathbf{a}_{\eta^{\{k\}}}$  and  $\mathbf{a}_{\xi\xi^{\{k\}}}$ ,  $\mathbf{a}_{\xi\eta^{\{k\}}}$ ,  $\mathbf{a}_{\eta\xi^{\{k\}}}$ ,  $\mathbf{a}_{\eta\eta^{\{k\}}}$  are the unit tangent vectors and their derivatives along the  $\xi$  and  $\eta$  axes at iterative step  $k$ , as given by Eqs. (4.35)-(4.40),  $\mathbf{t}$  is the orientation vector of the current linear sector or segment of  $\Gamma_c$  and  $g_{,\xi}$ ,  $g_{,\eta}$  are the derivatives of the constraint function with respect to  $\xi$  and  $\eta$ , respectively, which are given below for the 3 cases distinguished in Eq. (4.44):

- Vertical edges:  $\xi_{,\xi}^* = 1$ ,  $\xi_{,\eta}^* = 0$
- Horizontal edges:  $\xi_{,\xi}^* = 0$ ,  $\xi_{,\eta}^* = 1$
- Diagonal edge:  $\xi_{,\xi}^* = 1$ ,  $\xi_{,\eta}^* = 1$

Similar to AP1, the Newton-Raphson iterative procedure is terminated upon convergence of the vector function  $\mathbf{G}$  within the desired tolerance  $\gamma_1$ , which is set to  $1e^{-8}$ , while a maximum number of iterations  $k_{\max}$  is also introduced to avoid impacting the procedure computational efficiency in cases of diverging solutions.

A stepwise description of the iterative procedure is given below, while the concept is schematically illustrated in Figure 4.6.

---

Step 1: Initialisation of natural coordinate parameter vector  $\xi^{\{0\}}$  of trial point  $P^{\{0\}}$  along the coupling interface sector and its respective projection  $Q^{\{0\}}$  along the given edge:

$$\xi^{\{0\}} = \mathbf{0}$$

Step 2: Evaluation of global coordinate vectors of  $P^{\{0\}}$  and  $Q^{\{0\}}$ , and tangent vectors and respective derivatives at  $Q^{\{0\}}$ , at  $\xi^{\{0\}}$ :

$$\mathbf{X}^{\{0\}}, \tilde{\mathbf{X}}^{\{0\}}, \mathbf{a}_{\xi}^{\{0\}}, \mathbf{a}_{\eta}^{\{0\}}, \mathbf{a}_{\xi\xi}^{\{0\}}, \mathbf{a}_{\eta\eta}^{\{0\}}, \mathbf{a}_{\xi\eta}^{\{0\}}, \mathbf{a}_{\eta\xi}^{\{0\}}$$

Step 3: Evaluation of  $\mathbf{r}^{\{0\}}$ ,  $\mathbf{G}^{\{0\}}$  and  $\mathbf{J}_G^{\{0\}}$  for Newton-Raphson procedure at  $\xi^{\{0\}}$

Step 4: While  $(G_1^{\{k\}} > \gamma_1)$  and  $(G_2^{\{k\}} > \gamma_1)$  and  $(G_3^{\{k\}} > \gamma_1)$  and  $(k \leq k_{\max})$  iterate through steps 4.1, 4.2 and 4.3,  $k=0, 1, \dots, k_{\max}$

---

Step 4.1: Evaluation of updated vector of natural coordinates at trial projection point

$\xi^{\{k+1\}}$ :

$$\therefore \Delta \xi^{\{k+1\}} = -(\mathbf{J}_G^{\{k\}})^{-1} \cdot \mathbf{G}^{\{k\}}$$

$$\therefore \xi^{\{k+1\}} = \xi^{\{k\}} + \Delta \xi^{\{k+1\}}$$

Step 4.2: Evaluation of updated global coordinates vectors  $\mathbf{X}^{\{k+1\}}$ ,  $\tilde{\mathbf{X}}^{\{k+1\}}$  tangent vectors  $\mathbf{a}_{\xi}^{\{k+1\}}$ ,  $\mathbf{a}_{\eta}^{\{k+1\}}$  and tangent vector derivatives  $\mathbf{a}_{\xi\xi}^{\{k+1\}}$ ,  $\mathbf{a}_{\eta\eta}^{\{k+1\}}$ ,  $\mathbf{a}_{\xi\eta}^{\{k+1\}}$ ,  $\mathbf{a}_{\eta\xi}^{\{k+1\}}$  at trial projection point  $\xi^{\{k+1\}}$

Step 4.3: Evaluation of updated position vector  $\mathbf{r}^{\{k+1\}}$ , vector function  $\mathbf{G}^{\{k+1\}}$  and Jacobian  $\mathbf{J}_G^{\{k+1\}}$  at trial projection point  $\xi^{\{k+1\}}$

---

Step 5: Check obtained solution point  $\xi$  admissibility, in respect of it lying within the shell element boundaries and the interface sector or segment within an acceptable tolerance  $\gamma_2$ , which has been specified as  $10^{-8}$ :

- For 9-noded curved shell elements:

$$\therefore |\xi| \leq 1.0 + \gamma_2$$

$$\therefore |\eta| \leq 1.0 + \gamma_2$$

- For 6-noded curved shell elements:

$$\therefore 0 - \gamma_2 \leq \xi \leq 1.0 + \gamma_2$$

$$\therefore 0 - \gamma_2 \leq \eta \leq 1.0 + \gamma_2$$

$$\therefore 0 - \gamma_2 \leq \xi + \eta \leq 1.0 + \gamma_2$$

- For the coupling interface sector or segment:

$$\therefore \left| \tilde{\xi} \right| \leq 1.0 + \gamma_2$$


---

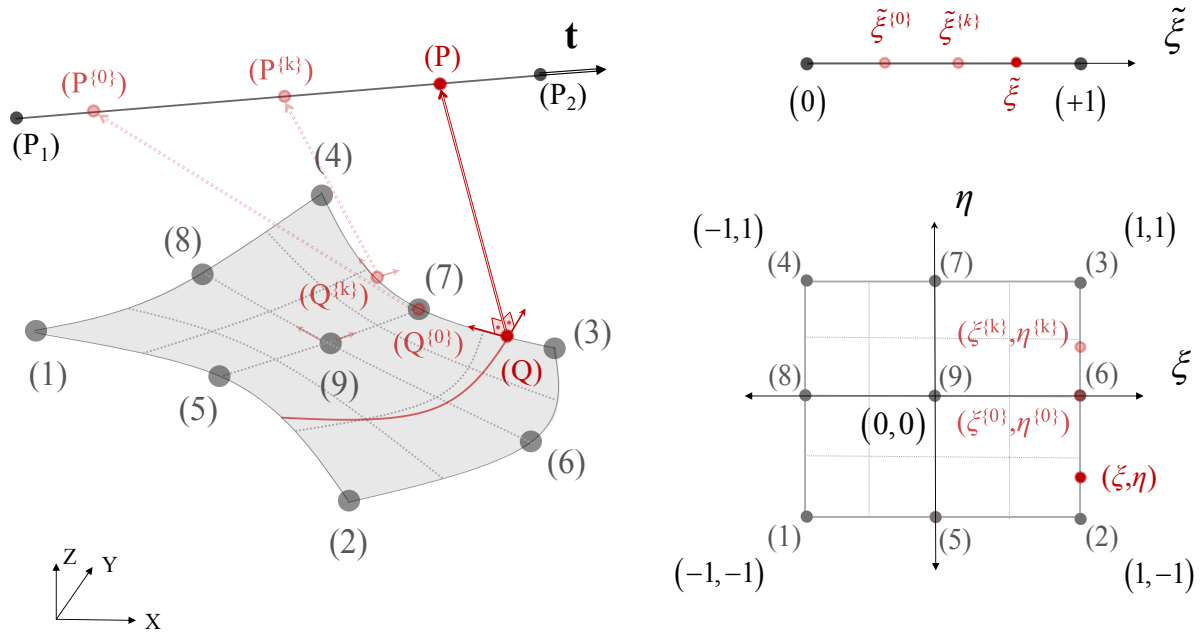


Figure 4.6: Algorithmic Process 2 (AP2) – conditional projection algorithm ( $\xi = 1$ )

#### 4.5.2.3 Algorithmic Process 3 (AP3) – Adjacent active element identification

The present section outlines the procedure employed for the classification of a shell element on the mesh of a surface as active in the following cases: (i) the starting point  $P_0$  along the coupling interface  $\Gamma_c$  is projected on the mesh of  $\Omega^{(i)}$  on edges or nodes shared by multiple elements, and the unique entry element  $e_1^{(i)}$  needs to be identified; (ii) the exit point of the coupling interface projection  $\Gamma_c^{(i)}$  from the domain  $\Gamma_k^{(i)}$  of an active shell element  $e_k^{(i)}$  coincides with a vertex node along its boundary, and the unique adjacent active element  $e_{k+1}^{(i)}$  traversed by  $\Gamma_c^{(i)}$  needs to be identified. The process is schematically illustrated in Figure 4.7.

In the succeeding mathematical formulation  $P$  denotes a point along a coupling interface segment or sector and  $Q$  denotes its projection on the domain of a candidate active shell element ( $e$ ). The superscript ( $i=1,2$ ), referring to the coupled surfaces, is omitted in the expressions presented henceforth, on account of simplicity and generality. The algorithmic process is outlined in a stepwise fashion hereafter:

Step 1: Mapping of coupling interface sector/segment orientation vector  $\mathbf{t}$  to the local coordinate system of trial active element ( $e$ )

The orientation vector  $\mathbf{t}$ , corresponding to the coupling interface linear sector or segment where  $P$  lies, is expressed in the local Cartesian coordinate system of a candidate shell element ( $e$ ) using the following transformation:

$$\mathbf{t}_{(e)} = \mathbf{T}_{(e)} \cdot \mathbf{t} \quad (4.47)$$

where the rotational transformation matrix of element ( $e$ ) is defined as:

$$\mathbf{T}_{(e)}^{(i)} = [\mathbf{c}_x \quad \mathbf{c}_y \quad \mathbf{c}_z]_{(e)}^T \quad (4.48)$$

The triad of unit orientation vectors of the local coordinate system axes is defined using a corotational approach, as earlier discussed in Chapter 3, for both 9-noded and 6-noded elements:

$$\left. \begin{aligned} \mathbf{c}_x &= \frac{\mathbf{c}_{13} - \mathbf{c}_{24}}{\|\mathbf{c}_{13} - \mathbf{c}_{24}\|}, \quad \mathbf{c}_y = \frac{\mathbf{c}_{13} + \mathbf{c}_{24}}{\|\mathbf{c}_{13} + \mathbf{c}_{24}\|}, \quad \mathbf{c}_z = \mathbf{c}_x \times \mathbf{c}_y & (9\text{-noded}) \\ \mathbf{c}_x &= \frac{\mathbf{v}_{12}}{\|\mathbf{v}_{12}\|}, \quad \mathbf{c}_z = \frac{\mathbf{v}_{12} \times \mathbf{v}_{13}}{\|\mathbf{v}_{12} \times \mathbf{v}_{13}\|}, \quad \mathbf{c}_y = \mathbf{c}_x \times \mathbf{c}_z & (6\text{-noded}) \\ \mathbf{c}_{jk} &= \frac{\mathbf{v}_{jk}}{\|\mathbf{v}_{jk}\|}, \quad \mathbf{v}_{jk} = \mathbf{X}_k - \mathbf{X}_j \end{aligned} \right\} \quad (4.49)$$

The assumption of negligible shell element out-of-flatness with mesh refinement, mentioned earlier in Sub-section 4.4.1, is embedded in all derivations presented henceforth. This allows for the out-of-plane abscissa  $z$  to be neglected, due to the planar abscissae ( $x,y$ ) being sufficiently larger in comparison, and hence the coordinate transformation of Eq. (4.47) effectively maps  $\mathbf{t}$  as a local planar vector. The corresponding local planar vector of  $\mathbf{t}$  expressed in the local coordinate system of element ( $e$ ) is henceforth denoted as  $\bar{\mathbf{t}}_{(e)}$ .

Step 2: Evaluation of element boundary tangent vectors at  $Q$

Two local element planar tangent vectors  $\bar{\mathbf{a}}_1$  and  $\bar{\mathbf{a}}_2$  are introduced at point  $Q$ , representing the tangent vectors of the closed element boundary curve oriented in the directions associated with clockwise and counter-clockwise circulation, respectively. Counter-clock-wise circulation defines the orientation of the positive local  $z$  semi-axis, in compliance with the nodal ordering specified in Sub-section 4.5.1. Vectors  $\bar{\mathbf{a}}_1$  and  $\bar{\mathbf{a}}_2$  are obtained by mapping two vectors  $\boldsymbol{\alpha}_1$  and  $\boldsymbol{\alpha}_2$  defined in the element natural coordinate system to the element local Cartesian coordinate system. Two cases can be distinguished:

- i. If  $Q$  lies in between the vertex nodes of an edge,  $\boldsymbol{\alpha}_1$  and  $\boldsymbol{\alpha}_2$  are defined as the vectors connecting the mid-node of the edge with its vertex-nodes, and  $(\bar{\mathbf{a}}_1, \bar{\mathbf{a}}_2)$  are both tangent to the edge.
- ii. If  $Q$  coincides with an element vertex node,  $\boldsymbol{\alpha}_1$  and  $\boldsymbol{\alpha}_2$  are defined as the vectors connecting the vertex node and the mid-nodes of the two edges sharing it, and  $(\bar{\mathbf{a}}_1, \bar{\mathbf{a}}_2)$  are tangent to the these edges.

For the mapping of  $\boldsymbol{\alpha}_1$  and  $\boldsymbol{\alpha}_2$  into  $\bar{\mathbf{a}}_1$  and  $\bar{\mathbf{a}}_2$ , the local element Jacobian for mapping between natural and planar local coordinates can be employed, on the basis of the negligible shell out-of-flatness assumption mentioned earlier:

$$\bar{\mathbf{a}}_j = \bar{\mathbf{j}}_{(e)} \cdot \boldsymbol{\alpha}_j, \quad j=1,2 \quad (4.50)$$

where the local Jacobian is given by the following expression, as will be discussed in Sub-section 4.7.2:

$$\bar{\mathbf{j}}_{(e)} = \begin{bmatrix} \bar{\mathbf{N}}_{,\xi} \cdot \bar{\mathbf{x}}_e & \bar{\mathbf{N}}_{,\eta} \cdot \bar{\mathbf{x}}_e \end{bmatrix} \quad (4.51)$$

Step 3: Check if orientation vector  $\mathbf{t}$  lies within the tangent vectors at  $Q$ .

Vectors  $\mathbf{n}_1$  and  $\mathbf{n}_2$ , corresponding to the cross products of  $\bar{\mathbf{t}}_{(e)}$  with  $\bar{\mathbf{a}}_1$  and  $\bar{\mathbf{a}}_2$ , are initially obtained:

$$\mathbf{n}_j = \bar{\mathbf{a}}_j \times \bar{\mathbf{t}}_{(e)}, \quad j=1,2 \quad (4.52)$$

The introduction of  $\bar{\mathbf{a}}_1$  and  $\bar{\mathbf{a}}_2$  effectively allows for two orientation boundaries for  $\bar{\mathbf{t}}_{(e)}$  to be established in the element local coordinate system x-y plane. Therefore, the classification of an element as active relies on assessing whether  $\bar{\mathbf{t}}_{(e)}$  lies in between  $\bar{\mathbf{a}}_1$  and  $\bar{\mathbf{a}}_2$ , and is oriented towards the element domain. This is assessed based on the sign of the dot product of  $\mathbf{n}_1$  and  $\mathbf{n}_2$ . The following cases are distinguished:

- i. If  $\mathbf{n}_1 \cdot \mathbf{n}_2 < 0$  the element is potentially active. In this case vectors  $\mathbf{n}_1$  and  $\mathbf{n}_2$  point in opposite directions, thereby indicating that  $\bar{\mathbf{t}}_{(e)}$  lies in between  $\bar{\mathbf{a}}_1$  and  $\bar{\mathbf{a}}_2$ . The normal vector  $\mathbf{n}^+$  corresponding to a counter-clockwise circulation of the shell element boundary, which coincides with the positive z- semi-axis orientation vector  $\mathbf{c}_z$  when the assumption of negligible shell element out-of-flatness with mesh refinement is adopted, is employed for the element classification as active/inactive:
  - If  $\mathbf{n}_1 \cdot \mathbf{n}^+ > 0$  and  $\mathbf{n}_2 \cdot \mathbf{n}^+ < 0$ , the element is active
  - If  $\mathbf{n}_1 \cdot \mathbf{n}^+ < 0$  and  $\mathbf{n}_2 \cdot \mathbf{n}^+ > 0$ , the element is inactive
- ii. If  $\mathbf{n}_1 \cdot \mathbf{n}_2 > 0$  the element is inactive. In this case vectors  $\mathbf{n}_1$  and  $\mathbf{n}_2$  point in the same direction, thereby indicating that  $\bar{\mathbf{t}}_{(e)}$  lies on the same side of  $\bar{\mathbf{a}}_1$  and  $\bar{\mathbf{a}}_2$ .
- iii. If  $\mathbf{n}_1 \cdot \mathbf{n}_2 = 0$  either of or both  $\mathbf{n}_1$  and  $\mathbf{n}_2$  are  $\mathbf{0}$ , which indicates that  $\bar{\mathbf{t}}_{(e)}$  is parallel to either of or both  $\bar{\mathbf{a}}_1$  and  $\bar{\mathbf{a}}_2$ . In this case a third vector  $\bar{\mathbf{a}}_3$  must be defined to guide the assessment process. The distinction of two further cases can be made:
  - If  $\mathbf{n}_j = \mathbf{0}$  and  $\mathbf{n}_k \neq \mathbf{0}$ , where  $j, k = 1, 2$  and  $j \neq k$ , then point  $Q$  is a vertex node of the shell element and  $\bar{\mathbf{t}}_{(e)}$  is parallel to  $\bar{\mathbf{a}}_j$ . In this case, tangent vector  $\bar{\mathbf{a}}_3$  is defined by mapping the direction of  $\alpha_j$  at the edge mid-node.
  - If  $\mathbf{n}_j = \mathbf{n}_k = \mathbf{0}$ , where  $j, k = 1, 2$  and  $j \neq k$ , then point  $Q$  lies on a shell element edge, in between its vertex nodes, and  $\bar{\mathbf{t}}_{(e)}$  is parallel to the tangent at point  $Q$ . In this case, tangent vector  $\bar{\mathbf{a}}_3$  is defined at the node of the edge with the smallest distance to  $Q$  in the counter-clockwise direction, by mapping the



direction of  $\mathbf{a}_j$  or  $\mathbf{a}_k$ , depending on which defines the orientation of  $\bar{\mathbf{t}}_{(e)}$  in the local system.

The cross product  $\mathbf{n}_3 = \bar{\mathbf{a}}_3 \times \bar{\mathbf{t}}_{(e)}$  is subsequently determined and used to guide the assessment of the element as active/inactive, alongside the normal vector  $\mathbf{n}^+$ . The following cases are distinguished:

- If  $\mathbf{n}_3 = \mathbf{0}$  then the element edge is straight, and the coupling interface projection traverses it. In this case the element is classified as neutrally active.
- If  $\mathbf{n}_3 \neq \mathbf{0}$  then if  $\mathbf{n}_3 \cdot \mathbf{n}^+ > 0$  the element is active, while if  $\mathbf{n}_3 \cdot \mathbf{n}^+ < 0$  the element is inactive

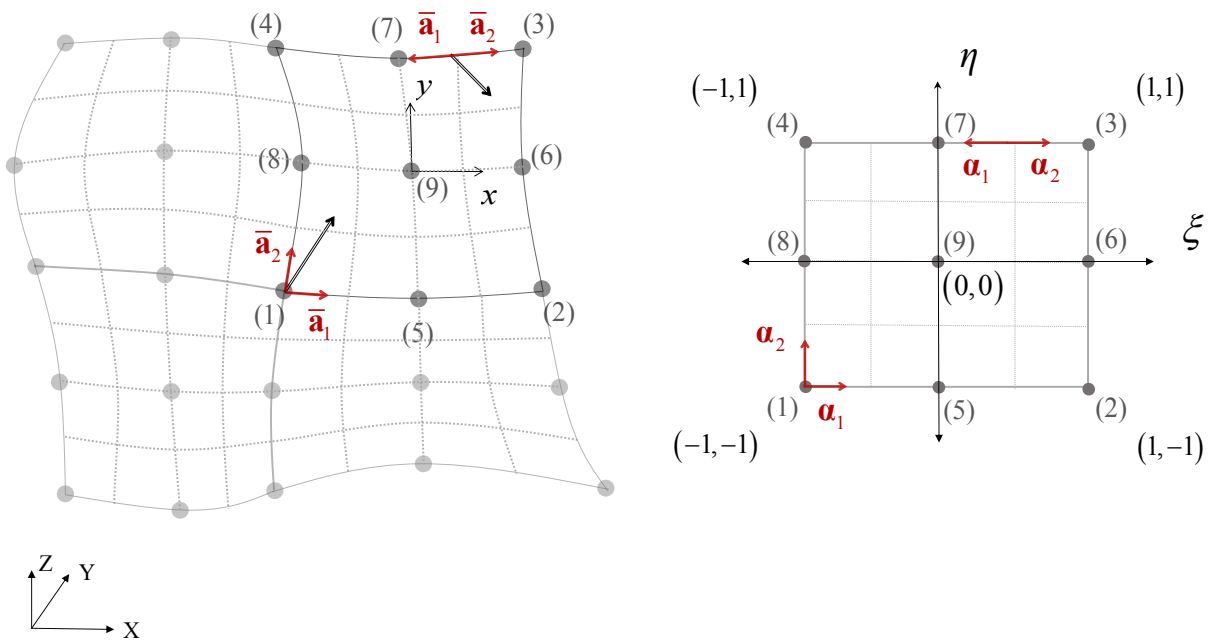


Figure 4.7: Algorithmic Process 3 (AP3) – adjacent active element identification

#### 4.5.2.4 Algorithmic Process 4 (AP4) – Active element exit point identification

The present section outlines the process for the identification of the coupling interface projection  $\Gamma_c^{(i)}$  exit point from the domain  $\Gamma_k^{(i)}$  of an active shell element  $e_k^{(i)}$ . The exit point lies on the element boundary, with the exception of the last active element  $e_{n_{ei}}^{(i)}$ , where the specified end point  $P_{np}$  of the coupling interface can be potentially projected inside its domain.

The process outlined herein is based on the simultaneous progression along  $\Gamma_c$  and  $\Gamma_c^{(i)}$ , and the identification of the points of  $\Gamma_c$  projecting on shell element edges on  $\Omega^{(i)}$ . As earlier discussed, a piece-wise linear approximation is employed for the geometric description of  $\Gamma_c$ , using a set of control points defining a sequence of linear sectors with distinct orientation vectors, as show in Eqs. (4.24) and (4.25). One or more control points are potentially projected inside the domain of specific active elements on  $\Omega^{(i)}$ , which in turn requires the consideration of different linear sector orientation vectors for the entry and exit point identification in the same active element. The simultaneous progression along  $\Gamma_c$  and  $\Gamma_c^{(i)}$  enables the monitoring of the transitions between the various sectors, thus allowing for the projection point search process to be readjusted using a different orientation vector when required.

On account of simplicity, the set of entry and exit points on an active element will be denoted as  $(R_1, S_1)$  and  $(R_2, S_2)$ , respectively, and the trial orientation vector as  $\mathbf{t}$  for the algorithmic process description following this point. The step-wise process outlined hereafter is employed to establish the exit point  $S_2$  on  $\Gamma_c^{(i)}$  from the domain of an active element ( $e$ ) and its corresponding point  $R_2$  on  $\Gamma_c$ , for a given set of starting points  $(R_1, S_1)$  and a given trial orientation vector  $\mathbf{t}$ , corresponding to a linear sector defined by control points  $P_1$  and  $P_2$ . The concept is schematically illustrated in Figure 4.8

---

Step 1: Mapping of coupling interface sector orientation vector  $\mathbf{t}$  to the planar local coordinate system of active element ( $e$ ) as  $\bar{\mathbf{t}}_{(e)}$

The orientation vector  $\mathbf{t}$  is expressed in the planar local Cartesian coordinate system of an active element ( $e$ ) as  $\bar{\mathbf{t}}_{(e)}$ , using the coordinate transformation of Eq. (4.47) and the assumption of negligible shell surface out-of-flatness with mesh refinement, as earlier discussed in Sub-section 4.5.2.3.

Step 2: Establishment of relative nodal orientation vectors  $\bar{\mathbf{a}}$  in the local coordinate system of active element ( $e$ ).

The vectors  $\bar{\mathbf{a}}_j$ , ( $j=1,2,\dots,m$ ), linking the starting point  $S_1$  with the perimetric boundary nodes of element ( $e$ ), where  $m=6$  or  $8$  for 6-noded triangular and 9-noded quadrilateral curved shell elements, respectively, are given by the following expressions:

$$\bar{\mathbf{a}}_j = \bar{\mathbf{x}}_j - \bar{\mathbf{x}}_{S_1} \quad (4.53)$$

Step 3: Establishment of vectors  $\bar{\mathbf{a}}_j$  and  $\bar{\mathbf{t}}_{(e)}$  relative orientation in the local coordinate system of active element ( $e$ ).

The normal vectors  $\mathbf{n}_j$  to the local shell element coordinate plane, defined as the cross products of  $\bar{\mathbf{a}}_j$  with  $\bar{\mathbf{t}}_{(e)}$ , are evaluated:

$$\mathbf{n}_j = \bar{\mathbf{a}}_j \times \bar{\mathbf{t}}_{(e)} \quad (4.54)$$

The dot products of  $\mathbf{n}_j$  with the unit vector  $\mathbf{n}^+$  corresponding to a counter-clockwise circulation of the shell element boundary, which coincides with the positive  $z$ - semi-axis orientation vector  $\mathbf{c}_z$  when the assumption of negligible shell element out-of-flatness with mesh refinement is adopted, are subsequently evaluated as follows:

$$n_j = \mathbf{n}_j \cdot \mathbf{n}^+ \quad (4.55)$$

The sign of  $n_j$  indicates whether  $\mathbf{n}_j$  is oriented in the direction of the positive or negative  $z$ - semi-axis, which in turn provides an indication of whether  $\bar{\mathbf{a}}_j$  is on the right or left side of  $\bar{\mathbf{t}}_{(e)}$ , respectively.

Step 4: Identification of trial exit point  $S_2$

The trial exit point  $S_2$  is identified on the basis of one of the following distinct cases, where circular indexing has been adopted with  $n_{j+1}^* = n_{j+1}$ ,  $n_{j-1}^* = n_{j-1}$  for  $j < m$ ,  $n_{j+1}^* = n_1$  for  $j = m$  and  $n_{j-1}^* = n_m$  for  $j = 1$ , where  $j = 1, 2, \dots, m$ :

- i. If  $n_j n_{j+1}^* < 0$ , the exit point lies on the shell element boundary, in between nodes  $j$  and  $j+1$ , and the exit point coordinates are determined by employment of AP2.
- ii. If  $n_{j-1}^* n_{j+1}^* < 0$  and  $n_j = 0$ , the exit point coincides with node  $j$ . A distinction should be made in this case for  $j$  being a vertex or non-vertex node, since this guides the search process for adjacent active elements on the surface mesh using AP3, as discussed earlier.
- iii. If  $n_{j-1}^* = n_j = 0$  and  $n_{j+1}^* \leq 0$ , which is the case if node  $j-1$  is the entry point of the coupling interface projection to the shell element domain, then two further cases are identified:
  - If  $n_{j+1}^* < 0$ , the shell element geometry is irregular, and thus node  $j$  is the exit point from the element domain.
  - If  $n_{j+1}^* = 0$ , the shell element geometry is regular, and thus the coupling interface traverses the respective straight edge and exits the shell element domain through node  $j+1$ .

Step 5: The vector linking the current trial exit point  $S_2$  with control point  $P_1$  at the start of the linear sector is defined in the global Cartesian coordinate system as follows:

$$\mathbf{r} = \mathbf{X}_{S_2} - \mathbf{X}_{P_1} \quad (4.56)$$

Vector  $\mathbf{r}$  is subsequently projected on the linear sector and its coordinate is normalised with the current interface linear sector length:

$$\tilde{\xi} = \frac{\mathbf{r} \cdot \mathbf{t}}{L} \quad (4.57)$$

where the sector length  $L = \sqrt{(\mathbf{X}_{P_2} - \mathbf{X}_{P_1})^2}$ .

The following cases are identified:

- i. If  $\tilde{\xi} \leq 1$  then  $S_2$  is the exit point from the element domain and  $R_2$  can be obtained by linear interpolation in the current sector, if AP2 was not previously employed.
- ii. If  $\tilde{\xi} > 1$  then  $S_2$  corresponds to a point  $R_2$  outside the current interface linear sector boundaries. Therefore, two more cases can be distinguished:
  - If the current interface sector is the last one, the process ends with the projection of the interface end point  $P_{np}$  on the shell element domain as  $Q_{np}$ .
  - Otherwise, the process is repeated from Step 1, starting from the projection  $Q_2$  of control point  $P_2$  on the element domain and using the orientation vector of the succeeding sector.

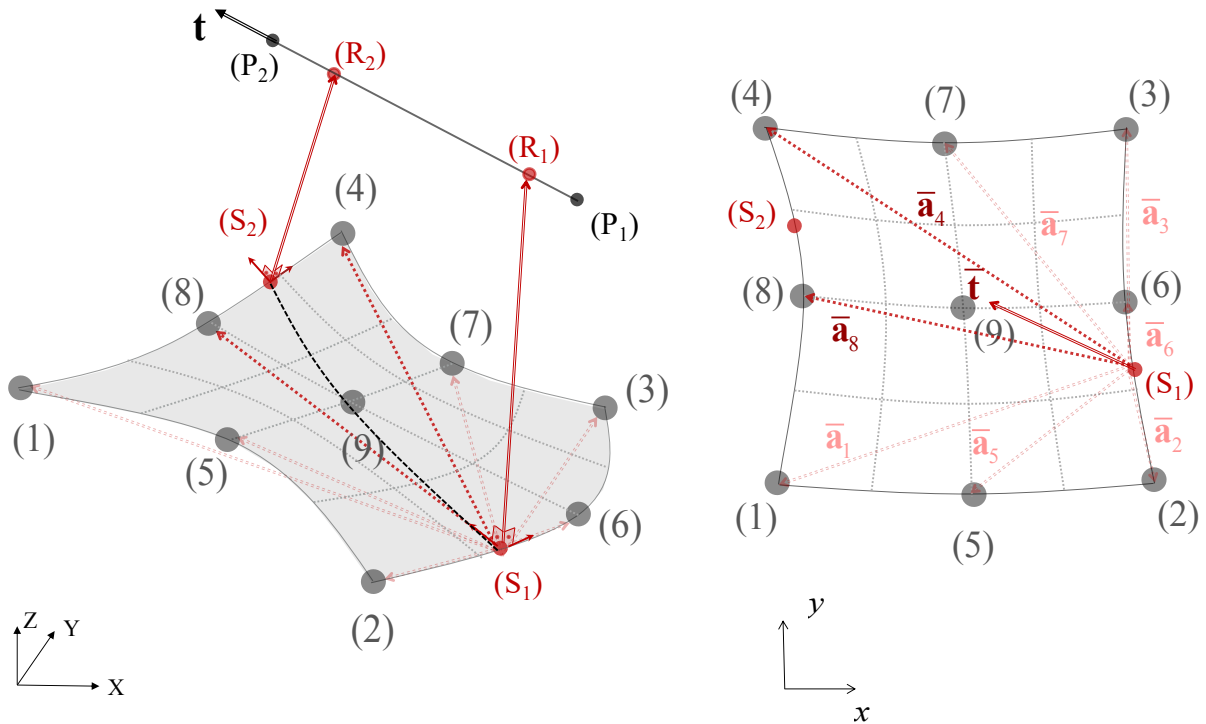


Figure 4.8: Algorithmic Process 4 (AP4) – active element exit point identification

### 4.5.3 Coupling element identification

Having previously identified the subset of active shell elements  $\mathbf{e}^{(i)}$  and the distinct sets of associated entry and exit points  $\mathbf{R}^{(i)}$  along  $\Gamma_c$  and  $\mathbf{S}^{(i)}$  along  $\Gamma_c^{(i)}$ , as shown in Eq. (4.27), the coupled surfaces  $\Omega^{(i)}$  are classified as slave and master. Without loss of generality,  $\Omega^{(1)}$  and  $\Omega^{(2)}$  are classified as slave and master, respectively, for the discussion following this point.

The interface segmentation is performed based on the set of points  $\mathbf{S}^{(i)}$  on  $\Gamma_c^{(i)}$ , corresponding to either the slave or both the slave and master surfaces, with each distinct couple being used as CPs at the ends of subsequent coupling segments. This leads to two distinct approaches, namely slave-only and slave-master interface segmentation, which have been considered in the development of the current methodology.

The slave-only segmentation approach has been adopted for the development of the translational and rotational coupling element formulation and has been incorporated in the default coupling element *modus operandi*. This is due to the slave-master segmentation generally resulting in a greater number of CPs along  $\Gamma_c^{(i)}$ , which potentially results in singularities in the coupled system tangent stiffness matrix, thus leading to convergence issues in the nonlinear solution procedure. The singularities arise in rare cases where the number of LMs at the CPs, introducing coupling constraints to the system, is greater than the number of unrestrained kinematic DOFs of the shell surfaces along  $\Gamma_c$ . This phenomenon is referred to as over-constraining.

The interface progressive segmentation process, as well as the coupling element discretisation into coupling elements, are outlined in a step-wise fashion hereafter:

Step 1: Establishment of coupling segments  $\Gamma_{c_j}^{(1)}$  and CPs along the coupling interface segment projection  $\Gamma_c^{(1)}$

The adoption of the slave-only segmentation approach allows for a sequence of segments  $\Gamma_{c_j}^{(1)}$ ,  $j=1,2,\dots,n_{e1}$  to be defined on  $\Gamma_c^{(1)}$ , with corresponding segments  $\Gamma_{c_j}$  on  $\Gamma_c$ , based on the set of points  $\mathbf{S}^{(1)}$  and  $\mathbf{R}^{(1)}$ , respectively, corresponding to the slave surface. The CPs at the ends

of each  $\Gamma_{cj}^{(1)}$  are defined in the locations of the corresponding points  $\mathbf{S}^{(1)}$ , while for a quadratic LM field interpolation a third CP is introduced at the mid-point of  $\Gamma_{cj}^{(1)}$ .

Step 2: Identification of slave and master active shell elements  $e_j^{(1)}$  and  $e_k^{(2)}$  associated with each coupling interface segment  $\Gamma_{cj}^{(1)}$

Each slave segment  $\Gamma_{cj}^{(1)}$  is associated with a unique active shell FE  $e_j^{(1)}$  on the slave surface  $\Omega^{(1)}$  and one or more  $e_k^{(2)}$  on the master surface  $\Omega^{(2)}$ , where  $k=1,2,\dots,n_{e2}$ . The set of active FEs on  $\Omega^{(2)}$  associated with  $\Gamma_{cj}^{(1)}$  corresponds to those traversed by the projection  $\Gamma_{cj}^{(2)}$  of  $\Gamma_{cj}^{(1)}$  on  $\Omega^{(2)}$ .

As discussed earlier, the projection of a segment on a surface in the present context only requires the projection of characteristic points, in this case points  $\mathbf{R}^{(1)}$ . As will be thoroughly discussed in Section 4.7, a Gaussian quadrature integration scheme has been adopted at the coupling element level, with the Gauss Points (GPs) being defined along the coupling segments  $\Gamma_{cj}^{(1)}$ . The efficiency of the above strategy can therefore be significantly enhanced, by establishing the set of master active FEs  $e_k^{(2)}$  associated with a given segment  $\Gamma_{cj}^{(1)}$  based on the former having at least one active GP projection on their surface. This allows only for the master FEs required for the numerical integration of the coupling constraint along  $\Gamma_c^{(1)}$  to be considered, thus excluding cases where a master FE  $e_k^{(2)}$  is intersected by a segment  $\Gamma_{cj}^{(2)}$ , but is inactive during the integration process.

Step 3: Establishment of coupling elements  $C_j$  associated with each coupling interface segment  $\Gamma_{cj}^{(1)}$

The identification of the unique active slave FE  $e_j^{(1)}$  and the set of active master FEs  $e_k^{(2)}$  associated with  $\Gamma_{cj}^{(1)}$  defines the set of interacting FEs on  $\Omega^{(1)}$  and  $\Omega^{(2)}$  along its length, where the constraint is enforced. Each distinct couple of  $e_j^{(1)}$  and  $e_k^{(2)}$  defines a new coupling element associated with  $\Gamma_{cj}^{(1)}$ , henceforth denoted as  $C_{jk}$ , comprising the shell FE surfaces  $\Gamma_j^{(1)}$  of  $e_j^{(1)}$  and  $\Gamma_k^{(2)}$  of  $e_k^{(2)}$  and the associated kinematic nodal DOFs, alongside the slave segment

$\Gamma_{cj}^{(1)}$  and the associated additional DOFs. The set of coupling elements defined along  $\Gamma_c^{(1)}$  are henceforth denoted as  $\mathbf{C}$ , with the respective set associated with a specific  $\Gamma_{cj}^{(1)}$  denoted as  $\mathbf{C}_j$ .  $\mathbf{C}$  and  $\mathbf{C}_j$  are effectively the coupling element connectivity matrices, encompassing the slave and master shell FEs associated with each coupling element.

As discussed earlier, the continuous LM field, obtained via interpolation of the LM vectors at the CPs defined along  $\Gamma_{cj}^{(1)}$ , is responsible for enforcing the constraint on all associated  $C_{jk}$ , which share the same slave shell FE and CPs. All  $C_{jk}$  associated with  $\Gamma_{cj}^{(1)}$  therefore share the kinematic nodal DOFs of  $e_j^{(1)}$ , as well as the additional DOFs defined at the respective CPs.

## 4.6 Coupling element formulation

As discussed previously, the classification of the coupled surfaces  $\Omega^{(i)}$  into master and slave guides the progressive segmentation of  $\Gamma_c$ , which is performed based on its projection  $\Gamma_c^{(1)}$  on the slave surface. The constraint is subsequently enforced along individual coupling segments  $\Gamma_{cj}^{(1)}$ , where a set of LMs is introduced at the respective CPs.

The discrete coupling constraint enforcement in a continuous sense along  $\Gamma_c^{(1)}$ , by virtue of a LM field, requires the mathematical derivation of the force vector and consistent tangent stiffness matrix expressions for coupling elements  $\mathbf{C}$ , and their subsequent assembly in the corresponding global quantities of the coupled system. Similar to the discussion in Section 4.2 for the simplified mechanical springs model, the expressions of the coupling element force vector and tangent stiffness matrix for a given constraint  $\mathbf{g}(\mathbf{u}^{(1)}, \mathbf{u}^{(2)})$  are obtained by establishing the expression of its contribution to the system total potential energy, and subsequently employing variational principles. The evaluation and assembly of the distinct coupling element  $C_{jk}$  contributions to the system global force vector and tangent system matrix, allows for an extended nonlinear system of coupled static or dynamic equilibrium equations to be obtained, where the primary and secondary unknowns are the kinematic and additional DOFs, respectively (Wriggers, 2006).



The solution of the extended equation system yields a set of nodal displacement values for the active shell elements  $\mathbf{e}^{(1)}$  and  $\mathbf{e}^{(2)}$  on  $\Omega^{(1)}$  and  $\Omega^{(2)}$ , which satisfies equilibrium for a given set of essential and natural boundary conditions, while also fulfilling the desired set of kinematic constraint in a weak sense along  $\Gamma_c^{(1)}$ . This is achieved by means of the LM vector components obtained at the CPs via the solution of the extended equation system, in its part associated with the additional DOFs, and their subsequent interpolation between consecutive distinct segments  $\Gamma_{c_j}^{(1)}$  in a piece-wise fashion.

#### 4.6.1 Coupling interface contribution to total potential energy

The contribution of  $\Gamma_c^{(1)}$  to the total potential energy of the coupled system is introduced by means of a two-field Lagrangian functional, in accordance with the Augmented LM formulation presented in Sub-section 2.3.1.3:

$$\Pi = \int_{\Gamma_c^{(1)}} \boldsymbol{\lambda} \cdot \mathbf{g}(\mathbf{u}^{(1)}, \mathbf{u}^{(2)}) \, d\Gamma_c^{(1)} + \frac{1}{2} \varepsilon \int_{\Gamma_c^{(1)}} \mathbf{g}^2(\mathbf{u}^{(1)}, \mathbf{u}^{(2)}) \, d\Gamma_c^{(1)}, \quad \varepsilon \geq 0 \quad (4.58)$$

where  $\boldsymbol{\lambda}$  is the LM vector field defined along  $\Gamma_c^{(1)}$ ,  $\mathbf{g}(\mathbf{u}^{(1)}, \mathbf{u}^{(2)})$  is the imposed kinematic constraint vector function expressed in terms of the displacement fields  $(\mathbf{u}^{(1)}, \mathbf{u}^{(2)})$  of the slave and master active shell elements  $\mathbf{e}^{(1)}$  and  $\mathbf{e}^{(2)}$ , and  $\varepsilon \in \mathbb{R}^+$  is a non-negative penalty parameter. It should be noted that since  $\mathbf{g}$  is a vector function, the following holds:

$$\mathbf{g}^2(\mathbf{u}^{(1)}, \mathbf{u}^{(2)}) = \mathbf{g}(\mathbf{u}^{(1)}, \mathbf{u}^{(2)}) \cdot \mathbf{g}(\mathbf{u}^{(1)}, \mathbf{u}^{(2)}) = \|\mathbf{g}(\mathbf{u}^{(1)}, \mathbf{u}^{(2)})\|^2$$

The first term of Eq. (4.58) represents the work done by the LM field over the kinematic constraint, which highlights the physical and dimensional correspondence of the former to a fictitious field of internal forces or moments. The second term is a penalty regularisation introduced to avoid zero diagonal terms in the part of the stiffness matrix associated with the nodal DOFs, which can be undesirable depending on the adopted procedure for solving the system of simultaneous equations, as discussed in Section 4.2. This is particularly important in cases where one of the coupled surfaces is unrestrained against rigid body motion and solvers that do not perform row-switching operations are employed for the solution of the system of

equations. In such cases, the elimination of the associated nodal DOFs using the corresponding equilibrium equations would not be possible without the use of a penalty stiffness parameter, which introduces non-zero pivots in the associated part of the tangent stiffness matrix.

As discussed earlier and confirmed here by virtue of dimensional correspondence, the LM vector field  $\boldsymbol{\lambda}$  comprises an identical amount of components to the kinematic constraint function  $\mathbf{g}(\mathbf{u}^{(1)}, \mathbf{u}^{(2)})$ , with each component of  $\boldsymbol{\lambda}$  being responsible for enforcing the constraint expressed by the corresponding term of  $\mathbf{g}(\mathbf{u}^{(1)}, \mathbf{u}^{(2)})$ .

The discretisation of  $\Gamma_c$  into a set of distinct coupling elements  $C_{jk}$ , in accordance with the systematic methodology outlined in Section 4.5, allows for Eq. (4.58) to be written in the following discrete form :

$$\Pi = \sum_{j=1}^{n_c} \left( \int_{\Gamma_{cj}^{(1)}} \boldsymbol{\lambda} \cdot \mathbf{g}(\mathbf{u}^{(1)}, \mathbf{u}^{(2)}) d\Gamma_c^{(1)} + \frac{1}{2} \varepsilon \int_{\Gamma_{cj}^{(1)}} \mathbf{g}^2(\mathbf{u}^{(1)}, \mathbf{u}^{(2)}) d\Gamma_c^{(1)} \right), \quad \varepsilon \geq 0 \quad (4.59)$$

where  $\Gamma_{cj}^{(1)}$  is the domain of the slave coupling segment associated with  $C_{jk}$  and  $n_c$  is the total number of coupling elements along  $\Gamma_c$ .

#### 4.6.2 Coupling element formulation notation

The focus is henceforth shifted from the coupled system to the individual coupling element. A simpler notation is adopted for simplicity of the presented formulation and the derived expressions. Subscripts  $j, k$  referring to individual coupling elements  $C_{jk}$  are omitted, along with the superscripts referring to projections of the coupling segments  $\Gamma_{cj}$  on the coupled surfaces  $\Omega^{(1)}, \Omega^{(2)}$ .

$\Gamma_c$ , previously referring to the entirety of the coupling interface, will henceforth be used instead of  $\Gamma_{cj}^{(1)}$  for reference to the individual coupling element interface segment, corresponding to the projection of the associated segment  $\Gamma_{cj}$  on the associated active slave shell element domain  $\Gamma_j^{(1)}$ . Accordingly,  $\Gamma_c^{(1)} \equiv \Gamma_c$  and  $\Gamma_c^{(2)}$  denote the projection of  $\Gamma_c$  onto

the slave and master active shell element domains, henceforth denoted as  $\Gamma^{(1)}$  and  $\Gamma^{(2)}$  instead of  $\Gamma_j^{(1)}$  and  $\Gamma_k^{(2)}$ .

The new notation effectively corresponds to the simplest setting of the discrete 1-D surface coupling problem, comprising a single coupling element, where the slave and master surfaces  $\Omega^{(1)}$  and  $\Omega^{(2)}$  are discretised with a single shell element each, and are coupled along a 1-D interface  $\Gamma_c$  defined onto or parallel to  $\Omega^{(1)}$ . In this system, the active slave and master domains  $\Gamma^{(1)}$  and  $\Gamma^{(2)}$  effectively degenerate into the respective shell element domains, while  $\Gamma_c$  comprises a single coupling segment, coinciding with its projection  $\Gamma_c^{(1)}$  on  $\Omega^{(1)}$ . The single coupling element defined therefore comprises  $\Gamma^{(1)}$  and  $\Gamma^{(2)}$  as its active slave and master shell FE domains, alongside  $\Gamma_c$  as its coupling segment.

Henceforth, all references to the surface coupling problem are made with reference to the individual coupling elements employed for the interface discretisation, and the notation discussed here is adopted.

### 4.6.3 Coupling element contribution to total potential energy

The expression of a single coupling element contribution to the total potential energy of the system can be obtained from Eq. (4.59), where the adoption of the notation outlined in the preceding sub-section allows for the corresponding expression to be written as follows:

$$\Pi_e = \Pi + \Pi_\varepsilon = \int_{\Gamma_c} \boldsymbol{\lambda} \cdot \mathbf{g}(\mathbf{u}^{(1)}, \mathbf{u}^{(2)}) d\Gamma_c + \frac{1}{2} \varepsilon \int_{\Gamma_c} \mathbf{g}^2(\mathbf{u}^{(1)}, \mathbf{u}^{(2)}) d\Gamma_c, \quad \varepsilon \geq 0 \quad (4.60)$$

At the coupling element level, the constraint function  $\mathbf{g}(\mathbf{u}^{(1)}, \mathbf{u}^{(2)})$  along  $\Gamma_c$  can be expressed in terms of the coupling element kinematic DOFs  $\mathbf{u}_e^{(i)}$ , corresponding to the global nodal DOFs of  $\Gamma^{(i)}$ :

$$\mathbf{g}(\mathbf{u}^{(1)}, \mathbf{u}^{(2)}) = \mathbf{g}(\mathbf{u}_e^{(1)}, \mathbf{u}_e^{(2)}) = \mathbf{g}(\mathbf{u}_e) \quad (4.61)$$

where  $\mathbf{u}_e = \left( \mathbf{u}_e^{(1)} \quad \mathbf{u}_e^{(2)} \right)^T$ .

The LM field  $\lambda$  along  $\Gamma_c$  can be expressed in terms of the additional DOFs  $\lambda_e$  as discussed in Sub-section 4.4.2:

$$\lambda = \Phi \lambda_e \quad (4.62)$$

where  $\Phi$  is the matrix of LM shape functions, comprising a number of rows equal to the number of LM vector components at the CPs.

Using Eqs. (4.61) and (4.62), Eq. (4.60) can be expressed in terms of  $\mathbf{u}_e = \left( \mathbf{u}_e^{(1)} \quad \mathbf{u}_e^{(2)} \right)^T$  and  $\lambda_e$  in the following form:

$$\Pi_e = \Pi(\mathbf{u}_e, \lambda_e) + \Pi_\varepsilon(\mathbf{u}_e) = \int_{\Gamma_c} \mathbf{g}(\mathbf{u}_e)^T \cdot \Phi \cdot \lambda_e \, d\Gamma_c + \frac{1}{2} \varepsilon \int_{\Gamma_c} \mathbf{g}^2(\mathbf{u}_e) \, d\Gamma_c, \quad \varepsilon \geq 0 \quad (4.63)$$

The coupling element force vector and tangent stiffness matrix are obtained from the above expression of the coupling element total potential energy contribution using variational principles, as elaborated in Sub-sections 4.6.4 and 4.6.5. The concept is qualitatively identical to the simple case of the coupled springs system presented in Section 4.2.

#### 4.6.4 Coupling element force vector

The coupling element force vector  $\mathbf{f}_e$  is obtained in an explicit manner by considering the 1<sup>st</sup> order variation of the total potential energy function  $\Pi_e$  with respect to the kinematic and additional DOFs  $\mathbf{u}_e = \left( \mathbf{u}_e^{(1)} \quad \mathbf{u}_e^{(2)} \right)^T$  and  $\lambda_e$ .

The 1<sup>st</sup> order variation of  $\Pi_e$  with respect to the kinematic DOFs  $\mathbf{u}_e = \left( \mathbf{u}_e^{(1)} \quad \mathbf{u}_e^{(2)} \right)^T$ , which expresses the virtual work performed by the LM field  $\lambda$  over an admissible infinitesimal deformation mode  $\delta \mathbf{u}_e$ , yields:

$$\delta \Pi_e^{\mathbf{u}_e} = \delta \mathbf{u}_e^T \cdot \frac{\partial \Pi_e}{\partial \mathbf{u}_e} = \delta \mathbf{u}_e^T \cdot \left( \int_{\Gamma_c} \frac{\partial \mathbf{g}(\mathbf{u}_e)^T}{\partial \mathbf{u}_e} \cdot \Phi \cdot \lambda_e \, d\Gamma_c + \varepsilon \int_{\Gamma_c} \frac{\partial \mathbf{g}(\mathbf{u}_e)^T}{\partial \mathbf{u}_e} \cdot \mathbf{g}(\mathbf{u}_e) \, d\Gamma_c \right) \quad (4.64)$$

The variation of  $\Pi_e$  with respect to the additional DOFs  $\lambda_e$  yields the discrete form of the constraint enforcement equation, for an admissible LM field along the coupling segment obtained by a corresponding variation  $\delta\lambda_e$  at the CPs:

$$\delta\Pi_e^{\lambda_e} = \delta\lambda_e^T \cdot \frac{\partial\Pi_e}{\partial\lambda_e} = \delta\lambda_e^T \int_{\Gamma_c} \Phi^T \cdot \mathbf{g}(\mathbf{u}_e) d\Gamma_c + 0 \quad (4.65)$$

where the optional penalty regularisation term vanishes, since it is only dependent on

$$\mathbf{u}_e = (\mathbf{u}_e^{(1)} \quad \mathbf{u}_e^{(2)})^T.$$

The coupling element force vector can be expressed in the following general form:

$$\mathbf{f}_e = \left\langle \frac{\partial\Pi_e}{\partial\mathbf{u}_e} \middle| \frac{\partial\Pi_e}{\partial\lambda_e} \right\rangle^T = \langle \mathbf{f}_g \mid \mathbf{f}_a \rangle^T + \langle \mathbf{f}_{g,\varepsilon} \mid \mathbf{f}_{a,\varepsilon} \rangle^T \quad (4.66)$$

where the expressions of the internal force vector components  $\mathbf{f}_g$  and  $\mathbf{f}_a$  associated with

$$\mathbf{u}_e = (\mathbf{u}_e^{(1)} \quad \mathbf{u}_e^{(2)})^T \quad \text{and} \quad \lambda_e, \quad \text{respectively, and their corresponding optional penalty}$$

regularisation terms  $\mathbf{f}_{g,\varepsilon}$  and  $\mathbf{f}_{a,\varepsilon}$  can be explicitly obtained from Eqs. (4.64) and (4.65), as given hereafter:

$$\mathbf{f}_g = \int_{\Gamma_c} \frac{\partial\mathbf{g}(\mathbf{u}_e)^T}{\partial\mathbf{u}_e} \cdot \Phi \cdot \lambda_e d\Gamma_c \quad (4.67)$$

$$\mathbf{f}_{g,\varepsilon} = \varepsilon \int_{\Gamma_c} \frac{\partial\mathbf{g}(\mathbf{u}_e)^T}{\partial\mathbf{u}_e} \cdot \mathbf{g}(\mathbf{u}_e) d\Gamma_c \quad (4.68)$$

$$\mathbf{f}_a = \int_{\Gamma_c} \Phi^T \cdot \mathbf{g}(\mathbf{u}_e) d\Gamma_c \quad (4.69)$$

$$\mathbf{f}_{a,\varepsilon} = \mathbf{0} \quad (4.70)$$

#### 4.6.5 Coupling element tangent stiffness matrix

The coupling element tangent stiffness matrix  $\mathbf{k}_e$  is also obtained explicitly by considering the 2<sup>nd</sup> order variation of the total potential energy function  $\Pi_e$  for admissible infinitesimal deformation modes  $\delta\mathbf{u}_e$  and variations  $\delta\lambda_e$  of the LM field along  $\Gamma_c$ . The four 2<sup>nd</sup> order energy variations are given below:

$$\begin{aligned} \delta^2 \Pi_e^{\mathbf{u}_e, \mathbf{u}_e} &= \delta\mathbf{u}_e^T \cdot \frac{\partial^2 \Pi_e}{\partial \mathbf{u}_e \partial \mathbf{u}_e^T} \cdot \delta\mathbf{u}_e = \\ &= \delta\mathbf{u}_e^T \cdot \left( \int_{\Gamma_c} \frac{\partial^2 \mathbf{g}(\mathbf{u}_e)^T}{\partial \mathbf{u}_e \partial \mathbf{u}_e^T} \cdot \Phi \cdot \lambda_e \, d\Gamma_c + \varepsilon \int_{\Gamma_c} \frac{\partial^2 \mathbf{g}(\mathbf{u}_e)^T}{\partial \mathbf{u}_e \partial \mathbf{u}_e^T} \cdot \mathbf{g}(\mathbf{u}_e) + \frac{\partial \mathbf{g}(\mathbf{u}_e)^T}{\partial \mathbf{u}_e} \cdot \frac{\partial \mathbf{g}(\mathbf{u}_e)}{\partial \mathbf{u}_e^T} \, d\Gamma_c \right) \cdot \delta\mathbf{u}_e \end{aligned} \quad (4.71)$$

$$\delta^2 \Pi_e^{\mathbf{u}_e, \lambda_e} = \delta\mathbf{u}_e^T \cdot \frac{\partial^2 \Pi_e}{\partial \mathbf{u}_e \partial \lambda_e^T} \cdot \delta\lambda_e = \delta\mathbf{u}_e^T \cdot \left( \int_{\Gamma_c} \frac{\partial \mathbf{g}(\mathbf{u}_e)^T}{\partial \mathbf{u}_e} \cdot \Phi \, d\Gamma_c \right) \cdot \delta\lambda_e \quad (4.72)$$

$$\delta^2 \Pi_e^{\lambda_e, \mathbf{u}_e} = \delta\lambda_e^T \cdot \frac{\partial^2 \Pi_e}{\partial \lambda_e \partial \mathbf{u}_e^T} \cdot \delta\mathbf{u}_e = \delta\lambda_e^T \cdot \left( \int_{\Gamma_c} \Phi^T \cdot \frac{\partial \mathbf{g}(\mathbf{u}_e)}{\partial \mathbf{u}_e^T} \, d\Gamma_c \right) \cdot \delta\mathbf{u}_e \quad (4.73)$$

$$\delta^2 \Pi_e^{\lambda_e, \lambda_e} = \delta\lambda_e^T \cdot \frac{\partial^2 \Pi_e}{\partial \lambda_e \partial \lambda_e^T} \cdot \delta\lambda_e = 0 \quad (4.74)$$

The above procedure is equivalent to the differentiation once of the coupling element force vector  $\mathbf{f}_e$  with respect to  $\mathbf{u}_e = (\mathbf{u}_e^{(1)} \quad \mathbf{u}_e^{(2)})^T$  and  $\lambda_e$ . Considering the prior distinction of the force vector components, the tangent stiffness matrix can be accordingly distinguished into 4 principal component matrices, where the contribution of the penalty regularisation terms is considered separately for clarity: (i)  $\mathbf{k}_{gg}$ , which is associated with the interaction of  $\mathbf{u}_e = (\mathbf{u}_e^{(1)} \quad \mathbf{u}_e^{(2)})^T$ ; (ii)  $\mathbf{k}_{ga}$  and  $\mathbf{k}_{ag}$ , which are associated with the interaction of  $\mathbf{u}_e = (\mathbf{u}_e^{(1)} \quad \mathbf{u}_e^{(2)})^T$  and  $\lambda_e$ ; and (iii)  $\mathbf{k}_{aa}$ , which is associated with the interaction of  $\lambda_e$ . This leads to the following general form for the tangent stiffness matrix  $\mathbf{k}_e$ :

$$\mathbf{k}_e = \begin{bmatrix} \frac{\partial^2 \Pi_e}{\partial \mathbf{u}_e \partial \mathbf{u}_e^T} & \frac{\partial^2 \Pi_e}{\partial \mathbf{u}_e \partial \boldsymbol{\lambda}_e^T} \\ \frac{\partial^2 \Pi_e}{\partial \boldsymbol{\lambda}_e \partial \mathbf{u}_e^T} & \frac{\partial^2 \Pi_e}{\partial \boldsymbol{\lambda}_e \partial \boldsymbol{\lambda}_e^T} \end{bmatrix} = \begin{bmatrix} \frac{\partial \mathbf{f}_e}{\partial \mathbf{u}_e^T} & \frac{\partial \mathbf{f}_e}{\partial \boldsymbol{\lambda}_e^T} \end{bmatrix} = \begin{bmatrix} \mathbf{k}_{gg} & \mathbf{k}_{ga} \\ \mathbf{k}_{ag} & \mathbf{k}_{aa} \end{bmatrix} + \begin{bmatrix} \mathbf{k}_{gg,\varepsilon} & \mathbf{k}_{ga,\varepsilon} \\ \mathbf{k}_{ag,\varepsilon} & \mathbf{k}_{aa,\varepsilon} \end{bmatrix} \quad (4.75)$$

where the component submatrices are given by the following expressions:

$$\mathbf{k}_{gg} = \int_{\Gamma_c} \frac{\partial^2 \mathbf{g}(\mathbf{u}_e)^T}{\partial \mathbf{u}_e \partial \mathbf{u}_e^T} \cdot \boldsymbol{\Phi} \cdot \boldsymbol{\lambda}_e \, d\Gamma_c \quad (4.76)$$

$$\mathbf{k}_{gg,\varepsilon} = \varepsilon \int_{\Gamma_c} \left( \frac{\partial^2 \mathbf{g}(\mathbf{u}_e)^T}{\partial \mathbf{u}_e \partial \mathbf{u}_e^T} \cdot \mathbf{g}(\mathbf{u}_e) + \frac{\partial \mathbf{g}(\mathbf{u}_e)^T}{\partial \mathbf{u}_e} \cdot \frac{\partial \mathbf{g}(\mathbf{u}_e)}{\partial \mathbf{u}_e^T} \right) d\Gamma_c \quad (4.77)$$

$$\mathbf{k}_{ga} = \mathbf{k}_{ag}^T = \int_{\Gamma_c} \frac{\partial \mathbf{g}(\mathbf{u}_e)^T}{\partial \mathbf{u}_e} \cdot \boldsymbol{\Phi} \, d\Gamma_c \quad (4.78)$$

$$\mathbf{k}_{ga,\varepsilon} = \mathbf{k}_{ag,\varepsilon}^T = \mathbf{0} \quad (4.79)$$

$$\mathbf{k}_{aa} = \mathbf{0} \quad (4.80)$$

$$\mathbf{k}_{aa,\varepsilon} = \mathbf{0} \quad (4.81)$$

## 4.7 Numerical integration scheme

### 4.7.1 Gaussian quadrature integration scheme

The integrals in the expressions of the force vector and tangent stiffness matrix derived in Section 4.6 are numerically evaluated employing Gaussian quadrature. The Gaussian quadrature rule allows for the approximation of the exact value of a function integral, by means of a weighted sum of the function values at specified GP abscissae. The number of employed GPs defines the order of the Gaussian quadrature rule, with an increased order leading to enhanced approximation accuracy. For a univariate integrand function  $f(x)$  defined in the interval  $[-1,1]$ , the  $m^{\text{th}}$ -order Gaussian quadrature rule is expressed in the following form:

$$\int_{-1}^1 f(x) dx \cong \sum_{p=1}^m w_p f(x_p) \quad (4.82)$$

where  $x_p \in [-1,1]$  is the abscissa of GP  $p$  and  $w_p$  is the corresponding weighting factor, with

$$\sum_{p=1}^m w_p = 2 \text{ for integration in 1 dimension.}$$

The GP abscissae and associated weights for the  $m^{\text{th}}$ -order Gaussian quadrature rule have been optimally established to minimise the integration error. The abscissae  $x_p$  correspond to the  $m$  roots of the orthogonal to the integrand function  $m^{\text{th}}$ -order Legendre polynomials  $P_m(x)$ , while the corresponding weights are given by the following expression (Abramowitz & Stegun, 1964):

$$w_p = \frac{2}{(1-x_p^2)P_m'(x_p)^2} \quad (4.83)$$

where  $P_m'(x_p)$  denotes the value of the  $m^{\text{th}}$ -order Legendre polynomial derivative at root  $x_p$ .

It should be noted that the employment of the  $m^{\text{th}}$ -order Gaussian quadrature rule allows for the exact integration of polynomial functions of order up to  $2m-1$ . This is an important accuracy consideration for the developed coupling element formulation, where the integrand functions are conditionally polynomial.

#### 4.7.2 Coordinate mapping

As earlier discussed in Section 4.6, the integrand functions of the coupling element force vector and tangent stiffness matrix components are related to the kinematic constraint function  $\mathbf{g}(\mathbf{u}^{(1)}, \mathbf{u}^{(2)})$  and the LM vector field  $\boldsymbol{\lambda}$  defined along the associated segment  $\Gamma_c$ . The employment of the discrete isoparametric frameworks discussed in Sub-sections 4.4.1 and 4.4.2 enables these to be expressed in the respective natural coordinate systems, using polynomial shape functions, which involves a mapping process from the respective natural coordinate system to the local or global Cartesian coordinate system.



The integration at the coupling element level is performed along the interface segment, in its natural coordinate system, and hence due account of the geometric change effect in real coordinates with respect to natural coordinates must be taken. This is achieved by means of the Jacobian associated with the respective mapping.

Beyond defining the Jacobian of the mapping at the interface segment level, which is essential for the integration procedures presented in the forthcoming sub-section, it is also useful to define the Jacobian of the shell FE geometry and displacement field mapping at this point, which is employed in the coupling formulations presented in Chapter 5.

In the case of curved shell FEs, both local and global Jacobians are (3x2) matrices expressing the rate of change of  $\mathbf{x}^{(i)} = (x^{(i)}, y^{(i)}, z^{(i)})$  and  $\mathbf{X}^{(i)} = (X^{(i)}, Y^{(i)}, Z^{(i)})$  with respect to  $(\xi^{(i)}, \eta^{(i)})$ , as given by the following expressions:

$$\begin{aligned} \mathbf{j}^{(i)}(\xi^{(i)}, \eta^{(i)}) &= \left[ \frac{\partial \mathbf{x}^{(i)}(\xi^{(i)}, \eta^{(i)})}{\partial \xi^{(i)}} \quad \frac{\partial \mathbf{x}^{(i)}(\xi^{(i)}, \eta^{(i)})}{\partial \eta^{(i)}} \right] = \\ &= \left[ \sum_{k=1}^{m_i} \frac{\partial N_k^{(i)}(\xi^{(i)}, \eta^{(i)})}{\partial \xi^{(i)}} \mathbf{x}_k^{(i)} \quad \sum_{k=1}^{m_i} \frac{\partial N_k^{(i)}(\xi^{(i)}, \eta^{(i)})}{\partial \eta^{(i)}} \mathbf{x}_k^{(i)} \right] = \left[ \mathbf{N}_{,\xi}^{(i)} \cdot \mathbf{x}_e^{(i)} \quad \mathbf{N}_{,\eta}^{(i)} \cdot \mathbf{x}_e^{(i)} \right] \end{aligned} \quad (4.84)$$

$$\begin{aligned} \mathbf{J}^{(i)}(\xi^{(i)}, \eta^{(i)}) &= \left[ \frac{\partial \mathbf{X}^{(i)}(\xi^{(i)}, \eta^{(i)})}{\partial \xi^{(i)}} \quad \frac{\partial \mathbf{X}^{(i)}(\xi^{(i)}, \eta^{(i)})}{\partial \eta^{(i)}} \right] = \\ &= \left[ \sum_{k=1}^{m_i} \frac{\partial N_k^{(i)}(\xi^{(i)}, \eta^{(i)})}{\partial \xi^{(i)}} \mathbf{X}_k^{(i)} \quad \sum_{k=1}^{m_i} \frac{\partial N_k^{(i)}(\xi^{(i)}, \eta^{(i)})}{\partial \eta^{(i)}} \mathbf{X}_k^{(i)} \right] = \left[ \mathbf{N}_{,\xi}^{(i)} \cdot \mathbf{X}_e^{(i)} \quad \mathbf{N}_{,\eta}^{(i)} \cdot \mathbf{X}_e^{(i)} \right] \end{aligned} \quad (4.85)$$

where  $\mathbf{N}_{,\xi}^{(i)}$  and  $\mathbf{N}_{,\eta}^{(i)}$  are the derivatives of matrix  $\mathbf{N}^{(i)}$  in Eq. (4.13) with respect to  $\xi^{(i)}$  and  $\eta^{(i)}$ .

The adoption of the negligible shell element out-of-flatness with mesh refinement assumption, earlier discussed in Sub-sections 4.4.1 and 4.4.2, allows for the local shell element geometry to be approximated as planar. The local Jacobian expressing the rate of change of the planar local coordinates  $\bar{\mathbf{x}}^{(i)} = (x^{(i)}, y^{(i)})$  accordingly reduces to a 2x2 matrix, which is given by the following expression:

$$\bar{\mathbf{j}}^{(i)} = \left[ \bar{\mathbf{N}}_{,\xi}^{(i)} \cdot \bar{\mathbf{x}}_e^{(i)} \quad \bar{\mathbf{N}}_{,\eta}^{(i)} \cdot \bar{\mathbf{x}}_e^{(i)} \right] \quad (4.86)$$

where  $\bar{\mathbf{N}}_{,\xi^{(i)}}$  and  $\bar{\mathbf{N}}_{,\eta^{(i)}}$  are the derivatives of matrix  $\bar{\mathbf{N}}^{(i)}$  in Eq. (4.15) with respect to  $\xi^{(i)}$  and  $\eta^{(i)}$ .

Based on the same assumption, the interface segment out-of-straightness can also be considered negligible in the limit with sufficient mesh refinement. The respective local Jacobian  $\tilde{j}$  is therefore a scalar quantity and the global Jacobian a  $3 \times 1$  vector, expressing the rate of change of  $\tilde{x}$  and  $\tilde{\mathbf{X}} = (\tilde{X}, \tilde{Y}, \tilde{Z})$  with respect to the interface natural coordinate  $\tilde{\xi}$ . These are given by the following set of equations:

$$\tilde{j}(\tilde{\xi}) = \frac{d\tilde{x}(\tilde{\xi})}{d\tilde{\xi}} = \sum_{k=1}^{m_\lambda} \frac{d\Phi_k(\tilde{\xi})}{d\tilde{\xi}} \tilde{x}_k = \boldsymbol{\varphi}_{,\tilde{\xi}} \cdot \tilde{\mathbf{x}}_e \quad (4.87)$$

$$\tilde{\mathbf{J}}(\tilde{\xi}) = \frac{d\tilde{\mathbf{X}}(\tilde{\xi})}{d\tilde{\xi}} = \sum_{k=1}^{m_\lambda} \frac{d\Phi_k(\tilde{\xi})}{d\tilde{\xi}} \tilde{\mathbf{X}}_k = \mathbf{\Phi}_{,\tilde{\xi}} \cdot \tilde{\mathbf{X}}_e \quad (4.88)$$

where  $\boldsymbol{\varphi}_{,\tilde{\xi}}$  and  $\mathbf{\Phi}_{,\tilde{\xi}}$  are the derivatives of matrices  $\boldsymbol{\varphi}$  and  $\mathbf{\Phi}$  in Eqs. (4.19) and (4.21) with respect to  $\tilde{\xi}$ . The mapping between the natural coordinate system and the local Cartesian coordinate system of the shell element and the coupling interface segment domains is illustrated in Figure 4.9.

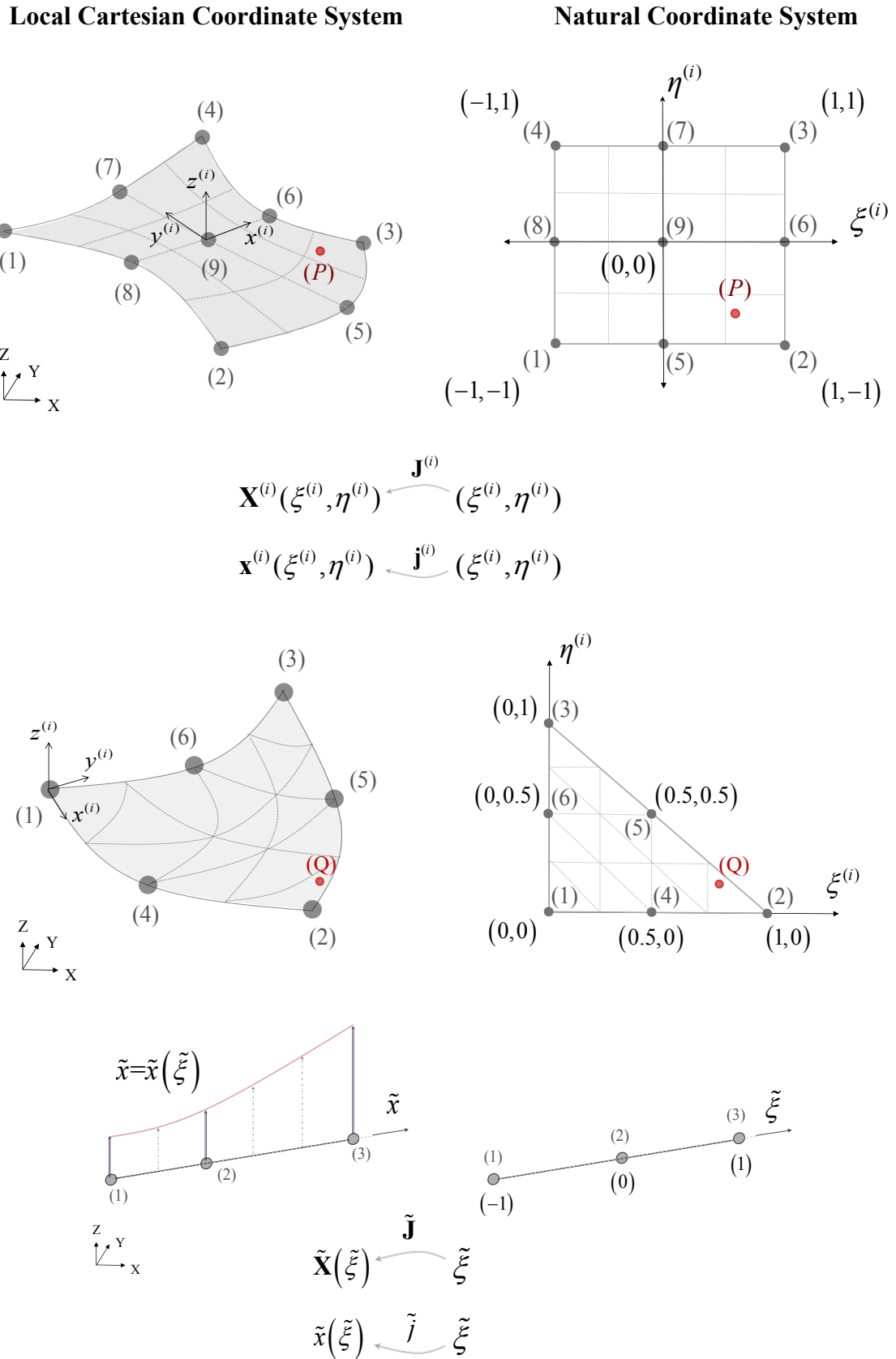


Figure 4.9: Coordinate mapping between the natural and Cartesian coordinate systems of the shell element domains and the 1-D coupling interface segments

### 4.7.3 Gaussian integration at the coupling element level

The integrand functions of the coupling element force vector and tangent stiffness matrix are expressed in terms of the three distinct sets of natural coordinates: (i) the slave element domain  $\Gamma^{(1)}$  natural coordinates  $(\xi^{(1)}, \eta^{(1)})$ ; (ii) the master element domain  $\Gamma^{(2)}$  natural coordinates  $(\xi^{(2)}, \eta^{(2)})$ ; and (iii) the coupling element interface segment  $\Gamma_c$  natural coordinate  $\tilde{\xi}$ . The integration is performed along  $\Gamma_c$ , with the corresponding integrals expressed in the following general form:

$$\int_{\Gamma_c} f(\xi^{(1)}, \eta^{(1)}, \xi^{(2)}, \eta^{(2)}, \tilde{\xi}) d\Gamma_c \quad (4.89)$$

where  $\tilde{\xi} \in [-1, 1]$ , while  $\{\xi^{(i)}, \eta^{(i)}\} \in [-1, 1]$  for 9-noded quadrilateral shell elements and  $\{\xi^{(i)}, \eta^{(i)}\} \in [0, 1] \mid 0 \leq \xi^{(i)} + \eta^{(i)} \leq 1$  for 6-noded triangular shell elements.

The GPs are defined along  $\Gamma_c$ , and hence the respective natural coordinate axis is defined such that its origin  $\tilde{\xi} = 0$  is located at the segment mid-point, with the segment end points abscissae being accordingly  $\tilde{\xi} = \pm 1$ . This allows for the individual GP abscissae  $\tilde{\xi}_p$  to be defined in the interval  $[-1, 1]$ , for consistency with what has previously been discussed in Sub-section 4.7.1.

The GPs are projected on  $\Gamma^{(1)}$  and  $\Gamma^{(2)}$  using the projection algorithm presented in Sub-section 4.5.2.1, which enables the direct evaluation of the projection coordinates  $(\xi_p^{(i)}, \eta_p^{(i)})$  in the respective natural coordinate system, when the global Cartesian coordinates  $\tilde{\mathbf{X}}_p(\tilde{\xi}_p)$  of the individual GPs are known. The establishment of an implicit relationship between  $\tilde{\xi}$  and  $(\xi^{(i)}, \eta^{(i)})$  by virtue of the employed projection algorithm, enables for Eq. (4.89) to be expressed purely as a function of  $\tilde{\xi}$ . Accordingly, the incorporation of geometric change effects due to coordinate mapping in the respective integral is limited to the integration domain  $\Gamma_c$ , where the scalar local Jacobian  $\tilde{j}$  can be used under the assumption of negligible shell element out-of-flatness and interface segment out-of-straightness. On the other hand, the effect of geometric change associated with  $\Gamma^{(1)}$  and  $\Gamma^{(2)}$  is readily accounted for in the projection algorithm.

Taking due account of the aforementioned considerations, Eq. (4.89) can be rewritten as:

$$\int_{-1}^1 f(\tilde{\xi}) \tilde{j}(\tilde{\xi}) d\tilde{\xi} = \int_{-1}^1 f\left(\xi^{(1)}(\tilde{\xi}), \eta^{(1)}(\tilde{\xi}), \xi^{(2)}(\tilde{\xi}), \eta^{(2)}(\tilde{\xi}), \tilde{\xi}\right) \tilde{j}(\tilde{\xi}) d\tilde{\xi} \quad (4.90)$$

The integral is numerically evaluated using Gaussian quadrature:

$$\int_{-1}^1 f(\tilde{\xi}) \tilde{j}(\tilde{\xi}) d\tilde{\xi} \cong \sum_{p=1}^m w_p f\left(\xi^{(1)}(\tilde{\xi}_p), \eta^{(1)}(\tilde{\xi}_p), \xi^{(2)}(\tilde{\xi}_p), \eta^{(2)}(\tilde{\xi}_p), \tilde{\xi}_p\right) \tilde{j}(\tilde{\xi}_p) \quad (4.91)$$

where  $\left(\xi^{(1)}(\tilde{\xi}_p), \eta^{(1)}(\tilde{\xi}_p)\right)$  and  $\left(\xi^{(2)}(\tilde{\xi}_p), \eta^{(2)}(\tilde{\xi}_p)\right)$  are the natural coordinates of the projections of GP  $p$ , with natural coordinate  $\tilde{\xi}_p$  along the interface, on the slave and master shell FE domains, respectively.

Two distinct integration schemes have been considered in the coupling element formulation, namely segment-specific and element-specific, which are discussed separately in the following sub-sections.

#### 4.7.3.1 Segment-specific integration scheme

The segment-specific integration scheme is based on the establishment of a unique set of GPs with fixed locations along the coupling segment length, which is employed for the integration of all associated coupling elements.

As discussed in Sub-section 4.5.2, the employment of the slave-only progressive segmentation scheme leads to the association of a single active slave shell element with multiple active master ones along the same segment. Accordingly, the specification of a unique set of GPs along the segment results into this being projected in its entirety on the slave shell FE surface, but only partially on each of the associated master shell FEs. At the coupling element level, only the subset of GPs with active projections on both its slave and master shell FE surfaces is employed for the numerical integration of the corresponding force vector and tangent stiffness matrix, which will henceforth be referred to as active GPs.

This leads to reduced integration order at the coupling element level, in comparison with the specified along the segment, which, in turn, results in an inferior overall accuracy of the coupling formulation. The inactive GPs of a given coupling element can either have active projections on adjacent master shell elements or be projected outside of the master surface domain. In the former case the contribution of an inactive GP is accounted for in the integration of the coupling element associated with the adjacent master FE, while in the latter case it is neglected. If a GP is projected on a shared edge between two master elements, its weighting factor is shared in the integration of the respective coupling elements.

The concept is schematically illustrated in Figure 4.10 for a coupled system encompassing two coupling elements, with a specified Gaussian quadrature rule of order 5 along the interface segment. As is evident in this example system, the unique set of GPs employed for the integration of both coupling elements, with fixed locations along the segment, are partially projected on the master surface shell FEs. 1 GP is projected outside the master surface, and hence a total of 4 GPs are employed for both coupling elements for a specified quadrature order of 5 along the segment.

Due to the specification of the same integration segment for multiple coupling elements, the part of the integrand functions associated with the master FE surface are potentially defined as piece-wise polynomial along the segment. Gaussian quadrature is incapable of accurately integrating piece-wise polynomial functions, irrespective of the employed integration order, and hence the segment-specific integration scheme potentially does not achieve exact integration along the segment, even with a large number of GPs.

These inaccuracies can be partially alleviated via the specification of a large quadrature order and the classification of the surface associated with the finer mesh as slave. This leads to smaller individual interface segment length, which allows for an overall greater number of GPs to be defined along the interface, as well as to an increased likelihood of active GP projection on master shell element domains of greater size. In the limit, with mesh refinement, the proposed treatment of GP contributions allows for adequate overall accuracy to be achieved along the interface, with a variable order of integration between different coupling elements, as will be discussed in more detail in Sub-section 5.5.5.2 of the coupling element patch tests.

#### 4.7.3.2 Element-specific integration scheme

The element-specific integration scheme is based on the establishment of multiple distinct, non-overlapping sets of GPs with the specified quadrature order along the segment, and the employment of each set for the integration of a unique associated coupling element.

The set of GPs for each coupling element is defined on the sub-segment that fully projects on both associated slave and master shell FE surfaces, which thus renders all GPs active. This allows for integration with the specified quadrature order to be achieved for all coupling elements along the interface, hence leading to a superior overall accuracy of the coupling formulation in comparison with the segment-specific scheme, even with a much lower overall number of GPs along the coupling interface. Moreover, the specification of integration domains with full projections on both shell element surfaces allows for the effective overcoming of inaccuracies arising from the integrand functions being piece-wise polynomial, and exact integration can therefore be achieved with a small number of GPs.

The concept is schematically illustrated in Figure 4.11 for the same coupled system shown in Figure 4.10. Contrary to the segment-based integration, a distinct set of 5 GPs is defined for each coupling element in this case, with the locations of the GPs changing to conform with the boundaries of the two subsegments shared by the slave and the distinct master shell elements. Each set of GPs is thus projected entirely on each shell FE surface, and hence a total of 10 GPs along the segment are employed for the integration of both coupling elements, for a specified quadrature order of 5.

Taking due account of the aforementioned considerations, the element-specific integration is selected as the integration scheme for the developed coupling element in its default *modus operandi*. A comparison of the accuracy and convergence rate achieved by the two schemes will be presented in Sub-section 5.5.5.2 of the coupling element patch tests.

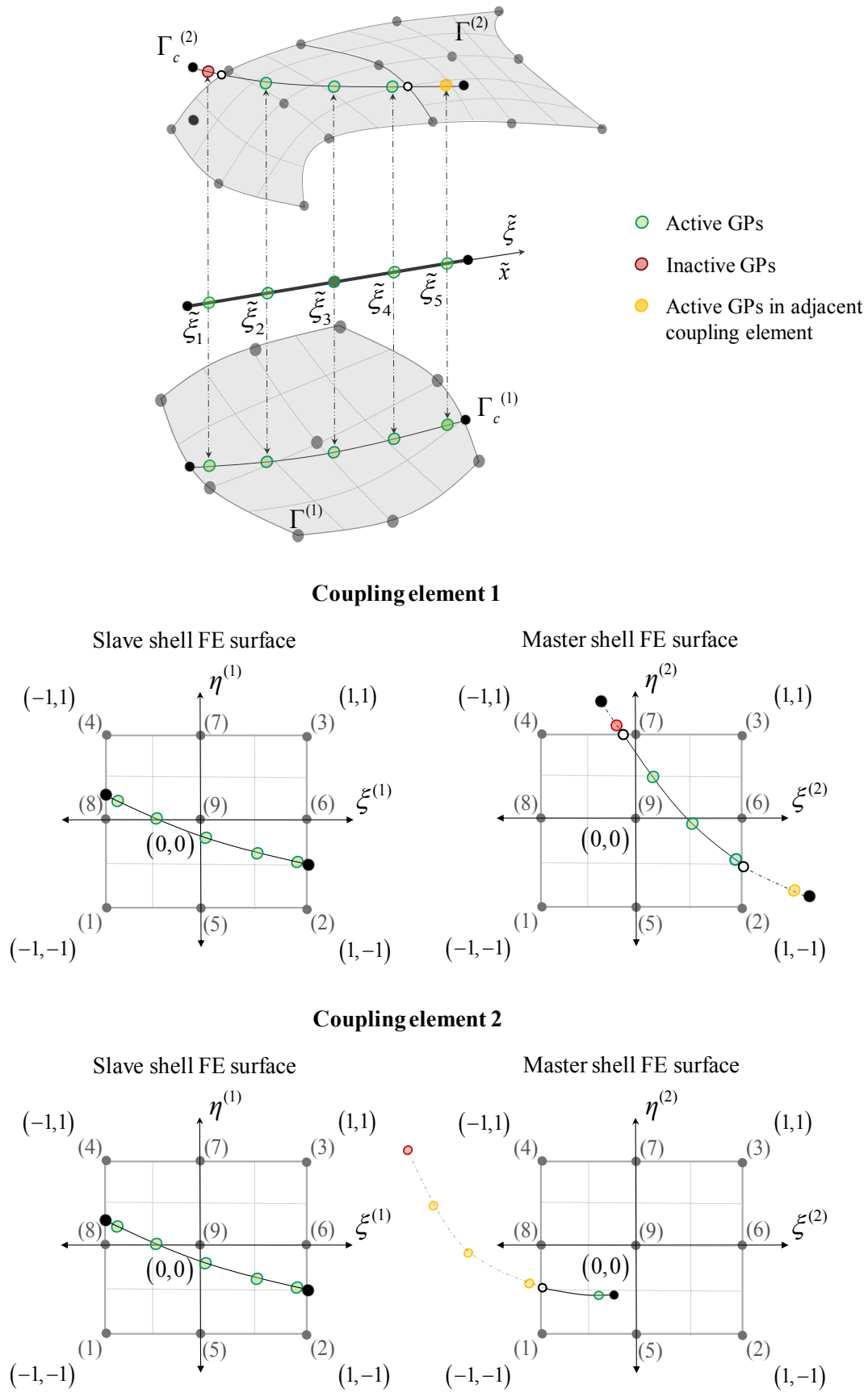


Figure 4.10: Segment-specific integration scheme and mapping of GPs on the slave and master shell element natural coordinate systems (Gaussian quadrature order 5)



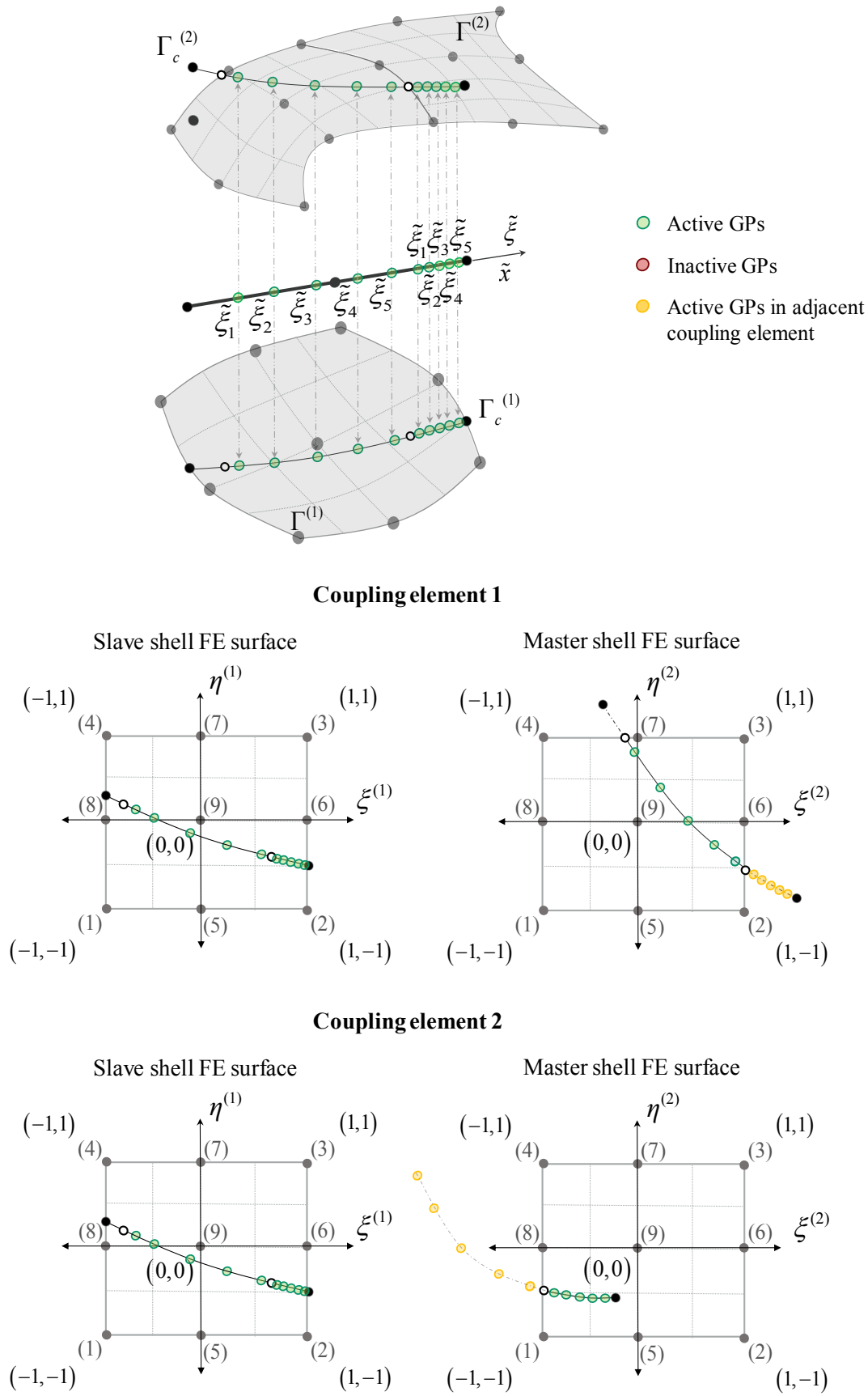


Figure 4.11: Element-specific integration scheme and mapping of GPs on the slave and master shell element natural coordinate systems (Gaussian quadrature order 5)

## **4.8 Concluding remarks**

An original and systematic methodology for surface coupling along a line is presented in this chapter, encompassing the employment of a novel 1-D coupling element formulation. The formulation is underpinned by the fundamental principles of the mortar method (Fischer & Wriggers, 2005b; Puso, 2004), employing an Augmented LM approach for the constraint enforcement along the 1-D interface. The developed 1-D coupling element facilitates discrete constraint enforcement along a straight or curved 1-D interface between planar, curved and folded surfaces of arbitrary relative spatial orientation, discretised with quadratic Reissner-Mindlin curved shell FEs. Therefore, it provides a systematic framework for geometric modelling of weld lines, the coupling of regions with different levels of discretisation detail or element types within a system, as well as for domain partitioning problems involving computationally heterogeneous partitions. Notwithstanding its development in compliance with the HF modelling strategy presented in Chapter 3, the formulation establishment within the most general setting enables the straightforward upgrade of existing FE programs to incorporate coupling elements applicable to any type of 2-D and 3-D FEs.

# Chapter 5

## 1-D Translational and Rotational Coupling Element

### 5.1 Introduction

In Chapter 4, a systematic methodology for the enforcement of surface coupling along a 1-D interface has been presented, which is based on the discretisation of the coupling interface into coupling elements. This allows for the enforcement of a set of distinct kinematic constraints  $\mathbf{g}(\mathbf{u}^{(1)}, \mathbf{u}^{(2)})$  along the interface using a multi-dimensional continuous Lagrangian Multiplier (LM) field  $\lambda$ , introduced in a piece-wise manner along successive coupling element segments.

In this context, a 1-D coupling element formulation has been developed using energy variational principles, encompassing the establishment of the coupling element internal force vector and tangent stiffness matrix associated with the given set of constraints  $\mathbf{g}(\mathbf{u}^{(1)}, \mathbf{u}^{(2)})$ . This allows for the individual coupling element contributions to be accounted for by means of their assembly to the coupled system global force vector and tangent stiffness matrix, thereby enabling the constraint enforcement to be effectively achieved in a discrete manner. The general form of the coupling element formulation has been presented earlier in Section 4.6.

This chapter focuses on the establishment of the coupling element force vector and tangent stiffness matrix for a set of rigid translational and rotational constraints along the 1-D coupling interface. The notation discussed previously in Section 4.6 is adopted throughout, the focus being on the individual coupling element formulation, encompassing the combination of translational and rotational coupling formulations. The chapter proceeds with presenting the translational and rotational coupling element formulations independently, where the derived

expressions for the coupling element internal force vector and consistent tangent stiffness matrix are presented for each case. Subsequently, the results associated with a series of patch tests, conducted to verify the element capability of effectively enforcing the coupling constraints and assess its accuracy and performance, are presented. The chapter concludes with a series of parametric studies for the developed coupling element, where its performance sensitivity to the various parameters embedded in the translational and rotational coupling formulations is thoroughly investigated.

## 5.2 1-D translational coupling element formulation

The present section presents the derivation of the mathematical formulation governing the response of the 1-D coupling element for 3-D rigid translational coupling constraint enforcement between two deformable surfaces  $\Omega^{(i)}$  ( $i=1,2$ ) with non-conforming shell Finite Element (FE) meshes. Without loss of generality, surfaces  $\Omega^{(1)}$  and  $\Omega^{(2)}$  are classified as slave and master, respectively.

The translational constraint is introduced in the global Cartesian coordinate system to alleviate complex nonlinear co-rotational transformations dependent on the relative surface orientation (Izzuddin & Liang, 2016). The constraint function for rigid translational surface coupling can be expressed in the following form:

$$\mathbf{g}(\mathbf{u}^{(1)}, \mathbf{u}^{(2)}) = \mathbf{u}^{(1)} - \mathbf{u}^{(2)} = \mathbf{0} \Rightarrow \left\{ \begin{array}{l} U^{(1)} - U^{(2)} \\ V^{(1)} - V^{(2)} \\ W^{(1)} - W^{(2)} \end{array} \right\} = \left\{ \begin{array}{l} 0 \\ 0 \\ 0 \end{array} \right\} \quad (5.1)$$

where  $\mathbf{u}^{(i)} = (U^{(i)} \quad V^{(i)} \quad W^{(i)})^T$ , ( $i=1,2$ ), are the independent shell surface displacement fields along the coupling interface in the global Cartesian (X,Y,Z) coordinate system.

The distinct isoparametric frameworks discussed in Sub-sections 4.4.1 and 4.4.2 are employed herein with a 3-D LM field  $\boldsymbol{\lambda} = (\lambda_x \quad \lambda_y \quad \lambda_z)^T$ .

This section proceeds with presenting the translational coupling element formulation in two sub-sections, where: (i) the element contribution to the total potential energy of the system is

established and the expressions for the coupling element internal force vector components are derived employing 1<sup>st</sup> order variational principles; and (ii) the expressions for the coupling element consistent tangent stiffness matrix components are derived from the established energy expression employing 2<sup>nd</sup> order variational principles.

### 5.2.1 Element contribution to total potential energy and internal force vector

For translational coupling of the active shell element domains  $\Gamma^{(i)}$  associated with the coupling element in the global Cartesian coordinate system, the constraint function in Eq. (5.1) can be expressed in terms of the coupling element kinematic Degrees of Freedom (DOFs)  $\mathbf{u}_e^{(i)}$  along  $\Gamma_c$ :

$$\mathbf{g} = \mathbf{g}(\mathbf{u}_e) = \mathbf{g}(\mathbf{u}_e^{(1)}, \mathbf{u}_e^{(2)}) = \mathbf{u}^{(1)}(\mathbf{u}_e^{(1)}) - \mathbf{u}^{(2)}(\mathbf{u}_e^{(2)}) = \mathbf{N}^{(1)} \cdot \mathbf{u}_e^{(1)} - \mathbf{N}^{(2)} \cdot \mathbf{u}_e^{(2)} \quad (5.2)$$

The expression of the total potential energy contribution of the coupling element to the system in Eq. (4.60) can therefore be rewritten in a discrete form, in terms of its kinematic and additional DOFs  $\mathbf{u}_e^{(i)}$  and  $\lambda_e$ , respectively:

$$\begin{aligned} \Pi_e = \Pi + \Pi_\varepsilon = & \int_{\Gamma_c} \left( \mathbf{N}^{(1)} \cdot \mathbf{u}_e^{(1)} - \mathbf{N}^{(2)} \cdot \mathbf{u}_e^{(2)} \right)^T \cdot \Phi \cdot \lambda_e \, d\Gamma_c + \\ & + \frac{1}{2} \varepsilon \int_{\Gamma_c} \left\| \mathbf{N}^{(1)} \cdot \mathbf{u}_e^{(1)} - \mathbf{N}^{(2)} \cdot \mathbf{u}_e^{(2)} \right\|^2 \, d\Gamma_c, \quad \varepsilon \geq 0 \end{aligned} \quad (5.3)$$

Having established the total potential energy function  $\Pi_e$  of an individual coupling element in terms of  $\mathbf{u}_e^{(i)}$  and  $\lambda_e$ , the force vector  $\mathbf{f}_e$  is obtained as its 1<sup>st</sup> order variation with respect to these parameters. The virtual work performed by the LM field over an admissible infinitesimal deformation mode  $\delta \mathbf{u}_e$  along  $\Gamma_c$  is given as the 1<sup>st</sup> order variation of  $\Pi_e$  with respect to  $\mathbf{u}_e = \left( \mathbf{u}_e^{(1)} \quad \mathbf{u}_e^{(2)} \right)^T$ , which yields:

$$\begin{aligned} \delta \Pi_e^{u_e} = & \delta \mathbf{u}_e^T \cdot \left( \int_{\Gamma_c} \frac{\partial (\mathbf{N}^{(1)} \cdot \mathbf{u}_e^{(1)} - \mathbf{N}^{(2)} \cdot \mathbf{u}_e^{(2)})^T}{\partial \mathbf{u}_e} \cdot \Phi \cdot \lambda_e \, d\Gamma_c \right) + \\ & + \delta \mathbf{u}_e^T \cdot \left( \varepsilon \int_{\Gamma_c} \frac{\partial (\mathbf{N}^{(1)} \cdot \mathbf{u}_e^{(1)} - \mathbf{N}^{(2)} \cdot \mathbf{u}_e^{(2)})^T}{\partial \mathbf{u}_e} \cdot (\mathbf{N}^{(1)} \cdot \mathbf{u}_e^{(1)} - \mathbf{N}^{(2)} \cdot \mathbf{u}_e^{(2)}) \, d\Gamma_c \right) \end{aligned} \quad (5.4)$$

while the variation with respect to  $\lambda_e$ , for an admissible field  $\delta \lambda_e$  of LM along the coupling segment, leads to the discrete form of the constraint enforcement equation, with the optional penalty term vanishing:

$$\delta \Pi_e^{\lambda_e} = \delta \lambda_e^T \left( \int_{\Gamma_c} \Phi^T \cdot (\mathbf{N}^{(1)} \cdot \mathbf{u}_e^{(1)} - \mathbf{N}^{(2)} \cdot \mathbf{u}_e^{(2)}) \, d\Gamma_c \right) \quad (5.5)$$

Eqs. (5.4) and (5.5) allow for the expressions of the internal force vector components  $\mathbf{f}_g$  and  $\mathbf{f}_a$  associated with the kinematic and additional DOFs  $\mathbf{u}_e$  and  $\lambda_e$ , respectively, to be explicitly obtained. These are given by the following expressions, where the contribution of the optional penalty terms is considered separately as  $\mathbf{f}_{g,\varepsilon}$  and  $\mathbf{f}_{a,\varepsilon}$  for clarity:

$$\mathbf{f}_g = \int_{\Gamma_c} \frac{\partial (\mathbf{N}^{(1)} \cdot \mathbf{u}_e^{(1)} - \mathbf{N}^{(2)} \cdot \mathbf{u}_e^{(2)})^T}{\partial \mathbf{u}_e} \cdot \Phi \cdot \lambda_e \, d\Gamma_c \quad (5.6)$$

$$\mathbf{f}_{g,\varepsilon} = \varepsilon \int_{\Gamma_c} \frac{\partial (\mathbf{N}^{(1)} \cdot \mathbf{u}_e^{(1)} - \mathbf{N}^{(2)} \cdot \mathbf{u}_e^{(2)})^T}{\partial \mathbf{u}_e} \cdot (\mathbf{N}^{(1)} \cdot \mathbf{u}_e^{(1)} - \mathbf{N}^{(2)} \cdot \mathbf{u}_e^{(2)}) \, d\Gamma_c \quad (5.7)$$

$$\mathbf{f}_a = \int_{\Gamma_c} \Phi^T \cdot (\mathbf{N}^{(1)} \cdot \mathbf{u}_e^{(1)} - \mathbf{N}^{(2)} \cdot \mathbf{u}_e^{(2)}) \, d\Gamma_c \quad (5.8)$$

$$\mathbf{f}_{a,\varepsilon} = \mathbf{0} \quad (5.9)$$

In the above expressions,  $\mathbf{f}_g$  and  $\mathbf{f}_{g,\varepsilon}$  can be further distinguished into two components associated with  $\mathbf{u}_e^{(1)}$  and  $\mathbf{u}_e^{(2)}$ , expressing the individual force contributions to the slave and master shell element domains  $\Gamma^{(1)}$  and  $\Gamma^{(2)}$ , respectively. The coupling element force vector can therefore be expressed in the following general form:

$$\mathbf{f}_e = \left\langle \frac{\partial \Pi_e}{\partial \mathbf{u}_e} \middle| \frac{\partial \Pi_e}{\partial \boldsymbol{\lambda}_e} \right\rangle^T = \langle \mathbf{f}_g | \mathbf{f}_a \rangle^T + \langle \mathbf{f}_{g,\varepsilon} | \mathbf{f}_{a,\varepsilon} \rangle^T = \langle \mathbf{f}_g^{(1)} \quad \mathbf{f}_g^{(2)} | \mathbf{f}_a \rangle^T + \langle \mathbf{f}_{g,\varepsilon}^{(1)} \quad \mathbf{f}_{g,\varepsilon}^{(2)} | \mathbf{f}_{a,\varepsilon} \rangle^T \quad (5.10)$$

The individual force contributions of the coupling element to the surfaces, alongside the respective penalty, terms are given by the following expressions:

$$\mathbf{f}_g^{(i)} = \int_{\Gamma_c} \frac{\partial (\mathbf{N}^{(1)} \cdot \mathbf{u}_e^{(1)} - \mathbf{N}^{(2)} \cdot \mathbf{u}_e^{(2)})^T}{\partial \mathbf{u}_e^{(i)}} \cdot \boldsymbol{\Phi} \cdot \boldsymbol{\lambda}_e \, d\Gamma_c$$

$$\therefore \mathbf{f}_g = (-1)^{i-1} \int_{\Gamma_c} \mathbf{N}^{(i)T} \cdot \boldsymbol{\Phi} \cdot \boldsymbol{\lambda}_e \, d\Gamma_c \quad (5.11)$$

$$\mathbf{f}_{g,\varepsilon}^{(i)} = \varepsilon \int_{\Gamma_c} \frac{\partial (\mathbf{N}^{(1)} \cdot \mathbf{u}_e^{(1)} - \mathbf{N}^{(2)} \cdot \mathbf{u}_e^{(2)})^T}{\partial \mathbf{u}_e^{(i)}} (\mathbf{N}^{(1)} \cdot \mathbf{u}_e^{(1)} - \mathbf{N}^{(2)} \cdot \mathbf{u}_e^{(2)}) \, d\Gamma_c$$

$$\therefore \mathbf{f}_{g,\varepsilon}^{(i)} = (-1)^{i-1} \varepsilon \int_{\Gamma_c} \mathbf{N}^{(i)T} \cdot (\mathbf{N}^{(1)} \cdot \mathbf{u}_e^{(1)} - \mathbf{N}^{(2)} \cdot \mathbf{u}_e^{(2)}) \, d\Gamma_c \quad (5.12)$$

In the derivation of Eqs. (5.6)-(5.12), the following relationships for the derivatives of the kinematic and additional DOFs have been employed:

$$\frac{\partial \mathbf{u}_e^{(i)}}{\partial \mathbf{u}_e^{(j)T}} = \frac{\partial (\mathbf{N}^{(i)} \cdot \mathbf{u}_e^{(i)})}{\partial \mathbf{u}_e^{(j)T}} = \mathbf{N}^{(i)} \cdot \frac{\partial \mathbf{u}_e^{(i)}}{\partial \mathbf{u}_e^{(j)T}} = \mathbf{N}^{(i)} \cdot \mathbf{I}_{3m_i} \delta_{ij} = \mathbf{N}^{(i)} \delta_{ij}$$

$$\frac{\partial \mathbf{u}_e^{(i)}}{\partial \boldsymbol{\lambda}_e^T} = \frac{\partial (\mathbf{N}^{(i)} \cdot \mathbf{u}_e^{(i)})}{\partial \boldsymbol{\lambda}_e^T} = \mathbf{0}$$

$$\frac{\partial \boldsymbol{\lambda}_e}{\partial \mathbf{u}_e^{(j)T}} = \frac{\partial (\boldsymbol{\Phi} \cdot \boldsymbol{\lambda}_e)}{\partial \mathbf{u}_e^{(j)T}} = \mathbf{0}$$

$$\frac{\partial \boldsymbol{\lambda}_e}{\partial \boldsymbol{\lambda}_e^T} = \frac{\partial (\boldsymbol{\Phi} \cdot \boldsymbol{\lambda}_e)}{\partial \boldsymbol{\lambda}_e^T} = \boldsymbol{\Phi} \cdot \mathbf{I}_{3m_\lambda} = \boldsymbol{\Phi}$$

where  $\delta_{ij}$  is the Kronecker delta:

$$\delta_{ij} = \begin{cases} 0, & i \neq j \\ 1, & i = j \end{cases}$$

### 5.2.2 Element tangent stiffness matrix

The derivation of the expression for the coupling element tangent stiffness matrix  $\mathbf{k}_e$  is based on the 2<sup>nd</sup> order variation of the total potential energy function  $\Pi_e$ , or equivalently the differentiation once of the internal force vector with respect to the element kinematic and additional DOFs  $\mathbf{u}_e$  and  $\lambda_e$ .

For consistency with the prior distinction of the force vector components, four principal component sub-matrices can be distinguished, with the associated penalty terms being considered separately: (i)  $\mathbf{k}_{gg}$ , which is associated with the interaction of  $\mathbf{u}_e$ ; (ii)  $\mathbf{k}_{ga}$  and  $\mathbf{k}_{ag}$ , which are associated with the interaction of  $\mathbf{u}_e$  and  $\lambda_e$ ; and (iii)  $\mathbf{k}_{aa}$ , which is associated with the interaction of  $\lambda_e$ . By considering the stiffness contributions to  $\Gamma^{(1)}$  and  $\Gamma^{(2)}$  separately,  $\mathbf{k}_{gg}$  can be further distinguished into four sub-matrices, while  $\mathbf{k}_{ga}$  and  $\mathbf{k}_{ag}$  into two, in accordance with Eq. (5.10). This allows  $\mathbf{k}_e$  to be expressed in the following general form:

$$\mathbf{k}_e = \begin{bmatrix} \mathbf{k}_{gg} & \mathbf{k}_{ga} \\ \mathbf{k}_{ag} & \mathbf{k}_{aa} \end{bmatrix} + \begin{bmatrix} \mathbf{k}_{gg,\varepsilon} & \mathbf{k}_{ga,\varepsilon} \\ \mathbf{k}_{ag,\varepsilon} & \mathbf{k}_{aa,\varepsilon} \end{bmatrix} = \begin{bmatrix} \frac{\partial \mathbf{f}_e}{\partial \mathbf{u}_e^T} & \frac{\partial \mathbf{f}_e}{\partial \lambda_e^T} \end{bmatrix} = \begin{bmatrix} \frac{\partial^2 \Pi_e}{\partial \mathbf{u}_e \partial \mathbf{u}_e^T} & \frac{\partial^2 \Pi_e}{\partial \mathbf{u}_e \partial \lambda_e^T} \\ \frac{\partial^2 \Pi_e}{\partial \lambda_e \partial \mathbf{u}_e^T} & \frac{\partial^2 \Pi_e}{\partial \lambda_e \partial \lambda_e^T} \end{bmatrix} \quad (5.13)$$

where:

$$\mathbf{k}_{gg} = \frac{\partial \mathbf{f}_g}{\partial \mathbf{u}_e^T} = \begin{bmatrix} \mathbf{k}_{gg}^{(11)} & \mathbf{k}_{gg}^{(12)} \\ \mathbf{k}_{gg}^{(21)} & \mathbf{k}_{gg}^{(22)} \end{bmatrix} \quad \mathbf{k}_{gg,\varepsilon} = \frac{\partial \mathbf{f}_{g,\varepsilon}}{\partial \mathbf{u}_e^T} = \begin{bmatrix} \mathbf{k}_{gg,\varepsilon}^{(11)} & \mathbf{k}_{gg,\varepsilon}^{(12)} \\ \mathbf{k}_{gg,\varepsilon}^{(21)} & \mathbf{k}_{gg,\varepsilon}^{(22)} \end{bmatrix} \quad (5.14a)$$

$$\mathbf{k}_{ga} = \mathbf{k}_{ag}^T = \frac{\partial \mathbf{f}_g}{\partial \lambda_e^T} = \begin{bmatrix} \mathbf{k}_{ga}^{(1)} \\ \mathbf{k}_{ga}^{(2)} \end{bmatrix} \quad \mathbf{k}_{ga,\varepsilon} = \mathbf{k}_{ag,\varepsilon}^T = \frac{\partial \mathbf{f}_{g,\varepsilon}}{\partial \lambda_e^T} = \begin{bmatrix} \mathbf{k}_{ga,\varepsilon}^{(1)} \\ \mathbf{k}_{ga,\varepsilon}^{(2)} \end{bmatrix} \quad (5.14b)$$

The final expressions for the various component sub-matrices are obtained by virtue of differentiation of the expressions in Eqs. (5.8), (5.9), (5.11) and (5.12):



$$\mathbf{k}_{gg}^{(ij)} = \frac{\partial \mathbf{f}_g^{(i)}}{\partial \mathbf{u}_e^{(j)T}} = \frac{\partial}{\partial \mathbf{u}_e^{(j)T}} \int_{\Gamma_c} (-1)^{i-1} \mathbf{N}^{(i)T} \cdot \Phi \cdot \lambda_e \, d\Gamma_c$$

$$\therefore \mathbf{k}_{gg}^{(ij)} = \mathbf{0} \quad (5.15)$$

$$\mathbf{k}_{gg,\varepsilon}^{(ij)} = \frac{\partial \mathbf{f}_{g,\varepsilon}^{(i)}}{\partial \mathbf{u}_e^{(j)T}} = \frac{\partial}{\partial \mathbf{u}_e^{(j)T}} \int_{\Gamma_c} (-1)^{i-1} \varepsilon \mathbf{N}^{(i)T} \cdot (\mathbf{N}^{(1)} \cdot \mathbf{u}_e^{(1)} - \mathbf{N}^{(2)} \cdot \mathbf{u}_e^{(2)}) \, d\Gamma_c$$

$$\therefore \mathbf{k}_{gg,\varepsilon}^{(ij)} = (-1)^{i+j-2} \varepsilon \int_{\Gamma_c} \mathbf{N}^{(i)T} \cdot \mathbf{N}^{(j)} \, d\Gamma_c \quad (5.16)$$

$$\mathbf{k}_{ga}^{(i)} = \mathbf{k}_{ag}^{(i)T} = \frac{\partial \mathbf{f}_g^{(i)}}{\partial \lambda_e^T} = \frac{\partial}{\partial \lambda_e^T} \int_{\Gamma_c} (-1)^{i-1} \mathbf{N}^{(i)T} \cdot \Phi \cdot \lambda_e \, d\Gamma_c$$

$$\therefore \mathbf{k}_{ga}^{(i)} = \mathbf{k}_{ag}^{(i)T} = (-1)^{i-1} \int_{\Gamma_c} \mathbf{N}^{(i)T} \cdot \Phi \, d\Gamma_c \quad (5.17)$$

$$\mathbf{k}_{ga,\varepsilon}^{(i)} = \mathbf{k}_{ag,\varepsilon}^{(i)T} = \frac{\partial \mathbf{f}_{g,\varepsilon}^{(i)}}{\partial \lambda_e^T} = \frac{\partial}{\partial \lambda_e^T} \int_{\Gamma_c} (-1)^{i-1} \varepsilon \mathbf{N}^{(i)T} \cdot (\mathbf{N}^{(1)} \cdot \mathbf{u}_e^{(1)} - \mathbf{N}^{(2)} \cdot \mathbf{u}_e^{(2)}) \, d\Gamma_c$$

$$\therefore \mathbf{k}_{ga,\varepsilon}^{(i)} = \mathbf{k}_{ag,\varepsilon}^{(i)T} = \mathbf{0} \quad (5.18)$$

$$\mathbf{k}_{aa} = \frac{\partial \mathbf{f}_a}{\partial \lambda_e^T} = \mathbf{0} \quad (5.19)$$

$$\mathbf{k}_{aa,\varepsilon} = \frac{\partial \mathbf{f}_{a,\varepsilon}}{\partial \lambda_e^T} = \mathbf{0} \quad (5.20)$$

### 5.2.3 Basic comparative evaluation of coupling element

A qualitative comparison of the derived expressions for the coupling element force vector and tangent stiffness matrix for a rigid translational constraint, presented in the preceding sections, against the results obtained for the simplified mechanical springs model earlier discussed in Section 4.2, is presented herein. Particular focus is given to the comparison of Eqs. (4.7) and

(4.8) for the force vector and tangent stiffness matrix of the simplified model against the two sets of expressions in Eqs. (5.8), (5.9), (5.11), (5.12) and (5.15)-(5.20), for the corresponding entities of the coupling element, which reveals the equivalence of the two systems in a qualitative sense.

In the case of the simplified mechanical model, each spring component is associated with a single kinematic DOF, leading to a discrete system with two DOFs ( $u_1, u_2$ ) in total, where the obtained expressions for the force vector and stiffness matrix contributions are readily associated with these. On the other hand, in the case of the coupling element the kinematic and additional DOFs  $\mathbf{u}_e$  and  $\lambda_e$  are 3-D vectors defined at the nodal and Collocation Point (CP) locations, along the global Cartesian coordinate axes (X,Y,Z). Hence, the force and stiffness contributions obtained in a continuous sense along the coupling interface segment must be transferred to these discrete locations along the (X,Y,Z) directions, using appropriate transformations. This is due to the coupling interface segment traversing the domain of the shell elements in an arbitrary orientation in the general setting of the coupling problem, resulting into a lack of spatial correspondence between its points and the discrete locations where the kinematic and additional DOFs are defined.

The process is identical to the transformation of a distributed load applied over a finite element domain to equivalent nodal loads. The transpose matrix of the 2-D shell element shape functions  $\mathbf{N}^{(i)T}$  allows for the transformation of a quantity defined along the interface projection on either shell element domain to equivalent discrete nodal quantities for the respective element domain  $\Gamma^{(i)}$ . Similarly, the transpose of the interface segment 1-D shape functions matrix  $\Phi^T$  allows for the transformation of any quantity defined continuously along the interface segment into a set of equivalent discrete quantities at the CPs. A combination of the above transformations is embedded in the final expressions for the force vector and tangent stiffness matrix quantities.

Furthermore, the mathematical expression of the penalty term in the coupling element energy function highlights its physical correspondence to a set of distributed fictitious springs along the 1-D interface, with constant stiffness  $\varepsilon \geq 0$  in the three global (X,Y,Z) directions. The system of distributed springs is only activated by the translational interaction of the deformable surfaces along the interface, while being completely uncoupled from the LM field, which is qualitatively identical to the simplified mechanical model of coupled springs.

Ultimately, in both systems the constraint enforcement equation, obtained as part of the force vector component  $\mathbf{f}_a$  associated with the additional DOFs, remains independent of the introduced penalty term, as shown in Eqs. (4.7) and (4.8). The penalty term only contributes to the terms of the force vector and the tangent stiffness matrix associated with the kinematic DOFs. The inclusion of the penalty term in the formulation therefore does not affect the constraint enforcement, but rather introduces non-zero entities in the terms of the force vector and tangent stiffness matrix associated with the kinematic DOFs, in both cases. As discussed in Chapter 4, the introduction of non-zero pivots in the tangent stiffness matrix diagonal is necessitated to avoid ill-conditioning and convergence bottlenecks when solvers which do not perform row switching operations for individual parameter elimination, such as the frontal solver (Irons, 1970), are employed.

### 5.3 1-D rotational coupling element formulation

Beyond achieving coupling of all displacement components of  $\Omega^{(i)}$  along the 1-D coupling interface  $\Gamma_c$ , the coupling element formulation presented in Section 5.2 can be enhanced to couple the rotations of the two surfaces transverse to  $\Gamma_c$ .

At any two points along the linear coupling interface, located at an infinitesimal distance apart, the coupled surfaces  $\Omega^{(i)}$  exhibit identical displacements. Hence, for any relative displacement increment between these points, the rotations exhibited by  $\Omega^{(i)}$  in the interface direction are readily coupled, and only the rotations of the two surfaces  $\Omega^{(i)}$  transverse to the coupling interface  $\Gamma_c$  may be considered for coupling.

Taking the above into consideration, the only mode that remains unconstrained when the translational coupling formulation is employed is the relative torsional rotation exhibited by  $\Omega^{(i)}$  along the longitudinal axis of  $\Gamma_c$ . The 1-D translational coupling element exhibits a singular behaviour in cases where such modes are unrestrained in the system, thereby necessitating the enhancement of the respective formulation to achieve torsional rotational coupling of  $\Omega^{(i)}$  along  $\Gamma_c$ .

As discussed in Chapter 3, the adopted hierarchically optimised, co-rotational Reissner-Mindlin shell elements utilise six DOFs in the global system, with three translational and three rotational DOFs per node. The local element response, however, is formulated with five nodal local DOFs, including two rotational DOFs for each node corresponding to the two smallest components of the normal to the surface nodal vector. Accordingly, these shell elements become insensitive to ‘drilling’ nodal rotations.

Two distinct approaches can be adopted to achieve rotational coupling of surfaces modelled with Reissner-Mindlin shell elements: (i) coupling of the transverse rotations of the two surface normals, which is more realistic for coupling rotations along a fold; and (ii) coupling of the transverse slopes of the two surfaces, which is more realistic for almost coplanar surfaces coupled along a ‘weld’ line. From a kinematic perspective, the constraints of the two approaches differ by the magnitude of transverse shear deformation in the two coupled surfaces, and hence the two approaches become identical for thin plates/shells. Even for moderately thick plates/shells within the scope of the Reissner-Mindlin assumption, the discrepancy between the two constraints is typically small, due to the transverse shear deformation being often small in comparison with the absolute rotations of the normals. Furthermore, noting the important computational benefit of the second approach in which the slopes of the two surfaces are fully determined by translational DOFs, thus allowing rotational DOFs to be excluded from the coupling element formulation, coupling of transverse slopes is adopted in this work.

The constraint is mathematically formulated by considering the field of tangent unit vectors of  $\Omega^{(i)}$ , with orientation transverse to  $\Gamma_c^{(i)}$ , and constraining the angle between them at any point along  $\Gamma_c$  to its value in the initial undeformed configuration. The angle between the unit tangent vector fields along  $\Gamma_c^{(i)}$  can be effectively constrained by constraining their dot product, which represents the cosine of the angle. The resulting scalar rotational constraint function is thus expressed in the following form:

$$g_R(\mathbf{u}^{(1)}, \mathbf{u}^{(2)}) = \mathbf{b}^{(1)} \cdot \mathbf{b}^{(2)} - \mathbf{b}_0^{(1)} \cdot \mathbf{b}_0^{(2)} \quad (5.21)$$

where  $\mathbf{b}_0^{(i)}$  and  $\mathbf{b}^{(i)}$  are the global tangent vector fields in the direction transverse to  $\Gamma_c^{(i)}$ , in the initial undeformed and the current deformed configurations, respectively, with  $\mathbf{b}^{(i)}$

depending on the respective surface  $\Omega^{(i)}$  displacement field  $\mathbf{u}^{(i)} = (U^{(i)} \quad V^{(i)} \quad W^{(i)})^T$  along  $\Gamma_c^{(i)}$ . The concept is schematically illustrated in Figure 5.1.

Even though the above constraint achieves the desired rotational coupling in a simple and elegant manner, its employment in the case of co-planar surfaces leads to ill-conditioning and potential singularities in the obtained tangent stiffness matrix. This is due to the use of the dot product which achieves upper/lower limits of  $\pm 1$  for coplanar vectors, with its 1<sup>st</sup> order variation thus being zero when the constraint is satisfied.

The arising singularity in this case can be circumvented by introducing a modification in the constraint, such that  $\mathbf{b}^{(2)}$  in Eq. (5.21) is defined as either the tangent vector field of  $\Omega^{(2)}$  transverse to  $\Gamma_c^{(2)}$  or as the normal vector to the surface, depending on whether the angle  $\mathcal{G}_0$  between  $\mathbf{b}^{(1)}$  and  $\mathbf{b}^{(2)}$  is  $\mathcal{G}_0 \in \left[\frac{\pi}{4}, \frac{3\pi}{4}\right]$  or  $\mathcal{G}_0 \in \left[0, \frac{\pi}{4}\right) \cup \left(\frac{3\pi}{4}, \pi\right]$ , respectively. It is worth noting that the normal vector in the latter case is normal to the surface defined by  $\Omega^{(2)}$  in both the initial and deformed configurations, hence it remains only a function of the translational DOFs. The selection of  $\pi/4$  for the intervals allows for ill-conditioning of the tangent stiffness matrix to be avoided in cases of small but non-zero relative orientation angles.

The kinematic DOFs of the individual rotational coupling elements remain the nodal translations  $\mathbf{u}_e^{(i)}$  of the active shell element surfaces  $\Gamma^{(i)}$  on  $\Omega^{(i)}$ , as in the case of the translational coupling element. Owing to the scalar nature of the constraint function in Eq. (5.21), the introduction of a single additional DOF per CP is required for the rotational constraint enforcement, leading to a 1-D rotational LM field  $\lambda_r$  along  $\Gamma_c^{(i)}$ .

This section proceeds with presenting the rotational coupling element formulation in two subsections, where: (i) the element contribution to the total potential energy of the system is established and the expressions for the coupling element internal force vector components are derived employing 1<sup>st</sup> order variational principles; and (ii) the expressions for the coupling element consistent tangent stiffness matrix components are derived from the established energy expression employing 2<sup>nd</sup> order variational principles .

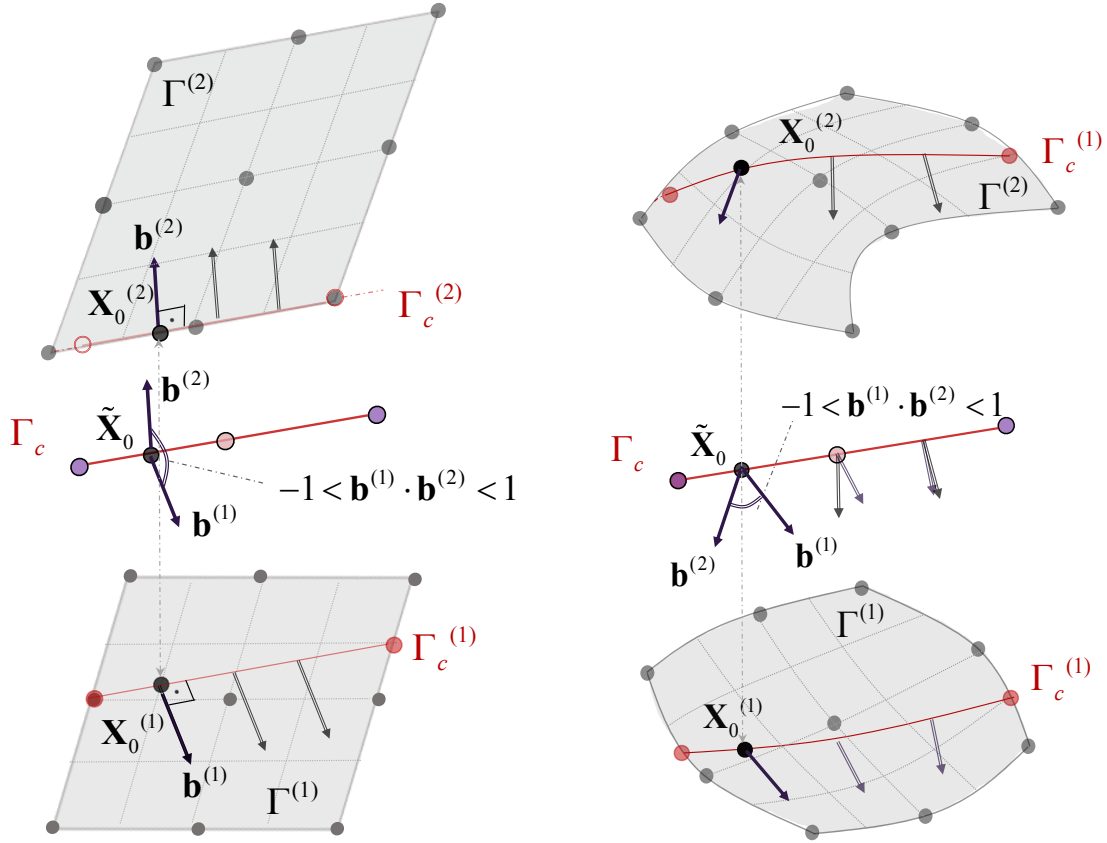


Figure 5.1: Rotational coupling based on the angle between the surface tangent vectors transverse to the coupling interface

### 5.3.1 Element contribution to total potential energy and internal force vector

For rotational coupling of the active shell element domains  $\Gamma^{(i)}$  associated with the coupling element in the global Cartesian coordinate system, the constraint function in Eq. (5.21) can be expressed in terms of the coupling element kinematic DOFs  $\mathbf{u}_e^{(i)}$  along  $\Gamma_c$ :

$$g_R(\mathbf{u}_e) = g_R(\mathbf{u}_e^{(1)}, \mathbf{u}_e^{(2)}) = \mathbf{b}^{(1)}(\mathbf{u}_e^{(1)}) \cdot \mathbf{b}^{(2)}(\mathbf{u}_e^{(2)}) - \mathbf{b}_0^{(1)} \cdot \mathbf{b}_0^{(2)} = \mathbf{b}^{(1)} \cdot \mathbf{b}^{(2)} - \mathbf{b}_0^{(1)} \cdot \mathbf{b}_0^{(2)} \quad (5.22)$$

The expression of the coupling element contribution to the total potential energy in Eq. (4.60) can therefore be rewritten in a discrete form, in terms of its kinematic and additional DOFs  $\mathbf{u}_e^{(i)}$  and  $\lambda_{Re}$ , respectively:

$$\begin{aligned} \Pi_{Re} = \Pi_R + \Pi_{Re} = \int_{\Gamma_c} \left( \mathbf{b}^{(1)}(\mathbf{u}_e^{(1)}) \cdot \mathbf{b}^{(2)}(\mathbf{u}_e^{(2)}) - \mathbf{b}_0^{(1)} \cdot \mathbf{b}_0^{(2)} \right) \boldsymbol{\varphi} \cdot \boldsymbol{\lambda}_{Re} \, d\Gamma_c + \\ + \frac{1}{2} \varepsilon_R \int_{\Gamma_c} \left\| \left( \mathbf{b}^{(1)}(\mathbf{u}_e^{(1)}) \cdot \mathbf{b}^{(2)}(\mathbf{u}_e^{(2)}) - \mathbf{b}_0^{(1)} \cdot \mathbf{b}_0^{(2)} \right) \right\|^2 \, d\Gamma_c, \quad \varepsilon_R \geq 0 \end{aligned} \quad (5.23)$$

The unit tangent vector field of  $\Gamma^{(i)}$  in the direction transverse to the longitudinal axis of  $\Gamma_c^{(i)}$  is obtained using the equations given hereafter:

$$\mathbf{b}^{(i)} = \mathbf{b}^{(i)}(\mathbf{u}_e^{(i)}) = \mathbf{J}^{(i)}(\mathbf{u}_e^{(i)}) \cdot \boldsymbol{\alpha}_0^{(i)} = \mathbf{N}_{,\xi}^{(i)} \cdot \mathbf{X}_e^{(i)} a_{0\xi}^{(i)} + \mathbf{N}_{,\eta}^{(i)} \cdot \mathbf{X}_e^{(i)} a_{0\eta}^{(i)} \quad (5.24)$$

$$\mathbf{b}_0^{(i)} = \mathbf{b}^{(i)}(\mathbf{0}) = \mathbf{J}^{(i)}(\mathbf{0}) \cdot \boldsymbol{\alpha}_0^{(i)} = \mathbf{J}_0^{(i)} \cdot \boldsymbol{\alpha}_0^{(i)} \quad (5.25)$$

where  $\mathbf{b}^{(i)}$  and  $\mathbf{b}_0^{(i)}$  denote the tangent vector fields, while  $\mathbf{J}^{(i)}$  and  $\mathbf{J}_0^{(i)}$  denote the Jacobian matrix of the mapping between natural and global Cartesian coordinates, in the current deformed and the initial undeformed configurations, respectively.

The tangent vector fields are obtained by means of mapping a direction vector field  $\boldsymbol{\alpha}_0^{(i)} = (a_{0\xi}^{(i)} \quad a_{0\eta}^{(i)})^T$ , expressed in the natural coordinate system, to global Cartesian coordinates, as illustrated in Figure 5.2. The latter defines the tangent direction transverse to  $\Gamma_c^{(i)}$  in the initial undeformed configuration and is assumed to remain constant for a given coupling element, which is realistic for small strain problems. The element deformation is thus accounted for solely through the Jacobian in the deformed configuration, which is given by Eq. (4.85) and can be rewritten in the following form:

$$\mathbf{J}^{(i)}(\mathbf{u}_e^{(i)}) = \begin{bmatrix} \mathbf{N}_{,\xi}^{(i)} \cdot \mathbf{X}_e^{(i)} & \mathbf{N}_{,\eta}^{(i)} \cdot \mathbf{X}_e^{(i)} \end{bmatrix} = \begin{bmatrix} \mathbf{N}_{,\xi}^{(i)} \cdot (\mathbf{X}_{e0}^{(i)} + \mathbf{u}_e^{(i)}) & \mathbf{N}_{,\eta}^{(i)} \cdot (\mathbf{X}_{e0}^{(i)} + \mathbf{u}_e^{(i)}) \end{bmatrix} \quad (5.26)$$

The vector field  $\boldsymbol{\alpha}_0^{(i)}$  can be obtained by means of an inverse Jacobian transformation of the respective vector  $\bar{\mathbf{a}}_0^{(i)}$  from the planar local to the natural element coordinate system:

$$\boldsymbol{\alpha}_0^{(i)} = \bar{\mathbf{j}}_0^{(i)-1} \cdot \bar{\mathbf{a}}_0^{(i)} \quad (5.27)$$

For the above inverse transformation process to be feasible,  $\bar{\mathbf{a}}_0^{(i)}$  needs to be a two-component vector, for dimensional correspondence with  $\boldsymbol{\alpha}_0^{(i)}$ , and accordingly  $\bar{\mathbf{j}}_0^{(i)}$  must be a square  $2 \times 2$  matrix. This is achieved by means of initially establishing  $\mathbf{a}_0^{(i)}$  in the local element coordinate

system, and subsequently employing its respective projection on the co-rotational coordinate system plane,  $\bar{\mathbf{a}}_0^{(i)}$ , based on the assumption that the shell element out-of-flatness is negligible with sufficient mesh refinement, as discussed previously in Section 4.4.

The Jacobian  $\bar{\mathbf{j}}_0^{(i)}$  of the mapping to the planar local element coordinate system in the initial undeformed configuration has been defined earlier in Eq. 4.86, and can be expressed in the following form:

$$\bar{\mathbf{j}}_0^{(i)} = \begin{bmatrix} \bar{\mathbf{N}}_{,\xi}^{(i)} \cdot \bar{\mathbf{x}}_{e0}^{(i)} & \bar{\mathbf{N}}_{,\eta}^{(i)} \cdot \bar{\mathbf{x}}_{e0}^{(i)} \end{bmatrix} \quad (5.28)$$

where  $\bar{\mathbf{x}}_{e0}^{(i)}$  is the local planar nodal coordinate vector on  $\Gamma^{(i)}$  and  $\bar{\mathbf{N}}_{,\xi}^{(i)}$ ,  $\bar{\mathbf{N}}_{,\eta}^{(i)}$  are the derivatives of matrix  $\bar{\mathbf{N}}^{(i)}$  in Eq. (4.15) with respect to  $\xi^{(i)}$  and  $\eta^{(i)}$ .

At any given point along  $\Gamma_c^{(i)}$ , the transverse to its longitudinal axis unit tangent vector  $\mathbf{a}_0^{(i)}$  can be obtained by normalising the cross product of the normal vector  $\mathbf{n}_0^{(i)}$  at that point and the orientation vector  $\mathbf{t}^{(i)}$  of  $\Gamma_c$ , with all aforementioned entities being expressed in the respective local coordinate system:

$$\mathbf{a}_0^{(i)} = \frac{\hat{\mathbf{a}}_0^{(i)}}{\|\hat{\mathbf{a}}_0^{(i)}\|}, \quad \hat{\mathbf{a}}_0^{(i)} = \mathbf{n}_0^{(i)} \times \mathbf{t}^{(i)} \quad (5.29)$$

The orientation vector  $\mathbf{t}^{(i)}$  is generally expressed in the global coordinate system as  $\mathbf{t}$ , and therefore a coordinate transformation is required:

$$\mathbf{t}^{(i)} = \mathbf{T}_0^{(i)} \cdot \mathbf{t} \quad (5.30)$$

where  $\mathbf{T}_0^{(i)}$  is the rotational transformation matrix of  $\Gamma^{(i)}$ , which is given by Eq. (4.48) and repeated here for ease of reference:

$$\mathbf{T}_0^{(i)} = \begin{bmatrix} \mathbf{c}_{x0}^{(i)} & \mathbf{c}_{y0}^{(i)} & \mathbf{c}_{z0}^{(i)} \end{bmatrix}^T \quad (5.31)$$

In the above expression the triad of unit orientation vectors of the local coordinate system axes are defined in Eq. (4.49) and are also repeated here for ease of reference:



$$\left. \begin{aligned}
 \mathbf{c}_{x0}^{(i)} &= \frac{\mathbf{c}_{130}^{(i)} - \mathbf{c}_{240}^{(i)}}{\|\mathbf{c}_{130}^{(i)} - \mathbf{c}_{240}^{(i)}\|}, & \mathbf{c}_{y0}^{(i)} &= \frac{\mathbf{c}_{130}^{(i)} + \mathbf{c}_{240}^{(i)}}{\|\mathbf{c}_{130}^{(i)} + \mathbf{c}_{240}^{(i)}\|}, & \mathbf{c}_{z0}^{(i)} &= \mathbf{c}_{x0}^{(i)} \times \mathbf{c}_{y0}^{(i)} & \text{(9-noded)} \\
 \mathbf{c}_{x0}^{(i)} &= \frac{\mathbf{v}_{120}^{(i)}}{\|\mathbf{v}_{120}^{(i)}\|}, & \mathbf{c}_{z0}^{(i)} &= \frac{\mathbf{v}_{120}^{(i)} \times \mathbf{v}_{130}^{(i)}}{\|\mathbf{v}_{120}^{(i)} \times \mathbf{v}_{130}^{(i)}\|}, & \mathbf{c}_{y0}^{(i)} &= \mathbf{c}_{x0}^{(i)} \times \mathbf{c}_{z0}^{(i)} & \text{(6-noded)} \\
 \mathbf{c}_{jk0}^{(i)} &= \frac{\mathbf{v}_{jk0}^{(i)}}{\|\mathbf{v}_{jk0}^{(i)}\|}, & \mathbf{v}_{jk0}^{(i)} &= \mathbf{X}_{k0}^{(i)} - \mathbf{X}_{j0}^{(i)}
 \end{aligned} \right\} \quad (5.32)$$

The normal vector  $\mathbf{n}_0^{(i)}$  at any given point along  $\Gamma_c^{(i)}$  is established as the cross product of the tangent vectors  $\mathbf{a}_{\xi 0}^{(i)}$  and  $\mathbf{a}_{\eta 0}^{(i)}$  along the shell element local planar axes:

$$\mathbf{n}_0^{(i)} = \mathbf{a}_{\xi 0}^{(i)} \times \mathbf{a}_{\eta 0}^{(i)} \quad (5.33)$$

$$\mathbf{a}_{\xi 0}^{(i)} = \frac{\partial \mathbf{x}_0^{(i)}}{\partial \xi^{(i)}} = \mathbf{N}_{,\xi}^{(i)} \cdot \mathbf{x}_{e0}^{(i)} \quad (5.34)$$

$$\mathbf{a}_{\eta 0}^{(i)} = \frac{\partial \mathbf{x}_0^{(i)}}{\partial \eta^{(i)}} = \mathbf{N}_{,\eta}^{(i)} \cdot \mathbf{x}_{e0}^{(i)} \quad (5.35)$$

The procedure discussed above is summarised in Figure 5.2. Evidently, the evaluation of the local Jacobian matrix  $\bar{\mathbf{j}}_0^{(i)}$  is only required once for the inverse vector transformation set out in Eq. (5.27). On the other hand, the global Jacobian  $\mathbf{J}$  is evaluated at every iterative step of the nonlinear solution procedure for an updated vector of global nodal translations  $\mathbf{u}_e^{(i)}$ .  $\mathbf{J}$  is therefore the prominent source of geometric nonlinearity in the constraint enforcement equation, and hence in the coupling element formulation.

Due to the assumption of negligible shell element out-of-flatness for a sufficiently dense mesh, alongside the incorporation of a co-rotational local coordinate axes definition, the planar components of  $\mathbf{a}_0^{(i)}$  are dominant in comparison to the out-of-plane one. Hence, in the limit, with mesh refinement,  $\bar{\mathbf{a}}_0^{(i)}$  is also approximately a unit vector. The inverse transformation of  $\bar{\mathbf{a}}_0^{(i)}$  to  $\mathbf{a}_0^{(i)}$ , which subsequently remains constant, allows for  $\mathbf{b}^{(i)}$  and  $\mathbf{b}_0^{(i)}$  to be readily obtained as approximately unit vectors, by employment of the direct transformations outlined in Eqs. (5.24) and (5.25), respectively. This is one of the main simplifying assumptions

embedded in the rotational coupling formulation, which makes  $\mathbf{b}^{(i)}$  linearly dependent on the translational DOFs, thus simplifying the application of the variational approach.

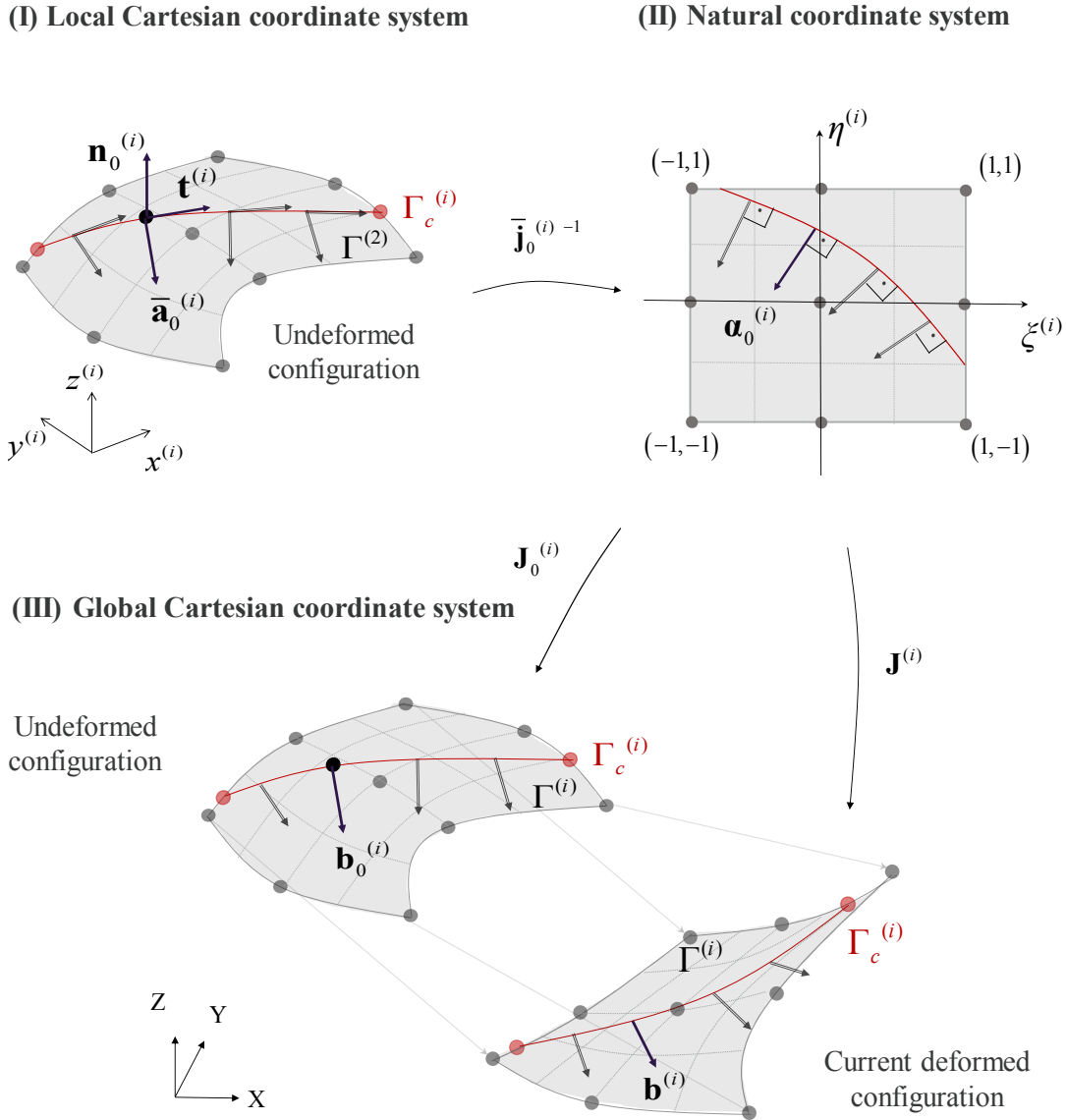


Figure 5.2: Vector mapping processes for the establishment of coupled shell element global tangent vector fields  $\mathbf{b}_0^{(i)}$  and  $\mathbf{b}^{(i)}$  in the initial undeformed and the current deformed configurations

Similar to the process employed for the translational coupling element, the force vector  $\mathbf{f}_e$  of the rotational coupling element is obtained as the 1<sup>st</sup> order variation of  $\Pi_{Re}$  with respect to  $\mathbf{u}_e^{(i)}$  and  $\lambda_{Re}$ . The 1<sup>st</sup> order variation of  $\Pi_{Re}$  with respect to  $\mathbf{u}_e = (\mathbf{u}_e^{(1)} \quad \mathbf{u}_e^{(2)})^T$ , representing the virtual work performed by the LM field over an admissible infinitesimal deformation mode  $\delta\mathbf{u}_e$  along  $\Gamma_c$ , yields:

$$\begin{aligned} \delta \Pi_{Re}^{\mathbf{u}_e} = & \delta \mathbf{u}_e^T \cdot \left( \int_{\Gamma_c} \frac{\partial (\mathbf{b}^{(1)} \cdot \mathbf{b}^{(2)} - \mathbf{b}_0^{(1)} \cdot \mathbf{b}_0^{(2)})}{\partial \mathbf{u}_e} \cdot \boldsymbol{\phi} \cdot \boldsymbol{\lambda}_{Re} \, d\Gamma_c \right) \\ & + \delta \mathbf{u}_e^T \cdot \left( \varepsilon_R \int_{\Gamma_c} \frac{\partial (\mathbf{b}^{(1)} \cdot \mathbf{b}^{(2)} - \mathbf{b}_0^{(1)} \cdot \mathbf{b}_0^{(2)})}{\partial \mathbf{u}_e} (\mathbf{b}^{(1)} \cdot \mathbf{b}^{(2)} - \mathbf{b}_0^{(1)} \cdot \mathbf{b}_0^{(2)}) \, d\Gamma_c \right) \end{aligned} \quad (5.36)$$

The discrete form of the constraint enforcement equation is obtained as the 1<sup>st</sup> order variation of  $\Pi_{Re}$  with respect to  $\boldsymbol{\lambda}_{Re}$ , for an admissible infinitesimal variation of the LM field  $\delta \boldsymbol{\lambda}_{Re}$  along  $\Gamma_c$ :

$$\delta \Pi_{Re}^{\boldsymbol{\lambda}_{Re}} = \delta \boldsymbol{\lambda}_{Re}^T \left( \int_{\Gamma_c} \boldsymbol{\phi}^T (\mathbf{b}^{(1)} \cdot \mathbf{b}^{(2)} - \mathbf{b}_0^{(1)} \cdot \mathbf{b}_0^{(2)}) \, d\Gamma_c \right) \quad (5.37)$$

where the penalty term vanishes. The expressions of the internal force vector components associated with  $\mathbf{u}_e^{(i)}$  and  $\boldsymbol{\lambda}_{Re}$  are explicitly obtained from equations (5.36) and (5.37) as given hereafter:

$$\mathbf{f}_g = \int_{\Gamma_c} \frac{\partial (\mathbf{b}^{(1)} \cdot \mathbf{b}^{(2)} - \mathbf{b}_0^{(1)} \cdot \mathbf{b}_0^{(2)})}{\partial \mathbf{u}_e} \cdot \boldsymbol{\phi} \cdot \boldsymbol{\lambda}_{Re} \, d\Gamma_c \quad (5.38)$$

$$\mathbf{f}_{g,\varepsilon} = \varepsilon_R \int_{\Gamma_c} \frac{\partial (\mathbf{b}^{(1)} \cdot \mathbf{b}^{(2)} - \mathbf{b}_0^{(1)} \cdot \mathbf{b}_0^{(2)})}{\partial \mathbf{u}_e} (\mathbf{b}^{(1)} \cdot \mathbf{b}^{(2)} - \mathbf{b}_0^{(1)} \cdot \mathbf{b}_0^{(2)}) \, d\Gamma_c \quad (5.39)$$

$$\mathbf{f}_a = \int_{\Gamma_c} \boldsymbol{\phi}^T (\mathbf{b}^{(1)} \cdot \mathbf{b}^{(2)} - \mathbf{b}_0^{(1)} \cdot \mathbf{b}_0^{(2)}) \, d\Gamma_c \quad (5.40)$$

$$\mathbf{f}_{a,\varepsilon} = \mathbf{0} \quad (5.41)$$

Similar to the translational coupling element formulation, the contribution of the LM and the penalty terms are considered separately in the above expressions for clarity. It is convenient to further distinguish the contributions associated with  $\Gamma^{(1)}$  and  $\Gamma^{(2)}$  in the above expressions for  $\mathbf{f}_g$  and  $\mathbf{f}_{g,\varepsilon}$ , by virtue of  $\mathbf{u}_e = (\mathbf{u}_e^{(1)} \quad \mathbf{u}_e^{(2)})^T$ , which allows  $\mathbf{f}_e$  to be stated in the general form given in Eq. (5.10). The respective components  $\mathbf{f}_g^{(1)}$ ,  $\mathbf{f}_g^{(2)}$ ,  $\mathbf{f}_{g,\varepsilon}^{(1)}$  and  $\mathbf{f}_{g,\varepsilon}^{(2)}$ , corresponding to the equivalent nodal forces on  $\Gamma^{(1)}$  and  $\Gamma^{(2)}$ , are given by the following expressions:

$$\mathbf{f}_g^{(1)} = \int_{\Gamma_c} \frac{\partial(\mathbf{b}^{(1)} \cdot \mathbf{b}^{(2)} - \mathbf{b}_0^{(1)} \cdot \mathbf{b}_0^{(2)})}{\partial \mathbf{u}_e^{(1)}} \cdot \boldsymbol{\varphi} \cdot \boldsymbol{\lambda}_{Re} \, d\Gamma_c =$$

$$\therefore \mathbf{f}_g^{(1)} = \int_{\Gamma_c} \frac{\partial \mathbf{b}^{(1)\top}}{\partial \mathbf{u}_e^{(1)}} \cdot \mathbf{b}^{(2)} \cdot \boldsymbol{\varphi} \cdot \boldsymbol{\lambda}_{Re} \, d\Gamma_c \quad (5.42)$$

$$\mathbf{f}_g^{(2)} = \int_{\Gamma_c} \frac{\partial(\mathbf{b}^{(1)} \cdot \mathbf{b}^{(2)} - \mathbf{b}_0^{(1)} \cdot \mathbf{b}_0^{(2)})}{\partial \mathbf{u}_e^{(2)}} \cdot \boldsymbol{\varphi} \cdot \boldsymbol{\lambda}_{Re} \, d\Gamma_c =$$

$$\therefore \mathbf{f}_g^{(2)} = \int_{\Gamma_c} \frac{\partial \mathbf{b}^{(2)\top}}{\partial \mathbf{u}_e^{(2)}} \cdot \mathbf{b}^{(1)} \cdot \boldsymbol{\varphi} \cdot \boldsymbol{\lambda}_{Re} \, d\Gamma_c \quad (5.43)$$

$$\mathbf{f}_{g,\varepsilon}^{(1)} = \varepsilon_R \int_{\Gamma_c} \frac{\partial(\mathbf{b}^{(1)} \cdot \mathbf{b}^{(2)} - \mathbf{b}_0^{(1)} \cdot \mathbf{b}_0^{(2)})}{\partial \mathbf{u}_e^{(1)}} (\mathbf{b}^{(1)} \cdot \mathbf{b}^{(2)} - \mathbf{b}_0^{(1)} \cdot \mathbf{b}_0^{(2)}) \, d\Gamma_c$$

$$\therefore \mathbf{f}_{g,\varepsilon}^{(1)} = \varepsilon_R \int_{\Gamma_c} \frac{\partial \mathbf{b}^{(1)\top}}{\partial \mathbf{u}_e^{(1)}} \cdot \mathbf{b}^{(2)} (\mathbf{b}^{(1)} \cdot \mathbf{b}^{(2)} - \mathbf{b}_0^{(1)} \cdot \mathbf{b}_0^{(2)}) \, d\Gamma_c \quad (5.44)$$

$$\mathbf{f}_{g,\varepsilon}^{(2)} = \varepsilon_R \int_{\Gamma_c} \frac{\partial(\mathbf{b}^{(1)} \cdot \mathbf{b}^{(2)} - \mathbf{b}_0^{(1)} \cdot \mathbf{b}_0^{(2)})}{\partial \mathbf{u}_e^{(2)}} (\mathbf{b}^{(1)} \cdot \mathbf{b}^{(2)} - \mathbf{b}_0^{(1)} \cdot \mathbf{b}_0^{(2)}) \, d\Gamma_c =$$

$$\therefore \mathbf{f}_{g,\varepsilon}^{(2)} = \varepsilon_R \int_{\Gamma_c} \frac{\partial \mathbf{b}^{(2)\top}}{\partial \mathbf{u}_e^{(2)}} \cdot \mathbf{b}^{(1)} (\mathbf{b}^{(1)} \cdot \mathbf{b}^{(2)} - \mathbf{b}_0^{(1)} \cdot \mathbf{b}_0^{(2)}) \, d\Gamma_c \quad (5.45)$$

In the derivation of the above expressions, the following chain rule for the differentiation of the dot product of  $\mathbf{b}^{(1)}$  and  $\mathbf{b}^{(2)}$  in the current deformed configuration is employed:

$$\frac{\partial(\mathbf{b}^{(1)} \cdot \mathbf{b}^{(2)})}{\partial \mathbf{u}_e^{(j)}} = \frac{\partial \mathbf{b}^{(1)\top}}{\partial \mathbf{u}_e^{(j)}} \cdot \mathbf{b}^{(2)} + \frac{\partial \mathbf{b}^{(2)\top}}{\partial \mathbf{u}_e^{(j)}} \cdot \mathbf{b}^{(1)}$$

with the derivative of the dot product in the initial undeformed configuration being a zero vector:

$$\frac{\partial(\mathbf{b}_0^{(1)} \cdot \mathbf{b}_0^{(2)})}{\partial \mathbf{u}_e^{(j)}} = \mathbf{0}$$

The derivatives of  $\mathbf{b}^{(1)}$  and  $\mathbf{b}^{(2)}$  with respect to  $\mathbf{u}_e = (\mathbf{u}_e^{(1)} \quad \mathbf{u}_e^{(2)})^T$  in the deformed configuration are given by the following expression:

$$\frac{\partial \mathbf{b}^{(i)}}{\partial \mathbf{u}_e^{(j)T}} = \frac{\partial (\mathbf{J}^{(i)} \cdot \boldsymbol{\alpha}_0^{(i)})}{\partial \mathbf{u}_e^{(j)T}} = (\mathbf{N}_{,\xi}^{(i)} a_{0\xi}^{(i)} + \mathbf{N}_{,\eta}^{(i)} a_{0\eta}^{(i)}) \delta_{ij} \quad (5.46)$$

with  $(i,j=1,2; i \neq j)$ , and where  $\delta_{ij}$  is the Kronecker delta. The above expression is obtained by differentiation of Eq. (5.24), using Eq. (5.26):

$$\frac{\partial (\mathbf{J}^{(i)} \cdot \boldsymbol{\alpha}_0^{(i)})}{\partial \mathbf{u}_e^{(j)T}} = \mathbf{N}_{,\xi}^{(i)} \frac{\partial (\mathbf{X}_{k0}^{(i)} + \mathbf{u}_e^{(i)})}{\partial \mathbf{u}_e^{(j)T}} a_{0\xi}^{(i)} + \mathbf{N}_{,\eta}^{(i)} \cdot \frac{\partial (\mathbf{X}_{k0}^{(i)} + \mathbf{u}_e^{(i)})}{\partial \mathbf{u}_e^{(j)T}} a_{0\eta}^{(i)} = (\mathbf{N}_{,\xi}^{(i)} a_{0\xi}^{(i)} + \mathbf{N}_{,\eta}^{(i)} a_{0\eta}^{(i)}) \delta_{ij}$$

### 5.3.2 Element tangent stiffness matrix

The derivation of the expression for the tangent stiffness matrix  $\mathbf{k}_e$  is based on the 2<sup>nd</sup> order variation of the total potential energy function  $\Pi_{Re}$ , or equivalently on the 1<sup>st</sup> order differentiation of the internal force vector with respect to the kinematic and additional DOFs  $\mathbf{u}_e$  and  $\boldsymbol{\lambda}_e$ .

Similar to Eq. (5.13) of the translational coupling element formulation, the tangent stiffness matrix is distinguished into four principal component sub-matrices  $\mathbf{k}_{gg}$ ,  $\mathbf{k}_{ga}$ ,  $\mathbf{k}_{ag}$  and  $\mathbf{k}_{aa}$ , where the LM and penalty terms contributions are considered separately for clarity and consistency. By considering the contributions to  $\Gamma^{(1)}$  and  $\Gamma^{(2)}$  separately,  $\mathbf{k}_{gg}$  can be further distinguished into four sub-matrices, while  $\mathbf{k}_{ga}$  and  $\mathbf{k}_{ag}$  into two, in accordance with Eqs. (5.14a) and (5.14b). The expressions for the various tangent stiffness matrix components can be explicitly obtained via 1<sup>st</sup> order differentiation of the coupling element internal force vector expressions in Eqs. (5.42)-(5.45) with respect to  $\mathbf{u}_e^{(i)}$  and  $\boldsymbol{\lambda}_{Re}$ :

$$\mathbf{k}_{gg}^{(11)} = \frac{\partial \mathbf{f}_g^{(1)}}{\partial \mathbf{u}_e^{(1)T}} = \mathbf{0} \quad (5.47)$$

$$\mathbf{k}_{gg}^{(12)} = \frac{\partial \mathbf{f}_g^{(1)}}{\partial \mathbf{u}_e^{(2)T}} = \int_{\Gamma_c} \frac{\partial \mathbf{b}^{(1)T}}{\partial \mathbf{u}_e^{(1)}} \cdot \frac{\partial \mathbf{b}^{(2)}}{\partial \mathbf{u}_e^{(2)T}} \cdot \boldsymbol{\varphi} \cdot \boldsymbol{\lambda}_{Re} \, d\Gamma_c \quad (5.48)$$

$$\mathbf{k}_{gg}^{(21)} = \frac{\partial \mathbf{f}_g^{(2)}}{\partial \mathbf{u}_e^{(1)T}} = \int_{\Gamma_c} \frac{\partial \mathbf{b}^{(2)T}}{\partial \mathbf{u}_e^{(2)}} \cdot \frac{\partial \mathbf{b}^{(1)}}{\partial \mathbf{u}_e^{(1)T}} \cdot \boldsymbol{\varphi} \cdot \boldsymbol{\lambda}_{Re} \, d\Gamma_c \quad (5.49)$$

$$\mathbf{k}_{gg}^{(22)} = \frac{\partial \mathbf{f}_g^{(2)}}{\partial \mathbf{u}_e^{(2)T}} = \mathbf{0} \quad (5.50)$$

$$\mathbf{k}_{gg,\varepsilon}^{(11)} = \frac{\partial \mathbf{f}_{g,\varepsilon}^{(1)}}{\partial \mathbf{u}_e^{(1)T}} = \varepsilon_R \int_{\Gamma_c} \frac{\partial \mathbf{b}^{(1)T}}{\partial \mathbf{u}_e^{(1)}} \cdot \mathbf{b}^{(2)} \cdot \mathbf{b}^{(2)T} \frac{\partial \mathbf{b}^{(1)}}{\partial \mathbf{u}_e^{(1)T}} \, d\Gamma_c \quad (5.51)$$

$$\begin{aligned} \mathbf{k}_{gg,\varepsilon}^{(12)} = \frac{\partial \mathbf{f}_{g,\varepsilon}^{(1)}}{\partial \mathbf{u}_e^{(2)T}} = & \varepsilon_R \int_{\Gamma_c} \left\{ \left( \frac{\partial \mathbf{b}^{(1)T}}{\partial \mathbf{u}_e^{(1)}} \cdot \frac{\partial \mathbf{b}^{(2)}}{\partial \mathbf{u}_e^{(2)T}} \right) \cdot (\mathbf{b}^{(1)} \cdot \mathbf{b}^{(2)} - \mathbf{b}_0^{(1)} \cdot \mathbf{b}_0^{(2)}) \right\} d\Gamma_c + \\ & + \varepsilon_R \int_{\Gamma_c} \left\{ \frac{\partial \mathbf{b}^{(1)T}}{\partial \mathbf{u}_e^{(1)}} \cdot \mathbf{b}^{(2)} \cdot \mathbf{b}^{(1)T} \frac{\partial \mathbf{b}^{(2)}}{\partial \mathbf{u}_e^{(2)T}} \right\} d\Gamma_c \end{aligned} \quad (5.52)$$

$$\begin{aligned} \mathbf{k}_{gg,\varepsilon}^{(21)} = \frac{\partial \mathbf{f}_{g,\varepsilon}^{(2)}}{\partial \mathbf{u}_e^{(1)T}} = & \varepsilon_R \int_{\Gamma_c} \left\{ \left( \frac{\partial \mathbf{b}^{(2)T}}{\partial \mathbf{u}_e^{(2)}} \cdot \frac{\partial \mathbf{b}^{(1)}}{\partial \mathbf{u}_e^{(1)T}} \right) \cdot (\mathbf{b}^{(1)} \cdot \mathbf{b}^{(2)} - \mathbf{b}_0^{(1)} \cdot \mathbf{b}_0^{(2)}) \right\} d\Gamma_c + \\ & + \varepsilon_R \int_{\Gamma_c} \left\{ \frac{\partial \mathbf{b}^{(2)T}}{\partial \mathbf{u}_e^{(2)}} \cdot \mathbf{b}^{(1)} \cdot \mathbf{b}^{(2)T} \frac{\partial \mathbf{b}^{(1)}}{\partial \mathbf{u}_e^{(1)T}} \right\} d\Gamma_c \end{aligned} \quad (5.53)$$

$$\mathbf{k}_{gg,\varepsilon}^{(22)} = \frac{\partial \mathbf{f}_{g,\varepsilon}^{(2)}}{\partial \mathbf{u}_e^{(2)T}} = \varepsilon_R \int_{\Gamma_c} \frac{\partial \mathbf{b}^{(2)T}}{\partial \mathbf{u}_e^{(2)}} \cdot \mathbf{b}^{(1)} \cdot \mathbf{b}^{(1)T} \frac{\partial \mathbf{b}^{(2)}}{\partial \mathbf{u}_e^{(2)T}} \, d\Gamma_c \quad (5.54)$$

$$\mathbf{k}_{ga}^{(1)} = \frac{\partial \mathbf{f}_g^{(1)}}{\partial \boldsymbol{\lambda}_{Re}^T} = \int_{\Gamma_c} \frac{\partial \mathbf{b}^{(1)T}}{\partial \mathbf{u}_e^{(1)}} \cdot \mathbf{b}^{(2)} \cdot \boldsymbol{\varphi} \, d\Gamma_c \quad (5.55)$$

$$\mathbf{k}_{ga}^{(2)} = \frac{\partial \mathbf{f}_g^{(2)}}{\partial \boldsymbol{\lambda}_{Re}^T} = \int_{\Gamma_c} \frac{\partial \mathbf{b}^{(2)T}}{\partial \mathbf{u}_e^{(2)}} \cdot \mathbf{b}^{(1)} \cdot \boldsymbol{\varphi} \, d\Gamma_c \quad (5.56)$$

## 5.4 Superposition of translational and rotational coupling formulations

The translational and rotational coupling element formulations, presented in Sections 5.2 and 5.3, individually achieve rigid coupling of the translational displacement field and the torsional rotations of  $\Gamma^{(i)}$  along  $\Gamma_c$ , respectively.

In both developed formulations, the constraint functions  $\mathbf{g}(\mathbf{u}^{(1)}, \mathbf{u}^{(2)})$  and  $\mathbf{g}_R(\mathbf{u}^{(1)}, \mathbf{u}^{(2)})$  are expressed in a discrete form in terms of the kinematic translational DOFs  $\mathbf{u}_e = (\mathbf{u}_e^{(1)} \quad \mathbf{u}_e^{(2)})^T$  along the global Cartesian coordinate axes (X,Y,Z). Accordingly, the coupling element force vector and tangent stiffness matrix are expressed in terms of  $\mathbf{u}_e = (\mathbf{u}_e^{(1)} \quad \mathbf{u}_e^{(2)})^T$ , and thus geometric nonlinearity is accounted for without necessitating the employment of complex co-rotational transformations for individual shell FEs.

Owing to the translational and rotational coupling element formulations being unrelated, their effects can be combined additively for the enforcement of multiple kinematic constraints along the interface. This is achieved by virtue of superposition of the derived expressions for the internal force vectors and consistent tangent stiffness matrices of the translational and rotational coupling elements, and allows for the establishment of a general formulation capable of achieving both forms of coupling.

The coupling element implementation in ADAPTIC (Izzuddin, 1991) v2.16.5 allows for basic translational coupling to be achieved when the element is introduced in a mesh, while the rotational coupling is switched on or off at the user's discretion. The developed coupling element can therefore be effectively employed for the modelling of a variety of coupling conditions in geometrically complex systems. This includes weld lines of various types, where the adopted welding process determines the capacity of the weld to accommodate relative rotations between the connected components. It should further be noted that the abridging of the element to achieve rigid coupling along only one or two of the three global translational axes is rendered a straightforward process by eliminating the desired coupling terms.

As is evident from Section 5.2, the coupling element tangent stiffness matrix is constant for a fully rigid translational constraint, which allows for its assembly once in the beginning of the analysis for each coupling element. The force vector can therefore be obtained as its product with the updated set of  $\mathbf{u}_e$  and  $\lambda_e$ , at every iterative step of the nonlinear solution procedure.

On the other hand, the force vector and tangent stiffness matrix components of the rotational coupling element are related to  $\mathbf{u}_e$  and  $\lambda_{Re}$  to a second- and first-order, respectively, which requires their evaluation at every iterative step of the nonlinear solution procedure. The associated computing wall-clock time and resources demands are therefore greater in comparison to the translational coupling element, which justifies the implementation in ADAPTIC (Izzuddin, 1991) to allow for rotational coupling to be switched off in cases where it is not required.

## 5.5 Patch tests

A series of patch tests has been conducted to verify the capability of the developed coupling element to enforce discrete kinematic constraints along a 1-D interface for surfaces with non-conforming shell FE meshes and to assess its performance under a variety of conditions. The results are presented and discussed in detail hereafter.

### 5.5.1 Preliminaries

Patch tests are generally employed for the performance assessment of FEs. Any sub-model comprising two or more FEs can qualify as a patch, if its configuration can be considered to represent a finite part of a mesh in the limit of a mesh refinement process. Therefore, the patch must comprise two or more elements arranged in the most general geometric configuration allowed by their formulation, with at least one internal node being shared by the entirety of elements (Zienkiewicz *et al.*, 1977).

The test process involves subjecting the patch to a prescribed mode associated with an *a priori* known exact solution over its boundary and assessing the element capability to capture the solution exactly, in a discrete sense. The prescribed mode can generally be a displacement or force field introduced along the patch boundary, while there are also mixed type patch tests (Zienkiewicz *et al.*, 1977).

The passing of the patch test by an element ensures that it can accurately capture the prescribed mode within a small finite patch of a mesh, and hence more complex modes can also be



captured over the mesh with sufficient refinement. Convergence to the exact solution is therefore ensured at a global level, however a monotonic convergence trend, which typically stems from the stiffer response with coarser mesh characteristic of FE solutions (Bathe, 1996), is not guaranteed.

The selection of an appropriate type of patch test for a given element type primarily requires the identification of the function that the element has been developed to perform. In the broader field of computational mechanics, constant strain patch tests are typically undertaken to verify the capability of a given element type with prescribed material and mechanical properties to model constant strain conditions. The passing of the patch test ensures that complex deformation states can be accurately modelled over the mesh with sufficient refinement, even if the element violates the continuity requirements under general strain conditions (Zienkiewicz *et al.*, 1977).

### 5.5.2 Coupling element patch tests

For the 1-D rigid coupling problem at hand, the set of imposed kinematic constraints enforces the fulfilment of surface deformation compatibility along the 1-D interface length. As discussed earlier, this is achieved in a discrete sense along the interface, over the segments of individual coupling elements, by means of a continuous piece-wise linear or quadratic LM field representing the required forces or moments. The element formulation therefore seeks to maintain the relative surface deformations, and correspondingly the interface deformations, as zero, rather than achieve their convergence to a constant value, and is thereby effectively rendered deformation-independent. Since the LM field is being approximated, rather than the displacement/strain fields, the purpose of the patch test would be to ensure that the element can represent constant LM fields for different 1-D element patches, while satisfying interface compatibility conditions.

Taking due account of the aforementioned considerations, two types of coupling element patch tests have been established: (i) rigid body mode patch tests, which aim at verifying the coupling element capability to generate a zero LM field along the interface under rigid body translations or rotations; and (ii) constant force/moment patch tests, which aim at verifying the coupling

element capability to generate a constant LM field along the interface under a constant force or moment field, equal to the prescribed value applied at the patch boundary.

Generalising the discussion of the preceding section, the passing of a constant LM patch test by the coupling element is indicative of its capability to model constant internal force and moment states within a small patch of a mesh. Consequently, convergence of the discrete coupling problem to the exact solution is guaranteed at the global level, in the limit, with mesh refinement, even if the element is unable to accurately model general force or moment LM states.

#### 5.5.2.1 Coupling element patch configuration

For an admissible coupling element patch configuration to be established, the following set of requirements should be fulfilled: (i) the patch must comprise two or more coupling elements; (ii) the patch must comprise at least one internal CP shared by the entirety of coupling elements; and (iii) the patch must encompass the most general geometric configuration allowed by the element formulation, representing part of a mesh in the limit of refinement. In the case of the developed coupling element, the interface segment is generally piece-wise linear, and hence the fulfilment of admissibility criterion (iii) would require the consideration of the most general coupled surface configuration.

The established patch comprises two planar surfaces, coupled along an interface with two segments and three distinct coupling elements associated with these, as illustrated in Figure 5.3. Each surface has a thickness  $t=1$  mm and is discretised with two 9-noded quadrilateral shell elements, while 6-noded triangular or mixed element types can also be employed for the discretisation, without loss of generality. Each coupling element encompasses two or three CPs, resulting into a linear or quadratic field of LMs along its length, respectively, where in both cases one CP is shared by the two interface segments. Both regular and irregular element geometries have been considered for one of the two surfaces.

For ease of reference to the distinct coupled surfaces and their respective shell elements, the bottom surface will henceforth be referred to as Surface 1 and the top as Surface 2, while their elements are numbered as 1A, 1B and 2A, 2B, from left to right along the global X-axis. The two surfaces are intersecting at a  $90^\circ$  angle and are appropriately arranged to avoid nodal

overlapping along all edges. This enables the most general configuration of interface segments and associated coupling elements to be obtained along the surface intersection for the given patch geometry. Linear elastic material parameters are considered, with Young's modulus  $E=10^5$  N/mm<sup>2</sup> and Poisson ratio  $\nu=0$ , for the effects of anticlastic curvature to be eliminated in cases where the applied force field induces out-of-plane surface deformation. Furthermore, the translational and rotational penalty parameters  $\varepsilon$  and  $\varepsilon_R$  for the coupling elements are both specified as 0.1, leading to ratios of  $\varepsilon/E$  and  $\varepsilon_R/(Et^2)$  both equal to  $10^{-6}$ .

### 5.5.2.2 Coupling element patch base-case and variants

The coupling element performance is assessed by subjecting it to the set of rigid body and constant force patch tests discussed earlier. The assessment is performed on the basis of the obtained error magnitude in the LM field, in relation to the *a priori* known exact solution associated with the respective rigid body or constant force mode. The element development and implementation in ADAPTIC (Izzuddin, 1991) allows for the values of the LMs at the CPs of each interface segment to be recovered at every iterative step of the nonlinear solution procedure. Subsequently, depending on the number of CPs defined per segment, a piecewise quadratic or linear interpolation of these values is employed to determine the LM field, as well as the corresponding error distribution along the coupling interface length, and identify the maximum error magnitude.

A series of parametric studies is also conducted to assess the sensitivity of the obtained patch test results to a variety of parameters embedded in the developed coupling element formulation, including: (i) the classification of Surfaces 1 and 2 as slave and master, (ii) the adopted integration scheme at the element level, including element-specific integration (E) and segment-specific (S) integration, (iii) the values of the translational and rotational coupling penalty parameters,  $\varepsilon$  and  $\varepsilon_R$ , and (iv) the element geometry, including regular (R) and irregular (I) elements.

The specification of a distinct set of values for the above parameters leads to variant patch configurations, which are assigned acronym keys in accordance with the following structure: (i) the first character is a letter denoting the element geometry (R/I); (ii) the second character is a single digit number (1/2) denoting the slave surface; (iii) the third character is a letter

denoting the adopted integration strategy (E/S); and (iv) the fourth character is a number denoting the number of CPs per segment (2/3). This leads to acronym keys such as R1E3 for a patch with regular elements, Surface 1 as the slave surface, element-specific integration and 3 CPs per segment, or I2S2 for a patch with irregular elements, Surface 2 as the slave surface, segment-specific integration and 2 CPs per segment.

Patch variants R1E2 and R1E3 are set as base-cases for the patch tests, encompassing regular element geometry and the default progressive segmentation and integration schemes specified in the developed coupling element formulation. Surface 1 is selected as the slave surface for the base cases without loss of generality, leading to the interface segmentation into two coupling segments, henceforth denoted as CS1 and CS2, with lengths of 30 mm and 20 mm, respectively, as illustrated in Figure 5.3 (b). Along CS1 and CS2, CPs (1)-(5) are defined, with (4) and (5) only being used for a quadratic LM field interpolation at the element level in variant R1E3. Along the interface, three coupling elements are accordingly defined: (1A-2A) and (1A-2B) associated with CS1, and (1B-2B) associated with CS2. The employment of the element-specific integration scheme leads to the identification of three complementary non-overlapping integration segments along the interface, henceforth denoted as IS1, IS2 and IS3, with endpoints [1]-[4]. For each coupling element, these correspond to the portion of the CS which is entirely projected on both the respective slave and master shell elements, thus allowing all GPs to be actively projected and the integration to be performed with the specified quadrature order on both surfaces.

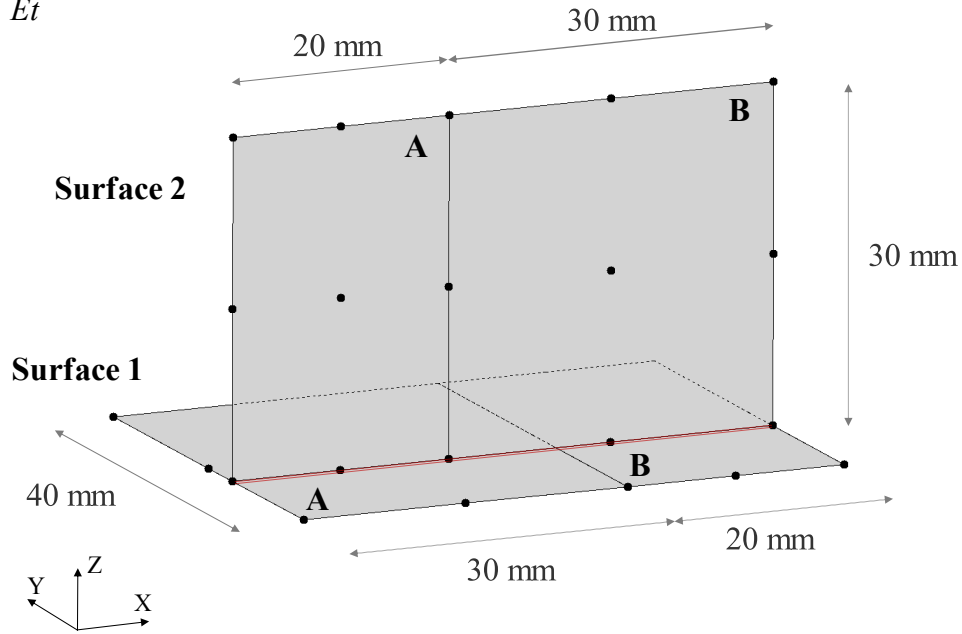
For each base-case patch test, the error for different values of the Gaussian quadrature order is evaluated to verify the monotonic convergence of the obtained LM field approximation to the exact solution with an increasing number of GPs. This procedure is carried out for CS with two and three CPs, in order for the accuracy of both the piece-wise linear and quadratic LM field approximations to be assessed. The obtained results are employed as performance indices for the coupling element in its default *modus operandi*, while also being used in the context of the subsequent parametric studies for the element performance sensitivity analysis to a variety of parameters. The results of the base-case patch tests, followed by those of the parametric studies, are presented and discussed in detail hereafter.

$$E=10^5 \text{ N/mm}^2$$

$$\nu=0$$

$$\varepsilon=10^{-6} E$$

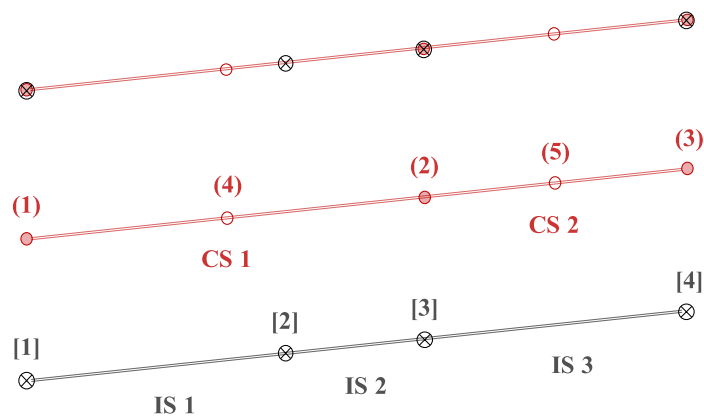
$$\varepsilon_R=10^{-6} Et^2$$



(a)

● Collocation Points

⊗ Integrations segment end-points



(b)

Figure 5.3: (a) Coupling element patch geometric configuration, material properties and coupling parameters, (b) coupling interface and integration segments

### 5.5.3 Rigid body mode patch tests

The rigid body mode patch tests aim at verifying the coupling element capability to generate a zero LM field along the interface CSs, when the patch is subjected to rigid body translations along or rigid body rotations about the global axes (X,Y,Z).

In the rigid body translation patch tests, Surface 2 is completely unrestrained, while Surface 1 is restrained at its four corners against all rotations. The rigid body translation in the direction of a given global axis is achieved by means of applying appropriate unit displacements and introducing translational restraints in the direction of the remaining axes, at the four corner nodes of Surface 1.

In the rigid body rotation patch tests, Surface 2 is completely unrestrained, while Surface 1 is restrained at its four corners against planar translations in the direction of the rigid body rotation global axis. The rigid body rotation about the X, Y planar axes is achieved by means of introducing translational restraints in the direction of the remaining axes along an edge of Surface 1 and applying appropriate unit displacements along the Z-axis at one corner node of the opposite edge. On the other hand, for a rigid body rotation about the Z planar axis, only one corner node of Surface 1 needs to be restrained against all translations, and a unit displacement to be applied along the global X or Y axes at the other corner node of the same edge, transverse to the edge.

In all cases, the recovered values of LMs at the CPs of the coupling segments are zero, leading to a zero LM field along the interface length, and thereby confirming the passing of the rigid body patch tests by the coupling element. The deformed configuration of the patch in each case is given in Figure 5.4. It should be noted that a zero value of the penalty parameters leads to a singular tangent stiffness matrix in this case when a frontal solver is employed, due to the patch exhibiting rigid body motion and Surface 2 being unrestrained. This highlights the necessity of the introduced penalty parameters in the augmented Lagrangian formulation for both translational and rotational coupling, as discussed earlier in Section 4.6.

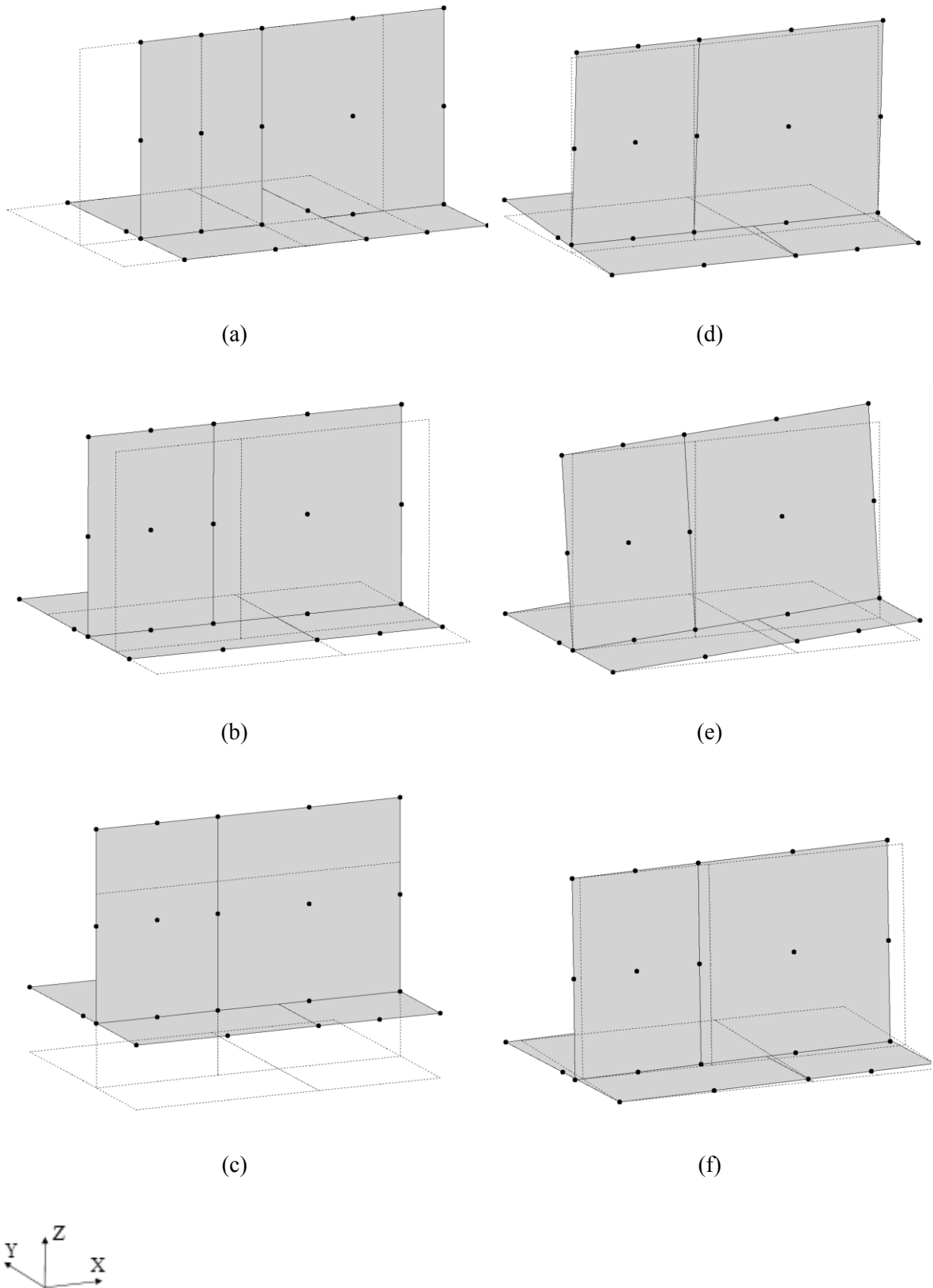


Figure 5.4: Rigid body mode coupling element patch tests: (a) translation in X, (b) translation in Y, (c) translation in Z, (d) rotation about X, (e) rotation about Y, (f) rotation about Z

#### 5.5.4 Constant force/moment patch tests

Constant force and moment patch tests aim at verifying the coupling element capability to generate a uniform LM field along the interface, with a constant value equal to the uniform force or moment loading applied at the patch boundary.

Four types of patch tests are considered herein, with three being associated with forces along the global X, Y and Z axes and one with moments about the global X axis, which coincides with the coupling interface longitudinal direction. All nodes of Surface 1 are fully restrained and the applied loading at the patch boundary is appropriately selected in each case to generate a uniform unit force or moment field over the domain of Surface 2. The coupling elements must be capable of transferring the induced uniform force or moment field between the coupled plates, by virtue of a uniform unit field of LM components in the direction of the load application only.

The LM field is obtained by means of interpolation of the LM vectors recovered at the CPs, each of which must comprise a single non-zero LM component and three zero ones. The non-zero LM component is activated to enforce the translational or rotational constraint in the direction dictated by the applied loading, and it should have a unit value at every CP for a uniform unit LM field to be obtained via interpolation along the interface.

Taking into consideration the patch geometric configuration and the arrangement of Surface 2, where the load is being applied, the following load cases are considered for the patch tests: (i) uniform planar shear applied to Surface 2, induced by means of a tangent force field applied over its top and side edges along the global X and Z axes, respectively; (ii) uniform membrane forces over the domain of Surface 2, induced by means of a force field applied over its top edge along the global Z axis; (iii) uniform transverse shear of Surface 2, induced by means of two superimposed fields of transverse forces along the global Y axis and counter-balancing moments along the global X axis, applied over its top edge; and (iv) uniform bending moment over the domain of Surface 2, induced by means of a moment field applied over its top edge about the global X axis.

For load cases (i)-(iii) described above, the coupling elements defined along the coupling interface must generate a uniform unit force LM component field along the global X, Z, Y axes, respectively, as well as a uniform moment LM field about the X axis for case (iv). For



both base-case patch variants R1E2 and R1E3, the values of the LM vector components in the respective directions are recovered at the CPs of the coupling segments. Subsequently, a piece-wise linear or quadratic interpolation is employed for the establishment of the LM field and the corresponding error distribution against the normalised longitudinal coordinate of the coupling interface,  $\tilde{\xi} = \tilde{x} / L \in [0,1]$ , with  $L=50\text{mm}$  being the length of the coupling interface.

The obtained error distribution along the interface is identical for all four patch tests, demonstrating the ability of the coupling element to generate an identical LM field for the enforcement of the translational and rotational constraints along the global coordinate axes. The error distribution for base-case patch variants R1E2 and R1E3 is graphically illustrated in Figures 5.5 and 5.6, respectively.

As can be observed from the graphs of Figures 5.5 and 5.6, the error distribution along the coupling interface for variant R1E2 is identical for a quadrature order greater than two, and is associated with a maximum error magnitude of 0.0007%. On the other hand, for variant R1E3, the maximum error magnitude of 0.0009% for a quadrature order of two drops to 0.0008% for a quadrature order greater than three. Evidently, the error distribution becomes insensitive to the employed Gaussian quadrature order for both variants, when the latter becomes greater than two and three, respectively. This is attributed to the employment of an element-specific integration scheme at the coupling element level.

As discussed earlier in Sub-section 4.7.3.2, the element-specific integration scheme enables the identification of a suitable integration sub-segment at the coupling element level, such that all GP projections on the associated slave and master shell elements are rendered active. The sub-segment is established by means of identifying the portion of the coupling element interface segment which is projected on the surface of both slave and master shell elements. More importantly, the establishment of the integration sub-segment in such a manner results in the respective integrand functions for all force vector and tangent stiffness matrix components being polynomial over the integration domain. Therefore, the piece-wise polynomial integrand forms encountered with segment specific integration can be effectively overcome at the element level, which allows for exact integration to be achieved with a small number of GPs.

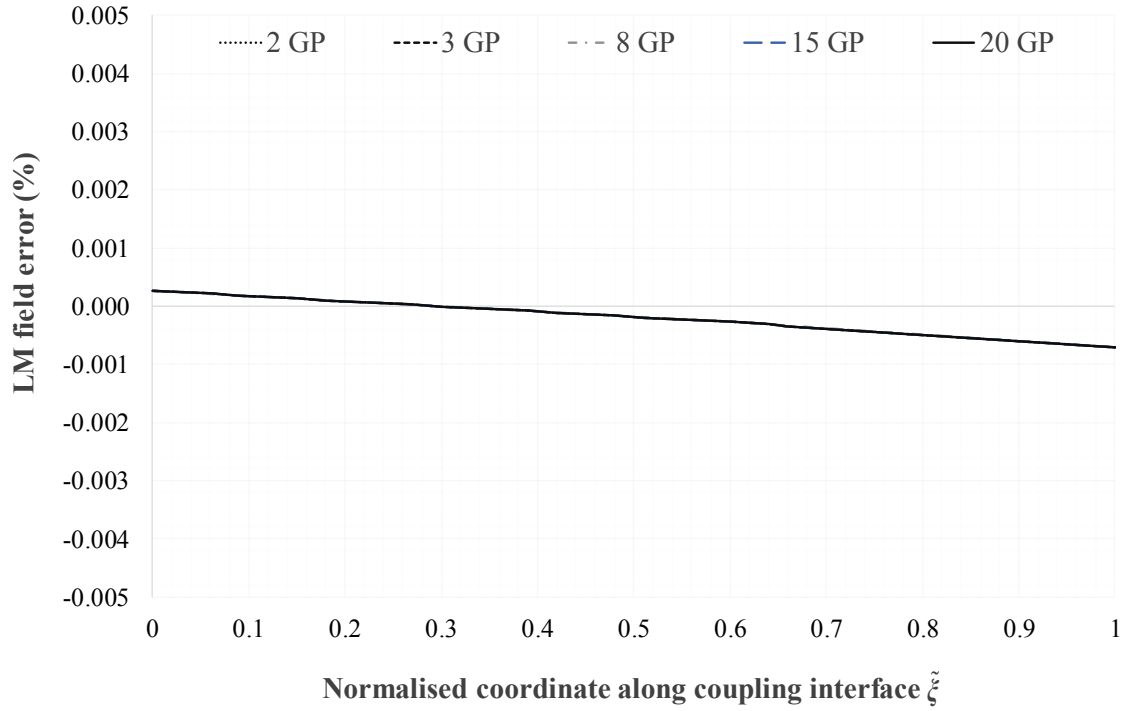


Figure 5.5: Lagrangian Multiplier field error distribution with variable Gaussian quadrature order for base-case patch variant R1E2

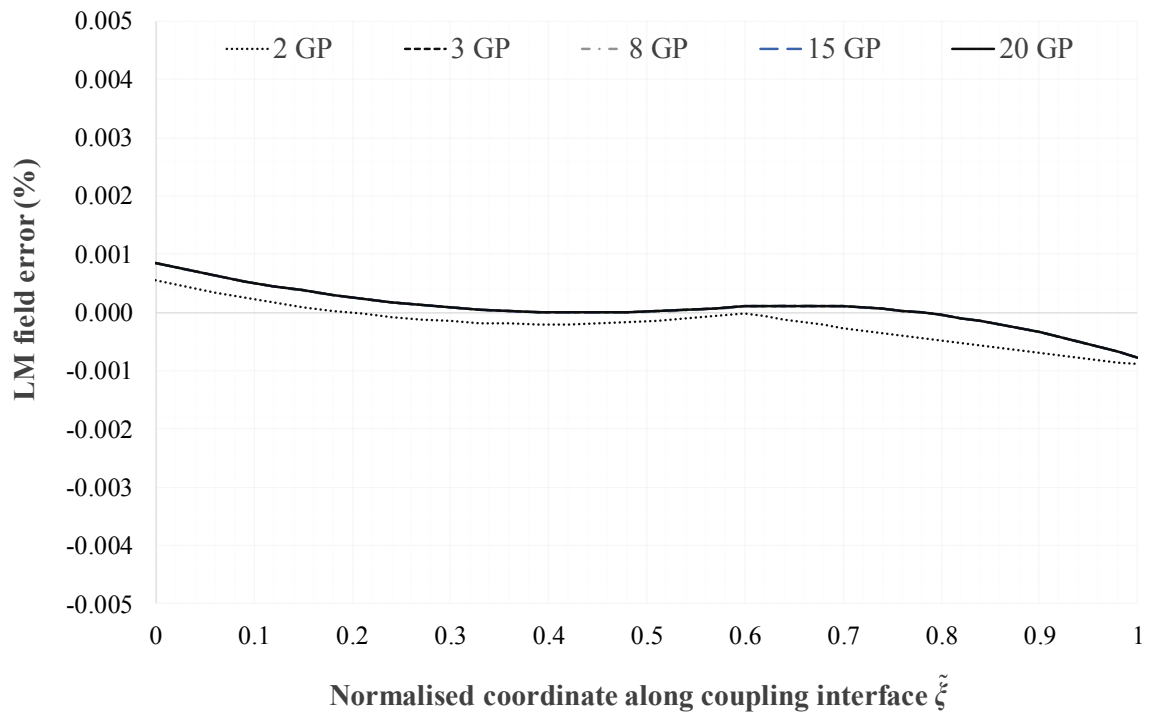


Figure 5.6: Lagrangian Multiplier field error distribution with variable Gaussian quadrature order for base-case patch variant R1E3

In the base-case patch variant configurations R1E2 and R1E3, characterised by regular shell FE and interface geometry, the integrand functions for the force vector and the tangent stiffness matrix are cubic or quartic polynomials with respect to the interface natural coordinate system, for two or three CPs per coupling segment, respectively. Accordingly, exact integration can be achieved with the employment of a Gaussian quadrature with order two and three, respectively, as confirmed by the patch test results.

Taking due account of the aforementioned considerations, the coupling element must be capable of generating a uniform unit field along the interface, in the direction of the activated LM component for each patch test, with exactly zero error when the element-specific integration scheme is employed. Despite the obtained error magnitude being sufficiently small for both variants to be considered negligible, it is not exactly zero. The element performance in approximating the *a priori* known exact solutions associated with the specified patch tests is therefore considered conditionally admissible.

The admissibility of the element performance is subject to the identification of the error source in one or more of the embedded numerical processes, rather than in the element formulation itself. This can be established by testing whether the error in the LM field converges to zero by enhancing the accuracy of these numerical processes, which verifies that the formulation allows for the exact solution to be obtained and the minor observed error in the patch test results is purely associated with these processes.

The error can be traced back to the employment of the projection algorithm discussed earlier in Sub-section 4.5.2.1 for the identification of the integration sub-segment end points, as well as of the GP projections on the slave and master shell surfaces, as discussed earlier in Sub-section 4.7.3. The specified tolerance in the projection algorithm results in a small numerical error in the evaluation of the integration sub-segment end points, which subsequently pollutes the abscissae of the GPs defined along its length. The projection of the already polluted GP abscissae from the segment to the slave and master shell element surfaces, using the same projection algorithm, results in further error accumulation in these projections. The integration error in the obtained active LM vectors at the CPs can be reduced by specifying a less generous tolerance in the projection algorithm, with the associated convergence measures being the orthogonality conditions at the projection point and the element boundary coordinates embedded in the final projection point admissibility criteria. This is illustrated in Figure 5.7.

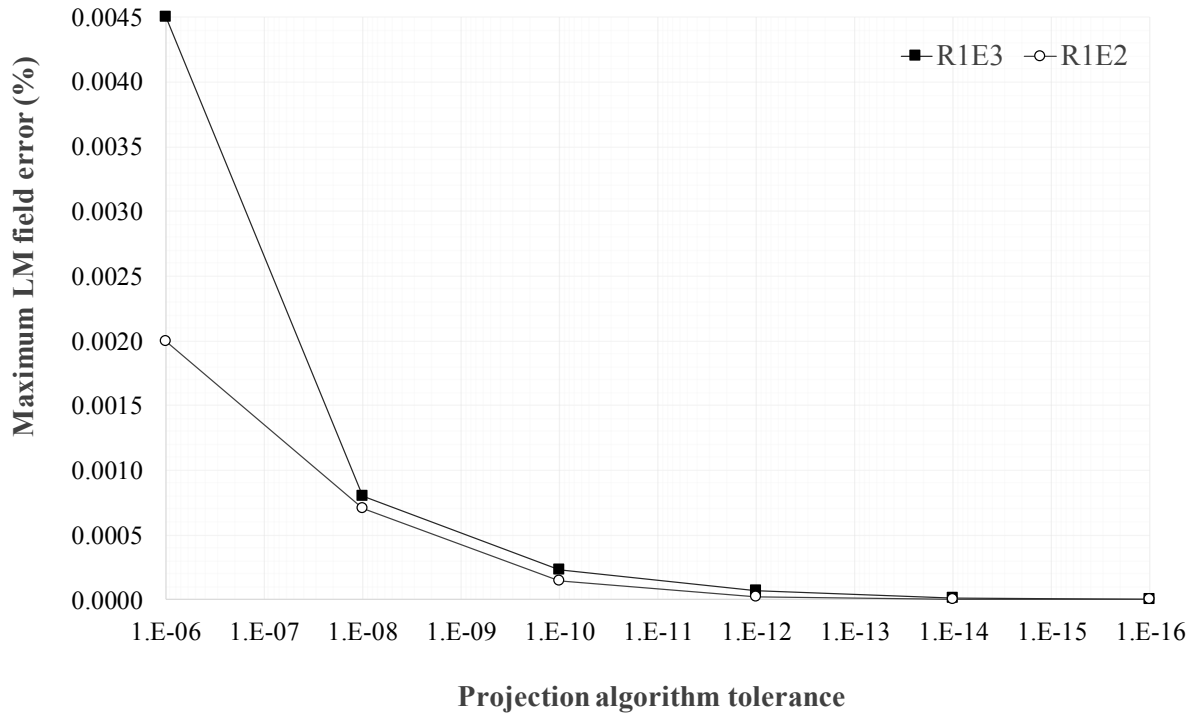


Figure 5.7: Maximum Lagrangian Multiplier field error variation with specified projection algorithm tolerance for base-case patch variants R1E2 and R1E3

Taking due account of the aforementioned considerations, it is concluded that the coupling element passes all four constant force/moment patch tests, due to the maximum error magnitude converging to zero with a decreasing projection algorithm tolerance. Evidently, the adopted value of  $10^{-8}$  for the projection algorithm tolerance leads to maximum errors of 0.0007% and 0.0008% for variants R1E2 and R1E3, respectively. This tolerance value was selected on the basis of achieving a maximum error magnitude sufficiently small to be considered negligible, while maintaining computational efficiency. The patch deformed configurations are illustrated in Figure 5.8(a)-(d).

The deflected shapes clearly indicate a uniform force distribution over the domain of Surface 2, resulting in a compatible deformation associated with constant planar shear and membrane strains, as well as constant curvature and out-of-plane strain over its domain, respectively, for cases (i)-(iv). Surface 1 is effectively irrelevant to the patch tests, due to its nodal kinematic DOFs being completely restrained. The aim is therefore to assess the coupling element capacity of accurately transferring the uniform force field between the coupled surfaces, by virtue of a uniform field of LM components in the direction of the kinematic constraint activated by the induced deformation of Surface 2.

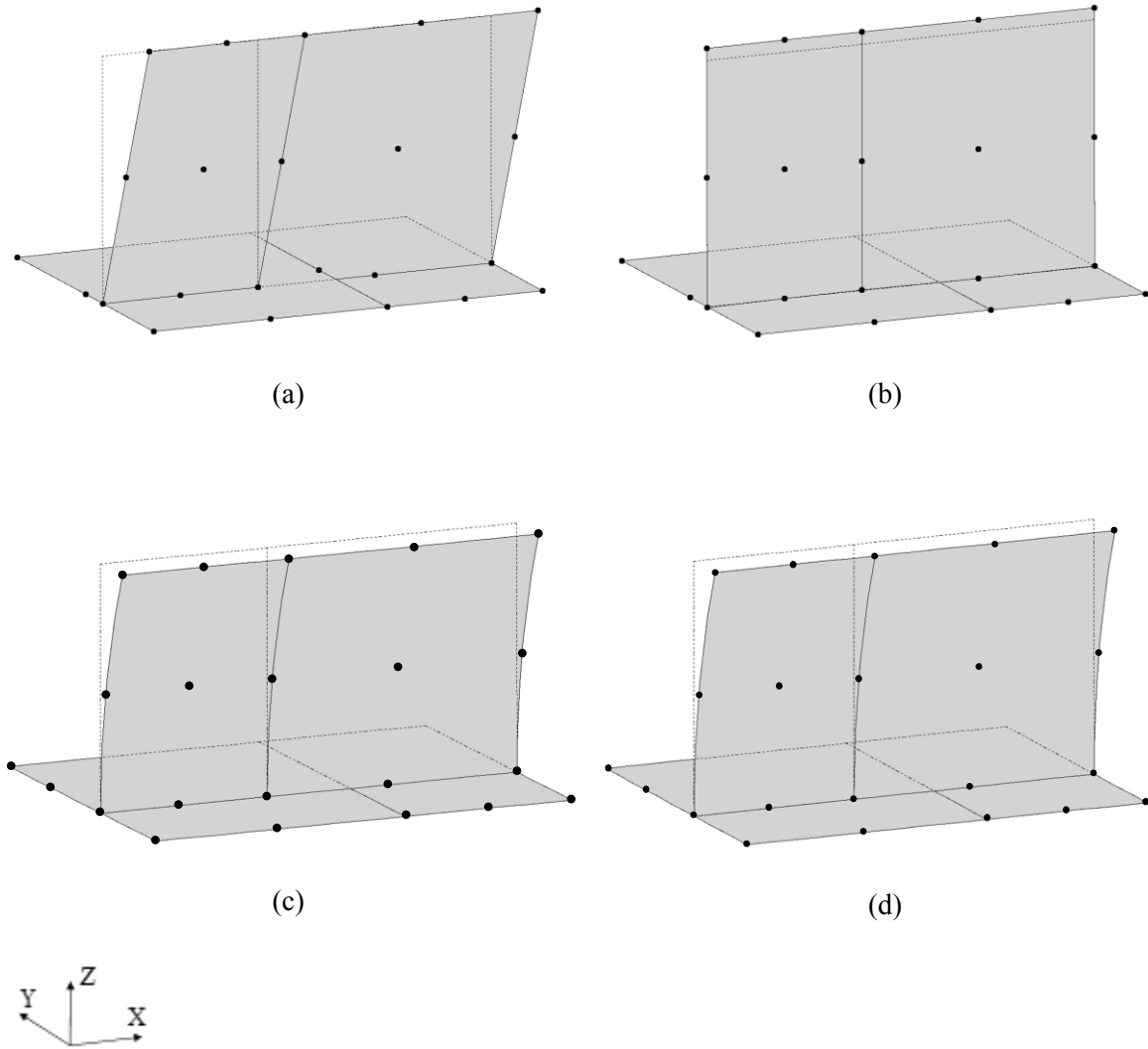


Figure 5.8: Constant force/moment coupling element patch tests: (a) planar shear force field, (b) planar membrane force field, (c) out-of-plane bending moment field, (d) out-of-plane shear force and moment fields

### 5.5.5 Coupling element performance sensitivity analysis

As discussed previously, a series of parametric studies is conducted to assess the coupling element performance sensitivity to the following parameters: (i) the surface classification, (ii) the adopted integration scheme, (iii) the penalty parameters  $\varepsilon$  and  $\varepsilon_R$ , and (iv) the shell FE geometric irregularities. The results are presented in separate sub-sections hereafter.

#### 5.5.5.1 Influence of master-slave surface classification

The influence of the surface classification as master and slave on the base-case patch test results is investigated here. The developed coupling element must be capable of passing the rigid body and constant force patch tests irrespective of the slave surface selection, achieving a monotonic convergence to the exact solution for an increasing quadrature order, even with a different level of achieved accuracy.

As discussed previously, for the base-case patch variants R1E2 and R1E3 Surface 1 has been selected as the slave surface, with the progressive segmentation algorithm resulting in two coupling segments CS1 and CS2, as illustrated in Figure 5.3(b). Herein, two new patch variants R2E2 and R2E3 are considered, with Surface 2 being the slave surface, which leads to the CS lengths being effectively interchanged. Three new coupling elements can therefore be defined: (2A-1A) associated with the new CS1, and (2B-1A), (2B-1B) associated with the new CS2. The obtained results for variants R2E2 and R2E3 are compared against those of R1E2 and R1E3 for all patch tests, to investigate the sensitivity of the coupling element performance to the selection of the slave surface.

For all six rigid body mode patch tests, R2E2 and R2E3 are associated with zero values for all LM components at the coupling segment CPs, similar to R1E2 and R1E3, thereby confirming the insensitivity of the respective results to the selection of the slave surface and the interface segmentation.

For the constant force/moment patch tests, the values of the LM components associated with the kinematic constraint activated by each load-case are recovered at the new CPs, and the error distribution is evaluated along the new CSs. The obtained error distributions for variants R2E2 and R2E3 are identical for all types of patch tests, similar to the base-case, as graphically illustrated in Figures 5.9 and 5.10 for a variable Gaussian quadrature order.

As is evident from the graphs of Figures 5.9 and 5.10, the employment of the element-specific integration scheme allows for the exact integration of the coupling element force vector and tangent stiffness matrix for variants R2E2 and R2E3, similar to the base-case. This is achieved with quadrature orders of two and three, respectively, beyond which the obtained error distribution becomes insensitive to the employed integration order. The comparison of the error distributions between the new and the base-case patch variants, obtained using a sufficient

Gaussian quadrature order to achieve exact integration, is illustrated in Figures 5.11 and 5.12. The comparison indicates minor discrepancies in the respective error distributions, as expected by the employment of different coupling segments for the LM field interpolation. The obtained distributions are symmetrical about the interface axis of symmetry, due to the obtained values at the CPs of the CSs being identical and interchanged in each case.

Conclusively, the element performance in its default *modus operandi* remains insensitive to the surface classification, allowing for an identical level of accuracy to be achieved with the employment of a small, but sufficient for exact integration, quadrature order. Evidently, a reduction in the projection algorithm tolerance results in a reduction in the maximum error magnitude in this case as well.

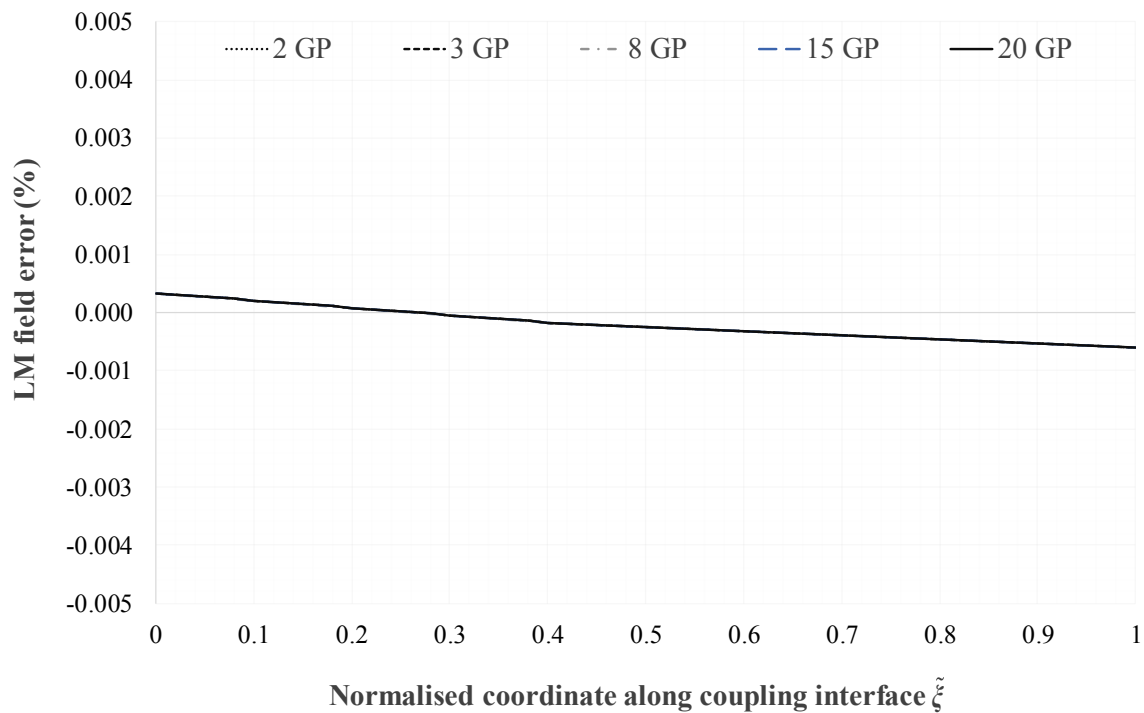


Figure 5.9: Lagrangian Multiplier field error distribution with variable Gaussian quadrature order for patch variant R2E2

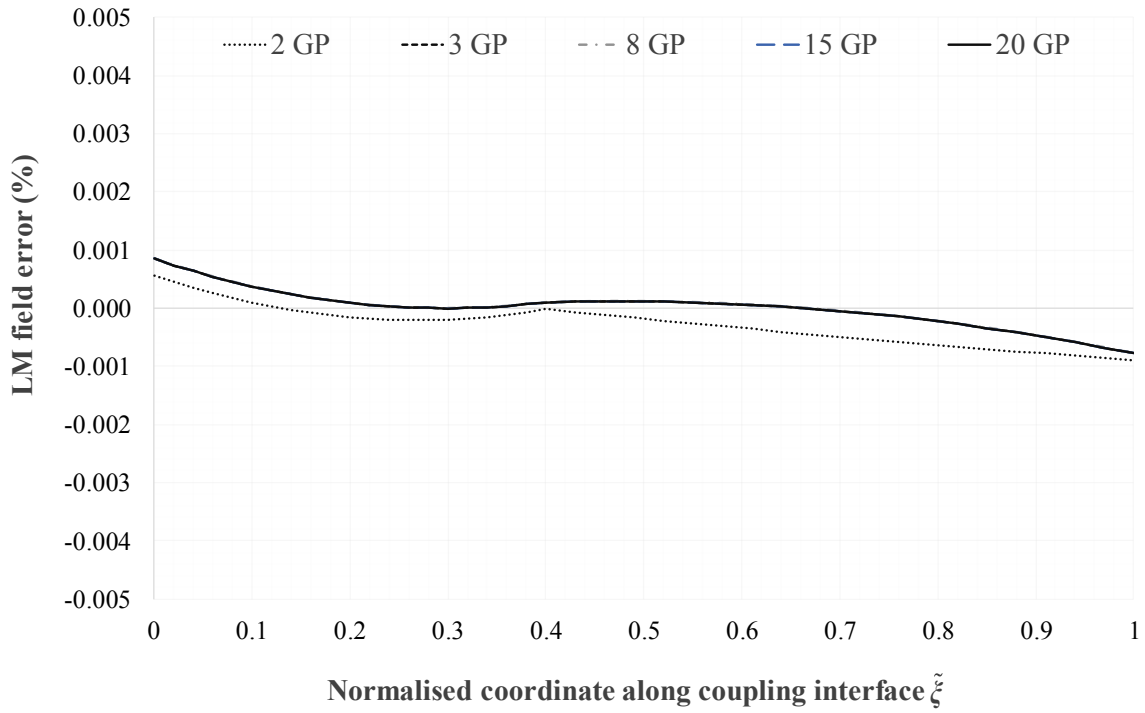


Figure 5.10: Lagrangian Multiplier field error distribution with variable Gaussian quadrature order for patch variant R2E3

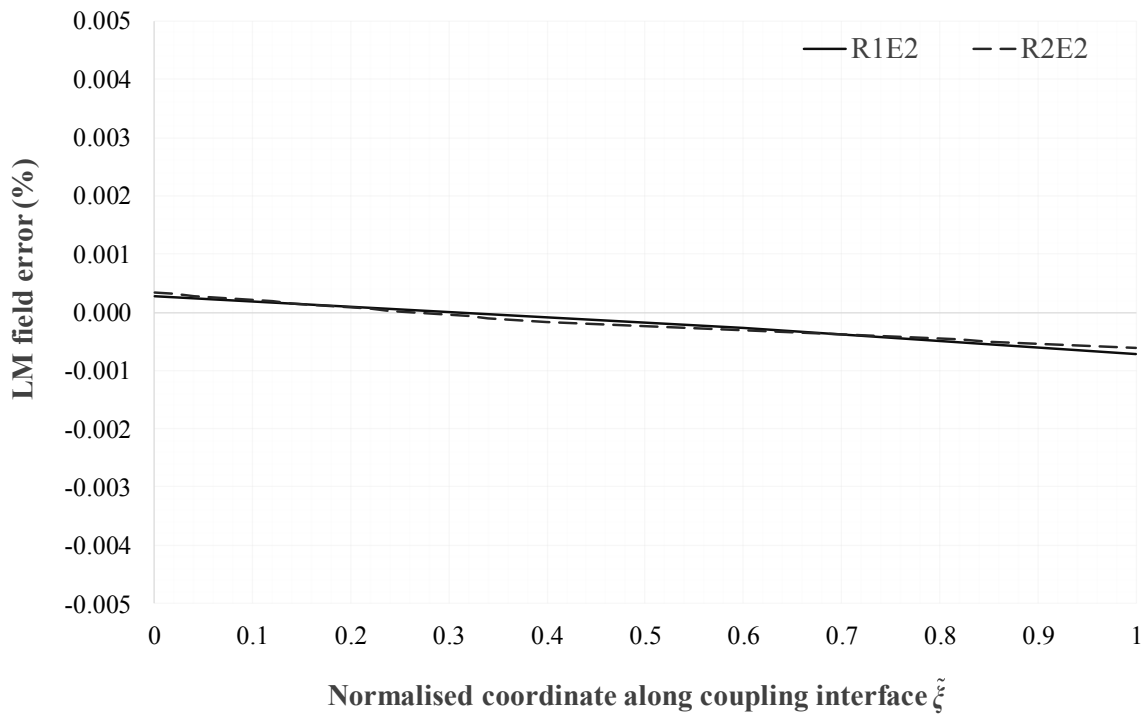


Figure 5.11: Lagrangian Multiplier field error distribution comparison for patch variants R1E2-R2E2



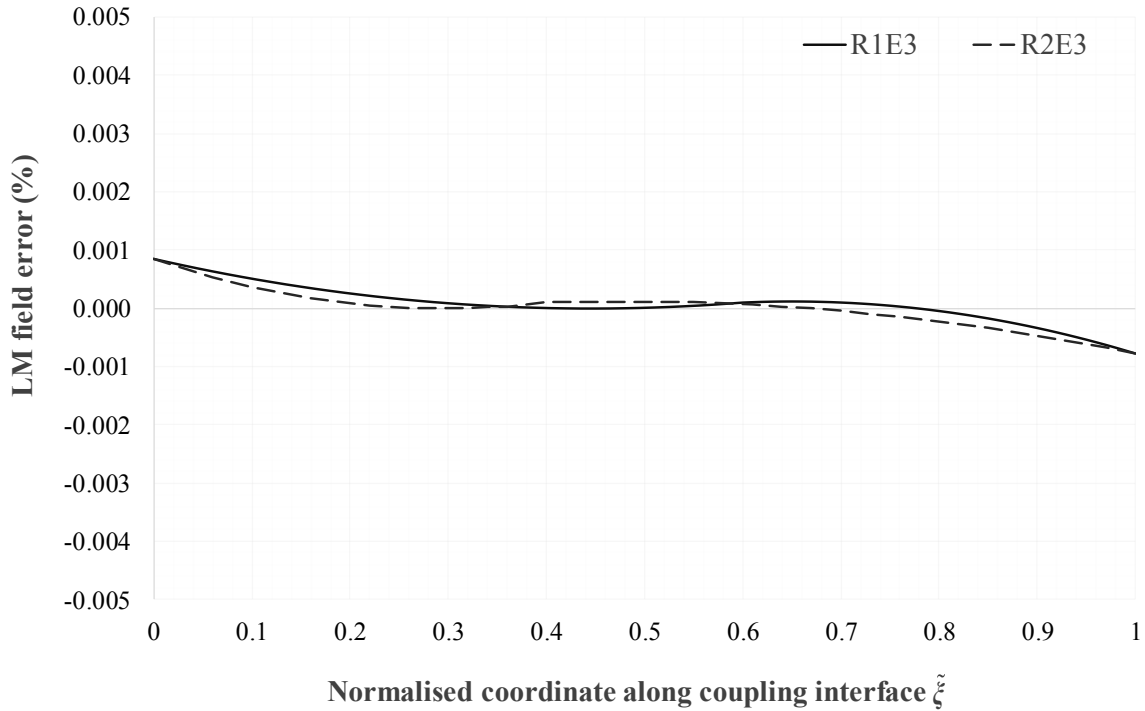


Figure 5.12: Lagrangian Multiplier field error distribution comparison for patch variants R1E3-R2E3

#### 5.5.5.2 Influence of adopted integration scheme

The influence of the adopted integration scheme at the element level on the base-case patch test results is investigated here. The developed coupling element must be capable of passing the rigid body and constant force patch tests irrespective of the integration scheme, with a monotonic convergence to the exact solution for an increasing quadrature order, even with a different level of achieved accuracy.

As discussed in Sub-section 4.7.3, the element-specific integration scheme is employed in the coupling element default *modus operandi*. This is based on the establishment of appropriate IS at the coupling element level, such that all GPs defined along these have active projections on both master and slave shell surfaces. Hence, it effectively enables the specified quadrature order to be maintained for all coupling elements, while overcoming the shortcomings associated with piece-wise polynomial integrand functions. Accordingly, exact integration of continuous cubic and quartic polynomial integrands over the specified IS can be achieved using two or three GPs, for linear and quadratic LM shape functions, respectively.

On the other hand, segment-specific integration is based on the definition of GPs along the CS associated with a given element, and the employment of the subset of these with active projections on both master and slave surfaces. Hence, it results into a variable and potentially reduced order of integration per coupling element, which however can achieve a sufficient overall level of accuracy with mesh refinement or/and a high quadrature order. As opposed to element-specific integration, the segment-specific scheme does not guarantee exact integration of the integrand functions, due to these being either polynomial or piece-wise polynomial, depending on the selection of the slave surface for slave-only interface segmentation.

In view of the above, patch variants R1S2 and R1S3 are considered herein to primarily verify the passing of the patch test and also establish the coupling element performance sensitivity in the respective cases. The coupling elements defined in this case are identical to R1E2 and R1E3, while the ISs coincide with the CSs illustrated in Figure 5.3(b). The obtained error distributions along the interface for patch variants R1S2 and R1S3 are illustrated in Figures 5.13 and 5.14, respectively, for a variable quadrature order.

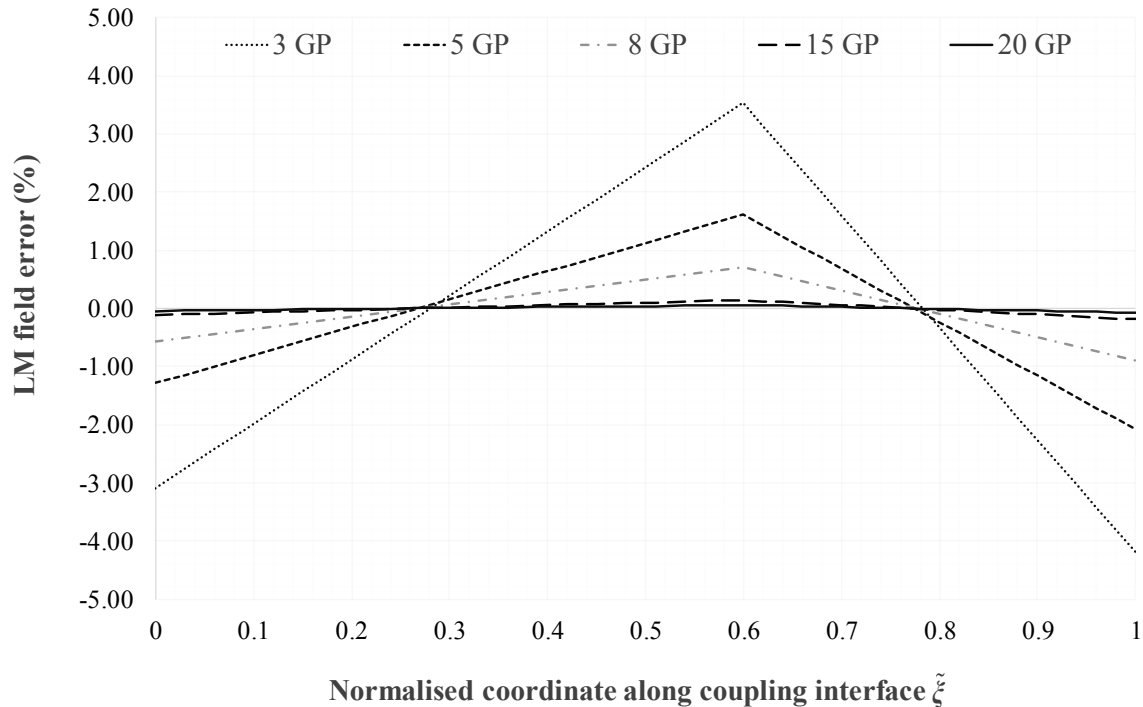


Figure 5.13: Lagrangian Multiplier field error distribution with variable Gaussian quadrature order for patch variant R1S2

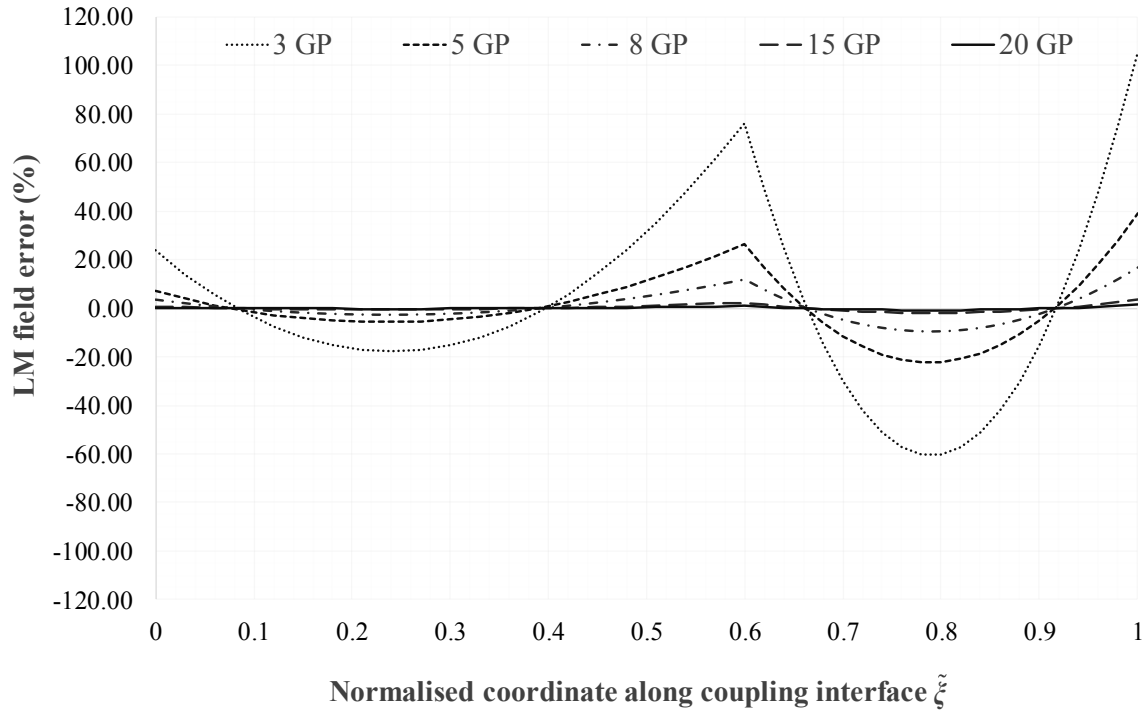


Figure 5.14: Lagrangian Multiplier field error distribution with variable Gaussian quadrature order for patch variant R1S3

The case of 2 GPs has not been considered, since it results into two of the three coupling elements being integrated with 1 GP, which does not allow for its direct comparison with the base-case patch variants with a quadrature order of two. It is evident from the graphs that the adoption of the segment-specific integration scheme at the element level leads to a significantly inferior approximation accuracy and convergence rate in comparison to element-specific integration, even for a high quadrature order. This is attributed in this case to the integrand functions of the force vector and the tangent stiffness matrix components associated with the master shell element 2A of coupling element (1A-2A) being piece-wise polynomial along CS1. Furthermore, the maximum error is significantly smaller for a given quadrature order in variant R1S2, as opposed to R1S3, dropping to 0.075% and 1.35% with 20 GPs, respectively.

The results of variants R1S2 and R1S3 are compared hereafter against those of variants R2S2 and R2S3, for the effect of the surface classification as slave and master on the segment-specific integration accuracy and convergence to be established. The obtained error distributions along the interface with variable quadrature order in the range of 3-20 GPs are illustrated in Figures 5.15 and 5.16 for variants R2S2 and R2S3, respectively. A comparison of the error distribution for variants R1S2 with R1E2, as well as for R1S3 with R1E3, are given in Figures 5.17 and 5.18, respectively.

The graphs of Figures 5.15 and 5.16 indicate an identical performance of patch variants R2S2 and R2S3 with R2E2 and R2E3, the latter of which have been proven to achieve the same level of accuracy and convergence rate with the base-case patch variants, as discussed in the preceding sub-section. The maximum observed error magnitude is 0.0007% and 0.0008% for piece-wise linear and quadratic LM fields, respectively, in both cases, which indicates the capability of R2S2 and R2S3 to achieve exact integration. This is due to the CSs when Surface 2 is selected as slave being coincident with the ISs with element-specific integration, as opposed to the case where Surface 1 is slave, where the integrand functions are defined as piece-wise polynomials along the CSs and thus cannot be integrated exactly .

Evidently, the coupling element performance is sensitive to the selection of the slave surface when segment-specific integration is employed, which can be partially alleviated by selecting the surface with the finer mesh of shell elements as slave. However, this integration scheme is unreliable in cases where the surface mesh densities are not considerably different. The convergence rate with increasing Gaussian quadrature order, for the variants with two and three CPs, is illustrated in Figures 5.19 and 5.20.

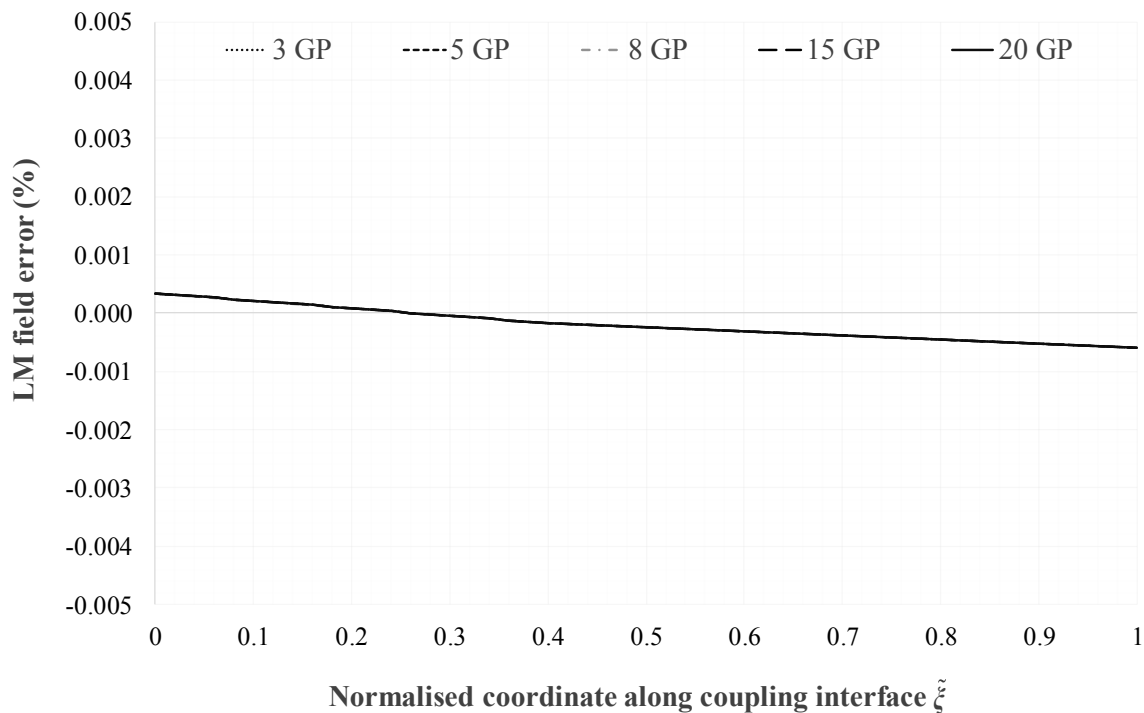


Figure 5.15: Lagrangian Multiplier field error distribution with variable Gaussian quadrature order for patch variant R2S2

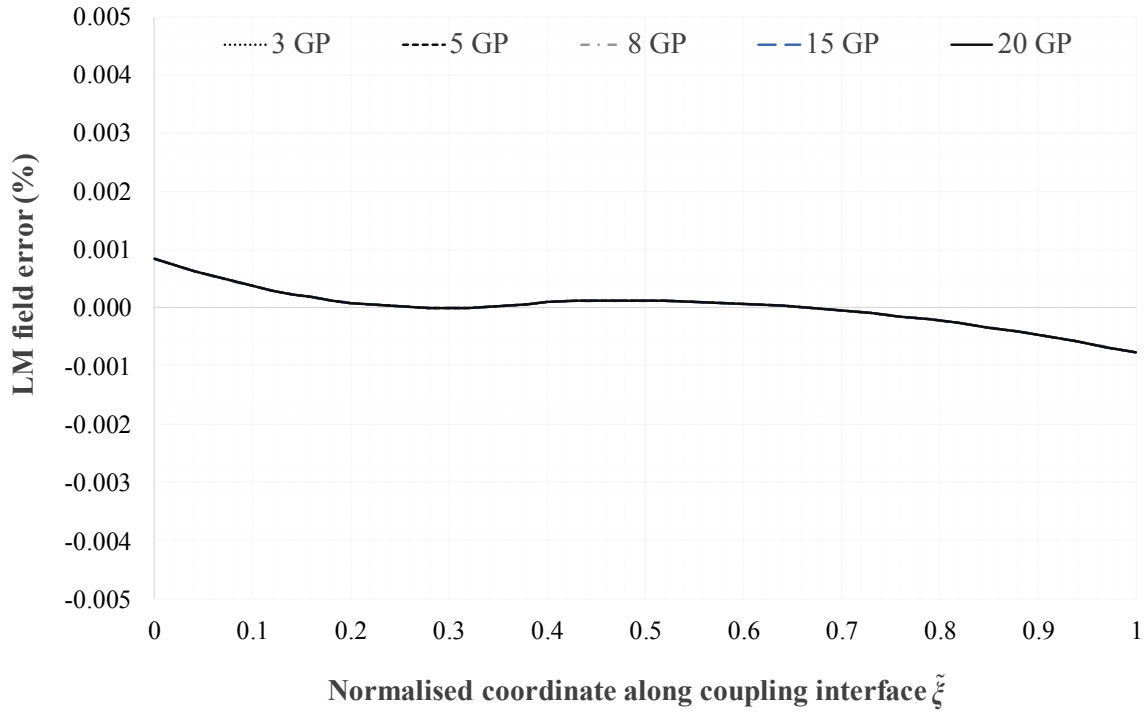


Figure 5.16: Lagrangian Multiplier field error distribution with variable Gaussian quadrature order for patch variant R2S3

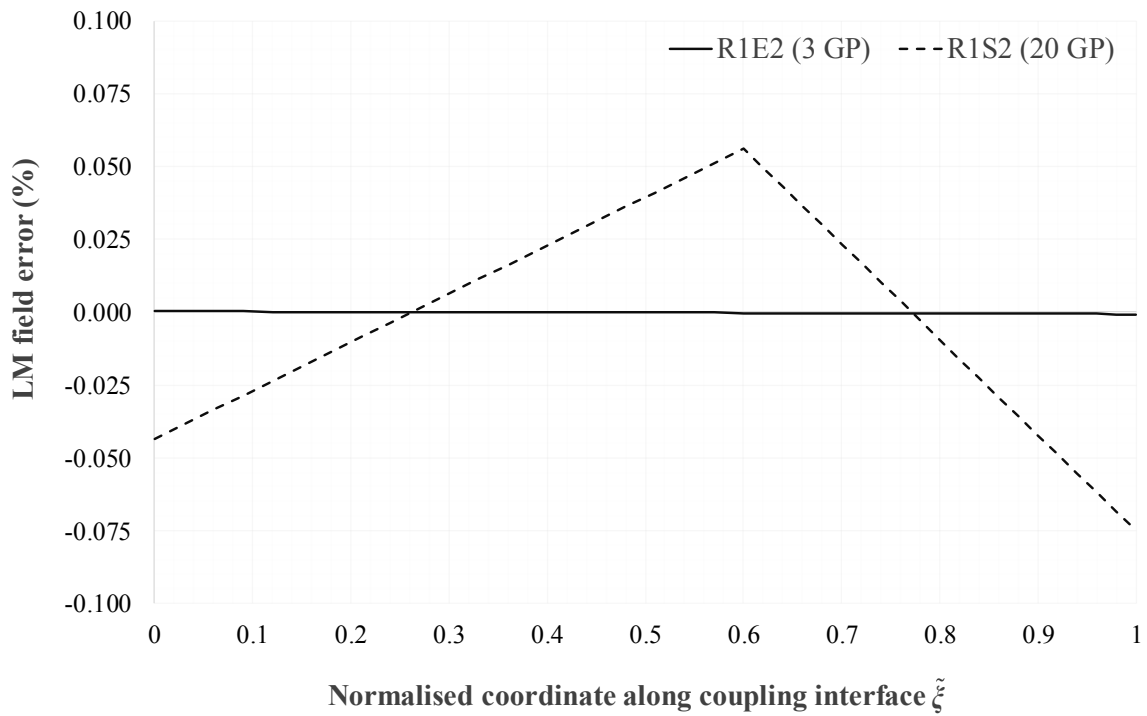


Figure 5.17: Lagrangian Multiplier field error distribution comparison for patch variants R1E2-R1S2

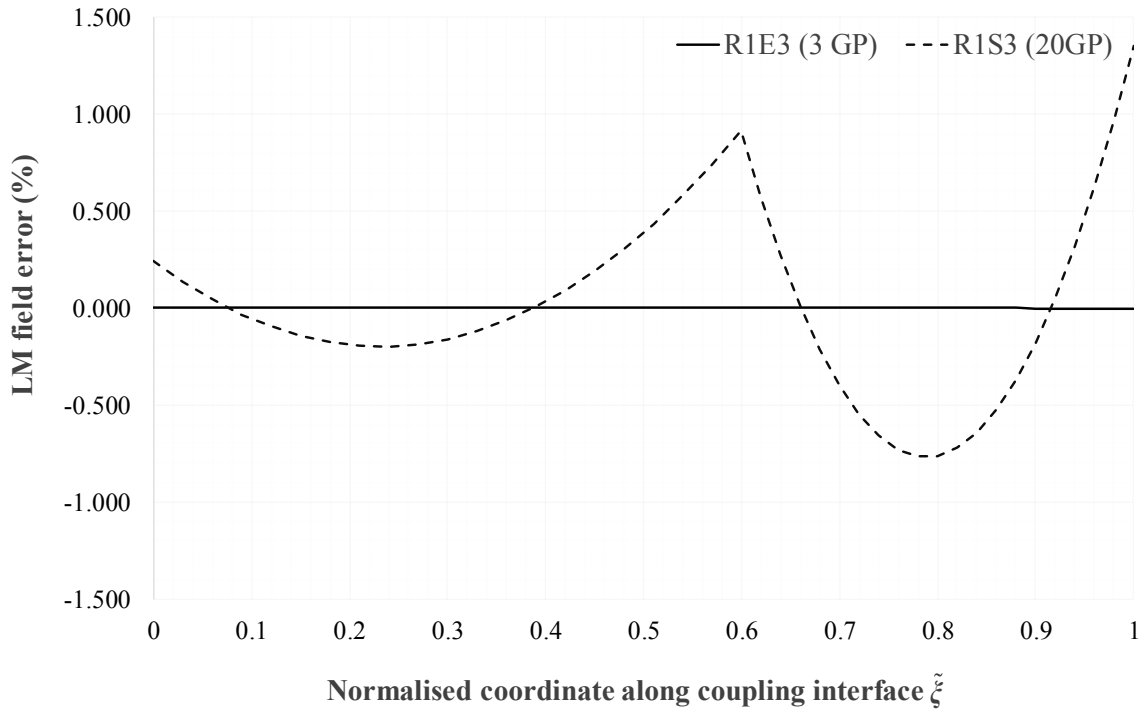


Figure 5.18: Lagrangian Multiplier field error distribution comparison for patch variants R1E3-R1S3

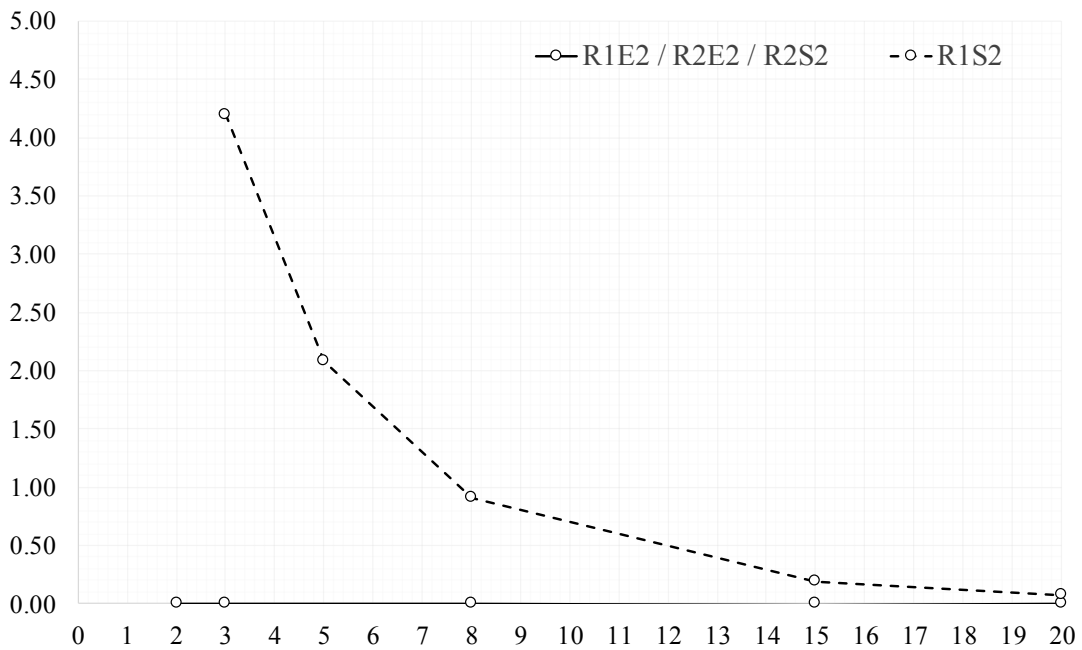


Figure 5.19: Convergence rate with increasing Gaussian quadrature order for patch variants R1E2/R2E2/R2S2 - R1S2

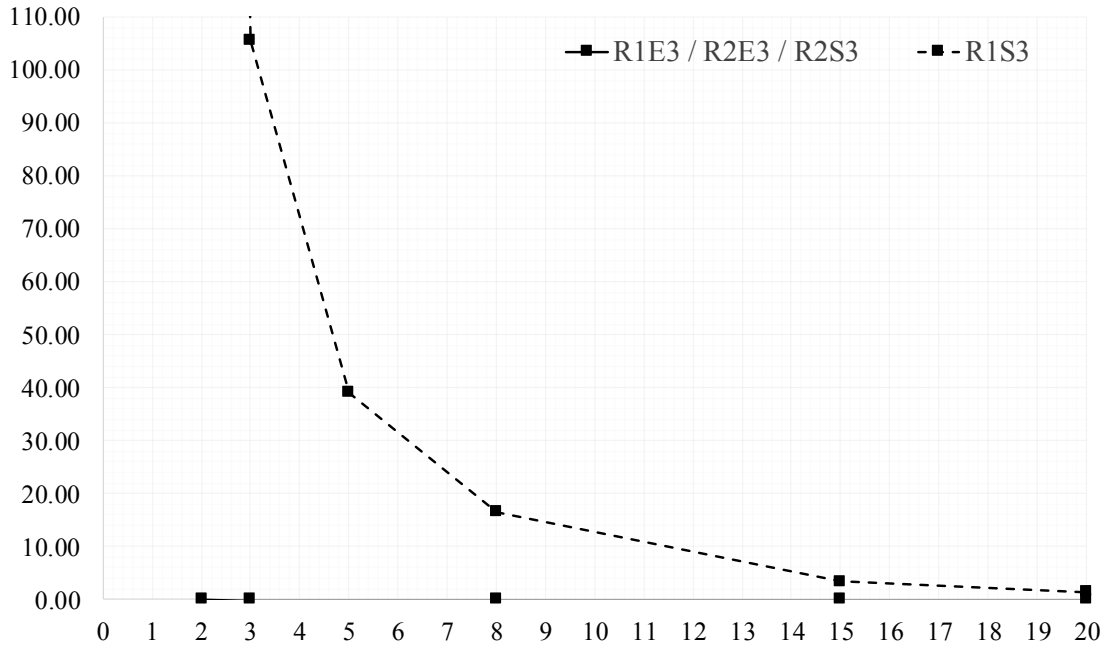


Figure 5.20: Convergence rate with increasing Gaussian quadrature order for patch variants R1E3/R2E3/R2S3 - R1S3

### 5.5.5.3 Influence of adopted penalty parameter values

The sensitivity of the base-case patch test results to the adopted translational and rotational coupling penalty parameter values is investigated here. The base-case patch variants R1E2 and R1E3 are considered for this purpose, and the specified values of the normalised coupling penalty parameters  $\varepsilon^* = \varepsilon/E$  and  $\varepsilon_R^* = \varepsilon_R/(Et^2)$  are varied within the range  $10^{-6}$  and  $10^{12}$ . The variation of the maximum obtained error magnitude in the LM field for the considered range of normalised coupling penalty parameters is illustrated in Figure 5.21, for both variants R1E2 and R1E3.

The graph of Figure 5.21 indicates an insensitivity of the coupling element performance to  $\varepsilon^*$  and  $\varepsilon_R^*$  within the range  $10^{-6}$  and  $10^6$ , with the maximum error magnitude of patch variant R1E2 slightly decreasing. For values greater than  $10^6$  the error is progressively increasing for both variants, becoming excessively large beyond  $10^{10}$ . This is attributed to the ill-conditioning

of the tangent stiffness matrix, resulting from it containing terms which are several orders of magnitude apart.

As discussed earlier, the penalty terms only contribute to the part of the coupling element tangent stiffness matrix associated with the kinematic DOFs of the coupled surfaces. The latter is subsequently assembled to the shell surface tangent stiffness matrix, for the constraint enforcement in a discrete sense along the interface, at the global system level. The terms of the shell surface tangent stiffness matrix are proportional to the Young's modulus  $E$  and depend on the surface thickness  $t$ . These parameters, therefore, provide an indication of the respective stiffness term order of magnitude. On the other hand, the order of magnitude of the coupling element tangent stiffness matrix terms associated with the kinematic DOFs of the coupled surfaces is governed by the selected values of the adopted penalty parameters  $\varepsilon$  and  $\varepsilon_R$ , and hence these are indicative of the condition number of the tangent stiffness matrix in a qualitative sense. For sufficiently large values of  $\varepsilon$  and  $\varepsilon_R$  the coupling element stiffness terms dominate over those of the shell surfaces, thus leading to ill-conditioning of the system tangent stiffness matrix, as well as to substantially inferior convergence characteristics. This is graphically illustrated in Figure 5.22.

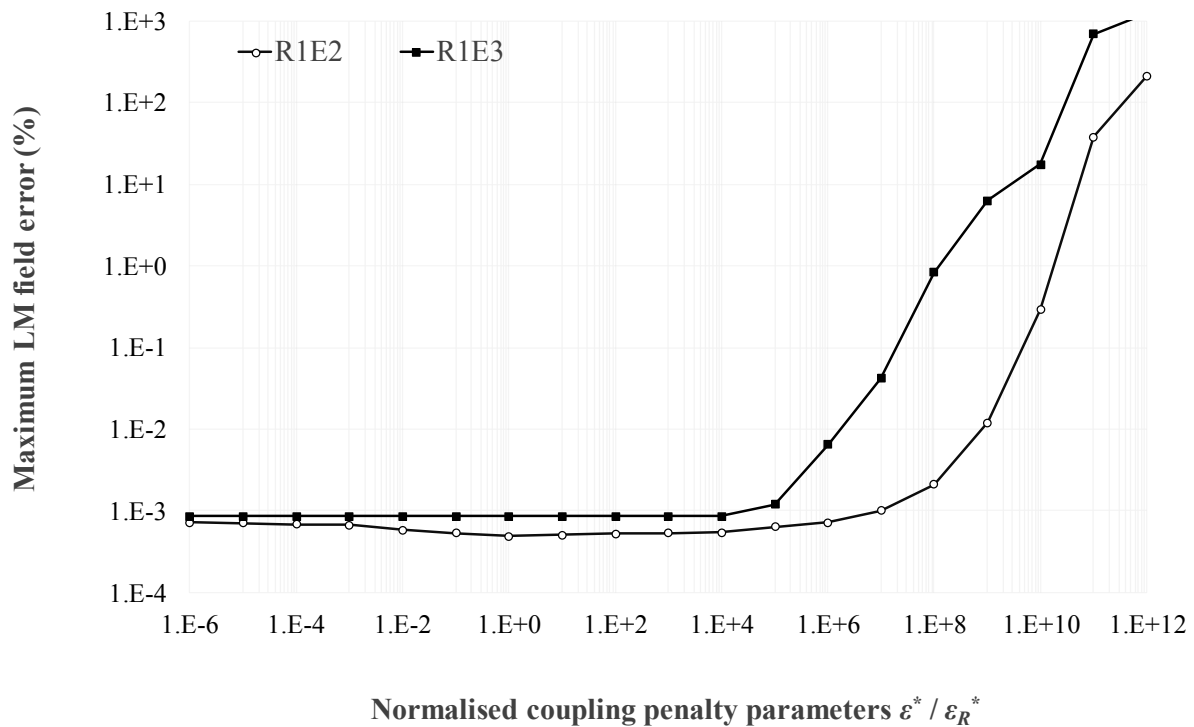


Figure 5.21: Maximum Lagrangian Multiplier field error variation with normalised translational and rotational coupling penalty parameters



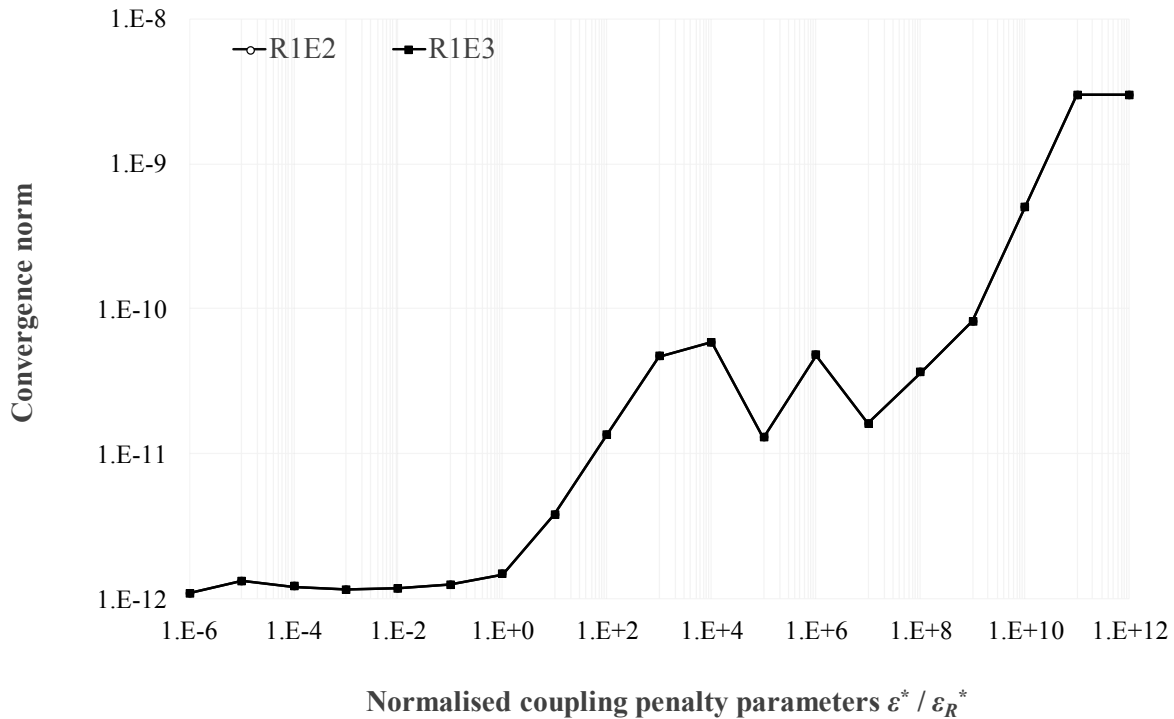


Figure 5.22: Convergence norm variation with normalised translational and rotational coupling penalty parameters

#### 5.5.5.4 Influence of shell element geometric irregularities

The sensitivity of the base-case patch test results to the geometric irregularities in the coupled surface shell element meshes is investigated here. Patch variants I1E2 and I1E3 are considered for this purpose, where the geometric irregularity is introduced by means of nodal dislocations on the edge shared between shell elements 2A and 2B.

In the general setting of a shell element mesh with irregular edges, the patch must represent the most general geometric configuration of a small part of the mesh, which is obtained as the result of a mesh refinement process. Taking this into consideration, the patch variants with irregular element geometry can be established by means of introducing a linear variation of nodal dislocations along the shared element edge of Surface 2, resulting in an inclined edge. This configuration can be considered representative of a mesh with curved shell element edges, which can be approximated as linear at the patch level. The geometric configuration of patch variants I1E2 and I1E3 is illustrated in Figure 5.23.

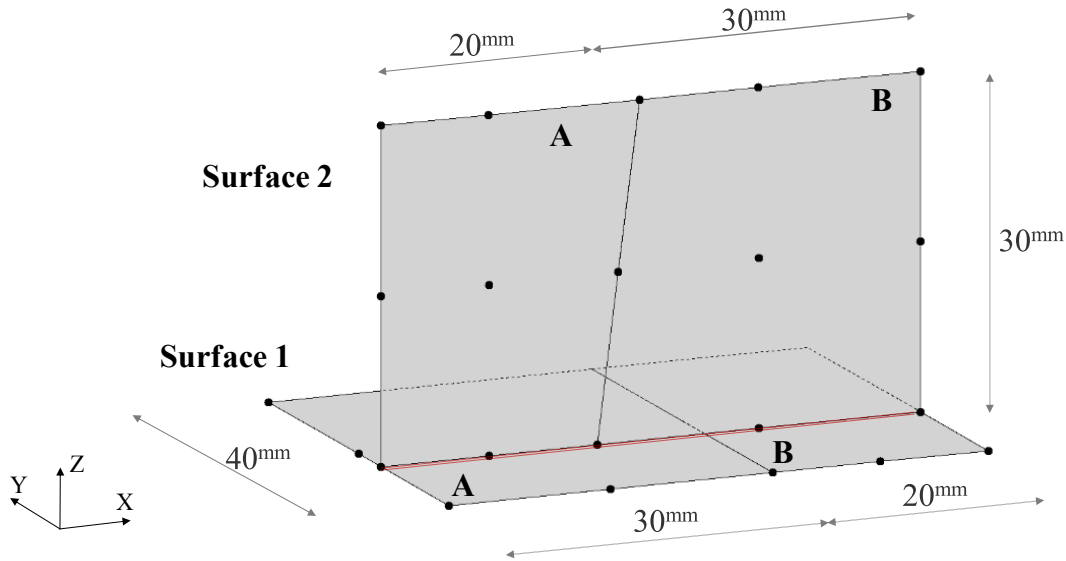


Figure 5.23: Coupling element patch geometric configuration with irregular element geometry

All rigid body mode patch tests are passed by the coupling element patch variants I1E2 and I1E3, while a variation of the obtained results is observed for the various types of constant force/moment patch tests. The planar shear and traction patch tests are both passed, with the element achieving an identical performance to that of the base-case-patch variants R1E2 and R1E3, illustrated in Figures 5.5 and 5.6, respectively. On the other hand, a performance deterioration is observed in the out-of-plane moment and shear-moment patch tests, with a considerable error introduced in the LM field approximation along the coupling interface.

The reason underlying the introduction of a greater error in patch tests associated with surface out-of-plane deformation, as opposed to those where the patch is subjected to planar loading, is the activation of the rotational coupling LM components in the former case. This is attributed to the adopted approach for rotational coupling, which does not achieve the same accuracy when discrepancies arise in the vector field variations with the introduction of geometric irregularities in the element geometry.

The ratio of the nodal dislocation to the characteristic shell element size can be employed for the quantification of the geometric irregularity magnitude, which can also be referred to as element distortion. Evidently, the error in the LM field increases for an increasing element distortion. Nevertheless, the element distortion reduces with mesh refinement, and hence, in the limit, the obtained error along the interface must converge to zero, due to the coupled shell element geometry becoming progressively more regular.

To establish the passing of the out-of-plane loading patch tests by the coupling element for irregular shell element geometry, the monotonic convergence of the LM field to the exact solution with mesh refinement should be verified. The patch mesh is only refined vertically, such that the number of coupled shell elements along the interface is maintained, and both these elements remain irregular with refinement, for the comparison of the obtained results to be feasible. The maximum error magnitude obtained along the interface for the LM field is plotted against the order of the mesh refinement processes in the graph of Figure 5.24, for both patch variants I1E2 and I1E3, and for an element distortion index of 5%. The refined patch mesh configuration in each case is illustrated in Figure 5.25.

The results in Figure 5.24 show a clear monotonic convergence to the exact solution with mesh refinement. This indicates that the patch test is not strictly passed with irregular elements, however mesh refinement leads effectively to regularisation and to the passing of the patch test.

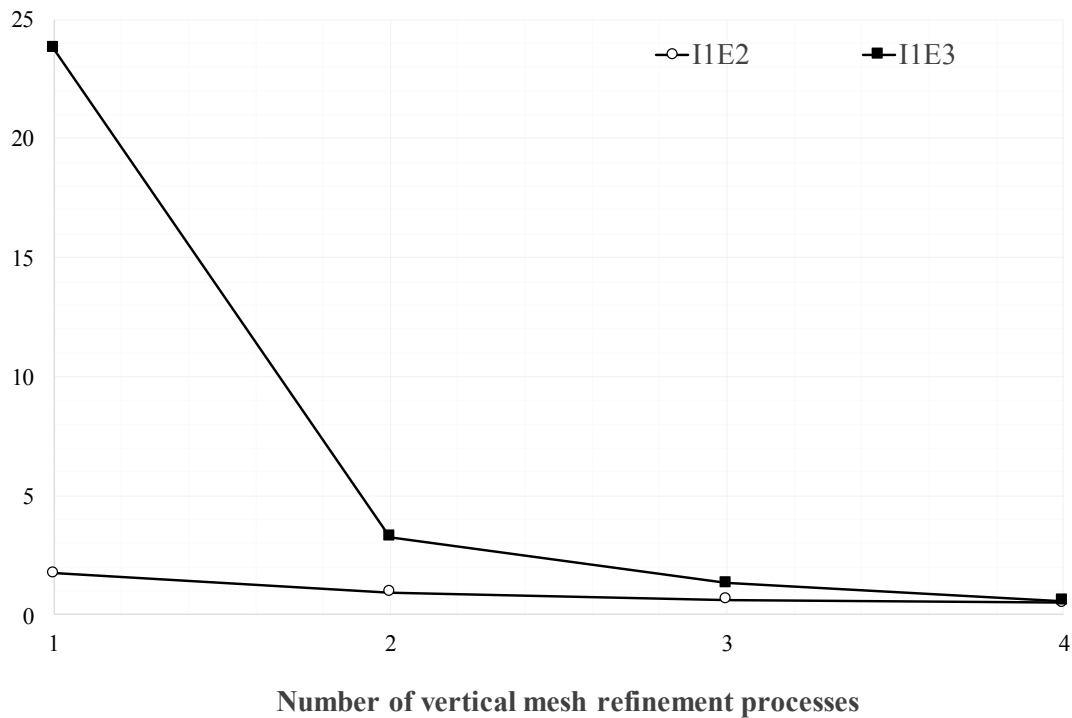
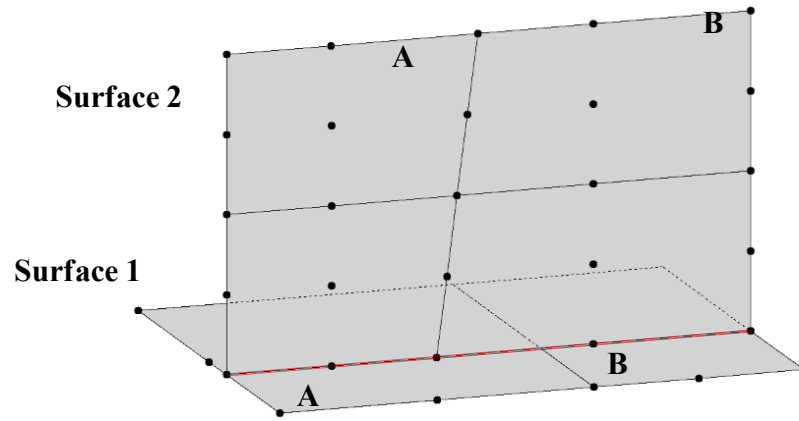
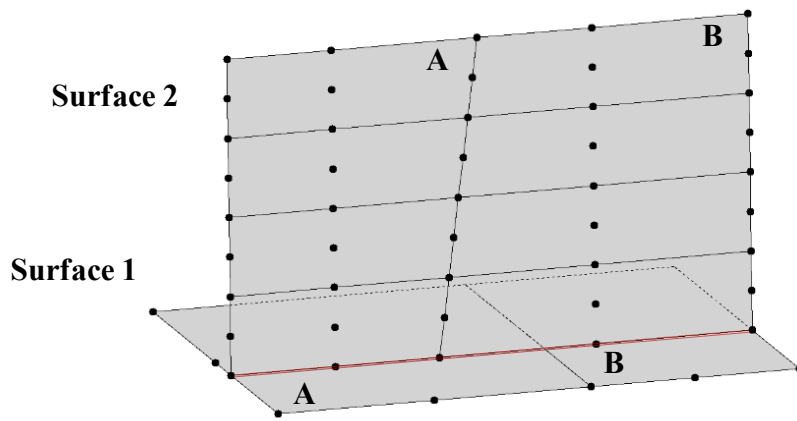


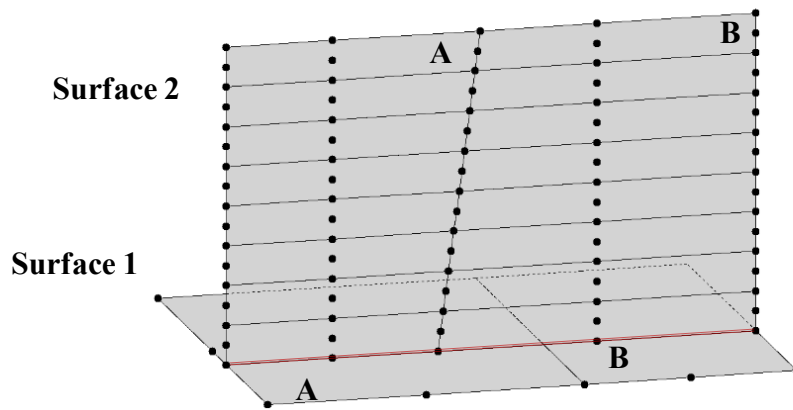
Figure 5.24: Convergence rate with increasing order of vertical mesh refinement for patch variants I1E2 and I1E3



(a)



(b)



(c)

Figure 5.25: Coupling element patch geometric configuration for irregular element geometry and different vertical mesh refinement order: (a) 2, (b) 3, (c) 4

## 5.6 Concluding remarks

Within the scope of the established systematic methodology for surface coupling along a line, presented in Chapter 4, translational and rotational coupling element formulations are proposed in this chapter, applicable to surfaces discretised with quadratic Reissner-Mindlin curved shell elements. Both formulations are developed using energy variational principles, enabling the determination of the coupling element internal force vector and tangent stiffness matrix associated with the individual sets of constraints along the interface. Translational coupling constraints enforce surface displacement compatibility along the interface in all three global directions, whereas rotational coupling is achieved by constraining the relative transverse slopes of the coupled surfaces. Accordingly, both coupling element formulations are expressed purely in terms of the global translational DOFs of the two surfaces and rotational DOFs are excluded. A set of rigid body and constant force/moment patch tests are conducted to verify the element ability of representing constant LM fields for different 1-D element patches, while satisfying interface compatibility conditions. The element passes all specified rigid body mode patch tests exactly and the constant force/moment patch tests with a maximum error in the LM field of less than 0.001% in its default *modus operandi*, where an element-based Gaussian quadrature integration scheme is adopted. A series of sensitivity analyses are further conducted to investigate the element performance sensitivity to a variety of parameters and algorithmic processes underpinning its formulation, and the main conclusions drawn are summarised hereafter: (i) the element performance is insensitive to the surface classification as master/slave; (ii) the element-based integration variant achieves exact integration, as opposed to the segment-based variant where the integrand functions are potentially piece-wise polynomial and thus cannot be integrated exactly, even with a large number of GPs; (iii) the element performance is generally insensitive to the selection of the penalty parameters, with excessively large values, nonetheless, leading to ill-conditioning of the tangent stiffness matrix and convergence failure; and (iv) the element performance deteriorates in the case of rotational coupling of geometrically irregular shell FEs, however monotonic convergence to the exact solution is still achieved with mesh refinement, and hence the element passes the respective patch tests for irregular shell FE geometries.

# Chapter 6

## 1-D Coupling Element Verification Studies

### 6.1 Introduction

The established high-fidelity (HF) nonlinear Finite Element (FE) modelling strategy presented in Chapter 3 is employed here in the context of a series of verification studies for the developed 1-D translational and rotational coupling element, the formulation of which was presented in Chapters 4 and 5. The selected studies aim to verify the ability of the coupling element to enforce effectively rigid kinematic constraints along a 1-D interface, between parallel or intersecting shell surfaces of arbitrary relative spatial orientation modelled with non-conforming meshes, taking due account of geometric and material nonlinearity. It is emphasised that, as discussed in Chapter 1, the term non-conforming is employed here to refer to non-matching coupled meshes with lack of nodal alignment along the coupling interface.

The passing of the set of patch tests, as elaborated in Section 5.5, confirms the ability of the coupling element to represent constant Lagrangian Multiplier (LM) force and moment fields along a 1-D interface, which is an essential requirement for convergence with mesh refinement. Herein, consideration is given to more complex plated and shell structural forms, with both developable and non-developable surfaces, coupled along a straight or curved interface, and discretised with regular or irregular shell elements. Particular focus is given to edgewise connected or intersecting planar, cylindrical and spherical shell surfaces, with the cases of folded plates, as well as mixed coupling of different surface types, being considered in the context of the larger-scale application study 5, presented in the next chapter.

Six verification studies are presented in this chapter, with the structural forms being investigated encompassing: (i) a rectangular planar plate, (ii) an L-frame, (iii) an annular plate, (iv) a cylindrical shell, (v) a hemispherical shell with a tip cut-off and (vi) and an imperfect I-beam. In each study, the deformed configuration, nonlinear equilibrium path and contour plots of the principal local shell FE generalised stress entities, obtained for the Coupled Mesh (CM) configuration from incremental nonlinear analyses, are compared against those of a monolithic model, henceforth referred to as the Base Mesh (BM). The latter corresponds to a standard mesh with the minimum employed level of discretisation detail determined by the denser of the coupled non-conforming meshes.

All verification studies are conducted using ADAPTIC (Izzuddin, 1991) v2.16.5, where the developed coupling element has been implemented. For the active coupling element identification along the 1-D interface in each case, the progressive segmentation algorithm presented in Section 4.5 with a slave-only approach is employed, considering the surface associated with the finest mesh as slave. At the coupling element level, a quadratic LM field interpolation using 3 Collocation Points (CPs) is adopted for all studies, with 4 LM entities introduced at each CP for the constraint enforcement, in accordance with the discussion in Section 4.4. The penalty parameters for both translational and rotational coupling are specified as 0.1, while the element-specific integration scheme presented in Sub-section 4.7.3.2 is employed, with a Gaussian quadrature order of 3.

## 6.2 Rectangular plate subjected to uniform stress states

A  $200 \times 100 \text{ mm}^2$  rectangular plate with a 1 mm thickness is considered in this study. A tri-linear elastoplastic material constitutive model is adopted, where the Young's modulus, Poisson's ratio and yield strength are specified as  $E = 210000 \text{ N/mm}^2$ ,  $\nu = 0.0$  and  $f_y = 355 \text{ N/mm}^2$ , respectively, and where strain-hardening is ignored.

The plate is represented with a coupled model CM-1, which comprises two  $100 \times 100 \text{ mm}^2$  plates coupled along a straight 1-D interface introduced at mid-length. The coarse and dense meshes comprise 4 and 64 9-noded shell FEs with regular edges, respectively. Similarly, a base model BM-1 is also employed which consists of a uniform mesh of 128 FEs, with an element

size equal to that of the finer mesh in CM-1. Configurations BM-1 and CM-1 are illustrated in Figure 6.1.

The plate is subjected to several displacement boundary conditions aimed at achieving uniform internal forces, as follows: (i) membrane forces along the global X-axis, (ii) planar shear forces along the planar global X- and Y-axes, (iii) bending moment about the global Y-axis, (iv) transverse shear forces along the global Z-axis, and (v) twisting moments about the global X- and Y-axes. The loading and boundary condition specifications for each of the aforementioned cases will be discussed in the following Sub-sections 6.2.1-6.2.5. It should be noted that the selection of a zero value for the Poisson's ratio  $\nu$  enables the elimination of anticlastic effects in the curvature-inducing load cases (iii) – (v) outlined above.

$$E = 210000 \text{ N/mm}^2$$

$$\nu = 0.0$$

$$f_y = 355 \text{ N/mm}^2$$

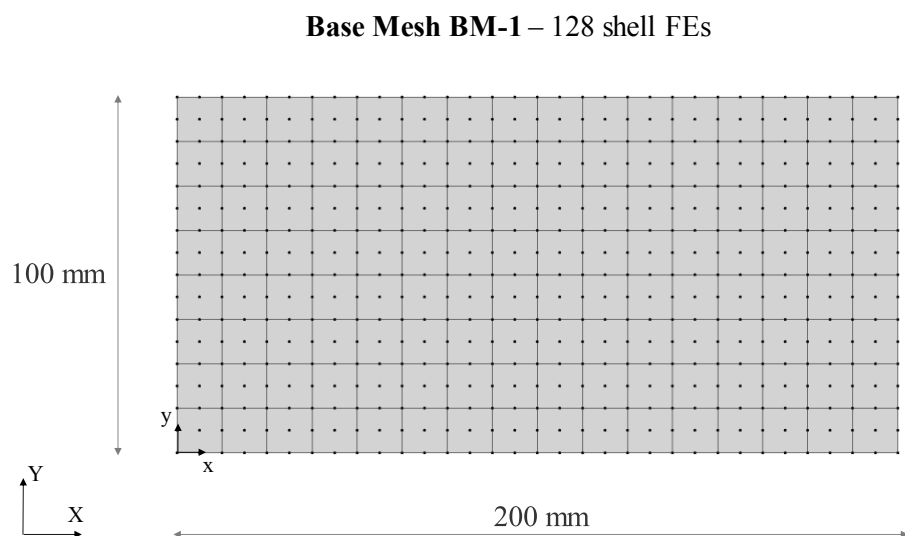
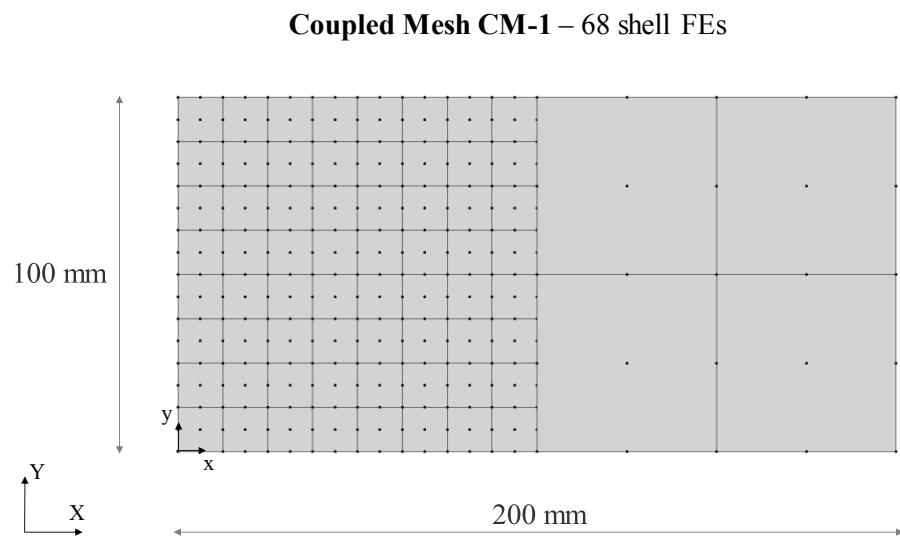


Figure 6.1: Geometric configuration, material properties and FE meshes for plate models CM-1 and BM-1



### 6.2.1 Uniform membrane force field

A uniform field of membrane forces is induced over the plate domain by applying a uniform unit displacement field  $d_{\text{nom}} = 1 \text{ mm}$  at its right end in the global X direction and restraining all nodes along the left edge against translations in the X-direction. Minimum restraints along the Y-axis are further introduced at two nodes along the left and right edges for rigid body motion to be avoided. Configurations CM-1 and BM-1 are illustrated in Figure 6.2. The maximum value of the applied displacement field is specified as 3mm, which exceeds the yield displacement of 0.338 mm with a corresponding maximum membrane force value of 355 N/mm.

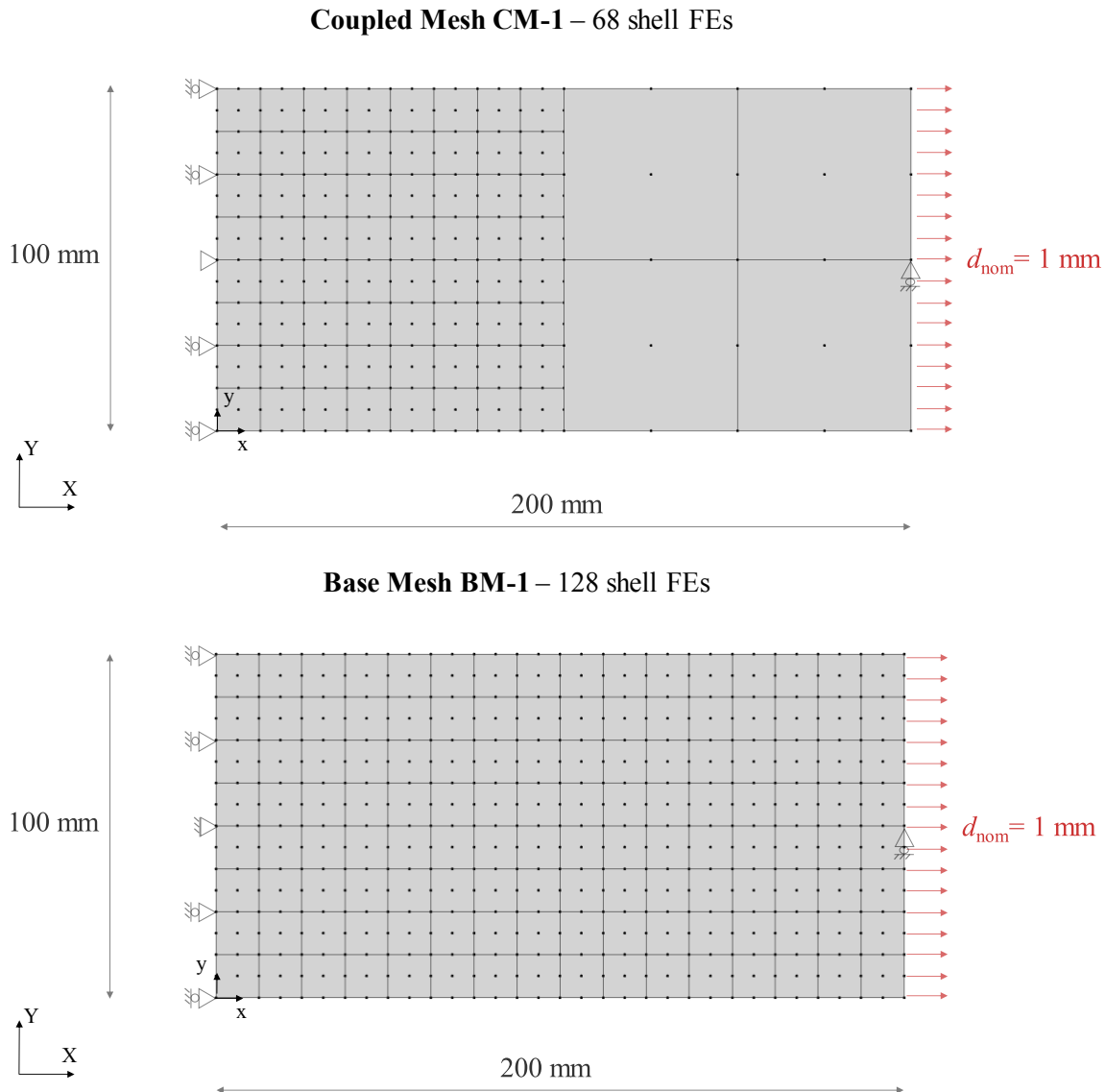


Figure 6.2: Geometric configuration, applied loading and boundary conditions for plate models CM-1 and BM-1

The plate deformed configuration, along with contour plots of the shell FE membrane force  $N_x$  generalised stress entity along the global X-axis, are provided in Figures 6.3 and 6.4, respectively. Identical nonlinear equilibrium paths for the translational Degree of Freedom (DOF) along the X-axis at the right plate edge nodes are obtained for the CM-1 and BM-1 models, as illustrated in Figure 6.5, where the load factor in the vertical graph axis is obtained by normalising the load with a nominal value of 355 N/mm.

As evident from the contour plots, the coupling element allows for a uniform membrane force field to be transferred exactly between the adjoining elements of the two coupled meshes in CM-1. This is achieved by means of a uniform LM force field along the interface in the X-direction, introduced to enforce the corresponding translational kinematic constraint.

The results of this study demonstrate the ability of the coupling element to transfer uniform force fields associated with translational constraints exactly, as will be also demonstrated in the following sub-section for a uniform planar shear loading.

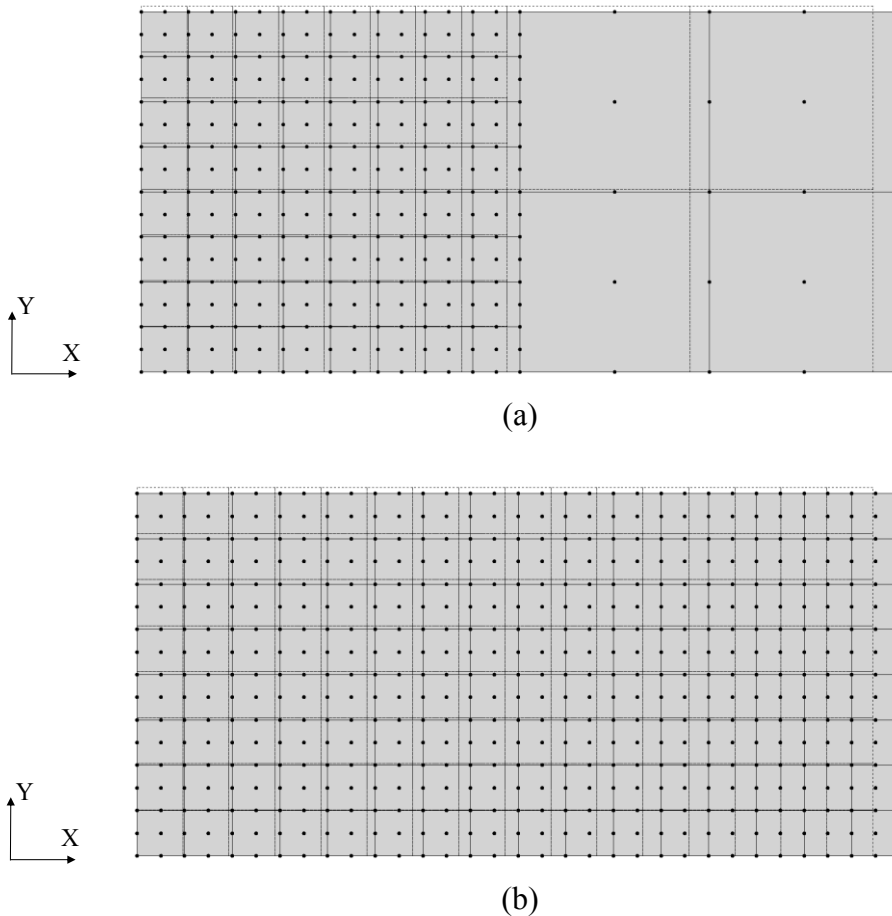


Figure 6.3: Deformed configuration at maximum displacement for plate models CM-1 (a) and BM-1 (b)

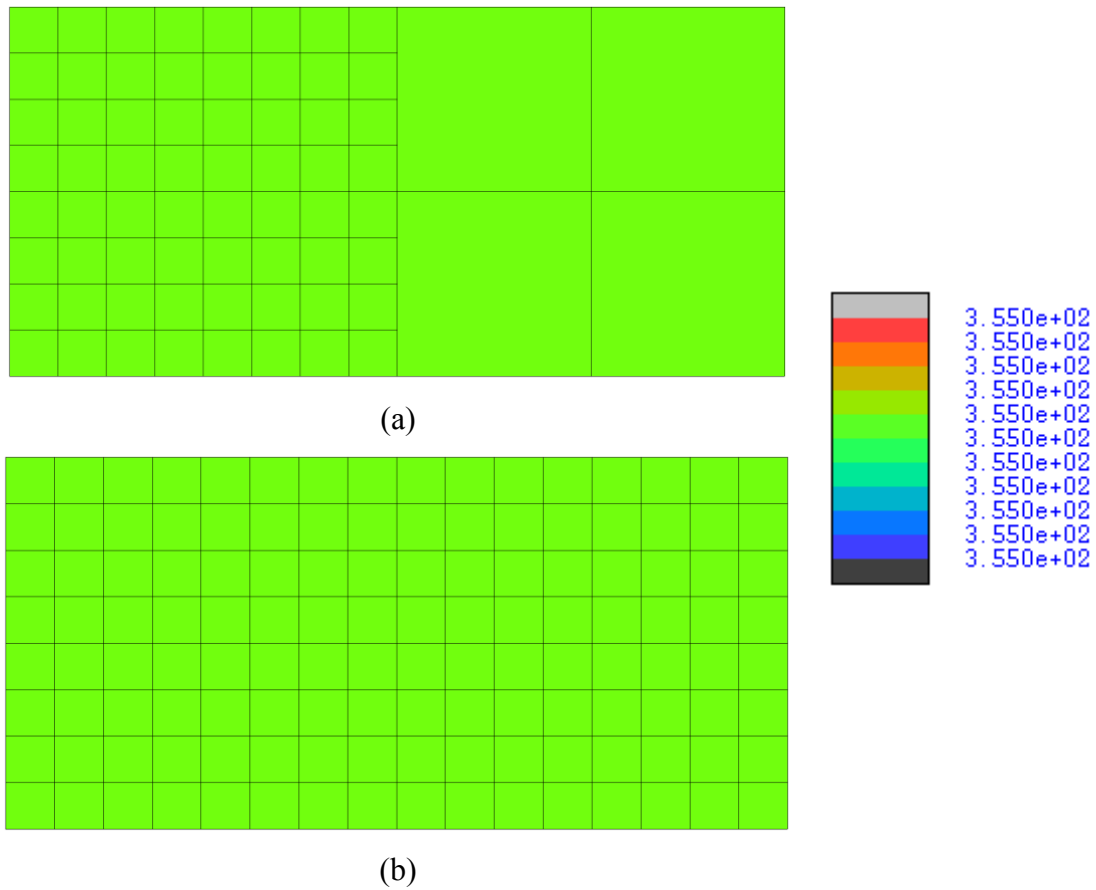


Figure 6.4: Contour plots of local shell FE membrane force  $N_x$  at first yield for plate models CM-1 (a) and BM-1 (b)

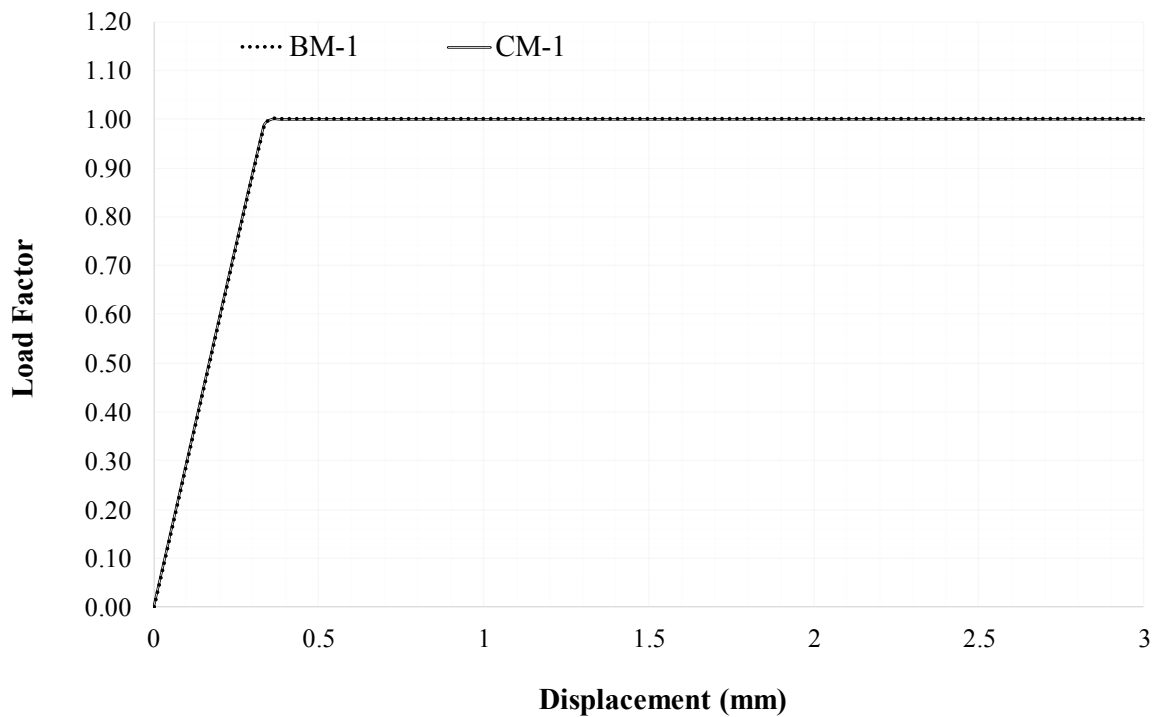


Figure 6.5: Nonlinear equilibrium path of translational DOF along the X-axis at right plate edge for plate models CM-1 and BM-1

### 6.2.2 Uniform planar shear force field

A uniform field of shear forces is induced over the plate domain by applying a uniform unit displacement field at its right end, alongside a linearly varying displacement field along its top and bottom edges, with values between 0 and 1 at their left and right ends, respectively, along the global Y-axis. All nodes along the left plate edge are restrained against translations in both the X- and Y-directions, while translational restraints in the X-direction are further introduced along the remaining three plate edges. Configurations CM-1 and BM-1 are illustrated in Figure 6.6. The maximum value of the applied displacement field is specified as 3mm, which exceeds the yield displacement of 0.390 mm with a corresponding maximum membrane force value of 205 N/mm.

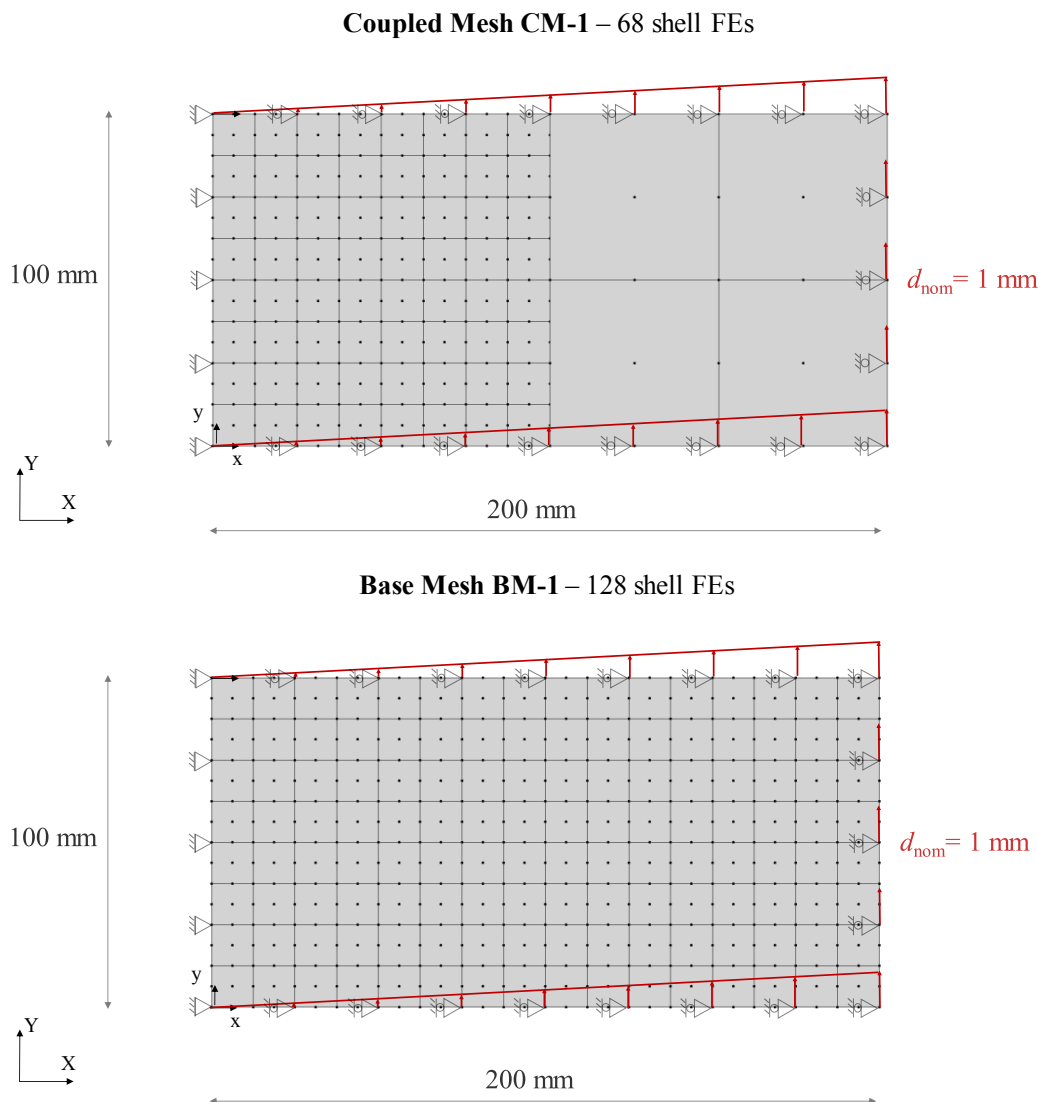


Figure 6.6: Geometric configuration, applied loading and boundary conditions for plate models CM-1 and BM-1

The deformed configuration and contour plots of the shell FE planar shear force  $N_{xy}$  generalised stress entity are provided in Figures 6.7 and 6.8, respectively. Identical nonlinear equilibrium paths for the displacement along the Y-axis at the right plate edge nodes are obtained for the CM-1 and BM-1 models, as illustrated in Figure 6.9, where the load factor in the vertical graph axis is obtained by normalising the load with a nominal value of 205 N/mm.

As is evident from the contour plots of Figure 6.8, the coupling element allows for a uniform planar shear force field to be transferred exactly between the adjoining elements of the two coupled meshes in CM-1. Similar to the case of membrane loading discussed in the preceding sub-section, this is achieved by means of a uniform LM force field along the interface in the Y-direction, introduced to enforce the corresponding translational kinematic constraint. The results of this study demonstrate the ability of the coupling element to transfer uniform force fields associated with translational constraints exactly.

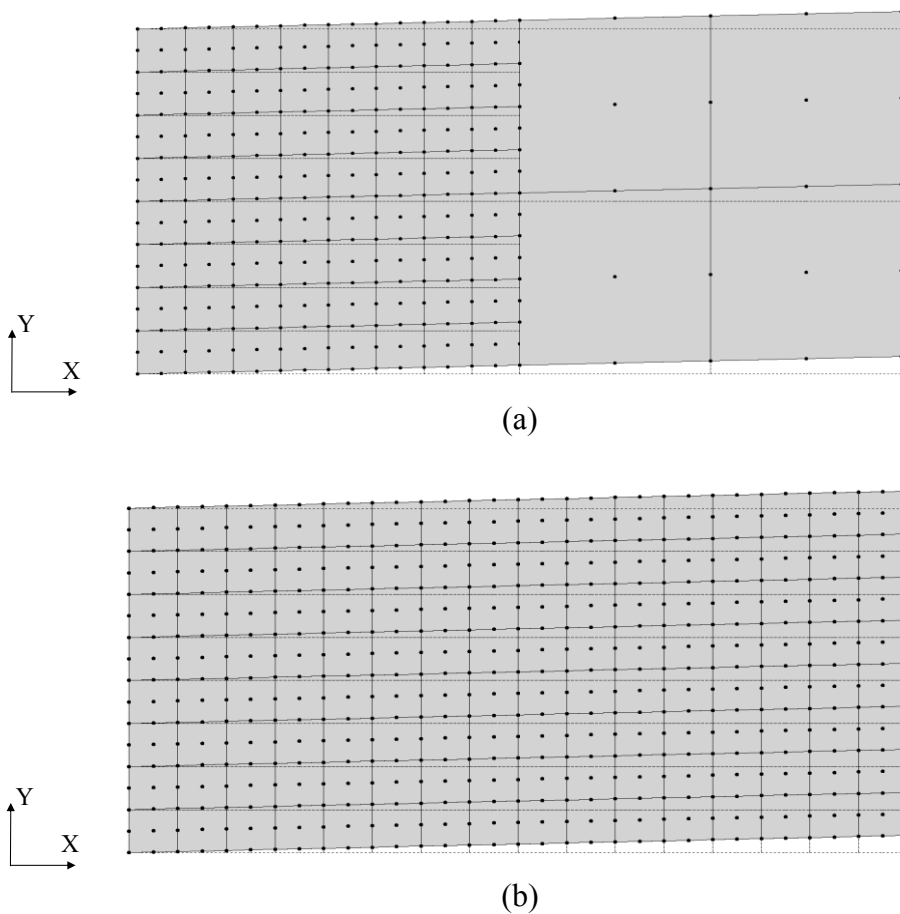


Figure 6.7: Deformed configuration at maximum displacement for plate models CM-1 (a) and BM-1 (b)

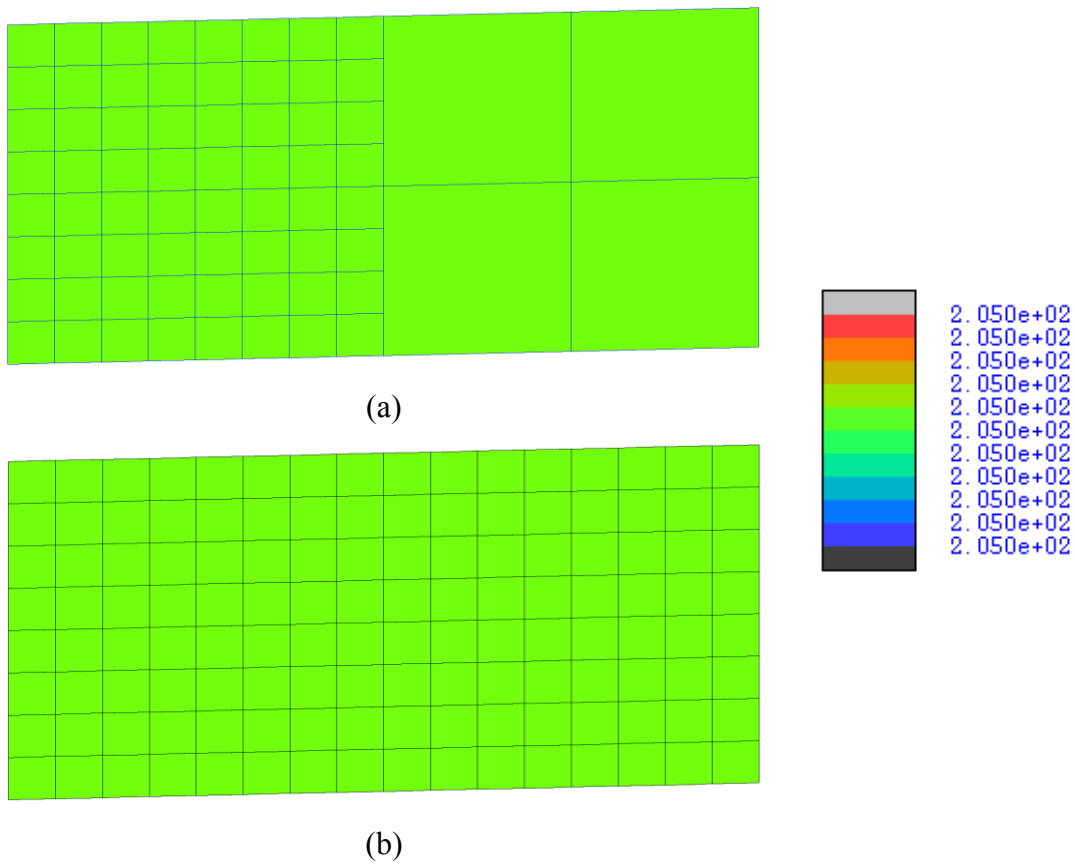


Figure 6.8: Contour plot of local shell FE planar shear force  $N_{xy}$  at maximum displacement for plate models CM-1 (a) and BM-1 (b)

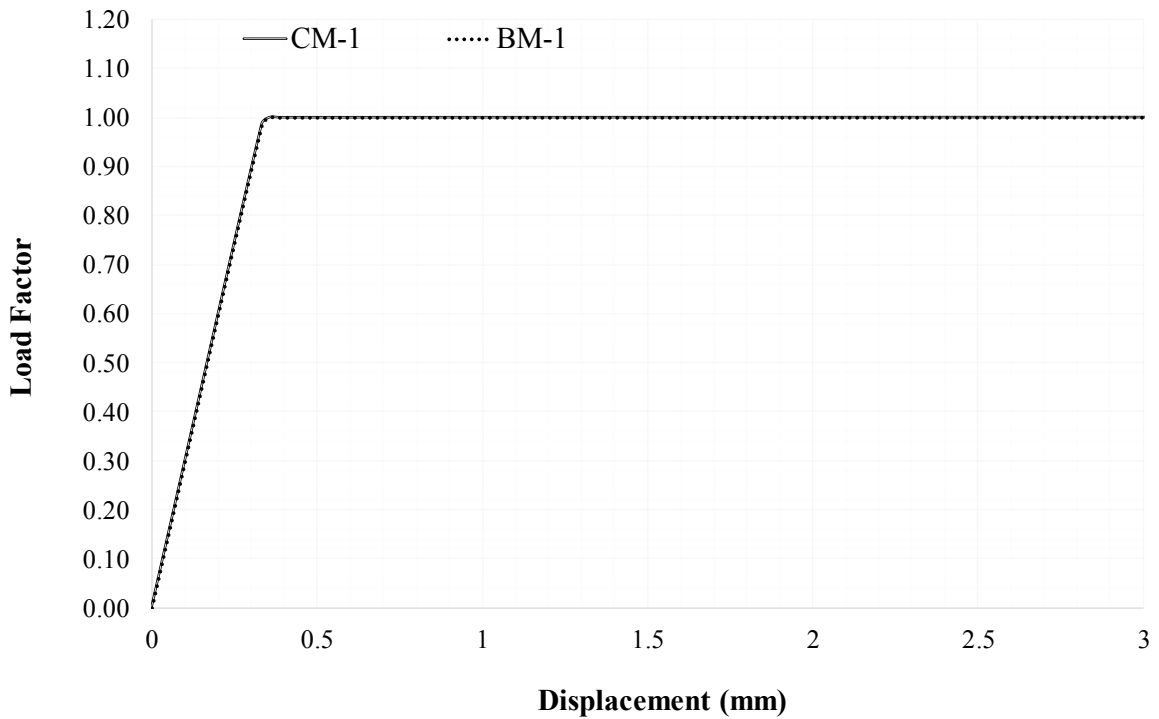


Figure 6.9: Nonlinear equilibrium path of translational DOF along the Y-axis at right plate edge for plate models CM-1 and BM-1

### 6.2.3 Uniform transverse bending moment field

A uniform transverse bending moment field is induced over the plate domain by applying a uniform unit rotational field along its right edge, alongside a linearly varying rotational field along its top and bottom edges with values between 0 and 1 at their left and right ends, respectively, about the global Y-axis. All nodes along the left plate edge are restrained against out-of-plane translations in the Z-direction and rotations about the Y-direction, while minimum translational restraints in the X- and Y-directions are further introduced on two of these nodes for rigid body motion to be avoided. Configurations CM-1 and BM-1 are illustrated in Figure 6.10. The maximum value of the applied rotational field is specified as  $\theta_{\max} = 6$  rad, which exceeds the yield rotation  $\theta_{\text{yield}} = 0.68$  rad.

The plate deformed configuration at the initiation of yielding, as well as at maximum rotation, are illustrated in Figure 6.11. The contour plots of the shell FE bending moment  $M_x$  about the global Y-axis, as well as of the transverse shear force  $Q_{xz}$  about the global Z-axis, at the corresponding response states are provided in Figures 6.12 and 6.13, respectively. The nonlinear equilibrium paths for the rotation about the Y-axis at the right plate edge nodes for CM-1 and BM-1 models are illustrated in Figure 6.14. The load factor in the vertical graph axis is obtained by normalising the applied bending moment with a nominal value of 59.17 Nmm/mm, corresponding to the yield bending moment.

The contour plots of Figures 6.12 (a) and 6.13 (a) demonstrate the principal mechanism of rotational constraint enforcement along the 1-D interface by the coupling element, which was discussed in detail in Section 5.3. This is based on coupling the orthogonal to the interface and tangent to the adjoining shell FE surface vector fields, which are expressed in terms of the respective global translational nodal DOFs in the deformed configuration. Thereupon, the introduced LM moment field required to achieve rotational coupling along the interface is transformed into a couple of equivalent nodal forces within each of the adjoining shell FE domains, along the global (X, Y, Z) Cartesian coordinate axes. This induces a set of transverse shear forces  $Q_{xz}$  in the adjoining elements, thus causing discontinuities in the respective distribution, as well as in the distribution of  $M_x$ , despite the plate being subjected to a constant curvature mode associated with zero shear throughout the domain.

A smoother distribution is obtained away from the adjoining shell FEs, which becomes virtually identical for both CM-1 and BM-1 at a sufficient distance, thus allowing for the correct

reaction forces and moments to be obtained at the supports and for equilibrium to be satisfied in a global sense. In moderate/large-scale structures discretised with relatively fine FE meshes, the effect of the discontinuities discussed above at the coupling interface vicinity becomes negligible, thereby allowing for an accurate response evaluation and internal force distribution approximation to be obtained at the global level. Moreover, the observed deviation of the nonlinear response in the range of very large displacements can be attributed to the approximation embedded in the coupling constraint enforcement, as well as to the employment of a coarser mesh in CM-1 leading to a stiffer response.

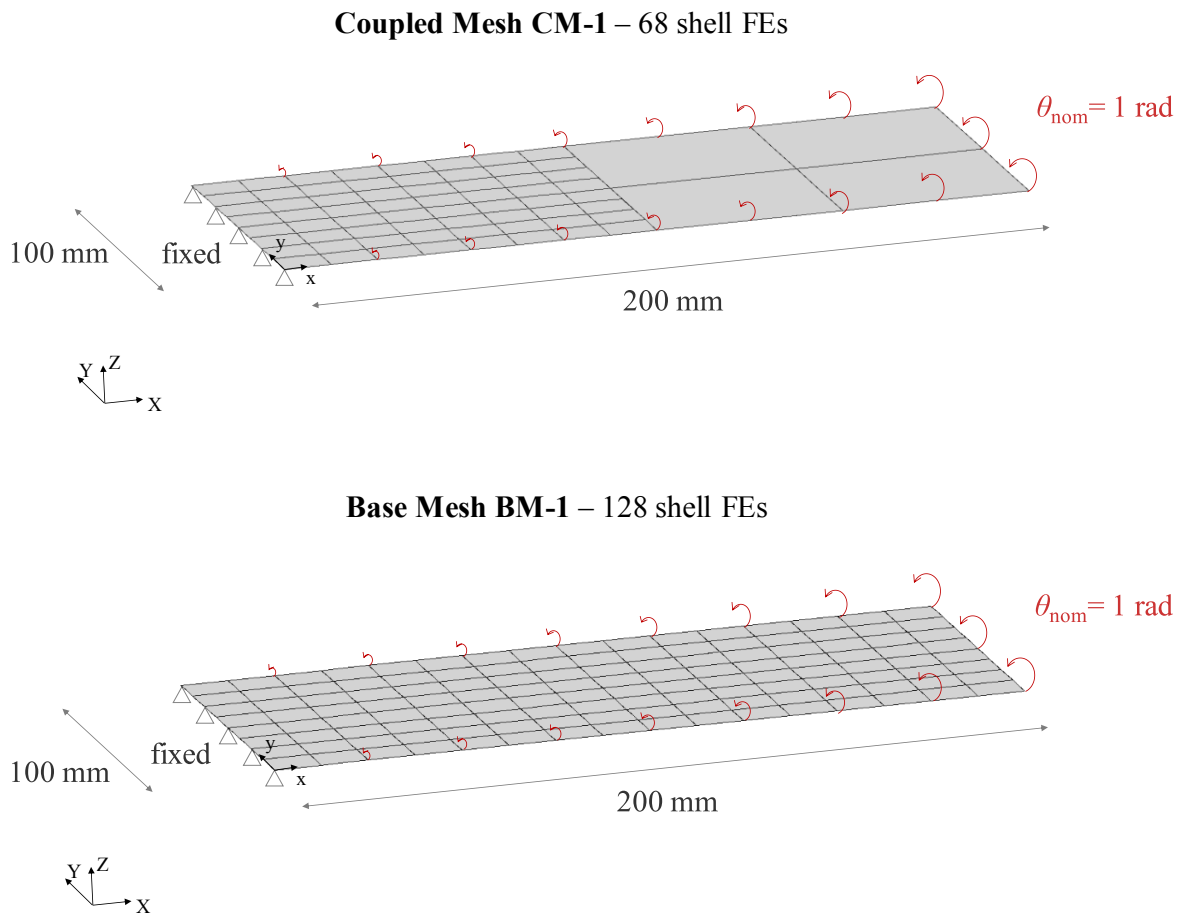
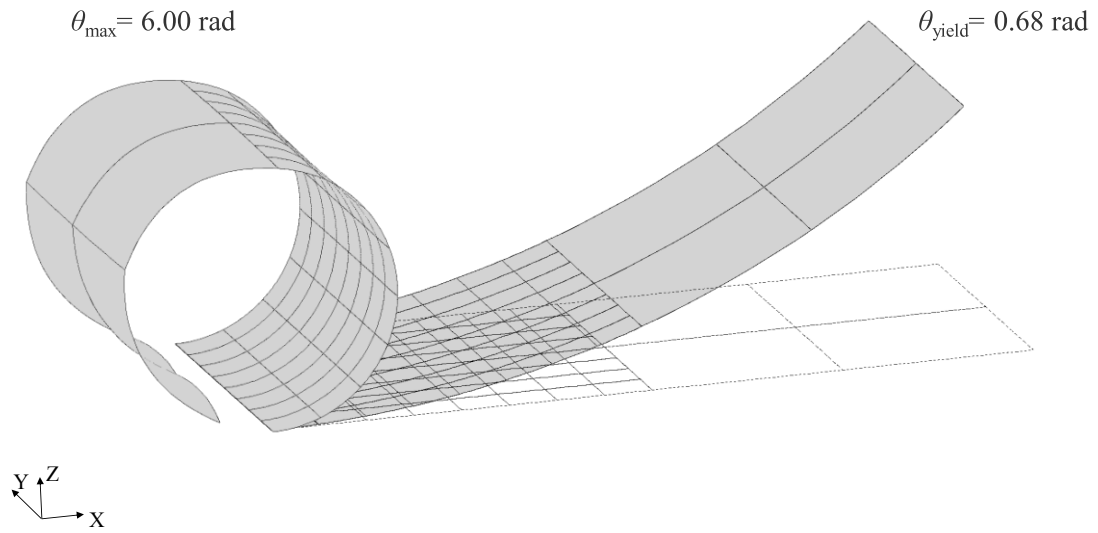
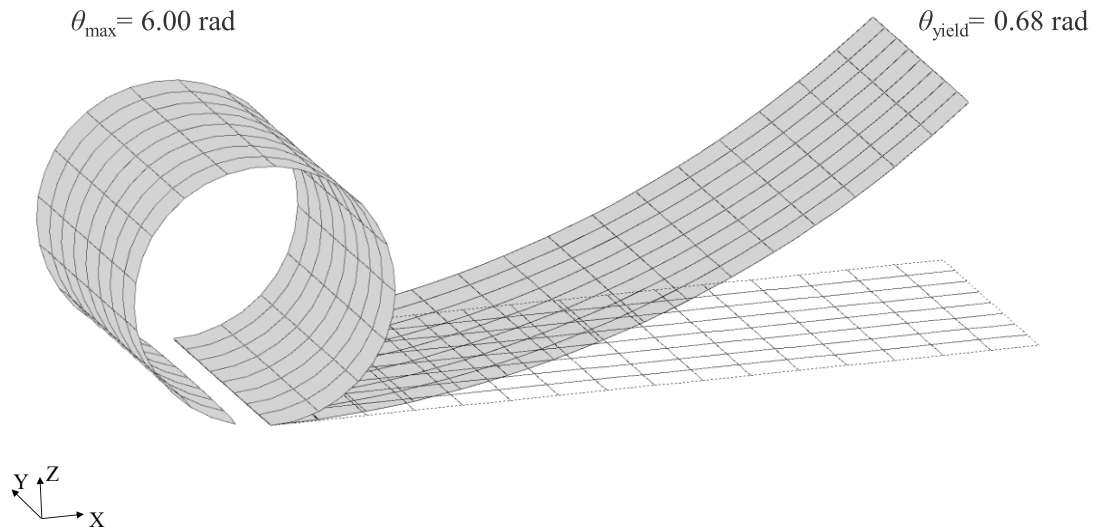


Figure 6.10: Geometric configuration, applied loading and boundary conditions for plate models CM-1 and BM-1





(a)



(b)

Figure 6.11: Deformed configuration at first yield and maximum rotation for plate models CM-1 (a) and BM-1 (b)

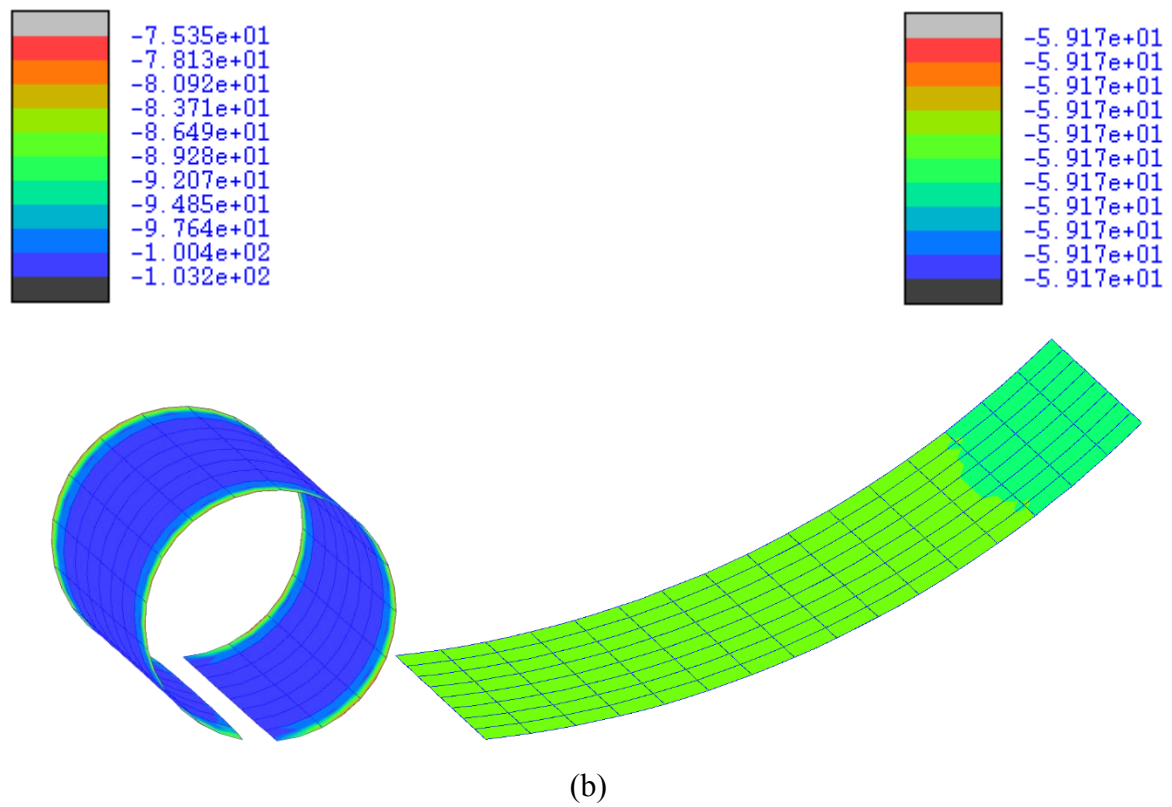
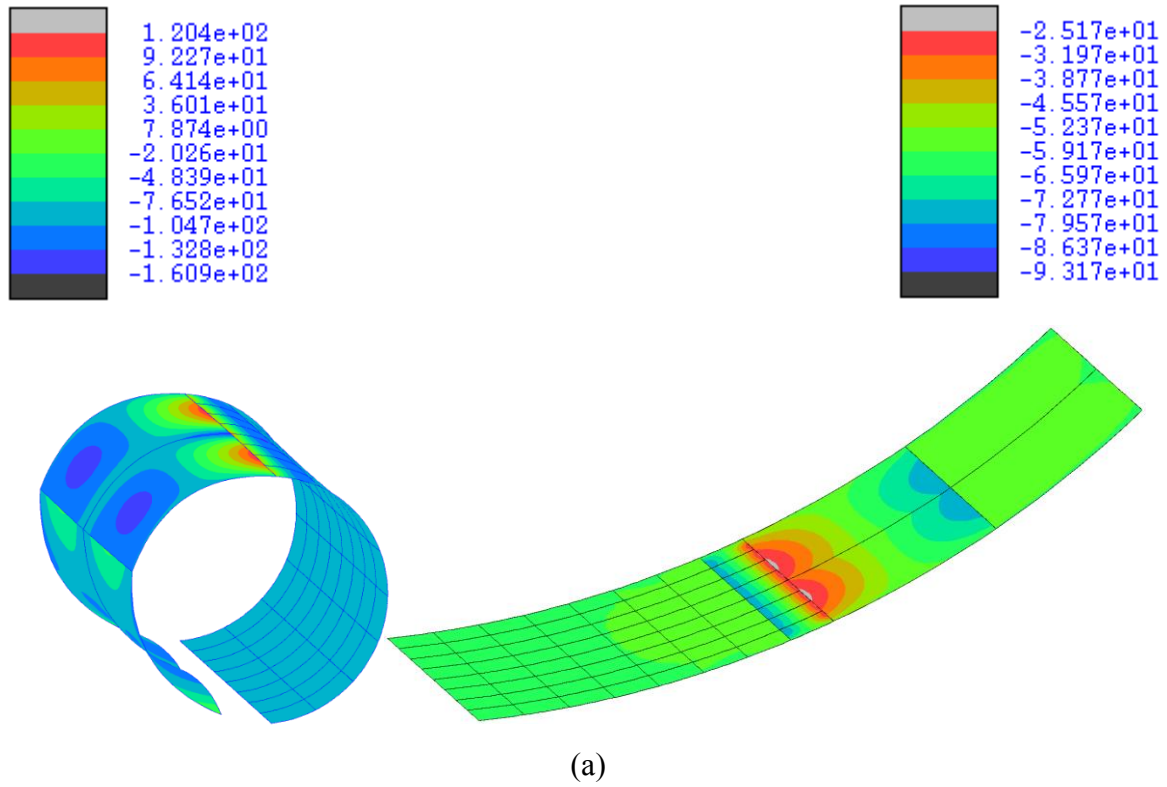


Figure 6.12: Contour plots of local shell FE bending moment  $M_x$  at first yield and maximum rotation for plate models CM-1 (a) and BM-1 (b)

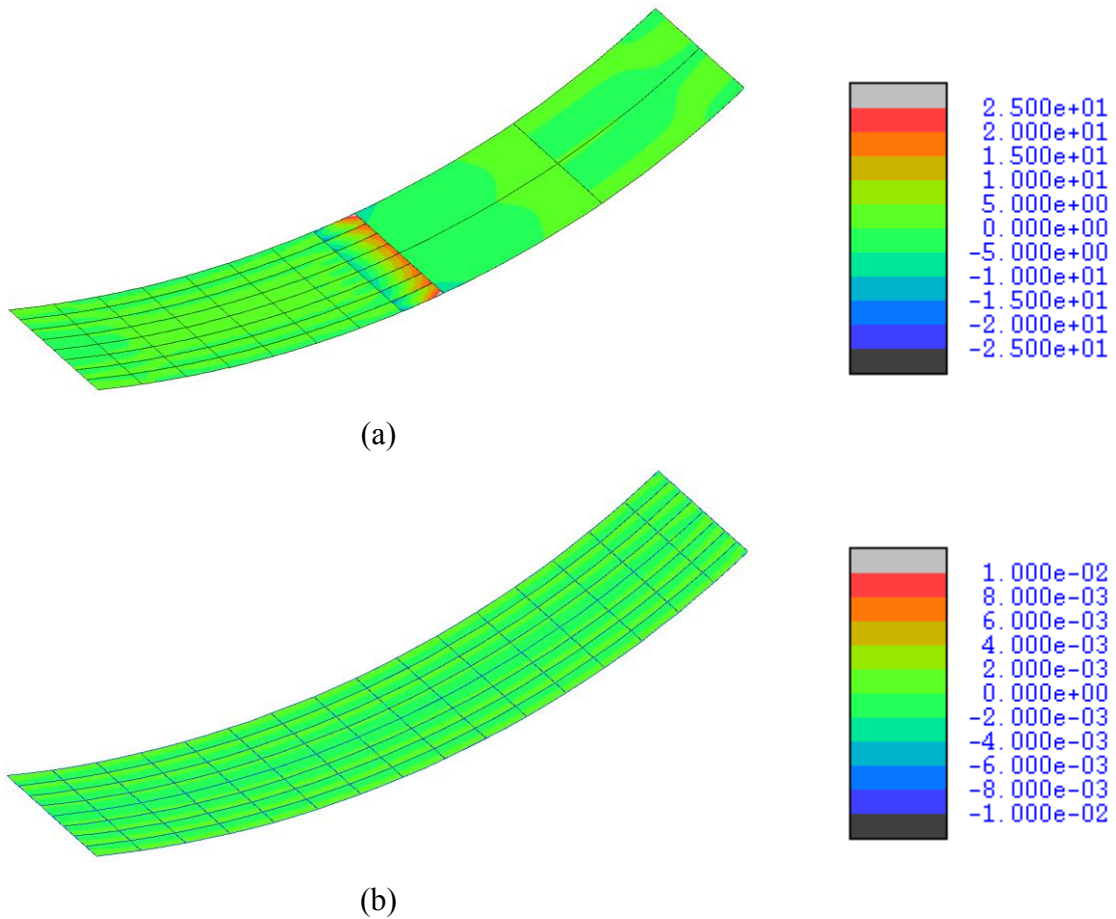


Figure 6.13: Contour plots of local shell FE transverse shear force  $Q_{xz}$  at first yield for plate models CM-1 (a) and BM-1 (b)

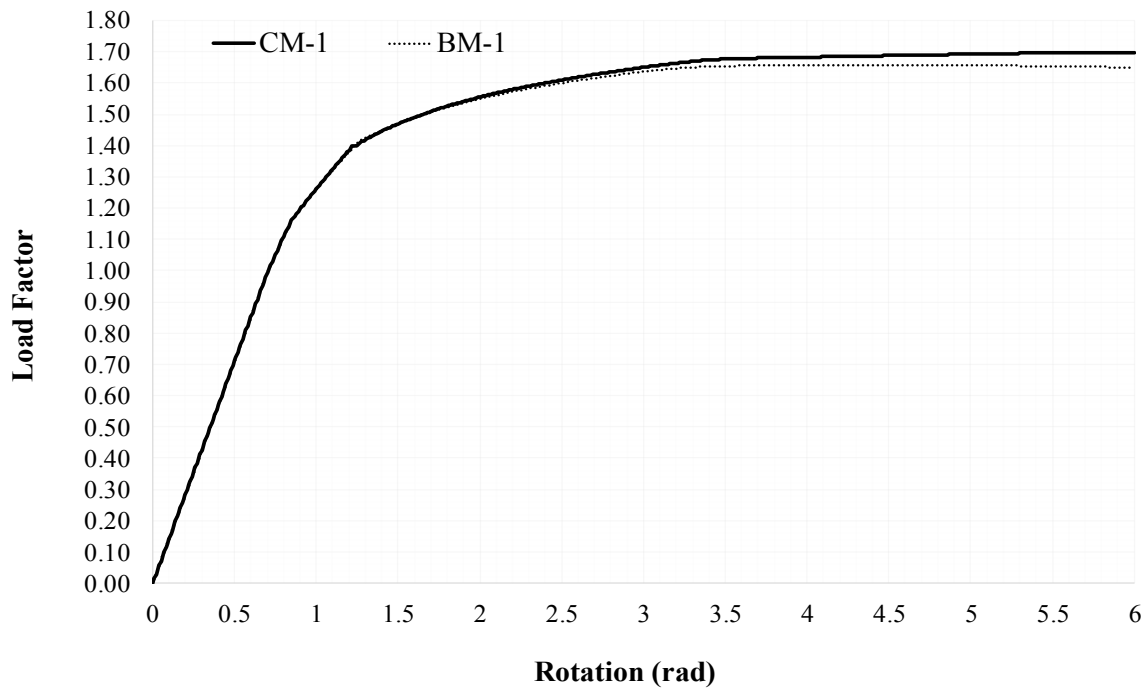


Figure 6.14: Nonlinear equilibrium path of rotational DOF about the Y-axis at right plate edge for plate models CM-1 and BM-1

### 6.2.4 Uniform transverse shear force field

A uniform transverse shear force field is induced over the plate domain by applying a uniform unit displacement field along its right edge along the global Z-axis. All nodes along the left plate edge are restrained against out-of-plane translations in the Z-direction and rotations about the Y-axis, while minimum translational restraints in the X- and Y-directions are further introduced on two of these nodes to avoid rigid body motion. Configurations CM-1 and BM-1 are illustrated in Figure 6.15. Naturally, the applied displacement field induces transverse bending about the global Y-axis, beyond shear, associated with a linear moment variation along the global X-axis. The maximum value of the applied displacement field is specified as  $d_{\max} = 200$  mm, which exceeds the yield displacement  $d_{\text{yield}} = 45$  mm. At first yield, the transverse shear force is constant over the plate domain and equal to 0.296 N/mm, while the corresponding yield bending moment is 59.17 Nmm/mm, similar to the preceding study.

The plate deformed configuration at the initiation of yielding, as well as at the maximum transverse displacement, are illustrated in Figure 6.16, while the contour plots of the shell FE transverse shear force  $Q_{xz}$ , bending moment  $M_x$  and membrane force  $N_x$  generalised stress entities at the corresponding response states are illustrated in Figures 6.17, 6.18 and 6.19, respectively. The nonlinear equilibrium paths for the translational DOF along the Z-axis at the right plate edge nodes for the CM-1 and BM-1 models are illustrated in Figure 6.20, where the load factor in the vertical graph axis is obtained by normalising the applied load with a nominal value of 0.296 N/mm.

Similar to the preceding study, subjecting the plate to a curvature inducing displacement field requires the enforcement of a rotational kinematic constraint along the interface, which is achieved by means of a couple of equivalent nodal forces introduced at the adjoining shell FEs. This is evident in the contour plots of all three  $Q_{xz}$ ,  $M_x$  and  $N_x$  entities of CM-1, shown in Figures 6.17 (a), 6.18 (a) and 6.19 (a), respectively, where discontinuities are observed at the interface vicinity.

In the range of moderate-large displacements, where the plate becomes progressively perpendicular to its undeformed configuration and the lever arm of the applied loading with respect to its restrained left edge reduces significantly, a transition between the principal load-transferring mechanism is exhibited. The bending and transverse shear principal load-transferring mechanisms in the range of small displacements progressively give place to a pure

membrane action mechanism, with virtually zero  $Q_{xz}$  and  $M_x$  over the plate domain. These only increase locally in the vicinity of the fully-formed plastic hinge adjacent to the left edge. The above transition becomes evident by virtue of comparison of the contour plots at the first yield and maximum displacement states.

The progressive load-transferring mechanism transition discussed above, alongside the associated reduction in the plate curvature in the range of large displacements, results in a transition in the kinematic constraint that the coupling element is called to enforce, which shifts from a rotational to a translational one. This study therefore further highlights the ability of the developed coupling element to achieve both forms of coupling in cases where either of the two constraints is eliminated, by means of the distinct allocated LM components for each constraint type, as earlier discussed in Section 4.4.

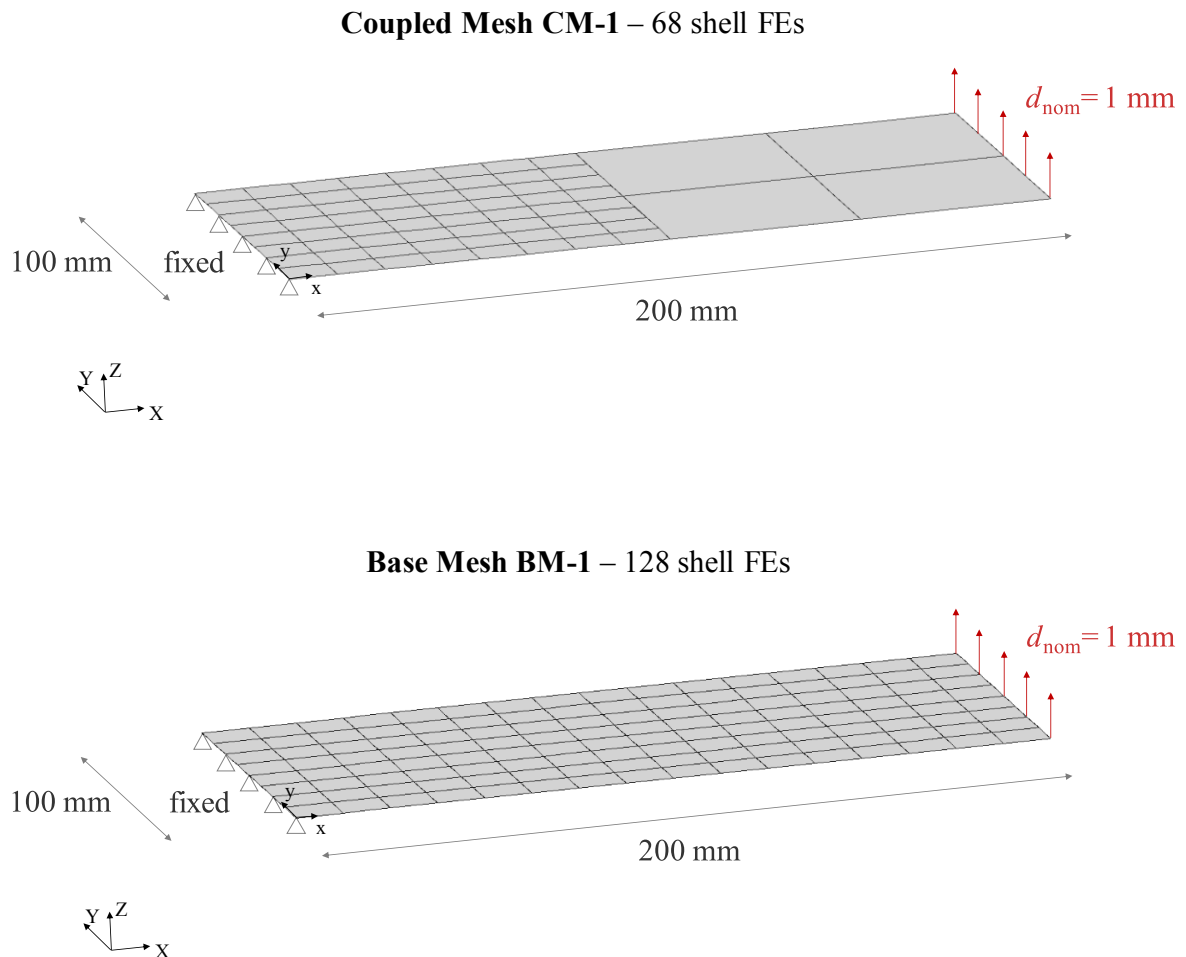
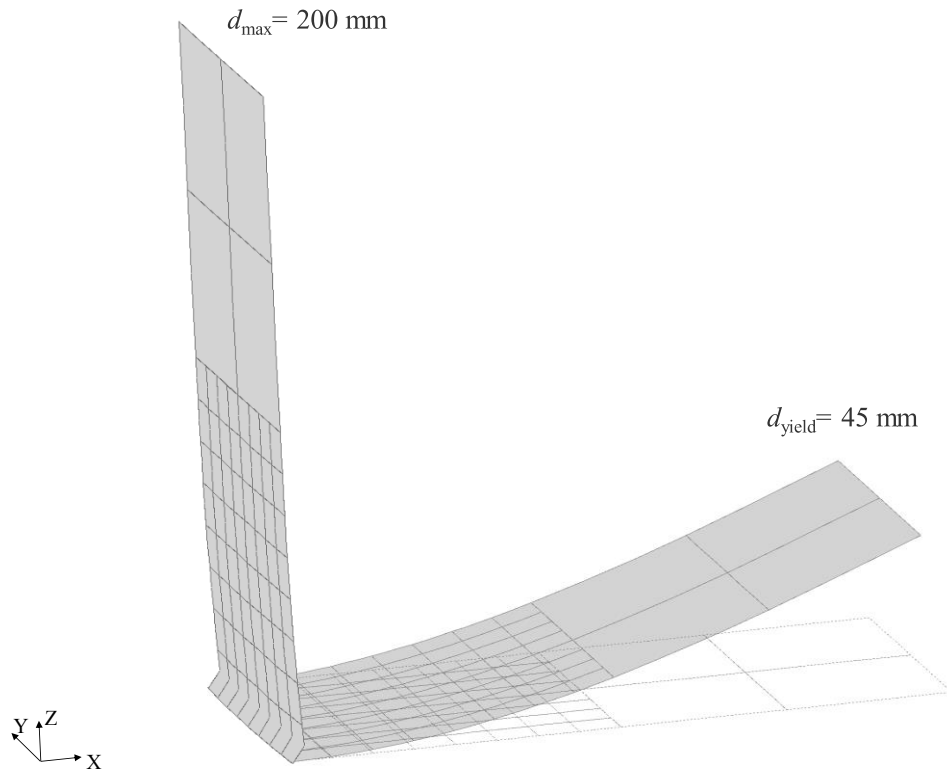
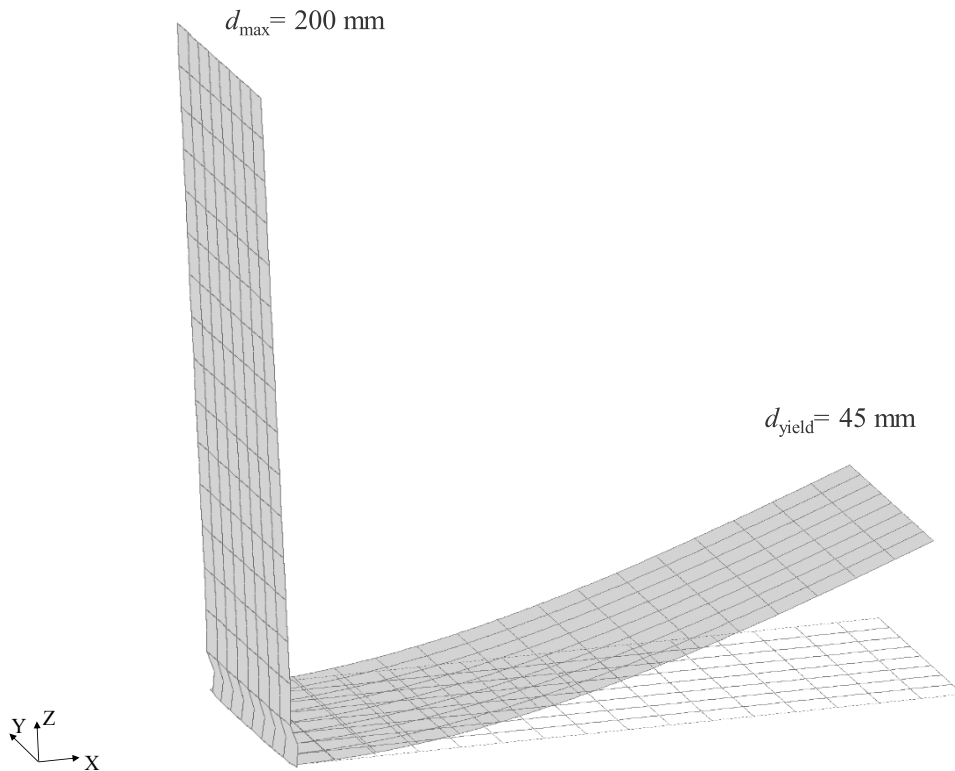


Figure 6.15: Geometric configuration, applied loading and boundary conditions for plate models CM-1 and BM-1

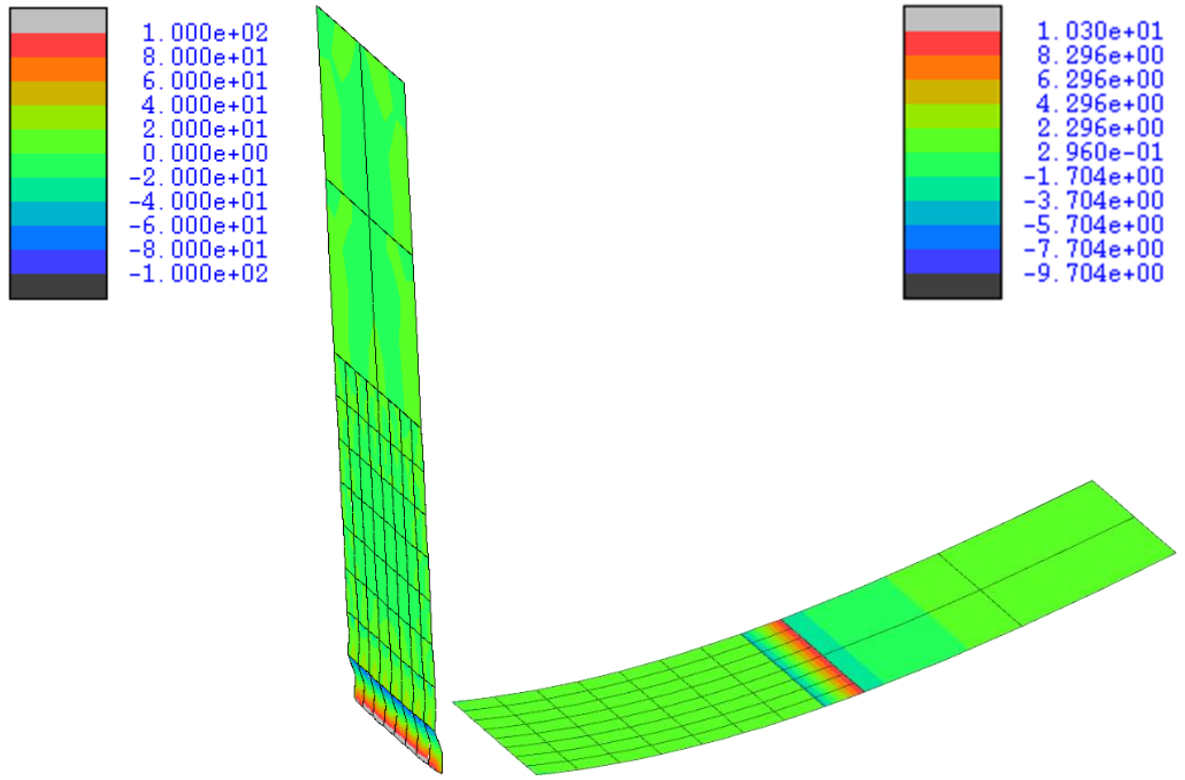


(a)

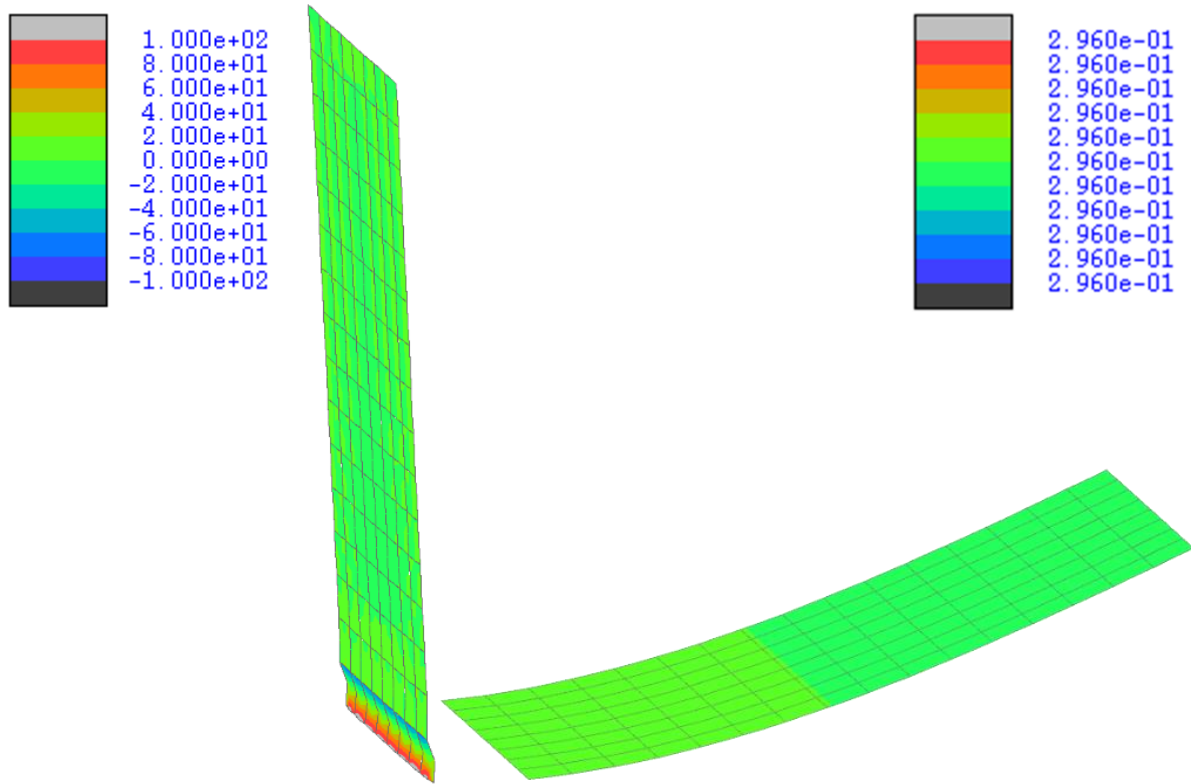


(b)

Figure 6.16: Deformed configuration at first yield and maximum displacement for plate models CM-1 (a) and BM-1 (b)

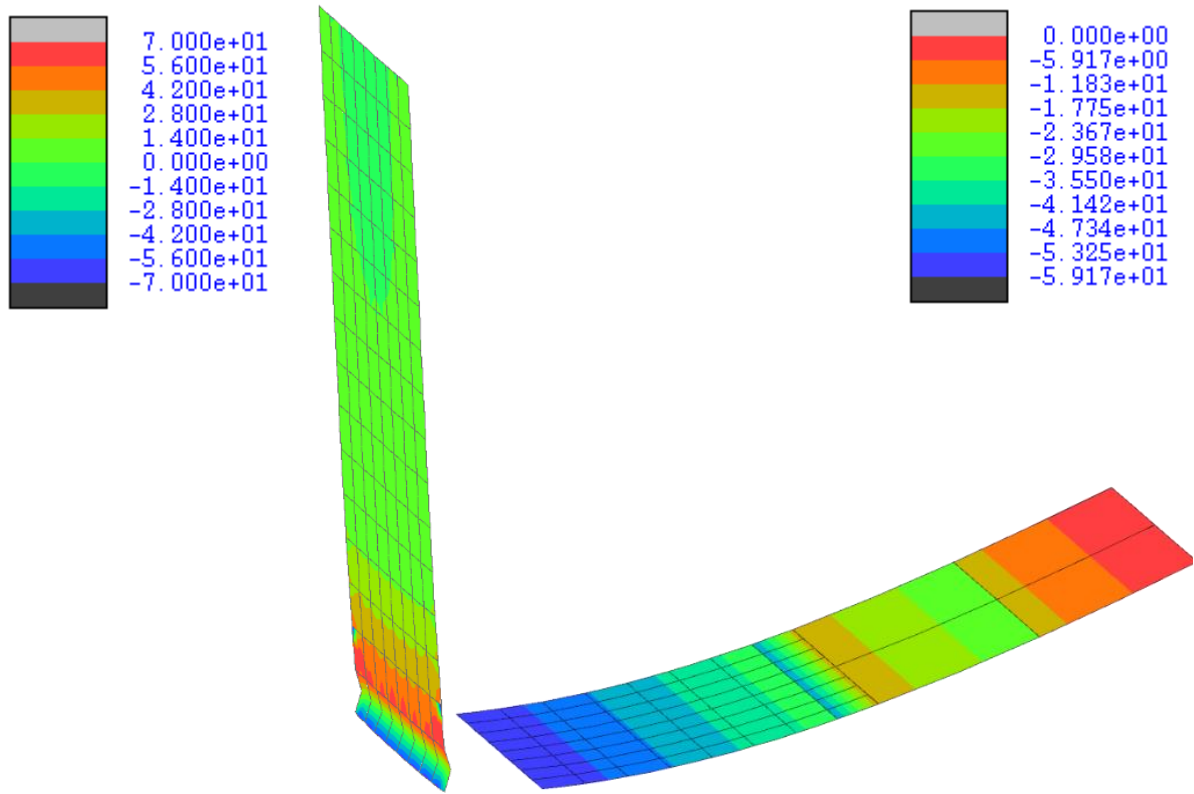


(a)

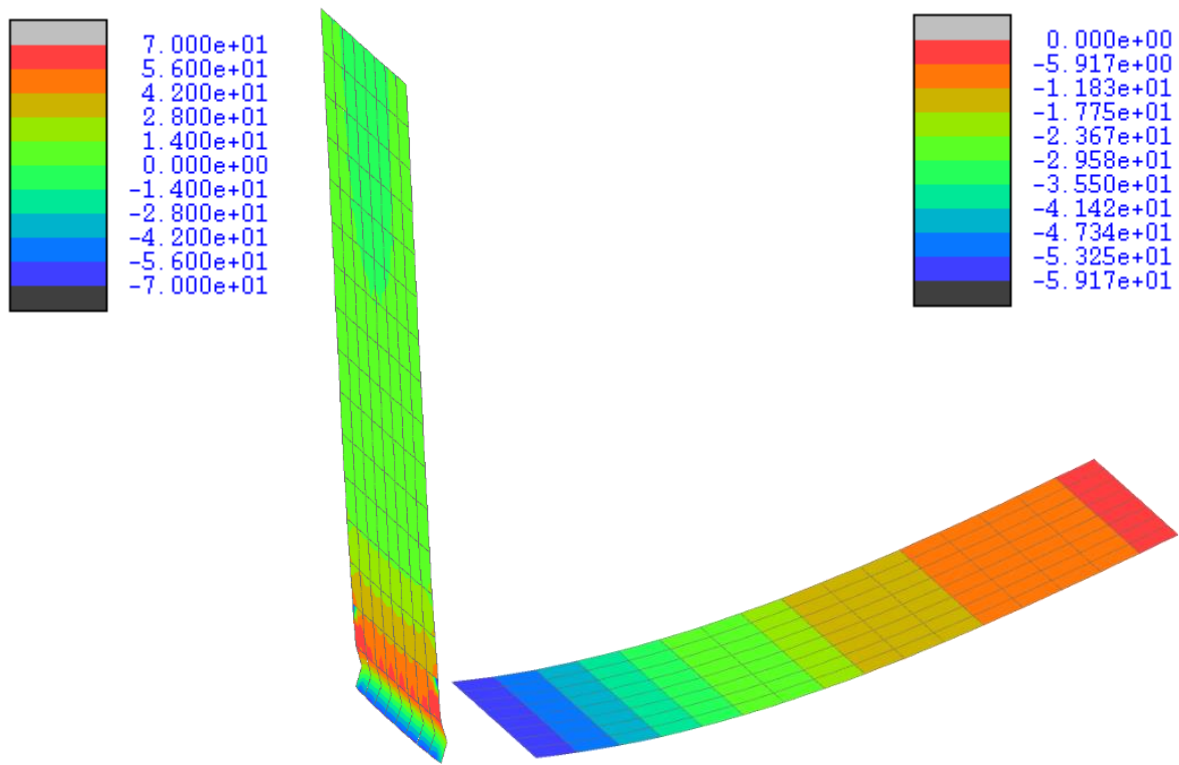


(b)

Figure 6.17: Contour plots of local shell FE shear force  $Q_{xz}$  at first yield and maximum displacement for plate models CM-1 (a) and BM-1 (b)



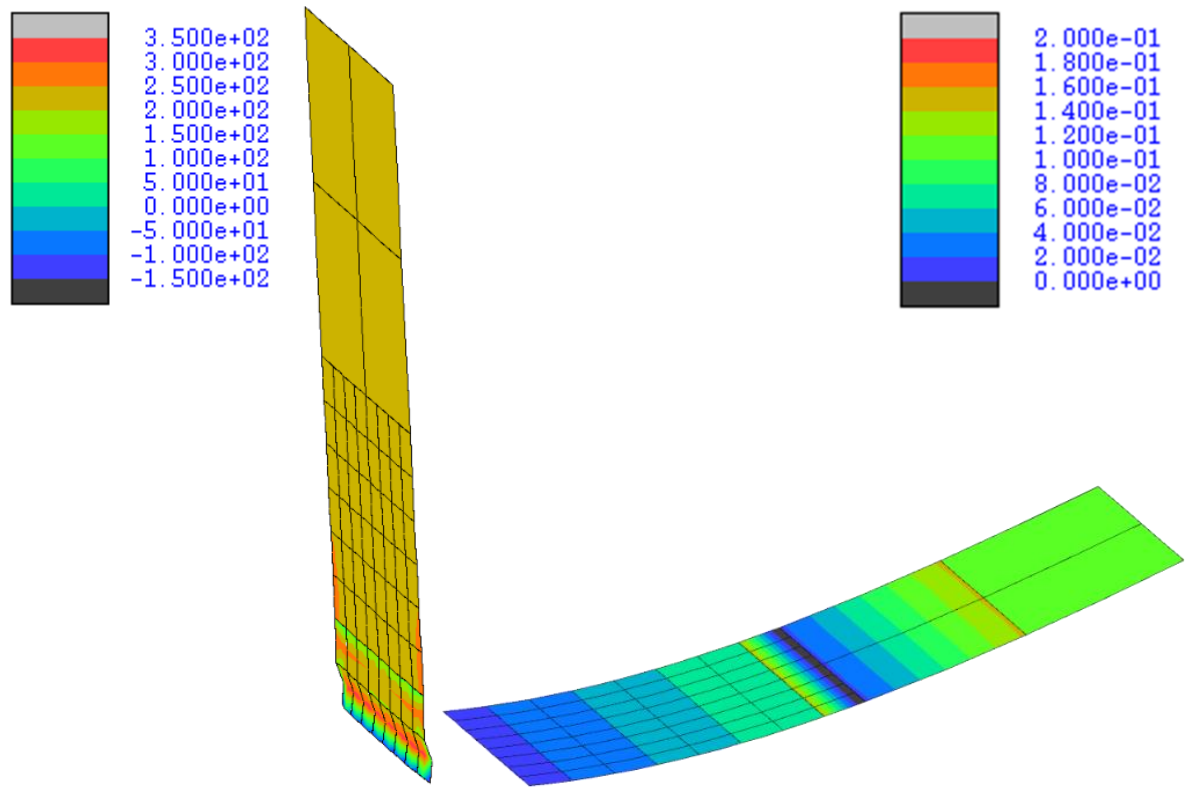
(a)



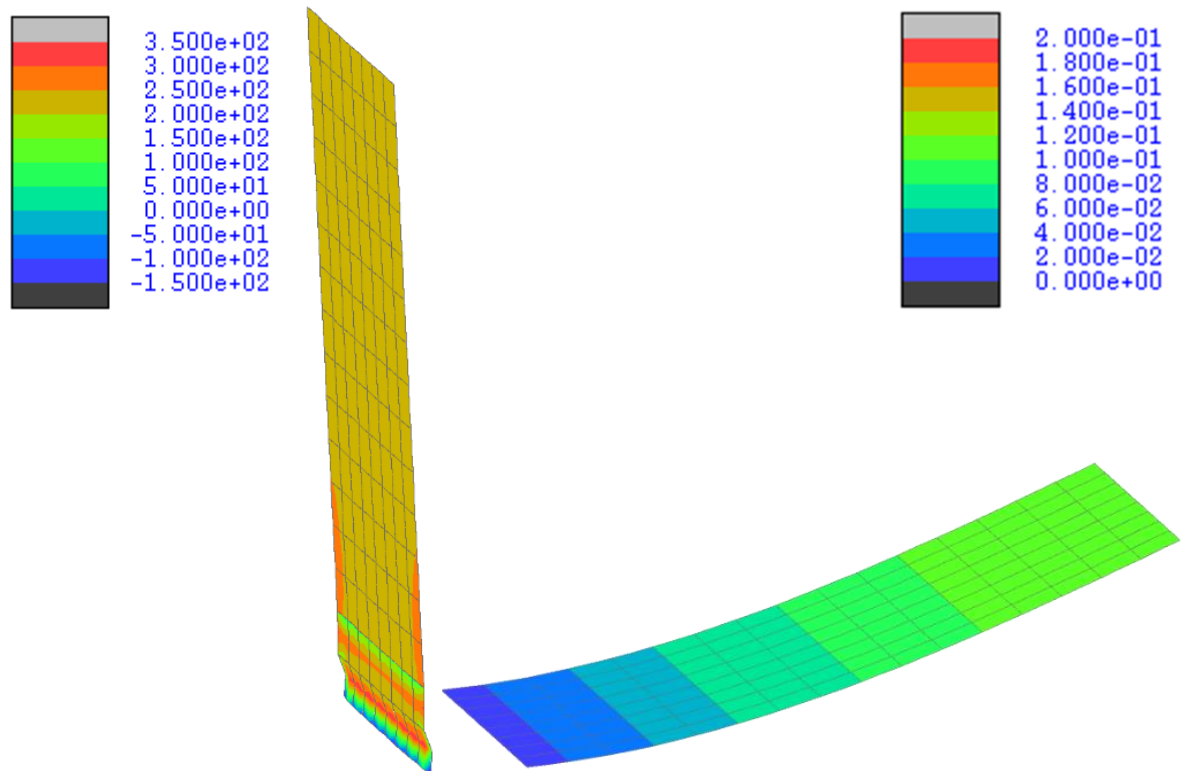
(b)

Figure 6.18: Contour plots of local shell FE bending moment  $M_x$  at first yield and maximum displacement for plate models CM-1 (a) and BM-1 (b)





(a)



(b)

Figure 6.19: Contour plots of local shell FE membrane force  $N_x$  at first yield and maximum displacement for plate models CM-1 (a) and BM-1 (b)

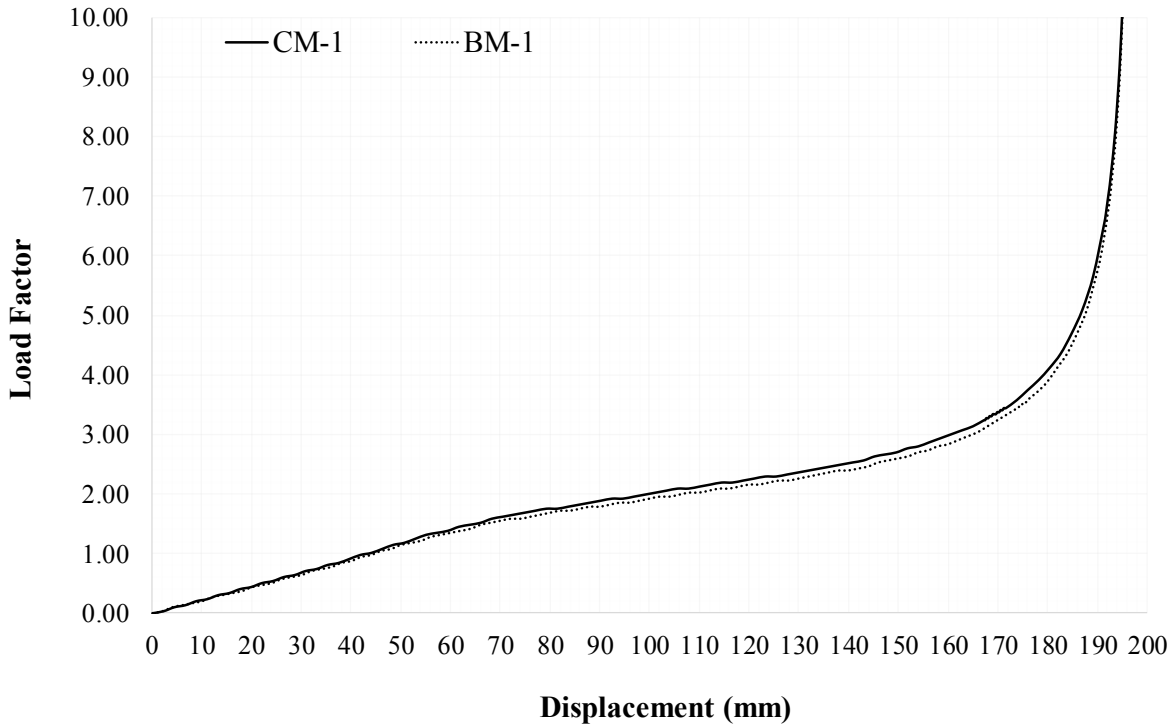


Figure 6.20: Nonlinear equilibrium path of translational DOF along the Z-axis at right plate edge for plate models CM-1 and BM-1

### 6.2.5 Uniform twisting moment field

A uniform twisting moment field is induced over the plate domain by applying uniform rotational fields with opposite values along its two sets of opposing edges: (i) rotational fields  $\theta_x$  with values 0.5 rad/mm and -0.5 rad/mm about the Y-axis at its top and bottom edges, respectively and (ii) rotational fields  $\theta_y$  with values 1 rad/mm and -1 rad/mm about the X-axis at its left and right edges, respectively. A single translational restraint is introduced in the Z-direction at the plate centre, alongside minimum planar restraints at the left and right edges for rigid body motion to be avoided. This allows for a linear variation of  $\theta_x$  and  $\theta_y$  to be obtained over the plate domain, along the Y- and X-axes, respectively, which induces a constant twisting curvature  $\kappa_{xy}$ , and hence a constant twisting moment, in the range of small rotations. Configurations CM-1 and BM-1 are illustrated in Figure 6.21. Material yielding is observed in the range of very small rotations, of the order of 0.02 and 0.04 rad for  $\theta_x$  and  $\theta_y$ , respectively. Hence, a maximum specified magnitude for the applied rotational fields of 0.05 and 0.1 rad, is adequate to investigate the coupling element ability to approximate the monolithic mesh response, taking due account of material nonlinearity.

The plate deformed configuration at a state in the small rotation range with  $\theta_x = 0.5$  mrad and  $\theta_y = 1$  mrad, where the response is perfectly elastic, is illustrated in Figure 6.22, while the contour plots of the local shell FE twisting moment  $M_{xy}$ , at the corresponding state are illustrated in Figure 6.23. The nonlinear equilibrium paths for rotations  $\theta_x$  and  $\theta_y$  at the bottom right corner plate node for CM-1 and BM-1 models are illustrated in Figures 6.24 and 6.25, where the load factor in the vertical graph axis is obtained by normalising the applied twisting moment with a value of 8 Nmm/mm obtained at first yield.

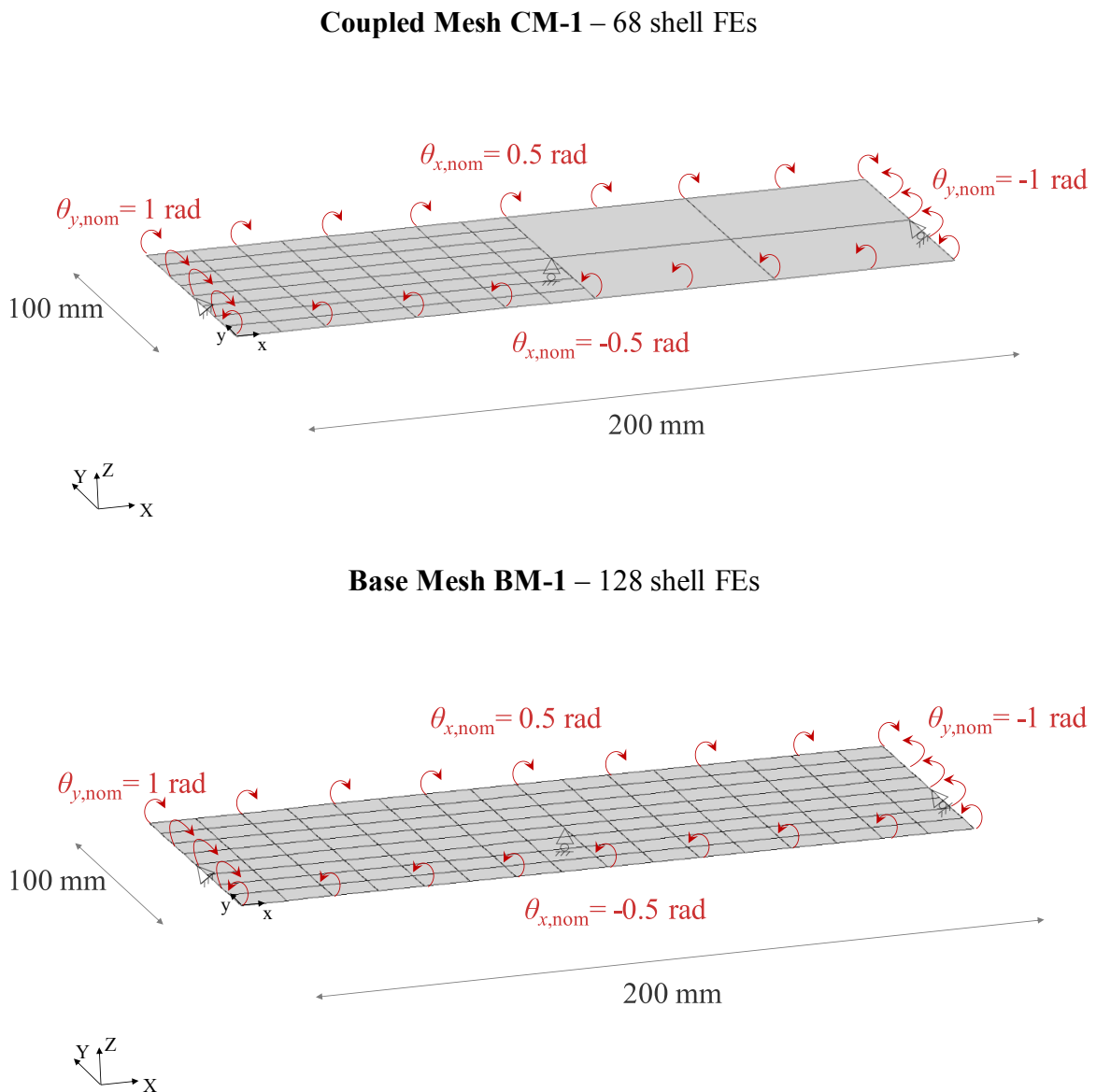
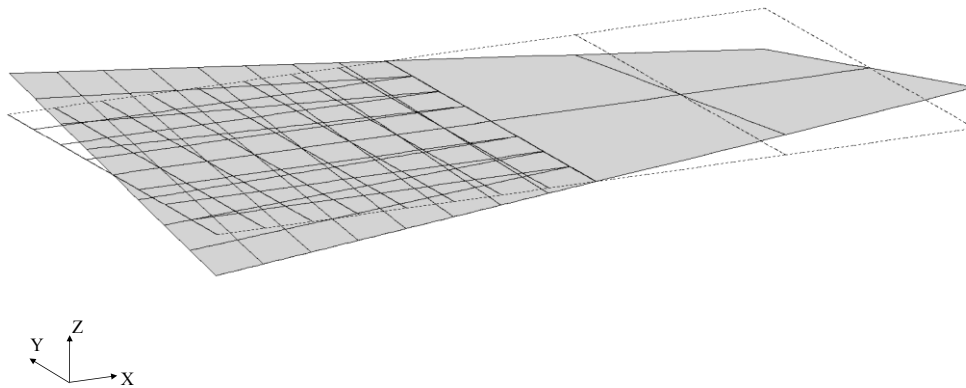


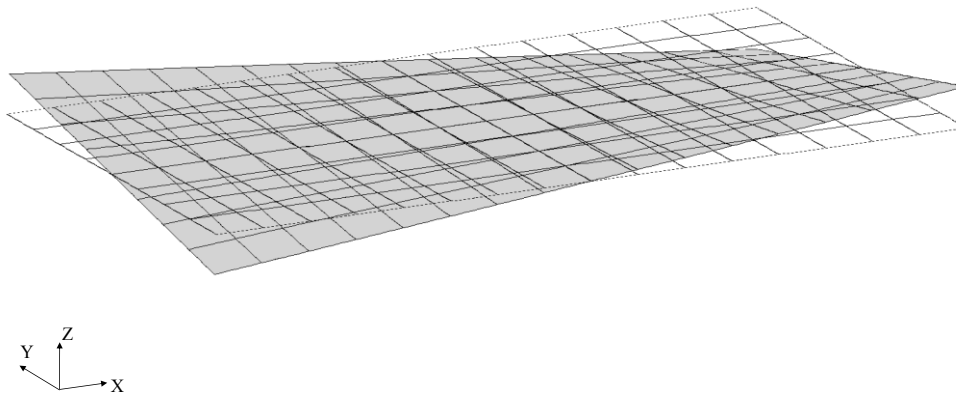
Figure 6.21: Geometric configuration, applied loading and boundary conditions for plate models CM-1 and BM-1

The applied perimetric rotational field does not induce bending curvature along the coupling interface in the range of small rotations, and hence the activated LM components are associated with translational constraints only. This allows for the coupling element to achieve an exact distribution of the internal forces over the plate domain in CM-1, including the adjoining shell FEs. The application of rotations at nodes along the coupling interface induces minor curvature at the shell FEs located at the two interface ends, and thus minor discontinuities are observed in the contour plots, due to the approximation embedded in the rotational coupling formulation.

The adopted ratio for the applied rotational fields along the horizontal and vertical plate edges does not enable these to remain straight in the range of large rotations, particularly in the presence of material plasticity. Therefore, the comparison of the coupled and monolithic meshes is limited to the considered range of rotations, where the ability of the coupling element to transfer a uniform twisting moment field between the coupled meshes is verified.

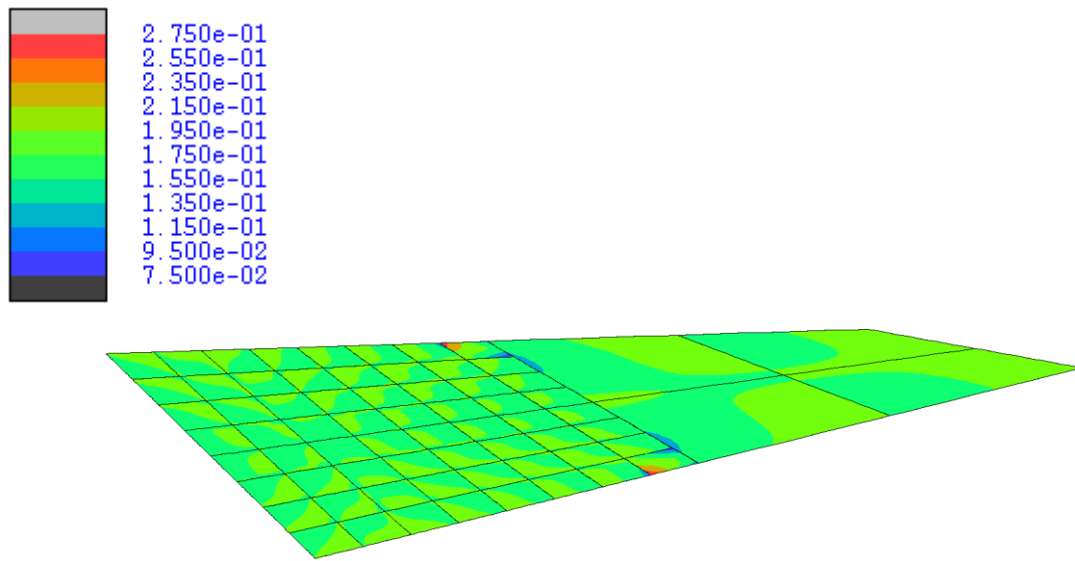


(a)

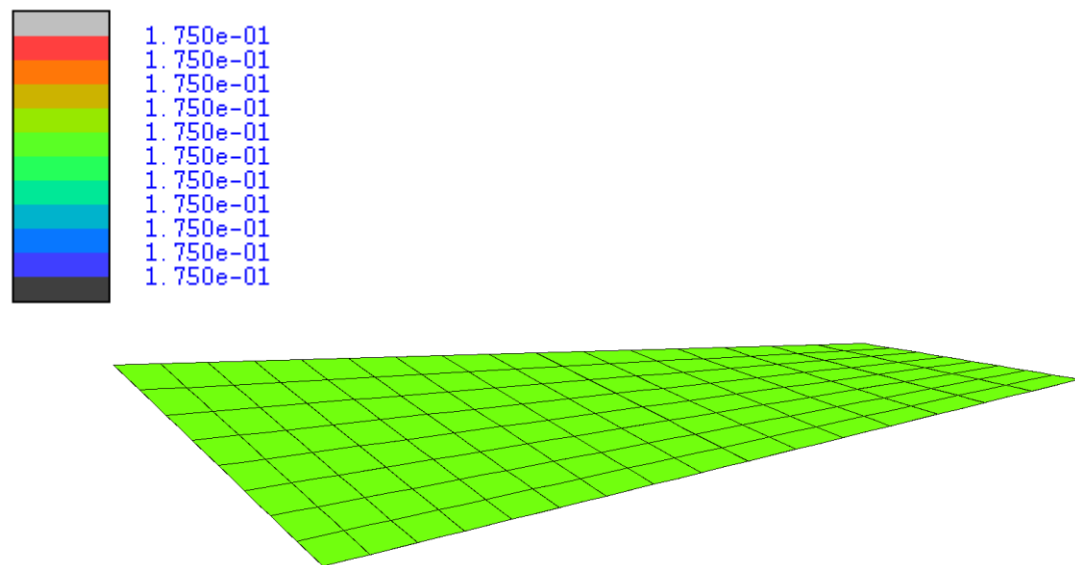


(b)

Figure 6.22: Deformed configuration at a small twisting rotation state for plate models CM-1 (a) and BM-1 (b)



(a)



(b)

Figure 6.23: Contour plots of local shell FE twisting moment  $M_{xy}$  at a small twisting rotation state for plate models CM-1 (a) and BM-1 (b)

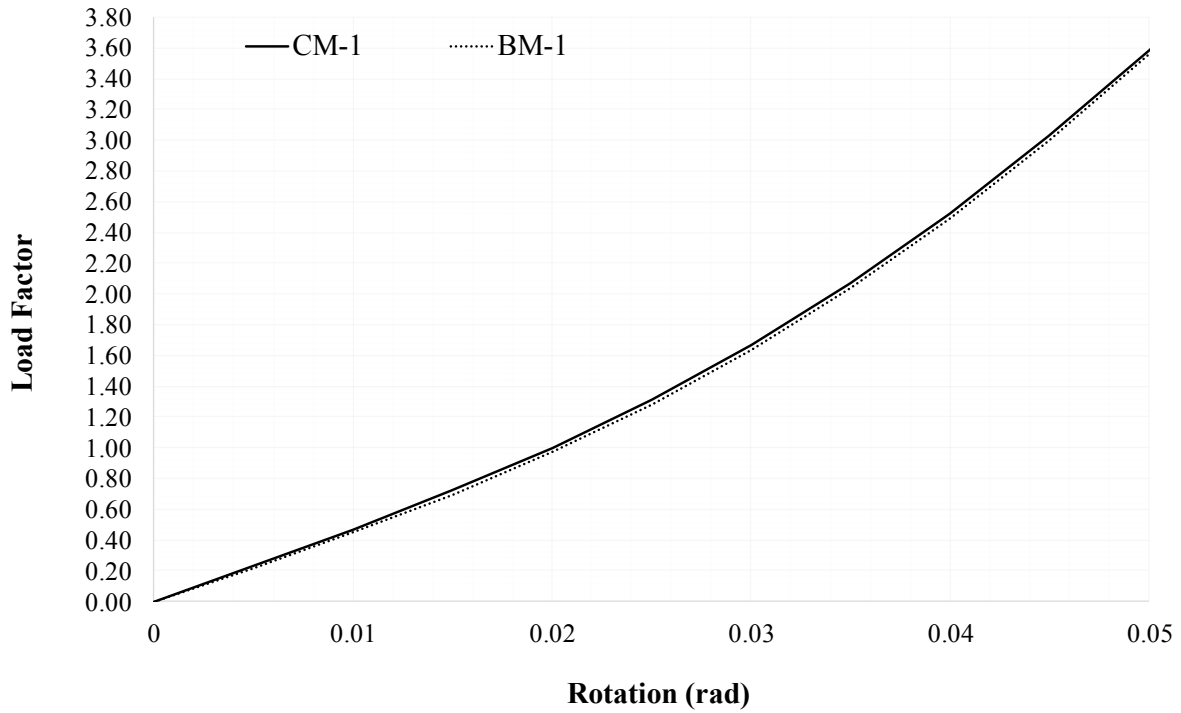


Figure 6.24: Nonlinear equilibrium path of rotational DOF  $\theta_x$  about the Y-axis at bottom right plate corner for plate models CM-1 and BM-1

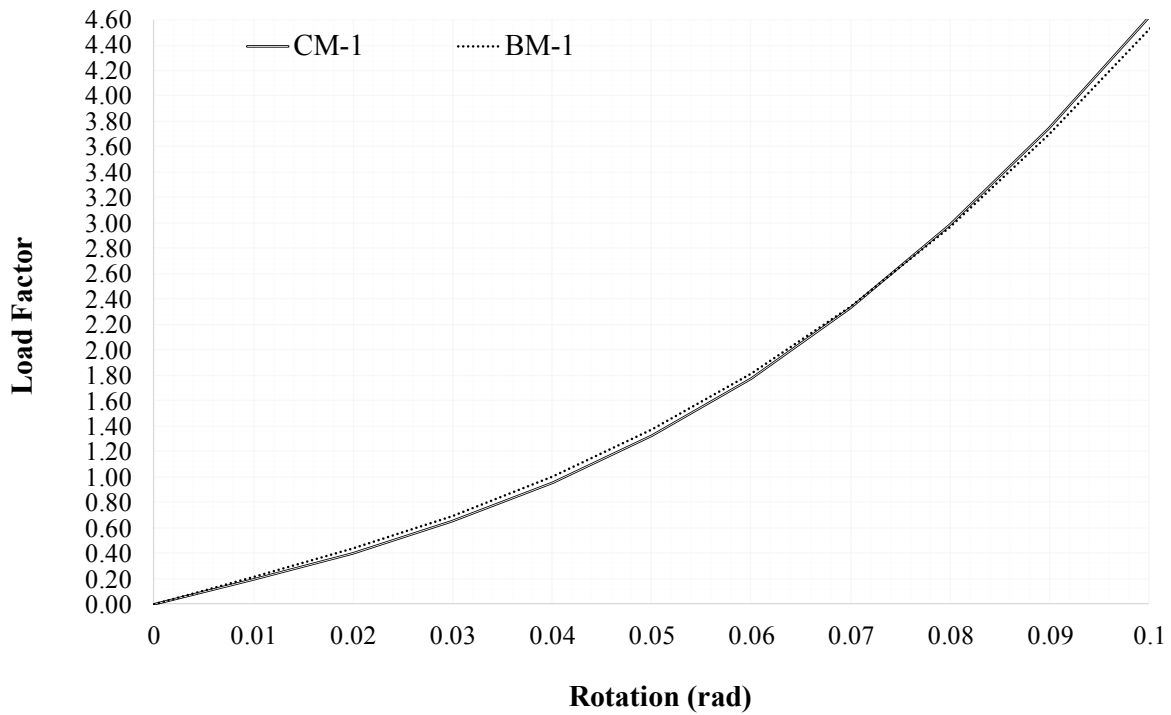


Figure 6.25: Nonlinear equilibrium path of rotational DOF  $\theta_y$  about the X-axis at bottom right plate corner for plate models CM-1 and BM-1

### 6.3 L-frame subjected to end forces

An L-frame consisting of two  $100 \times 10 \text{ mm}^2$  plates of 1 mm thickness is considered in this study, as illustrated in Figure 6.26. For distinction purposes, the two plates of the L-frame oriented with their large dimension along the Y- and X-axes will henceforth be referred to as plate 1 and plate 2, respectively. The L-frame is fully restrained against rotations and translations at the free end of plate 1 and is subjected to three distinct load cases, with the load applied in the form of a uniformly distributed force field introduced at the free end of plate 2. The load cases under consideration include a uniform force field along: (i) the global X-axis, (ii) the global Y-axis, and (iii) the global Z-axis. A tri-linear elastoplastic material constitutive model is adopted with Young's modulus  $E = 210000 \text{ N/mm}^2$ , Poisson's ratio  $\nu = 0.3$ , yield stress  $f_y = 355 \text{ N/mm}^2$  and a negligible strain-hardening parameter.

The coupled mesh configuration CM-2 comprises two independently discretised meshes for the plates, coupled along a straight 1-D interface oriented in the Y-direction and introduced at the frame corner, where these intersect. A coarse mesh comprising 8 9-noded shell FEs with regular edges is employed for the domain discretisation of plate 2, while a fine mesh of 128 elements is employed for plate 1. The base mesh configuration BM-2 consists of two matching meshes for plates 1 and 2, encompassing 320 and 16 shell FEs, respectively. Configurations CM-2 and BM-2 are illustrated in Figure 6.26. The adoption of a superior level of discretisation detail for the plate 1 is justified on the basis of it exhibiting more substantial stress variation under the load cases examined herein, in comparison to plate 2.

The focus of the present study remains the verification of the coupling element ability to achieve translational and rotational coupling between initially co-planar intersecting plated components under complex stress states, taking due account of geometric and material nonlinearity. Further consideration is given here to its capability of providing an accurate approximation of the internal force distribution at critical response states, thus enabling the capturing of the various transitions between load-transferring mechanisms in the range of large displacements.

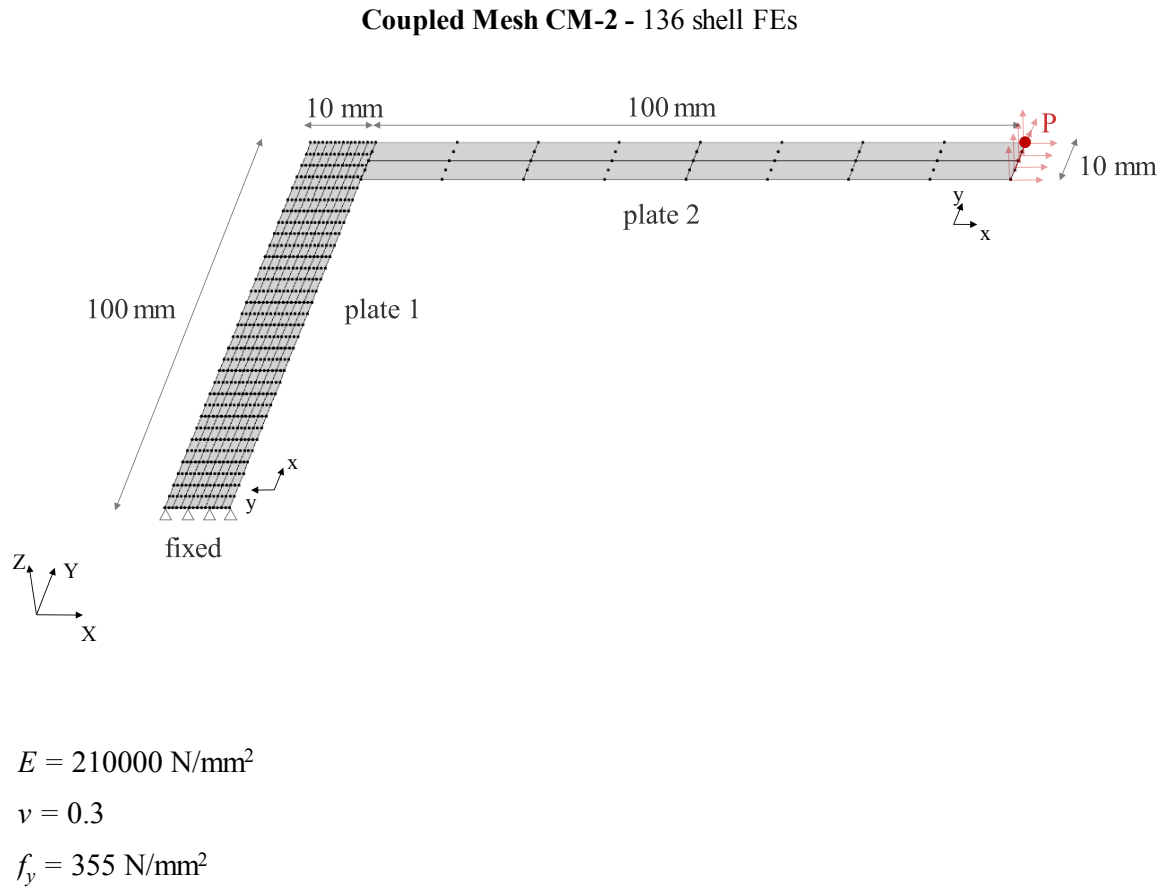


Figure 6.26: Geometric configuration, applied loading, boundary conditions and material properties for L-frame models CM-2 and BM-2

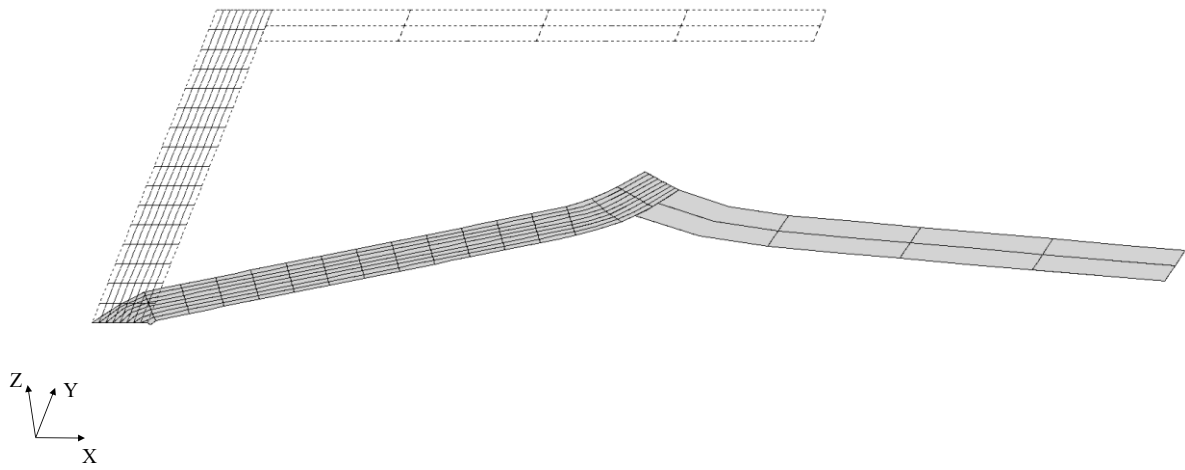


### 6.3.1 Planar end loading in X-direction

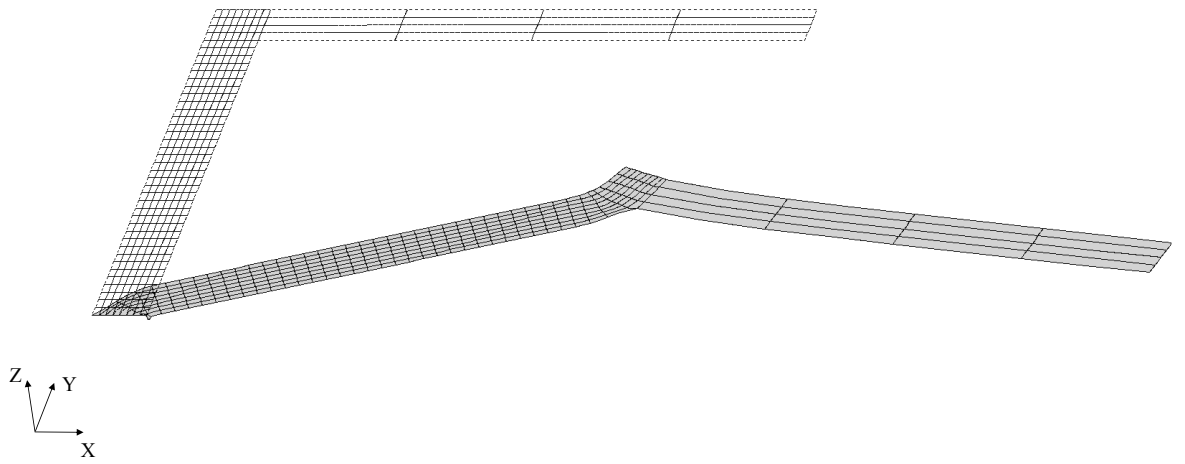
In the present study, a uniformly distributed force field with nominal magnitude 10 N/mm is applied incrementally at the free end of plate 2 along the global X-axis. Beyond the fixed support at the free end of plate 1, translational restraints along the global Z-axis are further introduced over the frame domain to prevent out-of-plane buckling. The L-frame deformed configuration corresponding to a maximum free end displacement of 80 mm for plate 2 at node P, which has been annotated in Figure 6.26, is illustrated in Figure 6.27 for both CM-2 and BM-2 configurations.

The frame response in the small displacement range is characterised by transverse bending of plate 1, with the corresponding effect being negligible for plate 2. Taking due account of the adopted material parameters, increasing loading leads to the formation of the first plastic hinge at the restrained bottom edge of plate 1, due to yielding of the respective section under substantial bending stresses and spread of the induced plasticity in the edge vicinity. Following the formation of the first plastic hinge, stiffness degradation leads to increased deformations along the global X-axis, thereby inducing substantial bending stresses over plate 2, and, ultimately, leading to the formation of a second plastic hinge at the frame corner. In the range of large displacements, the load application axis tends to align with both plastic hinges of the frame, which behaves as a mechanism and becomes virtually horizontal. Accordingly, substantial membrane action is exhibited, leading to stiffness hardening. The phenomena described above are observed both in the contour plots of the membrane force  $N_x$  generalised stress entity illustrated in Figure 6.28 and the nonlinear equilibrium paths provided in Figure 6.29, corresponding to the translational DOF along the X-axis of node P.

The nonlinear equilibrium paths are virtually identical throughout the full response range, with minor deviations observed only in the range of very large displacements. Furthermore, as observed in the contour plots, the coupling element employment allows for an accurate approximation of the internal force distribution to be obtained at the critical response states, i.e. at the formation of the two plastic hinges, thus enabling the accurate capturing of the spread of plasticity both away from the coupling interface and in its vicinity. Accordingly, the evolution of the deformed configuration can be accurately captured when the coupling element is employed, as highlighted by comparison of the contour plots of Figure 6.28 (a), (b) and (d), (e), at plastic hinge formation, as well as of Figure 6.28 (c) and (f), at maximum displacement.



(a)



(b)

Figure 6.27: Deformed configuration at maximum displacement for L-frame models CM-2 (a) and BM-2 (b)

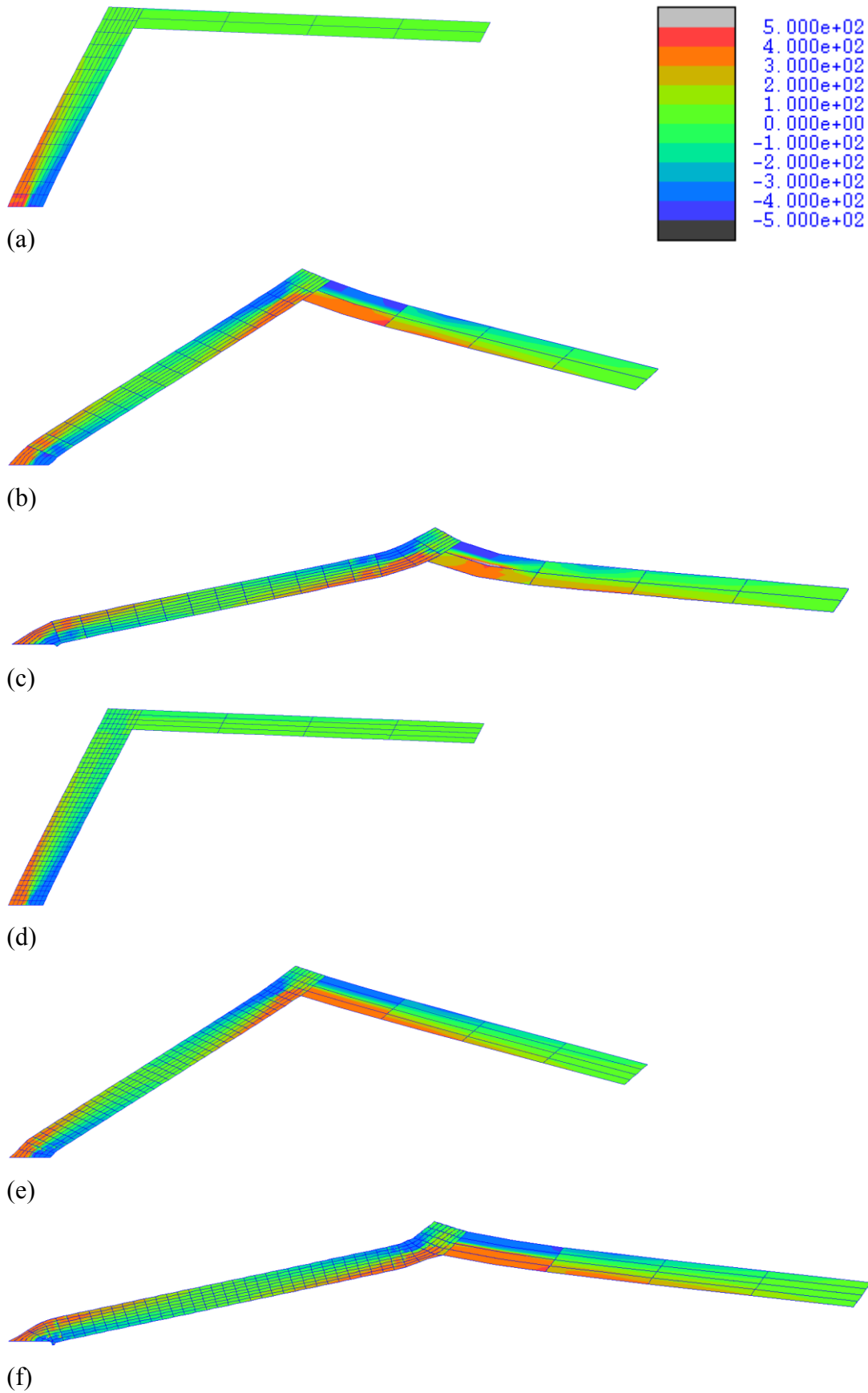


Figure 6.28: Contour plots of local shell FE membrane force  $N_x$  at plastic hinge formation and maximum displacement for L-frame models CM-2 (a, b, c) and BM-2 (d, e, f)

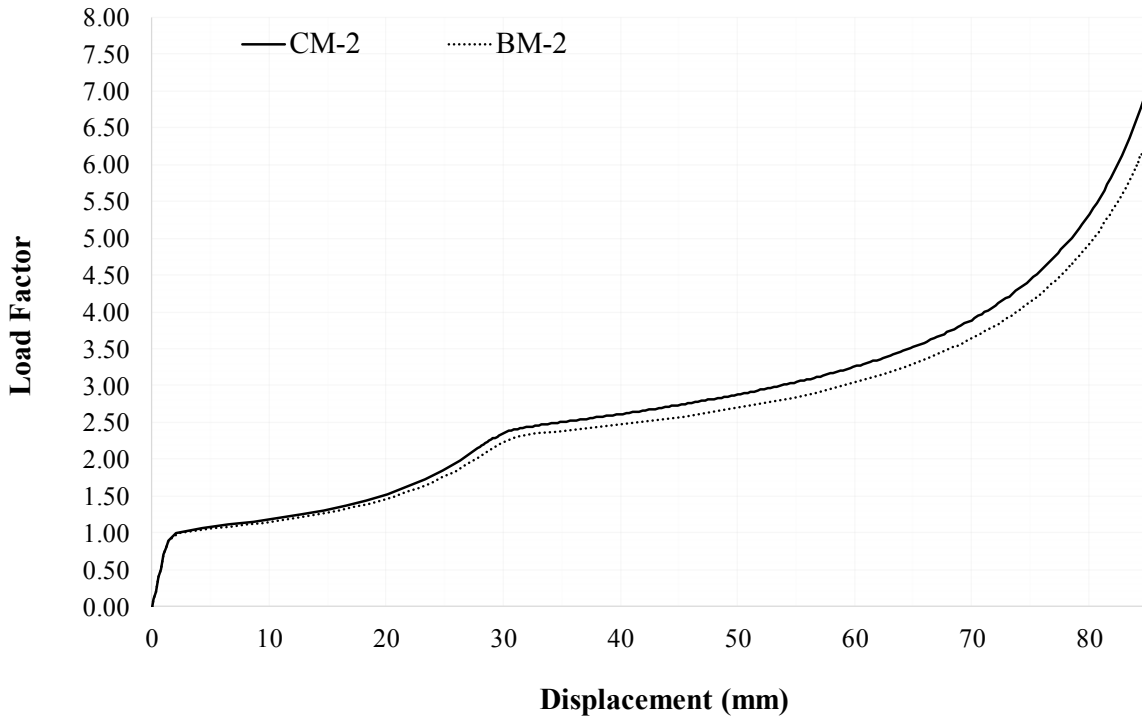


Figure 6.29: Nonlinear equilibrium path of translational DOF along the X-axis at node P for L-frame models CM-2 and BM-2

### 6.3.2 Planar end loading in Y-direction

In the present study, a uniformly distributed force field with nominal magnitude 10 N/mm is applied incrementally at the free edge of plate 2 along the global Y-axis. Similar to the preceding sub-section, restraints are introduced along the global Z-axis to prevent out-of-plane deformation due to buckling. The nonlinear equilibrium paths for both CM-2 and BM-2 configurations, corresponding to the translational DOF along the Y-axis of node P, are provided in Figure 6.30. The L-frame deformed configuration for a maximum free end displacement of 100 mm for plate 2 at node P is illustrated in Figure 6.31, for both CM-2 and BM-2 configurations.

The principal response attributes of the frame over the considered displacement range are similar to the previously considered load case, however the uniform bending moment distribution over plate 1, resulting from the orientation of the applied loading in this case, causes simultaneous yielding of all cross-sections along its longitudinal axis. Accordingly, the nonlinear response is characterised by a single yield point, corresponding to the state of

extensive yielding of plate 1, followed by a yielding plateau and a branch of substantial stiffness hardening in the range of large displacements, due to membrane action. The aforementioned response attributes are observed in the contour plots of the local shell FE membrane force  $N_x$  generalised stress entity illustrated in Figure 6.32, as well as in the nonlinear equilibrium paths of Figure 6.30.

Similar to the load-case discussed in the preceding sub-section, the results are indicative of the coupling element ability to accurately capture geometric nonlinearity effects, as well as the spread of plasticity, throughout the evolution of the L-frame deformed configuration and at the various load-transferring mechanism transitions.

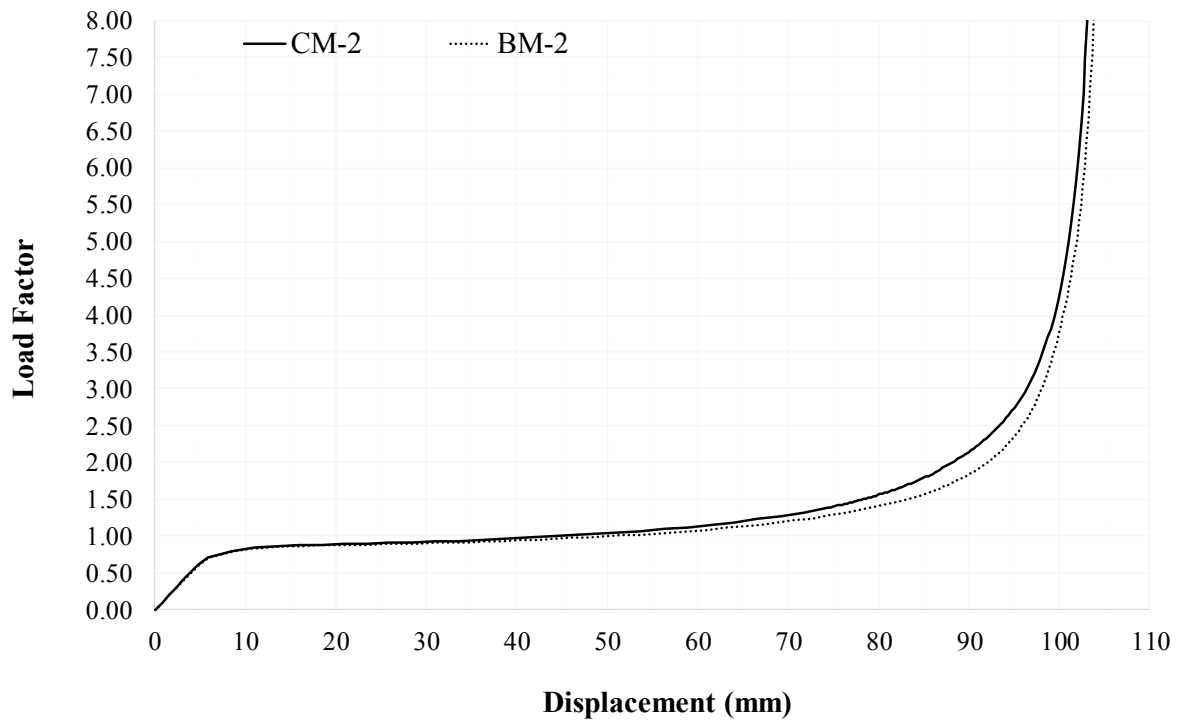


Figure 6.30: Nonlinear equilibrium path of translational DOF along the X-axis at node P for L-frame models CM-2 and BM-2

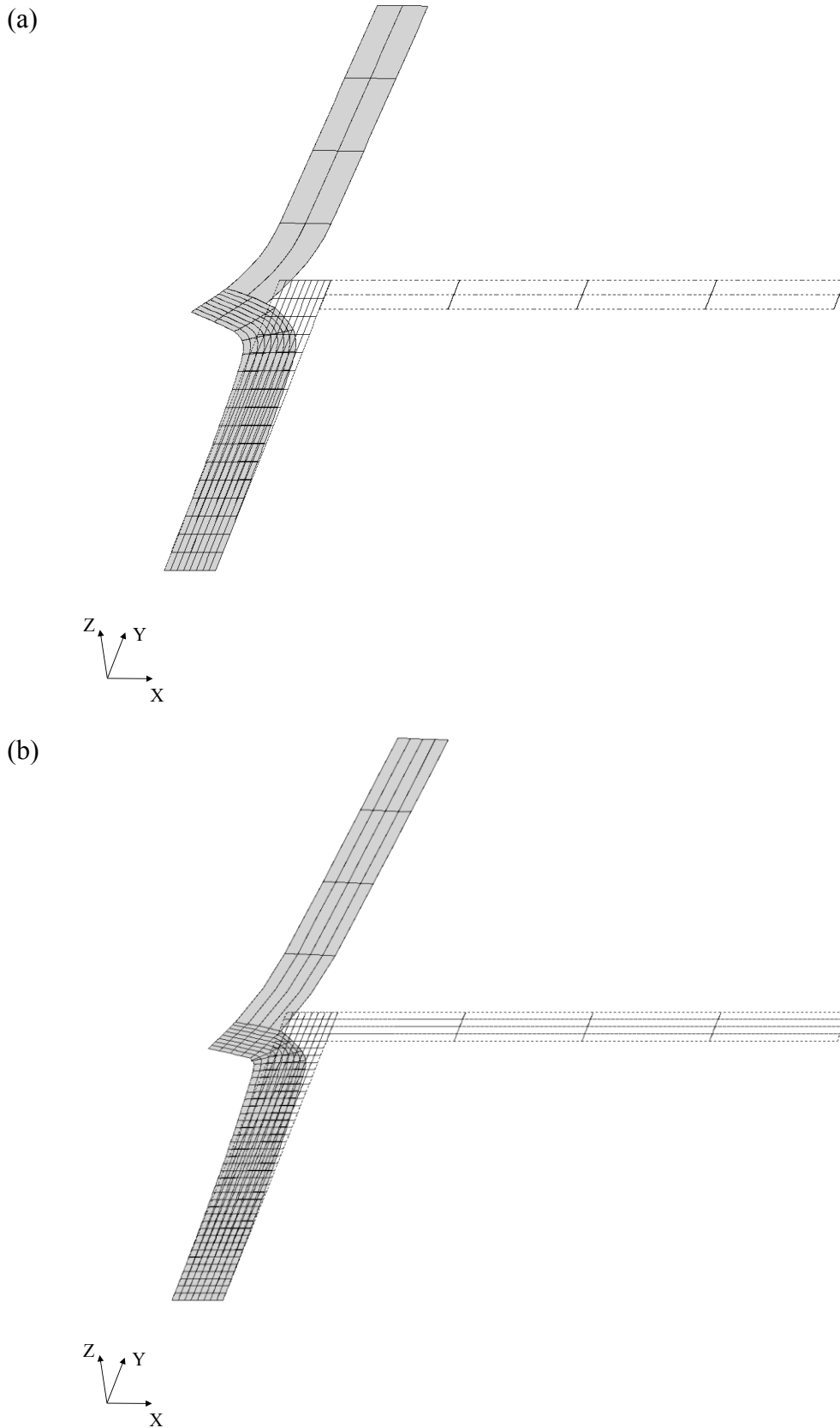


Figure 6.31: Deformed configuration at maximum displacement for L-frame models CM-2 (a) and BM-2 (b)

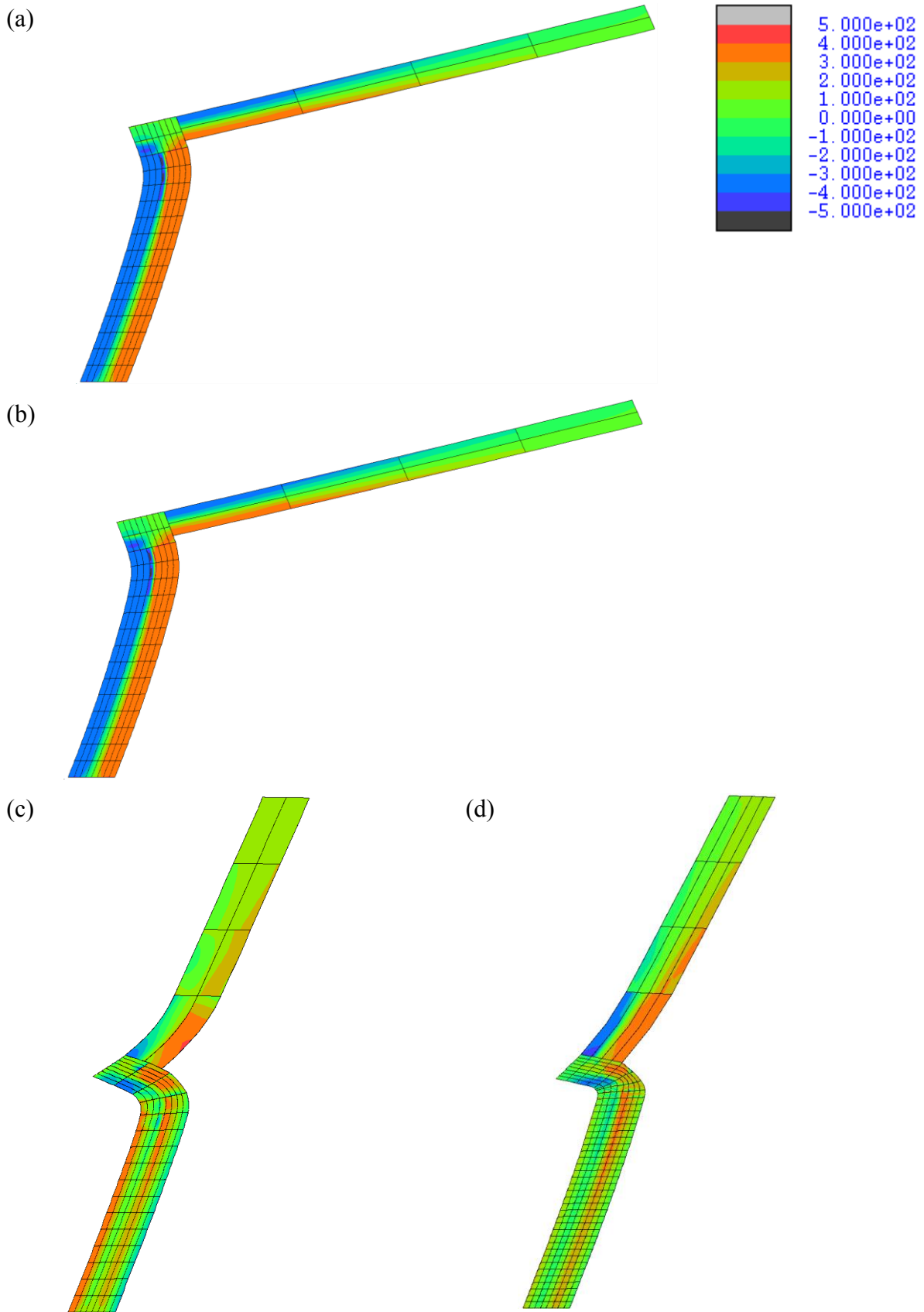


Figure 6.32: Contour plots of local shell FE membrane  $N_x$  for L-frame models: (a) CM-2 - plastic hinge formation, (b) BM-2 - plastic hinge formation, (c) CM-2 - maximum displacement, (d) BM-2 - maximum displacement

### 6.3.3 Out-of-plane end loading in Z-direction

In the present study, a uniformly distributed force field with nominal magnitude 1 N/mm is applied incrementally at the free edge of plate 2 along the global Z-axis. The L-frame deformed configuration at a maximum free end displacement of 140 mm for plate 2 at node P is illustrated in Figure 6.33, for both CM-2 and BM-2 configurations.

The frame response under transverse out-of-plane loading is principally characterised by bending of plate 2, as well as bending and twisting of plate 1, which ultimately leads to the yielding of the bottom restrained edge of the latter. The nonlinear response is associated with significantly reduced stiffness in the range of small displacements, in comparison with the two preceding studies, due to the bending moment acting about the plate section weak bending axis in this case. Following the plastic hinge formation, a yielding plateau is observed in the nonlinear equilibrium path, with the frame progressively exhibiting stiffness hardening before attaining the maximum displacement.

The aforementioned response attributes can be observed in the contour plots of the local shell FE membrane force  $N_x$ , twisting moment  $M_{xy}$  and bending moment  $M_x$  generalised stress entities illustrated in Figure 6.34, as well as in the nonlinear equilibrium paths provided in Figure 6.35, corresponding to the translational DOF along the Z-axis of node P.

Expanding on the conclusions of the two preceding studies, the results presented herein verify the coupling element ability to accurately capture complex stress states associated with both bending and twisting rotations, as well as the spread of plasticity throughout the evolution of the L-frame deformed configuration.



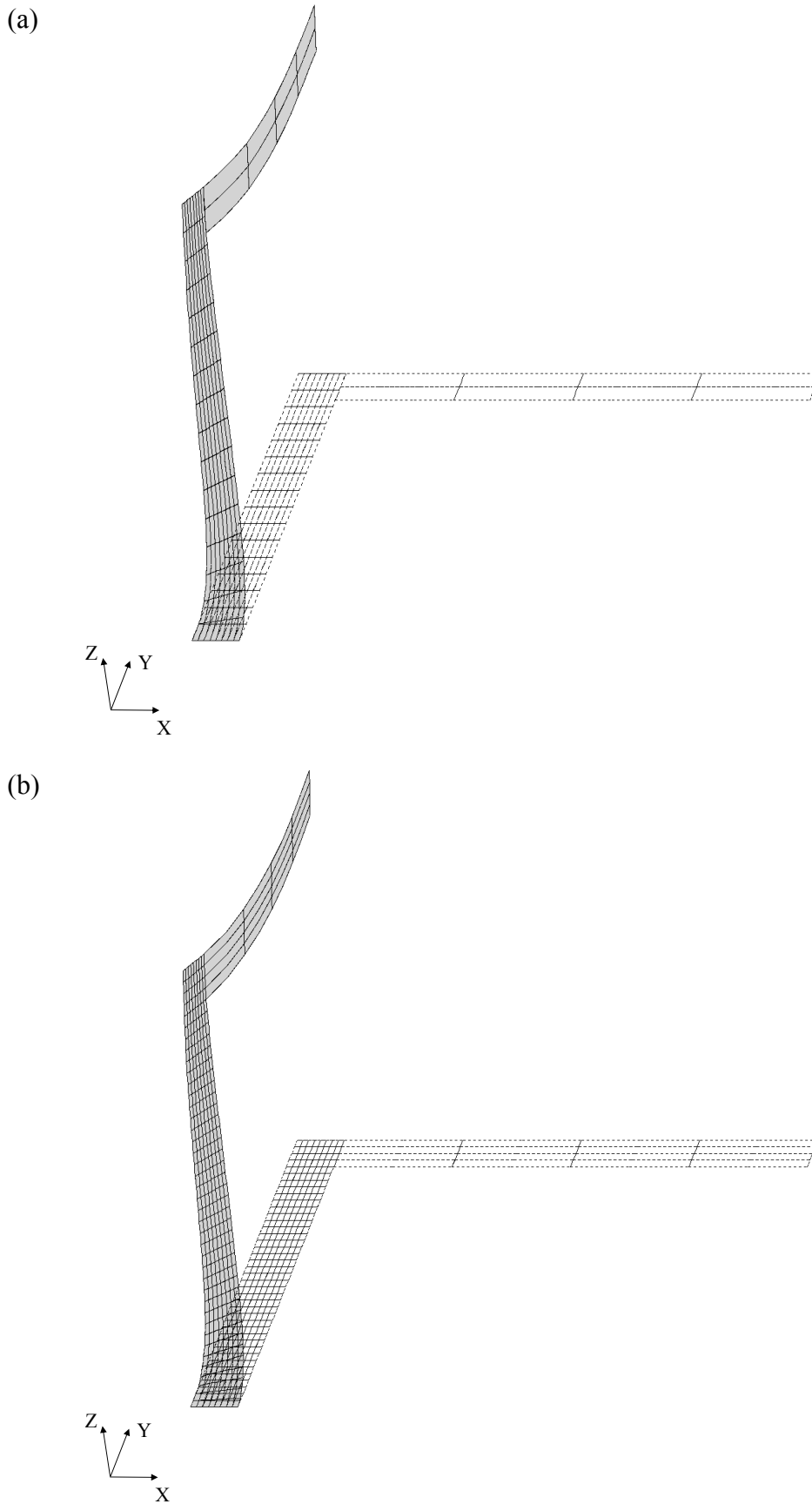


Figure 6.33: Deformed configuration at maximum displacement for L-frame models CM-2 (a) and BM-2 (b)

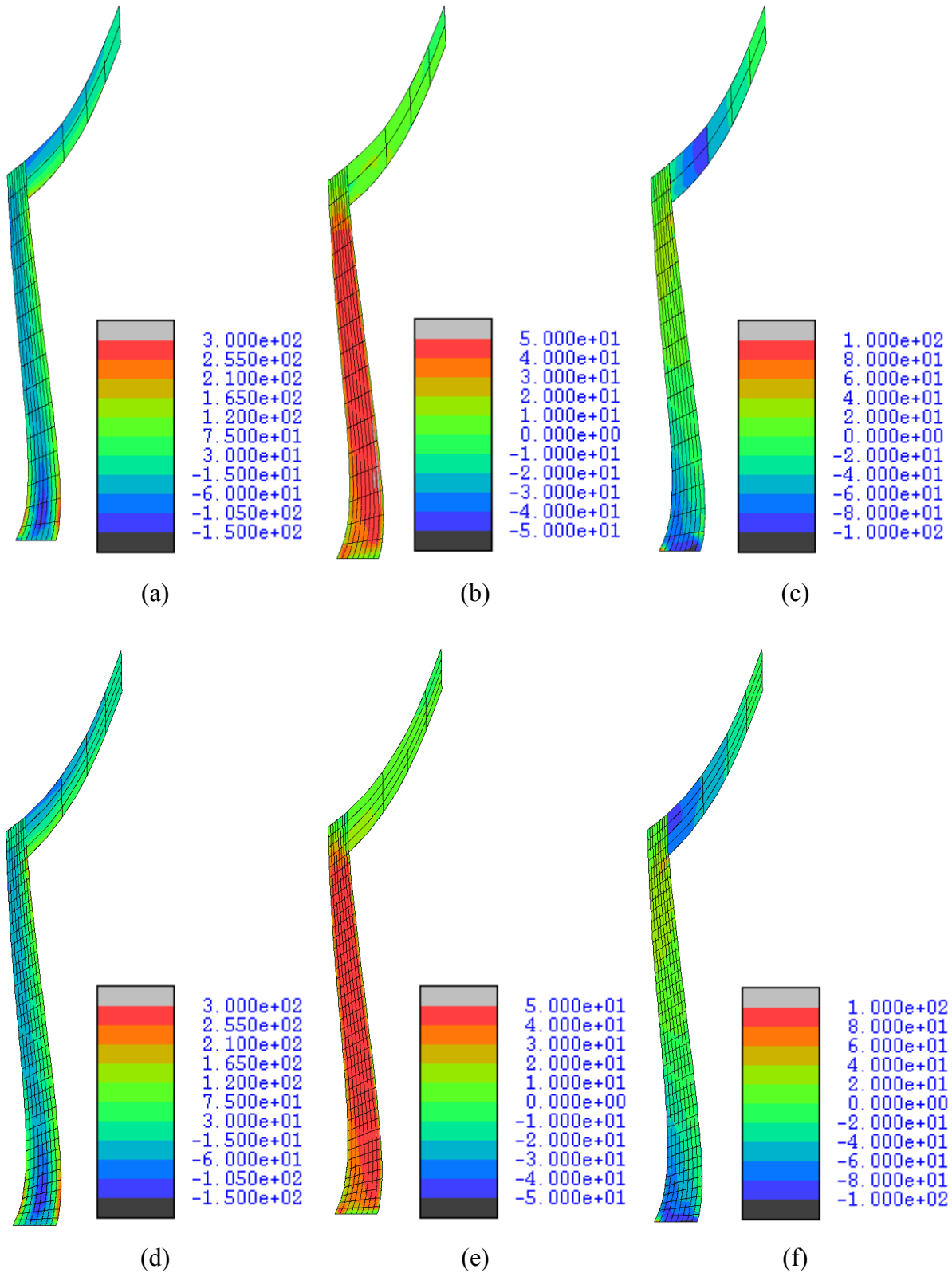


Figure 6.34: Contour plots of local shell FE generalised stress entities at maximum displacement for L-frame models: (a) CM-2 - membrane force  $N_x$ , (b) CM-2 - twisting moment  $M_{xy}$ , (c) CM-2 - bending moment  $M_x$ , (d) BM-2 - membrane force  $N_x$ , (e) BM-2 - twisting moment  $M_{xy}$ , (f) BM-2 - bending moment  $M_x$

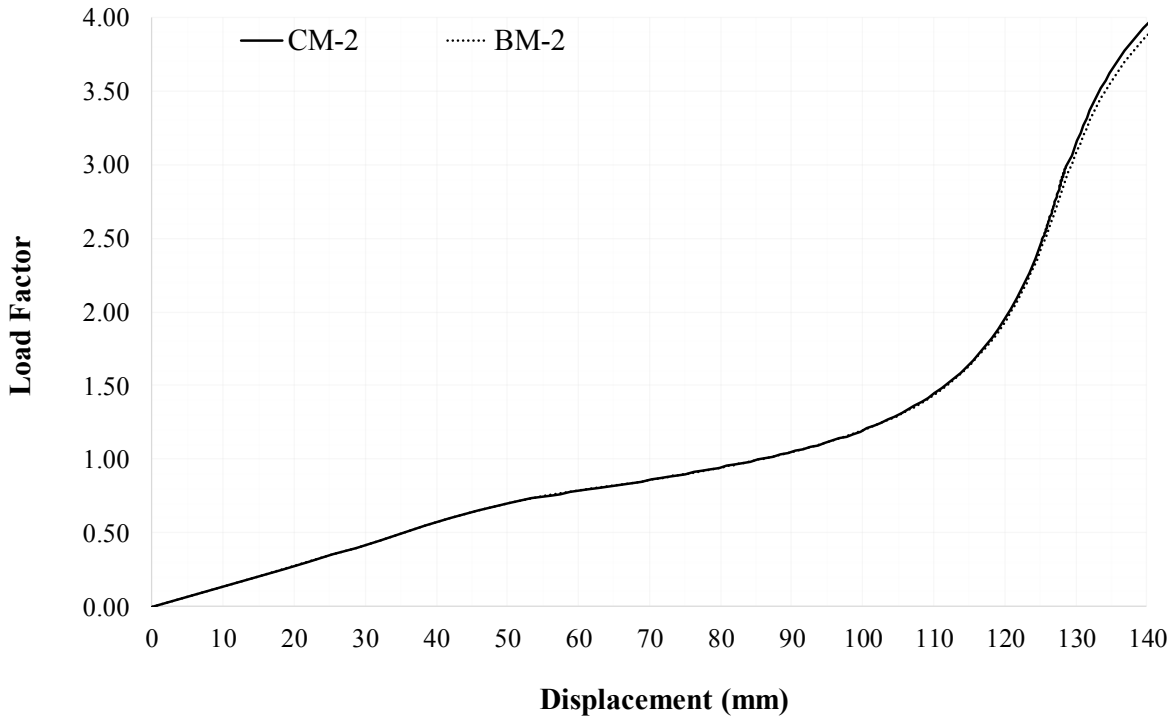


Figure 6.35: Nonlinear equilibrium path of translational DOF along the X-axis at node P for L-frame models CM-2 and BM-2

#### 6.4 Annular plate subjected to out-of-plane loading

An isotropic annular plate with a cut-off, fully fixed at one free end and subjected to a uniform transverse shear force field with nominal value 1 N/mm at the other, is considered herein, as illustrated in Figure 6.36. The plate external and internal radii are specified as  $R = 200$  mm and  $r = 100$  mm, respectively, and its thickness as 1 mm. A tri-linear elastoplastic material constitutive model is adopted, with Young's modulus  $E = 210000$  N/mm<sup>2</sup>, Poisson's ratio  $\nu = 0.3$ , yield stress  $f_y = 355$  N/mm<sup>2</sup> and a negligible strain-hardening parameter.

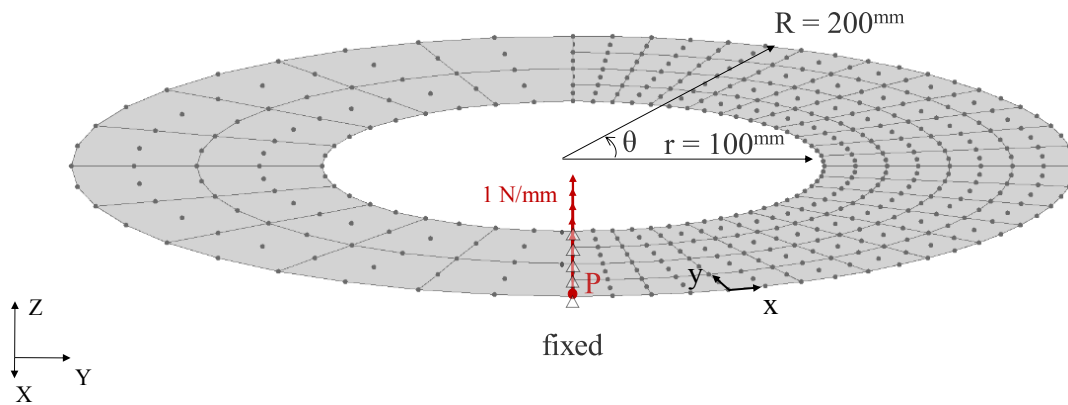
The coupled mesh configuration CM-3 comprises two edgewise adjoined semi-circular annular plates with identical geometric specifications, coupled along a straight 1-D interface oriented in the global X-direction, which is introduced at an angular polar coordinate  $\theta = \pi/2$  rad, opposite to the cut-off at  $\theta = 3\pi/2$  rad. Two non-conforming meshes, comprising 20 and 80 9-noded shell FEs with irregular edges, are employed for the domain discretisation of the two plate halves, while the base mesh configuration BM-3 is discretised with a uniform mesh of 160 shell FEs, obtained by refinement of the coarser mesh to achieve nodal alignment along the interface. Configurations CM-3 and BM-3 are illustrated in Figure 6.36.

The main focus of the present study is the verification of the coupling element ability to achieve translational and rotational coupling between initially co-planar plated components with irregular shell FE geometry under complex stress states, taking due account of geometric and material nonlinearity. The annular plate deformed configuration for a free end displacement of 500 mm at node P, which has been annotated in Figure 6.36, is illustrated in Figure 6.37 for both CM-3 and BM-3 configurations. Virtually identical equilibrium paths for the translational DOF along the Z-axis at node P are obtained for both BM-3 and CM-3 annular plate models, as illustrated in Figure 6.38. Contour plots do not provide an insight in a Cartesian coordinate framework, due to the plate geometry being circular, and hence the comparison of CM-3 and BM-3 is limited to the deformed configuration and the obtained nonlinear equilibrium paths in this study.

The applied out-of-plane loading principally induces twisting over the plate domain, as well as significant bending, thus activating both translational and rotational LM components to achieve coupling along the 1-D interface of CM-3. Substantial geometric nonlinearity is embedded in the response, even in the range of very small displacements, with the plate exhibiting a stable nonlinear equilibrium path. The stiffness is slightly reduced upon initiation of yielding at a load factor of 1.00 and the subsequent spread of plasticity over the plate domain, initiating from its internal perimeter, while in the range of very large displacements the plate exhibits substantial stiffness hardening due to membrane action.

The coupling element employment allows for the phenomena described above to be accurately captured, with minor deviations observed in the response at the maximum transverse displacement state. These are attributed to the coupling element moment transferring mechanism via equivalent nodal force couples introduced at the adjoining shell FE domains, as well as to the employment of a different discretisation level for BM-3 and CM-3.

**Coupled Mesh CM-3 – 100 shell FEs**



$$E = 210000 \text{ N/mm}^2$$

$$\nu = 0.3$$

$$f_y = 355 \text{ N/mm}^2$$

**Base Mesh BM-3 – 160 shell FEs**

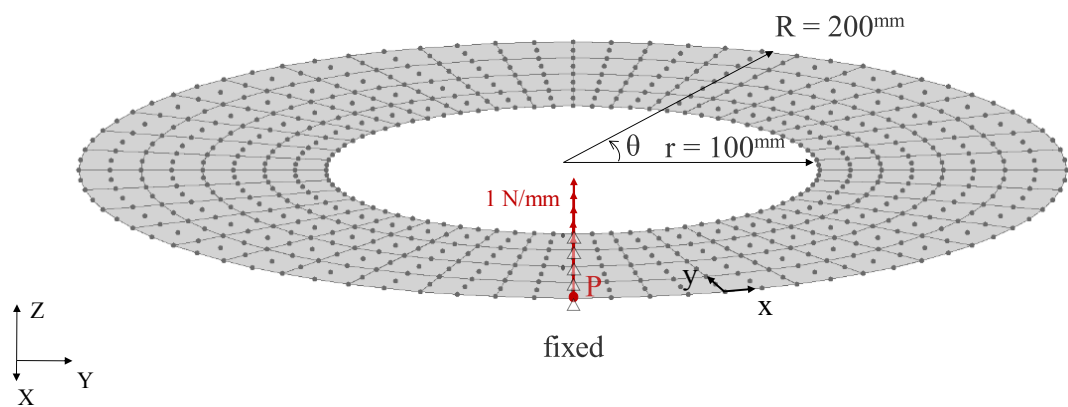


Figure 6.36: Geometric configuration, applied loading, boundary conditions and material properties for annular plate models CM-3 and BM-3

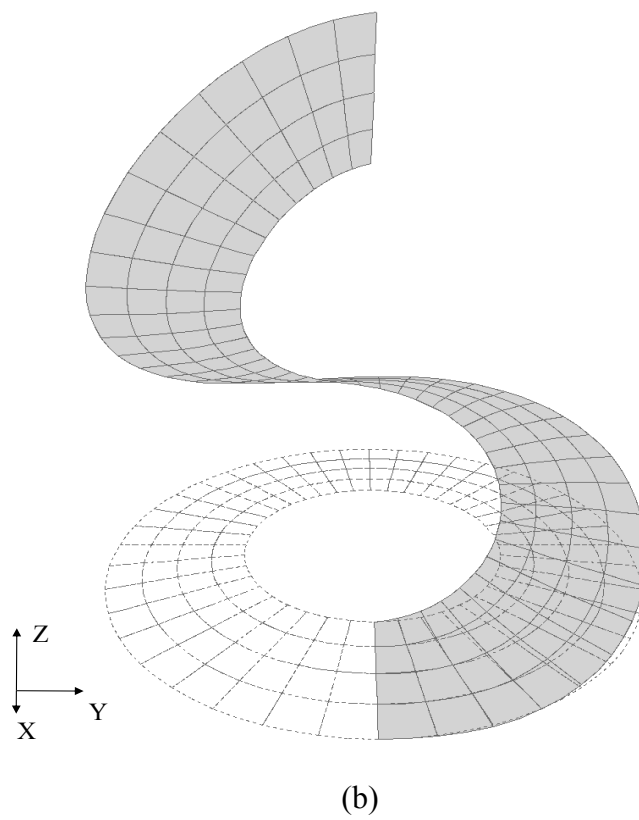
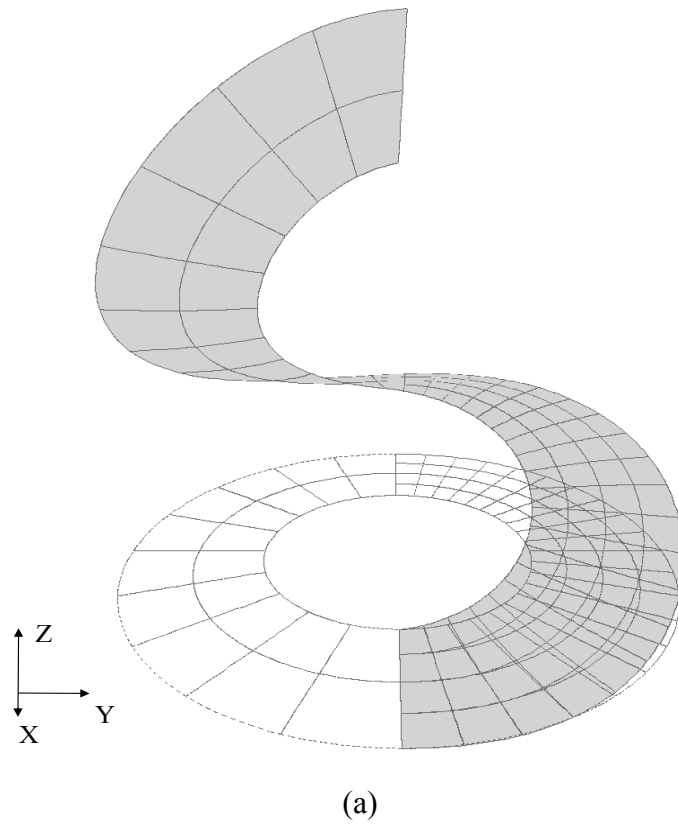


Figure 6.37: Deformed configuration at maximum displacement for annular plate models CM-3 (a) and BM-3 (b)

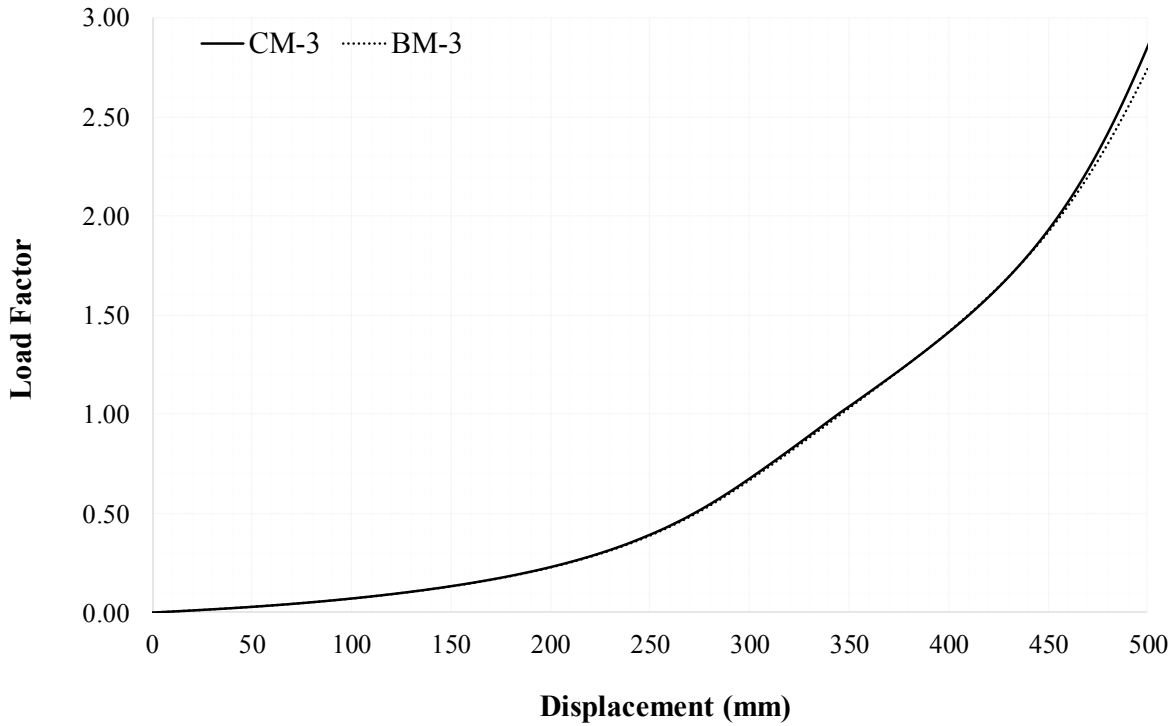


Figure 6.38: Nonlinear equilibrium path of translational DOF along the Z-axis at node P for annular plate models CM-3 and BM-3

## 6.5 Hinged cylindrical shell subjected to point load

A cylindrical shell, simply supported along its straight edges and subjected to a concentrated point load with unit nominal value applied transverse to its surface at its geometric centre, is considered herein, as shown in Figure 6.39. The shell length is specified as  $L = 508$  length units (LUs), its half-subtended angle as  $\beta = 0.1$  rad and its curvature radius as 2540 LUs, while two alternative thicknesses  $t = 12.5$  and 6.35 LUs are considered. An isotropic material constitutive model is adopted, with Young's modulus  $E = 3.105 \text{ FUs}/(\text{LUs})^2$  and Poisson's ratio  $\nu = 0.3$ , where FUs denotes the force units.

The coupled mesh configuration CM-4 comprises three edgewise adjoining cylindrical shells with identical curvature radii and half-subtended angles, and lengths of 127, 254 and 127 LUs, coupled along two curved 1-D interfaces along the curved shell edges in the global Y-direction, introduced at one and three quarters of the total shell length  $L$ . Two coarse meshes and a single fine mesh, encompassing 25 and 400 singly-curved, 9-noded shell FEs, respectively, are employed for the domain discretisation of the two shell quarters and its central part. A uniform

mesh with 800 elements is employed for the discretisation of the base mesh configuration BM-4, which is obtained by refinement of the two coarser meshes to achieve nodal alignment along each interface. Configurations CM-4 and BM-4 are illustrated in Figure 6.39.

The verification study is based on a numerical example presented by Izzuddin and Liang (2016) and aims at comparing the nonlinear response of CM-4, obtained with the employment of the developed coupling element, with that of a monolithic model investigated by the authors, which has been readily validated against a variety of results in the existing literature. Particular focus is given to highlighting the element performance in the case of surfaces discretised with curved shell FEs and coupled along a curved 1-D interface under complex stress states, taking due account of geometric and material nonlinearity.

The cylindrical shell deformed configuration corresponding to a maximum transverse displacement of 35 LUs at node P, where the central point load is being applied, is illustrated in Figure 6.40, for both CM-4 and BM-4 configurations. These correspond to the shell with thickness 12.7 LUs and are qualitatively identical for the configuration with a thickness of 6.35 LUs. Characteristic contour plots of the shell FE bending moment  $M_y$  and membrane force  $N_y$ , generalised stress entities are provided in Figures 6.41, 6.42 and 6.43 for the cylindrical shell model with thickness of 12.7 LUs, at three states over the shell deformed configuration evolution: (i) a state in the range of small displacements, prior to the limit point, associated with a transverse displacement of 1 LU, (ii) at the limit point, associated with a transverse displacement of 11 LUs, and (iii) at the maximum displacement state, associated with a transverse displacement of 35 LUs. The nonlinear equilibrium paths for the translational DOF along the Z-axis at node P for the two thicknesses under consideration are provided in Figures 6.44 and 6.45, for both CM-4 and BM-4 configurations.

The nonlinear equilibrium path of the cylindrical shell is initially thoroughly stable, with a limit point being subsequently reached for load factors of 2.25 and 0.6, for the models with thicknesses 12.7 LUs and 6.35 LUs, respectively. The shell response is thoroughly unstable after the limit point, with the sense of the initial shell curvature being fully reversed, and the shell subsequently exhibiting a stable branch associated with significant membrane action in the range of large displacements. In the case of the thinner shell, the nonlinear equilibrium path exhibits a snap-back response following the limit point. The capturing of these intricate response attributes requires the specification of a displacement control phase after the first limit point is reached.



As is evident from Figures 6.44 and 6.45, the employment of the developed coupling element allows for a virtually identical response to be obtained for CM-4 and BM-4, with a small deviation being observed only at the snap-back point in the case of the thinner shell. As can also be inferred from comparison of the contour plots in Figures 6.41, 6.42 and 6.43, the obtained force distribution for CM-4 in the various response states considered offers a good approximation of the actual distribution of BM-4, with deviations arising in the vicinity of the coupling interface due to the approximation embedded in the rotational coupling formulation. This study adds further verification to the accuracy of the proposed coupling element in the range of large displacements.

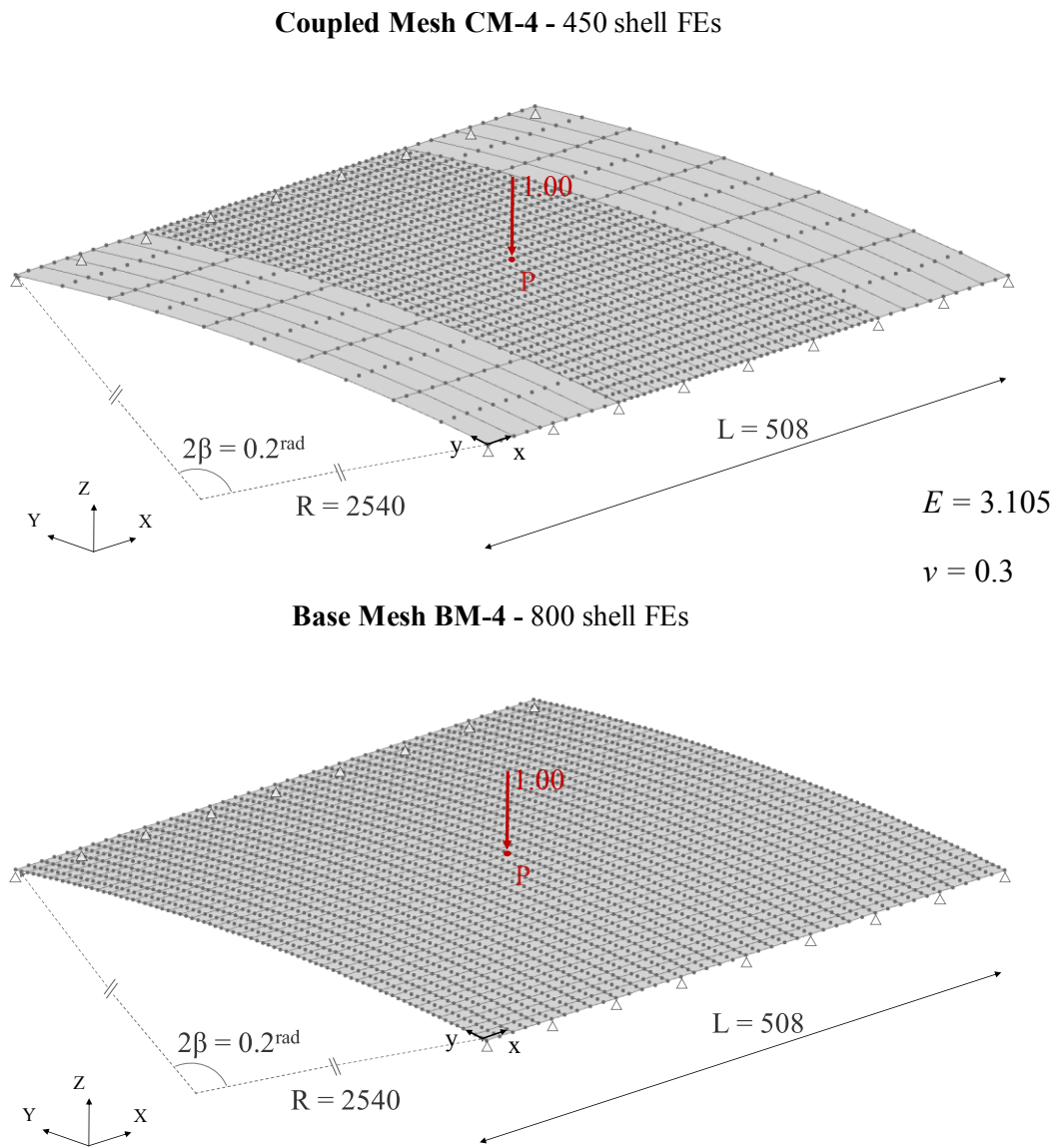
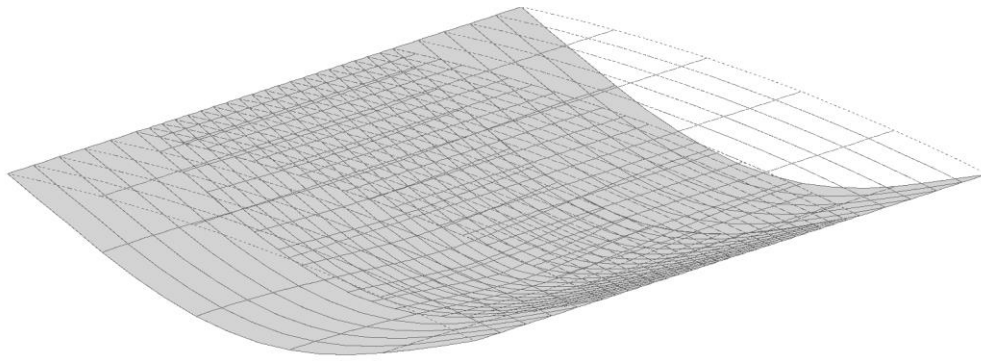
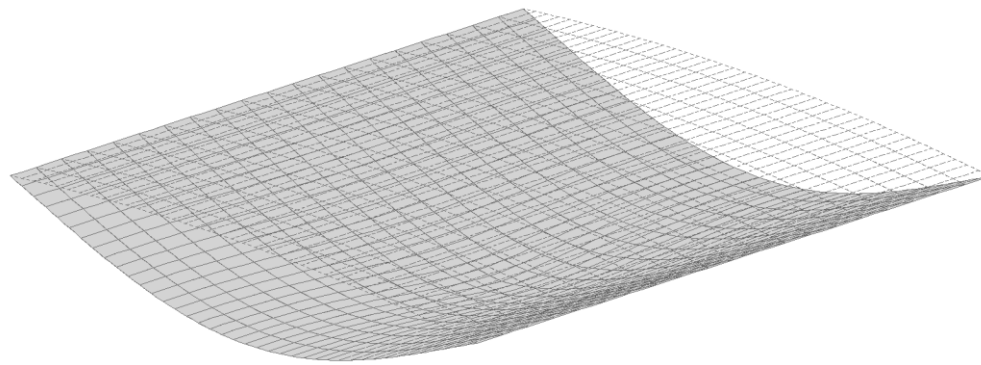


Figure 6.39: Geometric configuration, applied loading, boundary conditions and material properties for cylindrical shell models CM-4 and BM-4



(a)



(b)

Figure 6.40: Deformed configuration at maximum displacement for cylindrical shell models CM-4 (a) and BM-4 (b)

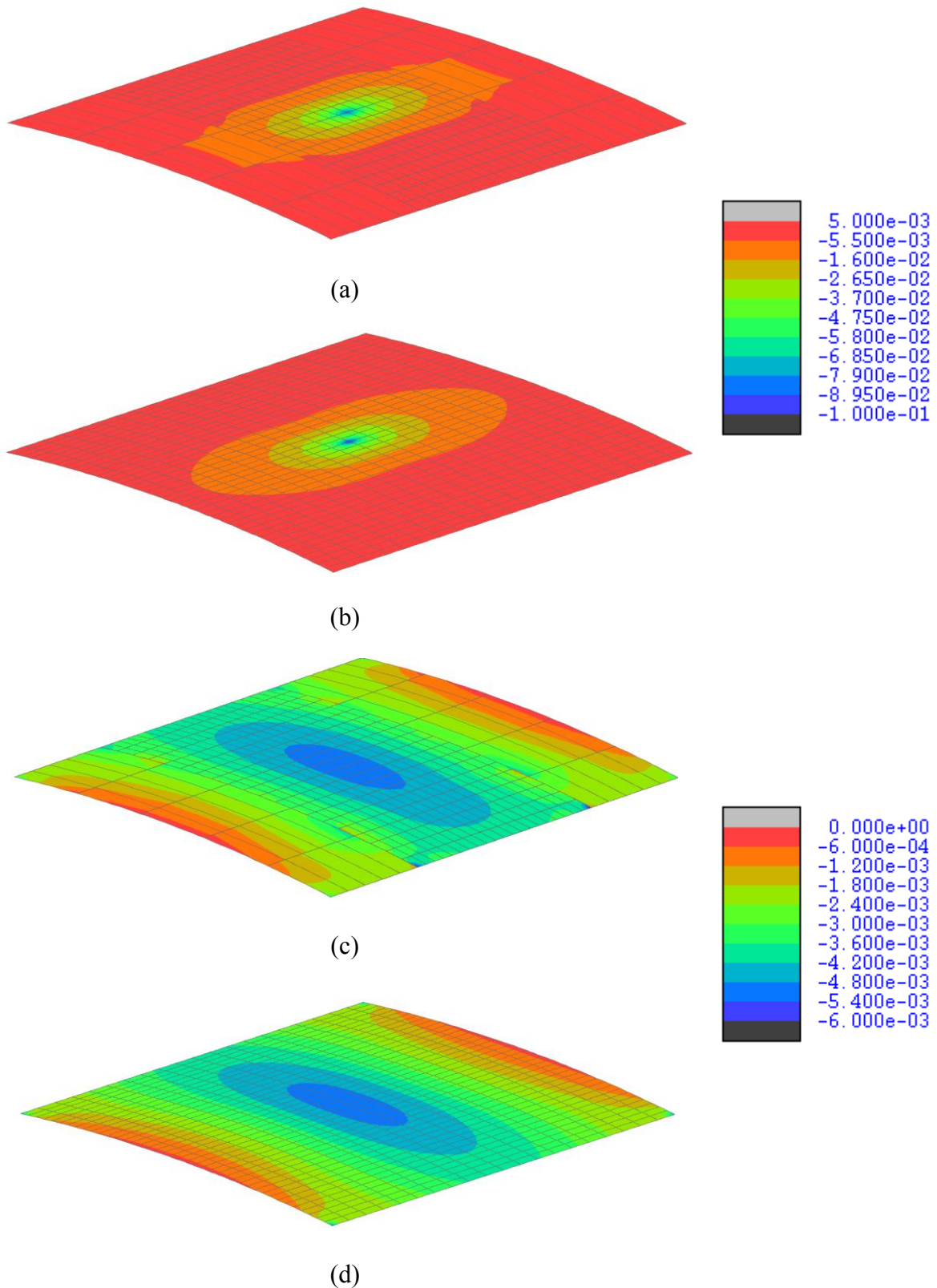


Figure 6.41: Contour plots of local shell FE generalised stress entities for cylindrical shell models with thickness  $t = 12.7$  at a small displacement state: (a) CM-4 - bending moment  $M_y$ , (b) BM-4 - bending moment  $M_y$ , (c) CM-4 - membrane force  $N_y$ , (d) BM-4 - membrane force

$N_y$

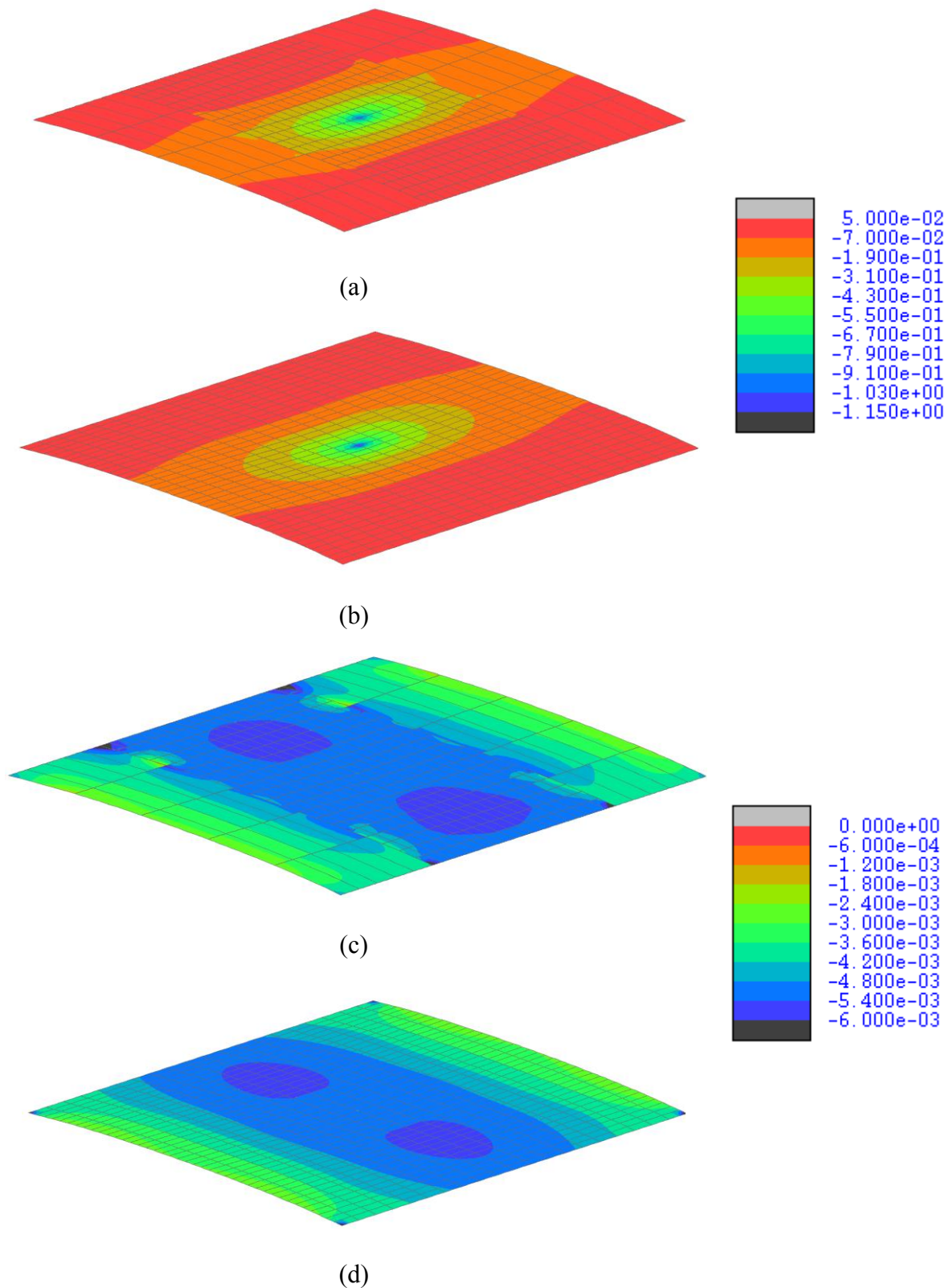


Figure 6.42: Contour plots of local shell FE generalised stress entities for cylindrical shell models with thickness  $t = 12.7$  at limit point state: (a) CM-4 - bending moment  $M_y$ , (b) BM-4 - bending moment  $M_y$ , (c) CM-4 - membrane force  $N_y$ , (d) BM-4 - membrane force  $N_y$

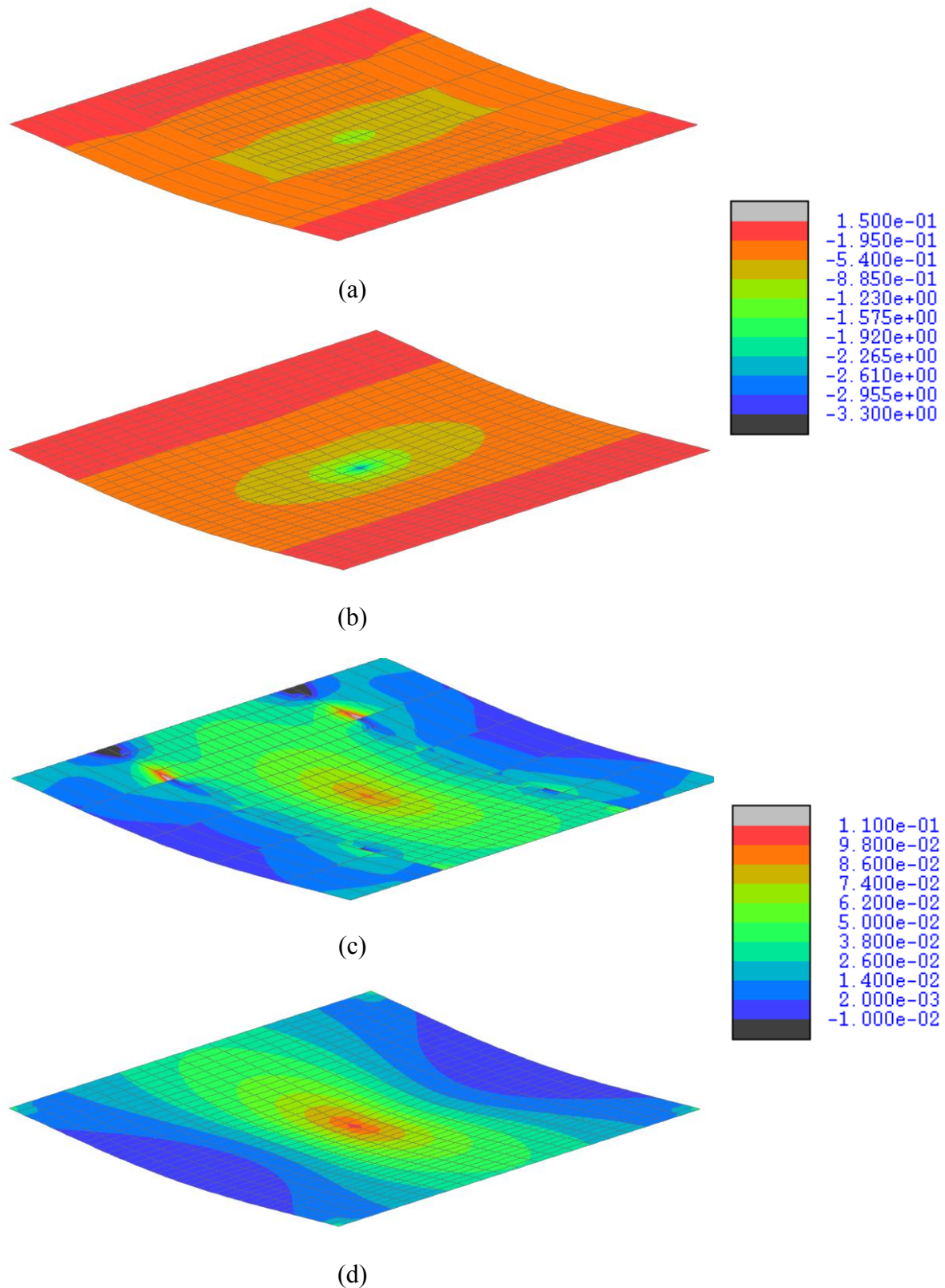


Figure 6.43: Contour plots of local shell FE generalised stress entities for cylindrical shell models with thickness  $t = 12.7$  at a maximum displacement: (a) CM-4 - bending moment  $M_y$ , (b) BM-4 - bending moment  $M_y$ , (c) CM-4 - membrane force  $N_y$ , (d) BM-4 - membrane force

$N_y$

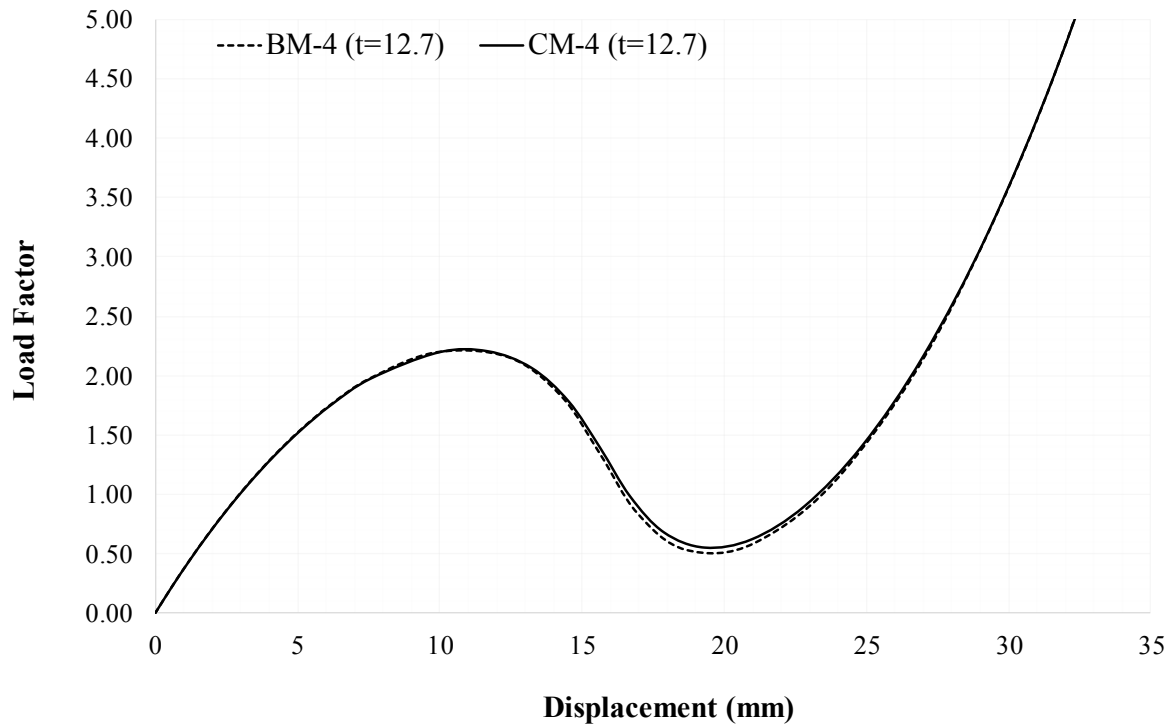


Figure 6.44: Nonlinear equilibrium path of translational DOF along the Z-axis at node P for cylindrical shell models CM-4 and BM-4 ( $t = 12.7$ )

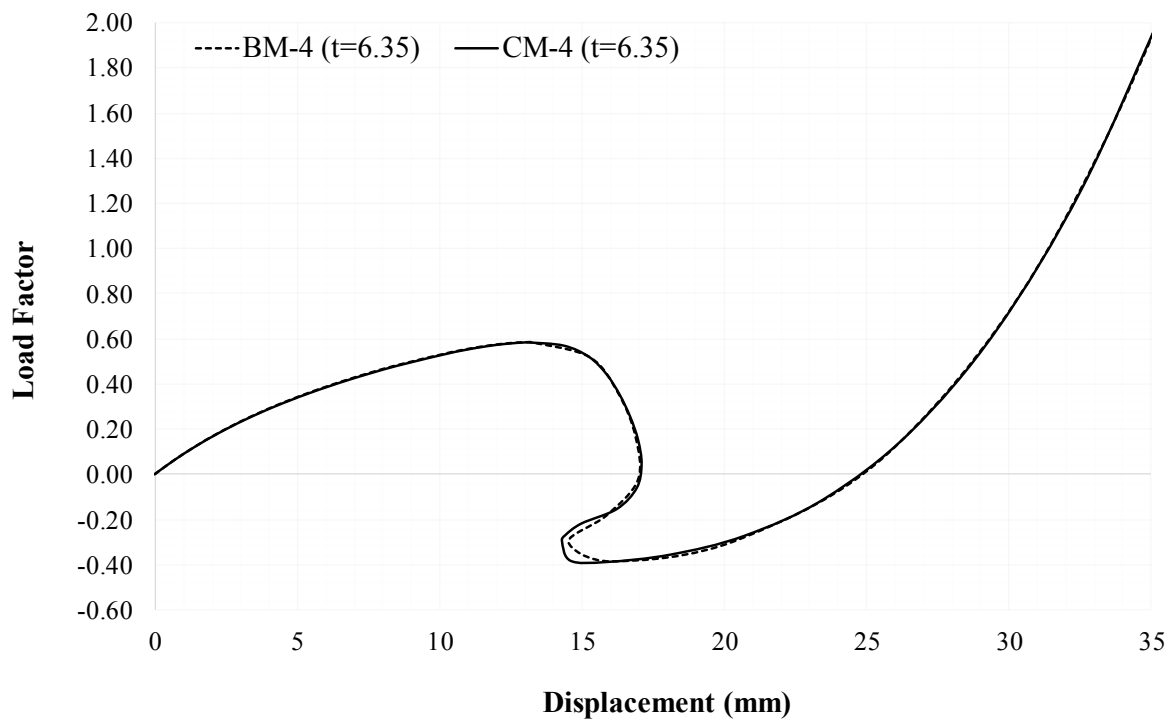


Figure 6.45: Nonlinear equilibrium path of translational DOF along the Z-axis at node P for cylindrical shell models CM-4 and BM-4 ( $t = 6.35$ )

## 6.6 Pinched hemispherical shell with cut-off

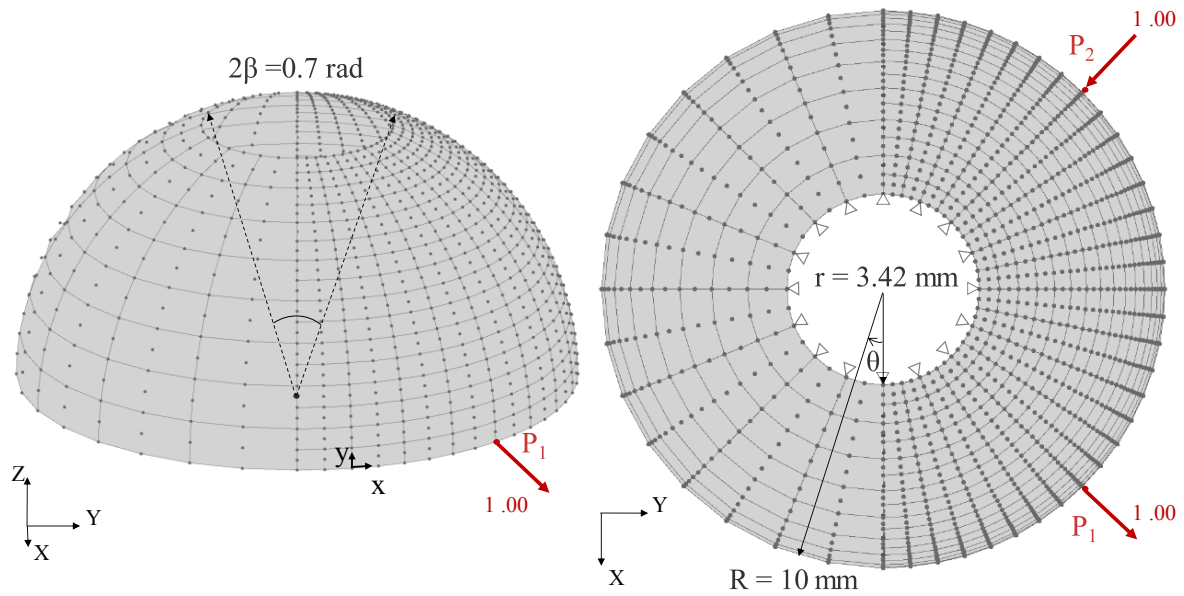
A hemispherical shell with a cut-off at its top corresponding to a half-subtended angle  $\beta = \pi/9$  rad, simply supported along its top curved edge and subjected to an orthogonal set of unit point loads acting inwards and outwards to its surface, is considered herein, as illustrated in Figure 6.46. The shell radius is specified as  $R = 10$  LUs and its thickness as  $t = 0.5$  LUs, while the point loads acting orthogonally to the surface are applied at two nodes  $P_2$  and  $P_1$  with angular polar coordinates  $\theta = 5\pi/4$  rad and  $\theta = 7\pi/4$  rad, respectively, along its bottom edge, which have been annotated in Figure 6.46. An isotropic material constitutive model is adopted, with Young's modulus  $E = 10$  FUs/(LUs)<sup>2</sup> and Poisson's ratio  $\nu = 0.2$ .

The coupled mesh configuration CM-5 comprises two edgewise adjoined half hemispherical shells with identical radii, coupled along two curved 1-D interfaces introduced over the shell sections with angular polar coordinates  $\theta = 0$  and  $\pi/2$  rad. Two meshes with 64 and 256 9-noded shell FEs with curved edges are employed for the domain discretisation of the two hemispherical halves, while a uniform mesh encompassing 1024 elements is employed for the BM-5 configuration. The verification study is an alteration of a numerical example presented by Izzuddin and Liang (2016), with particular consideration given herein to highlighting the element performance in achieving translational and rotational coupling of non-developable surfaces discretised with doubly-curved shell FEs along a curved 1-D interface under complex stress states, taking due account of geometric and material nonlinearity.

The hemispherical shell deformed configuration corresponding to maximum planar displacements of 8 and 4 LUs at nodes  $P_2$  and  $P_1$ , respectively, is illustrated in Figure 6.47, for both CM-5 and BM-5 configurations. The associated nonlinear equilibrium paths of the translational DOFs along both the X- and Y-axes at nodes  $P_1$  and  $P_2$  are collectively shown in Figure 6.48. On the basis of the justification provided in Section 6.4, contour plots are not considered herein for comparison of CM-5 and BM-5.

By comparing the nonlinear equilibrium paths and deflected shapes for BM-5 and CM-5, the element ability to achieve a virtually identical response in the range of large displacements for curved shell FEs coupled along a curved 1-D interface is highlighted, thus adding further verification to the accuracy of the proposed coupling element in the range of large displacements.

**Coupled Mesh CM-5 - 320 shell FE s**



$E = 10.0$

$\nu = 0.2$

**BaseMesh BM-5 - 1024 shell FEs**

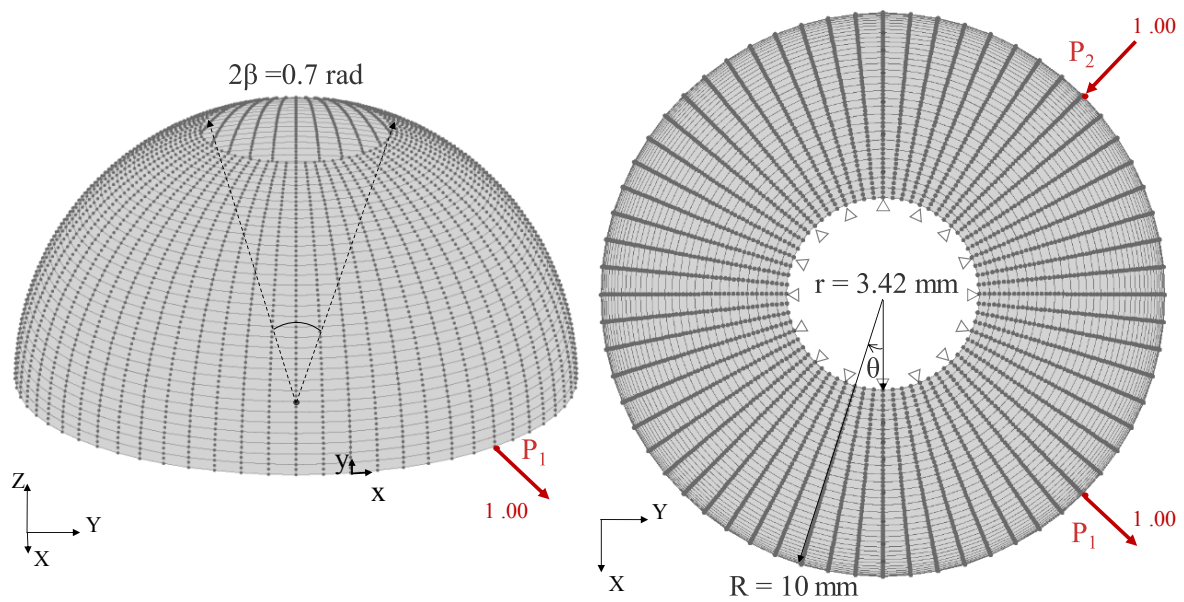


Figure 6.46: Geometric configuration, applied loading, boundary conditions and material properties for hemispherical shell models CM-5 and BM-5



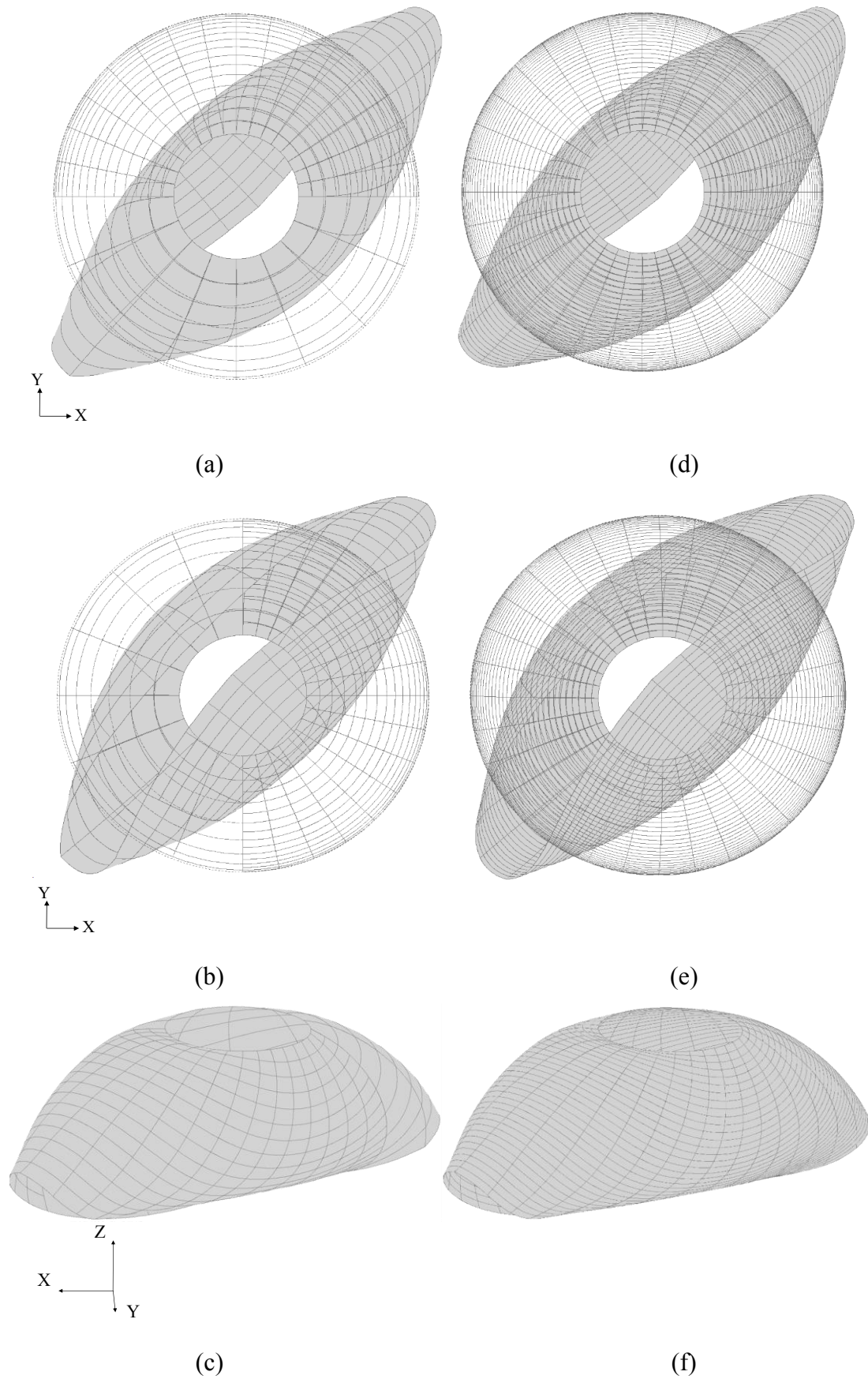


Figure 6.47: Deformed configuration at maximum displacement for hemispherical shell models CM-5 (a, b, c) and BM-5 (d, e, f)

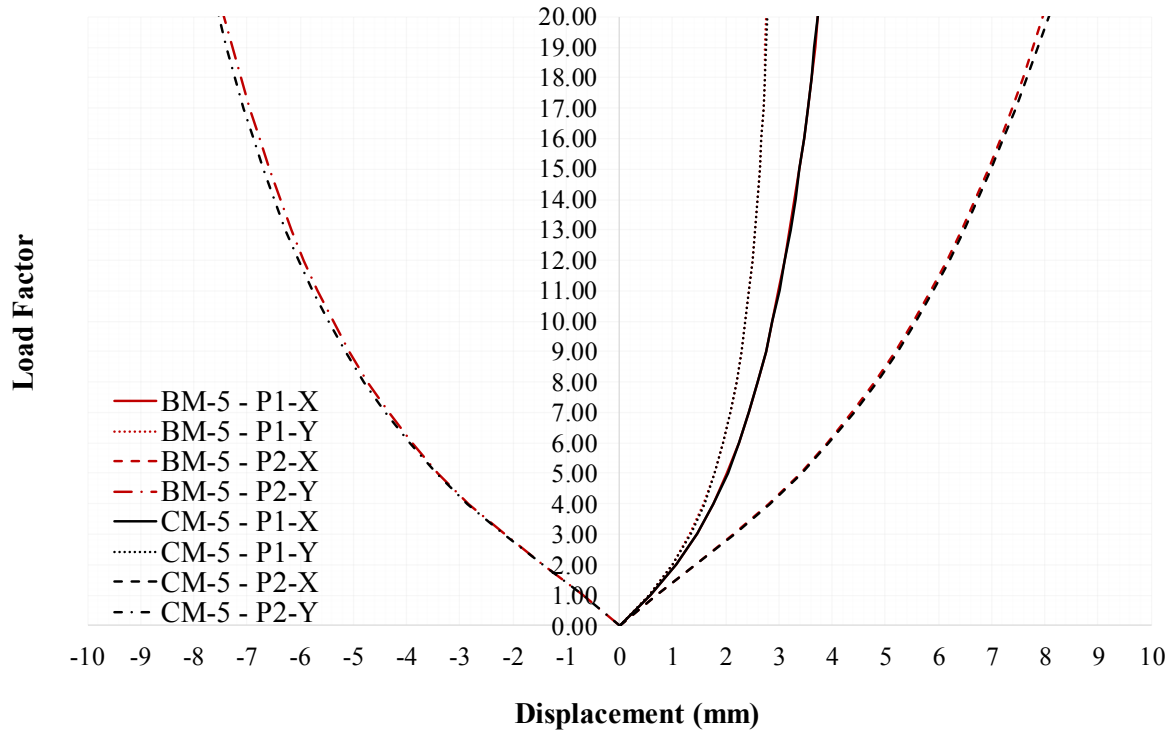
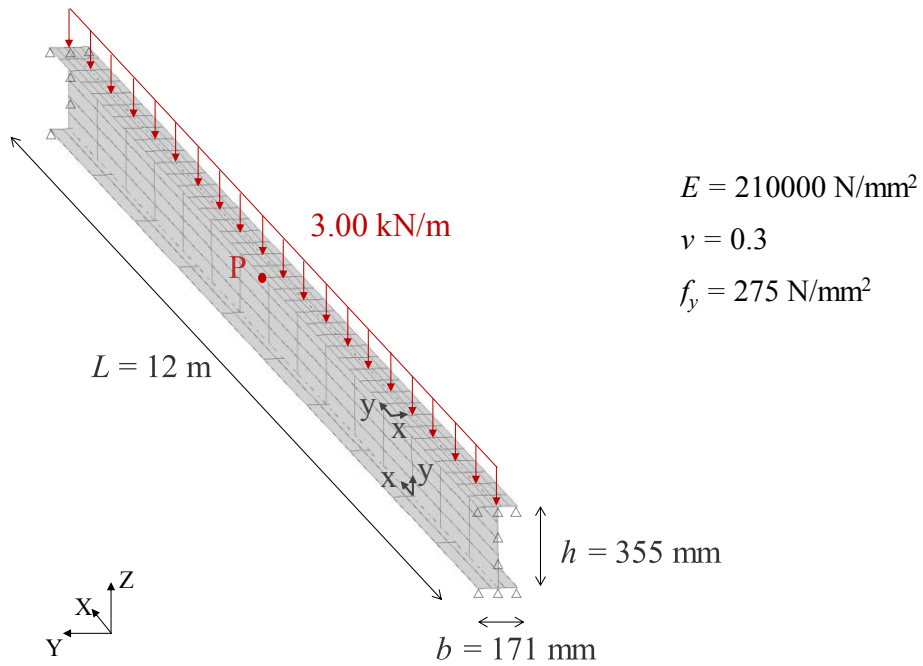


Figure 6.48: Nonlinear equilibrium path of translational DOFs along the X- and Y-axes at nodes P<sub>1</sub> and P<sub>2</sub> for hemispherical shell models CM-5 and BM-5

## 6.7 Imperfect I-beam subjected to transverse loading

A 12m long I-beam, simply supported at its two ends and subjected to a centrally applied uniformly distributed transverse load with a nominal value of 3 kN/m, is considered herein, as illustrated in Figure 6.49. A designated Universal Beam (UB) 356×171×51 cross-section in accordance with the provisions of BS EN 1993-1-1:2005 (BSI, 2005) is considered, with height  $h = 355$  mm, width  $b = 171$  mm, flange thickness  $t_f = 11.5$  mm and web thickness  $t_w = 11.5$  mm. Translational restraints in the global Z-direction are introduced over both the web and flanges at the two beam ends, with planar restraints in the global X- and Y-directions being introduced at one node on each end to restrain the beam against rigid body motion, while allowing for displacements in the X-direction. An isotropic constitutive model is adopted for structural steel, with Young's modulus  $E = 210000$  N/mm<sup>2</sup> and Poisson's ratio  $\nu = 0.3$ , where two cases are considered: (i) a perfectly elastic material response, and (ii) an elastoplastic material response with yield strength  $f_y = 275$  N/mm<sup>2</sup>, corresponding to S275 grade steel with negligible strain-hardening.

**Coupled Mesh CM-6 - 305 shell FEs**



**Base Mesh BM-6 - 1040 shell FEs**

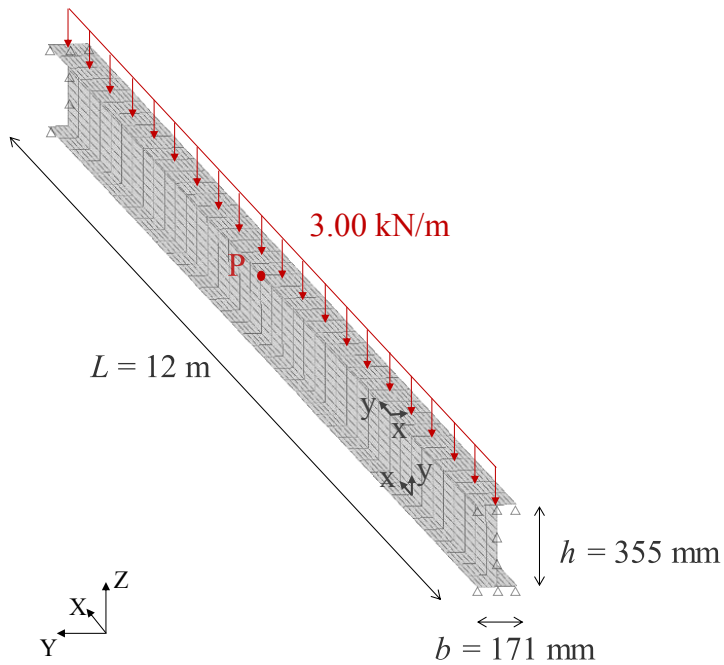


Figure 6.49: Geometric configuration, applied loading, boundary conditions and material properties for I-beam models CM-6 and BM-6

A sinusoidal imperfection is introduced at the top flange, along the global Y-axis, with maximum magnitude  $L/8000 = 1.5$  mm at mid-span, where  $L$  is the beam length. Owing to this imperfection, the beam exhibits lateral torsional buckling (LTB) prior to the attainment of its yielding moment, followed by substantial transverse and lateral deformations. Particular focus is given to highlighting the coupling element performance in achieving translational and rotational coupling of intersecting surfaces along a 1-D interface traversing their domains, under complex stress states involving combined bending and twisting rotations.

The coupled mesh configuration CM-6 comprises three independently discretised planar shell surfaces, corresponding to the beam web and flanges, coupled along two straight 1-D interfaces introduced at their intersections in the global X-direction. The bottom flange and web are discretised with 30 and 75 shell FEs, respectively, while a denser mesh is employed for the top flange, encompassing 200 elements. A uniform mesh with 1040 elements is employed for the discretisation of the base mesh configuration BM-6, with 400 and 320 elements employed for the web and each of the flanges, respectively. Configurations CM-6 and BM-6 are illustrated in Figure 6.49. The coupled and base configurations for the two distinct material specifications under consideration will henceforth be denoted as CM-6a, CM-6b and BM-6a, BM-6b, with (a) referring to perfectly elastic and (b) to perfectly elastoplastic material response.

The nonlinear equilibrium paths of the translational DOFs along both the Y- and Z-axes at node P are collectively shown in Figure 6.50, for both material specifications under consideration, where the vertical axis is normalised with the critical bending moment of 58.32 kN/m at the onset of LTB, as obtained from the model response. The deformed configurations of the beam for a displacement along the Y-axis of 450 mm at node P, as annotated in Figure 6.49, are illustrated in Figure 6.51 for the CM-6b and BM-6b models, while characteristic contour plots of the shell FE twisting moment  $M_{xy}$  generalised stress entity for these configurations at the same deformation state are given in Figure 6.52.

The nonlinear equilibrium paths of the translational DOFs along the Y- and Z-axes at node P are initially stable, with buckling observed at a load factor of around 1.0 for both material models under consideration, indicating that the beam is initially exhibiting elastic buckling due to being relatively slender.

Evidently, the employment of the developed coupling element allows for the progressive evolution of the beam deformed shape to be accurately captured, leading to a virtually identical

nonlinear response for CM-6 and BM-6, with a small deviation observed only in the range of very large displacements, of the order of  $L/30$ . A virtually identical deformed configuration is obtained in both cases, as shown in Figure 6.51, while the contour plots of Figure 6.52 indicate an accurate approximation of the internal twisting moment distribution. This study provides further verification of the proposed coupling element for the case of shells meeting at an angle, allowing for geometric and material nonlinearity to be accurately captured.

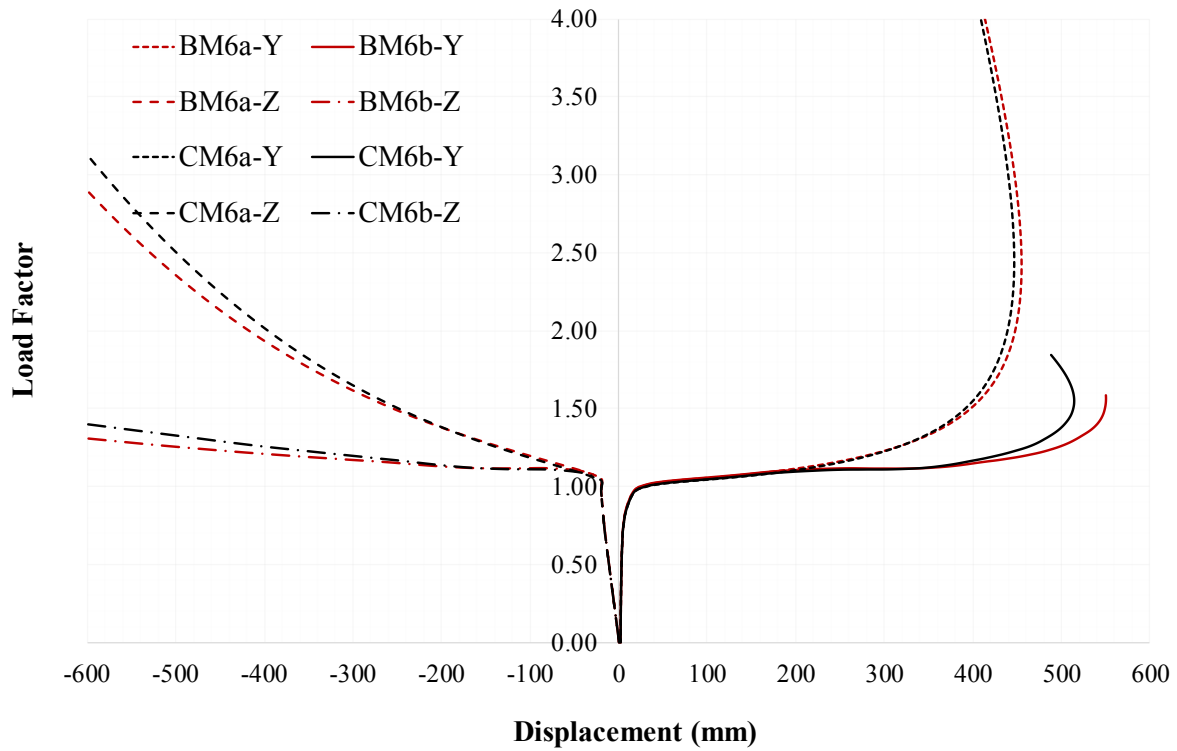
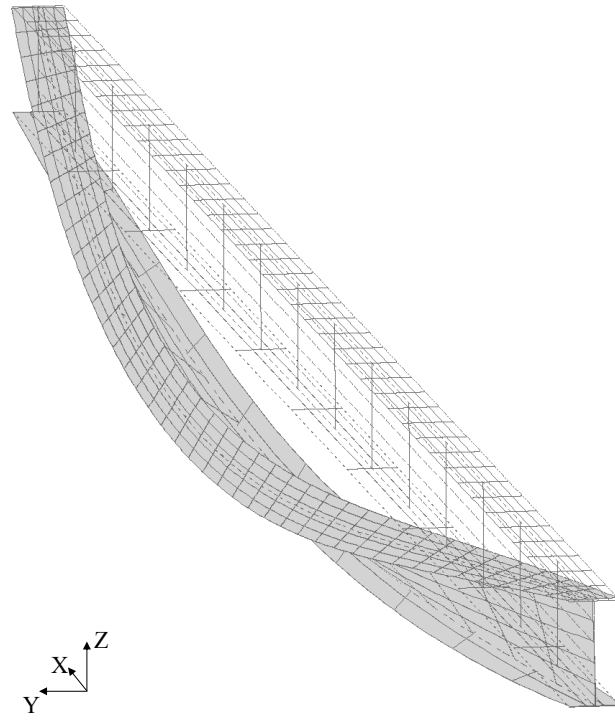
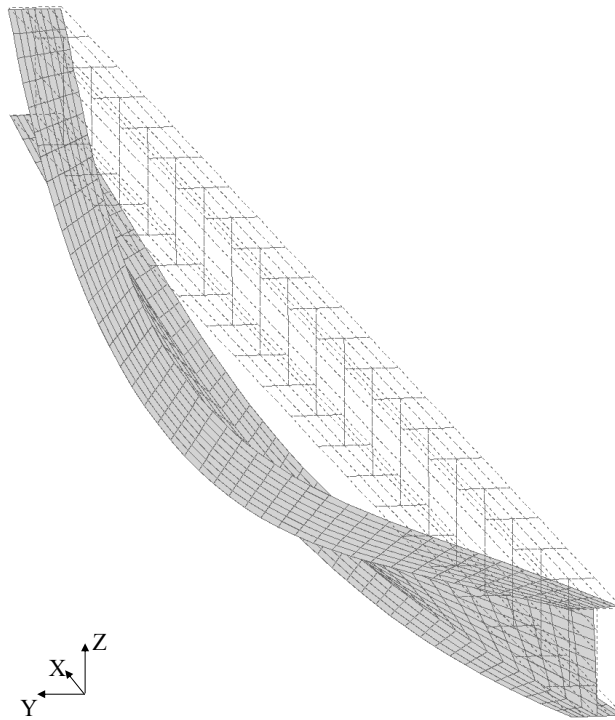


Figure 6.50: Nonlinear equilibrium paths of translational DOFs along the Y- and Z-axes at node P for I-beam models CM-6 and BM-6

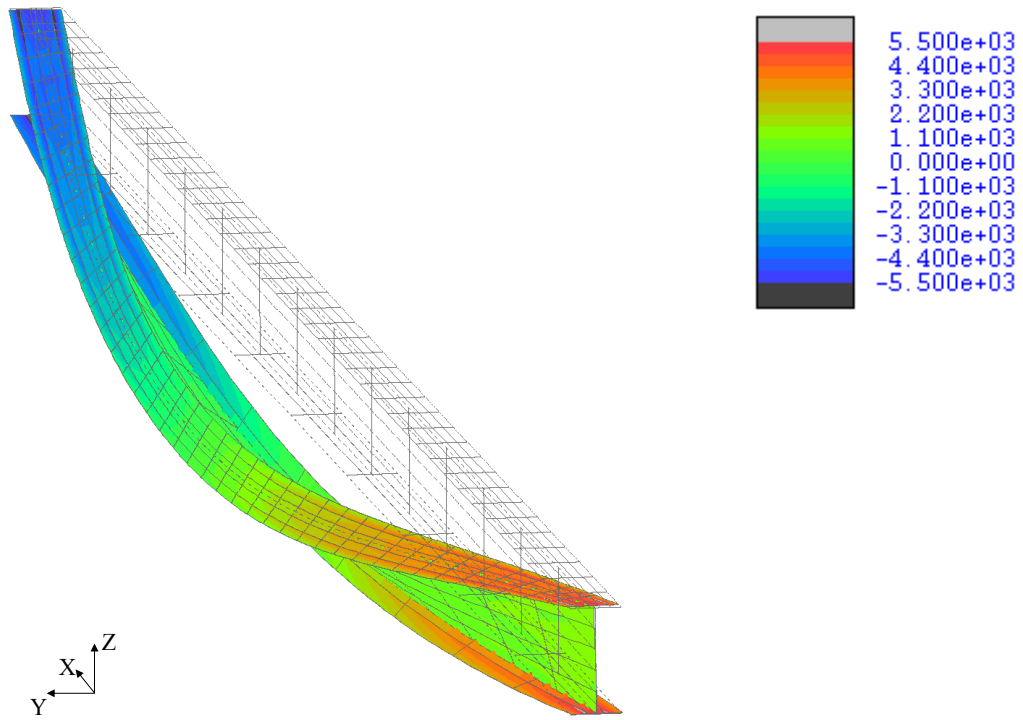


(a)

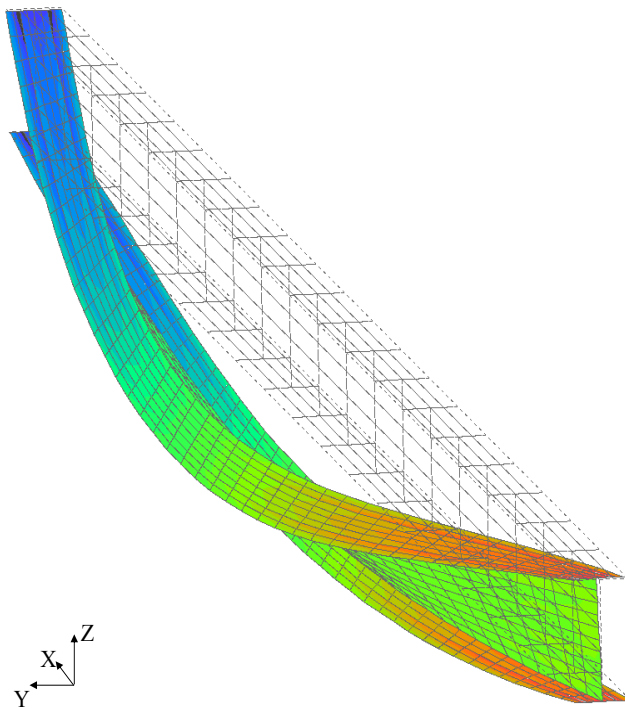


(b)

Figure 6.51: Deformed configuration at maximum displacement for I-beam models CM-6b (a) and BM-6b (b)



(a)



(b)

Figure 6.52: Contour plots of local shell FE twisting moment  $M_{xy}$  at maximum displacement for I-beam models CM-6b (a) and BM-6b (b)

## 6.8 Concluding remarks

A series of numerical studies has been presented in this chapter to verify the ability of the developed coupling element to enforce translational and rotational kinematic constraints along a 1-D interface, between planar or curved, edgewise-connected or intersecting shell surfaces, discretised with regular or irregular Reissner-Mindlin curved shell FEs. It is demonstrated that the proposed coupling element can achieve an accurate internal force distribution under constant membrane, bending, planar and transverse shear, as well as twisting stress states. The obtained distribution is exact in the case of stress states solely mobilising translational LMs for the constraint enforcement. On the other hand, the approximation embedded in the rotational coupling formulation, discussed in Section 5.3, introduces discontinuities in the transverse moment and shear distributions in the coupling interface vicinity, which however become smoother away from it. Nevertheless, this allows for global equilibrium to be satisfied, irrespectively, while the discontinuities reduce with mesh refinement to negligible local effects in the vicinity of coupling. For the considered cases of planar and curved shell surfaces with regular and irregular elements, the coupling element is capable of reproducing the deformed configuration evolution, achieving a virtually identical nonlinear response with the corresponding monolithic models, as well as an accurate internal force distribution. Minor deviations arise only in the range of very large displacements, which are partially attributed to the approximation embedded in rotational coupling, as well as to the employment of a relatively coarse mesh in the CM variants in some of the studies presented.



# Chapter 7

## Application Studies on High-Fidelity Modelling of Composite Structural Systems

### 7.1 Introduction

The established High-Fidelity (HF) nonlinear Finite Element (FE) modelling strategy and dual super-element domain partitioning methodology, presented in Chapter 3, alongside the developed 1-D coupling element, presented in Chapters 4 and 5 and verified in Chapter 6, are employed herein for a series of application studies on moderate- to large-scale composite structural systems. The principal objectives of the numerical studies conducted and presented here encompass the showcasing of the following aspects: (i) the effectiveness, accuracy and credibility of the established HF nonlinear FE modelling strategy for realistic 3-D nonlinear analysis of composite structures; (ii) the substantial benefits associated with the employment of dual super-element domain partitioning for HF modelling, in respect of the achieved reduction in the computing wall-clock time and the overcoming of memory bottlenecks; (iii) the substantial benefits associated with the incorporation of the developed 1-D coupling element in the established HF modelling strategy, in respect of modelling flexibility, computational efficiency and practicality; and (iv) the accuracy and versatility of a combined approach encompassing the conjunct employment of all the above for practical applications to real composite structural systems.

The accuracy and efficiency of the established HF modelling strategy for nonlinear FE analysis of composite structures is demonstrated in the context of application study 1, presented in

Section 7.2, where consideration is given to large-scale, all-metal sandwich composites. The study primarily focuses on the capturing of the various forms of local instabilities manifested over the domain and their interactions with the spread of plasticity using the proposed modelling strategy, which is critical in such structures due to their response sensitivity to such phenomena.

The computational benefits of partitioned modelling using the dual super-element approach (Jokhio & Izzuddin, 2015) for scalable parallel processing in High Performance Computing (HPC) systems with distributed memory is showcased in the context of application study 2, presented in Section 7.3, with reference to the results of application study 1. The limitations of excessive partitioning are discussed, and practical guidance is also provided for the selection of the optimal domain partitioning configuration, offering maximum speedup, beyond which further partitioning leads to excess in both the nonlinear solution procedure and the communication overhead between parallel processors.

The modelling flexibility and computational efficiency of the 1-D coupling element incorporation in the HF modelling strategy, allowing for selective discretisation of independent substructures within a mesh, is illustrated in the context of application study 3, presented in Section 7.4, with reference to the results of application study 1. The additional benefits of enhancing the selective discretisation approach with domain partitioning capabilities are also discussed, with reference to the results of application study 2, in view of establishing a unified HF modelling framework for composite systems.

The credibility of the established HF strategy for realistic 3-D modelling of composite structural systems is demonstrated in application study 4, presented in Section 7.5, where this is validated against experimental results. The results have been obtained from physical testing of the novel, all-steel, sandwich panel composites envisioned to be incorporated in offshore topside decks in the context of the INFLOAT project.

Having established the accuracy and credibility of the HF modelling approach, as well as the efficiency of the 1-D coupling element incorporation in it, the combined modelling strategy is used in application study 5, presented in Section 7.6, for the realistic 3-D modelling of a passive explosion-protective barrier installed on an offshore platform topside deck. The performance assessment of the barrier is compared for the cases where this is modelled individually, as is common in industrial practice, and where a selective discretisation approach using the 1-D

coupling element is adopted to incorporate the contribution of surrounding structural elements in the system modelling. A discussion is also provided on the potentially unconservative nature of commonly adopted design assumptions in engineering practice.

The chapter proceeds with presenting the five application studies, all of which have been conducted using ADAPTIC (Izzuddin, 1991) v2.16.5, where the developed 1-D coupling element has also been implemented.

## **7.2 Application study 1: High-fidelity nonlinear analysis of large-scale all-metal sandwich composites**

The HF modelling strategy presented in Chapter 3 is employed herein for the nonlinear response investigation and buckling mode characterisation of large-scale, all-metal, sandwich panel composites with rectangular and hexagonal honeycomb core topologies. Particular focus is given to two-way spanning, large-scale, composite deck system applications, where all-metal sandwich panels are employed as deck components subject to extreme static and dynamic loading.

As discussed in Chapter 3, the modelling strategy based on the employment of hierarchically optimised, lock-free, co-rotational shell FEs (Izzuddin & Liang, 2016; 2017) allows for the effects of geometric and material nonlinearity on the structural response to be accurately captured in the range of large displacements. In sandwich composites comprising individual plated components in the faceplates and core, arranged in a periodic honeycomb cell topological pattern, various forms of local instabilities are manifested at several locations over the domain and spread from its centre to the four edges. For large-scale composite deck systems in particular, the capturing of all local instabilities is essential for an accurate nonlinear response evaluation and failure mode characterisation, as well as for a reliable robustness and energy dissipation capability assessment in the case of extreme accidental loading. Therefore, the establishment of a HF nonlinear FE modelling approach for this type of structural system, enabling the capturing of the various local buckling phenomena, necessitates the employment of the proposed modelling strategy with a substantial mesh density.

The aim of the present section is to demonstrate the capabilities and efficiency of the proposed HF modelling strategy, rather than the detailed investigation of the sandwich component response to various load types, hence consideration is given only to extreme static loading. The two most commonly encountered static load cases in composite deck systems are therefore considered, namely uniformly distributed loading (UDL) and localised patch loading (PL).

The results obtained from static incremental nonlinear analyses are presented to highlight the ability of the proposed strategy to accurately capture the variety of complex buckling phenomena, alongside the spread of plasticity, in the large displacement range. The results obtained with both a coarse and dense mesh of shell FEs are compared to demonstrate the necessity of employing a substantial mesh density for the domain discretisation, so as to achieve good accuracy. Furthermore, an imperfection sensitivity analysis is conducted on panels with rectangular honeycomb core topology, to highlight the influence of imperfections on the global panel response and emphasise the importance of their incorporation in the HF modelling strategy for accurate response prediction.

### **7.2.1 Problem Description**

For the numerical studies presented herein, consideration is given as base cases to large-scale  $3000 \times 3000 \text{ mm}^2$  sandwich panels, as illustrated in Figure 7.1 (a), with 100 mm depth between the mid-planes of the top and bottom plates, and 3 mm thickness for the top and bottom plates and the core cell walls. Regular cell geometries have been adopted for both topologies under consideration, with  $90^\circ$  and  $120^\circ$  cell wall angles for rectangular and hexagonal honeycomb core configurations, respectively, as illustrated in Figure 3.3 (b) and Figure 7.1 (b), (c). The rectangular cell dimensions along the orthogonal global planar X- and Y- axes are set to  $100 \times 100 \text{ mm}^2$ , while for the hexagonal cells a core configuration of equivalent density is considered, with 60 mm cell wall width and  $120 \times 104 \text{ mm}^2$  planar cell dimensions.

A triaxial elastoplastic constitutive model for mild steel is adopted, with yield strength  $f_y = 355 \text{ N/mm}^2$ , Young's Modulus  $E = 210000 \text{ N/mm}^2$  and Poisson's ratio  $\nu = 0.3$ . The strain hardening parameter is neglected to allow for the influence of local buckling and the spread of plasticity on the panel response to be more effectively demonstrated.

All panels are modelled as simply supported along all 4 edges, with translational restraints introduced at the nodes along the bottom plate perimeter in the global Z direction and minimal planar restraint provided along the global X- and Y- axes to prevent rigid body motion, as illustrated in Figure 7.1 (a). Moreover, all welded connections at the core cell intersections, as well as between the core and the faceplates, are considered to be fully rigid.

For the two transverse load cases under consideration the load is applied incrementally, with nominal values  $p_{nom}=260 \text{ kN/m}^2$  for UDL and  $P_{nom}=800 \text{ kN}$  for PL, where in the latter case the localised load is applied uniformly over a stiff, practically rigid baseplate with  $300 \times 300 \text{ mm}^2$  planar dimensions, located at the panel centre, as illustrated in Figure 7.1 (a).

For the imperfection sensitivity analyses, alternative sympathetic sinusoidal imperfections are introduced over the faceplate and core cell walls of rectangular honeycomb panels, considering zero displacements and compatible rotations along the boundaries, as illustrated previously in Figure 3.3 (c). The values of imperfection amplitude considered correspond to 0.1%, 0.2%, 0.5%, 1.0% and 2.0% of the minimum plated component dimension forming individual rectangular honeycomb cells, leading to 0.1 mm, 0.2 mm, 0.5 mm, 1.0 mm and 2.0 mm maximum nodal transverse dislocations, respectively.

The terminating condition for all analyses is specified as a maximum value of global transverse displacement of 300 mm, corresponding to 10% of the global panel dimensions, beyond which excessive strains, of the order of the ultimate strain for mild steel, are typically observed.

Shell FE meshes are employed for the discretisation of both the rectangular (R) and hexagonal (H) core topology models under consideration, with two different densities for each model: (i) 43200 and 230400 elements for the R models, and (ii) 59256 and 314496 elements for the H models. For each of the R and H models, the coarser and denser configurations will henceforth be denoted as Conventional (C) and High-Fidelity (HF), which enables the establishment of four distinct model variants with corresponding acronyms (R-C), (R-HF), (H-C) and (H-HF).

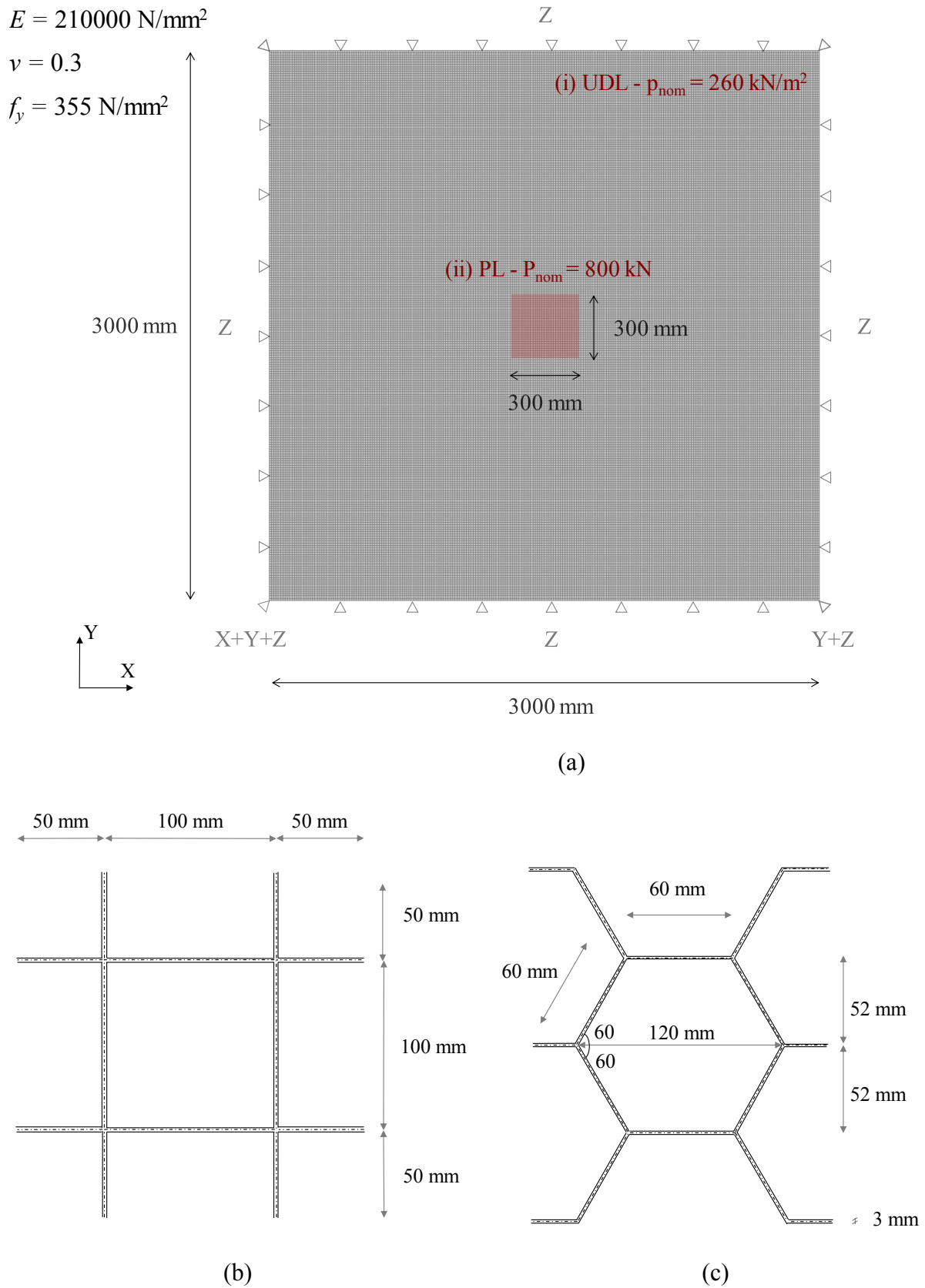


Figure 7.1: (a) Geometric configuration, applied loading, boundary conditions and material properties for sandwich composite models R-C, R-HF, H-C and H-HF, (b) core topology of R-C and R-HF, (c) core topology of H-C and H-HF

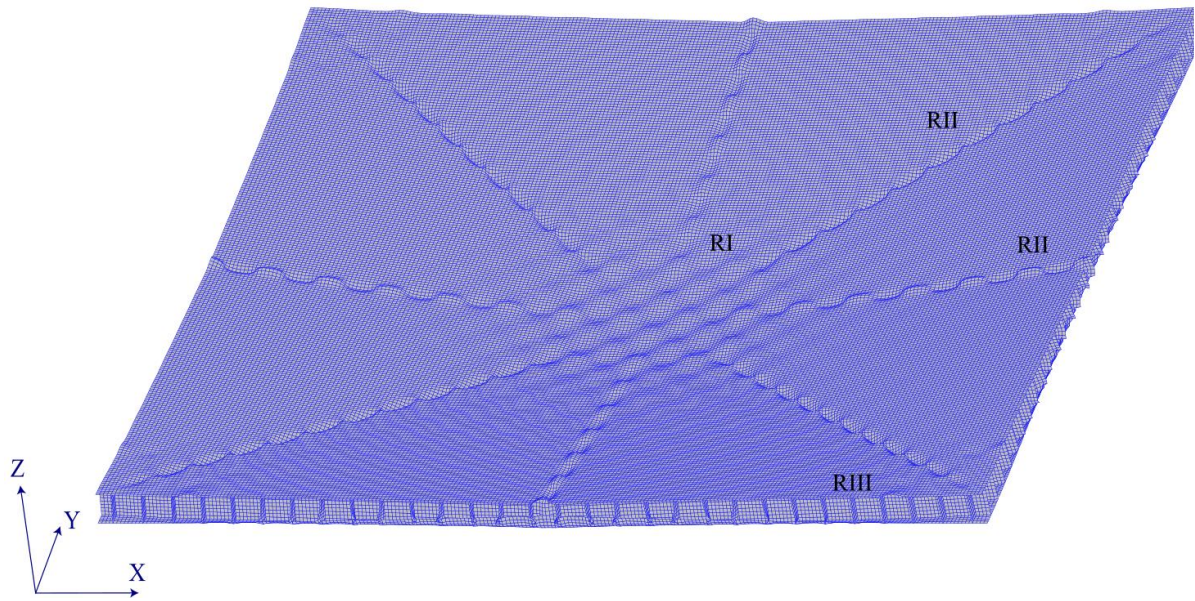
### 7.2.2 Response of large-scale all-metal sandwich composites subject to UDL

The deformed configurations at maximum displacement for the R-HF and H-HF model variants subject to UDL are illustrated in Figure 7.2. The nonlinear equilibrium paths of the translational Degrees of Freedom (DOF) along the global Z-axis at the bottom faceplate central node for the R-C, R-HF variants are provided in Figure 7.3, and for the H-C and H-HF variants in Figure 7.4. Three distinct response ranges can be identified in the nonlinear equilibrium paths of Figures 7.3 and 7.4, which have been annotated on the respective graphs, as well as on the deflected shapes of Figure 7.2 (a) and (b), as RI, RII and RIII. Various forms of local instabilities are manifested in these response regions, which are illustrated in the local contour plots of the shell element bending moment  $M_y$  generalised stress entity for variants R-HF and H-HF in Figures 7.5 and 7.6, respectively. The contour plots have been resolved along the global Y-axis, while the direction of the local y-axis for the shell elements on the faceplates and the core cell walls have been defined as in Figure 3.3 (b).

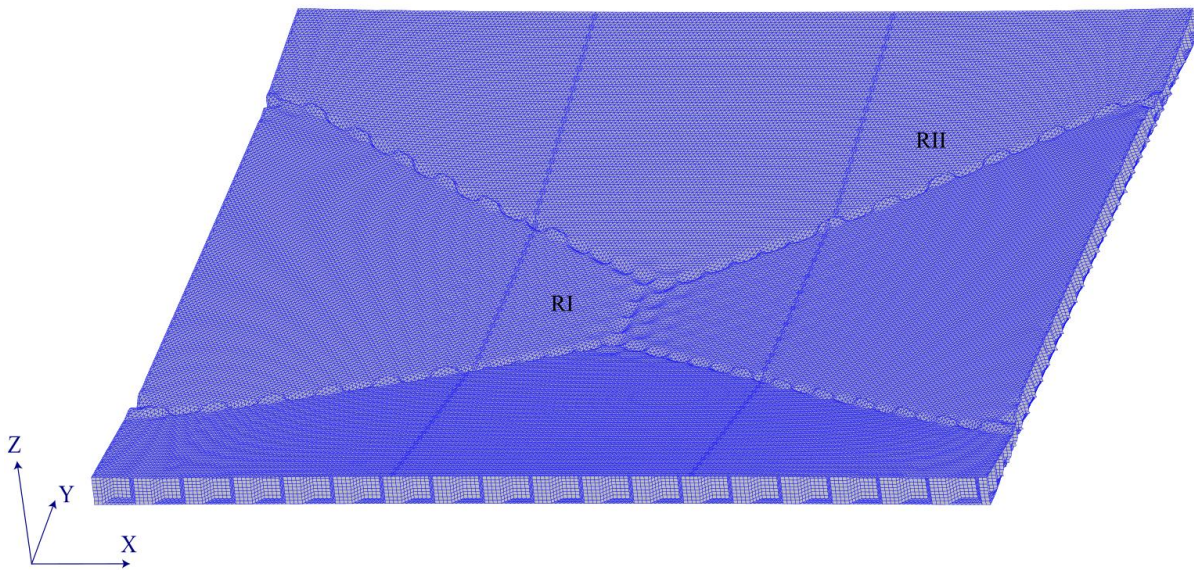
Considering more closely the nonlinear response under UDL in Figures 7.3 and 7.4, the elastic flexural response of both rectangular and hexagonal honeycomb configurations in range I is followed by yielding of both faceplates at the central region, along with elastoplastic intercellular buckling of the top faceplate between the cell walls. These phenomena are demonstrated in Figures 7.5 (a) and 7.6 (a) for the R-HF and H-HF model variants, respectively.

Range II is associated with yield line formation, extending towards the 4 panel corners in the direction of maximum shear stresses at 45° epicentral angles, as shown in Figures 7.5 (b) and 7.6 (b) for model variants R-HF and H-HF, respectively. The yield line propagation induces primarily shear yielding and subsequent plastic penetration (transverse shear deformation) local buckling in the vicinity of yield lines, on top of the intersected cells. This is further accompanied by the formation of lines of buckled cells along the horizontal and vertical planar axes in the R-HF variant, as illustrated in Figure 7.5 (c).

In range III, which is related to large displacements, the sandwich composites exhibit membrane action, resulting in the response stiffening observed in the graphs of Figures 7.3 and 7.4, as well as in the development of a perimetric compressive stress field. The ‘hoop’ action induced by the compressive stress field induces buckling of the top faceplate of R-HF on top of half-cells in the panel perimeter, as illustrated in Figure 7.2 (a).



(a)



(b)

Figure 7.2: Deformed configuration at maximum displacement for sandwich composite models subject to UDL: (a) R-HF, (b) H-HF



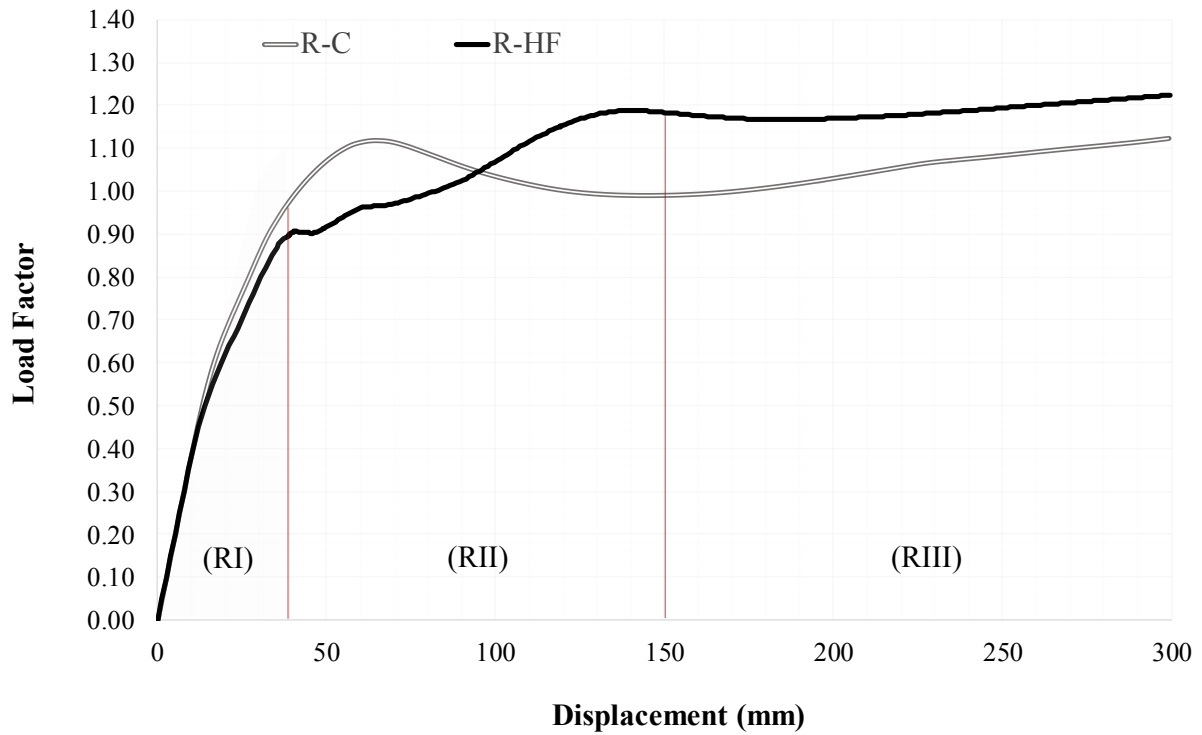


Figure 7.3: Nonlinear equilibrium path of translational DOF along the Z-axis at bottom faceplate centre for sandwich composite models R-C and R-HF subject to UDL

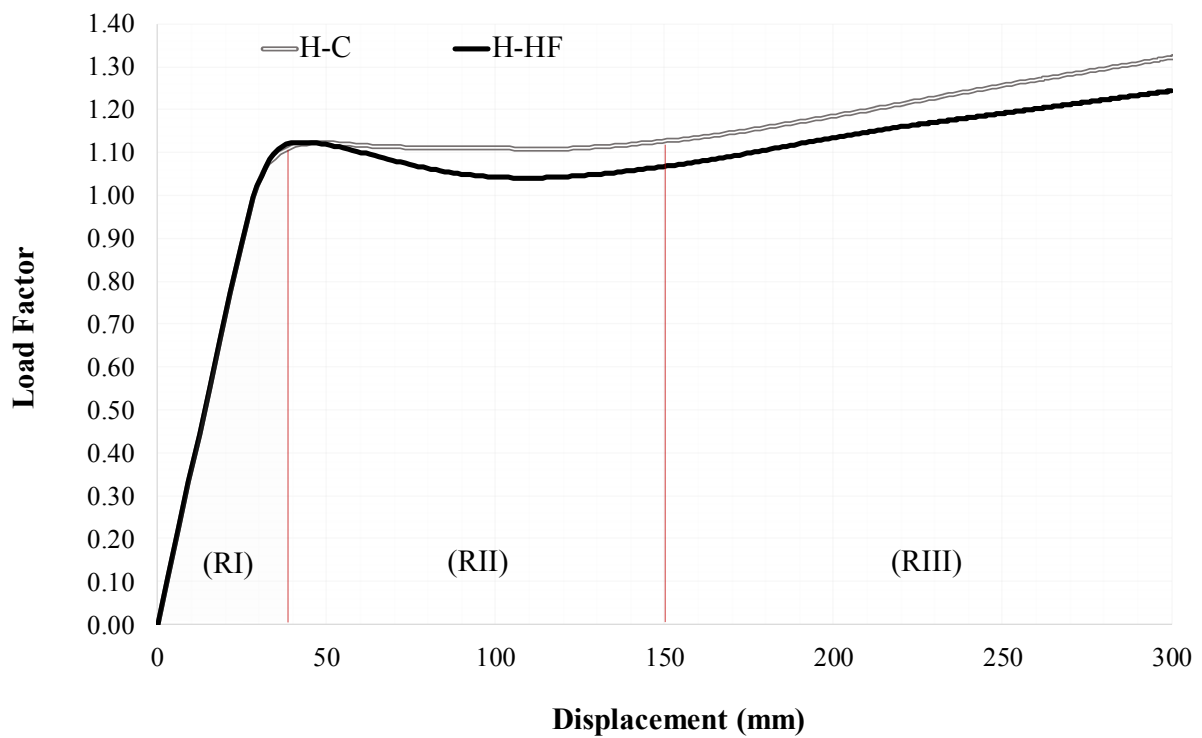


Figure 7.4: Nonlinear equilibrium path of translational DOF along the Z-axis at bottom faceplate centre for sandwich composite models H-C and H-HF subject to UDL

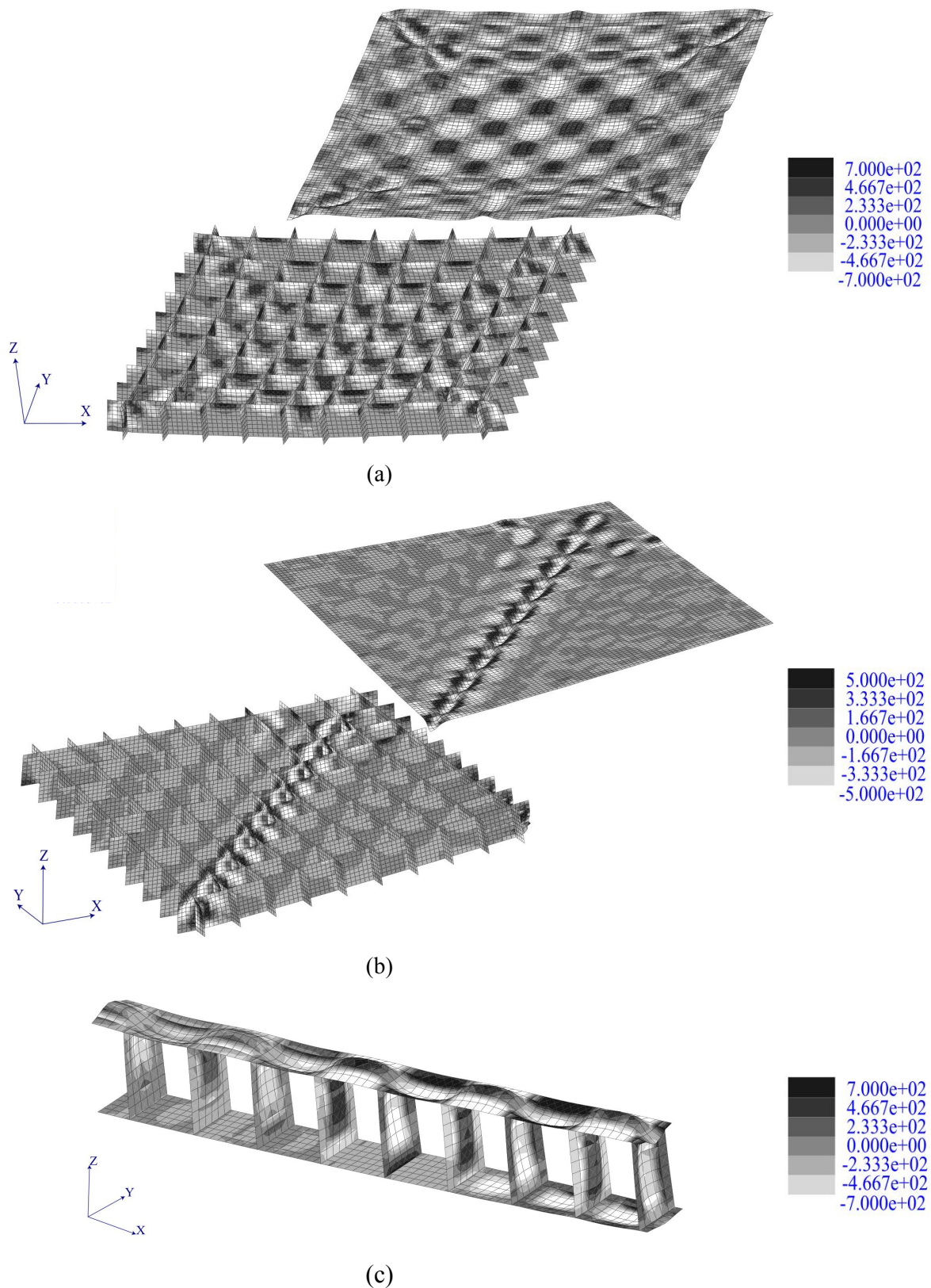
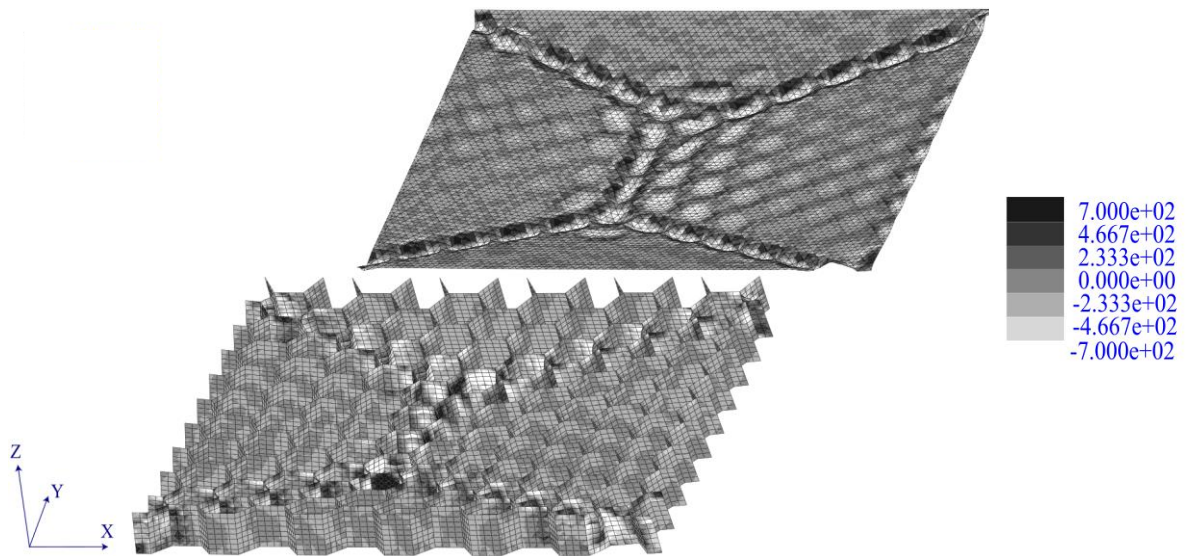
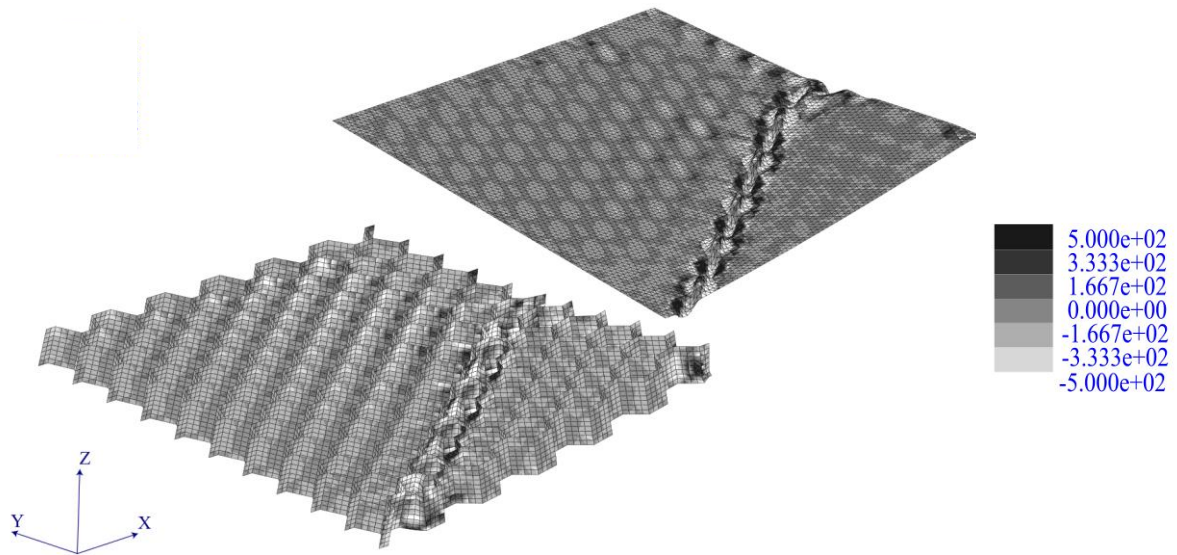


Figure 7.5: Contour plots of local shell FE bending moment  $M_y$  at maximum displacement for sandwich composite model R-HF subject to UDL: (a) intercellular buckling at panel centre, (b) penetration buckling of top faceplate and shear buckling of core strips at yield line vicinity, (c) intercellular buckling at cross-pattern lines



(a)



(b)

Figure 7.6: Contour plots of local shell FE bending moment  $M_y$  at maximum displacement for sandwich composite model H-HF subject to UDL: (a) intercellular buckling at panel centre, (b) penetration buckling of top faceplate and shear buckling of core strips at yield line vicinity

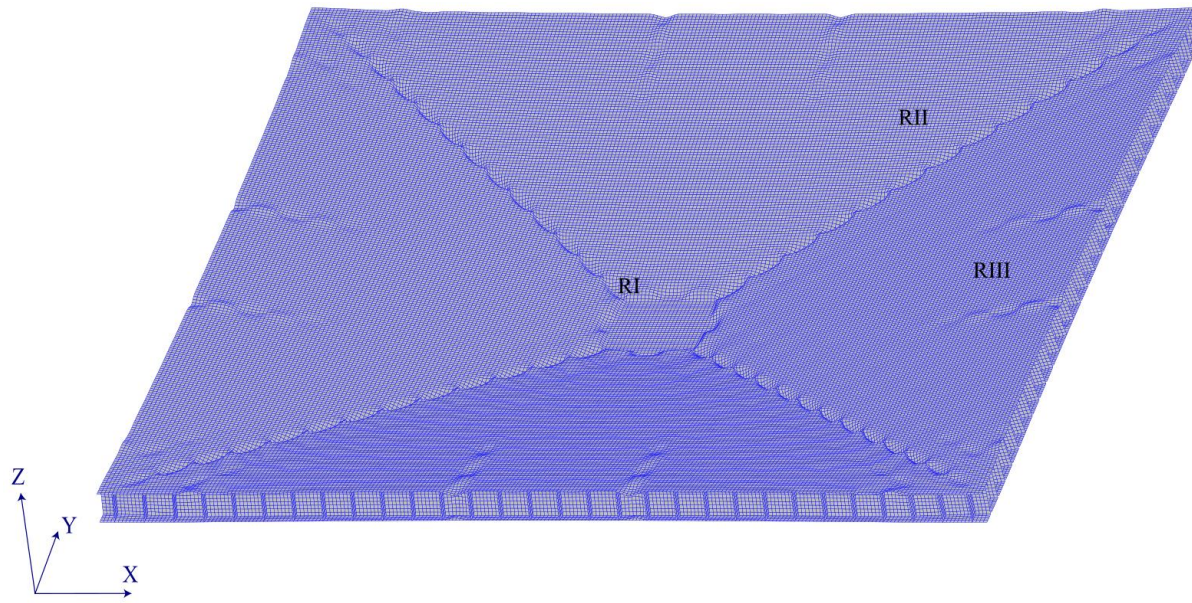
### 7.2.3 Response of large-scale all-metal sandwich composites to PL

The deformed configurations at maximum displacement for the R-HF and H-HF model variants subject to PL are illustrated in Figure 7.7. The nonlinear equilibrium paths corresponding to the translational DOF along the global Z-axis at the bottom faceplate central node for the R-C and R-HF variants are provided in Figure 7.8, and for the H-C and H-HF variants in Figure 7.9. Similar to the UDL case, three distinct response ranges can be identified in the nonlinear equilibrium paths, which have been annotated on the respective graphs, as well as on the deformed configurations, as RI, RII and RIII. Local contour plots of the shell element bending moment  $M_y$  generalised stress entity, resolved along the global Y-direction, are provided in Figures 7.10 and 7.11 for variants R-HF and H-HF, respectively, demonstrating the principal instability phenomena manifested over the panel domains.

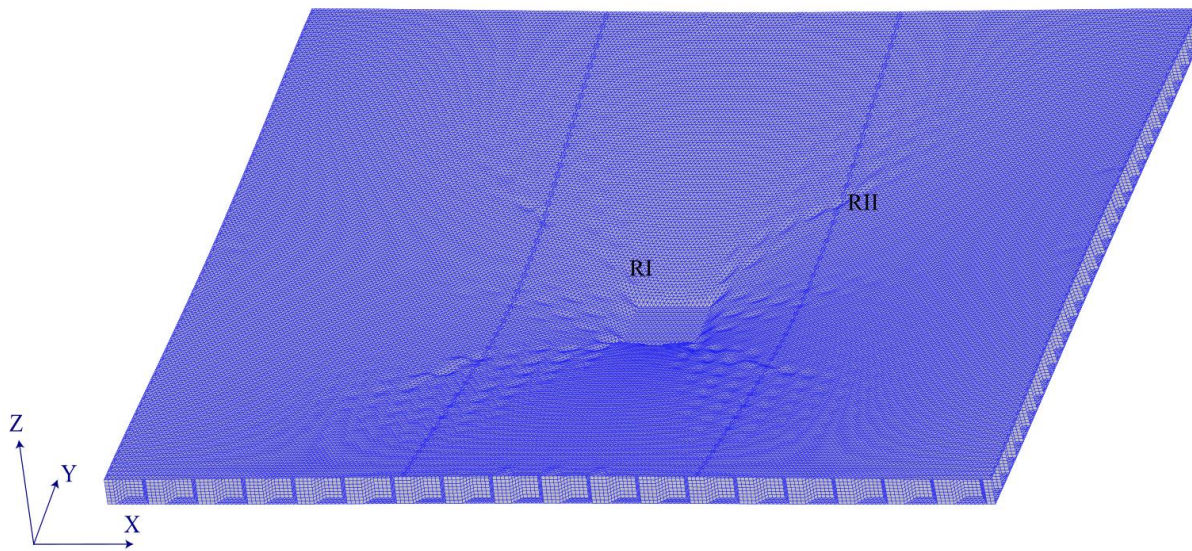
Examining more closely the composite nonlinear response under PL in Figures 7.8 and 7.9, the elastic response in range I is characterised by global flexural deformation of the panel and localised shear deformation of the core underneath the load patch, where the cells are subjected to substantial shear and compression. Ultimately, the regions of the composites underneath the patch exhibit shear yielding at the patch perimeter.

Shear yielding at the patch perimeter is followed by penetration of the top faceplate plate and compressive buckling of the underlying cells in range II, along with penetration local buckling of the top faceplate between the cell walls in the patch vicinity, as illustrated in Figures 7.10 (a), (c) and 7.11 (a), (b). Plasticity spreads in a regular pattern via yield line formation and expansion to the 4 panel corners for R-HF, as illustrated in Figure 7.10 (b), while a more dispersive pattern is observed for H-HF, as shown in Figure 7.11 (a).

Similar to the UDL case, excessive displacements in range III induce perimetric ‘hoop’ action, ultimately leading to buckling of the top faceplate on top of lines of cells in the R-HF model variant, with the buckled cell pattern initiating from the panel perimeter and being oriented towards the panel centre, as shown in Figure 7.7 (a).



(a)



(b)

Figure 7.7: Deformed configuration at maximum displacement for sandwich composite models subject to PL: (a) R-HF, (b) H-HF

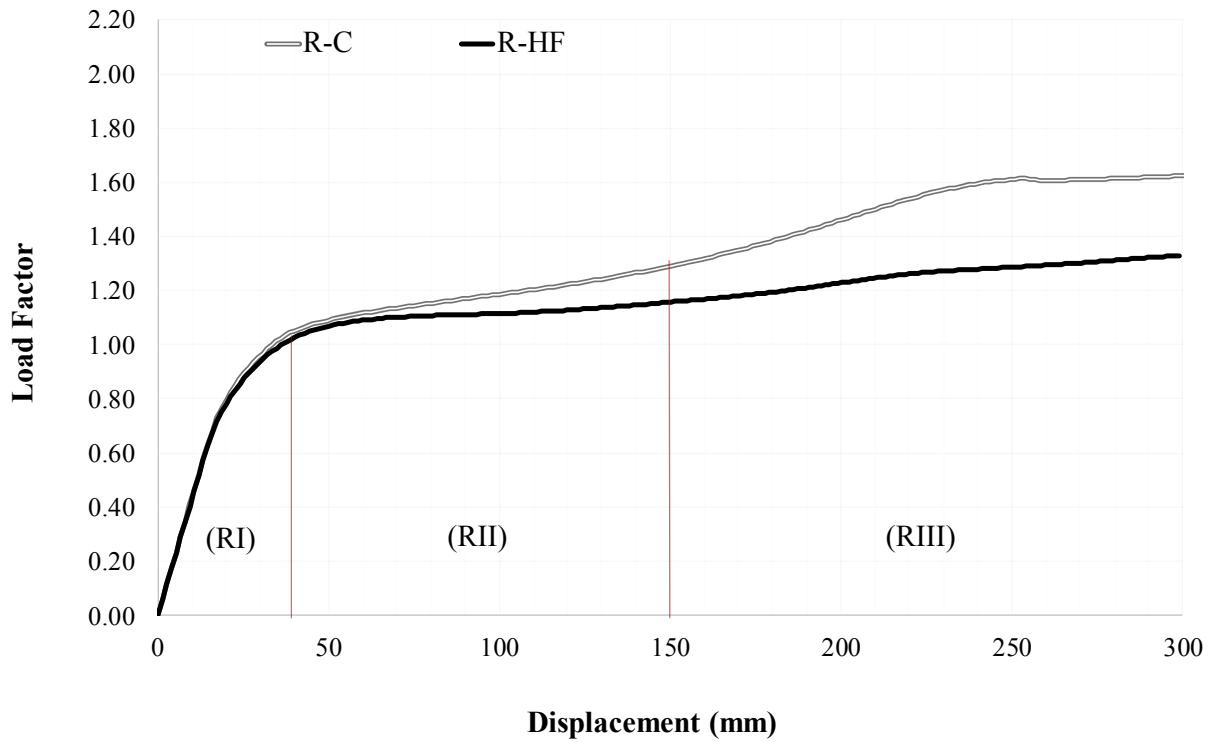


Figure 7.8: Nonlinear equilibrium path of translational DOF along the Z-axis at bottom faceplate centre for sandwich composite models R-C and R-HF subject to PL

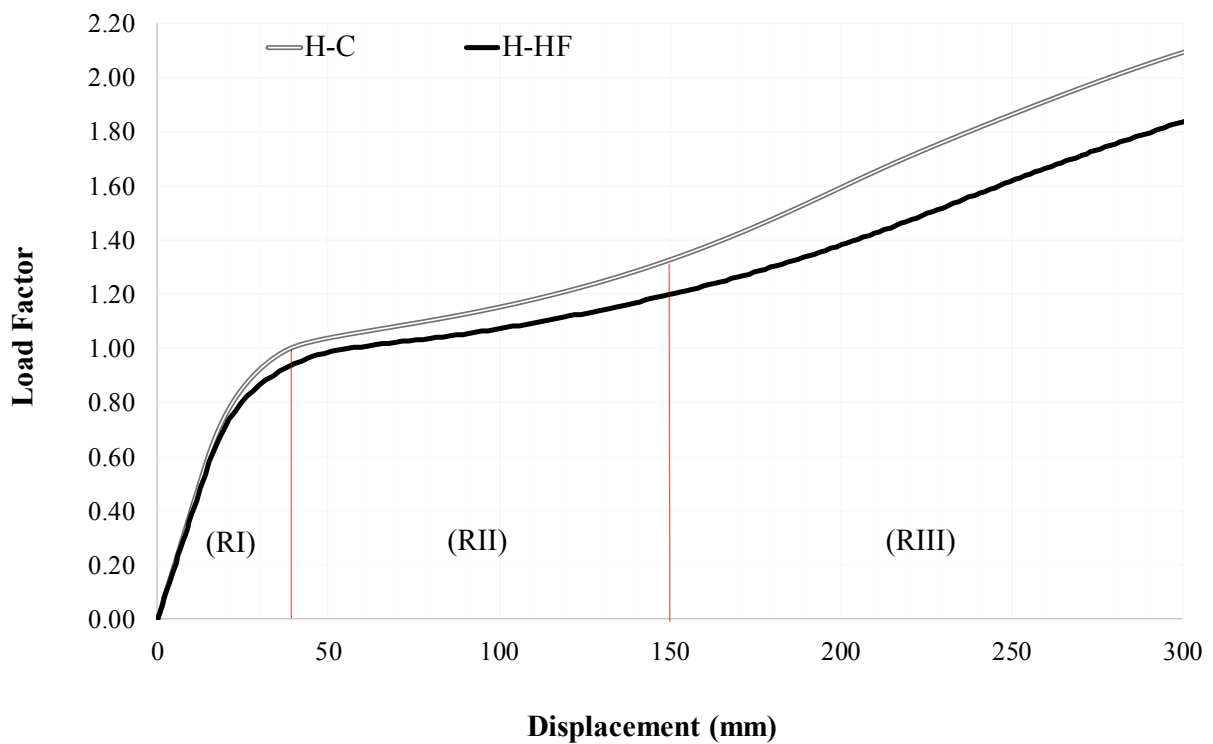


Figure 7.9: Nonlinear equilibrium path of translational DOF along the Z-axis at bottom faceplate centre for sandwich composite models H-C and H-HF subject to PL

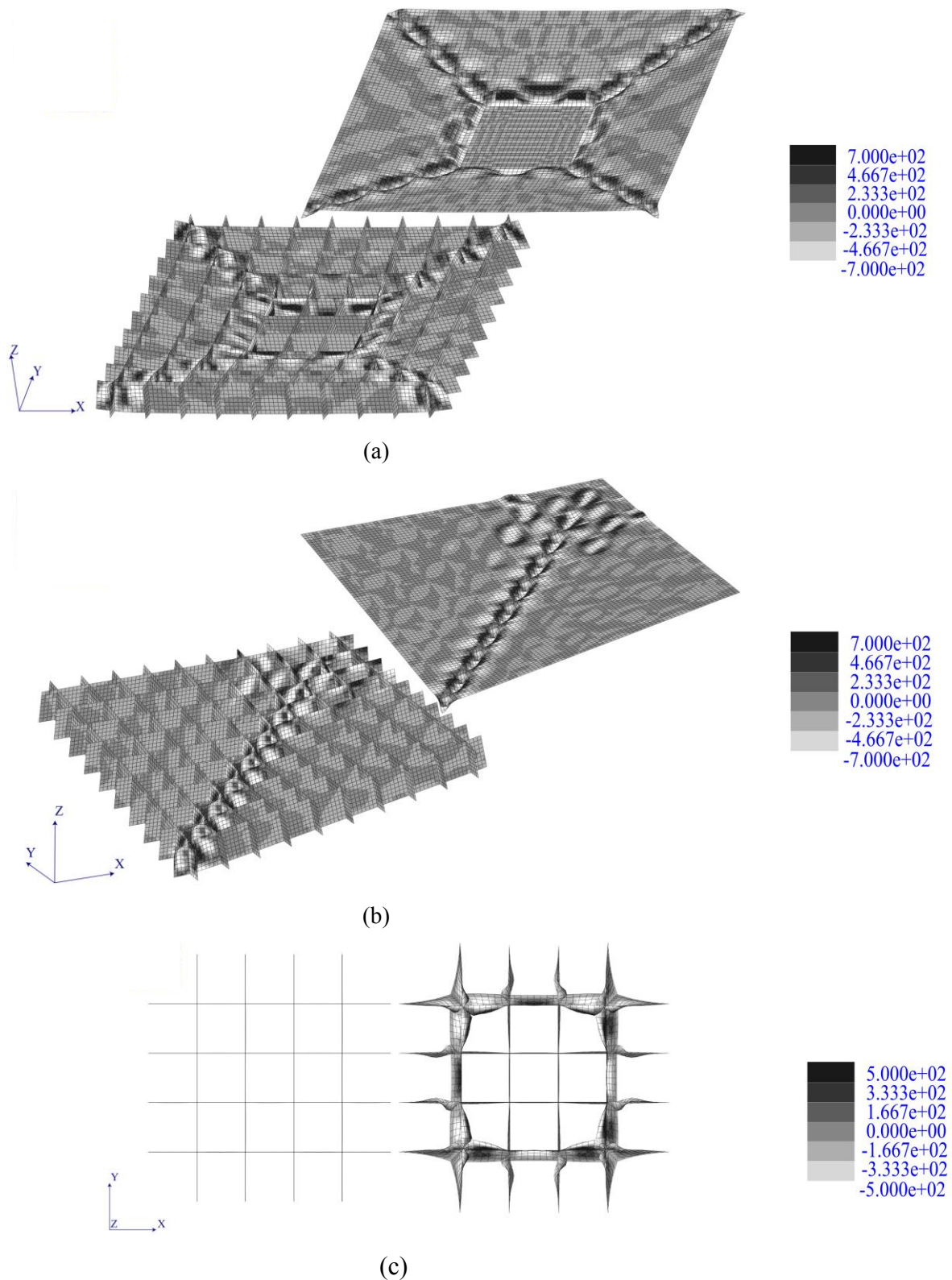


Figure 7.10: Contour plots of local shell FE bending moment  $M_y$  at maximum displacement for sandwich composite model R-HF subject to PL: (a) penetration buckling of top faceplate and compressive/shear buckling of core strips at patch vicinity, (b) penetration buckling of top faceplate and shear buckling of core strips at yield line vicinity, (c) direct compressive buckling of core strips underneath the patch

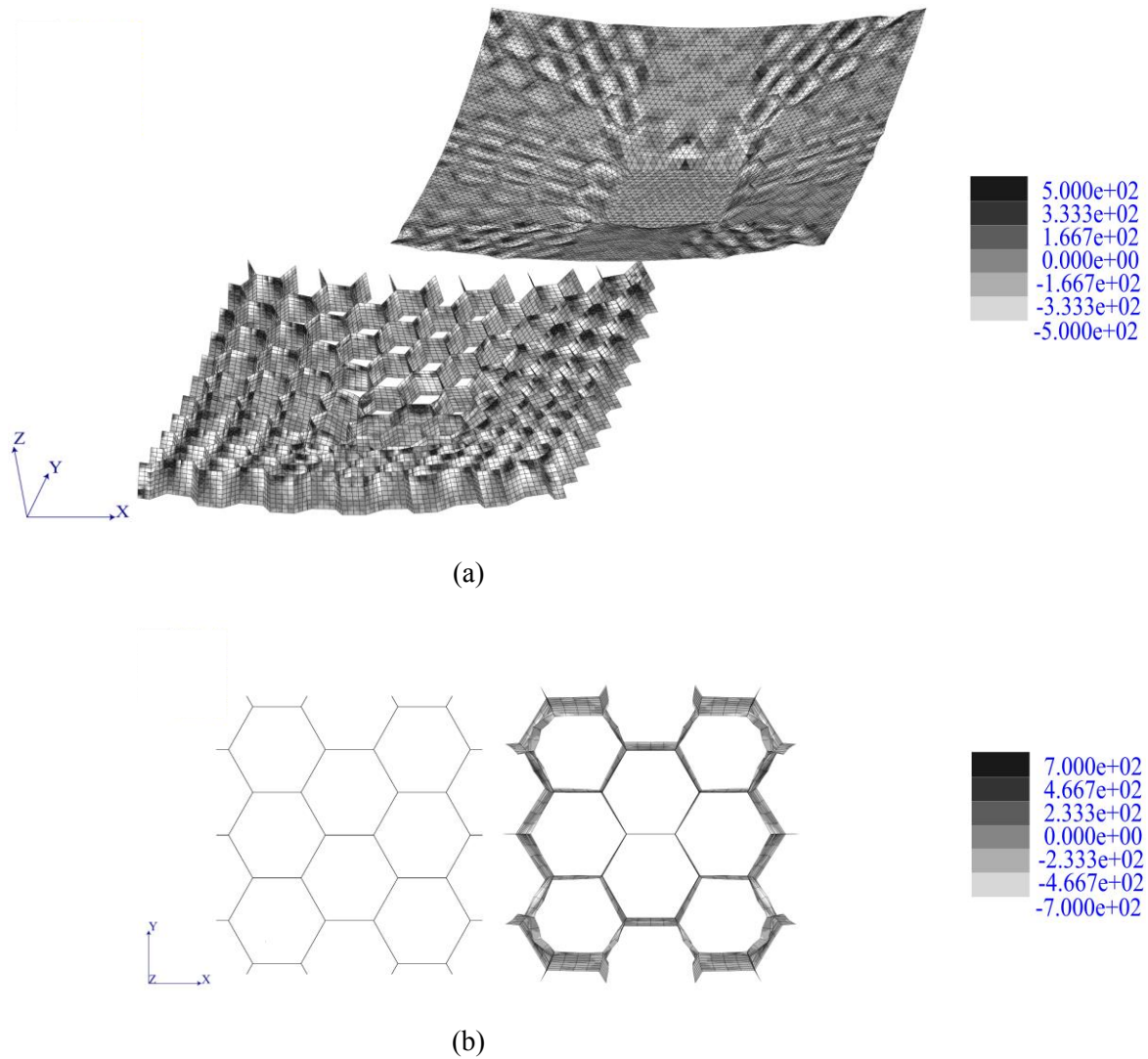


Figure 7.11: Contour plots of local shell FE bending moment  $M_y$  at maximum displacement for sandwich composite model H-HF subject to PL: (a) penetration buckling of top faceplate and compressive/shear buckling of core strips at patch vicinity, (b) direct compressive buckling of core strips underneath the patch

#### 7.2.4 Imperfection sensitivity analysis

Although seemingly unimportant for large-scale systems, imperfections can significantly alter the global nonlinear response of all-metal sandwich composites, due to the latter being governed by local instability phenomena in the large-displacement range. An imperfection sensitivity analysis is therefore conducted on the R-HF sandwich composite model and the results are illustrated in Figures 7.12 and 7.13 for the UDL and PL cases, respectively, considering the nonlinear equilibrium path of the bottom faceplate central node.



Imperfection sensitivity is more prevalent in the UDL case, which is attributed to the various local buckling phenomena being manifested over a greater extent of the panel domain. A virtually 25% reduction is observed in the yielding capacity and a 10% change in the ultimate capacity over the considered imperfection range. In the PL case the panel response is less sensitive to imperfections, due to the local loading application, nonetheless a reduction in the ultimate panel yielding capacity is observed.

### **7.2.5 Discussion**

The substantial response sensitivity to the employed level of discretisation detail, as illustrated in Figures 7.3 and 7.4 for the UDL case, as well as in Figures 7.8 and 7.9 for the PL case, highlights the necessity of accurately capturing the influence of local plate buckling, including material nonlinearity, which profoundly affect the global panel response. The stiffness and strength deviations observed between the R-C and R-HF models, as well as the substantial post-yield softening exhibited by the H-HF in comparison with the H-C models, cannot be captured without employing a high level of discretisation detail. Furthermore, considering the response sensitivity to imperfections, the incorporation of these in the modelling of large-scale sandwich composites and deck systems is particularly crucial for the energy dissipation capability and robustness assessment, where extreme static and dynamic loading can be important design and assessment considerations, as earlier discussed.

The accuracy of the proposed HF modelling approach, stemming from the employment of hierarchically optimised, co-rotational shell elements (Izzuddin & Liang, 2016; 2017), in conjunction with the use of a dense FE mesh, enable the accurate capturing of these intricacies in the range of large displacements. However, this type of modelling is generally associated with high computational and memory demands that can become prohibitive for large-scale applications, particularly where multiple interacting panels are considered. The following application study demonstrates the benefits of partitioned modelling towards addressing these shortcomings of the conventional modelling approach.

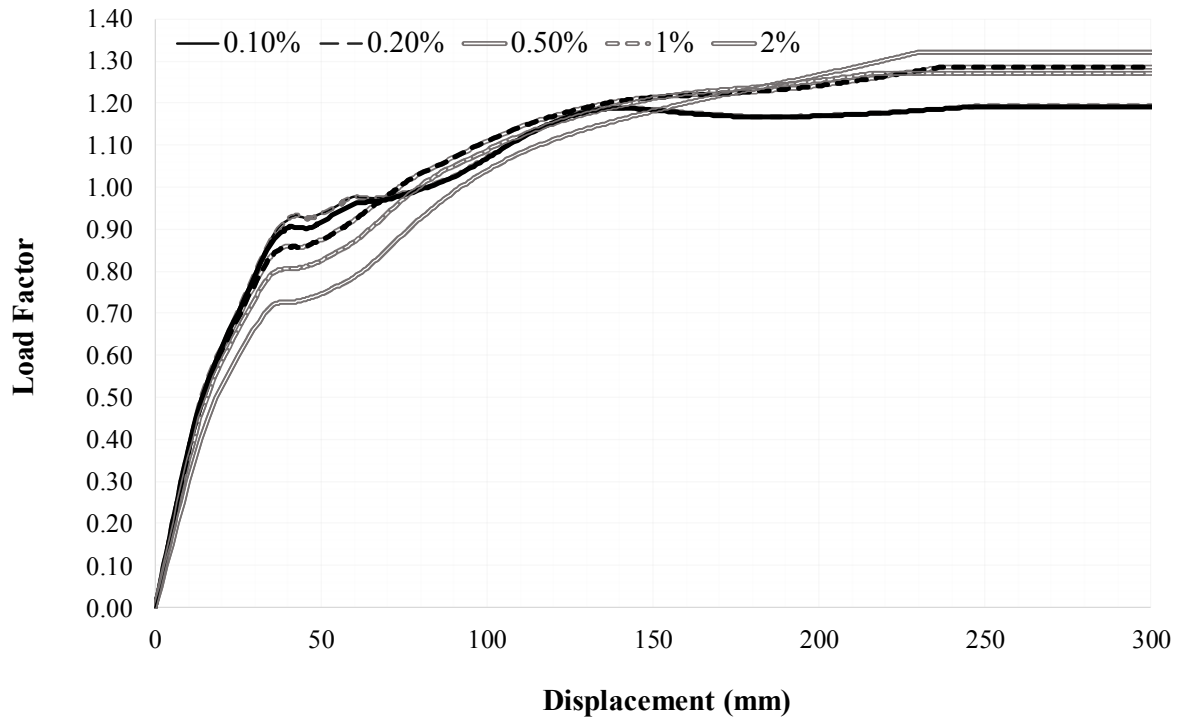


Figure 7.12: Imperfection sensitivity of sandwich composite model R-HF subject to UDL

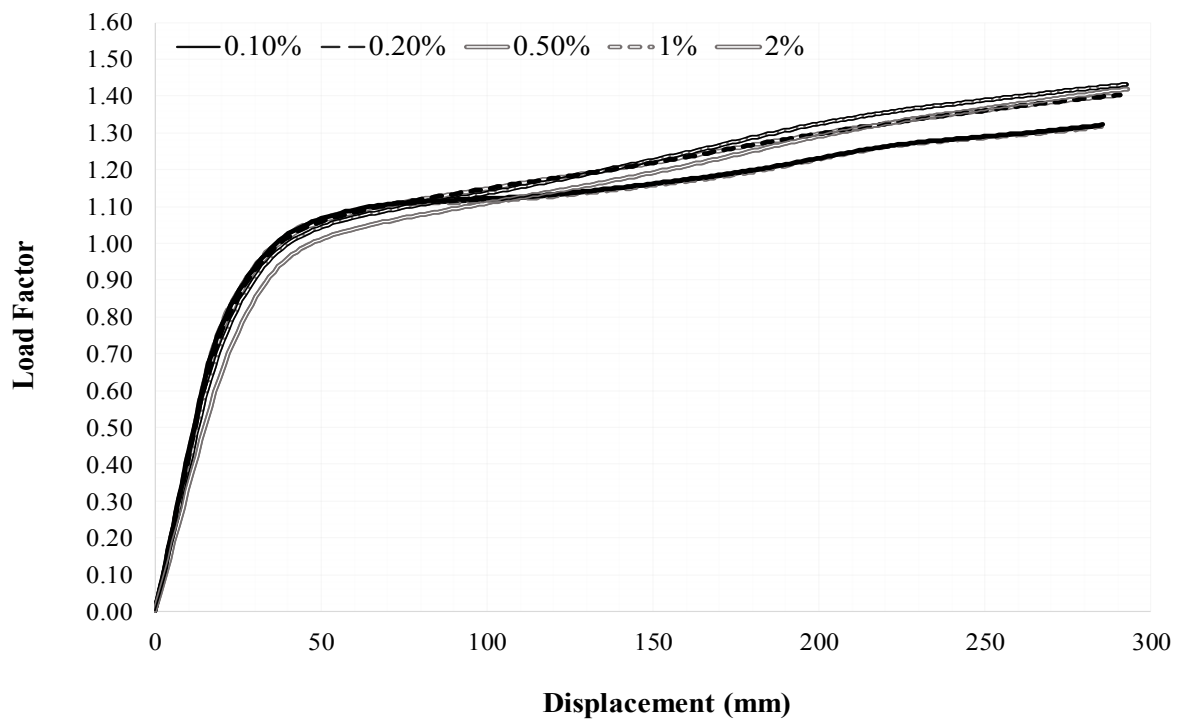


Figure 7.13: Imperfection sensitivity of sandwich composite model R-HF subject to PL

## **7.3 Application study 2: Computational benefits of dual super-element domain partitioning**

### **7.3.1 Problem description**

The HF nonlinear FE modelling strategy is enhanced here with dual super-element domain partitioning capabilities (Jokhio & Izzuddin, 2015) allowing for scalable parallel processing using HPC distributed memory systems, as discussed in Sections 3.6 and 3.7. A thorough investigation of the dual super-element domain partitioning efficiency is conducted, considering configurations with different number of child partitions for the large-scale sandwich composite models presented in the preceding application study.

Two discretisation levels are considered, employing 43200 and 230400 elements, corresponding respectively to R-C and R-HF models subjected to PL, in order for the relative efficiency of domain partitioning for a moderate and high level of discretisation detail to be investigated. Taking due account of the geometric symmetry and mesh uniformity, configurations with 2 (PM-4), 3 (PM-9), 4 (PM-16), 5 (PM-25), 6 (PM-36), 7 (PM-49) and 8 (PM-64) child partitions along both the global X- and Y-axes are considered, leading to a similar number of DOFs per child partition. All analyses are processed using the HPC facility of Imperial College London, where computing nodes with identical processing specifications, including 20 Central Processing Units (CPUs) and 128GB memory, are used in a fully dedicated mode to minimise the inter-processor communication overhead.

### **7.3.2 Comparative evaluation of domain partitioning configurations**

The comparative efficiency evaluation of the various domain partitioning configurations for R-C and R-HF is conducted on the basis of the achieved wall-clock time speedup in relation to the equivalent monolithic models. Wall-clock time can be employed as the principal efficiency quantification index, considering identical memory allocation to individual processes associated with the various partitions. For scalable parallel processing in HPC distributed memory systems, the wall-clock time encompasses the CPU time related to the determination of the nonlinear element response and the numerical solution of the algebraic system of nonlinear equations, along with the communication overhead between different processors.

The speedup achieved by a partitioned model with  $p$  child partitions can be quantified using a simple speedup factor  $SF_p$ , which is defined by the following expression:

$$SF_p = \frac{t_{mono}}{t_p} \quad (7.1)$$

where  $t_{mono}$  and  $t_p$  are the wall-clock times required for the incremental nonlinear analysis by the monolithic and partitioned models, respectively.

The absolute wall-clock times for the adopted set of partitioned models with  $p = 4, 9, 16, 25, 36, 49, 64$ , as well as the relative times with respect to the equivalent monolithic models and the achieved speedup factors  $SF_p$ , are provided in Table 7.1, for both R-C and R-HF. The variation of the speedup factor with an increasing number of child partitions for R-C and R-HF is graphically illustrated in Figure 7.14, where the maximum speedup and the corresponding optimal number of child partitions are clearly annotated for each case.

Figure 7.14 and Table 7.1 indicate an initially increasing speedup factor with an increasing number of child partitions, for both R-C and R-HF models. A maximum speedup value of 3.80 is achieved by R-C with 25 partitions, with R-HF achieving an equivalent value. R-C exhibits a branch of progressively decreasing partitioning efficiency for a further increasing number of child partitions, while the speedup associated with R-HF increases further, achieving a maximum value of 4.81 with 49 partitions, after which it also exhibits a descending branch.

Evidently, the employment of a higher level of discretisation detail in R-HF, as compared to R-C, leads to a substantially larger value of maximum achieved speedup, allowing for an almost 80% reduction of the associated wall-clock time to be achieved, as well as to an overall enhanced domain partitioning efficiency, extending to a greater number of child partitions. This highlights the particular computational benefits associated with the incorporation of dual super-element domain partitioning in the established HF modelling strategy, when it comes to the modelling of large-scale systems with a substantial mesh density.

The progressively decreasing speedup rate observed for an increasing number of child partitions, ultimately leading to a descending branch for both R-C and R-HF, is indicative of an efficiency deterioration of the domain decomposition approach in the case of excessive partitioning. This is due to an increasing communication overhead between parallel processors,

which significantly impacts the parallelisation efficiency, ultimately leading to slowdown (Jokhio & Izzuddin, 2015). Moreover, physical limitations imposed by the available number of CPUs in a single computing node of the HPC system require the distribution of models with a very large number of partitions to multiple nodes, which further encumbers the inter-processor communication.

Table 7.1: Computing wall-clock time and achieved speedup for different domain partitioning configurations of sandwich composite models R-C and R-HF

Model Configuration	Wall-Clock Time (min)	Normalised Wall-Clock Time (%)	Percentage Reduction (%)	SF (-)
<b>(R-C) - 43200 Elements, 156842 Nodes, 784210 DOF</b>				
MM	4472	100.00	0.00	1.00
PM-4	2166	48.45	51.55	2.06
PM-9	1556	34.79	65.21	2.87
PM-16	1233	27.58	72.42	3.63
<b>PM-25</b>	<b>1177</b>	<b>26.31</b>	<b>73.69</b>	<b>3.80</b>
PM-36	1225	27.40	71.68	3.65
PM-49	1351	30.21	69.68	3.31
PM-64	1445	32.32	67.68	3.09
<b>(R-HF) - 230400 Elements, 882122 Nodes, 4410610 DOF</b>				
MM	36454	100.00	0.00	1.00
PM-4	20252	55.56	44.44	1.80
PM-9	13113	35.97	64.03	2.78
PM-16	10659	29.24	70.76	3.42
PM-25	9182	25.19	74.81	3.97
PM-36	8210	22.52	77.48	4.44
<b>PM-49</b>	<b>7579</b>	<b>20.79</b>	<b>79.21</b>	<b>4.81</b>
PM-64	10269	28.17	71.83	3.55

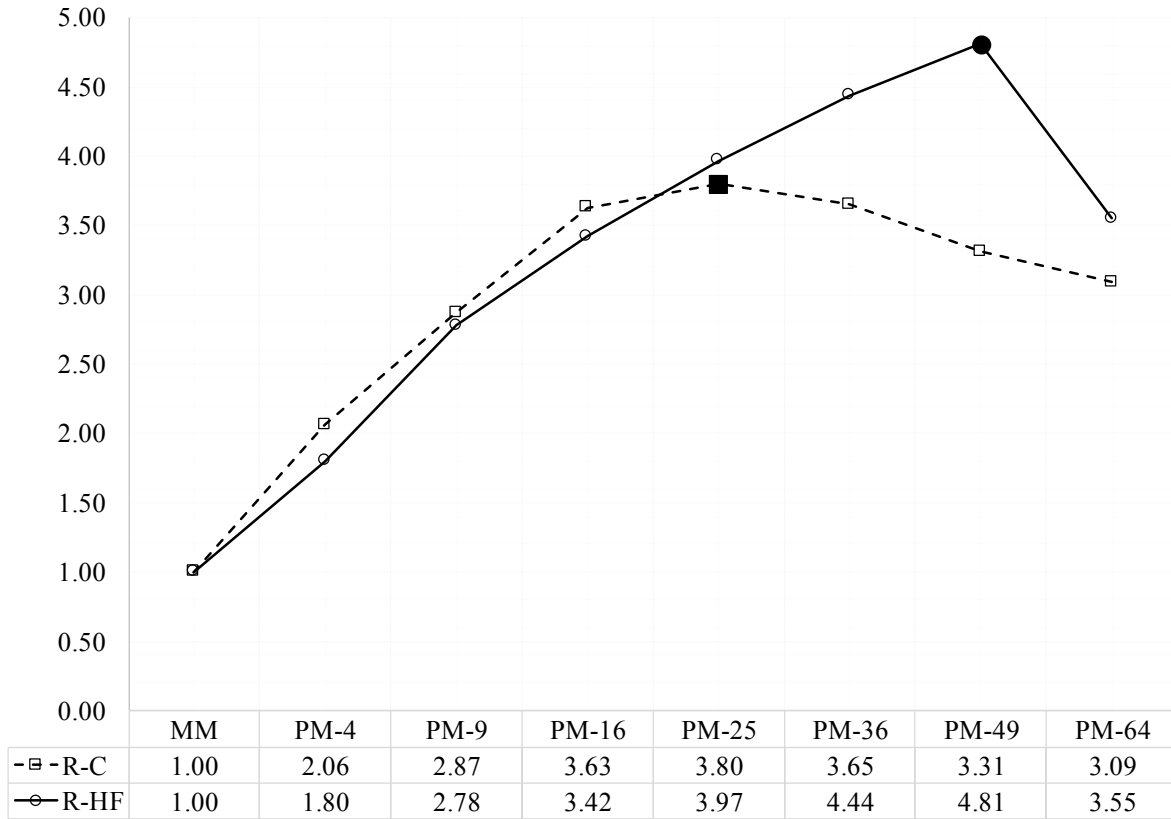


Figure 7.14: Computing wall-clock time speedup for different domain partitioning configurations of sandwich composite models R-C and R-HF

### 7.3.3 Practical guidance for optimal partitioning

Taking due account of the aforementioned considerations, a qualitative guide for establishing the optimal partitioning configuration is proposed here, based on the Nodal Ratio  $NR_p$ . This is defined by the following expression for a configuration with  $p$  child partitions:

$$NR_p = \frac{n_i^{(p)}}{N_b^{(p)}} = \frac{n^{(p)} - n_b^{(p)}}{N_b^{(p)}} \quad (7.2)$$

where  $N_b^{(p)}$  is the number of nodes along the partition boundary at the parent level,  $n^{(p)}$  is the average total number of nodes of a child partition,  $n_b^{(p)}$  is the average number of nodes on the child partition boundary, and  $n_i^{(p)}$  is the average number of internal nodes in the child partition domain. For the partitioned model configurations under consideration, the values of the nodal

quantities  $N_b^{(p)}$ ,  $n^{(p)}$ ,  $n_b^{(p)}$  and  $n_i^{(p)}$  defined above are presented in Table 7.2, while the variation of  $N_b^{(p)}$  and  $n_i^{(p)}$  with an increasing number of child partitions is graphically illustrated in Figure 7.15, for both R-C and R-HF.

Under idealised process parallelisation conditions, with identical CPU specifications, communication overhead and processing time for problems of the same size, optimal efficiency for partitioned modelling of all-metal sandwich panels is achieved for  $NR_p = 1$ . This corresponds to the distribution of equivalently sized problems, in respect of the associated number of DOFs, over all CPUs. As presented in Table 7.2 and shown in Figure 7.15, the previously determined optimal speedup values 3.80 and 4.81 for the two discretisation levels R-C and R-HF, achieved with 25 and 49 child partitions, respectively, are both associated with a nodal ratio  $NR_p = 1$ . This graphically corresponds to the intersection of the  $N_b^{(p)}$  and  $n_i^{(p)}$  lines for each of R-C and R-HF, which defines the nodal distribution equilibrium point between the parent and child partitions.

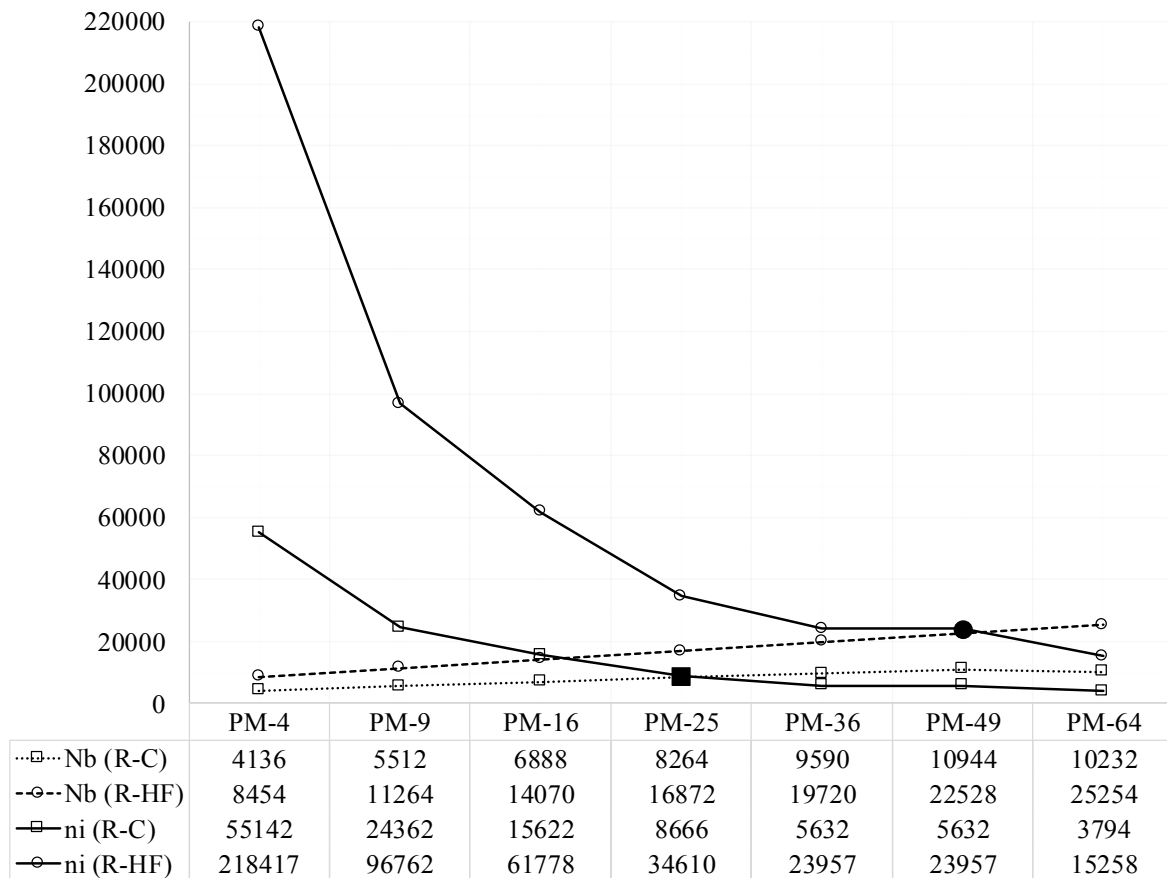


Figure 7.15: Parent and child partition process nodal quantities for different domain partitioning configurations of sandwich composite models R-C and R-HF

Table 7.2: Parent and child partition process nodal quantities and nodal ratio for different domain partitioning configurations of sandwich composite models R-C and R-HF

Model Configuration	n	n <sub>b</sub>	n <sub>i</sub> =n-n <sub>b</sub>	N <sub>b</sub>	Nodal Ratio NR=n <sub>i</sub> /N <sub>b</sub>
<b>(R-C) - 43200 Elements, 156842 Nodes, 784210 DOF</b>					
PM-4	56282	1140	55142	4136	13.3
PM-9	25122	760	24362	5512	4.4
PM-16	16230	608	15622	6888	2.3
<b>PM-25</b>	<b>9122</b>	<b>456</b>	<b>8666</b>	<b>8264</b>	<b>1.0</b>
PM-36	6092	460	5632	9590	0.6
PM-49	6092	460	5632	10944	0.5
PM-64	4098	304	3794	10232	0.4
<b>(R-HF) - 230400 Elements, 882122 Nodes, 4410610 DOF</b>					
PM-4	221237	2820	218417	8454	25.8
PM-9	98642	1880	96762	11264	8.6
PM-16	63282	1504	61778	14070	4.4
PM-25	35738	1128	34610	16872	2.1
PM-36	24897	940	23957	19720	1.2
<b>PM-49</b>	<b>24897</b>	<b>940</b>	<b>23957</b>	<b>22528</b>	<b>1.1</b>
PM-64	16010	752	15258	25254	0.6

For values of the Nodal Ratio greater than 1, graphically corresponding to the region left of the respective nodal distribution equilibrium points, the computing demand is dictated by the child partitions. On the other hand, for values of the nodal ratio lower than 1, graphically corresponding to the region right of the respective nodal distribution equilibrium points, computing demand is dictated by the number of nodes on the partition boundary at the parent level. In both cases, the allocation of partitions with significantly different number of DOFs to CPUs with identical specifications for processing results into the wall-clock time and the respective speedup being dictated by the partitions with the greater number of DOFs, which effectively compromises the essence of domain partitioning and scalable process parallelisation. This outcome can even be better illustrated by considering the extreme case



where the number of partitions becomes the same as the number of finite elements employed for the domain discretisation, where the partitioned model effectively degenerates into the monolithic model, but with a significant communication overhead, thus achieving virtually zero speedup.

The comparison of the nonlinear response of R-HF obtained for a monolithic model and a partitioned configuration with 64 child partitions is illustrated in Figure 7.16. Evidently, the two configurations exhibit a virtually identical nonlinear equilibrium path, which highlights the domain partitioning capability of achieving substantial computational benefits, without compromising the accuracy and convergence rate of the monolithic approach, as earlier discussed in Section 3.6.

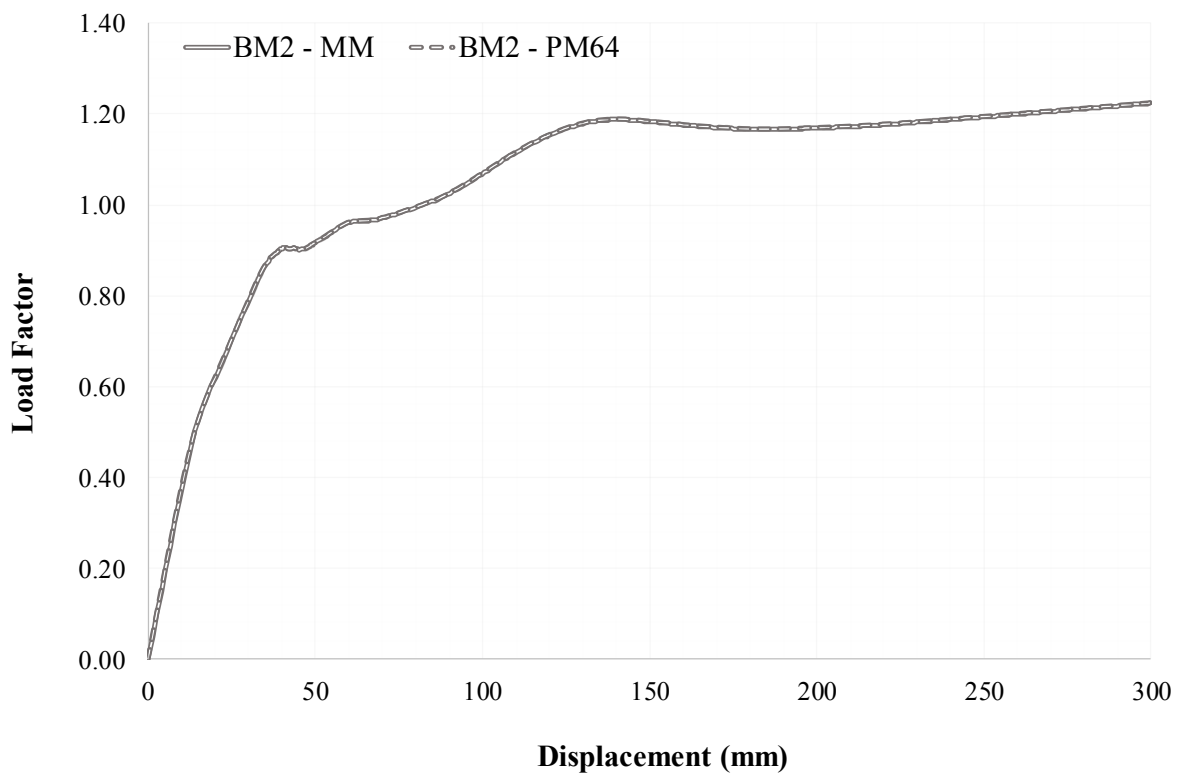


Figure 7.16: Nonlinear equilibrium path of translational DOF along the Z-axis at bottom faceplate centre for monolithic and partitioned sandwich composite models R-HF

## **7.4 Application study 3: Computational and modelling benefits of 1-D translational and rotational coupling element**

### **7.4.1 Problem description**

The application study presented herein aims at illustrating the substantial benefits associated with the incorporation of the developed 1-D translational and rotational coupling element, presented in Chapters 4 and 5, in the established HF nonlinear FE modelling strategy. The benefits of the coupling element are emphasised here in respect of: (i) the enhancement of the modelling flexibility and the overcoming of mesh conformity requirements in large-scale meshes; and (ii) the enhanced computing speed-up and the overcoming of potential memory bottlenecks.

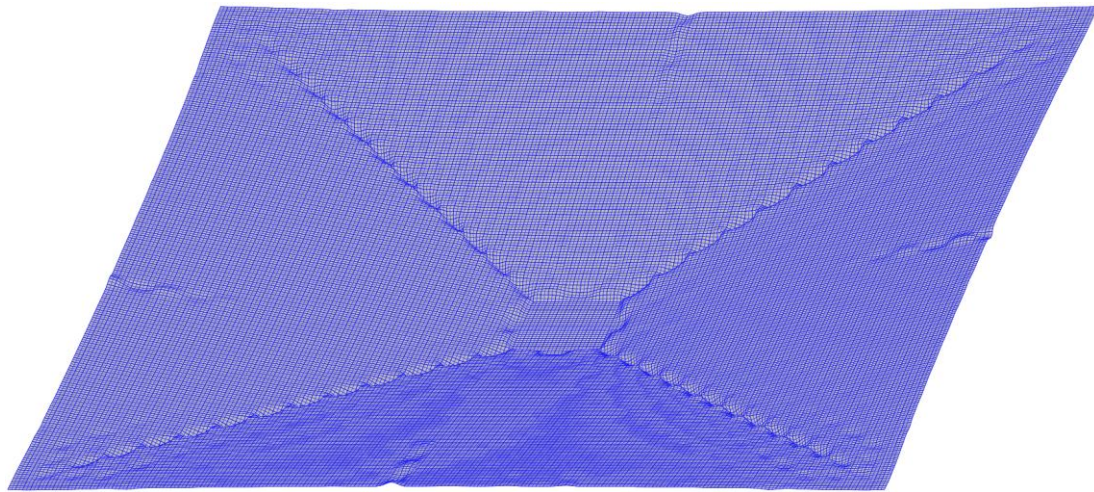
In this context, the R-HF FE model presented in Section 7.2, subjected to the PL load case, is employed as the basis for a selectively-discretised configuration, henceforth referred to as R-HF-A, where A stands for adaptive with reference to the employed FE discretisation strategy. Identical geometric and material specifications as well as loading and boundary conditions to the R-HF model are considered, as specified in Section 7.2. A distinction should be made between the employment of the term adaptive herein, which refers to the established manually implemented selective discretisation strategy, and the adaptive meshing capabilities of commercial FE softwares, encompassing the automated establishment of an optimal conforming mesh configuration of variable density over the domain.

R-HF-A encompasses a fine shell element mesh in the core region underneath the patch and over the entire top faceplate, coupled to a coarser mesh over the rest of the core domain and the entire bottom faceplate. The adopted discretisation strategy has been established to allow the various local instabilities governing the panel global nonlinear response, as demonstrated in Section 7.2 by virtue of the R-HF response to PL, to be effectively captured by R-HF-A. These include: (i) penetration (transverse shear deformation) buckling of the top faceplate in the vicinity of the loading patch; (ii) penetration buckling of the top faceplate in the vicinity of the yield line and the four corners; (iii) shear buckling of the core strips traversed by the yield lines; (iv) direct compressive buckling of the core strips underneath the patch; and (v)

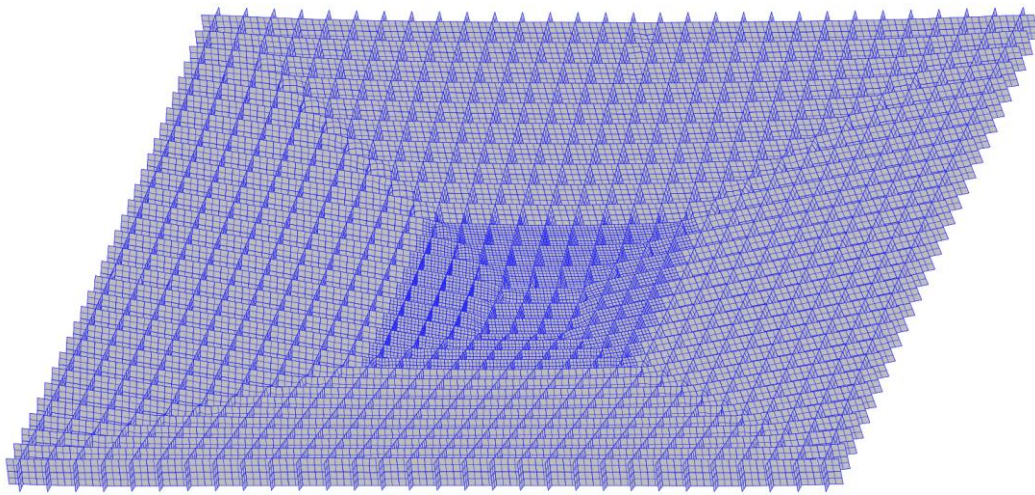
compressive buckling of the panel perimetric half cells, due to the substantial membrane action exhibited by the panel in large displacements leading to perimetric compressive ‘hoop’ action.

At the panel domain extending symmetrically over an area of  $1000 \times 1000 \text{ mm}^2$  on the X-Y Cartesian coordinate plane about its geometric centre, a mesh of  $8 \times 8$  elements is employed for the discretisation of each cell wall on the core strips, resulting in a uniform mesh of 12800 FEs. The same level of discretisation detail is employed over the entire top faceplate domain, resulting in a uniform mesh of 57600 shell elements, conforming only with the central core domain mesh. Over the core domain surrounding its central densely discretised region, a mesh of  $4 \times 4$  FEs is employed over the strip cell walls, leading to a mesh of 25600 FEs, while the bottom faceplate encompasses a uniform mesh of 6400 FEs, which is accordingly non-conforming with the core strips mesh over the entire panel domain. The above discretisation strategy leads to a final mesh configuration with 102400 elements in total, which is less than half of that employed for the R-HF domain discretisation (230400). The individual panel compartment mesh configurations discussed above for R-HF-A are illustrated in Figure 7.17, at the panel deformed configuration associated with a maximum displacement of 300 mm, in accordance with the nonlinear solution procedure outlined in Section 7.2.

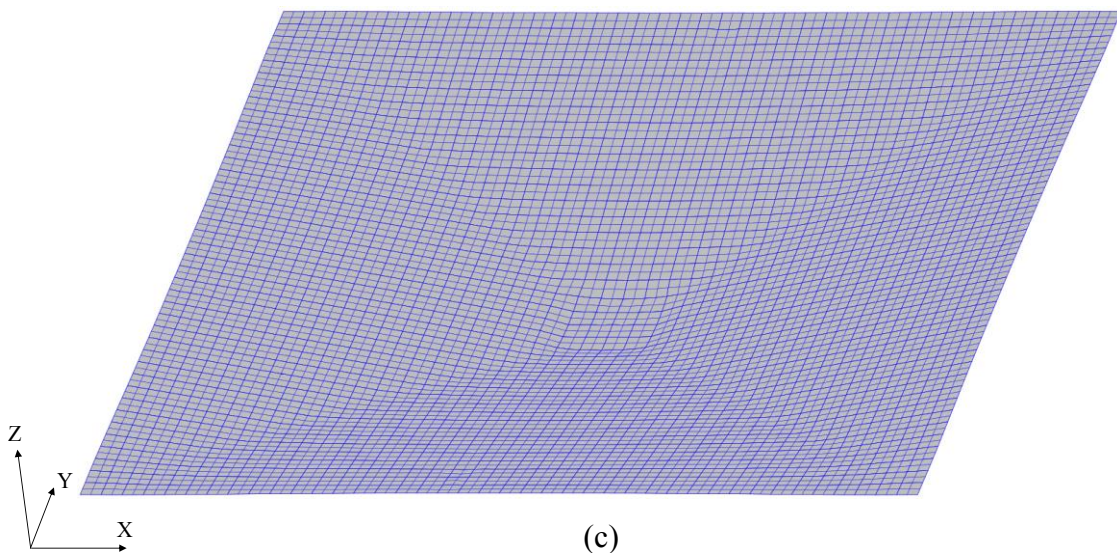
The non-conforming meshes of the various independently discretised regions over the panel domain are coupled along 1-D interfaces introduced at their intersections, using the developed translational and rotational coupling element. The coupling interfaces are established along the intersections of both faceplates with the core strips, as well as along the strip height at the adjoining boundary between the core central densely discretised region and its surrounding coarser mesh. For the active coupling element identification along each interface, the progressive segmentation algorithm presented in Section 4.5 is employed, where a slave-only progressive segmentation approach has been adopted herein, using the denser of each two coupled regions as the slave surface. At the coupling element level, 3 Collocation Points (CPs) with 4 Lagrangian Multiplier (LM) entities each are employed along the associated segment, with 3 of these being allocated for translational and 1 for rotational constraint enforcement, in accordance with Section 4.4. The translational and rotational coupling penalty parameters are both specified as 0.1, while the element-specific scheme discussed in Sub-section 4.7.3.2 is employed for integration at the element level, with a specified Gaussian quadrature order of 3 providing exact integration.



(a)



(b)



(c)

Figure 7.17: Deformed configuration at maximum displacement for selectively-discretised sandwich composite model R-HF-A: (a) top faceplate, (b) core, (c) bottom faceplate

### 7.4.2 Comparison of adaptive and monolithic HF modelling approaches

The deformed configurations of R-HF and R-HF-A at maximum displacement are illustrated in Figure 7.18, while a comparison of the nonlinear equilibrium paths, corresponding to the translational DOFs along the global Z-axis at the bottom faceplate centre, for sandwich composite models R-C, R-HF and R-HF-A is provided in Figure 7.19.

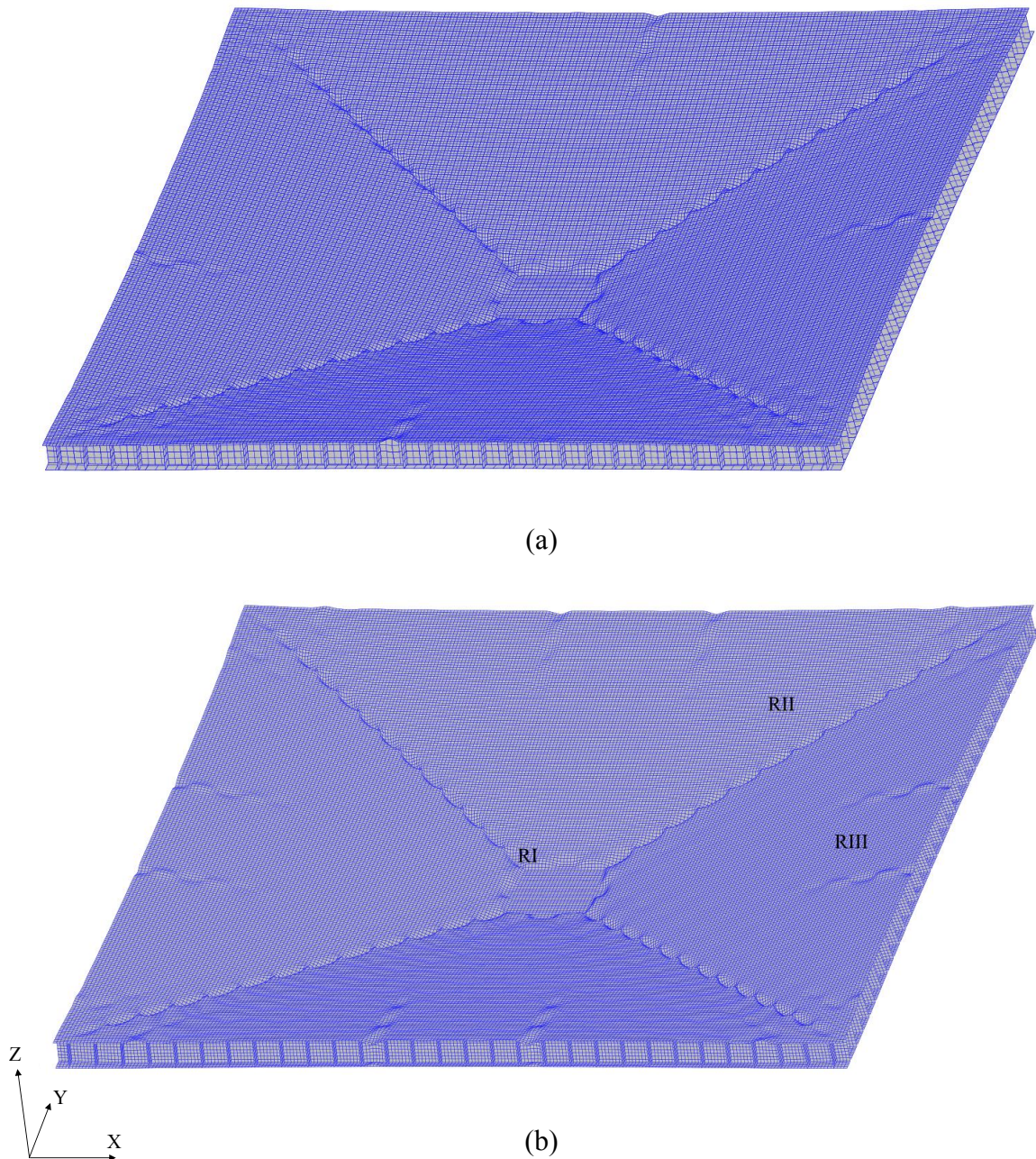


Figure 7.18: Deformed configuration at maximum displacement for sandwich composite models R-HF and R-HF-A

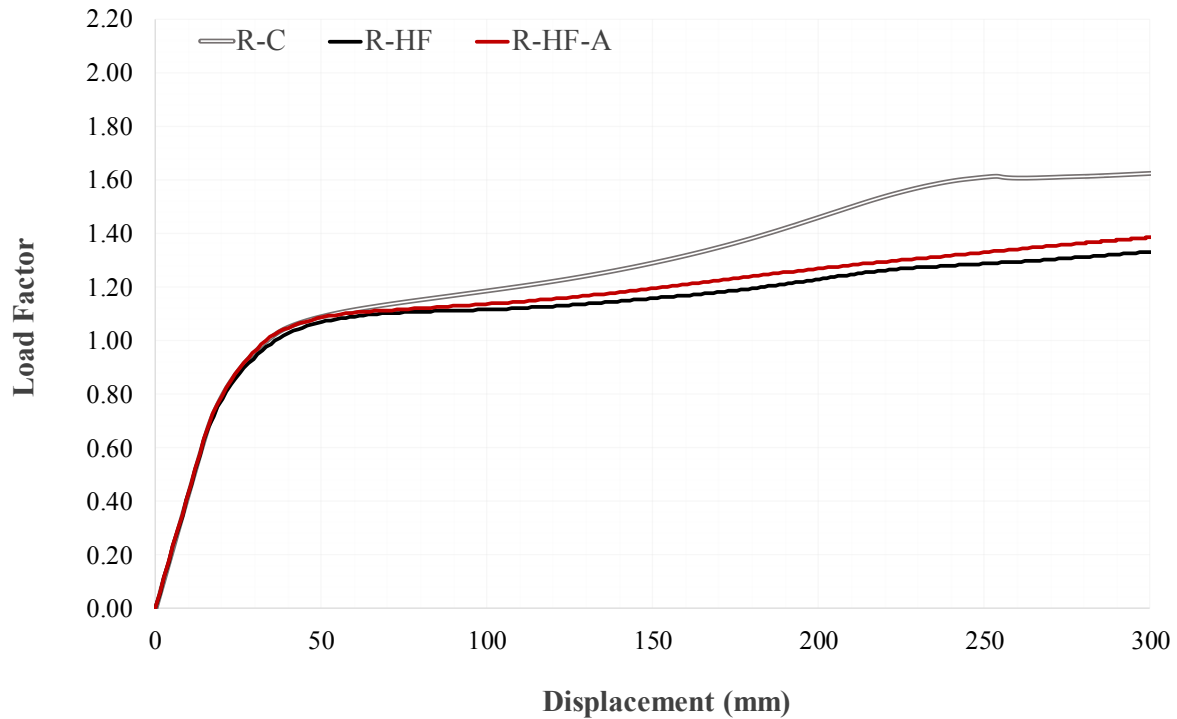


Figure 7.19: Nonlinear equilibrium path of translational DOF along the global Z-axis at bottom faceplate centre for sandwich composite models R-C, R-HF and R-HF-A

As evident from Figure 7.19, R-HF-A allows for an accurate response evaluation in the linear elastic range, alongside the capturing of the panel yielding capacity, with minor discrepancies observed only in the range of large displacements, leading to a slightly stiffer response. Comparing the deflected shapes obtained for the two configurations in Figure 7.18 and observing the various panel compartment deformations in Figure 7.17, it can be seen that R-HF-A captures the principal local instabilities at the faceplates and the core strips manifested: (i) at the patch vicinity, (ii) along the yield lines, (iii) at the panel corners, and (iv) underneath the loading patch. However, it leads to the buckling of fewer and different perimetric half-cells, thus resulting in a marginally different panel deformed configuration at maximum displacement and causing minor discrepancies in the obtained response in the range of large displacements, where the latter is governed by local instabilities.

These minor discrepancies can be attributed to the discontinuities induced in the stress distribution over the faceplates and core at the interface vicinities, due to the embedded approximation in the rotational coupling formulation based on achieving moment transferring by means of an equivalent nodal force couple at the adjoining shell element domains.

Furthermore, despite the selective discretisation approach comprising a dense mesh where required, a substantial portion of the domain is still discretised with an overall coarser mesh compared to R-HF, thus potentially contributing to the observed slightly stiffer response. Despite the minor discrepancies in the nonlinear response evaluation and the deformed configuration of the panel in the range of large displacements, the adopted selective discretisation approach enables an accurate capturing of all principal instability phenomena that govern the panel response.

### **7.4.3 Computational benefits of adaptive HF modelling**

Beyond providing a highly accurate approximation of the R-HF response, R-HF-A additionally enables a reduction of more than 50% in the number of employed shell elements, thus leading to substantial speedup. A 40% reduction is achieved in the absolute computing wall-clock time required for extensive HF nonlinear FE analysis under extreme static loading, from 36454 min required for R-HF to 21856 min for R-HF-A. A more extensive investigation of the computational benefits associated with the additional incorporation of dual-super-element domain partitioning is conducted hereafter, where the relative efficiency of partitioned models with different number of child partitions is assessed for R-HF-A, considering the achieved speedup relative to equivalent monolithic model.

Beyond what was discussed in Section 7.3, the wall-clock time associated with each partition of R-HF-A further encompasses the CPU time related to the nonlinear coupling element response evaluation, which is considerable due to the total number of coupling elements employed over the panel domain being of the order of 12520. It is emphasized here that the coupling element tangent stiffness matrix assembly at every iterative step of the nonlinear solution procedure is only required for its rotational components, whereas the respective translational entity needs only be evaluated once before the analysis, as discussed in Sections 5.2 and 5.3. Furthermore, the LM additional DOF incorporation in the algebraic system of nonlinear equations associated with each partition leads to a substantial increase in the problem size, and consequently the time required for solving the system of simultaneous equations, though there are still clear computational benefits in using the coupling elements for selective mesh refinement.

Configurations with 2 (PM-4), 3 (PM-9), 4 (PM-16), 5 (PM-25), 6 (PM-36), 7 (PM-49) and 8 (PM-64) equivalently-sized child partitions along both the global X- and Y- axes are considered, in accordance with Section 7.3, for comparison with the obtained results for R-C and R-HF. As before, all numerical analyses are conducted on the distributed memory HPC system of Imperial College London, making use of the same resources noted in Sub-section 7.3.1.

The variation of the speedup factor for the adopted set of partitioned models with  $p = 4, 9, 16, 25, 36, 49, 64$  is graphically illustrated in Figure 7.20 for the R-C, R-HF and R-HF-A configurations, with the maximum value and the corresponding optimal number of child partitions being clearly annotated for each case. The absolute wall-clock times for R-HF-A, as well as the relative times with respect to the equivalent monolithic model and the achieved speedup factors  $SF_p$ , as given by Eq. (7.1), are provided in Table 7.3.

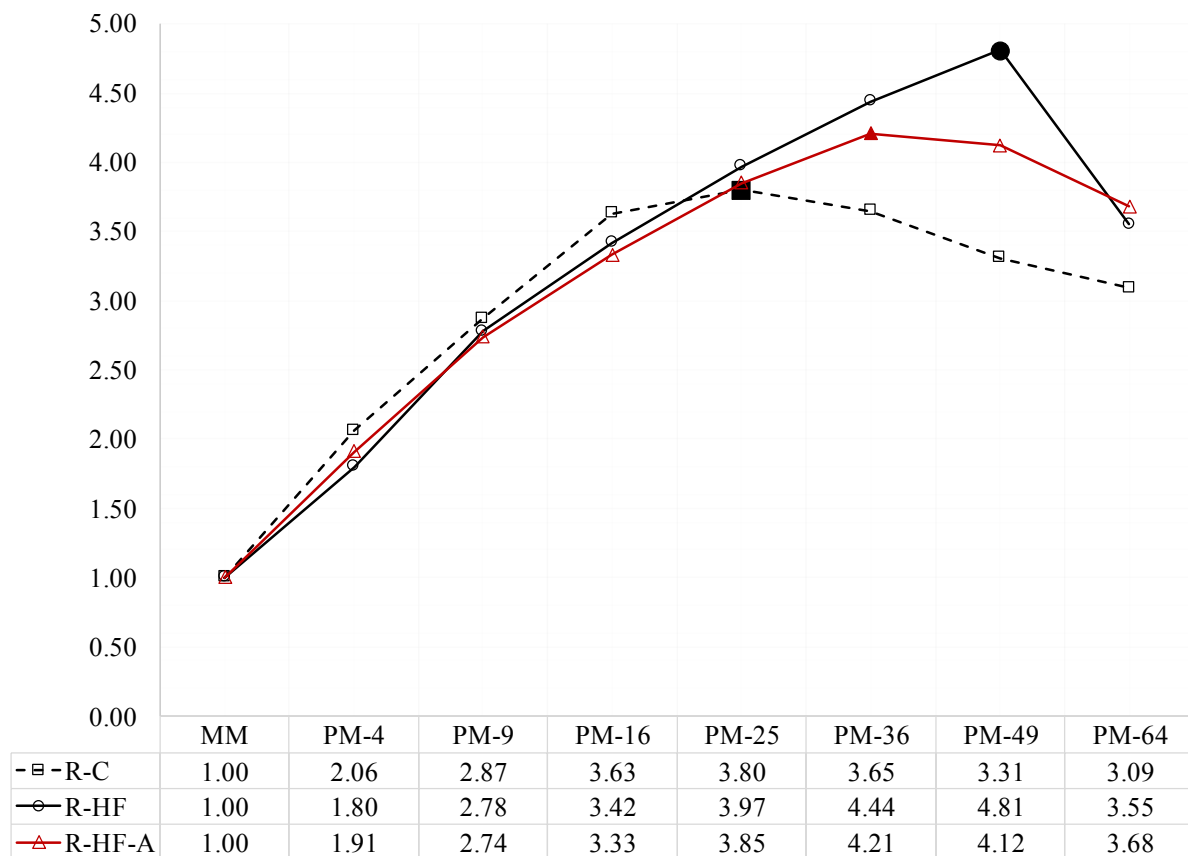


Figure 7.20: Computing wall-clock time speedup for different domain partitioning configurations of sandwich composite models R-C, R-HF and R-HF-A



Table 7.3: Computing wall-clock time and achieved speedup for different domain partitioning configurations of sandwich composite model R-HF-A

Model Configuration	Wall-Clock Time (min)	Normalised Wall-Clock Time (%)	Percentage Reduction (%)	SF (-)
<b>R-HF-A - 102400 Elements, 419042 Nodes, 2095210 DOF, 54620 Additional DOFs</b>				
MM	21856	100.00	0.00	1.00
PM-4	11443	52.36	47.64	1.91
PM-9	7977	36.50	63.50	2.74
PM-16	6563	30.03	69.97	3.33
PM-25	5677	25.97	74.03	3.85
<b>PM-36</b>	<b>5191</b>	<b>23.75</b>	<b>76.25</b>	<b>4.21</b>
<b>PM-49</b>	<b>5305</b>	<b>24.27</b>	<b>75.73</b>	<b>4.12</b>
PM-64	5939	27.17	72.83	3.68

Evidently, a maximum speedup of 4.21 is achieved for the R-HF-A configuration with 36 partitions, while the configuration with 49 partitions is associated with a speedup factor of 4.12, with the shape of the speedup variation curve indicating that the optimal configuration encompasses an intermediate number of partitions to these two configurations. Accordingly, more than 75% reduction in the computing wall-clock time associated with the respective monolithic model can be achieved, which, in turn, corresponds to more than 85% overall reduction in comparison to the R-HF monolithic model.

Similar to R-C and R-HF, an increasing number of child partitions leads to increasing speedup, with a gradually decreasing rate, until the maximum value is reached, which is followed by a descending branch due to the adverse effect of excessive partitioning and the associated increased communication overhead between parallel processors (Jokhio & Izzuddin, 2015). The level of discretisation detail of R-HF-A is intermediate in relation to R-C and R-HF, and hence the former is associated with an enhanced partitioning efficiency compared to R-C, but not as substantial as in the case of R-HF. This is further highlighted by the configuration with 36 child partitions, leading to maximum speedup in the case of R-HF-A, being between the respective configurations of R-C and R-HF, encompassing 25 and 49 partitions, respectively.

It should be emphasised that the adopted partitioning scheme for the configurations under consideration, encompassing the domain decomposition of the monolithic model into equivalently-sized child partitions, is sub-optimal in the case R-HF-A. In the case of R-C and R-HF, this scheme leads to child partitions with equivalent number of nodes and DOFs over their domain and along their respective partition boundaries, due to the mesh uniformity and conformity. Conversely, due to the selective discretisation approach adopted for the establishment of the R-HF-A configuration, the same scheme leads to a substantially increased number of nodes and DOFs for the child partitions defined at the panel centre, as compared to those adjacent to its domain edges. The wall-clock time required for parallel processing is therefore dictated by the central child partitions, which are substantially less compared to the edge child partitions, thus compromising the overall efficiency of domain partitioning.

Irrespective, the configuration leading to maximum speedup is still dictated by the balance between the maximum number of DOFs for individual child partition domains and the number of DOFs along the partition boundary at the parent level, which in this case also accounts for the additional LM DOFs at the child partition level. This is evidently achieved by the configuration of 36 partitions for R-HF-A, which allows for substantial speedup to be achieved, despite the partitioning scheme being sub-optimal. The partitioned modelling efficiency can be further enhanced by adopting an optimal partitioning scheme adjusted to the selective discretisation strategy employed for R-HF-A. The latter would encompass the domain decomposition into larger partitions towards the panel edges and smaller towards its centre, with maximum efficiency being achieved when the number of DOFs and additional DOFs is identical for all child partition processes, and equal to the number of DOFs along the partition boundary at the parent level. This equivalently corresponds to the distribution of identically-sized problems to parallel CPUs with identical specifications, as discussed in Section 7.3.

It should be noted that the employment of domain partitioning requires the consideration of different 1-D coupling interfaces within each child partition process, as opposed to the monolithic model where these are continuously defined. Accordingly, the interfaces are entirely defined within the individual child partition domains, and the respective additional DOFs at the CPs located at individual domain edges are not shared between these along the partition boundary. This approach can potentially compromise the performance and accuracy of the coupled model, due to CP and associated LM entity multiplicity at distinct locations over the domain. However, irrespective of the attained accuracy in the response evaluation, this

approach allows for the required wall-clock time for the analyses to be determined, when individual incremental steps of the nonlinear solution procedure are associated with the same number of iterations as in the monolithic model. Therefore, it has been employed herein to assess the speedup achieved by the R-HF-A configuration.

## **7.5 Application study 4: Validation of high-fidelity nonlinear analysis - 4-point bending of all-steel sandwich composites**

The application study presented here aims at validating the established HF nonlinear FE modelling strategy for realistic 3-D nonlinear analysis of composite structural systems against the results of physical tests. In this context, the established methodology is employed for the numerical modelling of two all-steel, laser-welded, sandwich panel specimens with rectangular honeycomb core, which were tested under 4-point bending.

The 4-point bending tests form part of an extensive experimental programme for the investigation of various performance aspects of novel, all-metal, sandwich panel composites, which has been undertaken as part of the joint industrial Research and Development (R&D) collaboration between Imperial College London, POSCO and AMEC Foster Wheeler. All experimental testing has been conducted at the POSCO R&D testing facility. It is emphasised that the main purpose of this application study is not conducting an extensive and detailed experimental validation, but highlighting the accuracy of the established HF nonlinear FE modelling strategy as one of the main contributions of the present research work.

### **7.5.1 Sandwich composite specimen manufacturing and specifications**

Both faceplates and the core strips of the sandwich panel composite specimens are fabricated from structural steel and have a 3 mm thickness. The specimens have  $600 \times 300$  mm<sup>2</sup> planar global dimensions and 100 mm centre-plane distance between the top and bottom faceplates. The core comprises 3 longitudinal and 6 transverse mutually orthogonal strips, with  $300 \times 97$  mm<sup>2</sup> and  $600 \times 97$  mm<sup>2</sup> dimensions, connected orthogonally to the faceplates by means of laser welding to form a regular honeycomb topological pattern with  $100 \times 100$  mm<sup>2</sup> planar

cell dimensions, measured from the strip centre-planes. The specimen geometric specifications are illustrated in Figure 7.21.

The core strips are manufactured as slotted, with 3 mm wide vertical cut-offs along half their height and a  $\pm 0.05$  mm tolerance to account for minor imperfections associated with the employed laser-cutting process. This allows for a straightforward transverse and horizontal strip assembly process to be established, without necessitating the implementation of welded connections at the intersection locations. The geometric configuration, dimensions and detailing of the sandwich panel specimens and the core strips are illustrated in Figure 7.21 (a)-(c), where  $\delta_1$  and  $\delta_2$  denote the aforementioned slot manufacturing tolerances.

Laser welding enables the connection implementation between the strip edges and faceplates from the external surface of the latter, thus resolving one of the principal challenges associated with the fabrication of all-metal sandwich panel composites. The laser-welding parameters, such as the welding rate, and the welding machine head focal length and inclination, have been particularly optimised for the specimen type, material grade and plated component thicknesses, while special preparation of the individual plated components has further been undertaken prior to the connection implementation. This allows for porosity, insufficient penetration and various other forms of undesirable welding imperfections and defects to be alleviated, thus ensuring the superiority of the weld material mechanical properties in comparison to the parent material. Accordingly, delamination failure does not precede the principal shear failure mode of the specimens, but only arises in the late stages of their nonlinear response following the exhibition of an extensive yielding plateau, as will be discussed in more detail in due course. The laser welding facility employed for the specimen manufacturing is shown in Figure 7.22 (a)-(c), while typical forms of welding defects, including porosity and lack of penetration, are compared against a laser weld section with no defects in Figure 7.22 (d)-(f).

The specimens are tested at a Universal Testing Machine (UTM) with 1000 kN test capacity, available at the POSCO R&D testing facility. The load, applied via the load cell at a rate of 0.01 mm/sec, is shared between two cylinders in contact with the top faceplate, on top of the central transverse cell strips, as illustrated in Figure 7.23. 5 Linear Variable Differential Transformers (LVDTs) have been installed underneath the specimen to measure the displacements at 5 points of the bottom faceplate, while 4 strain gauges with diagonal orientation have been further installed at the end longitudinal strips, as shown in Figure 7.21 (a), (d).

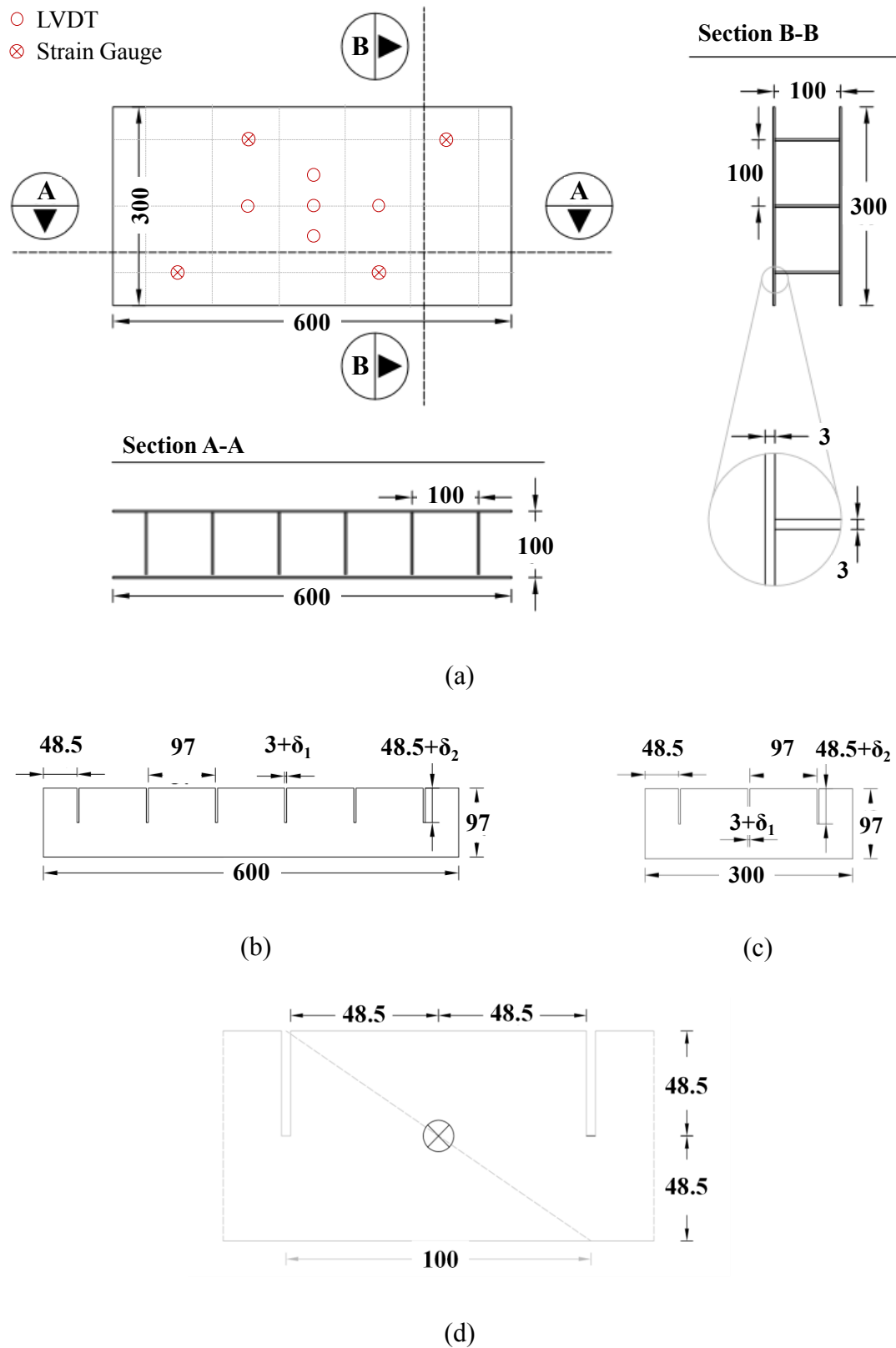


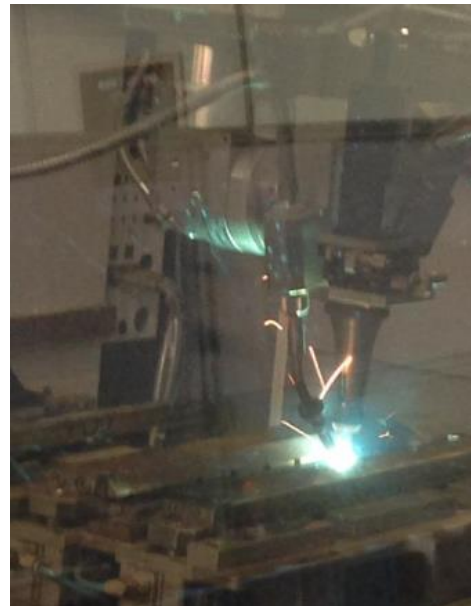
Figure 7.21: (a) Geometric configuration, detailing and LVDT locations (in red) for all-steel sandwich composite specimens, (b) dimensions and detailing of longitudinal strips, (c) dimensions and detailing of transverse strips, (d) strain gauge arrangement



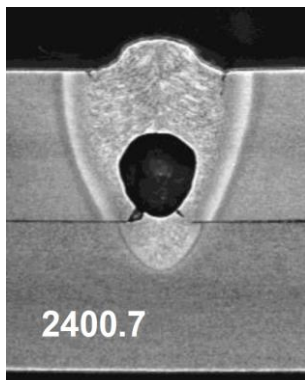
(a)



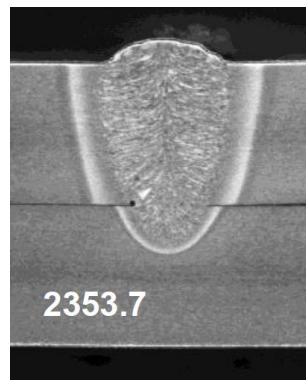
(b)



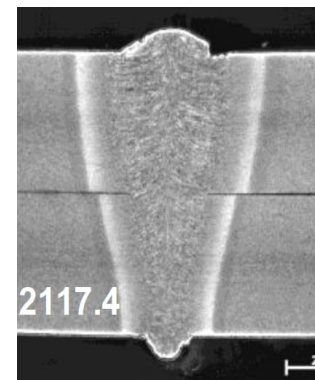
(c)



(d)



(e)



(f)

Figure 7.22: Laser welding machine employed for specimen fabrication (a-c) and laser welding section with porosity defect (d), lack of penetration (e) and no defects (f)

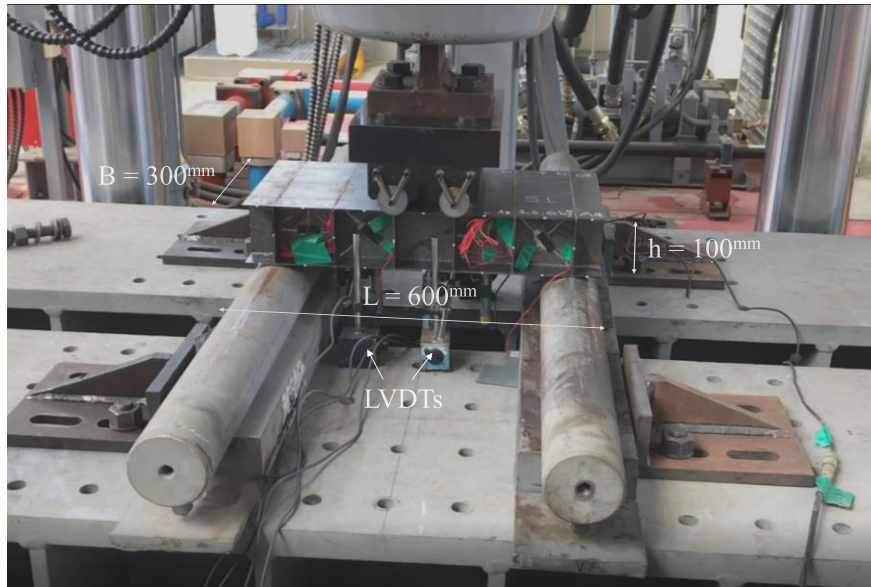


Figure 7.23: Experimental setup of the 4-point bending tests for all-steel sandwich panels

### 7.5.2 Coupon tests and nonlinear material constitutive model calibration

The results of a series of tensile coupon tests, conducted on rectangular section specimens of the steel grade employed for the sandwich composite specimen fabrication, have been used to establish average material parameter values. These have been subsequently employed for the calibration of the tri-linear elastoplastic material constitutive model adopted for the HF modelling of the two specimens in ADAPTIC (Izzuddin, 1991).

The coupon specimen configuration following tensile failure, alongside the stress-strain curve for 4 specimens A-1, A-2, B-1 and B-2 of the employed steel grade, are illustrated in Figure 7.24 (a), (b), respectively, with the associated principal material properties summarised in Table 7.4. Following a coupon test calibration process, the material parameters for the adopted constitutive model are specified as follows: Young's modulus  $E = 218$  GPa, Poisson's ratio  $\nu = 0.3$ , yield strength (proof stress at a strain level of 0.2%)  $f_y = 428$  MPa, strain hardening parameter  $\mu = 0.00655$ , plastic strain at the onset of hardening  $\varepsilon_h = 0.015$  and plastic strain at ultimate strength  $\varepsilon_m = 0.15$ . The specification of quadratic hardening allows for an ultimate strength of  $f_u = 525$  MPa to be achieved at  $\varepsilon_m$  for the adopted values of  $\varepsilon_h$  and  $\mu$ , in accordance with the following expression:

$$\sigma_u = \sigma_y + \frac{\mu E}{1 - \mu} \frac{\varepsilon_m - \varepsilon_h}{2} \quad (7.3)$$

Table 7.4: Characteristic material properties for coupon test specimens A-1, A-2, B-1 and B-2 of the employed steel grade

Coupon Specimen	$f_{y,0.2}$ (N/mm <sup>2</sup> )	$f_{y,0.5}$ (N/mm <sup>2</sup> )	$f_{y,l}$ (N/mm <sup>2</sup> )	$f_{y,h}$ (N/mm <sup>2</sup> )	$f_u$ (N/mm <sup>2</sup> )	$\epsilon_u$	$E$ (N/mm <sup>2</sup> )
A-1	401.3	400.5	398.9	407.4	509.4	13.4	213295
A-2	404.4	394.4	393.3	407.4	505.7	14.3	221284
B-1	421.9	420.7	418.9	435.4	525.9	13.9	216206
B-2	420.8	420.2	417.4	433.8	523.7	13.6	219734

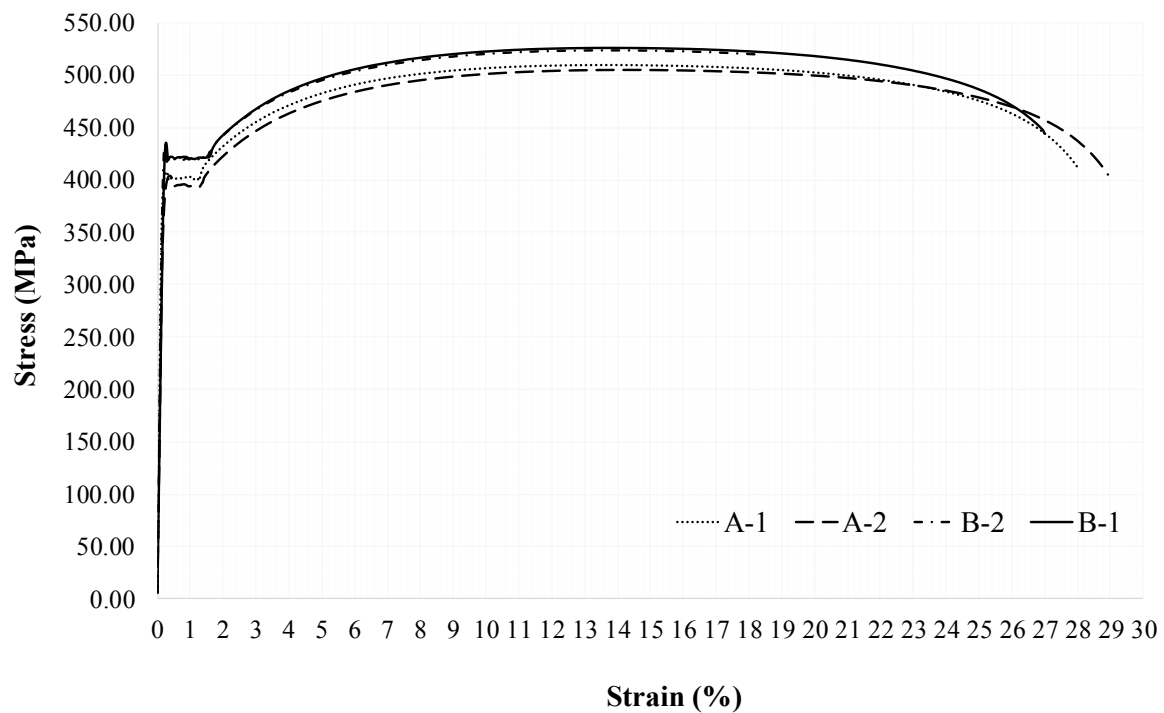


Figure 7.24: (a) Experimental stress-strain curve obtained from coupon tests for the steel grade employed for specimen fabrication, (b) coupon test specimens

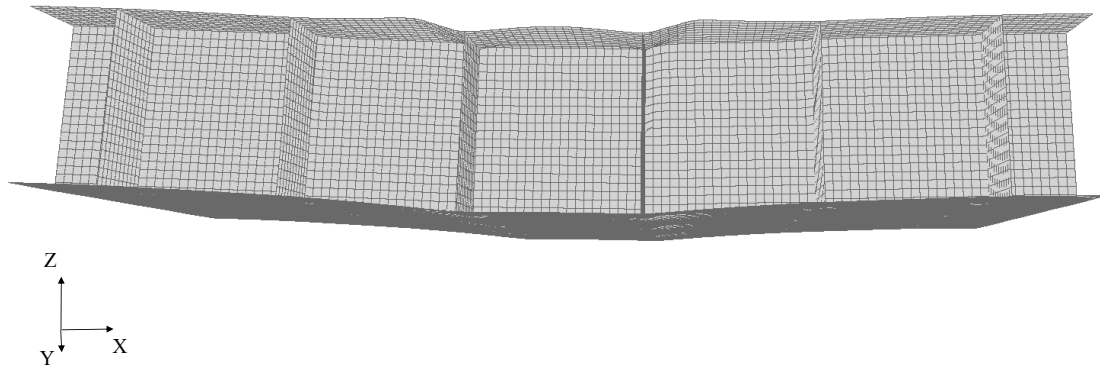


### **7.5.3 Results**

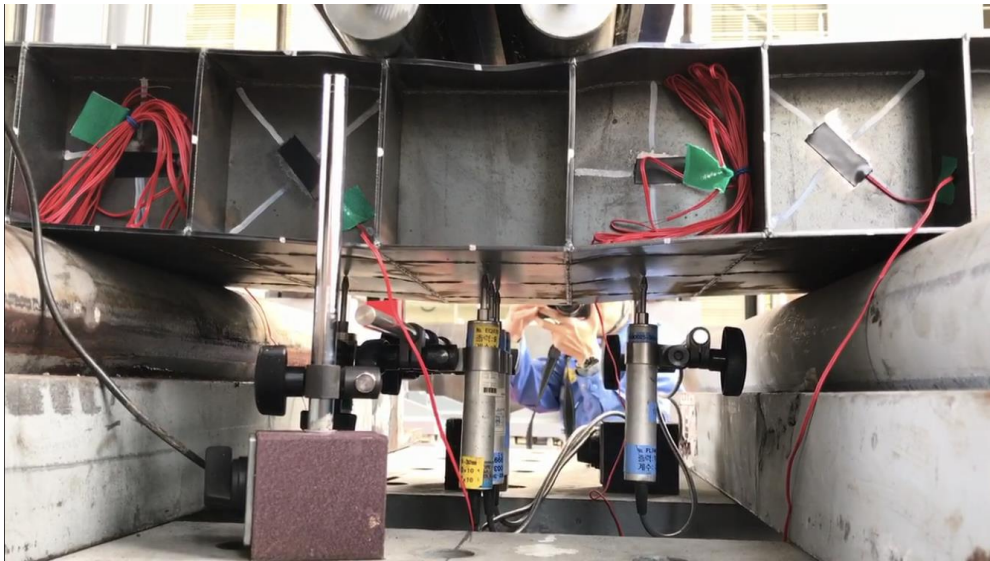
The HF FE models established for the validation against the experimental results comprise a uniform mesh of 28800 shell elements (Izzuddin & Liang, 2016; 2017), corresponding to a mesh of 20×20 elements on each individual cell wall. Duplicate nodes are introduced along the strip slots, to model the material discontinuity and allow for independent deformation of the two slot edges located on either side of the orthogonal strip traversing it. The slots in the HF FE model are introduced at the bottom half of the longitudinal strips and the top half of the transverse strips, which is the case in the actual specimens, as can be observed in Figure 7.25 (b) and (c), where the specimen deformed configuration at ultimate conditions is shown.

The introduction of duplicate nodes enables either side of each slot to displace independently from the orthogonal strip, while at the same time maintaining deformation continuity between the top and bottom strip edges and the faceplates. The potential contact of transverse and longitudinal strips in the actual specimen is accounted for by means of joint elements. These connect the slot edge nodes with the nodes of the orthogonal strip traversing it that are located in between the slot edges, and provide rigid axial contact between these when their relative deformation is negative, thus signifying penetration of the two strips.

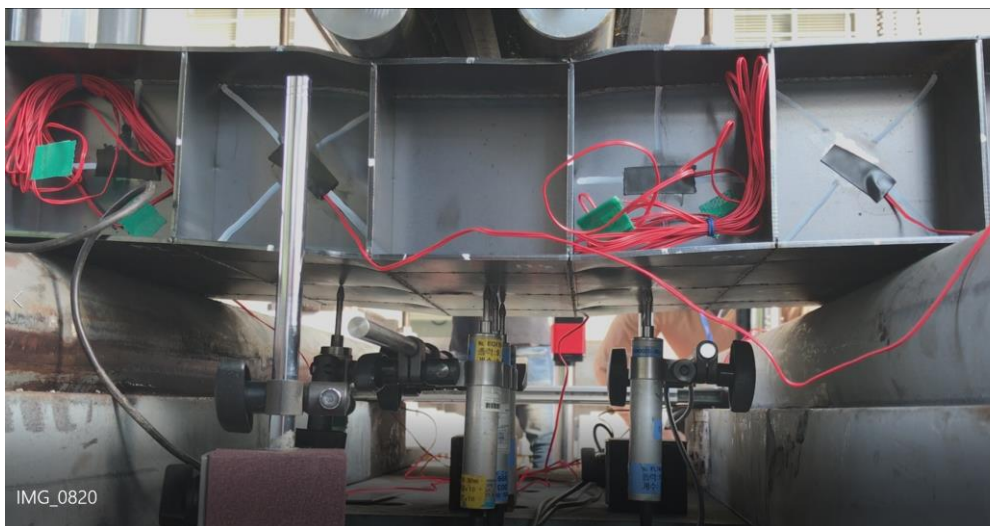
The specimen response is characterised by an initial elastic branch, preceding shear yielding of the longitudinal strips outside the central cell load span at a maximum transverse displacement of roughly 2.5 mm, recorded at the central LVDT. The specimens subsequently exhibit a yielding plateau with an apparent effect of hardening, ultimately leading to delamination of the longitudinal strip laser welds adjacent to the load cylinders. Local buckling of the longitudinal strips adjacent to the load span occurs after delamination, leading to a loss of stiffness and strength, at a level of transverse displacement equal to 10 mm. The nonlinear response subsequently becomes unstable, with the specimens exhibiting a progressive loss of their load bearing capacity, and the tests are terminated at a displacement of 22 mm. The deformed configuration of the HF FE model and the specimens at an ultimate state prior to delamination, associated with 10 mm maximum transverse displacement, are illustrated in Figure 7.25 (a)-(c), while the final specimen deformed configuration at the end of the test is illustrated in Figure 7.26.



(a)



(b)

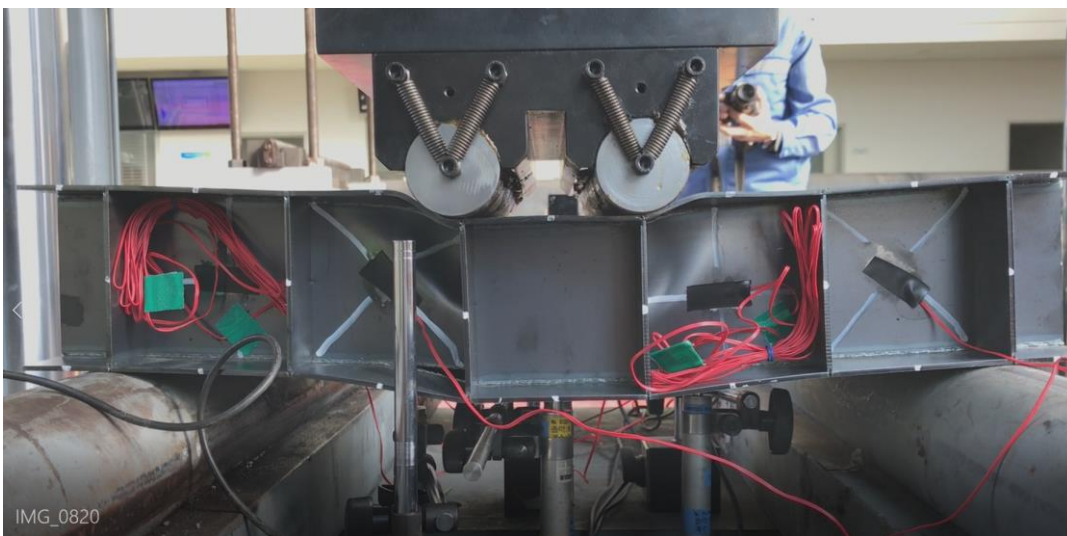


(c)

Figure 7.25: Deformed configuration at ultimate state prior to laser weld delamination (transverse displacement 10 mm): (a) HF FE model, (b) specimen S1, (c) specimen S2



(a)



(b)

Figure 7.26: Deformed configuration of specimens S1 (a) and S2 (b) at failure following laser weld delamination (transverse displacement 22 mm)

It is infeasible for the HF FE model to capture delamination of the laser welds, due to the exclusion of brittle material fracture. This would require a detailed modelling of the laser welds connecting the top faceplate to the longitudinal specimen strips, accounting for potential welding defects during the manufacturing process, which is outside of the scope of the present research work and thesis.

Taking the above into consideration, the primary focus for the validation process is shifted to the transverse displacement range between 0-10 mm, corresponding to the region of elastic deformation, shear yielding of the longitudinal strips and subsequent exhibiting of the yield plateau. The nonlinear response of the HF FE models at the centre of the bottom faceplate is

compared against that of the two specimens S1 and S2, as recorded by the central LVDT illustrated in Figure 7.21 (a), in the graph of Figure 7.27, where equilibrium states marking transitions between principal behavioural bounds of the specimen response have been annotated. Moreover, contour plots of the shell element planar shear force  $N_{xy}$  generalised stress entity are provided in Figure 7.28 for the top faceplate and the core.

Evidently, a highly accurate nonlinear response prediction of the two specimens is achieved by the established HF FE model, which enables the capturing of both the initial elastic stiffness and the shear yielding capacity. The adopted FE modelling strategy, encompassing slot-strip contact modelling, alongside the employed calibrated tri-linear elastoplastic material constitutive model, further allow for an accurate capturing of the specimen response over the yielding plateau. Accordingly, the applicability of the HF modelling strategy to realistic nonlinear 3-D modelling of composite structural systems is highlighted. This is particularly important in cases where the significance of the structure, or the embedded risk of extensive damage due to accidental loading, require a detailed nonlinear response evaluation for the structural integrity and robustness assessment, or for the energy dissipation capability quantification under extreme loading. This will be also demonstrated in the context of the last application study of the present chapter.

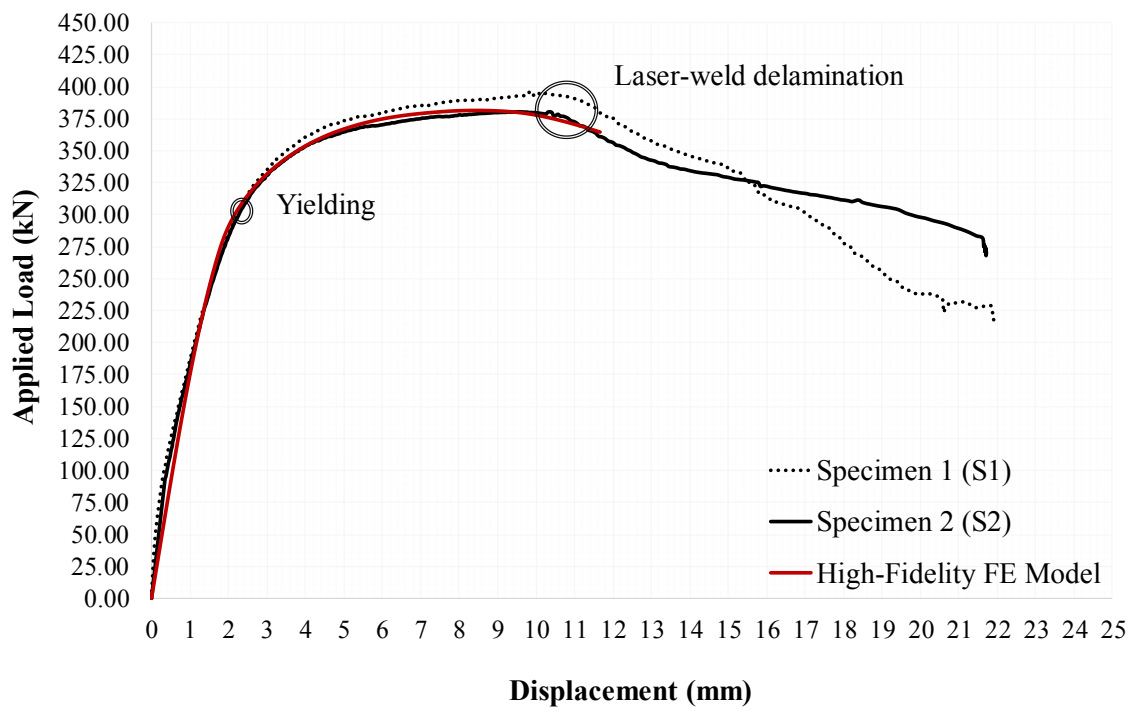
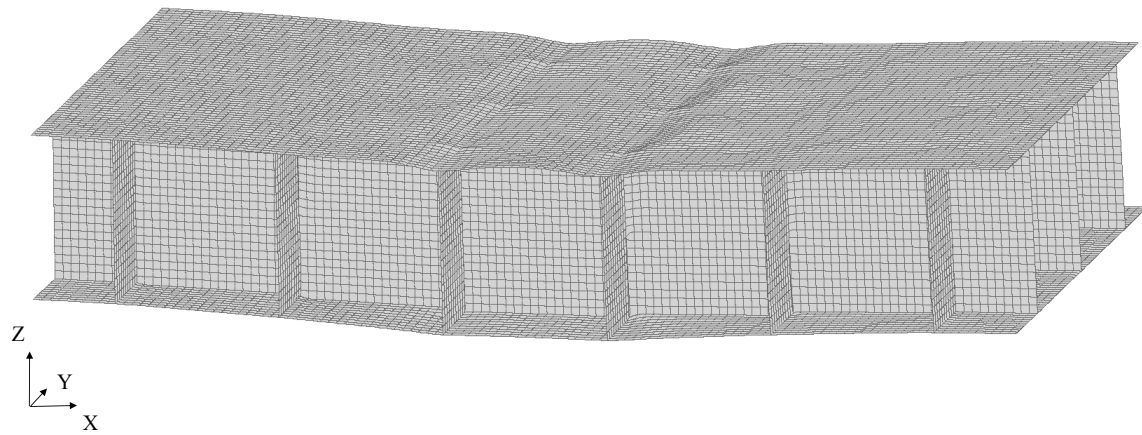
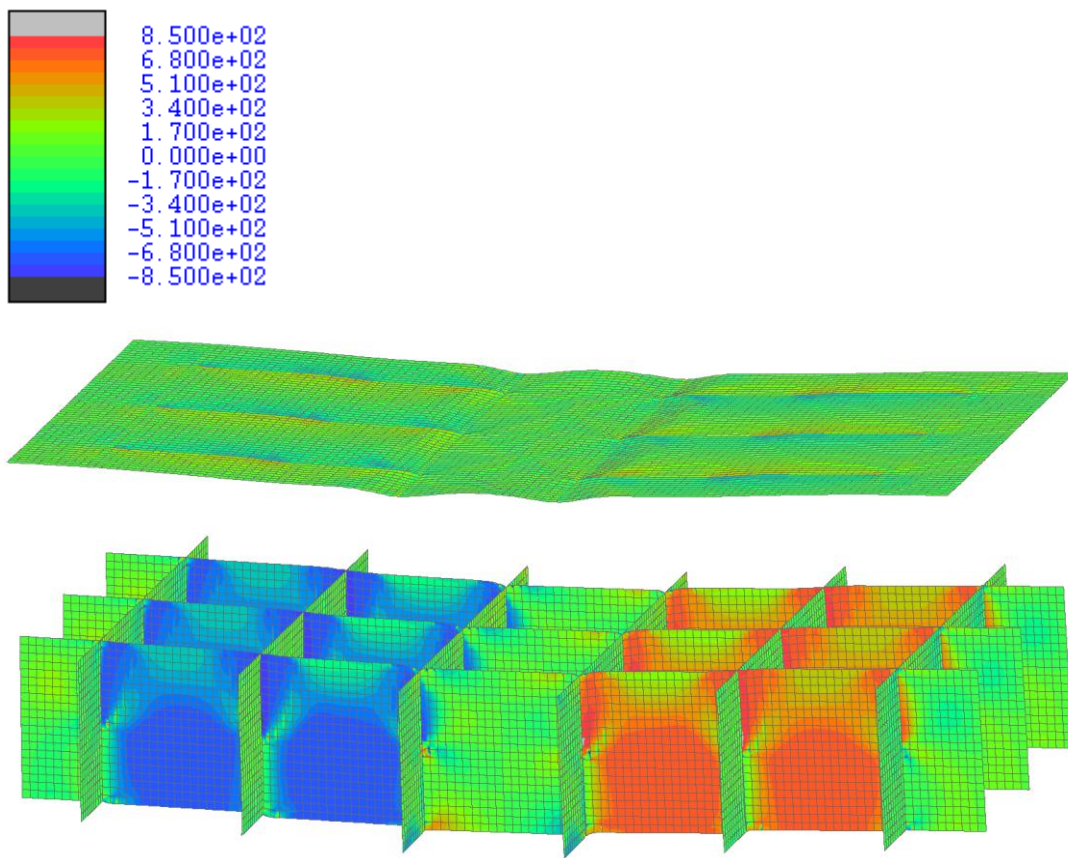


Figure 7.27: Validation of high-fidelity FE model nonlinear response against experimental results for 4-point bending specimens S1 and S2



(a)



(b)

Figure 7.28: Deformed configuration (a) and contour plots of local shell element planar shear force  $N_{xy}$  (b) for high-fidelity FE model

## **7.6 Application study 5: Passive explosion-protective barrier on offshore platform topside module**

The aim of the present application study is to demonstrate the significant benefits associated with the conjunct employment of the HF nonlinear FE modelling strategy and the developed coupling element for realistic 3-D modelling and analysis of composite structural systems, on both the modelling flexibility and practicality fronts. A passive explosion-protective barrier of corrugated type, integrated into the primary structural frame of an offshore platform topside module and subjected to blast loading, is considered for this purpose

As discussed in Chapter 1, offshore platforms installed in shallow-deep water generally comprise a jacket or alternative frame supporting structure, underlying or integrated with the topside module. The latter is a large-scale deck system where the main equipment required for petroleum drilling or natural gas extraction and a variety of other operational processes is installed, alongside the staff living quarters. Due to the variety and size of the installed equipment on the platform topside, the accidental explosion (blast) hazard is one of the most critical design scenarios, which often governs the deck system primary and secondary component sizing in the offshore oil and gas engineering practice (British Standards Institution, 2014).

### **7.6.1 Accidental explosion loading and passive explosion-protective barriers on offshore platform topside modules**

Blast is associated with the combustion of fluid or gas substances and its sub-sonic propagation via heat transfer, referred to as deflagration, or of fluid, gas or solid explosives and its super-sonic propagation as a shock wave via decomposition of the propagated substance, which is referred to as detonation (Williams, 1985). In offshore platform topsides, the risk of liquid or gas leakage and combustion leading to deflagration is considerable (British Standards Institution, 2014), and thus significant research has been conducted in the respective field, particularly after the Piper Alpha oil rig incident in 1988, where a gas pump leakage caused the death of 167 people.

The main characteristics of blast impulses are summarised in pressure time-history profiles, describing the combustion wave-front pressure variation with time. Deflagrations and detonations have distinct pressure time-history profiles, with the former being associated with smaller peak pressures and larger durations and the latter with a steeper pressure variation of substantial peak pressure and reduced duration (Zeldovich *et al.*, 1985).

Pressure impulses can be associated with both positive and negative values, with the associated time-history peak pressure values and duration being of primary significance in the assessment and design of engineering structures subject to blast loading. For deflagration combustions, the overpressure durations range between the order of milliseconds and seconds, with the peak pressure reaching values of up to 8 bar in very congested offshore topside modules (British Standards Institution, 2014). A typical deflagration pressure profile is illustrated in Figure 7.29.

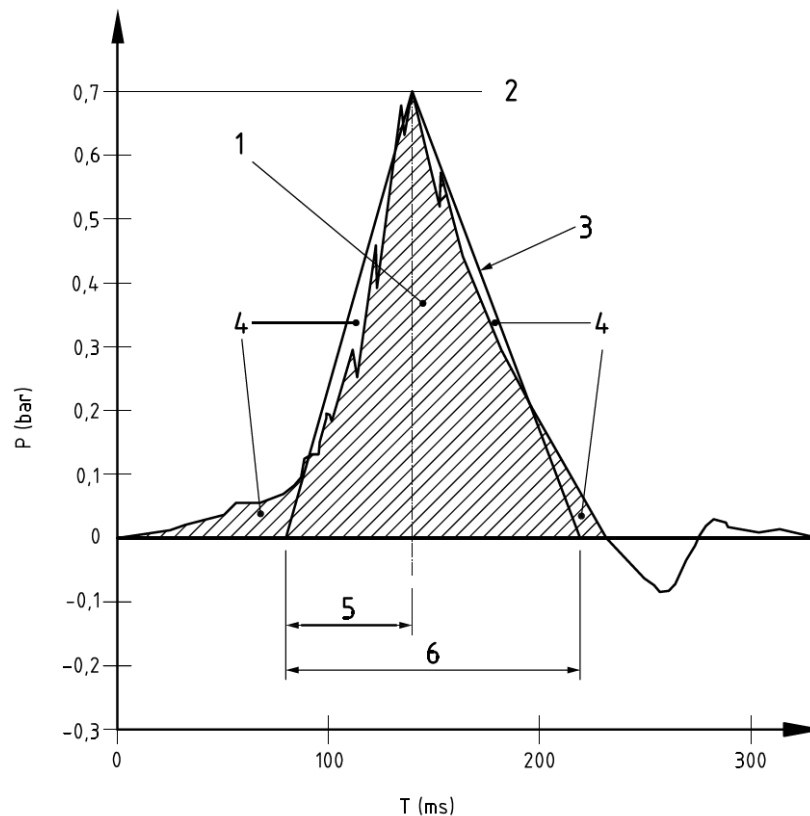


Figure 7.29: Typical deflagration pressure time-history in offshore platform topside modules (British Standards Institution, 2014)

In the offshore oil and gas industrial engineering practice, a common approach for limiting the induced damage in the case of accidental explosions is the installation of passive explosion- or

fire-protective barrier structures, with consideration being given herein to the former, which will henceforth be referred to as blast walls.

Blast walls are installed perimetrically in critical topside deck spans where the explosion hazard from the installed equipment is severe (Det Norske Veritas, 2010). These serve the purpose of dissipating the induced impact loading kinetic energy by means of plastic deformation, thus limiting the structural damage to a local scale and preserving the global structural integrity and robustness, while being easily replaceable in the case of accidental events. Blast walls can either be integrated in the topside structure primary frame by means of their connection to the perimetric columns and beams of the latter, in which case they are also potentially traversed by a diagonal bracing, or non-integrated, in which case they are connected to the overlying primary beam by means of angle cleats.

Taking due consideration of the above, the detailed nonlinear response evaluation and energy dissipation capability quantification of blast walls are of principal importance for the structural integrity and robustness assessment of offshore platform topsides at a global structural level. Blast wall failure in accidental explosion events must therefore be avoided, due to the resulting extensive damage over the topside deck leading to potential global structural failure and the loss of human lives.

### **7.6.2 Blast wall HF nonlinear FE modelling**

A blast wall of corrugated profile, with geometric specifications provided in Figure 7.30, is considered herein, integrated in a part of the topside module primary frame structure between two columns C1 and C2 of circular-hollow cross-sectional profiles and an overlying I-beam, as illustrated in Figure 7.31. The width and height of the blast wall are 10528 and 5000 mm, respectively, while both columns are 6000 mm tall, with cross-sectional radii of 1000 and 508 mm and thicknesses of 30 and 19 mm for columns C1 and C2, respectively. The overlying I-beam is a plate girder with 1000 mm height, 400 mm top and bottom flange widths and 5 mm web and flange thicknesses. At its bottom edge, the corrugated profile is welded to a 10528 mm long and 170 mm wide faceplate with 6 mm thickness.



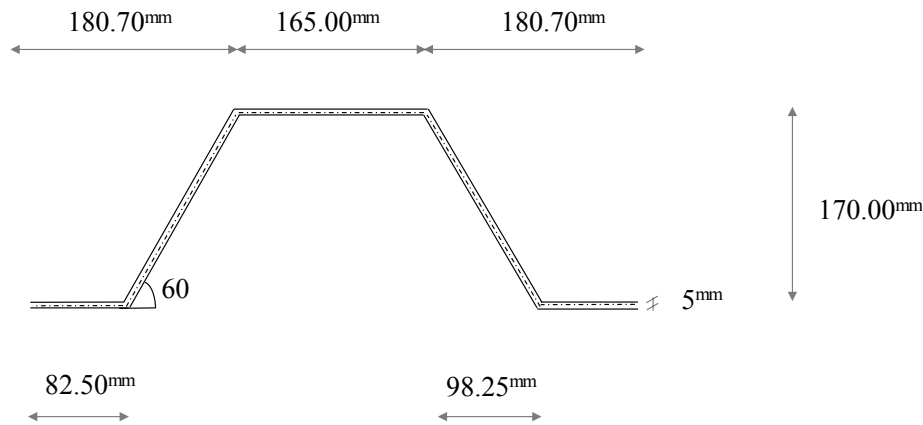


Figure 7.30: Blast wall corrugated profile geometric specifications and centreline distances

The blast pressure time-history is idealised as a piece-wise linear impulse with peak overpressure of 0.75 bar, rise time of 100 msec and total overpressure duration of 200 msec, The negative pressure portion of the impulse is neglected, while the total considered duration for the blast wall nonlinear response evaluation is 250 msec. The blast load is assumed to be acting only on the wall surface as a UDL, which allows for a comparison of the accuracy of the adopted FE modelling strategy with that commonly adopted in engineering practice. The latter involves the independent modelling of the blast wall and the accounting for its connection to the surrounding structural elements by means of appropriate restraints introduced along its edges.

A tri-linear elastoplastic material constitutive model is adopted for mild steel, with Young's modulus  $E = 210$  GPa, Poisson's ratio  $\nu = 0.3$  and yield stress  $f_y = 355$  MPa and quadratic strain-hardening with an onset strain  $\epsilon_h = 0.02$  and initial tangential strain-hardening parameter  $\mu = 0.00835$ , allowing for an ultimate stress  $f_u = 470$  MPa to be achieved at an ultimate strain level  $\epsilon_u = 0.15$ . A Cowper-Symonds strain rate sensitivity model with parameters  $D = 4000$  s<sup>-1</sup> and  $q = 5$  is further adopted to capture the effect of increasing material stiffness and strength under the imposed impact loading, which provides an overstress estimate  $\sigma_o$  on the basis of the following equation:

$$\sigma_o = \sigma_y \left( \frac{\dot{\epsilon}_p}{D} \right)^{1/q} \quad (7.4)$$

where  $\dot{\epsilon}_p$  expresses the rate of change of plastic strains in the temporal domain (Cowper & Symonds, 1957). The material mass is modelled as uniformly distributed over the volume of the shell FEs employed for the system discretisation, while a damping parameter of 5% is adopted. It should be noted that the adopted values for all specified material parameters comply with the provisions of DNV GL (2013) for structural capacity evaluation using nonlinear FE modelling methods.

The Newmark average acceleration method with parameters  $\beta = 0.25$  and  $\gamma = 0.5$  is employed for the numerical solution of the nonlinear system of dynamic equilibrium equations in the temporal domain, with a time step  $\Delta t = 1$  msec. This is sufficiently small to ensure adequate accuracy in the response evaluation, despite the implicit scheme unconditional stability (Newmark, 1959).

The various plated components of the structural elements incorporated in the HF nonlinear FE model herein, i.e. the two cylindrical columns, the blast wall, the faceplate and the beam web and flanges, are discretised independently with non-conforming meshes of 9-noded shell FEs, in accordance with the modelling strategy presented in Chapter 3. For the blast wall domain discretisation, a dense mesh of 28800 shell FEs is employed with characteristic element size of 50 mm, due to it being the structural component of principal interest. For the two columns, meshes encompassing 900 FEs are employed, while 360 elements are employed for the discretisation of the faceplate, as well as of the beam flanges and web.

Rigid translational and rotational coupling of the various meshes is achieved using the developed coupling element along six 1-D interfaces [1]-[6], as illustrated in Figure 7.31. Interfaces [1]-[4] couple the blast wall with the bottom faceplate, the beam bottom flange, column C2 and column C1, respectively, while interfaces [5] and [6] are introduced to couple the beam web with columns C2 and C1, respectively. For the active coupling element identification along each interface, the progressive segmentation algorithm presented in Section 4.5 is employed, with a slave-only progressive segmentation approach, using the surface associated with the denser mesh in each case as slave, i.e. the blast wall for interfaces [1]-[4], and columns C2 and C1 for interfaces [5] and [6], respectively. At the coupling element level, 3 CPs with 4 LM entities each are employed for the constraint enforcement along the corresponding coupling segment. The penalty parameters for both translational and rotational coupling are specified as 0.1, while the element-specific integration scheme is employed with a Gaussian quadrature order of 3.

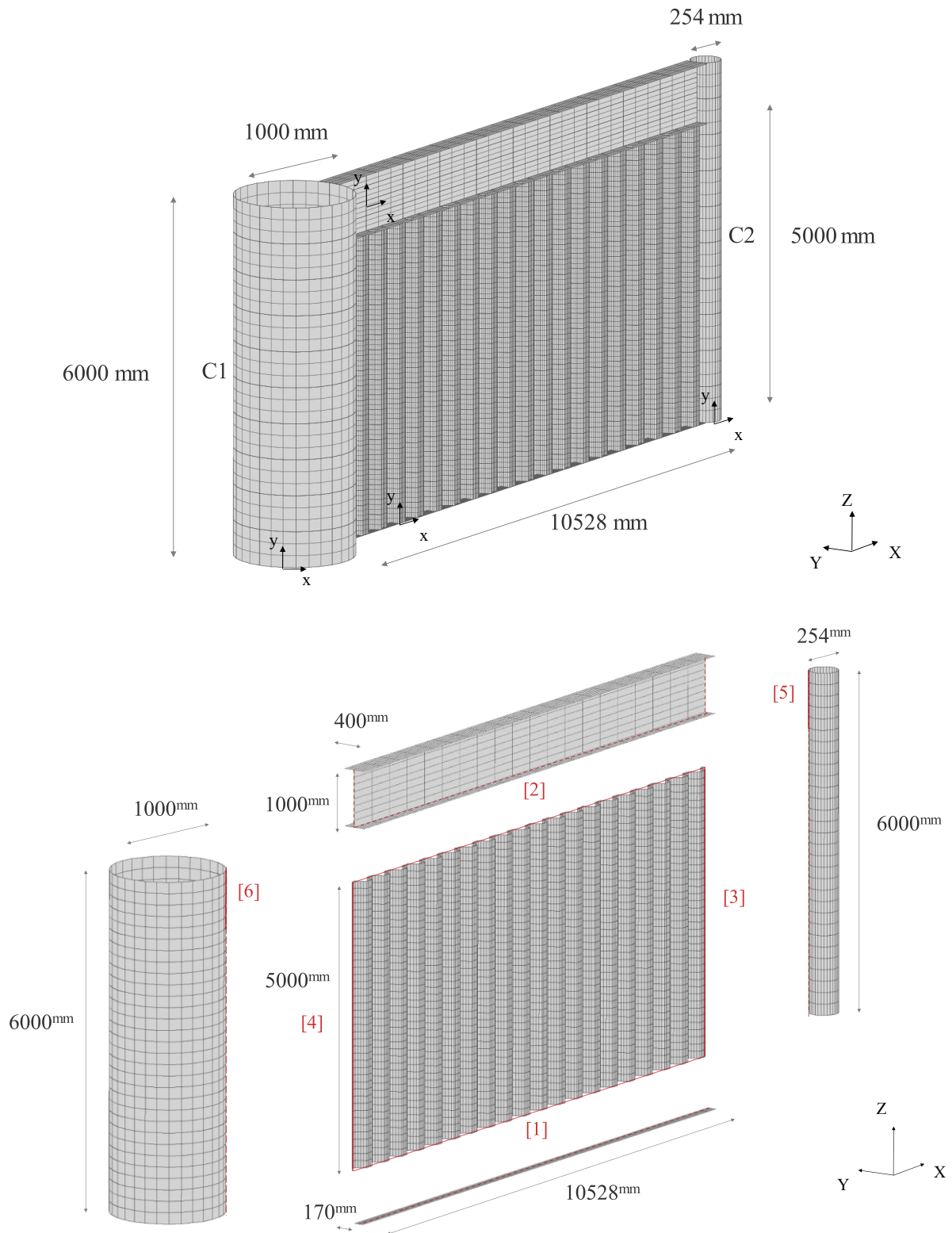


Figure 7.31: HF FE model configuration, global component dimensions and 1-D coupling interface definition (slave surface continuous – master surface dotted) for integrated blast wall and surrounding structural elements

The bottom faceplate is modelled as fully restrained against all translations and rotations, similar to the bottom section of column C2 and both the top and bottom sections of column C1, to account for continuity of the modelled domain with the surrounding structure. Two distinct cases are investigated herein, with the blast wall and column C2 being free to move or connected to an overlying deck, where translational restraints in the three global directions are introduced in the latter case. The two blast wall integrated model (IM) configurations under consideration, encompassing the modelling of the overlying beam top flange and the top section of column C2 as free or restrained, will henceforth be referred to as IM-1 and IM-2, for the purpose of distinction.

The obtained response for IM-1 and IM-2 is compared against the conventional modelling approach in engineering practice, encompassing the HF nonlinear FE modelling of the blast wall only and the accounting for the surrounding structural element contributions via approximate boundary conditions. The corresponding blast wall conventional models (CMs) for the two cases under consideration will henceforth be assigned the acronyms CM-1 and CM-2. In CM-1 the blast wall is fully restrained along its bottom and left edges, with its top and right edges restrained only along the global Z-axis, while in CM-2 all edges are modelled as fully restrained.

### **7.6.3 Results**

The comparison of the maximum transverse displacement time-history over the corrugated blast wall profile domain is illustrated in Figure 7.32 for IM-1 and CM-1, and in Figure 7.33 for IM-2 and CM-2. The strain energy time-history curves for all configurations under consideration are collectively illustrated in Figure 7.34. The deformed configurations of IM-1, IM-2, CM-1 and CM-2, at the time instance corresponding to a maximum deflection over the wall domain along the out-of-plane global Y-axis in each respective case, are illustrated in Figures 7.35 - 7.38, whereas contour plots of the local shell FE  $\epsilon_y$  strain and von Mises stress entities are shown in Figures 7.39 - 7.42.

The comparison of the strain energy and displacement time-histories, as well as of the  $\epsilon_y$  strain and von Mises stress contour plots, for the IM and CM configurations indicates a substantial underestimation of the maximum transverse displacement, and accordingly the level of induced

strains due to plastic deformation in the system, when the conventional modelling approach is employed. This can be attributed to the CM configurations failing to capture the interaction between the blast wall and the surrounding structural elements with the established set of boundary conditions. Accordingly, the contributions to the blast wall response of the twisting and bending flexibility of columns C1 and C2, as well as of their significant plastic deformations due to material yielding and the spread of plasticity are neglected, thus leading to substantial inaccuracies in the system ultimate response evaluation.

As evident from the transverse displacement and strain energy time-histories of IM-1, the blast wall in this case undergoes permanent plastic deformations, associated with an extensive spread of plasticity following the blast impact, with a maximum displacement 2.5 times greater than the predicted by CM-1. Due to the beam top flange and column C2 being unrestrained in this case, column C2 undergoes substantial plastic deformations following yielding at its base, leading to an increased maximum displacement over the wall domain, which in this case behaves as effectively unrestrained at its right end. This is accounted for in CM-1 by only restraining the right edge along the Z-axis. The contour plots indicate an induced maximum strain of the order of  $\varepsilon_u = 0.15$  in the vicinity of the faceplate at the blast wall lower right region, where the corresponding von Mises stresses surpass the ultimate strength of 470 MPa for mild steel. Accordingly, there is an increased risk of material fracture and subsequent failure of the wall in that region, even with the beneficial contribution of the overstress due to strain rate effects allowing for an increased material resistance to be attained.

In the case of IM-2, the system also exhibits substantial plastic deformations, which are however significantly lower compared to IM-1, due to the top beam flange and C2 column section being restrained. CM-2 underestimates the level of maximum displacements and strain energy dissipation of the system by roughly 5 times, which can be principally attributed to the beam web exhibiting substantial deformations, thus leading to increased overall deformations over the blast wall domain. The contour plots of IM-2 indicate overall reduced strains in comparison to IM-1; however, the blast wall exhibits substantial stresses in its upper left corner, which are not captured by CM-2 and can potentially lead to failure for a loading scenario associated with a slightly increased blast overpressure.

Both CM-1 and CM-2 evidently fail to capture the phenomena described above, thus providing: (i) unconservative estimates of the blast wall failure hazard and its energy dissipation capability at ultimate conditions, when a performance assessment of an existing system is being looked

at; and (ii) unconservative estimates of the design actions for the wall and the surrounding structural elements, when the design of the system is being looked at.

The establishment of a conforming shell FE mesh for the discretisation of three different shell surface types, namely folded, cylindrical curved and planar, becomes a particularly challenging undertaking in this case, without the modelling flexibility offered by the developed coupling element. Furthermore, the establishment of a conforming mesh results in a substantially fine mesh at a global level, if the same level of discretisation detail for the blast wall is to be achieved, accordingly imposing a prohibitive demand in relation to modelling effort, computing time and memory resources.

The developed coupling element allows for these shortcomings to be effectively overcome by enabling the independent discretisation and coupling of the various components, thus enabling a substantially reduced overall mesh density to be achieved. This application study therefore profoundly highlights the practical benefits of the HF modelling strategy employment for a realistic response evaluation, energy dissipation quantification and performance assessment of composite structural systems where this is critical, which would otherwise be virtually infeasible.

Besides highlighting the substantial versatility of the established combined modelling strategy, this application study further serves as a general and extensive verification study for the developed 1-D coupling element. Evidently, the latter is capable of effectively enforcing rigid translational and rotational coupling between mixed surface types, intersecting along 1-D interfaces which traverse the shell FE domains in arbitrary orientations. Furthermore, the attainment of numerical convergence in the case of dynamic analysis in large-scale FE meshes where the coupling element is employed, alongside the element capability of accurately capturing the spread of plasticity in cases of blast loading where the strain rate effect is accounted for, are demonstrated.

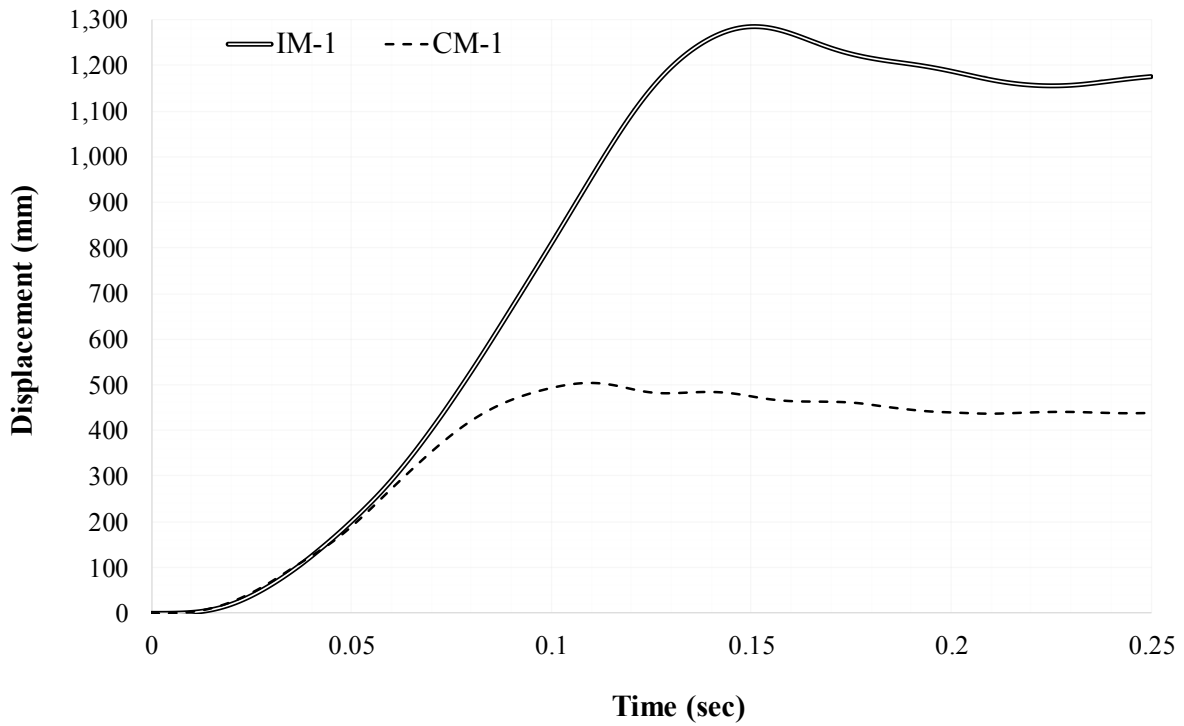


Figure 7.32: Maximum transverse displacement time-history for blast wall models IM-1 and CM-1

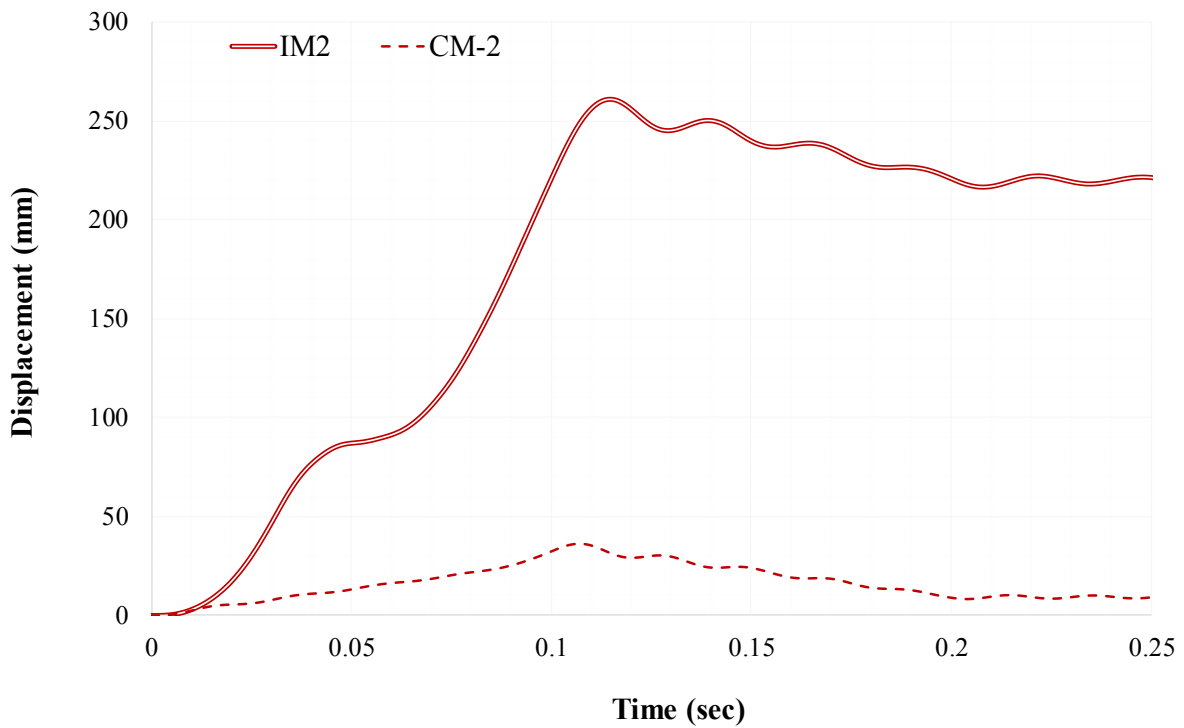


Figure 7.33: Maximum transverse displacement time-history for blast wall models IM-2 and CM-2

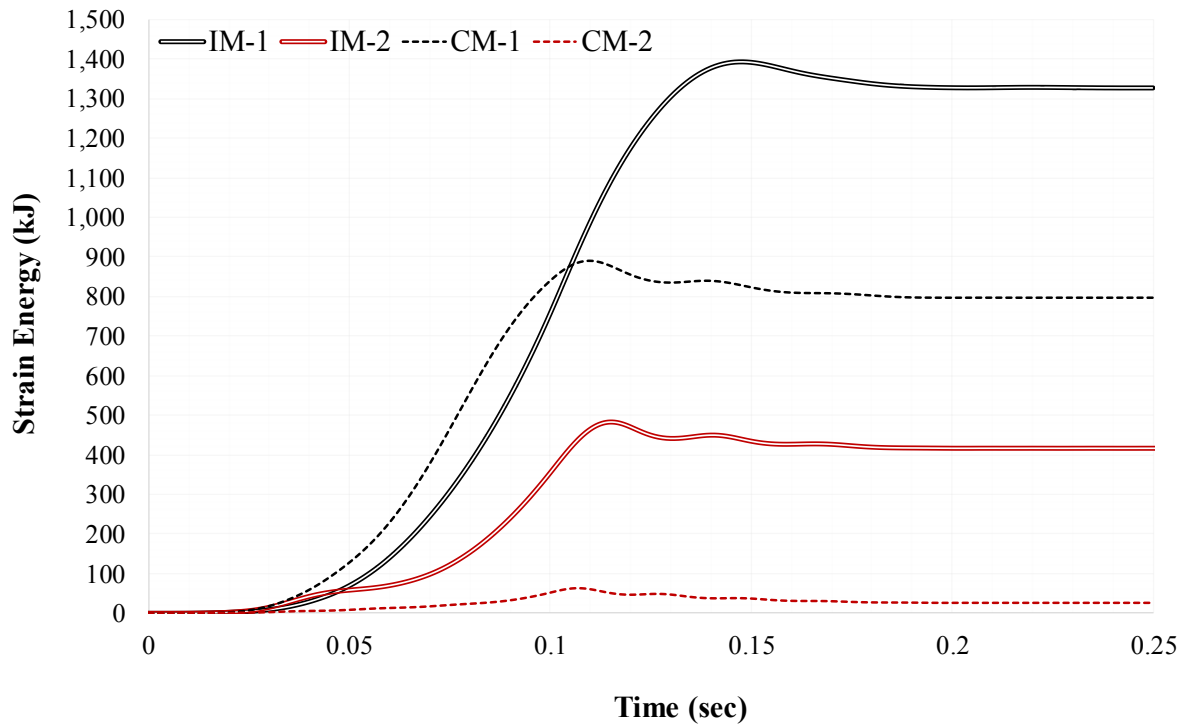


Figure 7.34: Strain energy time-history for blast wall models IM-1/2 and CM-1/2



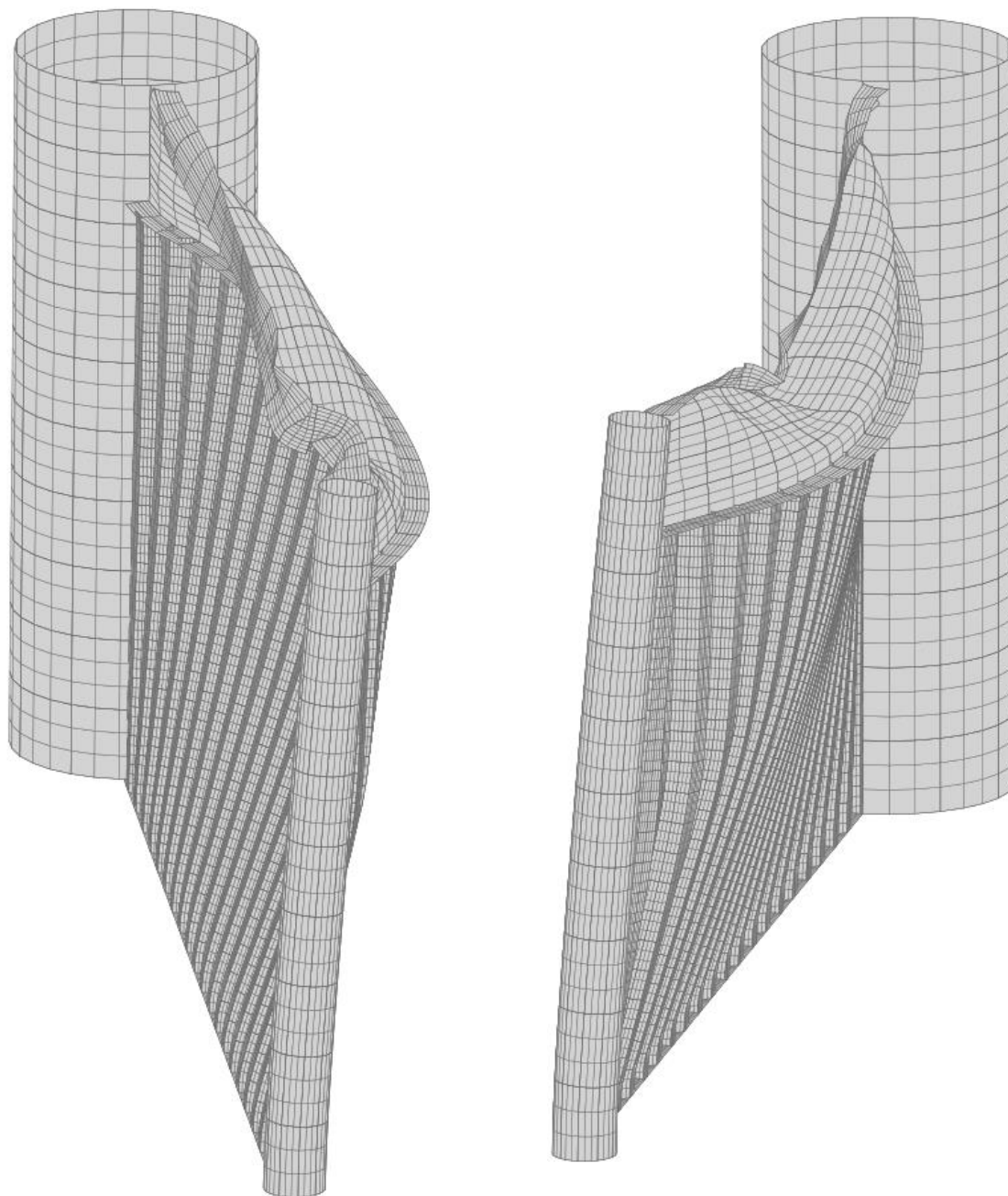


Figure 7.35: Deformed configuration at maximum displacement for blast wall model IM-1

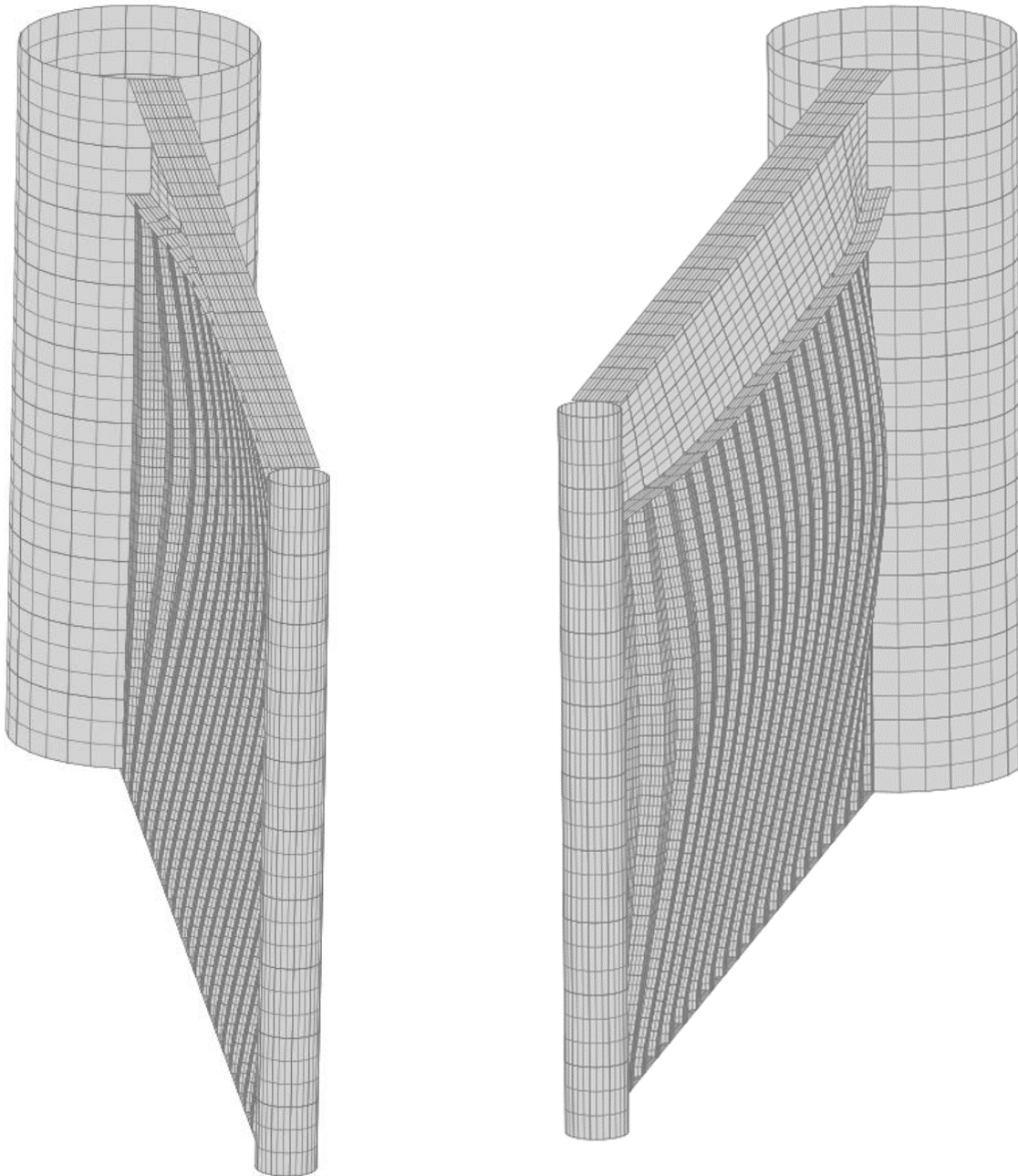


Figure 7.36: Deformed configuration at maximum displacement for blast wall model IM-2  
(scale factor 2.0)

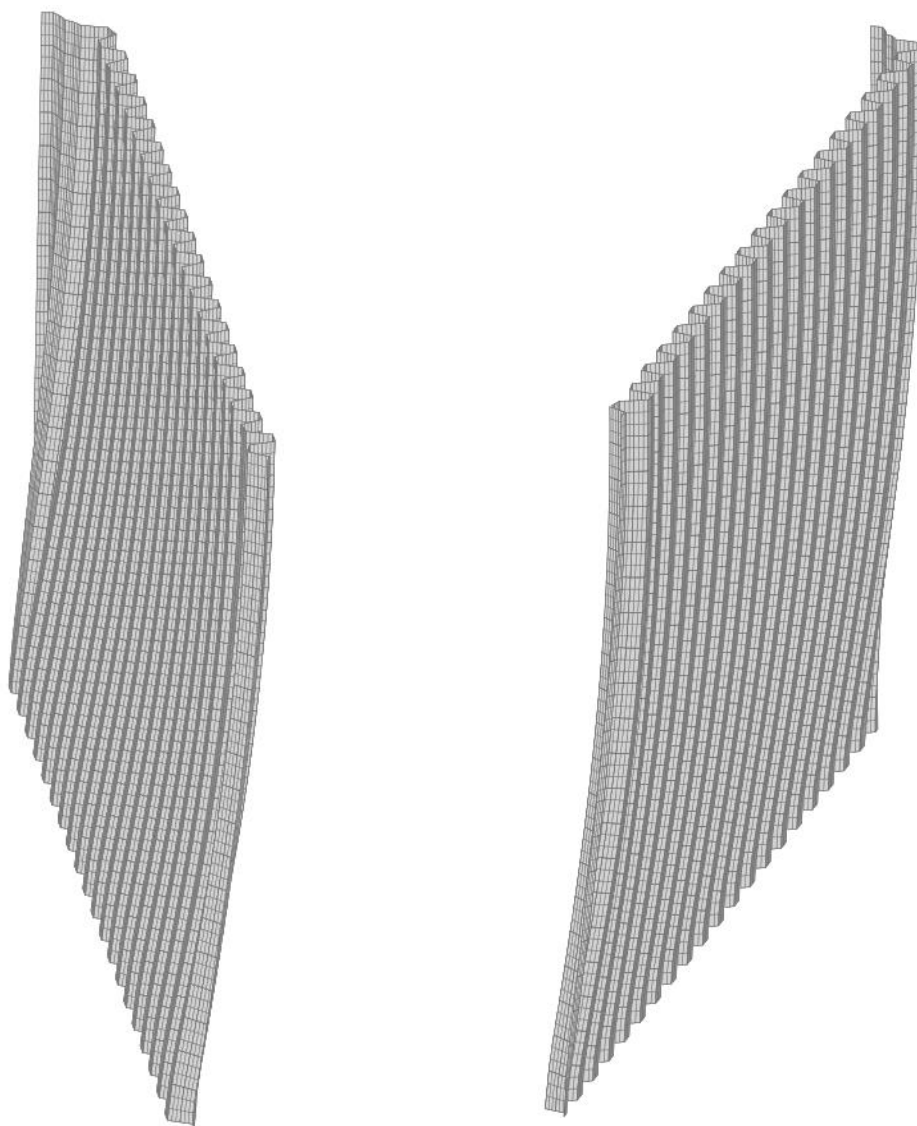


Figure 7.37: Deformed configuration at maximum displacement for blast wall model CM-1

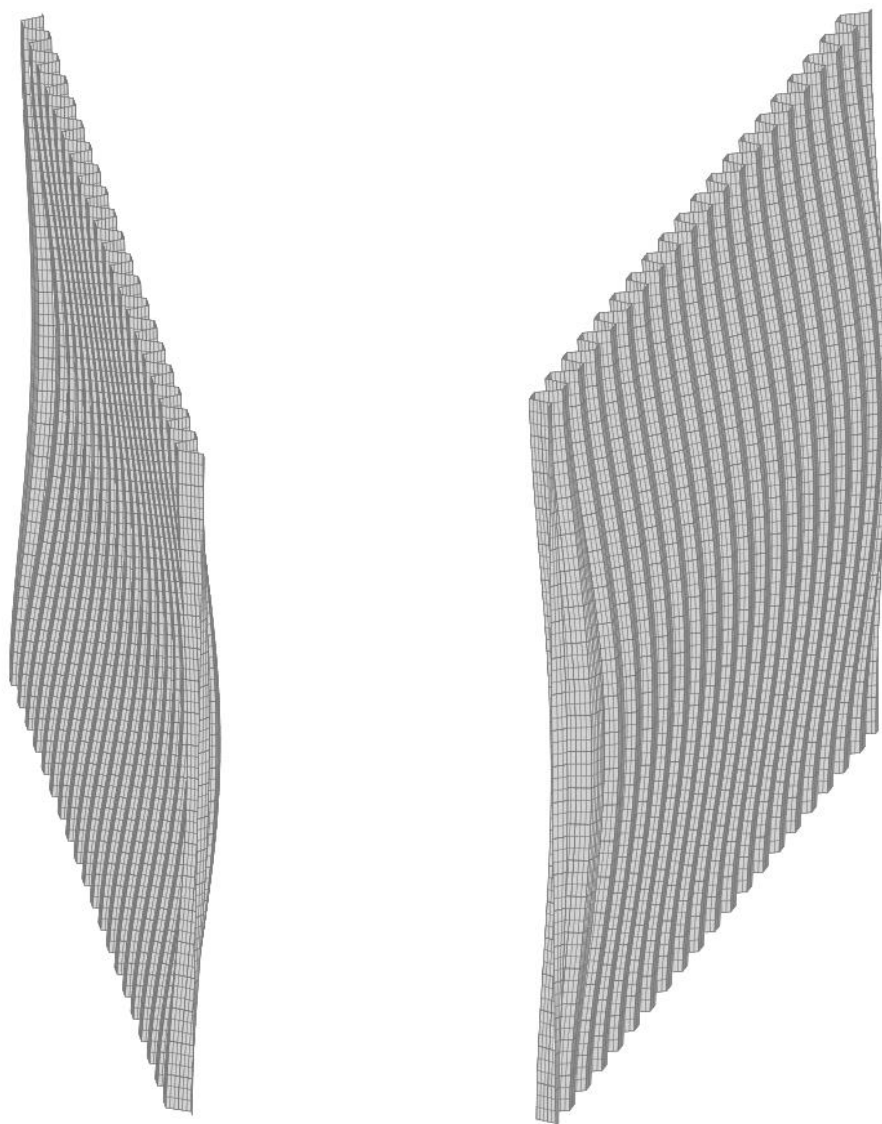


Figure 7.38: Deformed configuration at maximum displacement for blast wall model CM-2  
(scale factor 2.0)

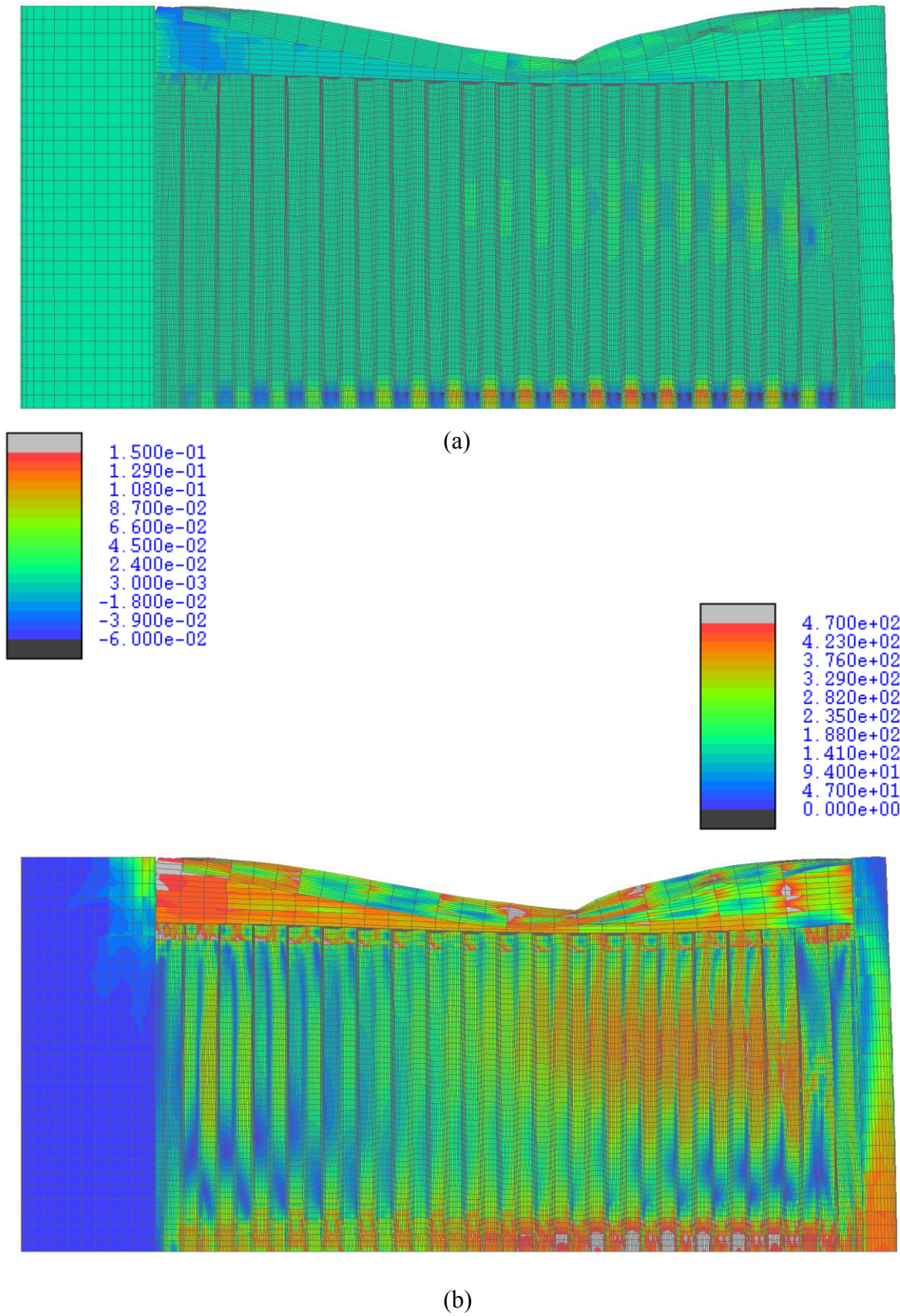
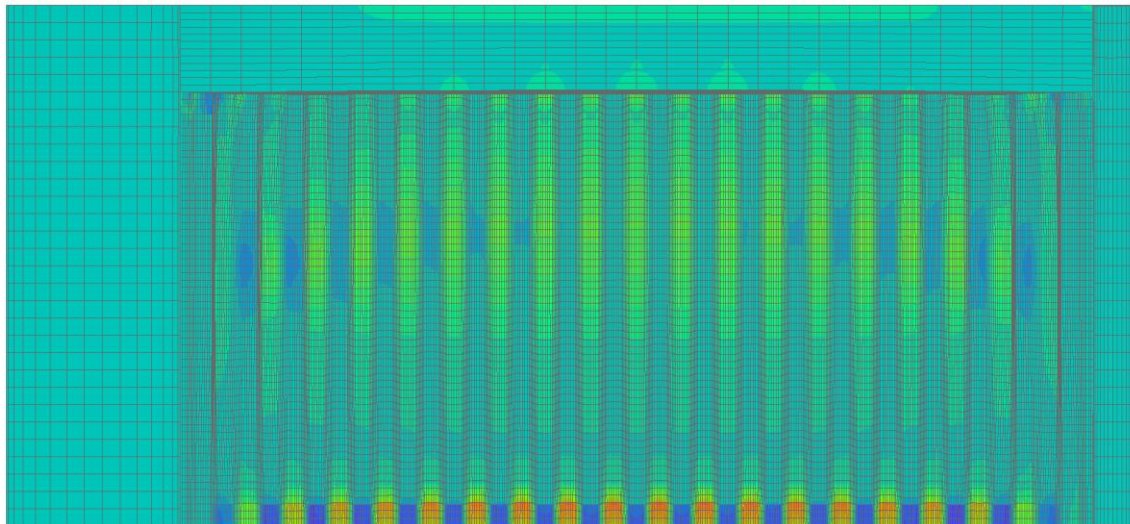
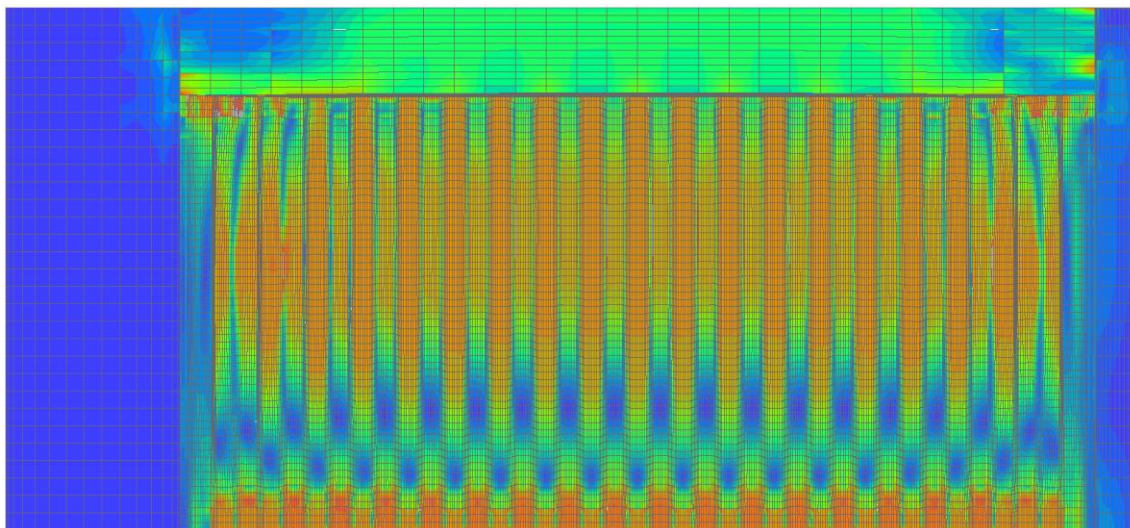
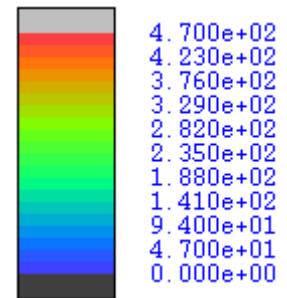
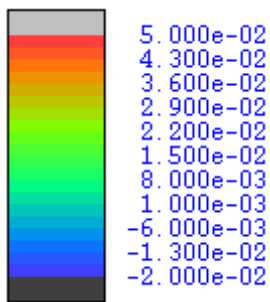


Figure 7.39: Contour plots of local shell FE entities at maximum displacement for blast wall model IM-1: (a) strain  $\epsilon_y$ , (b) von Mises stress



(a)



(b)

Figure 7.40: Contour plots of local shell FE entities at maximum displacement for blast wall model IM-2: (a) strain  $\epsilon_y$ , (b) von Mises stress

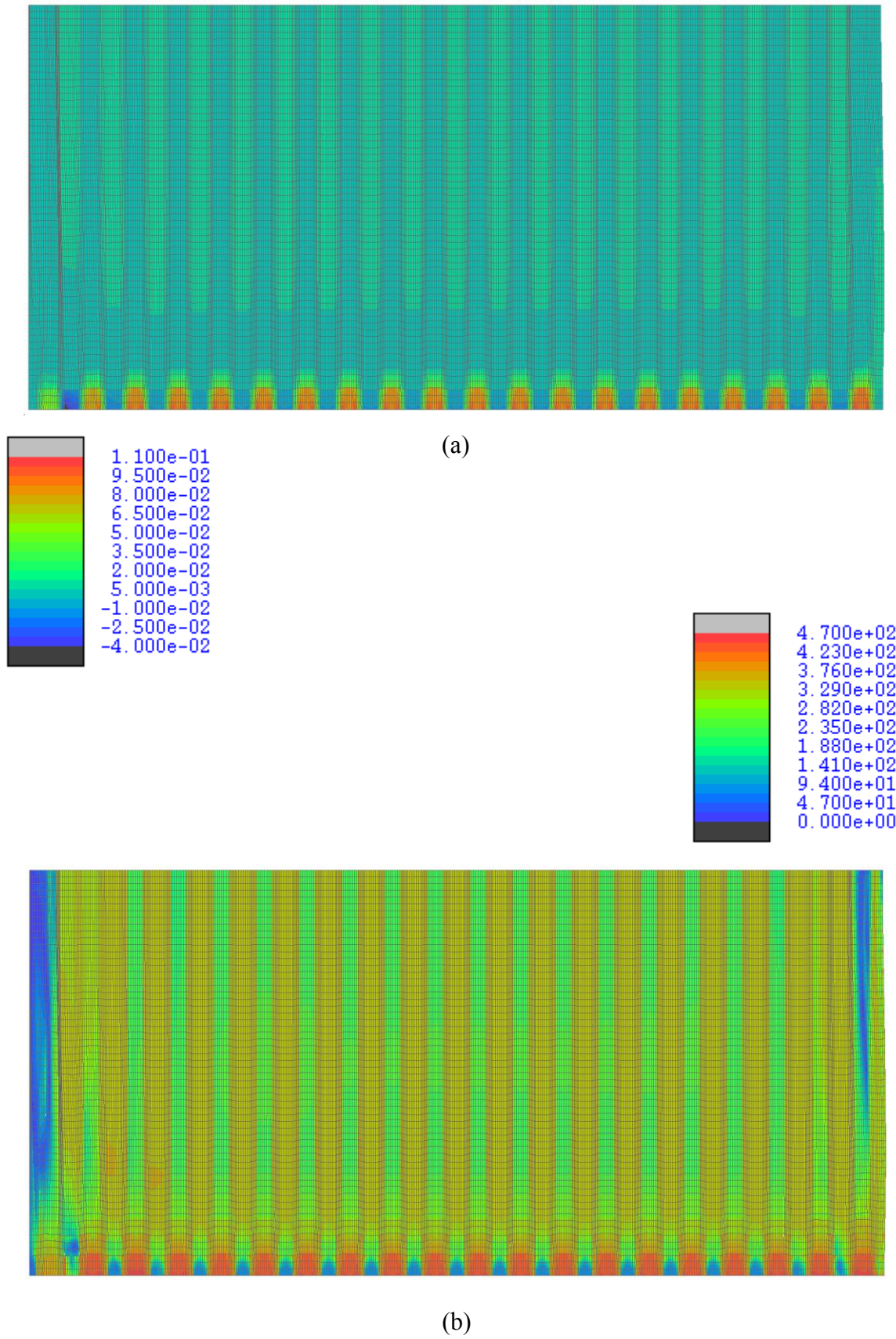


Figure 7.41: Contour plots of local shell FE entities at maximum displacement for blast wall model CM-1: (a) strain  $\epsilon_y$ , (b) von Mises stress

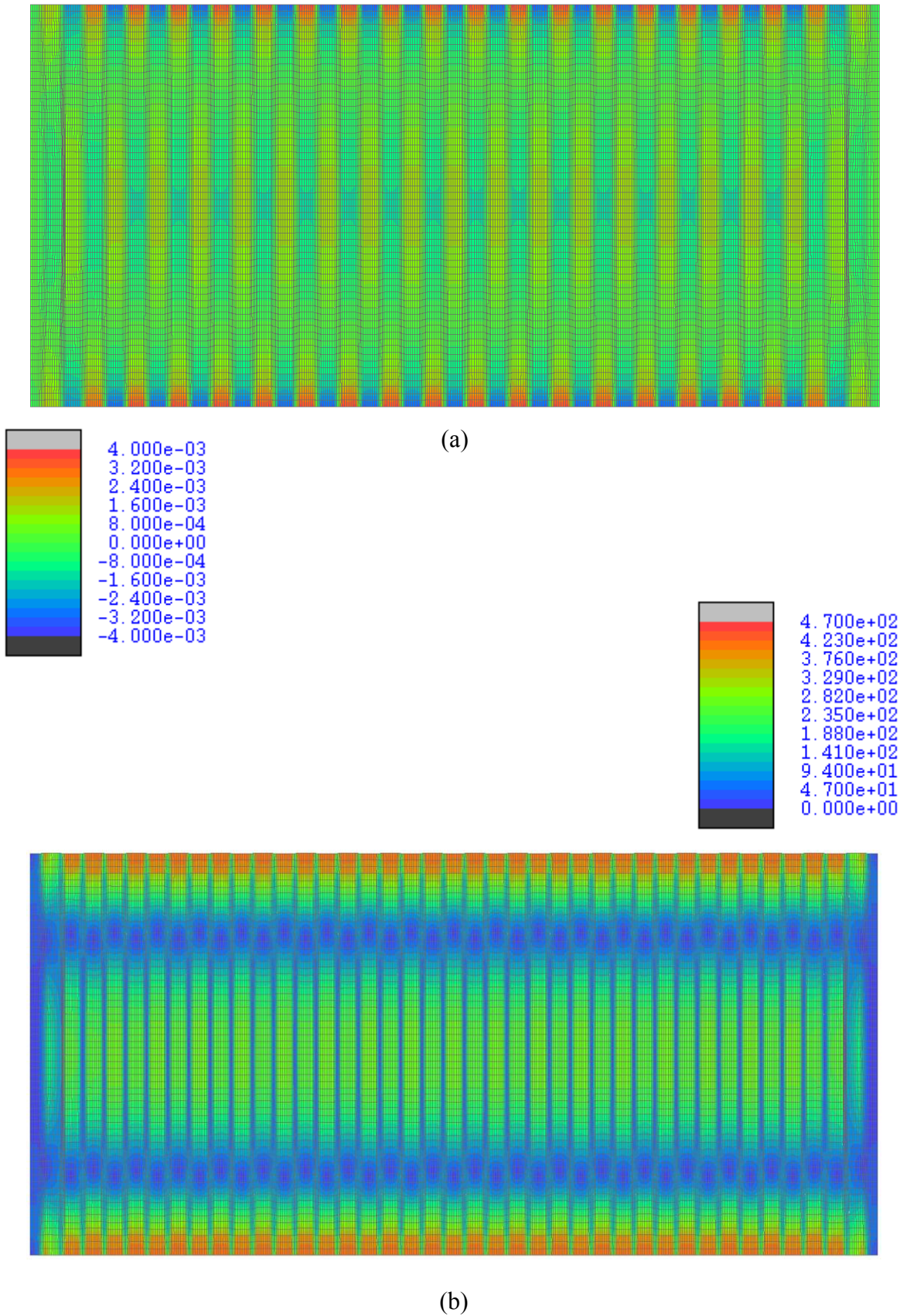


Figure 7.42: Contour plots of local shell FE entities at maximum displacement for blast wall model CM-2: (a) strain  $\epsilon_y$ , (b) von Mises stress



## **7.7 Concluding remarks**

A series of numerical studies focusing on offshore topside deck applications is presented in this chapter, with consideration being specifically given to large-scale metal sandwich composites employed as deck components, as well as to composite passive explosion protective barriers (blast walls). A summary of the conclusions drawn from the results of the conducted application studies is provided hereafter: (i) the proposed HF nonlinear FE modelling strategy enables the capturing of the spread of plasticity and the interaction of the various forms of local buckling in the range of large displacements, which is essential for large-scale sandwich and composite systems due to their substantial response sensitivity to such phenomena; (ii) the proposed HF modelling strategy is successfully validated against experimental results, obtained from physical testing of novel, metal, sandwich panel components as part of the INFLOAT project; (iii) dual super-element domain partitioning allows for a wall-clock time reduction of virtually 80% to be achieved for large-scale sandwich composites, in comparison with the monolithic HF models, through effective process parallelisation on HPC systems with distributed memory; (iv) The optimal number of child partitions for a given system, leading to maximum speedup, is achieved for an equivalent distribution of DOFs in all partitions, with the efficiency of partitioned modelling being more prevalent in systems associated with a high discretisation level; (v) the employment of the developed 1-D coupling element formulation for selective domain discretisation in large-scale composite systems enables the response of the corresponding HF monolithic model to be effectively approximated, while leading to a substantial reduction in the employed number of FEs for domain discretisation; (vi) the employment of the 1-D coupling element in conjunction with dual super-element domain partitioning leads to further computational benefits, even with a sub-optimal partitioning configuration; (vii) the employment of the HF modelling strategy and 1-D coupling element provide a systematic and reliable methodology for the realistic HF 3-D modelling of composite systems, enabling the capturing of effects that significantly alter the response and are neglected with the adoption of a simplified modelling approach, which is particularly crucial in applications involving substantial hazard.

# Chapter 8

## Conclusions

### 8.1 Summary

The research work presented in this thesis was motivated by a joint project between Imperial College London, POSCO and AMEC Foster Wheeler, namely the INFLOAT project, aiming towards the establishment of a novel and systematic design methodology for offshore platform topside decks. The envisioned undertaking encompasses the incorporation of novel large-scale metal sandwich composites as deck components, which enables the overcoming of several limitations of the conventional design approach of such systems. Within this scope, this research work was originally oriented towards the establishment of a systematic high-fidelity (HF) nonlinear Finite Element (FE) modelling strategy, facilitating extensive numerical investigation of the novel sandwich composite and composite deck system response attributes, which had not been addressed at this scale in previous work. In the process of this development, the modelling limitations posed by the requirement of achieving FE mesh conformity in large-scale composite systems, comprising independent deformable components intersecting along a line, motivated the development of a novel approach for surface-to-surface coupling along a line, offering complete discretisation flexibility. In view of its broad application spectrum, substantial technical content and lack of previous work in this area, the developed coupling approach received significant attention throughout this research and became the centrepiece of the present thesis.

A summary of the main contributions of this research and the conclusions drawn from the individual chapters is provided hereafter.

### 8.1.1 HF partitioned modelling of composite and sandwich structures

The establishment of a sufficient level of confidence in the response predictions for large-scale metal honeycomb core sandwich composites is essential for the development of an all-steel sandwich panel system, as it represents a novel application for offshore topside decks. The extensive nonlinear response of such composites has not been investigated adequately in previous work, while the effects of the adopted manufacturing and laser welding processes on the composite response must be established and accounted for in the established design methodology. In this context, a HF nonlinear FE modelling strategy is proposed in this work, which provides an accurate and systematic approach for realistic modelling of large-scale composite structural systems.

The proposed approach is based on the employment of Reissner-Mindlin quadratic curved shell elements, the local formulation of which is underpinned by two principal aspects: (i) a co-rotational framework for the local element coordinate system definition, (Izzuddin & Liang, 2016); and (ii) a hierarchic optimisation approach that enables the relief of inaccuracies arising from shear, membrane and distortion locking phenomena, typically encountered in curved shell elements (Izzuddin & Liang, 2017).

The advanced features of the utilised shell elements allow for a strategy of enhanced accuracy and robustness to be established, which enables the accurate nonlinear response evaluation in the range of large displacements, taking due account of geometric and material nonlinearity effects. This is imperative in the modelling of large-scale metal composite structures, particularly of sandwich composites with discrete core topologies, due to the global system response and failure modes being sensitive to the progressive manifestation and interaction of various local instability forms over their domain. The efficiency of the proposed strategy in the modelling of large-scale metal sandwich composites with rectangular and hexagonal honeycomb core topologies is demonstrated in an application study presented in Section 7.2. The employment of the proposed strategy in conjunction with a high level of discretisation detail allows the effective modelling of the spread of plasticity over the domain, as well as of intercellular, compressive and shear local buckling over the panel faceplates and core, which substantially alter the nonlinear response of such composites.

The proposed HF modelling strategy has been successfully validated against experimental results, obtained from physical testing of the novel sandwich panels undertaken as part of the

INFLOAT project, which provides a high level of confidence in its accuracy for application to the modelling of all-steel sandwich panels within the project framework and beyond. Part of the experimental validation is illustrated in Section 7.5, for a set of 4-point bending tests.

The approach is further enhanced with the utilisation of recently developed domain partitioning capabilities, allowing for the effective overcoming of limitations arising from excessive computational demand in large-scale systems by exploiting parallel computing architectures. The incorporated partitioned modelling approach is based upon a novel dual super-element concept introduced by Jokhio and Izzuddin (2015), allowing for scalable parallel processing of individual partitions in High Performance Computing (HPC) systems with distributed memory. The adopted methodology enables a substantial reduction of computing wall-clock time and the overcoming of potential memory bottlenecks, without compromising the accuracy and convergence characteristics of the monolithic approach.

The studies undertaken in Section 7.3 show that the adopted partitioned modelling approach with a single hierarchic partitioning level leads to virtually 80% wall-clock time reduction when applied to large-scale sandwich composites, with the use of hierarchic partitioning (Jokhio, 2012; Jokhio & Izzuddin, 2015) potentially enhancing the efficiency of the approach further. Moreover, this work provides further guidance on the establishment of the optimal partitioning configuration which leads to maximum speedup for a given system, beyond which the efficiency of the method is compromised by excesses in both the nonlinear solution procedure and the communication overhead between parallel processors.

### **8.1.2 Surface coupling along a 1-D interface with non-conforming meshes**

A novel 1-D coupling element formulation is presented in this work, facilitating discrete constraint enforcement along a line between shell surfaces of arbitrary relative spatial orientation, which has not been addressed in computational mechanics research hitherto. The developed formulation provides a systematic framework for geometric modelling of weld lines, mesh tying of regions with different levels of discretisation detail or element types within a system, as well as domain partitioning problems involving computationally heterogeneous partitions.

The formulation adopts the fundamental principles of the mortar method (Puso, 2004; Fischer & Wriggers, 2005), thus inheriting its benefits in respect of the discretisation scheme convergence and stability. The principal features of the development are summarised hereafter:

- i. A master (mortar)/slave (non-mortar) surface classification.
- ii. An augmented Lagrangian Multiplier (LM) formulation for the constraint enforcement, with the independent LM field introduced along the interface projection on the slave surface.
- iii. A systematic algorithmic treatment for the 1-D interface projection discretisation into coupling elements, encompassing: (a) establishment of the active sets of coupled FEs and interface progressive segmentation on the two surfaces, based on the identification of its projection intersections with the FE domain boundaries on the respective meshes; (b) identification of a unique set of interacting segments on the two surfaces, on the basis of active Gauss Point (GP) projections from the slave to the master surface; and (c) establishment of a unique set of coupling elements contributing to the constraint enforcement, each comprising a slave and master FE surface and the associated interface segment projection on the slave surface.
- iv. An isoparametric framework for the approximation of the discrete geometry, as well as of the displacement and LM fields, within each distinct coupling element, with two variants allowing for linear and quadratic interpolation along its interface segment.
- v. A systematic Gaussian quadrature integration scheme at the element level, based on establishing a set of GPs along the interface segment and determining their projections from the slave to the master surface, with two variants facilitating element-based and segment-based integration (Farah *et al.*, 2015).
- vi. A consistent formulation for the coupling element force vector and tangent stiffness matrix, for any set of kinematic constraints.

The developed approach has several benefits on the modelling front, including: (i) discretisation flexibility in relation to the employed FE types and mesh parameters; (ii) overcoming of the modelling shortcomings associated with the requirements of mesh conformity; (iii) accuracy enhancement arising from the employment of component- or

domain-specific optimal discretisation strategies at a local level; and (iv) substantial reduction of the associated computational demands.

The developed coupling approach provides a unified discretisation strategy of enhanced computational efficiency, applicable to large-scale, geometrically complex, composite structural systems and beyond. While the developed approach has been applied with recently developed shell elements (Izzuddin & Liang, 2016; 2017) utilising ADAPTIC (Izzuddin, 1991), the underlying formulation has been developed for application to surface-to-surface coupling along a line for meshes consisting of any type of 2-D or 3-D finite elements.

### **8.1.3 1-D translational and rotational coupling element**

Within the scope of the established systematic methodology for surface coupling along a line, translational and rotational coupling element formulations are proposed in this work, applicable to surfaces discretised with quadratic Reissner-Mindlin curved shell elements. The developed formulations enable the fulfilment of translational and rotational compatibility conditions and the accurate transferring of internal forces along the coupling interface for independently discretised domains.

Both translational and rotational coupling formulations have been developed using energy variational principles, enabling the determination of the coupling element internal force vector and tangent stiffness matrix associated with the individual sets of constraints along the interface. The translational coupling constraints enforce surface displacement compatibility along the interface in all three global coordinate system axes directions, whereas rotational coupling is achieved by constraining the relative orientation of the coupled surface slopes transverse to the interface along its length. Contrary to the alternative of coupling the rotations of the surface normals along the interface, the adopted approach has the important computational benefit of enabling the coupling element formulation to be expressed purely in terms of the global translational Degrees of Freedom (DOFs) of the two surfaces, thus allowing rotational DOFs to be excluded. Notwithstanding the approximation embedded in the adopted approach for specific configurations, the discrepancies between the two methods become negligible for small-thickness plate/shell FE problems.

Considering the nature of the developed coupling element formulation, which is based on the approximation of the LM field rather than the displacement/strain fields, a set of rigid body and constant force/moment patch tests are established. These aim to verify the element ability of representing constant LM fields for different 1-D element patches, while satisfying interface compatibility conditions. The element has been shown to pass all specified patch tests with a maximum error in the LM field of less than 0.001% in its default modus operandi, where an element-based Gaussian quadrature integration scheme is adopted.

A series of sensitivity analyses has been further conducted to investigate the element performance sensitivity to a variety of parameters and algorithmic processes underpinning its formulation. The main conclusions drawn from these parametric investigations are summarised hereafter:

- i. The element performance is insensitive to the surface classification as master/slave.
- ii. The element performance is sensitive to the adopted Gaussian quadrature integration variant. The element-based variant achieves exact integration, while the segment-based is associated with a considerable error, particularly for quadratic LM and displacement field interpolations along the interface, even with the employment of a large number of GPs. This is attributed to the Gaussian quadrature integration scheme being incapable of exactly integrating piece-wise polynomial functions, arising in cases where the integration is performed over the entire coupling segment in non-matching meshes.
- iii. The element performance is insensitive to the selection of the penalty parameter for a wide range of values, with excessively large values, nonetheless, leading to ill-conditioning of the tangent stiffness matrix and convergence failure.
- iv. The element performance deteriorates in the case of rotational coupling of geometrically irregular shell FEs, which is reflected in the results of the constant moment patch tests. Nonetheless, monotonic convergence to the exact solution is achieved with mesh refinement, and hence the element passes the respective patch tests for irregular shell FE geometries. Accordingly, in large scale FE meshes with irregular element geometry, a sufficiently high discretisation level enables the accurate enforcement of rotational constraints.

#### 8.1.4 1-D coupling element verification studies

The ability of the developed coupling element to enforce effectively translational and rotational kinematic constraints along a 1-D interface, between independently discretised parallel or intersecting shell surfaces of arbitrary relative spatial orientation, is verified through a series of numerical studies. Consideration is given to planar, cylindrical and spherical shell surfaces, coupled along a straight or curved interface, and discretised with regular and irregular hierarchically optimised, co-rotational, Reissner-Mindlin curved shell FEs (Izzuddin & Liang, 2016; 2017).

The coupling element performance is assessed via the response comparison of models with non-matching meshes, where the 1-D coupling element is employed for the coupling of independently discretised regions, and the corresponding monolithic models. For each study, the comparative evaluation of the coupled and monolithic models is conducted on the basis of: (i) the deformed configuration, (ii) the nonlinear equilibrium path, and (iii) the internal distribution of characteristic generalised FE stress entities. The main conclusions drawn from the conducted series of verification studies, in respect of the element performance, are summarised hereafter:

- i. An accurate internal force distribution is achieved under constant membrane, bending, planar and transverse shear, as well as twisting stress states.
- ii. The obtained distribution is exact in the case of stress states solely mobilising translational LMs for the constraint enforcement.
- iii. The approximation embedded in the rotational coupling formulation, encompassing coupling of the transverse to the interface surface slopes, introduces discontinuities in the transverse moment and shear distributions in the coupling interface vicinity. These are attributed to the associated moment transferring mechanism, achieved via equivalent nodal force couples at the adjoining shell elements. The discontinuities reduce away from the interface, always allowing for global equilibrium to be satisfied, while mesh refinement enables these to be reduced to negligible local effects in the vicinity of coupling.
- iv. Minor deviations between the response of the coupled and monolithic models arise in the range of very large displacements. These are partially attributed to the



approximation embedded in the rotational coupling formulation, as well as to the employment of a relatively coarse mesh in the coupled model variants in some of the studies presented.

### **8.1.5 Application studies on high-fidelity modelling of composite structural systems**

A series of numerical studies focusing on offshore topside deck applications is conducted, with consideration being specifically given to large-scale metal sandwich composites employed as deck components, as well as to composite passive explosion protective barriers (blast walls). The main conclusions drawn from the conducted series of application studies are summarised hereafter:

- i. The employment of the proposed HF nonlinear FE modelling strategy with a high level of discretisation detail provides a highly accurate, robust and systematic approach for modelling the spread of plasticity and the interaction of the various local buckling phenomena in the range of large displacements. This is illustrated through a series of numerical studies on large-scale, metal, honeycomb core, sandwich composites. The capturing of such phenomena is essential in large-scale composite systems with distinct topological configurations, due to the substantial response sensitivity of such systems to local instabilities and imperfections.
- ii. The HF modelling strategy provides a reliable and systematic framework for realistic 3-D modelling of composite structural systems. The accuracy of the proposed HF modelling strategy is established by means of its successful validation against experimental results, obtained from physical testing of novel, metal, sandwich panel components as part of the INFLOAT project.
- iii. Dual super-element domain partitioning facilitates extensive HF nonlinear analyses of large-scale composite systems, achieving a substantial reduction in the associated wall-clock time and memory demands, while overcoming potential memory bottlenecks. Process parallelisation on HPC systems with distributed memory allows for a wall-clock time reduction of virtually 80% to be achieved for large-scale sandwich composites, in comparison with the respective monolithic HF models, when an optimal partitioning configuration is considered.

- iv. The efficiency of domain partitioning increases with an increasing discretisation level, and hence the approach has particular computational benefits when employed in the HF modelling of composite systems with a substantial mesh density,
- v. The optimal number of child partitions for a given system, leading to maximum speedup, is achieved for an equivalent distribution of DOFs in all partitions, under the assumption of idealised process parallelisation conditions. Beyond the optimal number of partitions, further domain partitioning leads to performance deterioration, due to excess in both the nonlinear solution procedure and the communication overhead between parallel processors.
- vi. The developed 1-D coupling element formulation substantially enhances the discretisation flexibility in geometrically complex composite systems, comprising independent deformable plate components coupled along a line, by enabling selective domain discretisation. This is demonstrated for large-scale metal sandwich composites subject to localised patch loading, where a dense mesh is only employed in regions of the domain associated with substantial stress variations. The selective discretisation approach enables the response of the corresponding HF monolithic model to be effectively approximated, while further leading to a substantial reduction in the employed number of FEs for domain discretisation.
- vii. The employment of the 1-D coupling element in conjunction with dual super-element domain partitioning leads to further computational benefits. For selectively-discretised large-scale sandwich composites, a sub-optimal partitioning configuration of equivalently-sized partitions, which is not associated with an equal distribution of DOFs over all partitions, allows for a 75% computing wall-clock time reduction to be achieved in comparison with the respective monolithic model. This, in turn, corresponds to an overall 85% reduction in relation to the monolithic model with a uniform conforming mesh, while further speedup can be achieved with an optimal partitioning configuration.
- viii. The developed 1-D coupling element enables the integrated modelling of geometrically complex composite systems, incorporating the contribution of a wide range of structural components in the response. Due to the modelling complexity and limitations associated with the establishment of a monolithic mesh in such cases,

industrial practice typically circumvents it by modelling only the structural components of interest, and accounting for the contribution of surrounding structural elements through appropriately introduced boundary conditions. In applications involving substantial hazard, such as the assessment or design of blast walls in ultimate conditions, an accurate response evaluation is required, accounting for the contribution of the surrounding structural elements. In this context, the employment of the HF modelling strategy and 1-D coupling element provides a systematic and reliable methodology for the realistic 3-D modelling of composite systems, enabling the capturing of effects that significantly alter the response and are neglected with the adoption of a simplified modelling approach.

## 8.2 Recommendations for future work

The proposed HF modelling strategy, alongside the developed 1-D coupling element, provide a systematic, reliable and versatile framework for realistic 3-D modelling of composite structures, whereas the additional incorporation of dual super-element domain partitioning renders the extensive nonlinear response evaluation of large-scale systems a realistic prospect. Notwithstanding these contributions, there is still scope for further improvement on both the coupling element and HF partitioned modelling fronts.

From the perspective of the developed 1-D coupling element formulation, potential extensions and enhancements include:

- i. Extension of the formulation to facilitate discrete contact constraint enforcement. The adaptation of the 3-D mortar method embedded in the element formulation, presented in Chapter 4, provides a systematic algorithmic treatment for the 1-D interface progressive segmentation and discretisation. The developed formulation, underpinned by the use of an augmented LM approach for the constraint enforcement, can be extended to incorporate contact kinematic constraints, expressed in the form of inequalities. Accordingly, the formulation would enable the establishment of a new contact interface in each iterative step of the nonlinear incremental solution procedure, conforming with the relative deformations of the two domains in contact. This process generally enables modelling of effects such as separation or slip between the

independent regions, which is important in the context of the following recommendation, as well as of potential contact interface expansion. Practical applications include the modelling of weld lines in problems involving parallel or intersecting surfaces with large relative deformations, where contact of the independent domains potentially occurs adjacent to the weld lines.

- ii. Investigation of alternative mathematical optimisation formulations for kinematic constraint enforcement. The employment of an augmented LM approach for the constraint enforcement in the context of the developed coupling element formulation achieves enhanced accuracy; nonetheless it introduces additional DOFs to the global system, associated with the independent LM field defined along the interface. Despite this being unimportant when coupling is over a relatively small part of the domain, in some large-scale application where several coupling interfaces are introduced the additional DOFs potentially increase the associated computational demand considerably. Notwithstanding the effectiveness of domain partitioning, the adoption of an approach that enables the condensation of the additional LM DOFs, such as dual LM interpolation spaces, or completely eliminates them, such as the Nitsche approach, could potentially prove beneficial. These approaches are associated with a variety of shortcomings, as discussed in Section 2.3, which require the implementation of algorithmic treatments to remedy various inaccuracies or sources of numerical instability. Nonetheless, a comparative evaluation of such formulations has not been performed in this work and could potentially prove efficient for particular classes of problems. In this context, the element implementation in FE programs could allow for selection between a range of adopted constraint enforcement formulations.
- iii. Incorporation of cross-sectional deformation and eccentricity effects in the coupling element formulation. As discussed in Section 4.3, due to the developed coupling element formulations primarily dealing with thin plates and shells, a principal embedded assumption is the constraint enforcement at the shell surface mid-plane, thus ignoring cross-sectional deformation and eccentricity over the shell thickness. The incorporation of these effects in the developed formulation will lead to enhanced accuracy in its present form, while, most importantly, enabling its employment for the coupling of moderately thick shells, which is not considered in the present work.

- iv. Incorporation of nonlinear interface constitutive model for weld material along the coupling interface. The developed coupling formulation utilises a purely geometric definition of the coupling constraints as non-penetration conditions, and hence the LM field along the interface is obtained on the basis of enforcing compatibility between the coupled surfaces. The introduction of a nonlinear constitutive model for the weld material along the interface will enable the capturing of weld fracture in the coupled system response. Practical applications include problems where potential weld delamination must be accounted for, such as in the late response stages of the 4-point bending tests conducted in the context of the INFLOAT project and presented in Section 7.5.
- v. Expansion of the coupling element formulation to iso-geometric elements. In view of recent developments in the field of computational contact mechanics, extending beyond conventional FE procedures (De Lorenzis *et al.*, 2012; Florez & Wheeler, 2016), potential extensions include the formulation incorporation in iso-geometric analysis. The benefit of such approaches is the smooth surface description, for example using NURBS, which enables inaccuracies or stiffening effects due to the mesh non-conformity along the interface to be overcome.

With regards to the HF partitioned discretisation strategy that has been implemented using MATLAB, potential extensions and enhancements include:

- i. Utilisation of hierarchic domain partitioning capabilities in the HF modelling approach for all-metal sandwich composites. The current work adopts a single level of partitioning, even though the previously developed approach (Jokhio, 2012; Jokhio & Izzuddin, 2015) allows hierarchic partitioning to any number of levels. Notwithstanding the efficiency and substantial wall-clock time speedup achieved with single-level partitioning, hierarchic partitioning to further levels could potentially lead to enhanced speedup, subject to an appropriate selection of the partitioning scheme.
- ii. Establishment of a systematic domain partitioning framework to incorporate the developed coupling element. In Section 7.4, the computational benefits of domain partitioning in cases where the coupling element is employed for selective domain discretisation are demonstrated considering a sub-optimal partitioning configuration, as well as discontinuous LM fields at the partitioned boundary. The enhancement of

the HF partitioned modelling strategy to allow for continuity of the LM field at the partitioned boundary enables the surplus additional DOFs, associated with collocation point multiplicity, to be eliminated. Accordingly, consistency with the monolithic approach can be achieved, with the additional benefit of reducing the number of additional DOFs. Moreover, the potential extension of the discretisation approach to allow for coupling element introduction at the parent level would enable more flexible independent discretisation of different child partitions. Finally, the approach would greatly benefit from the establishment of a systematic methodology for identifying the optimal partitioning configuration in such cases, corresponding to equal DOF distribution over the various partition processes, along the lines of the qualitative guidance provided in Section 7.3.

## Bibliography

- Abramowitz, M. & Stegun, I. (1964) *Handbook of Mathematical Functions with Formulas, Graphs, and Mathematical Tables (Applied Mathematics Series 55)*. Washington, DC, National Bureau of Standards.
- Allen, H. G. (1969) *Analysis and design of structural sandwich panels*. Oxford, Pergamon.
- Andrews, E. & Moussa, N. (2009) Failure mode maps for composite sandwich panels subjected to air blast loading. *International Journal of Impact Engineering*. 36 (3), 418-425.
- Bathe, K. (1996) *Finite element procedures*. London, Prentice Hall.
- Bathe, K. (2001) The inf-sup condition and its evaluation for mixed finite element methods. *Computers & Structures*. 79 (2), 243-252.
- Bathe, K. & Chaudhary, A. (1985) A solution method for planar and axisymmetric contact problems. *International Journal for Numerical Methods in Engineering*. 21 (1), 65-88.
- Becker, R., Hansbo, P. & Stenberg, R. (2003) A finite element method for domain decomposition with non-matching grids. *ESAIM: Mathematical Modelling and Numerical Analysis*. 37 (2), 209-225.
- Belgacem, F. B. (1999) The mortar finite element method with Lagrange multipliers. *Numerische Mathematik*. 84 (2), 173-197.
- Belgacem, F. B., Hild, P. & Laborde, P. (1998) The mortar finite element method for contact problems. *Mathematical and Computer Modelling*. 28 (4), 263-272.
- Belgacem, F. B. & Maday, Y. (1997) The mortar element method for three dimensional finite elements. *ESAIM: Mathematical Modelling and Numerical Analysis*. 31 (2), 289-302.
- Berggren, S. A., Lukkassen, D., Meidell, A. & Simula, L. (2001) On stiffness properties of square honeycombs and other unidirectional composites. *Composites Part B: Engineering*. 32 (6), 503-511.
- Berggren, S. A., Lukkassen, D., Meidell, A. & Simula, L. (2003) Some Methods for Calculating Stiffness Properties of Periodic Structures. *Applications of Mathematics*. 48 (2), 97-110.
- Bernardi, C., Debit, N. & Maday, Y. (1990) Coupling finite element and spectral methods: First results. *Mathematics of Computation*. 54 (189), 21-39.
- Bernardi C., Maday Y. & Patera A.T. (1993) Domain Decomposition by the Mortar Element Method. In: Kaper H.G., Garbey M. & Pieper G.W. (eds) *Asymptotic and Numerical Methods for Partial Differential Equations with Critical Parameters*. NATO ASI Series (Series C: Mathematical and Physical Sciences), vol 384. Dordrecht, Springer.

- Bertsekas, D. P. (1982) *Constrained optimization and Lagrange multiplier methods*. New York, Academic Press.
- Brezzi, F. & Bathe, K. (1990) A discourse on the stability conditions for mixed finite element formulations. *Computer Methods in Applied Mechanics and Engineering*. 82 (1-3), 27-57.
- Brezzi, F. & Fortin, M. (1991) *Mixed and hybrid finite element methods*. New York, Springer-Verlag.
- British Standards Institution. (2005) BS EN 1993-1-1: 2005 A1: 2014. *Eurocode 3: Design of steel structures - General rules and rules for buildings*. London, British Standards Institution.
- British Standards Institution. (2014) BS EN ISO 19901-3:2014. *Petroleum and natural gas industries - Specific requirements for offshore structures Part 3: Topsides structure*. London, British Standards Institution.
- Carrera, E. (1998) Evaluation of layerwise mixed theories for laminated plates analysis. *AIAA Journal*. 36 (5), 830-839.
- Cavaleri, F. J. & Cardona, A. (2013) An augmented Lagrangian technique combined with a mortar algorithm for modelling mechanical contact problems. *International Journal for Numerical Methods in Engineering*. 93 (4), 420-442.
- Correia, J. R. & Garrido, M. (2018) Composite sandwich panels for building floors: recent developments and main challenges. In: Keller, T., Yanes Armas, S., Carlsson, L. A. & Frostig, Y. (eds.) *12th International Conference on Sandwich Structures ICSS-12: Proceedings, ICSS-12, 19-22 August 2018, Lausanne, Switzerland*. Lausanne, EPFL-CCLab Composite Construction Laboratory. pp.3-5.
- Cote, F., Deshpande, V. & Fleck, N. (2006) The shear response of metallic square honeycombs. *Journal of Mechanics of Materials and Structures*. 1 (7), 1281-1299.
- Cote, F., Deshpande, V., Fleck, N. & Evans, A. (2004) The out-of-plane compressive behavior of metallic honeycombs. *Materials Science and Engineering: A*. 380 (1-2), 272-280.
- Cowper, G. R. & Symonds, P. S. (1957) *Strain-Hardening and Strain-Rate Effects in the Impact Loading of Cantilever Beams*. Brown University Division of Applied Mathematics. Report number: TR-C11-28.
- Crisfield, M. (2000) Re-visiting the contact patch test. *International Journal for Numerical Methods in Engineering*. 48 (3), 435-449.
- Crupi, V., Epasto, G. & Guglielmino, E. (2012) Collapse modes in aluminium honeycomb sandwich panels under bending and impact loading. *International Journal of Impact Engineering*. 43, 6-15.
- De Lorenzis, L., Wriggers, P. & Zavarise, G. (2012) A mortar formulation for 3D large deformation contact using NURBS-based isogeometric analysis and the augmented Lagrangian method. *Computational Mechanics*. 49 (1), 1-20.



- Det Norske Veritas. (2010) DNV-RP-C204. *Design against accidental loads*. Norway, Det Norske Veritas.
- Det Norske Veritas. (2013) DNV-RP-C208. *Determination of Structural Capacity by Non-Linear FE Analysis Methods*. Norway, Det Norske Veritas
- Dharmasena, K. P., Wadley, H. N., Xue, Z. & Hutchinson, J. W. (2008) Mechanical response of metallic honeycomb sandwich panel structures to high-intensity dynamic loading. *International Journal of Impact Engineering*. 35 (9), 1063-1074.
- Dias, A., Serpa, A. & Bittencourt, M. (2015) High-order mortar-based element applied to nonlinear analysis of structural contact mechanics. *Computer Methods in Applied Mechanics and Engineering*. 294, 19-55.
- Dohrmann, C., Key, S. & Heinstein, M. (2000) A method for connecting dissimilar finite element meshes in two dimensions. *International Journal for Numerical Methods in Engineering*. 48 (5), 655-678.
- El-Abbasi, N. & Bathe, K. (2001) Stability and patch test performance of contact discretizations and a new solution algorithm. *Computers & Structures*. 79 (16), 1473-1486.
- ESDEP [The European Steel Design Education Program]. (2009) *Lecture Series, Offshore Structures, Lecture 15A.10*. Available from: <http://fgg-web.fgg.uni-lj.si/~pmoze/ESDEP/master/wg15a/11000.htm> [Accessed 2<sup>nd</sup> February 2019]
- Farah, P., Popp, A. & Wall, W. A. (2015) Segment-based vs. element-based integration for mortar methods in computational contact mechanics. *Computational Mechanics*. 55 (1), 209-228.
- Farah, P., Wall, W. & Popp, A. (2018) A mortar finite element approach for point, line, and surface contact. *International Journal for Numerical Methods in Engineering*. 114 (3), 255-291.
- Fischer, K. & Wriggers, P. (2005) Frictionless 2D contact formulations for finite deformations based on the mortar method. *Computational Mechanics*. 36 (3), 226-244.
- Flemisch, B., Puso, M. & Wohlmuth, B. (2005) A new dual mortar method for curved interfaces: 2D elasticity. *International Journal for Numerical Methods in Engineering*. 63 (6), 813-832.
- Flemisch, B. & Wohlmuth, B. I. (2007) Stable Lagrange multipliers for quadrilateral meshes of curved interfaces in 3D. *Computer Methods in Applied Mechanics and Engineering*. 196 (8), 1589-1602.
- Fletcher, R. (2000) *Practical methods of optimization*. 2nd edition. Chichester, Wiley.
- Florez, H. & Wheeler, M. F. (2016) A mortar method based on NURBS for curved interfaces. *Computer Methods in Applied Mechanics and Engineering*. 310, 535-566.

- FrancaVilla, A. & Zienkiewicz, O. (1975) A note on numerical computation of elastic contact problems. *International Journal for Numerical Methods in Engineering*. 9 (4), 913-924.
- Galletti, G. G., Vinqvist, C. & Es-Said, O. S. (2008) Theoretical design and analysis of a honeycomb panel sandwich structure loaded in pure bending. *Engineering Failure Analysis*. 15 (5), 555-562.
- Gibson, L. J. & Ashby, M. F. (1999) *Cellular solids: structure and properties*. 2nd ed. Cambridge, Cambridge University Press
- Grediac, M. (1993) A finite element study of the transverse shear in honeycomb cores. *International Journal of Solids and Structures*. 30 (13), 1777-1788.
- Hallquist, J., Goudreau, G. & Benson, D. (1985) Sliding interfaces with contact-impact in large-scale Lagrangian computations. *Computer Methods in Applied Mechanics and Engineering*. 51 (1-3), 107-137.
- Holt, P. & Webber, J. (1982) Exact solutions to some honeycomb sandwich beam, plate, and shell problems. *The Journal of Strain Analysis for Engineering Design*. 17 (1), 1-8.
- Hughes, T. J., Taylor, R. L., Sackman, J. L., Curnier, A. & Kanoknukulchai, W. (1976) A finite element method for a class of contact-impact problems. *Computer Methods in Applied Mechanics and Engineering*. 8 (3), 249-276.
- Irons, B. M. (1970) A frontal solution program for finite element analysis. *International Journal for Numerical Methods in Engineering*. 2 (1), 5-32.
- Izzuddin, B. A. (1991) *Nonlinear dynamic analysis of framed structures*. Ph.D. Thesis. Imperial College London, University of London.
- Izzuddin, B. A. (2005) An enhanced co-rotational approach for large displacement analysis of plates. *International Journal for Numerical Methods in Engineering*. 64 (10), 1350-1374.
- Izzuddin, B. (2006) Simplified buckling analysis of skeletal structures. *Proceedings of the Institution of Civil Engineers-Structures and Buildings*. 159 (4), 217-228.
- Izzuddin, B. A. (2007) Rotational spring analogy for buckling analysis. *Journal of Structural Engineering*. 133 (5), 739-751.
- Izzuddin, B. A. & Liang, Y. (2016) Bisector and zero-macrospin co-rotational systems for shell elements. *International Journal for Numerical Methods in Engineering*. 105 (4), 286-320.
- Izzuddin, B. A. & Liang, Y. (2017) A hierarchic optimisation approach towards locking-free shell finite elements. *Computers & Structures*. Available from: <http://dx.doi.org/10.1016/j.compstruc.2017.08.010>.
- Jelovica, J., Romanoff, J., Ehlers, S. & Varsta, P. (2012) Influence of weld stiffness on buckling strength of laser-welded web-core sandwich plates. *Journal of Constructional Steel Research*. 77, 12-18.

- Jelovica, J., Romanoff, J. & Remes, H. (2014) Influence of general corrosion on buckling strength of laser-welded web-core sandwich plates. *Journal of Constructional Steel Research*. 101, 342-350.
- Jeyakrishnan, P. R., Chockalingam, K. K. S. K. & Narayanasamy, R. (2012) Studies on buckling behavior of honeycomb sandwich panel. *The International Journal of Advanced Manufacturing Technology*. 65 (5-8), 803-815.
- Jokhio, G. A. (2012) *Mixed Dimensional Hierarchic Partitioned Analysis of Nonlinear Structural Systems*. Ph.D. Thesis. Imperial College London.
- Jokhio, G. A. & Izzuddin, B. A. (2015) A Dual Super-Element Domain Decomposition Approach for Parallel Nonlinear Finite Element Analysis. *International Journal for Computational Methods in Engineering Science and Mechanics*. 16 (3), 188-212.
- Kaman, M. O., Solmaz, M. Y. & Turan, K. (2010) Experimental and Numerical Analysis of Critical Buckling Load of Honeycomb Sandwich Panels. *Journal of composite materials*. 44 (24), 2819-2831.
- Karagiozova, D., Nurick, G. & Langdon, G. (2009) Behaviour of sandwich panels subject to intense air blasts–Part 2: Numerical simulation. *Composite Structures*. 91 (4), 442-450.
- Kee Paik, J., Thayamballi, A. K. & Sung Kim, G. (1999) The strength characteristics of aluminium honeycomb sandwich panels. *Thin-Walled Structures*. 35 (3), 205-231.
- Kikuchi, N. & Oden, J. T. (1988) *Contact problems in elasticity: a study of variational inequalities and finite element methods*. Philadelphia, PA, SIAM.
- Kim, J. & Youn, S. (2012) Isogeometric contact analysis using mortar method. *International Journal for Numerical Methods in Engineering*. 89 (12), 1559-1581.
- Kolsters, H. & Zenkert, D. (2006a) Buckling of laser-welded sandwich panels. Part 1: Elastic buckling parallel to the webs. *Proceedings of the Institution of Mechanical Engineers, Part M: Journal of Engineering for the Maritime Environment*. 220 (2), 67-79.
- Kolsters, H. & Zenkert, D. (2006b) Buckling of laser-welded sandwich panels. Part 2: elastic buckling normal to the webs. *Proceedings of the Institution of Mechanical Engineers, Part M: Journal of Engineering for the Maritime Environment*. 220 (2), 81-94.
- Kolsters, H. & Zenkert, D. (2010) Buckling of laser-welded sandwich panels: ultimate strength and experiments. *Proceedings of the Institution of Mechanical Engineers, Part M: Journal of Engineering for the Maritime Environment*. 224 (1), 29-45.
- Landers, J. A. & Taylor, R. L. (1986) *An Augmented Lagrangian Formulation for the Finite Element Solution of Contact Problems*. Naval Civil Engineering Laboratory Port Hueneme CA. NCEL Contract Report.
- Laursen, T. & Heinstein, M. (2003) Consistent mesh tying methods for topologically distinct discretized surfaces in non-linear solid mechanics. *International Journal for Numerical Methods in Engineering*. 57 (9), 1197-1242.

- Laursen, T., Puso, M. A. & Sanders, J. (2012) Mortar contact formulations for deformable–deformable contact: past contributions and new extensions for enriched and embedded interface formulations. *Computer Methods in Applied Mechanics and Engineering*. 205, 3-15.
- Laursen, T. & Simo, J. (1993a) Algorithmic symmetrization of Coulomb frictional problems using augmented Lagrangians. *Computer Methods in Applied Mechanics and Engineering*. 108 (1-2), 133-146.
- Laursen, T. & Simo, J. (1993b) A continuum-based finite element formulation for the implicit solution of multibody, large deformation-frictional contact problems. *International Journal for Numerical Methods in Engineering*. 36 (20), 3451-3485.
- Liang, S. & Chen, H. L. (2006) Investigation on the square cell honeycomb structures under axial loading. *Composite structures*. 72 (4), 446-454.
- Liang, Y. & Izzuddin, B. A. (2016) Large displacement analysis of sandwich plates and shells with symmetric/asymmetric lamination. *Computers & Structures*. 166, 11-32.
- López Jiménez, F. & Triantafyllidis, N. (2013) Buckling of rectangular and hexagonal honeycomb under combined axial compression and transverse shear. *International Journal of Solids and Structures*. 50 (24), 3934-3946.
- Luenberger, D. G. & Ye, Y. (2008) *Linear and nonlinear programming*. 3<sup>rd</sup> ed. New York, Springer.
- Maplesoft (2016) *Maple* (Release 2016.2) [software] Waterloo Maple Inc.
- Masters, I. G. & Evans, K. E. (1996) Models for the elastic deformation of honeycombs. *Composite Structures*. 35 (4), 403-422.
- MathWorks Inc. (2017) *MATLAB* (Release 2017b) [software] The MathWorks Inc.
- McDevitt, T. & Laursen, T. (2000) A mortar-finite element formulation for frictional contact problems. *International Journal for Numerical Methods in Engineering*. 48 (10), 1525-1547.
- Minga, E., Macorini, L. & Izzuddin, B. A. (2018) Enhanced mesoscale partitioned modelling of heterogeneous masonry structures. *International Journal for Numerical Methods in Engineering*. 113 (13), 1950-1971.
- Morcous, G., Cho, Y., El-Safty, A. & Chen, G. (2010) Structural behavior of FRP sandwich panels for bridge decks. *KSCCE Journal of Civil Engineering*. 14 (6), 879-888.
- Newmark, N. M. (1959) A method of computation for structural dynamics. *Journal of the Engineering Mechanics Division*. 85 (3), 67-94.
- Nilsson, P. (2017) Laser-welded corrugated core steel sandwich panels for bridge application. Thesis for the Degree of Licentiate of Engineering. Chalmers University of Technology

- Nitsche, J. (1971) Über ein Variationsprinzip zur Lösung von Dirichlet-Problemen bei Verwendung von Teilräumen, die keinen Randbedingungen unterworfen sind. *Abhandlungen aus dem mathematischen Seminar der Universität Hamburg*. 36 (1), 9-15.
- Nurick, G., Langdon, G., Chi, Y. & Jacob, N. (2009) Behaviour of sandwich panels subjected to intense air blast—Part 1: Experiments. *Composite Structures*. 91 (4), 433-441.
- Pantelides, C. P., Surapaneni, R. & Reaveley, L. D. (2008) Structural performance of hybrid GFRP/steel concrete sandwich panels. *Journal of Composites for Construction*. 12 (5), 570-576.
- Papadopoulos, P. & Taylor, R. L. (1992) A mixed formulation for the finite element solution of contact problems. *Computer Methods in Applied Mechanics and Engineering*. 94 (3), 373-389.
- Parisch, H. (1989) A consistent tangent stiffness matrix for three-dimensional non-linear contact analysis. *International Journal for Numerical Methods in Engineering*. 28 (8), 1803-1812.
- Parisch, H. & Lübbing, C. (1997) A formulation of arbitrarily shaped surface elements for three-dimensional large deformation contact with friction. *International Journal for Numerical Methods in Engineering*. 40 (18), 3359-3383.
- Perić, D. & Owen, D. (1992) Computational model for 3-D contact problems with friction based on the penalty method. *International Journal for Numerical Methods in Engineering*. 35 (6), 1289-1309.
- Petras, A. (1999) *Design of sandwich structures*. Ph.D. thesis. University of Cambridge.
- Petras, A. & Sutcliffe, M. (1999) Failure mode maps for honeycomb sandwich panels. *Composite Structures*. 44 (4), 237-252.
- Plantema, F. J. (1966) *Sandwich construction*. Wiley, New York.
- Popp, A., Seitz, A., Gee, M. W. & Wall, W. A. (2013) Improved robustness and consistency of 3D contact algorithms based on a dual mortar approach. *Computer Methods in Applied Mechanics and Engineering*. 264, 67-80.
- Popp, A., Wohlmuth, B. I., Gee, M. W. & Wall, W. A. (2012) Dual quadratic mortar finite element methods for 3D finite deformation contact. *SIAM Journal on Scientific Computing*. 34 (4), B421-B446.
- Puso, M. A. (2004) A 3D mortar method for solid mechanics. *International Journal for Numerical Methods in Engineering*. 59 (3), 315-336.
- Puso, M. A. & Laursen, T. A. (2003) Mesh tying on curved interfaces in 3D. *Engineering Computations*. 20 (3), 305-319.

- Puso, M. A. & Laursen, T. A. (2004a) A mortar segment-to-segment contact method for large deformation solid mechanics. *Computer Methods in Applied Mechanics and Engineering*. 193 (6-8), 601-629.
- Puso, M. A. & Laursen, T. A. (2004b) A mortar segment-to-segment frictional contact method for large deformations. *Computer Methods in Applied Mechanics and Engineering*. 193 (45-47), 4891-4913.
- Puso, M. A., Laursen, T. & Solberg, J. (2008) A segment-to-segment mortar contact method for quadratic elements and large deformations. *Computer Methods in Applied Mechanics and Engineering*. 197 (6-8), 555-566.
- Rebel, G., Park, K. & Felippa, C. (2002) A contact formulation based on localized Lagrange multipliers: formulation and application to two-dimensional problems. *International Journal for Numerical Methods in Engineering*. 54 (2), 263-297.
- Robbins Jr, D. & Reddy, J. (1993) Modelling of thick composites using a layerwise laminate theory. *International Journal for Numerical Methods in Engineering*. 36 (4), 655-677.
- Romanoff, J. (2011) Interaction between laser-welded web-core sandwich deck plate and girder under bending loads. *Thin-Walled Structures*. 49 (6), 772-781.
- Romanoff, J. & Varsta, P. (2006) Bending response of web-core sandwich beams. *Composite Structures*. 73 (4), 478-487.
- Romanoff, J. & Varsta, P. (2007) Bending response of web-core sandwich plates. *Composite Structures*. 81 (2), 292-302.
- Romanoff, J., Varsta, P. & Klanac, A. (2007a) Stress analysis of homogenized web-core sandwich beams. *Composite Structures*. 79 (3), 411-422.
- Romanoff, J., Varsta, P. & Remes, H. (2007b) Laser-welded web-core sandwich plates under patch loading. *Marine Structures*. 20 (1-2), 25-48.
- Santos, L., Nordas, A. N., Izzuddin, B. A. & Macorini, L. (2018) Mechanical models for local buckling of metal sandwich panels. *Proceedings of the Institution of Civil Engineers - Engineering and Computational Mechanics*. 171 (2), 65-78.
- Seitz, A., Farah, P., Kremheller, J., Wohlmuth, B. I., Wall, W. A. & Popp, A. (2016) Isogeometric dual mortar methods for computational contact mechanics. *Computer Methods in Applied Mechanics and Engineering*. 301, 259-280.
- Simo, J. C. & Laursen, T. (1992) An augmented Lagrangian treatment of contact problems involving friction. *Computers & Structures*. 42 (1), 97-116.
- Simo, J. C., Wriggers, P. & Taylor, R. L. (1985) A perturbed Lagrangian formulation for the finite element solution of contact problems. *Computer Methods in Applied Mechanics and Engineering*. 50 (2), 163-180.

- Song, Y., Youn, S. & Park, K. (2015) A gap element for treating non-matching discrete interfaces. *Computational Mechanics*. 56 (3), 551-563.
- Stadter, J. & Weiss, R. (1979) Analysis of contact through finite element gaps. *Computers & Structures*. 10 (6), 867-873.
- Taczała, M. & Banasiak, W. (2004) Buckling of I-core sandwich panels. *Journal of Theoretical and Applied Mechanics*. 42 (2), 335-348.
- Taylor, R. L. & Papadopoulos, P. (1991) On a patch test for contact problems in two dimensions. In: Wriggers, P. & Wagner W. (eds.) *Nonlinear Computational Mechanics*. Berlin, Springer-Verlag, pp. 690-702.
- Tur, M., Fuenmayor, F. & Wriggers, P. (2009) A mortar-based frictional contact formulation for large deformations using Lagrange multipliers. *Computer Methods in Applied Mechanics and Engineering*. 198 (37-40), 2860-2873.
- TWI - The Welding Institute. (2019a) *Laser Welding*. Available from: <https://www.twi-global.com/what-we-do/research-and-technology/technologies/welding-joining-and-cutting/lasers/laser-welding> [Accessed 16/02/2019].
- TWI - The Welding Institute. (2019b) *Trends in welding processes in engineering construction for infrastructure projects*. Available from: <https://www.twi-global.com/technical-knowledge/published-papers/trends-in-welding-processes-in-engineering-construction-for-infrastructure-projects-july-2003> [Accessed 19/02/2019].
- Wadley, H. N. (2005) Multifunctional periodic cellular metals. *Philosophical Transactions of the Royal Society A: Mathematical, Physical and Engineering Sciences*. 364 (1838), 31-68.
- Wadley, H. N., Fleck, N. A. & Evans, A. G. (2003) Fabrication and structural performance of periodic cellular metal sandwich structures. *Composites Science and Technology*. 63 (16), 2331-2343.
- Williams, F. A. (1985) *Combustion theory: the fundamental theory of chemically reacting flow systems*. 2nd ed. Boca Raton, FL, CRC Press.
- Wohlmuth, B. I. (2000) A mortar finite element method using dual spaces for the Lagrange multiplier. *SIAM Journal on Numerical Analysis*. 38 (3), 989-1012.
- Wriggers, P. (2006) *Computational contact mechanics*. Berlin, Springer.
- Wriggers, P. & Simo, J. (1985) A note on tangent stiffness for fully nonlinear contact problems. *Communications in Applied Numerical Methods*. 1 (5), 199-203.
- Wriggers, P., Van, T. V. & Stein, E. (1990) Finite element formulation of large deformation impact-contact problems with friction. *Computers & Structures*. 37 (3), 319-331.
- Wriggers, P. & Zavarise, G. (1993) Application of augmented Lagrangian techniques for non-linear constitutive laws in contact interfaces. *Communications in Numerical Methods in Engineering*. 9 (10), 815-824.

- Wriggers, P. & Zavarise, G. (2008) A formulation for frictionless contact problems using a weak form introduced by Nitsche. *Computational Mechanics*. 41 (3), 407-420.
- Zavarise, G. & De Lorenzis, L. (2009a) A modified node-to-segment algorithm passing the contact patch test. *International Journal for Numerical Methods in Engineering*. 79 (4), 379-416.
- Zavarise, G. & De Lorenzis, L. (2009b) The node-to-segment algorithm for 2D frictionless contact: classical formulation and special cases. *Computer Methods in Applied Mechanics and Engineering*. 198 (41-44), 3428-3451.
- Zavarise, G. & Wriggers, P. (1999) A superlinear convergent augmented Lagrangian procedure for contact problems. *Engineering Computations*. 16 (1), 88-119.
- Zeldovich, I., Barenblatt, G. I., Librovich, V. & Makhviladze, G. (1985) *Mathematical theory of combustion and explosions*. New York, Consultants Bureau.
- Zenkert, D. (1995) *An introduction to sandwich construction*. West Midlands, Warley: Engineering Materials Advisory Services Ltd.
- Zenkert, D. (1997) *The handbook of sandwich construction*. West Midlands, Warley: Engineering Materials Advisory Services Ltd.
- Zhang, J. & Ashby, M. (1992) The out-of-plane properties of honeycombs. *International Journal of Mechanical Sciences*. 34 (6), 475-489.
- Zhu, F., Zhao, L., Lu, G. & Wang, Z. (2008) Deformation and failure of blast-loaded metallic sandwich panels-Experimental investigations. *International Journal of Impact Engineering*. 35 (8), 937-951.
- Zhu, F., Zhao, L., Lu, G. & Gad, E. (2009) A numerical simulation of the blast impact of square metallic sandwich panels. *International Journal of Impact Engineering*. 36 (5), 687-699.
- Zienkiewicz, O. C. & Taylor, R. L. (1977) *The finite element method*. London, McGraw-Hill.
- Zok, F. W., Rathbun, H., He, M., Ferri, E., Mercer, C., McMeeking, R. M. & Evans, A. G. (2005) Structural performance of metallic sandwich panels with square honeycomb cores. *Philosophical Magazine*. 85 (26-27), 3207-3234.